Modern applications of machine learning in quantum sciences

Anna Dawid[1,2*], Julian Arnold[3†], Borja Requena[2†], Alexander Gresch[4†], Marcin Płodzień[2], Kaelan Donatella[5], Kim Nicoli[6,7], Paolo Stornati[2], Rouven Koch[8], Miriam Büttner[9], Robert Okuła[10], Gorka Muñoz–Gil[11], Rodrigo A. Vargas–Hernández[12,13], Alba Cervera-Lierta[14], Juan Carrasquilla[13], Vedran Dunjko[15], Marylou Gabrié[16,17], Patrick Huembeli[18,19], Evert van Nieuwenburg[20], Filippo Vicentini[18], Lei Wang[21,22], Sebastian J. Wetzel[23], Giuseppe Carleo[18], Eliška Greplová[24], Roman Krems[25], Florian Marquardt[26,27], Michał Tomza[1], Maciej Lewenstein[2,28] and Alexandre Dauphin[2*]

1 Faculty of Physics, University of Warsaw, Poland
2 ICFO - Institut de Ciències Fotòniques, The Barcelona Institute of Science and Technology, 08860 Castelldefels (Barcelona), Spain
3 Department of Physics, University of Basel, Switzerland
4 Quantum Technology Research Group, Heinrich-Heine-Universität Düsseldorf, Germany
5 Université de Paris, CNRS, Laboratoire Matériaux et Phénomènes Quantiques, France
6 Machine Learning Group, Technische Universität Berlin, Germany
7 BIFOLD, Berlin Institute for the Foundations of Learning and Data, 10587 Berlin, Germany
8 Department of Applied Physics, Aalto University, Espoo, Finland
9 Institute of Physics, Albert-Ludwig University of Freiburg, Germany
10 International Centre for Theory of Quantum Technologies, University of Gdańsk, Poland
11 Institute for Theoretical Physics, University of Innsbruck, Austria
12 Department of Chemistry, University of Toronto, Canada
13 Vector Institute for Artificial Intelligence, MaRS Centre, Toronto, Canada
14 Barcelona Supercomputing Center, Spain
15 LIACS, Leiden University, The Netherlands
16 CMAP, École Polytechnique, France
18 Institute of Physics, École Polytechnique Fédérale de Lausanne (EPFL), Switzerland
19 Menten AI, Inc., Palo Alto, California, United States of America
20 Niels Bohr International Academy, Copenhagen, Denmark
21 Beijing National Lab for Condensed Matter Physics and Institute of Physics, Chinese Academy of Sciences, Beijing, China
22 Songshan Lake Materials Laboratory, Dongguan, China
23 Perimeter Institute for Theoretical Physics, Waterloo, Canada
24 Kavli Institute of Nanoscience, Delft University of Technology, NL-2600 GA Delft, The Netherlands
25 Department of Chemistry, University of British Columbia, Vancouver, Canada
26 Max Planck Institute for the Science of Light, Erlangen, Germany
27 Department of Physics, Friedrich-Alexander Universität Erlangen-Nürnberg, Germany
28 ICREA, Pg. Lluís Companys 23, 08010 Barcelona, Spain
† These authors contributed equally.

* Anna.Dawid@fuw.edu.pl, Alexandre.Dauphin@icfo.eu

April 8, 2022

Abstract

In these Lecture Notes, we provide a comprehensive introduction to the most recent advances in the application of machine learning methods in quantum sciences. We cover the use of deep learning and kernel methods in supervised, unsupervised, and reinforcement learning algorithms for phase classification, representation of many-body quantum states, quantum feedback control, and quantum circuits optimization. Moreover, we introduce and discuss more specialized topics such as differentiable programming, generative models, statistical approach to machine learning, and quantum machine learning.

In memory of Peter Wittek

Contents

1   Introduction

Making *intelligent* machines, i.e., machines capable of learning and utilizing gathered knowledge in thinking and reasoning, is a long-lived dream of human civilization. The more we know about the human brain, intelligence, and psychology, the more challenging it seems. However, despite the many obstacles and challenges in creating proper artificial intelligence (AI), the joint effort of researchers working in natural, cognitive, mathematical, and computer sciences has produced impressive machinery that is already revolutionizing our everyday life, industry, and science.

1.1   How to make computers learn?

The ultimate goal of AI is to endow machines with the ability to conceptualize and create abstractions. Both of these features are mechanisms that underlie learning representations of knowledge and reasoning based on experience in humans. We have multiple ways to represent ideas. For instance, we can encode a piece of music in digital format on a computer, in analog format on a vinyl disc, or we can write it down in a music score. While the representations have entirely different natures, the piece of music is the same. Hence, the properties of abstract ideas do not depend on the data source.

Furthermore, conceptualization and abstraction bring the possibility to consider various levels of details within a particular representation or the capability to switch from one level to another while preserving the relevant information [1–5]. Our brain excels at extracting abstract ideas from different knowledge representations. In our daily lives, we constantly process information from multiple sources that represent the same concept in completely different ways. For example, we can identify the concept of a dog by seeing one, hearing or smelling it, reading the word "dog", painting a snout on someone's face, or even casting shadows with our hands that resemble the shade of a dog. This level of abstraction and conceptualization allows us to reason, connecting high-level ideas. All the aforementioned properties of our brain form what we call intelligence. Conferring these properties to a computer would result in a general problem-solving machine.

Today, we are at a point in our technological advances at which the human brain and computers have a disjoint set of tasks in which they naturally excel.[1] Some tasks are easy for computers but difficult for humans. These are problems that can be described by a list of formal, mathematical rules. Therefore, computers excel at solving logic, algebra, geometry, and optimization problems, which we can tackle with hard-coded solutions or knowledge-based AI. However, we would like to tackle problems that are not easy to present in a formal mathematical way, such as face recognition, or whose exact mathematical formulation is not yet known, as detecting new quantum phases.

A particularly exciting direction is the development of algorithms that are not explicitly programmed. The main principle is to allow computers to learn from experience (or data). The shift toward this data-driven paradigm led to the birth of *machine learning (ML)*, schematically depicted in fig. 1.1. This field leverages fundamental concepts of applied statistics, emphasizing the use of computers to estimate complicated functions and with a decreased emphasis on proving confidence intervals around them [7]. Such trend has increased even more with the arising of *deep learning (DL)*, where enormous and heavily parametrized hierarchical models are used to deal with complex patterns from real-world data and do this with unprecedented

---

[1]This observation was first made in the 1980s and it is called Moravec's paradox. As Moravec wrote in 1988 [6], "it is comparatively easy to make computers exhibit adult level performance on intelligence tests or playing checkers, and difficult or impossible to give them the skills of a one-year-old when it comes to perception and mobility".

Figure 1.1: Schematic representation of the difference between the traditional programming, based on the algorithmic approach, and the experience-based/data-driven approach, which is the backbone of the ML paradigm. The ML paradigm is the first step toward learning abstractions by computers through the extraction of common features from data.

accuracy. Interestingly, many DL architectures are designed to mimic some of the properties of the human thinking process, such as the understanding of correlations in visual patterns or the recurrence in sound signals. We present a schematic representation of the relationship between these three fields (AI, ML, and DL) in fig. 1.2.

> To make a computer learn, we need three main ingredients:
>
> 1. a *task* to solve (section 1.4),
>
> 2. *data* that can be considered as an equivalent of *experience*. The latter can be provided in the form of, e.g., an interacting environment, and allows for solving the task (section 1.5),
>
> 3. a *model* that learns how to solve the task (section 2.4).
>
> To check whether a computer successfully learns how to solve a task, we need to define a performance measure, which can be as simple as the comparison between the model's prediction and the expected answer. In these terms, the learning process can be described as the iterative minimization of the model's error or maximization of the model's performance over the given task and data.

1.2 Historical view on learning machines

The foundations of the theory of learning were established already in the 1940s. Its development has followed two parallel paths: a knowledge-based approach, which dominated the AI research field for decades, and a data-based one, which is currently on the rise. Throughout the years, ML has gone under various names (like cybernetics or connectionism) and experienced a few cycles of intense popularity,[2] followed by criticism and disappointment, followed by funding cuts, followed by renewed interest years or decades later [7]. To give the reader some insight into the giants on whose arms we stand, we briefly present milestones in the development of ML, following Refs. [7, 9, 10]:

---

[2]Some argue that the "AI winter" is upon us unless we rethink AI or combine it with knowledge-based approaches [8]. It is also important to remember that such hype cycles are frequent with emerging new technologies.
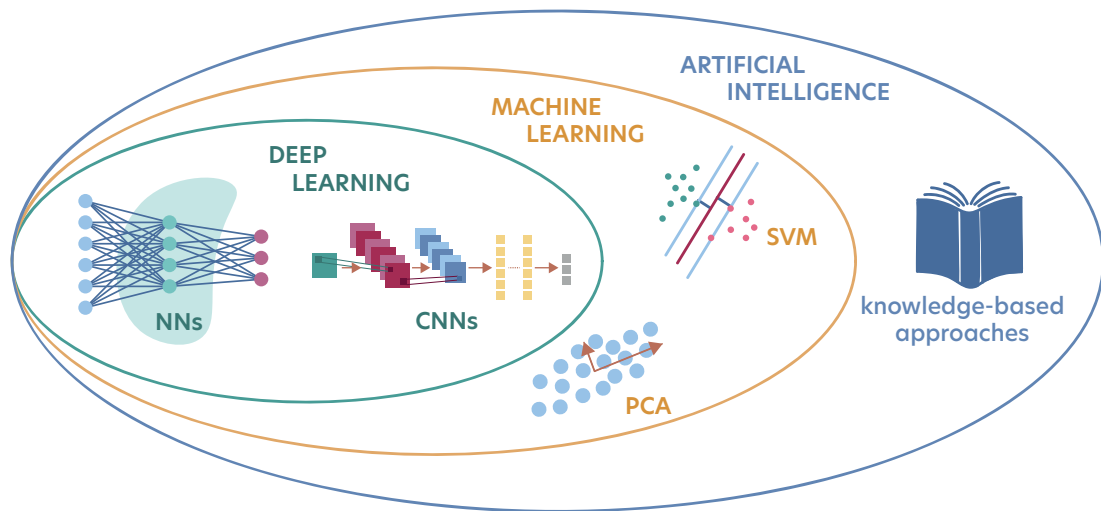
Figure 1.2: Sketch of the relation between AI, ML, and DL with examples from each field including support vector machines (SVMs), principal component analysiss (PCAs), neural networks (NNs), and convolutional neural networks (CNNs).

- 1943 – Walter Pitts and Warren McCulloch create a computer model based on the neural networks of the human brain called *threshold logic*. Their field of expertise is called *cybernetics*.

- 1949 – Donald Hebb hypothesizes how learning in biological systems works and formulates *Hebbian learning*. For example, if certain neurons "fire together, they wire together".

- 1957 – Frank Rosenblatt introduces a *Rosenblatt perceptron* modeling a single neuron. A perceptron is also called "an artificial neuron" and after modifications in 1969 by Marvin Minsky and Seymour Papert to this day remains widely used as a building block of artificial neural networks (ANNs).

- 1962 – David Hubel and Torsten Wiesel present, for the first time, response properties of single biological neurons recorded with a microelectrode.

- 1969 – Marvin Minsky and Seymour Papert point out the computational limitations and disadvantages of linear models, including a single artificial neuron, contributing to the first "AI winter".

- 1986 – David Rumelhart, Geoffrey Hinton, and Ronald Williams use *backpropagation* to train an NN with one or two hidden layers which, next to the revival of Hebb's ideas, causes renewed interest in the field that at this time is called *connectionism*. In the same year, David Rummelhart, James McClelland, *et al.* publish a widely discussed two-volume book "Parallel Distributed Processing" discussing known and collecting original contributions from the field including backpropagation and Boltzmann machines.

- the mid-1990s – second AI winter whose appearance is ascribed [7] to exceedingly ambitious claims of the community, which led to the disappointment of investors, and the simultaneous progress of kernel methods, that require less computational resources.

Interestingly, we can see how closely the development of AI was intertwined with neuroscience. This makes sense, as the human brain provides proof by example that intelligent behavior is possible. A natural approach to AI would be to try to reverse engineer the brain to reproduce its functionality. However, while the perceptron was inspired by biological neurons and some ML models are loosely inspired by neurological discoveries, there is nowadays a consensus that models should not be designed to be realistic simulators of biological functions [7].[3] Instead, scientists attempt to solve the mysteries of the human brain using ML.

Since 2006, DL has been thriving again thanks to a breakthrough in the efficient training of deep NNs [11] via backpropagation, followed by multiple analyses confirming the importance of its depth. At the same time, there has been a rapid improvement in computational power over the last decades which allowed the exploration of larger ML models. Here, the development of graphics processing units (GPUs) has played a particularly important role: highly parallelizable algorithms, such as NNs which are based on matrix and vector operations, can profit immensely from the parallel architecture of GPUs allowing them to process large amounts of data more efficiently than central processing units (CPUs). Additionally, we have started producing and storing large amounts of easily accessible electronic data all over the world [12–14], enabling data-driven programming approaches. Since then, the progress in the field has enabled realizations of concepts known, so far, only in science-fiction literature, such as self-driving cars or robots mimicking human emotions on their artificial faces. DL has dominated the field of computer vision for years, and it has found great success in time-series analysis, with applications like stock-market and weather forecasting [15]. Another fruitful direction is natural language processing, where sequence-to-sequence models have achieved great feats, even combining text with images [16,17]. Recently, DL-based algorithms obtained superhuman performance in video games [18,19] and complex board games, such as Go [20].

Overall, the continuous progress in the field of ML is supported by the steady increase of computational power as well as its easy applicability to real-world problems. The increasing amount of data produced by our society and the monetary benefit of its processing have made that the largest technological companies focus enormous economic efforts in the development of ML models. It is hence not a coincidence that the most important research groups in the field are associated with such companies. Importantly, one should understand the extend to which the trends of the field are dictated by the thirst for scientific discovery or by the particular needs of one or another technological giant. In summary, ML has become a day-by-day tool, acting in the shades of most of the technological tools we use nowadays, with the potential of solving some of the most important problems of the modern world and thereby contributing to improving the quality of life of people around the globe.

1.3 Learning machines viewed by a statistical physics

It is also worth noticing that the above sketched developments of AI, data science, cognitive science, and neuroscience, related to ML and NN, were also intertwined with the development of the statistical physics of spin glasses and NN. A wonderful retrospective of these developments can be found in the lecture of the late Naftali Tishby, "Statistical physics and ML: A 30-year perspective". Therefore, here we present a similar list of historical milestones as in section 1.2, but focused on statistical physics achievements:

- 1975 – Philipp W. Anderson and Samuel F. Edwards formulate the Edwards-Anderson spin glass model with short-range random interactions between Ising spins.

---

[3]Interestingly, we know that actual biological neurons compute very different functions than the perceptrons constituting our modern NNs, but greater realism has not yet led to any improvement in model performance [7].

- 1975 – a little later David Sherrington and Scott Kirpatrick formulate the Sherrington-Kirkpatrick spin glass model with infinite-range interactions, for which the mean-field solution should be exact. They propose to solve it using the replica trick, but this approximate solution turns out to be clearly incorrect at low temperatures.

- 1979 – Giorgio Parisi proposes an ingenious replica symmetry-breaking solution of the Sherrington-Kirkpatrick model.

- 1982 – John J. Hopfield publishes his seminal paper on attractor NNs, where by assuming the symmetry of interneuron coupling, he relates the model to a disordered Ising model of N spins, very much analogous to spin glasses. The maximal storage capacity is found to be $0.14N$.

- 1985 – Daniel Amit, Hannoch Gutfreund, and Haim Sompolinski formulate the statistical physics of the Hopfield model and relate limited storage capacity to the spin glass transition.

- 1987 – Marc Mezard, Giorgio Parisi, and Miguel Angel Virasoro publish the book "Spin glass theory And beyond: An introduction to the replica method and its applications". Interestingly, it is one of the first works bringing together statistical physics and NNs but also putting them in a more general context of complex systems like optimization and protein folding.

- 1988 – Elisabeth Gardner formulates the, so-called, Gardner's program to ML, where learning abilities are related to the relative volume in the space of those NNs that realize learning tasks and teacher-student scenarios (see section 8.1.1).

- 1989 – Daniel Amit publishes the book "Modeling brain function: The world of attractor NNs" where he brings closer neurophysiology and artificial NNs by introducing dynamical patterns whose temporal sequence encodes the information.

- 1990 – Géza Györgyi shows that sharp phase transitions from bad to good generalization can occur in learning using the Gardner's program on the perceptron.

- 1995 – David Saad, Sara Solla, Michael Biehl, and Holm Schwarze adapt Gardner's idea to study the dynamics of gradient descent in perceptrons and simple two-layer NNs called committee machines.

- late 2010s – The statistical mechanics predictions for the perceptron and the committee machine start being made mathematically rigorous by Nicolas Macris, Jean Barbier, Lenka Zdeborová, and Florent Krzakala.

- 2010s-today – With the explosion of DLs, interest in the statistical mechanics approach to learning is rekindled. Analyses are developed for increasingly complex models starting to bridge the gap from perceptrons to deep NNs.

- 2021 – Giorgio Paris receives the Nobel Prize in Physics "for the discovery of the interplay of disorder and fluctuations in physical systems from atomic to planetary scales."

We discuss the intersection of statistical physics and ML in more detail in section 8.1.

1.4 Examples of tasks

As stated above, the first ingredient needed for a computer to learn is the notion of a *learning task*. The archetypical ML task is the study of a response variable, $y(x)$, influenced by an explanatory variable x. In principle, there is no restriction whether y or x or both are continuous, discrete or even categorical.[4] Throughout the Lecture Notes, we restrict both variables, possibly encoded accordingly, to be of quantitative nature. That is, we can treat the variables straightforwardly from a numerical perspective, and we can adjust them easily to fit our needs.

Regression. We start by considering *regression* tasks. In this setting, we typically assume an immediate relationship between the two variables x and y, which is often of deterministic nature. More precisely, we seek to express the variable y, a.k.a. the output or target, in terms of the variable x, a.k.a. the input. In general, both variables can be multi-dimensional, as indicated by our notation. The objective of regression is to find the function f that yields the mapping $y = f(x)$ for all possible tuples of (x, y). Of course, from a practical point of view, we can neither optimize over the set of all possible functions nor over the full domain of x. Instead, we resort to a finite data set for which we opt to find a model that maps every input x to its corresponding target y. Usually, the model is predefined up to some parameters,[5] which are tuned to fit the data set. The most simple model assumes a linear relationship between the input and the output. We give more details of this model archetype in section 2.4.1. From here, there is a multitude of ways to extend the model by incorporating non-linear dependencies on both the model parameters and the input x. We find interesting regression problems in a large range of study fields, such as sociology (e.g., annual salary as a function of years of work experience), psychology (e.g., perceived happiness relative to wealth), finance (e.g., housing market prices depending on socio-economic factors) or, of course, (quantum) physics and chemistry. We cover some examples in these Lecture Notes, as for instance the prediction of potential energy surfaces (PESs) in quantum chemistry in section 4.5, or the estimation of the Hamiltonian's parameters given measurement data in section 7.3.

Classification. Another large class of tasks is *classification*. In this case, our goal is to use an algorithm to assign *discrete* class labels to examples. In contrast to regression, we are optimizing a model to find a mapping from an input vector x to a target y, which encodes a representation of the different possible classes. The simplest example of this kind of task is the binary classification, in which an algorithm has to distinguish between two classes, e.g., true or false. When the task involves more than two classes, we speak of multi-class classification. A canonical example for such a task is the classification of the images of handwritten digits contained in the famous MNIST [21] data set (named after Modified National Institute of Standards and Technology) over ten classes, one for each number from zero to nine. Other famous ML classification data sets are Iris [22], CIFAR-10 and 100 [23], and ImageNet [24].[6] A popular example from physics is the classification of different classical and quantum phases of matter, described in chapter 3. Another set of examples is provided by the classification subroutines in the automation of (quantum) experiments highlighted in section 7.3.

Both regression and classification tasks require a training data set consisting of examples of inputs x together with their corresponding labels y. Nonetheless, there are also tasks that

---

[4]When the inputs are, for example, words in a sentence as they are in the field of natural language processing, we can still process them by representing words by a suitable encoding which can be either continuous or discrete.

[5]There are also non-parametric approaches, e.g., see section 7.2.1 and section 4.4.2.

[6]The Iris database contains 150 data points with four features of three species of iris. The CIFAR-10 data set consists of 60 000 32x32 color images in 10 classes and was named after the Canadian Institute for Advanced Research. Finally, the ImageNet is a gigantic project with over 10 million labeled images whose the most popular subset spans 1000 object classes.

do not require explicit labels. An example of such is *density estimation*, where one aims at inferring the probability density function of the data set. This is directly related to the field of *generative problems*, where the goal is to *generate* new data instances that resemble some given input data. The distinction between the two fields is that the latter does not require explicit knowledge or reconstruction of the underlying data distribution to sample new instances. We present more details on density estimation in section 7.2.

In all the previous cases, we try to infer properties of a given pre-defined data set. Nevertheless, there are other tasks that involve starting from scratch and building a data set on the fly, from which we can then learn. A paradigmatic example of such a task is learning how to play a game. In this case, we start tabula rasa and progressively build a data set with the experience gathered as we play the game. From this data (or during its retrieval) our goal is to learn a function that chooses the best possible action or move according to the current state of the game. In this example, we can periodically alternate between collecting experience and learning, or we can do both at the same time.

This list of tasks is, of course, not exhaustive. Other examples which do not directly fall into the previous categories include text translation, imputation of missing values, anomaly detection, and data denoising, to name a few.

1.5 Types of learning

The second learning ingredient is the *data*, whose accessibility also often determines the type of learning we have to consider. It is clear, of course, that the notions of task, as presented in the previous section, and data are intertwined: certain tasks can only be solved if sufficient data is available and, in turn, a richer data set allows to transition from one task to another with seemingly low effort. Although the term data is often used for a variety of concepts accross many fields, there is a precise definition of it in the ML community. We usually refer to the *data* in terms of a data set $\mathcal{D}$, containing a finite amount of data instances often called *data points*, which may be presented as is, i.e., $\mathcal{D} = \{x_i\}$ or may be accompanied by predefined labels, i.e. $\mathcal{D} = \{(x_i, y_i)\}$. To shorten the notation, we also represent the input data $\{x_i\}$ by a matrix X, that can either be stacked row- or column-wise.

While the notation is clear-cut, there is much less convention and an even lesser understanding of how the data is *represented*. This is because, on one hand, the data can be arbitrarily preprocessed (for example, the data mean is often substracted prior to any further analysis), which already provides some degree of freedom. On the other hand, even choosing the right descriptors to characterize our object of interest is challenging: too few might not capture all relevant aspects of the object wheras too many can lead to spurious correlations that can interfere with the conclusions that we want to gain out of the data. We refer to every element in each data point x_i as a *feature*. As stated before, a central problem in ML relates to the correct representation of the data and its features. This is the core of the field of representation learning on which we only touch, e.g., by means of autoencoders (AEs) and principal component analysis (PCA) in chapter 3 and section 7.2.

Lastly, we emphasize that data can, loosely speaking, be identified with experience: data can be produced as the result of a repeated interaction with an entity (such as an experiment or a simulation) that then leaves us with a certain amount of experience about its underlying mechanism. In some cases, this experience may be used to further interact with such entity and learn from it. To this end, we set up a model. In summary, the type of data we have access to effectively defines the types of learning our model can be faced with. These are usually split in three: supervised, unsupervised and reinforcement learning.

Supervised learning. *Supervised learning* can be seen as a generalized notion of regression and classification, introduced in section 1.4, and describes ML algorithms that learn from *labeled* data, i.e., $\mathcal{D} = \{(\boldsymbol{x}_i, \boldsymbol{y}_i)\}$. There exists various approaches to supervised learning, ranging from statistical methods to classical ML and DL, both introduced in section 2.4. The concept of supervised learning appears repeatedly in these Lecture Notes and forms the basis of many chapters, including phase classification (chapter 3), Gaussian processes (chapter 4), as well as in the selected topics of DL for quantum sciences (chapter 8). Importantly, some of the latter are specially suited to deal with experimental data, as for instance in the efficient read-out of quantum dots or the identification of Hamiltonian parameters describing quantum experimental setups. In most of these examples (but there are notable exceptions), large amounts of data are required for the training process. On top of data, as stated, supervised learning requires correctly labeled data. This is usually considered one of its most prominent downsides, as perfectly matching labels are not always accessible or have to be added manually by humans.

Unsupervised learning. Supervised learning is not always the best option: the scarcity of labeled data is one example in which a classical input-output design might fail. Instead, we often have access to data where no prior information, e.g. in terms of labels, is given (i.e. $\mathcal{D} = \{\boldsymbol{x}_i\}$). In this case, we can employ *unsupervised learning*. Unsupervised learning can either be used for preliminary preprocessing steps, such as dimensionality reduction, or for representation learning, such as in clustering. In the opposite way, the dimensionality can also be increased by adding features via generative models. In these Lecture Notes, we discuss the application of unsupervised learning for phase classification in chapter 3 and density estimation in section 7.2. This example is particularly interesting because it demonstrates how the choice of unsupervised learning over supervised learning can aid in the automated discovery of new physics when the interpretation of a process, e.g., the nature of two different phases in a transition is unknown.

Reinforcement learning. In contrast to the two previous types of learning, in reinforcement learning (RL), we typically do not have a data set available *at all*. What we have instead is an *environment* with which we have to interact to achieve a certain task. This interaction is augmented with feedback, i.e., some extra information on whether the action has been beneficial or harmful in achieving the task at hand. The collection of visited environment states, action taken and rewards or penalizations received take the role of a data set. Feedback is very important in RL because we do not have a clear-cut route in achieving our task. In fact, initially, we typically do not even know the necessary ingredients for achieving the task. Often, we only know that we *achieved* a specific goal but not *why* we did it. The field of RL is precisely concerned with tackling the issue of how. In order to introduce it properly, we devote to it chapter 6.

Other types of learning. While supervised, unsupervised, and reinforcement learning are the most common learning schemes, there are ML approaches that go beyond this classification. An interesting example is active learning. This field includes selection strategies that allow for an iterative construction of a model's training set in interaction with a human expert or environment. The aim of active learning is to select the most informative examples and minimize the cost of labeling [25, 26]. We touch on this topic by means of Bayesian optimization (BO) in section 4.3 and local ensembles (LEs) in section 3.5.3. Another example is the so-called semi-supervised learning in which unlabeled data is explored to get better feature representations and improve the models trained on the labeled data [27].
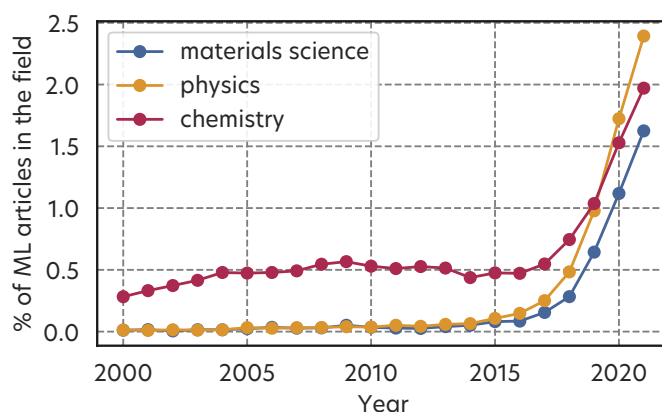
Figure 1.3: The number of ML-based publications in physics, materials science, and chemistry is growing exponentially. Adapted from Ref. [28].

1.6 What are these Lecture Notes about

We live in fascinating times where scientists start to incorporate AI algorithms for knowledge discovery. The breakthroughs of this booming field have led to a rapid increase in the confidence of the scientific community in these methods. This trend can be observed by tracking the percentage of ML-based publications in physics, chemistry, and material science, shown in fig. 1.3. As the number of ML applications grows, keeping track of all advances becomes challenging. Moreover, it is difficult to find reliable learning material of intermediate level which allows to efficiently bridge the gap between the quickly developing field of ML and scientists interested in incorporating ML tools into their own research.

Therefore, the aim of these Lecture Notes is to give an educational and self-contained overview of modern applications of ML in quantum sciences. We discuss in detail four ML paradigms that have already been successfully explored in quantum physics and chemistry. What we believe to be unique and very much needed before diving into the specifics of numerous application examples is an informative introduction to each paradigm, which prepares a quantum scientist for doing their own ML project. In particular, in chapter 3 we describe how supervised and unsupervised learning can be utilized to classify phases of matter. In chapter 4 we introduce kernel methods with a special focus on Gaussian processes (GPs) and Bayesian optimization (BO). Chapter 5 presents an overview of various representations of quantum states based on neural networks (NNs). Finally, in chapter 6 we dive into the foundations of reinforcement learning (RL) and how it can be applied to quantum experiments. To make the Lecture Notes self-contained, we devote chapter 2 to the ML prerequisites that are necessary to fully enjoy further, more advanced contents of this work.

Next to these well-recognized contributions of ML in quantum sciences, we observe an exciting two-way interplay between the natural sciences and AI. In chapter 7 we present more specialized examples on how ML-related methods revolutionize quantum science. In particular, we introduce the paradigm of differentiable programming (∂P) and describe how it is becoming an important numerical research tool. Moreover, we discuss how ML methods assist researchers in tasks related to density estimation, as well as optimizations and speed-up of scientific experiments. We also acknowledge a vibrant reverse influence on ML coming from statistical physics (which we discuss in section 8.1) and finally, quantum computing. We describe the promises of quantum machine learning (QML) in section 8.2. All in all, these Lecture Notes discuss the fruitful interplay of AI and quantum sciences, presented schematically in fig. 1.4. Their content with references to relevant sections is illustrated in fig. 1.5.
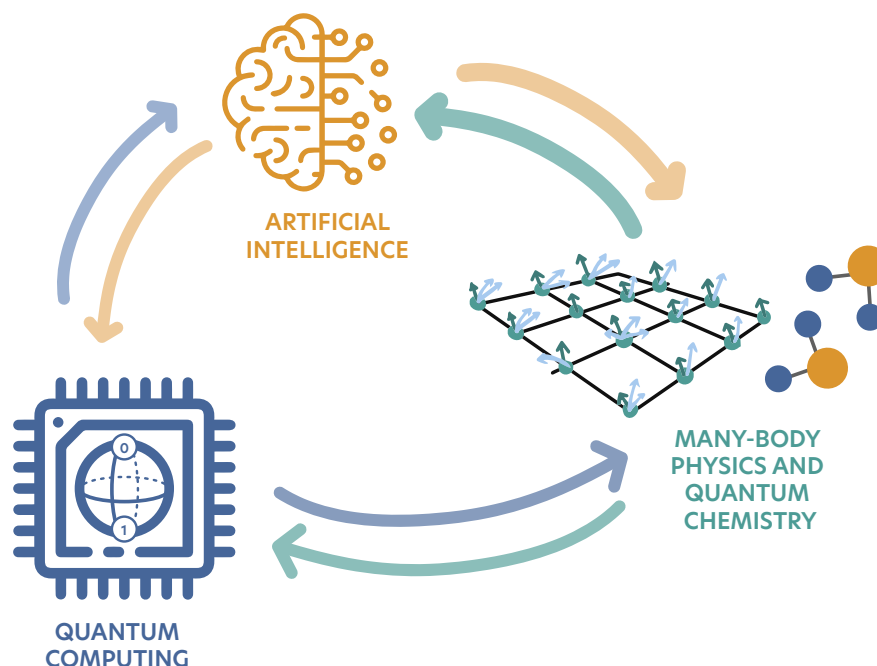
Figure 1.4: Interplay of AI and quantum sciences, in particular quantum computing, many-body physics, and quantum chemistry. Within these Lecture Notes we focus on the influence of AI onto quantum sciences but also cover the reverse impact of the statistical physics and quantum computing onto ML.

These Lecture Notes do not aim at providing an exhaustive list of ML applications in quantum sciences and becoming a complete review of the field. Such reviews already exist and nicely summarize the latest achievements [29–31]. Instead, we aim at providing the reader with enough knowledge, intuition, and tricks of the trade to start implementing ML methods of choice in their own research. As such, we selected the ML applications presented in this work that, we believe, are pedagogically appealing, while keeping a broad overview of the field. To this end, we focus on what a reader could do, and not only on what has been done. To fulfill this ambition, we conclude each chapter with an outlook and open problems that we recognize as important and promising.

These Lecture Notes are aimed at quantum scientists that want to familiarize themselves with ML methods. Therefore, we assume a basic knowledge of linear algebra, probability theory, and quantum information theory. We also expect familiarity with concepts such as Lagrange multipliers, Hilbert space, and Monte Carlo methods. We also assume the reader is familiar with quantum mechanics and has a basic grasp of the current challenges in quantum sciences.

Finally, note that the idea of creating these Lecture Notes was born out of the *Summer School: Machine Learning in Quantum Physics and Chemistry* which took place between Aug, 23 - Sept, 03, 2021, in Warsaw, Poland. As a result, the scientific content of this work is inspired by the topics covered by lecturers and invited speakers of the school. We also invite the reader to take a look at the school tutorials in Ref. [32] and to reuse figures prepared for these Lecture Notes, which are available in Ref. [33].

UNSUPERVISED
LEARNING
sec. 3.2,
3.4, 7.2

SUPERVISED
LEARNING
sec. 3.3,
4.5, 7.3

REINFORCEMENT
LEARNING
ch. 6

**FORM OF
TRAINING
DATA**

BIAS-VARIANCE
TRADE-OFF
sec. 2.2

INTERPRETABILITY
sec. 3.5

**MECHANICS
OF ML**

AUTOMATIC
DIFFERENTIATION
sec. 7.1

STATISTICAL
PHYSICS
FOR ML
sec. 8.1

QUANTUM
sec. 8.2

**ML IN
QUANTUM
SCIENCES**

TASK

ARCHITECTURE

CNN
sec. 2.4.4,
3.3, 3.5.2

NF
sec. 7.2.1

CLASSICAL

RNN
sec. 2.4.6,
5.2.2

KERNEL
METHODS
ch. 4

AE
sec. 2.4.5,
3.4.1

CLASSIFICATION
ch. 3,
sec. 4.2.2

REGRESSION
ch. 4,
sec. 7.3.2

GENERATIVE
PROBLEMS
sec. 7.2

DENSITY
ESTIMATION
sec. 7.2

APPLICATION

PHASE
CLASSIFICATION
ch. 3

REPRESENTATION
OF QUANTUM STATES
ch. 5

QUANTUM
COMPUTING
sec. 6.6.4 - 6.6.5

QUANTUM
TOMOGRAPHY
sec. 5.3.7

QUANTUM CHEMISTRY
sec. 4.5

QUANTUM
EXPERIMENTS

OPTIMIZATION
AND SPEED-UP
sec. 6.6.3, 7.3.1

HAMILTONIAN
LEARNING
sec. 7.3.2

Figure 1.5: Content of these Lecture Notes. We cover (1) three main learning schemes, i.e., supervised, unsupervised, and reinforcement learning (RL), (2) examples of ML tasks like classification, regression, and density estimation, (3) various applications in quantum chemistry and quantum many-body physics, (4) quantum and classical ML architectures. Finally, we also dive into mechanics of ML.

Further reading

- Carleo, G. *et al.* (2019). *Machine learning and the physical sciences*. Rev. Mod. Phys. 91, 045002. This detailed review summarizes the development of ML in physics and achievements till 2019 [30].

- Carrasquilla, J. (2020). *Machine learning for quantum matter*. Adv. Phys. X 5, 1. The concise review focused on phase classification and quantum state representation [31].

- Chollet, F. (2019). *On the measure of intelligence*. The review about different measures used to quantify *intelligence* providing the perspective on AI development [34].

- Krenn, M. et al. (2022) *On scientific understanding with artificial intelligence*. arXiv: 2204.01467 [35]. A beautiful paper discussing ways in which AI could contribute to the scientific discovery. It touches upon the philosophy of understanding as well as draws conclusions from dozens of anecdotes from scientists on their computer-guided discoveries.

- Recordings of lectures of the Summer School: Machine Learning in Quantum Physics and Chemistry which took place between Aug, 23 - Sept, 03, 2021, in Warsaw, Poland.

- Jupyter notebooks prepared as tutorials for the Summer School: Machine Learning in Quantum Physics and Chemistry [32].

2 Basics of machine learning

In this section, we describe basic machine learning (ML) concepts connected to optimization and generalization. Moreover, we present a probabilistic view on ML that enables us to deal with the uncertainty in the predictions we make. Finally, we discuss various ML models. Together, these topics form the ML preliminaries needed for understanding the contents of the next chapters.

2.1 Learning as an optimization problem

We have already discussed that ML can solve various tasks (e.g., classification or regression) and that there are different ways for the machine to access the data. The final ingredient is a model that learns how to solve the given task with the data at hand. In general, it is a function of the input data, $f(x)$, whose output is interpreted as a prediction made for the input data. The form of the output depends on the task. It can be, e.g., a class from a discrete set of possible classes in the classification task or a tensor from a continuous target distribution in the regression task. Finding the function that provides the best mapping between data and the desired outcome for a specific task is at the heart of ML. We start with declaring a certain parametrization of a model (function), e.g., $f(x) = \theta^\mathsf{T} x + b$. Then, all possible parametrizations of this function form the set of functions, i.e., the hypothesis class. Section 2.4 presents specific examples of the hypothesis classes (or spaces), but for now we focus on the learning process itself.

The mentioned learning schemes, i.e., supervised, unsupervised, or reinforcement learning, have the same underlying process of learning: finding an optimal model $\hat{f} \equiv f_{\theta^*}$ with optimal parameters θ^* in the hypothesis space, which minimizes the target loss function or maximizes a model performance. For the remainder of this section, for clarity, we focus on minimizing the loss function, $\mathcal{L}$, which intuitively plays a role of a penalty for errors of a model.

> Machines "learn" by minimizing the loss function of the training data, i.e., all the data accessible to the ML model during the learning process. The minimization is done by tuning the parameters of the model. The loss function formula varies between tasks and there is a certain freedom of how it can be chosen. In general, the loss function compares model predictions or a developed solution against the reality or expectations. Therefore, learning becomes an optimization problem.

In these Lecture Notes, we use the terms of loss, error, and cost functions[1] interchangeably following Ref. [7]. Popular examples of loss functions include the mean-squared error (MSE) and the cross-entropy (CE), used for supervised regression and classification[2] problems. The output of the loss function depends on the model (which enters into formulas via predictions) and the data set. They are also normalized by the number of data points n to compare their

---

[1]The literature also uses the terms of criterion or cost, error, or objective functions. Their definitions are not very strict. Following [7]: "The function we want to minimize or maximize is called the objective function, or criterion. When we are minimizing it, we may also call it the cost function, loss function, or error function. In this book, we use these terms interchangeably, though some ML publications assign special meaning to some of these term". For example, loss function may be defined for a single data point, the cost or error function may be a sum of loss functions, so check the definitions used in each paper.

[2]For classification, a more intuitive measure of the performance could be, e.g., accuracy, which is the ratio between the number of correctly classified examples and the data set size. Note, however, that gradient-based optimization requires measures of performance that are smooth and differentiable. These conditions distinguish loss functions from evaluation metrics such as accuracy, recall, precision, etc.
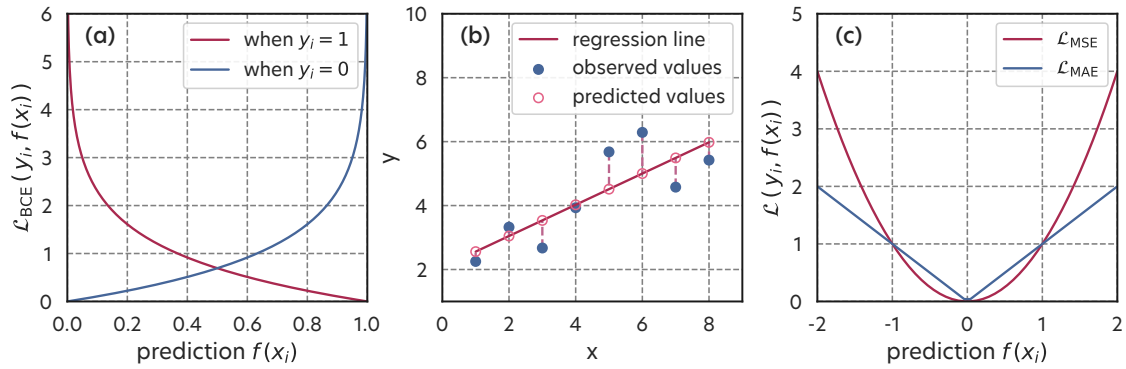
Figure 2.1: Examples of loss functions. (a) Plot of the binary cross-entropy (CE) for a single data point, x_i, when the ground-truth label $y_i = 0$ (blue) or 1 (purple). (b) Intuition behind loss functions used in regression problems. Dashed lines are differences between the labels, y_i, and values predicted by a model, $f(x_i)$. (c) Plots of the MSE (purple) and MAE (blue) for a single data point, x_i, when the ground-truth label $y_i = 0$.

values between problems with different data set sizes. The MSE is a popular loss function inherited from linear regression problems and is defined as

$$\mathcal{L}_{\text{MSE}} = \frac{1}{n} \sum_{i=1}^{n} (y_i - f(\boldsymbol{x}_i))^2. \tag{2.1}$$

It has an information-theoretic justification discussed in more detail in section 2.4.1 and section 2.2. In the former, we also introduce the mean absolute error (MAE) as another viable loss function, which is more sensitive to small errors than the MSE as shown in fig. 2.1(b)-(c). Cross-entropy (CE) is also a concept drawn from information theory and has connections to probability theory (see section 2.3). In the binary classification task, we can use the binary CE (BCE) known also as the log loss (eq. (2.2) and panel (a) in fig. 2.1), while for the multi-class classification, we use the categorical CE (CCE). They are defined as

$$\mathcal{L}_{\text{BCE}} = -\frac{1}{n} \sum_{i=1}^{n} y_i \cdot \log(f(\boldsymbol{x}_i)) + (1 - y_i) \cdot \log(1 - f(\boldsymbol{x}_i)), \tag{2.2}$$

$$\mathcal{L}_{\text{CCE}} = -\frac{1}{n} \sum_{i=1}^{n} \sum_{c=1}^{K} y_{i,c} \cdot \log(f(\boldsymbol{x}_i)), \tag{2.3}$$

where K is the number of classes. This formula requires representing labels in a way called *one-hot encoding*. For example, in a K-class problem, instead of having a label with K possible values such as $y_i = 1, 2, \ldots, K$, each label is encoded as a K-element vector with all-zero elements except for one at the index corresponding to the class. For example, $\boldsymbol{y}_i = [0, 0, 1, \ldots, 0]$, means a sample i belongs to the third class, as only $y_{i,3}$ is non-zero.

Once we choose a loss function, we can minimize it by varying the parameters of the ML model, using any optimization method of our choice. In general, we can reach the minimum of the loss function either via analytical construction or optimization methods that can be either gradient-based or gradient-free. A popular example of a gradient-based method is *gradient descent*. The optimization usually starts in a random place within the loss landscape (meaning
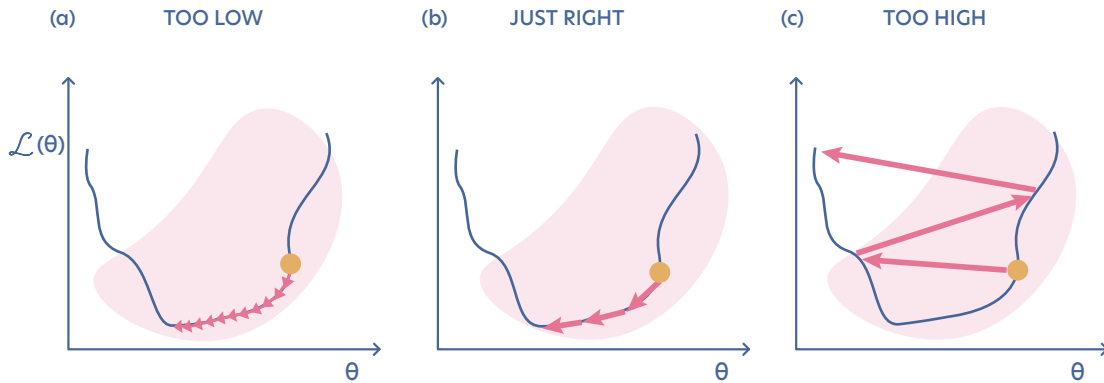
Figure 2.2: Choosing a learning rate has an impact on convergence to the minimum. (a) If η is too small, the training needs many epochs. (b) The right η allows for a fast convergence to a minimum and needs to be found. (c) If η is too large, optimization can take you away from the minimum (you "overshoot"). This figure suggests that loss function is convex which is rarely true.

with a model with randomly initialized parameters, $\theta = \theta_0$).[3] Using the model with θ_0, one makes prediction over the training data and from here, computes the loss function. The next step consists of computing the gradients of the loss function with respect to each model parameter, θ_j. The final step is to update the parameters by subtracting the respective gradients multiplied by a learning rate, η, i.e.,

$$\theta_j := \theta_j - \eta \frac{\partial \mathcal{L}}{\partial \theta_j}. \tag{2.4}$$

These steps need to be repeated until the minimum is reached, and each repetition is called an *epoch*. The intuition is that gradient descent updates model parameters by making steps toward the minimum of the function (so in the opposite direction than the gradient, which indicates where the function value grows). The learning rate controls the size of these steps. Figure 2.2 presents in a simplified way the importance of the η choice. Both too large and too small ηs make the optimization more challenging, and only an optimal η promises efficient convergence to a minimum. There is rarely an obvious way of choosing η which, therefore, has to be found, e.g., by trial and error. As such, the learning rate is one of the so-called *hyperparameters* of the learning process. Hyperparameters are parameters whose values control the learning process (especially speed of convergence and quality of the minimum) and are chosen by a user (in contrast to model parameters, which are derived via training). The total number of epochs or the choice of the loss function are hyperparameters too. We encounter more examples of the hyperparameters in this introductory chapter.

To find optimal hyperparameters, a good practice is to form (in addition to the training data set) a separate *validation data set*. This data is only used to *validate* the model, and not used for training. Then, we can set various hyperparameters and choose them in such a way that the error on the validation set is minimized.[4] Dividing the data set into smaller subsets

---

[3]In practice, parameters are usually initialized randomly but with the constraint to have a mean at zero and constant variance across layers, otherwise we may encounter problems with vanishing or exploding gradients [36].

[4]One can even use optimization methods to find optimal hyperparameters which minimize the validation error (a popular library is Optuna [37]) but a choice of hyperparameters guided by intuition may prove to be a faster and cheaper approach.

can be problematic in case of the limited number of data. Alternative approaches for model validation exist like k-fold *cross-validation* [7], which consists in splitting the data set into k non-overlapping subsets. The validation error can be then estimated by taking average error over k trials where the i-th trial uses i-th subset as a validation set and the rest as training data. Note that the cross-validation comes at the price of increased computational cost.

Coming back to the gradient descent, note that to perform it, we must first compute the gradient of the loss function with respect to the parameters to be tuned, $\nabla_{\boldsymbol{\theta}}\mathcal{L}$, before each step, see eq. (2.4). *A priori*, there exist several different approaches how to compute these derivatives. For example, one could work our the analytical derivatives by hand or approximate them numerically based on finite differences. When we are concerned with the accurate numerical evaluation of derivatives and not their symbolic form, automatic differentiation (AD) is a good choice. AD makes use of the fact that the computer programs which compute the corresponding loss function can be decomposed into a sequence of a handful of elementary arithmetic operations (e.g., additions or multiplications) and functions (e.g., exp or sin). The numerical value of the derivative of the program, i.e., the loss function, can therefore be computed in an automated fashion by repeated applications of basic pre-defined differentiation rules, such as the chain rule

$$\frac{df(g(x))}{dx} = f'(g(x))g'(x). \tag{2.5}$$

For more details on how to compute derivatives of computer programs, in particular AD, see section 7.1.[5]

The optimization procedure that we have described in the previous paragraphs and in fig. 2.2 is very efficient when the *loss landscape*, i.e., the representation of the loss values around the parameter space of the model, is convex. Especially for DL, however, loss landscapes are highly non-convex and usually exhibit multiple local minima [38,39]. Two immediate questions arise from this non-convexity: firstly, how getting stuck in local minima corresponding to large loss function values or in saddle points of such landscapes can be avoided? Secondly, whether some minima are better than others? Currently, such questions concerning learning dynamics are still being explored in various on-going research directions, but some intuitions are already provided by statistical physics (see section 8.1). A popular approach to deal with the aforementioned problems considers a slight modification of the gradient descent algorithm, so-called *stochastic gradient descent (SGD)*. This optimization method (whose pseudocode is provided in algorithm 1) consists in computing the loss function at each epoch on randomly selected mini-batches (subsets) of the training data. This means that during each epoch the gradients may point in various directions. Effectively, the resulting stochasticity has been shown to help in escaping saddle points and narrow local minima [40].[6] Moreover, computing the loss function and gradients only for a mini-batch of data instead for the whole data set provides a nice computational speed-up for large data sets.

Let us look into the minimum reached during the optimization of DL models in more detail. To do that, and to describe the curvature around such a minimum, we use the Hessian of the training loss function, $\boldsymbol{H}_{\boldsymbol{\theta}^*} = \frac{\partial^2}{\partial\theta_i\theta_j}\mathcal{L}_{\text{train}}|_{\boldsymbol{\theta}=\boldsymbol{\theta}^*}$, i.e., the square matrix of second-order partial derivatives of $\mathcal{L}$ with respect to the model parameters, calculated at the minimum, $\boldsymbol{\theta} = \boldsymbol{\theta}^*$. The eigenvectors of $\boldsymbol{H}_{\boldsymbol{\theta}^*}$ corresponding to the largest positive eigenvalues indicate directions with the steepest ascent around the minimum. A high curvature implies that the training data strongly determines the model parameters along that direction. What may be surprising, the

---

[5]The special case where AD is applied in *reverse-mode* to NNs is known as backpropagation and constitutes the workhorse that enables efficient NN training.

[6]In practice, stochasticity is helpful in avoiding saddle points but there are theoretical works showing it is not a necessary condition for a proper convergence [41].

Algorithm 1 Minibatch stochastic gradient descent (SGD)

Require: Learning rate η
  Initialize $\boldsymbol{\theta}$ to random values
  for epoch $= 1$ to no_epochs **do**
    Shuffle $\mathcal{D}_{\text{train}}$
    for i $= 1$ to m (where m is a minibatch size) **do**
      $z_i = \{\boldsymbol{x}_i, y_i\} \sim \mathcal{D}_{\text{train}}$ ▷ Draw random data point from data set without replacement
      $\mathcal{L} \leftarrow \frac{1}{m} \sum_{i=1}^{m} \mathcal{L}(y_i, f(\boldsymbol{x}_i))$ ▷ Compute loss function on the minibatch
      $(\nabla\mathcal{L})_j \leftarrow \frac{\partial \mathcal{L}}{\partial \theta_j}$ ▷ Compute gradients
      $\theta_j \leftarrow \theta_j - \eta \frac{\partial}{\partial \theta_j} \mathcal{L}$ ▷ Update parameters
    end for
  end for
  return $\boldsymbol{\theta}$

---

training of an ML model leads to a local minimum or a saddle point[7] [43–45]: the vast majority of the eigenvalues are close to zero, indicating various flat directions and some small negative eigenvalues are also present, indicating directions with negative curvature. We present more examples on what information one can gain out of $\boldsymbol{H}_{\boldsymbol{\theta}^*}$ in section 3.5.3.

Up until this point, the only gradient based optimization method we have described is SGD. Popular alterations to this scheme consist of, for example, including a momentum term that takes previous update directions into account [46, 47] or adaptive learning rates between epochs [48] or both, culminating in the celebrated Adam optimizer [49, 50]. Another different idea is to incorporate the second derivative in the update rule as is accomplished by the limited-memory Broyden–Fletcher–Goldfarb–Shanno algorithm (L-BFGS) algorithm [51]. There are also gradient-free optimization approaches which are used especially when the gradients or loss function itself are expensive or impossible to compute, e.g., when optimizing experiments. Examples include genetic algorithms, particle swarm optimization, random search and simulated annealing [52]. Another example we discuss in more detail in section 4.3 is Bayesian optimization.

2.2 Generalization and regularization

So far, ML looks like cleverly named function fitting. This changes when we put the emphasis on the generalization rather than merely maximizing the model performance on the training data.

> The heart of ML lies in the *generalization*, which is the ability to make correct predictions on new data, never seen during the training.

Checking whether your model generalizes well requires an additional data set, commonly referred to as the *test set*, composed of data points that are used neither for optimization

---

[7]One can wonder why we should trust a model which does not land in the global minimum. A series of empirical results as well as applying spin-glass theory to deep learning [42] indicate, among others, that for large-size networks, most local minima are equivalent and yield similar performance on a test set. Also, the probability of finding a "bad" (high value) local minimum is non-zero for small-size networks and decreases quickly with network size. Finally, attempting at finding the global minimum on the training set (as opposed to one of the many good local ones) is not useful in practice and may lead to overfitting, i.e., much better performance on training set than test set, which is equivalent to bad generalization.

of model parameters nor for searching for the best hyperparameters describing the learning process. The test set is only used for reporting the final performance of the model.[8] Therefore, the original full data set needs to be separated into a training, a validation, and a test set.[9] One needs to be particularly careful in the preparation of these data set as to prevent *information leakage*, i.e., the use of information in the training process that is expected to be available at prediction time.[10]

A common problem encountered during the training of an ML model is a higher test error than the training error: their difference is called the generalization error. This lower model performance on the test set compared to the training set persists, even when all data points are generated by an identical probability distribution (but disappears in the infinite data limit). The main reason is the large capacity of DL models.[11]

> The *capacity* can be loosely understood as the measure of a model's ability to fit a variety of functions. When the model capacity is much higher than one needs to solve the task, the model tends to *overfit*, i.e., memorize all possible properties of the training set which may not be true for the general distribution (and in particular, the test set).

In particular, the model can even fit the noise in the training data. As a result, overfitting increases the test error while keeping the training error low (or even decreasing it). An optimal capacity allows for the lowest gap between the test and training error, so the lowest generalization error. However, a capacity that is too low results in an overly constrained model which can *underfit*, i.e., have a high training error. The intuition behind the under- and overfitting is schematically shown in fig. 2.3. Therefore, we can improve the generalization of the model by controlling its capacity.

> Every modification of the model aiming to improve the generalization of a model (possibly at the cost of the increased training error) is called a *regularization* technique.

One can think of regularization in terms of Occam's razor.[12] The additional motivation for using regularization is the *no free lunch theorem*, which states that, when averaged over all possible data generating distributions, every classification algorithm has the same error rate when classifying previously unobserved points [7, 54]. Therefore, no ML model is universally better than another; and no regularization technique is universally better than another. This implies that we need to design our ML algorithms to perform well on a specific tasks, e.g., by regularizing it in a way which is tailored to this task.

A straightforward way of restricting the model's capacity is to limit the magnitude of its trainable parameters which effectively limits the hypothesis space of a parametrized model. This can be done by adding a penalizing term to the training loss function which increases with the parameters' magnitude. Such an approach is used within the two popular regularization

---

[8]We need the test set, as the performance measure obtained from the validation test may be overestimated because we use it to find the best hyperparameters of the learning process.

[9]The ratio between sizes of these sets depends on how much data is available in total, but we suggest starting with, e.g., 8:1:1.

[10]A common mistake is to first normalize the whole data set and then separate it into a training, a validation, and a test set. As a result, a model may "know" about the most extreme data points which are not part of the training set.

[11]DL models are even able to fit large data sets with random labels [53]!

[12]This principle states that among competing hypotheses that explain known observations equally well, one should choose the simplest one. It is sometimes summarized as *"entities should not be multiplied beyond necessity"*.
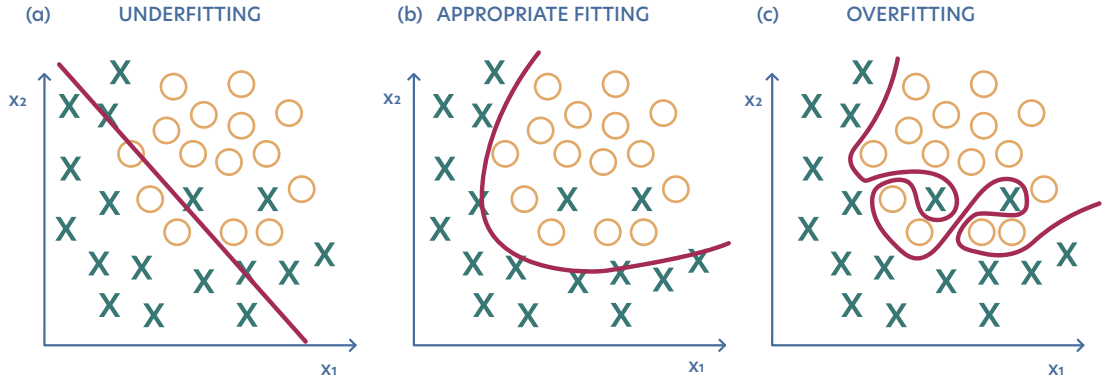
Figure 2.3: Scheme of under- and overfitting. (a) When the model capacity is too low, the model cannot fit the training data properly. (b) With the model capacity corresponding to the task complexity, the fitting is optimal. (c) When the model capacity exceeds the task complexity, the model tends to overfit and the generalization error increases.

techniques, i.e., ℓ_1 and ℓ_2 regularization. In particular, ℓ_2 regularization is described in more detail in sections 2.4.1 and 4.2.1.

Up to now, we have discussed the relationship between a model's complexity and its performance on the training and test set in intuitive terms. In the following, we formalize this intuition through the *bias-variance trade-off*. Consider the standard situation encountered in regression problems: We are given an ensemble of data points $\mathcal{D} = \{\boldsymbol{x}, f(\boldsymbol{x}) + \epsilon\}$ that derives from the function $f(\boldsymbol{x})$ and some noise ϵ inherent to the data. The function $f(\boldsymbol{x})$ is generally unknown and our goal is to infer it. We do this by constructing a regression fit of the data $\hat{f}(\boldsymbol{x})$. What we are eventually interested in for the test error (or generalization error) to be as small as possible. The test error is given as an average of the loss function $\mathcal{L}$ evaluated over test points

$$\text{Err}_{\mathcal{T}} = \mathbb{E}\left[\mathcal{L}(\boldsymbol{y}, \hat{f}(\boldsymbol{x})) \,|\, \mathcal{T}\right], \tag{2.6}$$

where $\mathcal{T}$ is a fixed training set. This quantity is difficult to calculate, and we can instead resort to the expected prediction error obtained by averaging the generalization error over many training sets

$$\text{Err} = \mathbb{E}\left[\mathcal{L}(\boldsymbol{y}, \hat{f}(\boldsymbol{x}))\right] = \mathbb{E}\left[\text{Err}_{\mathcal{T}}\right]. \tag{2.7}$$

Let us look at the expected prediction error at a given point $\boldsymbol{x}_0$

$$\text{Err}(\boldsymbol{x}_0) = \mathbb{E}\left[\left(f(\boldsymbol{x}_0) + \epsilon - \hat{f}(\boldsymbol{x}_0)\right)^2\right], \tag{2.8}$$

where, for now, we consider an MSE as the loss function (eq. (2.1)). The averaging in eq. (2.8) is performed over all random variables inside the expression $\mathbb{E}[\cdot]$, namely the noise ϵ as well as the model through the choice of different training sets. We can expand this expression as

$$\text{Err}(\boldsymbol{x}_0) = \mathbb{E}\left[\left(f(\boldsymbol{x}_0) - \hat{f}(\boldsymbol{x}_0)\right)^2\right] + \mathbb{E}\left[2\epsilon(f(\boldsymbol{x}_0) - \hat{f}(\boldsymbol{x}_0))\right] + \mathbb{E}\left[\epsilon^2\right], \tag{2.9}$$

where $\mathbb{E}\left[\epsilon^2\right]$ is the (fixed) variance of the underlying noise in the data. Next, we use the property of independent random variables $\mathbb{E}[AB] = \mathbb{E}[A]\,\mathbb{E}[B]$ to obtain

$$\mathbb{E}\left[2\epsilon(f(\boldsymbol{x}_0) - \hat{f}(\boldsymbol{x}_0))\right] = 2\mathbb{E}[\epsilon]\,\mathbb{E}\left[f(\boldsymbol{x}_0) - \hat{f}(\boldsymbol{x}_0)\right] = 0, \tag{2.10}$$

where we assumed unbiased noise $\mathbb{E}[\epsilon] = 0$. Thus, we are left with

$$\mathbb{E}\left[(f(x_0) - \hat{f}(x_0))^2\right] + \mathbb{E}\left[\epsilon^2\right] = \mathbb{E}\left[(\hat{f}(x_0))^2\right] - 2f(x_0)\mathbb{E}\left[\hat{f}(x_0)\right] + (f(x_0))^2 + \mathbb{E}\left[\epsilon^2\right]. \quad (2.11)$$

We modify eq. (2.11) by adding and subtracting $\mathbb{E}\left[\hat{f}(x_0)\right]\mathbb{E}\left[\hat{f}(x_0)\right]$ to get

$$\text{Err}(x_0) = \left(\mathbb{E}\left[\hat{f}(x_0)\right] - f(x_0)\right)^2 + \left(\mathbb{E}\left[(\hat{f}(x_0))^2\right] - \mathbb{E}\left[\hat{f}(x_0)\right]\mathbb{E}\left[\hat{f}(x_0)\right]\right) + \mathbb{E}\left[\epsilon^2\right]. \quad (2.12)$$

We can identify the first term as the squared bias of our model

$$\text{Bias}^2[\hat{f}(x_0)] := \left(\mathbb{E}\left[\hat{f}(x_0)\right] - f(x_0)\right)^2, \quad (2.13)$$

and the second as its variance

$$\text{Var}[\hat{f}(x_0)] := \mathbb{E}\left[(\hat{f}(x_0))^2\right] - \mathbb{E}\left[\hat{f}(x_0)\right]\mathbb{E}\left[\hat{f}(x_0)\right]. \quad (2.14)$$

This results in

$$\text{Err}(x_0) = \text{Bias}^2[\hat{f}(x_0)] + \text{Var}[\hat{f}(x_0)] + \mathbb{E}\left[\epsilon^2\right]. \quad (2.15)$$

The average prediction error at a given unseen test point x_0 can therefore be decomposed into the bias of our model, its variance as well as the variance of the noise underlying our data (which is irreducible from a model perspective).[13]

> The more complex a model $\hat{f}(x)$ is, the lower its bias is after training. However, the increased model complexity generally also results in larger fluctuations in capturing the data points, resulting in a larger variance – a situation we refer to as overfitting. This is referred to as the bias-variance trade-off.

Figure 2.4 shows an illustration of the bias-variance trade-off which makes clear that the ideal model realizes an optimal trade-off between the training error and the model complexity. Interestingly, empirical studies indicate that modern large DL models with enormous capacities are able to generalize very well [56]. How overparametrized models can generalize so well remains a challenging puzzle of the field[14] but some insight is provided with tools of statistical physics (see section 8.1).

2.3 Probabilistic view on machine learning

The need for a probabilistic approach to ML becomes apparent when we consider that this field has to tackle three sources of uncertainty (following Ref. [7]). Firstly, there may be an inherent stochasticity of the system generating the data we have access to (especially when dealing with quantum data). Secondly, we need to account for a possible incomplete observability, i.e., an unavoidable lack of information regarding all possible variables influencing the system. In other words, we have only partial access (by means of the available data) to all relevant parts of the mechanism or distribution underlying the system. Finally, the models we use are rarely complete and need to discard some available information. An example of incomplete modeling may be a robot whose movement space we discretize. Such a discretization immediately makes the robot uncertain about "omitted" parts of the space. To mathematically account for the uncertainty of a model, we can follow the so-called Bayesian approach to probability which interprets the probability as an expectation or quantification of a *belief*.

In this section, we provide a concise reminder of basic concepts from the probability theory which appear in the rest of these Lecture Notes:

---

[13]This does not only hold for an MSE loss as many variations of the bias-variance decomposition are known [55].

[14]Promising observations are provided by the lottery ticket hypothesis [57].
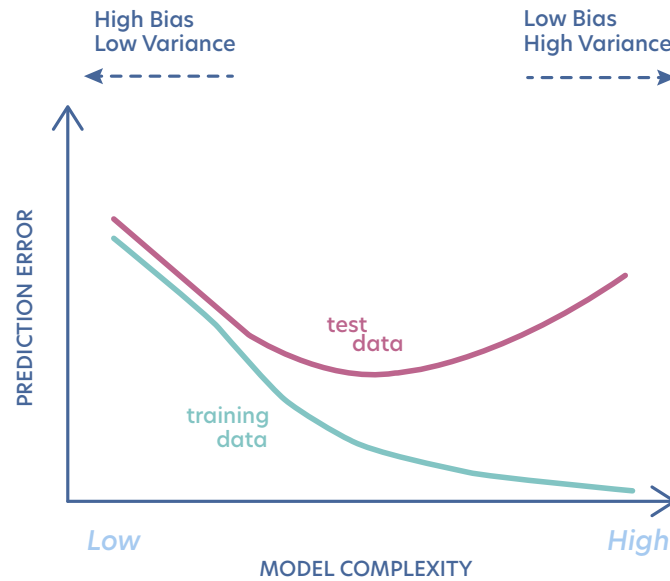
Figure 2.4: Illustration of the bias-variance trade-off and its relation to the prediction error observed on training (green curve) and test sets (red curve). The ideal model which results in the lowest test error has both intermediate model complexity (e.g. capacity) and training error.

- Random variables are variables taking random values. If they are independent and identically distributed (i.e., drawn independently from the same probability distribution), they are called *i.i.d.* random variables.

- A *probability distribution* is a measure of how likely a random variable X is to take on each of its possible states x[15], e.g., $p(X = x)$. A probability distribution over discrete (continuous) variables is called a probability mass function (probability density function). A *joint* probability distribution is a probability distribution over many variables at the same time and is denoted, e.g., as $p(X = x, Y = y)$. When the notation is clear, we typically also drop the random variable and just write $p(X = x) \equiv p(x)$, instead.

- Two random variables X and Y are *independent* if their joint probability distribution can be expressed as a product of two factors, one involving only X and one involving only Y:

$$\forall x, y, \quad p(X = x, Y = y) = p(X = x)p(Y = y).\tag{2.16}$$

You can denote this independence by $X \perp Y$.

- A vector whose elements consists of random variables is called a *random vector* and we denote it simply with $\boldsymbol{x}$.

- A *conditional* probability is a probability of one event given that some other event has happened. We denote the conditional probability with $p(Y = y \mid X = x)$, meaning the probability of $Y = y$ given the observation that $X = x$. It can be calculated as:

$$p(Y = y \mid X = x) = \frac{p(Y = y, X = x)}{p(X = x)}.\tag{2.17}$$

---

[15]This notation is easily generalized to vector-valued random variables.

- Any joint probability distribution over many random variables may be decomposed into conditional distributions over only one variable each, which is called the *chain rule* or *product rule* of probability:

$$p\left(x^{(1)}, \ldots, x^{(n)}\right) = p\left(x^{(1)}\right) \prod_{i=2}^{n} p\left(x^{(i)} \mid x^{(1)}, \ldots, x^{(i-1)}\right). \tag{2.18}$$

- Finally, let us discuss a situation where we know the conditional probability $p(y \mid x)$ and need to know the opposite one, $p(x \mid y)$. Fortunately, if we also know $p(x)$, we can compute the desired quantity using *Bayes' rule*:

$$p(x \mid y) = \frac{p(y \mid x)p(x)}{p(y)}. \tag{2.19}$$

If we do not know $p(y)$, we can compute it via $p(y) = \sum_x p(y \mid x)p(x)$, the *sum rule* of probabilities. Bayes' rule is a direct consequence of the definition of conditional probability in eq. (2.17).

We are now armed with enough tools to look at ML models in a probabilistic way. In particular, we can reformulate the definition of supervised and unsupervised learning. Unsupervised learning consists of observing some examples of a random variable X, e.g., $x_1, x_2, \ldots, x_n$, and then learning the probability distribution $p(X)$ or some of its properties.[16] Supervised learning is about observing some examples of a random vector X and an associated vector Y, e.g., $\{x_1, y_1\}, \{x_2, y_2\}, \ldots, \{x_n, y_n\}$, and learning to predict y from x, usually by estimating $p(Y = y \mid X = x)$. An ideal ML model perfectly learns the probability distribution that generates the data.[17]

Combining this with what we have discussed in section 2.1, now we know that ML models (typically parametrized) are used to estimate probability distributions. Therefore, the concept of likelihood enters the picture. The *likelihood function* is the joint probability of the observed data as a function of the parameters of the chosen model, $p(\mathcal{D} \mid \boldsymbol{\theta})$, estimating the data-generating probability distribution.[18] How it enters ML problems is explained on the example of linear regression in section 2.4.1.

Finally, sometimes it is useful to compare two probability distributions over the same random variable X, e.g., $p(x)$ and $q(x)$. Such a measure is provided by a *relative entropy*, called the Kullback-Leibler (KL) divergence, $D_{\mathrm{KL}}(p\|q)$. To be precise, it is a measure of how the probability distribution q is different from a reference probability distribution p. As we typically employ it in classification tasks where p and q are both discrete distributions, it is defined as:

$$D_{\mathrm{KL}}(p\|q) = \left\langle \log \frac{p(\mathrm{x})}{q(\mathrm{x})} \right\rangle_p = \frac{1}{n} \sum_{i}^{n} p(x_i) \log \frac{p(x_i)}{q(x_i)}. \tag{2.20}$$

For continuous distributions, the sum has to be replaced by an integral. $D_{\mathrm{KL}}(p\|q)$ has some properties of distance, i.e., is non-zero and is zero if and only if p and q are equal.[19] But it

---

[16]Again, we can easily generalize this notion to random vectors or vector-valued random variables.

[17]If there is any kind of stochasticity in the underlying distribution, then even an ideal model can be wrong. Such an error is called the *Bayes optimal error* that poses a fundamental limit on statistical models.

[18]Do not confuse likelihood and probability! Intuitively, probability is a property of a sample coming from some distribution. Likelihood, on the other hand, is a property of a parametrized model. In particular, if you plot $p(\mathcal{D} \mid \boldsymbol{\theta})$ as a function of possible $\boldsymbol{\theta}$, it does not have to integrate to one.

[19]Equal in case of discrete variables, and equal "almost everywhere", i.e., throughout all of space except for on a set of measure zero, in case of continuous variables.

is not a proper distance measure as it is not symmetric, $D_{\text{KL}}(p||q) \neq D_{\text{KL}}(q||p)$.[20] Using the properties of the logarithm, $D_{\text{KL}}(p||q)$ can be expressed as

$$D_{\text{KL}}(p||q) = \frac{1}{n} \sum_i^n p(x_i) \log p(x_i) - \frac{1}{n} \sum_i^n p(x_i) \log q(x_i) =: -\mathcal{S}(p) + \mathcal{L}_{\text{CE}}(p,q), \qquad (2.21)$$

where $\mathcal{S}(p)$ is the Shannon entropy of the reference probability distribution p, and as the second term we obtain the CE, which we have already introduced in eqs. (2.2) and (2.3)! We rediscover it by noting that minimizing $D_{\text{KL}}(p||q)$, i.e., the difference of p with respect to q, is equivalent to minimizing the cross-entropy, because q does not appear in $\mathcal{S}(p)$.

While the utility of comparing probability distributions is clear in the case of estimating a true probability distribution with a parametrized one, it may not be immediately obvious for arbitrary ML models. Let us discuss the case of supervised learning with a model f. Consider the labeled training data set consisting of n tuples $\{x_i, y_i\}$, where x_i is a given sample with label y_i. Each label belongs to one out of K classes. Next, we can think of each one-hot-encoded label $y_i = k$ as a very specific probability distribution $y_i = q(x_i) = \delta_{k,j}$, where $k, j \in \{1, \ldots, K\}$ (one-hot encoding). Next, the training data x_i are fed to the model, f, and as an output we obtain the probability distribution $p(x_i) = f(x_i)$, which gives us the probabilities of a given sample x_i belonging to each class. In the last step, we have to compare two probability distributions p and q. Therefore, we rediscover the categorical cross-entropy from eq. (2.3).

2.4 Machine learning models

We have already described two out of three ingredients of the ML: tasks (section 1.4) and data (section 1.5). The final element is a model which learns how to solve a task given some data. ML models can be broadly divided into two classes which are *standard* ML and DL. In sections 2.4.1 to 2.4.3, we give the overview on the former while the latter is explained in more depth in sections 2.4.4 to 2.4.6. Let us start by stressing the following point:

> DL is a sub-field of ML itself as depicted in fig. 1.2. It is customary, however, to distinguish between ML methods based on whether they use neural networks (NNs). Henceforth, in the remainder of the chapter, we refer to *standard* ML as any algorithm which does not make use of NNs.

The distinction here becomes more subtle: in a nutshell, what distinguishes traditional learning from DL is the level of abstraction and the flexibility the algorithm has in extracting the features. In other words, traditional ML requires very specific algorithms specifically designed and tailored to the problem at hand. What model is to be applied then often comes down to experience and further intuition of the task of interest. On the other hand, NNs are a very flexible yet general tool whose core goal is to reproduce a target function without any (or little) constraints on the functional class from which to search. As a down-side, they usually do not support an easy interpretation of their mapping (compared to traditional ML methods) and are often referred to as *black-box* functions. We explain to what extent this actually is the case in section 3.5. The distinction we can infer is that DL does not require an explicit set of instructions on how to connect the input with the output. Traditional ML methods, on the other hand, are often constructed by geometric or information-theoretic arguments which already provide intuition into the method by their very construction, hence their immediate interpretability.

---

[20]We recommend an illustrative discussion of the asymmetry of $D_{\text{KL}}(p||q)$ in Fig. 3.6 of Ref. [7].

A natural question that arises now is: which approach to choose, traditional ML or DL? As always: it depends. For instance, DL performs at the state-of-the-art level in the big-data regime where an NN has enough available information to infer and perform the feature extraction. The low-data limit is where traditional ML is still prevailing. Here, we need to incorporate as much information as possible into the algorithm of choice to make learning efficient. Thus, algorithms become much less general and more problem-dependent.

Let us now focus on the standard ML algorithms and leave the discussion about NNs for section 2.4.4 and forward. Some prominent examples of traditional ML we encounter during the rest of these Lecture Notes are the following: Principal component analysis (PCA) is a very elegant approach for the task of dimensionality reduction, i.e., for data compression. It takes multi-dimensional samples and compresses their feature space while maintaining only a few relevant features. The compressed data can undergo further ML routines (see section 3.2.1). Gaussian processes (GPs) are another examples of a traditional ML algorithm which deal well with learning tasks when only limited data is available. Jointly with BO, they represent one of the most powerful examples of the variational inference (see chapter 4). They are furthermore an instance of so-called *kernel methods* which is as powerful as widely used. The elegance comes from the efficient application of a feature transformation of the input data. In this way, the data which typically resides in a representation that is not amenable to treat, get mapped into a domain where they are easier to analyze.

The mentioned methods are discussed in more detail across the Lecture Notes. The following sections constitute a primer of the standard ML models, describing basic approaches like linear and logistic regression, linear support vector machines (SVMs), and continue into the DL regime with description of NNs with focus on convolutional neural networks (CNNs) and autoregressive neural networks (ARNNs).

2.4.1 Linear (ridge) regression

Before diving into the details of the topic, let us restate the problem of regression sketched in section 1.4. We encounter a labeled data set $\mathcal{D} = \{(\boldsymbol{x}_i, y_i)\}_{i=1}^{n} \equiv \{(\boldsymbol{X}, \boldsymbol{y})\}$ of observations that are derived from an underlying function f, possibly subject to some (stochastic) noise ϵ. The latter is often assumed to be sampled from an unknown noise distribution $\mathcal{E}$, i.e., $\epsilon \sim \mathcal{E}$:

$$y_i = f(\boldsymbol{x}_i) + \epsilon_i \quad \forall \, (\boldsymbol{x}_i, y_i) \in \mathcal{D}. \tag{2.22}$$

The function f is generally unknown and our goal is to infer it. To this end, we build a regression fit of the data $\hat{f}$ such that $\hat{f}(\boldsymbol{x}) \approx y$.[21]

Arguably, the simplest parametrized fitting method one can produce is a linear model, where we seek to find parameters $\boldsymbol{\theta} \in \mathbb{R}^d$ that linearly connect the input variable $\boldsymbol{x}$ with the prediction $\hat{y}$, i.e.,

$$\hat{y} = \sum_{i=1}^{d-1} \theta_i x_i + b \equiv \sum_{i=0}^{d-1} \theta_i x_i = \boldsymbol{x}^{\mathsf{T}} \boldsymbol{\theta}. \tag{2.23}$$

To shorten the notation, we have absorbed the constant $\theta_0 = b$, the so-called *bias*, in the definition of the input $\boldsymbol{x}$ via setting $x_0 = 1$. Up to now, the linear model aims to find a hyperplane[22] through the data points. We can extend the model by a non-linear transformation

---

[21] For the sake of simplicity, we consider one-dimensional output. The following derivations, however, can easily be extended to multi-dimensional output as well.

[22] For one-dimensional input and output, the hyperplane simply is a line.

ϕ of the input, i.e., $x \mapsto \phi(x)$. This is still linear regression as we maintain linearity in the parameters θ that we seek to optimize. As an example of a non-linear transformation, the map $\phi_p : x \mapsto (1, x, x^2, x^3, \ldots, x^p)$ promotes our model to polynomial regression up to the p-th degree. To simplify the notation in the rest of the section, we consider the case where no feature maps are applied. The inclusion of a feature map is central element of chapter 4 and discussed there to a far greater extent.

Once a certain hyperplane is defined, by means of its parameters θ, we need to define a quality measure that compares our predictions to their corresponding ground-truth values. That is, we have to choose a suitable loss function $\mathcal{L}$. The most conventional choice for the loss is the mean-squared error (MSE) over the data set $\mathcal{D}$ as

$$\mathcal{L}_{\text{MSE}}(\theta \mid \mathcal{D}) := \frac{1}{n} \sum_{i=1}^{n} (y_i - x_i^\mathsf{T} \theta)^2 = \| y - X^\mathsf{T} \theta \|^2. \tag{2.24}$$

To attain the right-most equation, we stack all inputs x_i vertically next to each other, to form the matrix $X \in \mathbb{R}^{(d-1) \times n}$. The same procedure is applied to y_i, now to be promoted to y. The last step allows to find the set of parameters θ that minimize the MSE. This yields the least-squares estimator (for the derivation, see the first half of appendix B)

$$\theta_{\text{MLE}} = (X^\mathsf{T} X)^{-1} X^\mathsf{T} y = X^+ y, \tag{2.25}$$

where the notation X^+ denotes the Moore-Penrose inverse [58].

To see why we have to employ the MSE as the choice of our loss function, we have to consider the likelihood of the labeled data given the model's parameters $p(y \mid X, \theta)$. To this end, we assume that our targets y are actually sampled from a Gaussian with a mean given by our linear model, i.e., $x^\mathsf{T} \theta$ with some variance σ which models the noise on the data. We can then write the likelihood of observing the targets y given the locations X and model parameters θ as

$$p(y \mid X, \theta) = \mathcal{N}(y \mid X^\mathsf{T} \theta, \sigma^2 \mathbb{1}) \tag{2.26}$$

$$= \prod_{i=1}^{n} \mathcal{N}(y_i \mid x_i^\mathsf{T} \theta, \sigma^2). \tag{2.27}$$

In the last step, we furthermore assumed a data set $\mathcal{D}$ of i.i.d. random variables to factorize the multivariate Gaussian. A common assumption is to regard the observed data set $\mathcal{D}$ as the most probable one of the underlying linear model. We therefore seek to maximize the likelihood in order to find the set of parameters θ that have led to the most probable data. This is the idea of maximum likelihood estimation (MLE). Its estimator is defined as the argument of the maximum likelihood of eq. (2.26). We can modify this estimator by including a logarithm and obtain:

$$\theta_{\text{MLE}} := \arg \max_{\theta} \ p(y \mid X, \theta) \tag{2.28}$$

$$= \arg \max_{\theta} \ \log p(y \mid X, \theta) \tag{2.29}$$

$$= \arg \max_{\theta} \left(-\frac{1}{2\sigma^2} \sum_{i=1}^{n} (y_i - x_i^\mathsf{T} \theta)^2 + \text{const.} \right) \tag{2.30}$$

$$= \arg \min_{\theta} \left(\sum_{i=1}^{n} (y_i - x_i^\mathsf{T} \theta)^2 \right) \equiv \arg \min_{\theta} (\mathcal{L}_{\text{MSE}}). \tag{2.31}$$

The constants appearing in eq. (2.30) can be ignored as they are independent of $\boldsymbol{\theta}$. From the previous results, we hence see that the i.i.d.-assumption, together with the concept of MLE leads to the MSE as the preferred loss function.

However, the estimator fully ignores the data noise modelled by σ^2, as it was also drop out in the maximization procedure of the $p(\boldsymbol{y} \mid \boldsymbol{X}, \boldsymbol{\theta})$. Thus, even if we correctly chose the model, the minimization procedure of the MSE in eq. (2.24) typically performs well on the provided data set $\mathcal{D}$ but not on previously unencountered data points. The reason is *overfitting* which we already introduced as a concept in section 2.2. This phenomenon occurs as we incorporate the noise on the targets in our model parameters $\boldsymbol{\theta}_{\text{MLE}}$. As a way out to this issue, we have introduced the notion of regularization. In our linear model (2.23), we can introduce regularization by means of Bayesian inference. This means, instead of maximizing merely the data likelihood in eq. (2.26), we encode any prior knowledge of the model[23] into a so-called *prior* distribution $p(\boldsymbol{\theta})$. By virtue of the Bayes theorem from eq. (2.19), we can calculate the *posterior* distribution[24] $p(\boldsymbol{\theta} \mid \boldsymbol{X}, \boldsymbol{y})$ over the parameters given the data set and maximize this quantity, instead. This yields the maximum a posteriori estimator (MAP) defined as

$$\boldsymbol{\theta}_{\text{MAP}} := \arg\max_{\boldsymbol{\theta}} \; p(\boldsymbol{\theta} \mid \boldsymbol{X}, \boldsymbol{y}) \tag{2.32}$$

$$= \arg\max_{\boldsymbol{\theta}} \; \frac{p(\boldsymbol{\theta})p(\boldsymbol{y} \mid \boldsymbol{X}, \boldsymbol{\theta})}{p(\boldsymbol{X}, \boldsymbol{y})}, \tag{2.33}$$

where we have used the Bayes theorem from eq. (2.19) in the second step. The denominator does not depend on $\boldsymbol{\theta}$ and can therefore be ignored. For the likelihood, we keep the assumptions introduced for eq. (2.26). As the prior, we now draw the parameter values from a Gaussian distribution centered around $\boldsymbol{0}$ with some variance τ^2, i.e.,

$$p(\boldsymbol{\theta}) = \mathcal{N}(\boldsymbol{\theta} \mid \boldsymbol{0}, \tau^2 \mathbb{1}). \tag{2.34}$$

The product of two Gaussian distribution is Gaussian itself, hence allowing us to apply the same trick with the logarithm as before in eq. (2.29). We arrive at

$$\boldsymbol{\theta}_{\text{MAP}} = \arg\min_{\boldsymbol{\theta}} \left(\mathcal{L}_{\text{MSE}}(\boldsymbol{\theta} \mid \mathcal{D}) + \frac{\sigma^2}{\tau^2} \|\boldsymbol{\theta}\|^2 \right) = \left(\boldsymbol{X}^\intercal \boldsymbol{X} + \frac{\sigma^2}{\tau^2} \mathbb{1} \right)^{-1} \boldsymbol{X}^\intercal \boldsymbol{y}. \tag{2.35}$$

We can picture the parameter $\lambda = \sigma^2/\tau^2$ as a signal-to-noise ratio which effectively penalizes large magnitudes of the parameter values by the additional term in the loss function. Hence, λ is referred to as the *regularization strength*. This particular choice of the loss term is called *Tikhonov* regularization. Its corresponding MAP is also called the linear *ridge regression* estimator.

Let us compare the two estimators of eqs. (2.25) and (2.32). The additional term in the estimator stems from the fact that we take both the data noise as well as a parameter constraint into account. Both are discarded in the limit of $\tau \to \infty$[25], where we have $\boldsymbol{\theta}_{\text{MAP}} \to \boldsymbol{\theta}_{\text{MLE}}$.

> In order to consider the underlying noise in the training data, we have to constrain the linear model. Dealing with overfitting in such a way is usually referred as (ridge) regression.

---

[23]The prior knowledge correspond to our initial assumptions on the parameters before we are handed any data.
[24]We call it posterior because it is computed *after* the observation of the data set $\mathcal{D}$.
[25]This corresponds to a uniform prior of the parameters $\boldsymbol{\theta}$.

Finally, the choice of the prior in eq. (2.34) is by no means unique. In fact, there is a plethora of regularization ideas and corresponding penalty terms [7]. An easy variation could, for example, be to replace the ℓ_2-norm with an ℓ_1-norm. This is achieved by choosing a Laplace distribution for the parameters as the prior. The corresponding estimator is the result of least absolute shrinkage and selection operator (LASSO) regression [59]. Because the ℓ_1-norm punishes already small parameter values severely, it favors sparse solutions for the parameters $\boldsymbol{\theta}$, instead. This can, for example, be desired to detect the significant features out of a pool of possible candidates in certain tasks [60].

2.4.2 Logistic regression

In the previous section, we have discussed the linear regression problem. The discussion can be extended to the classification task in a very straightforward way as we show in the following.

> The basic idea of *logistic regression* is to adapt the linear model such as to estimate the probability that a given input falls in either one of the possible classes.

Let us consider two classes K_1 and K_2 and an input $\boldsymbol{x}$ to classify. We introduce the class-conditional densities $p(\boldsymbol{x}|K_i)$ and the corresponding baseline class prior probabilities $p(K_i)$. Bayes' theorem of eq. (2.19) immediately gives us an expression for the posterior probability that the input belongs to class K_1. It reads as

$$
\begin{aligned}
p(K_1 \mid \boldsymbol{x}) &= \frac{p(\boldsymbol{x} \mid K_1)p(K_1)}{p(\boldsymbol{x} \mid K_1)p(K_1) + p(\boldsymbol{x} \mid K_2)p(K_2)} \\
&= \frac{1}{1 + \exp(-\theta)} =: \varsigma(\theta) \\
\text{where } \theta &:= -\log\left(\frac{p(\boldsymbol{x} \mid K_2)p(K_2)}{p(\boldsymbol{x} \mid K_1)p(K_1)}\right)
\end{aligned}
\tag{2.36}
$$

and equips us with the *logistic sigmoid* function ς that maps any real-valued input θ to the interval $[0, 1]$. We can now use the linear model (or any other ML model) to yield a value for θ and map it to the corresponding posterior probability. This additional layer turns the regression model into a classifier.

In order to extend the situation to more than two classes, we perform a similar reformulation as done in eq. (2.36). In this case, one obtains the *softmax* function

$$
p(K_k \mid \boldsymbol{x}) = \frac{\exp(\theta_k)}{\sum_i \exp(\theta_i)} =: \text{softmax}(\boldsymbol{\theta})
\tag{2.37}
$$

that maps the output score vector $\boldsymbol{\theta}$ to a proper probability density over all classes at once. Its name is derived from the fact that in the limiting case of $\theta_i \gg \theta_k \ \forall k \neq i$, the softmax converges to the maximum function, i.e., softmax $\to$ max.

In both cases, the model's parameters are trained by parsing the output scores through either eq. (2.36) or eq. (2.37) to obtain and subsequently minimize the loss in eq. (2.2) or eq. (2.3), respectively. An interesting aspect of any classifier is how it draws a line between data from two different phases, known as the *decision boundary*. In case of the linear model the decision boundary is linear, which is a simple consequence of the model choice. Because this boundary is derived from the likelihood of the data due to the particular choice for the loss function, the model is highly prone to outliers. One way to circumvent this issue is to take a geometric approach in finding the decision boundary. This is done in the next section.
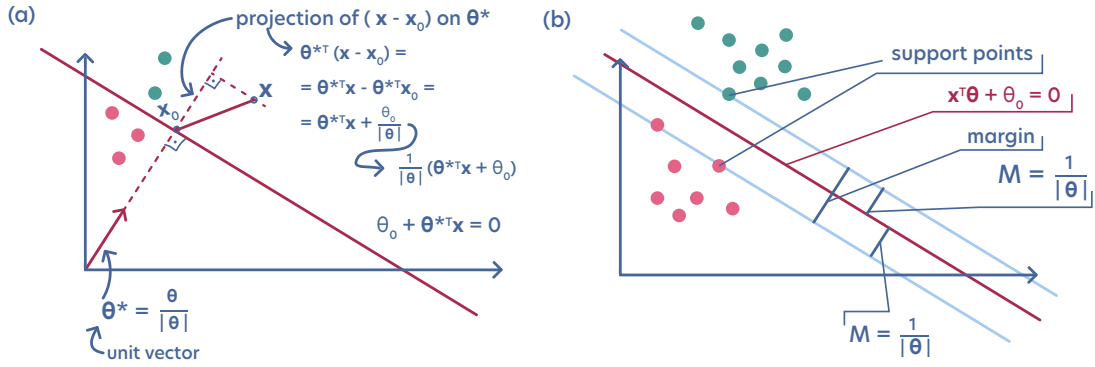
Figure 2.5: Geometric construction of an SVM in a 2D problem. (a) Purple line, described fully by $\boldsymbol{\theta}$, is an exemplary hyperplane separating two classes of data (pink and green points). (b) The optimal hyperplane maximizes the margin, M, between itself and the support points which are training data points closest to the hyperplane.

2.4.3 Support vector machines

The alternative approach to the classification, instead of maximizing a model likelihood, is to analyze the geometrical properties of the data. Take a look at the the linearly separable problem presented in fig. 2.5. In panel (a), you see that to classify two types of data, we can draw a line (or more generally, a hyperplane) which separates the training data. Then, instead of making probabilistic predictions on test data, we can just check on which side of the hyperplane the test points are. Panel (a) contains also a simple geometric analysis which shows that the equation for the hyperplane separating the data is $\boldsymbol{\theta}^{\mathrm{T}} \boldsymbol{x} + \theta_0 = 0$. The unit vector in the direction perpendicular to the hyperplane is $\boldsymbol{\theta}^* = \boldsymbol{\theta}/|\boldsymbol{\theta}|$, and the shortest distance between a point $\boldsymbol{x}$ and the hyperplane is

$$d(\boldsymbol{x}, \boldsymbol{\theta}) = \left(\boldsymbol{\theta}^{\mathrm{T}} \boldsymbol{x} + \theta_0\right)/|\boldsymbol{\theta}|. \tag{2.38}$$

If we do not impose any additional constraints, there are many possible hyperplanes separating the data into the two classes. How do we choose the best one? One way is by maximizing the distance between the hyperplane and the data points. Therefore, let us formulate the constraint that all data points need to be at least the distance M away from the hyperplane. The data points separated from the hyperplane exactly by M, hence the closest to the hyperplane, become the support points presented in fig. 2.5(b). The classification problem boils down to finding the $\boldsymbol{\theta}$ which maximizes the margin. From eq. (2.38), we can write:

$$y_i \left(\boldsymbol{\theta}^{\mathrm{T}} \boldsymbol{x}_i + \theta_0\right) \geq M|\boldsymbol{\theta}|, \tag{2.39}$$

where elements of the vector of observations y_i are ± 1 in order to ensure that this formulation is always positive, regardless of the class to which the data point belongs. Note that if we scale each of the $\boldsymbol{\theta}$ coefficients by the same factor, the above (in)equality still holds. Therefore, we can arbitrarily rescale $\boldsymbol{\theta}$ and θ_0 to have $|\boldsymbol{\theta}| = \frac{1}{M}$ that leads to the following canonical condition for every data point in the data set:

$$y_i \left(\boldsymbol{\theta}^{\mathrm{T}} \boldsymbol{x}_i + \theta_0\right) \geq 1. \tag{2.40}$$

Therefore, to find the optimal hyperplane, we need to minimize $|\boldsymbol{\theta}|$, while ensuring $y_i \left(\boldsymbol{\theta}^{\mathrm{T}} \boldsymbol{x}_i + \theta_0\right) \geq 1$ for every data point. This is the optimization with constraints, and we

can use Langrange multipliers for that! Minimizing $|\boldsymbol{\theta}|$ with constraints comes down to minimizing the following Lagrange function:

$$L = \frac{1}{2}|\boldsymbol{\theta}|^2 - \sum_i^n \alpha_i \left[y_i \left(\boldsymbol{\theta}^{\mathrm{T}} \boldsymbol{x}_i + \theta_0 \right) - 1 \right], \tag{2.41}$$

where the Lagrange multipliers α_i are chosen such that

$$\alpha_i \left[y_i \left(\boldsymbol{\theta}^{\mathrm{T}} \boldsymbol{x}_i + \theta_0 \right) - 1 \right] = 0 \text{ for each } i. \tag{2.42}$$

Interestingly, the loss function in eq. (2.41) with the above constraints is a so-called quadratic program as the function itself is quadratic and the constraints are linear with respect to $|\boldsymbol{\theta}|$. It has, therefore, a global minimum found usually via so-called sequential minimal optimization [61] instead of any iterative gradient-based methods.

Also note that the condition put on the Lagrange multipliers in eq. (2.42) implies the following:

- If $\alpha_i > 0$, then $\left[y_i \left(\boldsymbol{\theta}^{\mathrm{T}} \boldsymbol{x}_i + \theta_0 \right) - 1 \right] = 0$, which means the point $\boldsymbol{x}_i$ lies on the boundary of the margin slab.

- If $\left[y_i \left(\boldsymbol{\theta}^{\mathrm{T}} \boldsymbol{x}_i + \theta_0 \right) - 1 \right] > 0$, the points is outside the margin and $\alpha_i = 0$.

Therefore, the final model coefficients are given only in terms of such points $\boldsymbol{x}_i := \boldsymbol{x}_{s,i}$ that lie on the boundary of the slab. These points are the support points and give the SVM its name. The SVM problem relies then on minimizing L^{26} numerically to find the coefficients α_i which are non-zero only for support points.

> Therefore, classification with support vector machines (SVMs) consists in finding the optimal hyperplane separating the data by maximizing the margin between the hyperplane and the support points which are data points closest to the decision boundary. This optimization problem with constraints is solved with Lagrange multipliers and is convex.

With the found optimal hyperplane $\hat{f}$ we can then make predictions at an arbitrary test point $\boldsymbol{x}^*$:

$$\hat{f}(\boldsymbol{x}^*) = \boldsymbol{\theta}^T \boldsymbol{x}^* + \theta_0 = \sum_i^n \alpha_i y_i \boldsymbol{x}_i^T \boldsymbol{x}^* + \theta_0 = \sum_i \alpha_i y_i \boldsymbol{x}_{s,i}^T \boldsymbol{x}^* + \theta_0, \tag{2.43}$$

where the last summation is only over support points. Finally, in order to turn this value into a class prediction, we take the sign of $\hat{f}$ as the corresponding class label.

Until now, we only considered binary classification problems of linearly separable data sets. There are two obvious ways on how to extend the SVM to classification problems that have more than two classes, say K many. The first, known as the one-to-one approach, breaks the multi-class situation down to a binary classification between every combination of two classes, individually. This way, we are required to train $\mathcal{O}(K^2)$ SVMs to make predictions afterwards. This numerical overhead is eased in the second approach: one-to-rest classification. Here, we only require a single SVM for each of the K classes that simply predicts whether a test point belongs to the class or not. As a second extension possibility, we can ask about the classification problem that is not linearly separable. We explain this case later in section 4.2.2.

---

[26] In practice, rather than minimizing L, one maximizes a Lagrange dual, L_D, which provides the lower bound for L. We explain it in more detail in section 4.2.2.
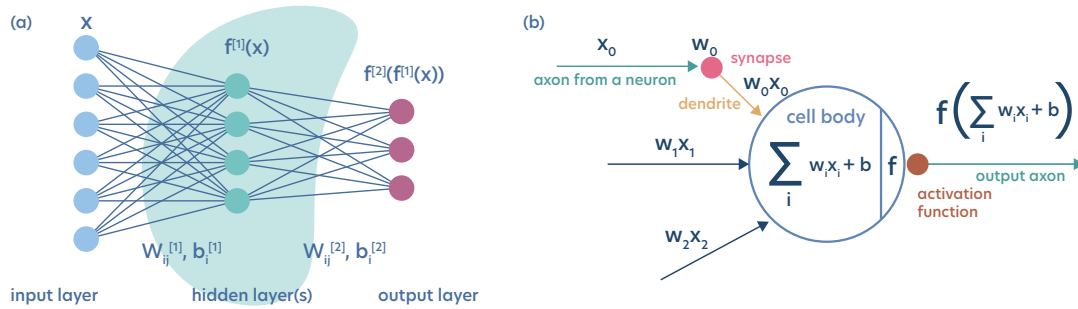
Figure 2.6: Illustration of (a) a typical fully-connected (here: single-layer) NN and (b) one of its neurons (simple perceptron) and the computations associated with it.

2.4.4 Neural networks

Artificial neural networks (ANNs), typically referred to as neural networks (NNs), are a large class of models used to process data in ML tasks. They are parametrized functions that are themselves composed of many simple functions. As the name suggests, ANNs were originally proposed by taking inspiration from the neural networks that constitute our brains. They are typically composed of interconnected layers that sequentially process information, see fig. 2.6. Each layer contains multiple nodes or units, also called *artificial neurons* or *perceptrons*[27]. Each node i takes as input a vector $x = (x_1, x_2, \ldots, x_m) \in \mathbb{R}^m$, corresponding to the activations of all nodes in the previous layer. Each node outputs a scalar value $y \in \mathbb{R}$ (its activation) that is computed as $y = f(w_i^\mathsf{T} x + b_i)$, where the parameters $w_i \in \mathbb{R}^m$ and $b_i \in \mathbb{R}$ are the node's weights and bias, respectively. The weights of a node control the strength of its connection to the neurons of the previous layer. The function f is a non-linear function called *activation function*. Common choices are the rectified linear unit (ReLU)

$$f(x) = \max(0, x), \tag{2.44}$$

the sigmoid function (eq. (2.36)), or the tanh function

$$f(x) = \tanh(x) = \frac{e^x - e^{-x}}{e^x + e^{-x}}. \tag{2.45}$$

The first layer is called input layer, where the activations of its nodes are set according to the vector x encoding the input data. The last layer is called output layer and the activations of its nodes constitute the output of the NN. All intermediate layers are called hidden layers. NNs where each node is by default connected to all nodes in the subsequent layer are referred to as *fully connected*. The number of layers, nodes, and their connections is known as the *architecture* of an NN. NNs are considered deep if they are composed of many hidden layers[28]. ML methods based on deep neural networks (DNNs) as models fall under the name of DL [7].

A central question regarding NNs is what types of functions they can represent (recall our previous discussion on traditional ML vs. DL). First, consider an NN without its nonlinear activation functions. The function realized by such an NN is a simple affine map, i.e., consists of multiplying the input by a weight matrix and adding to it an additional bias vector.

---

[27]Here and in the following, we refer to the modern perceptron introduced by Minsky and Papert [62] which can contain smooth activation functions in contrary to the Heaviside step function utilized in Rosenblatt's original perceptron [63].

[28]There is no clear consensus on the threshold of depth that divides shallow and deep NNs.

Thus, the addition of nonlinear activation functions is crucial for NNs to be able to represent a larger class of functions. For example, Kolmogorov and Arnold [64] have shown that any arbitrary continuous high-dimensional function can be expressed as a linear combination of the composition of a set of nonlinear functions

$$f(\boldsymbol{x}) = \sum_{q=0}^{2m} \Phi_q \left(\sum_{p=1}^{m} \phi_{q,p}(x_p) \right), \tag{2.46}$$

where $\Phi_q, \phi_{q,p}$ are nonlinear functions that act on the individual components of the input $\boldsymbol{x} \in \mathbb{R}^m$. This means that we could represent any function $f(\boldsymbol{x})$ with a polynomial number $O(m^2)$ of one-dimensional nonlinear functions. This strongly resembles the structure of an NN with two hidden layers. Note, however, that the nonlinear functions must be carefully chosen depending on the target function. In NNs, the non-linearities are typically fixed $\Phi_q = \phi_{q,p} \; \forall q, p$. It turns out that fully-connected NNs composed of a single hidden layer and nonlinear activation functions are also *universal function approximators*. That is, given that the target function is reasonably well-behaved it can be approximated to any desired accuracy given that its hidden layer contains enough nodes [7, 65, 66]. Note that this may still require a hidden layer that is exponentially large in the number of nodes. This raises the question what one can achieve with NNs that have multiple hidden layers.

The universal approximation theorem guarantees that there exists an NN, i.e., choice of NN architecture, as well as weights and biases, which approximates the given target function arbitrarily well. However, it does not guarantee that we are able to find this choice. It turns out that, in practice, DNNs are capable of solving many problems with much less nodes, i.e., trainable parameters, compared to shallow NNs. In that sense, choosing a DNN over a shallow NN yields a useful prior over the space of functions which the NN can approximate.

The parameters of an NN are typically optimized by gradient-based methods, such as stochastic gradient descent (SGD) or Adam, to minimize a given loss function $\mathcal{L}$ (see section 2.1). Computing the gradient of the loss function with respect to each parameter numerically is typically done by means of *backpropagation* [67]. In contrast, when evaluating an NN with a given input, information flows forwards through the networks. As such, this is called *forward propagation*. The backpropagation algorithm is part of a larger class of approaches to calculate numerical derivatives accurately, efficiently, and in an automated fashion, known as automatic differentiation (AD). These methods are described in detail in section 7.1.

Convolutional neural networks Convolutional neural networks (CNNs) are a special class of NNs where, in contrast to fully-connected NNs, not every node is connected to all nodes of the subsequent layer. Instead, convolutions replace matrix multiplications in the computation of the activations of subsequent layers. This reduction of the number of parameters per layer allows us to build and train deeper architectures. Moreover, this model architecture makes use of the spatial hierarchy typically present in input data. In image-like data, pixels that are spatially close to each other generally show more correlation than pixels which are far apart. By replacing the *full* connectivity of the standard NN with multiple convolutional layers with *local* connectivity, CNNs make use of this vanishing correlation at large distances.

Figure 2.7 illustrates the working principle behind a CNN – the *convolutions*: A filter (also called kernel) with trainable weights is slid across a given layer. The resulting activation are then obtained by element-wise multiplication of the neuron activations and the filter's weights, followed by an overall sum and the application of a non-linear activation function. This filtering causes the NN to be only locally connected (as opposed to fully connected). Note that the number of weights, therefore, does not depend on the size of the input, but rather on the size
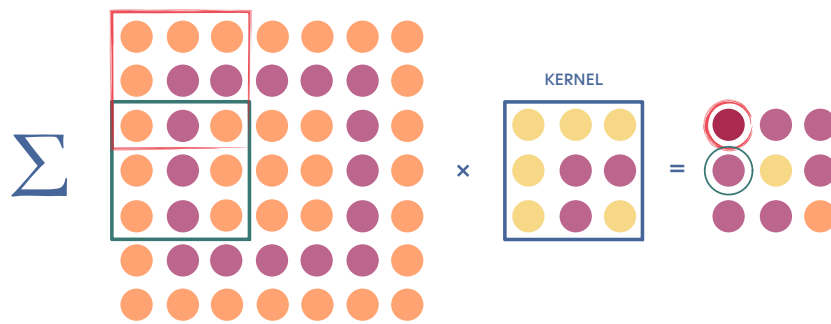
Figure 2.7: Schematic representation of a convolutional layer in two dimensions: A kernel/filter of fixed size (here 3x3) is convolved with a two-dimensional input image. The grey scale corresponds to the magnitude of the neuron activations and kernel (filter) weights.

of the filter. The filter size controls the range over which spatial correlations in the input data are registered. One can build one- or two-dimensional CNNs (with filters of corresponding dimension) depending on whether the input data is naturally represented as a vector or a matrix. In a typical CNN, after application of several such convolutional layers, the activations are flattened to a single feature vector. This corresponds to a lower-dimensional representation of the input data that is further processed using a fully-connected architecture. To reduce the dimension of the data representation resulting from the application of convolutional layers, one typically also uses *pooling operations*. These combine the activations resulting from applications of close-by filters, e.g., by taking the maximum or mean.

2.4.5 Autoencoders

Autoencoders (AEs) [68, 69] are widely used ML tools for unsupervised learning. Unlabeled data (e.g., images, audio signals, texts) may often be high-dimensional, hence very difficult to analyze and to extract any patterns when working in the data domain. However, dimensionality reduction techniques (see, e.g., section 3.2.1) represent an advantageous approach to extract useful knowledge from such unlabeled data. In a nutshell, the goal of AEs is to precisely *encode* some knowledge, patterns, attributes of the given input data into some latent variable[29] on a lower dimensional manifold. By means of a so-called bottleneck structure (as shown in fig. 2.8), the latent representation of the input data is the mapped back into the input space (decoding) by leveraging on the information extracted by the architecture at the time of feature extraction (encoding). This bottleneck architecture is based on two NNs performing the encoding and decoding parts. Such NNs are trained by minimizing the so-called error reconstruction loss, meaning that the optimal setup for such encoder-decoder pair is the one for which the output x_{rec} is reconstructed as similar as possible to the original input data x. These NNs are jointly optimized with an iterative process. In other words, for a given set of possible encoders and decoders, we are looking for the pair that keeps the maximum of information when encoding and, so, has the minimum of reconstruction error when decoding. This joint optimization forces the model to maintain only the variations in the data required to reconstruct the input without holding on to redundancies within the input. Henceforth, likewise in PCA, only the most relevant features describing the data are distilled during the learning process. One important remark is that the bottleneck is a key attribute of such a network

---

[29] A latent variable is a random variable that we cannot observe directly. In this case, we call variables latent because we do not observe them in the data.
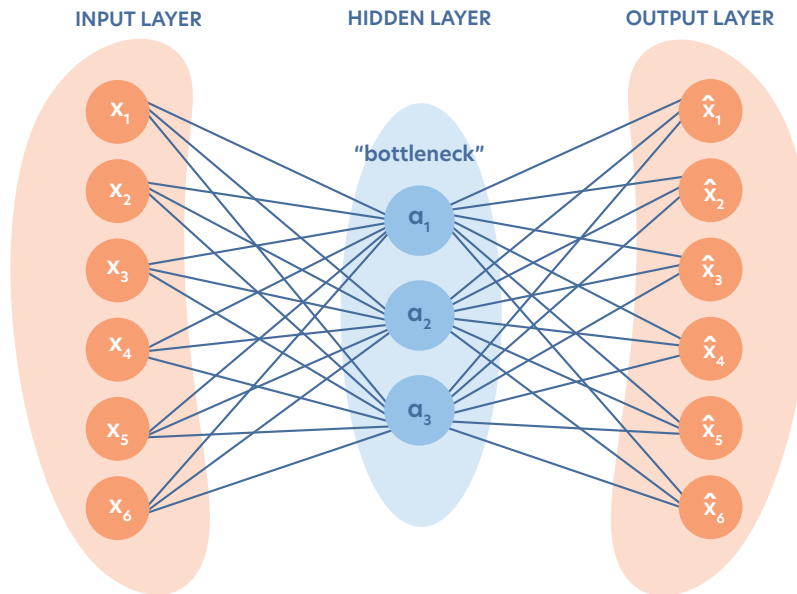
Figure 2.8: Example of the bottleneck architecture of an AE. The input is connected to the bottleneck by an encoder-NN on the left while the decoder-NN connects it with the output on the right.

design; without the presence of an information bottleneck, our network could easily learn to simply memorize the input values by passing these values along through the network. On top of this, by relying on such a pair of NNs, AEs are inherently more flexible yet expressive compared to standard dimensionality reduction algorithms (e.g., PCA) which rely on sub-manifold projection of input data through constrained linear or non-linear transformations.

There are several kinds and variations of AEs, all of which share this fundamental bottleneck property as their base structure. A concrete example of a further development of AEs in the context of generative models are variational autoencoders (VAEs). As the name suggests, VAEs [68] have to do with variational inference. What they do in practice is to train the encoding-decoding pair in a slightly more complicated way. The knowledge extracted from the data in the encoding part is nested into a base probability density (e.g., initialized as a Gaussian) which is trained and tuned in such a way that it becomes a good approximation (sampler) of the underlying data distribution. Once the training is done, the latent representation of the input data becomes thus a probability density from which one can sample new, unseen data which resembles the one used for training, as being characterized by the same learned features. As such, the goal here is not to reconstruct the input data from the extracted knowledge anymore, but to produce new samples as similar as possible to the training set. Further example of AEs are: sparse AEs [70, 71], denoising AEs [72], importance weighted AEs [73], etc.

2.4.6 Autoregressive neural networks

To complete this section, let us briefly present autoregressive neural networks (ARNNs). These networks were originally inspired by autoregressive models in statistics and economics, which one can employ to predict future values of a time-series (for instance, a financial asset). ARNNs are formalized for the general task of density estimation [74], in which the goal is to estimate a complex, high-dimensional probability density function, see als section 7.2. They are con-
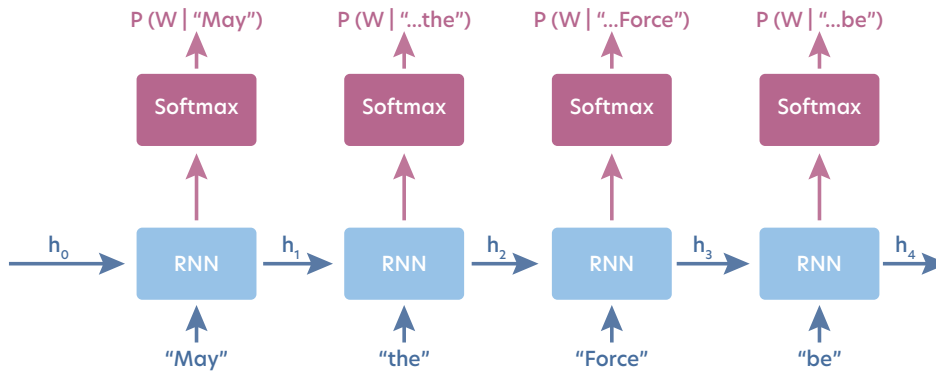
Figure 2.9: Pictorial representation of an recurrent neural network (RNN). One can directly see that the model is autoregressive, as conditional probabilities only depend on the previous input data. Here, the blue box represents a non-linear transformation as described in the main text. The task here is to be able to generate meaningful sentences. The input data is a sentence, and the output is the probability for the word "W" to be the next word in the sentence, conditioned on previous words. The h_i are the hidden vectors that take into account memory effects inherited from previous RNN transformations. Adapted from [75].

structed to satisfy the following property on the outputs of the network, satisfying a conditional structure

$$f_{\boldsymbol{\theta}}(\boldsymbol{x}) = \prod_{i=1}^{m} f_i(x_i \mid x_{i-1}, \ldots, x_1) \tag{2.47}$$

with $\boldsymbol{x} = (x_1, x_2, \ldots, x_m)$ the inputs for the model. In the case of time-series, the inputs x_i would be values of a variable at times t_i, and the model f tries to predict future values based on past ones. A generic example of such networks is the recurrent neural network (RNN) that was popularized in the context of natural language processing tasks. The main idea behind this class of models is that information "loops back" into the model, introducing correlations between different parts of the network, as opposed to feed-forward networks. Broadly speaking, a sentence has a causal order, but the correlations between words is not necessarily highest between words that are close together, hence the idea of introducing a back loop, with a memory can be understood somewhat intuitively. The long-short-term memory (LSTM) is an extension of this idea with two memory length scales (long- and short-term), and was also found to be successful for such tasks [76]. A sketch of an RNN is presented in fig. 2.9, with an example use-case from a language processing task. The goal here is to predict the next word in the sentence, based on previous words. The parameters of such a network are hidden in the RNN cell, and take part in a nonlinear transformation given by:

$$h_i = \varsigma(\boldsymbol{W}_h \boldsymbol{h}^{(i-1)} + \boldsymbol{W}_i \boldsymbol{x}^{(i)})$$

with $\boldsymbol{W}_h$ and $\boldsymbol{W}_i$ two weight matrices, $\boldsymbol{h}^{(i)}$ the i-th hidden vector, that represents information coming out of the previous cells, $\boldsymbol{x}^{(i)}$ the i-th element of the input data, and ς some nonlinear activation function [30]. For words, $\boldsymbol{x}^{(i)}$ represents the i-th word of the sentence that is encoded in some form (for example, using a one-hot encoding). Note that there exists several variants of this transformation, the most popular being the gated recurrent unit [77]. Recently,

---

[30]One also has to choose an initialization $\boldsymbol{x}^{(0)}, \boldsymbol{h}^{(0)}$, which are generally null vectors.

autoregressive models have been applied to different problems in physics such as statistical mechanics [78–80], quantum tomography [81], and ground state search [82]. In chapter 5 and section 7.2, we stress the advantages of using such models and present impressive results for quantum physics and chemistry that have been obtained using them.

Further reading

1. Bishop, C. M. (2006). *Pattern Recognition and Machine Learning*. Springer "Information Science and Statistics" series. The standard book about standard ML [83].

2. Goodfellow, I., Bengio, Y. & Courville, A. (2016). *Deep Learning*. An MIT Press book. One of the best textbooks on DL with explanation of all preliminaries [7].

3. Zhang, A. *et al.* (2021). *Dive into Deep Learning*. Interactive DL book with code, math, and discussions. Implemented with NumPy/MXNet, PyTorch, and TensorFlow [84].

4. Mehta, P. *et al.* (2019). *A high-bias, low-variance introduction to machine learning for physicists*. Phys. Rep. 810, 1-124. For the physicist-friendly introduction to ML [85].

5. Recordings of lectures on "ML for physicists" from 2020/21 and "Advanced ML for physics, science, and artificial scientific discovery" from 2021/22 by Florian Marquardt.

6. Introductory ML course developed specifically with STEM students in mind: ML-lectures.org and accompanying content: Neupert, T. *et al.* (2021). *Introduction to machine learning for the sciences*. arXiv:2102.04883 [86].

7. Carrasquilla, J. & Torlai, G. (2021). *How to use neural networks to investigate quantum many-body physics*. PRX Quantum 2, 040201. Tutorial on ML for selected physical problems with code [87].

3 Phase classification

One of the fields in physics where machine learning (ML), in particular neural networks (NNs), could be particularly useful is condensed-matter physics [30], which revolves around the study of the collective behavior of interacting particles. The difficulties associated with describing such systems arise due to the rapid growth of the number of degrees of freedom as the particle number grows leading to a large configuration space. The "standard" approach to circumvent these challenges is to find suitable order parameters – quantities which represent the important "macroscopic" degrees of freedom in a system without keeping track of all the microscopic details. The order as quantified by these order parameters naturally separates matter into different states, i.e., phases [88, 89]. For some systems, the order parameter is quite simple: in ferromagnets, for example, the order parameter simply corresponds to the magnetization which is given by a sum of *local* magnetic moments. In general, however, the identification of order parameters and the classification of matter into distinct phases are difficult tasks. Topological phases of matter, for example, are characterized by topological properties which are intrinsically *non-local*. The identification of order parameters represents a crucial first step toward understanding the physics that underlies a many-body system and identifying an appropriate order parameter for novel phases of matter typically requires lots of physical intuition and educated guessing.

On the other hand, in fields such as computer vision, it has been demonstrated that NNs can be trained to correctly classify intricate sets of labeled data naturally living in high dimensions (see MNIST [21] or CIFAR [23]). This motivates us to explore ML techniques as a novel tool to probe the enormous state space of relevant many-body systems that are currently intractable with other algorithms [31]. Among all potential applications of ML to condensed-matter physics, learning phases from (simulated or experimental) data is a particularly intriguing one: It could allow us to discover new phases and new physics without prior human knowledge or supervision. In what follows, we aim to give the reader a first introduction to the field of phase classification using ML.

3.1 Prototypical physical systems for the study of phases of matter

In the following, we briefly describe the two prototypical physical systems for which we demonstrate the task of phase classification in the next sections: the Ising model [90], which exhibits a *symmetry-breaking* phase transition and can be characterized by a simple local order parameter, as well as the Ising gauge theory (IGT) [91], which shows a *topological* phase without a local order parameter.[1]

3.1.1 Ising model

We consider the two-dimensional square-lattice ferromagnetic Ising model, which is one of the simplest classical statistical models to show a phase transition and serves as a simple description of ferromagnetism. Ferromagnetism arises when a collection of spins aligns, yielding a net magnetic moment that is macroscopic in size. In the Ising model , for each lattice site k there is a discrete (classical) spin variable $\sigma_k \in \{+1, -1\}$ leading to a state space of size 2^N given N lattice sites. The energy of a spin configuration is specified by the following Hamiltonian

$$H(\boldsymbol{\sigma}) = -J \sum_{\langle i,j \rangle} \sigma_i \sigma_j, \qquad (3.1)$$

---

[1]In the Landau paradigm of phase transitions [92, 93], changes between phases of matter are fundamentally connected to changes in the underlying symmetries. Interestingly, Landau's symmetry-breaking theory of phase transitions breaks down for topological phases of matter [94].
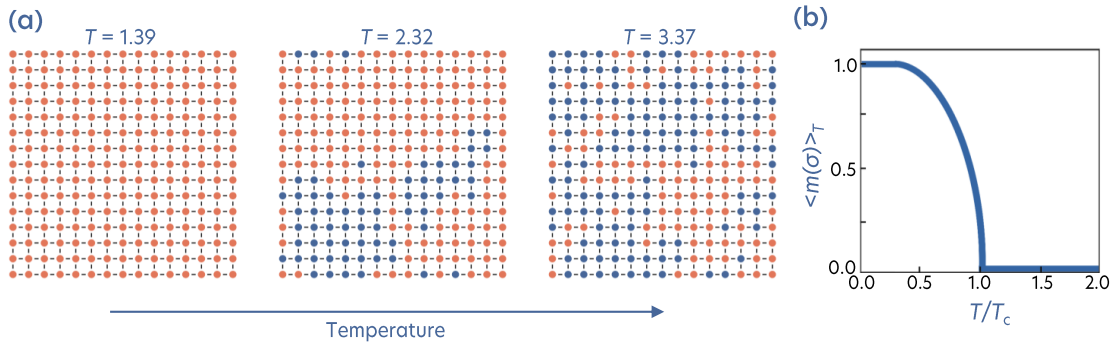
Figure 3.1: (a) Example spin configuration samples of the Ising model with $J = 1$ and $k_B = 1$ at various temperatures, where $T_c \approx 2.27$ (see eq. (3.5)). Here, the blue (orange) colored dots on each lattice site denote the value of the spin variable at that site $\sigma_k = 1$ ($\sigma_k = -1$). Panel reproduced from [32, Notebook A1]. (b) Mean magnetization per site $\langle m(\boldsymbol{\sigma}) \rangle_T$ of the Ising model as a function of the temperature T.

where the sum runs over nearest-neighboring sites (with periodic boundary conditions) and J is the interaction strength $J > 0$ (ferromagnetic interaction).[2] Let us assume that the system is at equilibrium at an inverse temperature $\beta = 1/k_B T$, where k_B is the Boltzmann constant and T the temperature. Then, the probability of finding the system in a state with a spin configuration $\boldsymbol{\sigma}$ is described by the Boltzmann distribution

$$P_T(\boldsymbol{\sigma}) = \frac{e^{-\beta H(\boldsymbol{\sigma})}}{Z_T}. \tag{3.2}$$

Here $Z_T = \sum_{\boldsymbol{\sigma}} e^{-\beta H(\boldsymbol{\sigma})}$ is the partition function, where the sum runs over all possible spin configurations. Example spin configurations of the Ising model at various temperatures are shown in fig. 3.1(a). Using eq. (3.2) the expectation value of a given observable $O(\boldsymbol{\sigma})$ can be expressed as

$$\langle O(\boldsymbol{\sigma}) \rangle_T = \sum_{\boldsymbol{\sigma}} P_T(\boldsymbol{\sigma}) O(\boldsymbol{\sigma}). \tag{3.3}$$

For example, the observable corresponding to the magnetization per site is given by

$$m(\boldsymbol{\sigma}) = \frac{1}{N} \sum_i \sigma_i. \tag{3.4}$$

In 1944, Onsager [90] obtained the following analytical expression for the critical temperature

$$T_c = \frac{2J}{k_B \ln(1 + \sqrt{2})}, \tag{3.5}$$

at which a phase transition between a *high-temperature paramagnetic* (disordered) phase and a *low-temperature ferromagnetic* (ordered) phase occurs, see fig. 3.1. For temperatures below the critical temperature T_c spontaneous magnetization occurs, i.e., the interaction is sufficiently strong to cause neighboring spins to spontaneously align leading to a non-zero mean magnetization. At temperatures above T_c thermal fluctuations completely dominate over any

---

[2]The case $J < 0$ corresponds to the two-dimensional square-lattice *antiferromagnetic* Ising model which exhibits a phase transition at the same critical temperature.
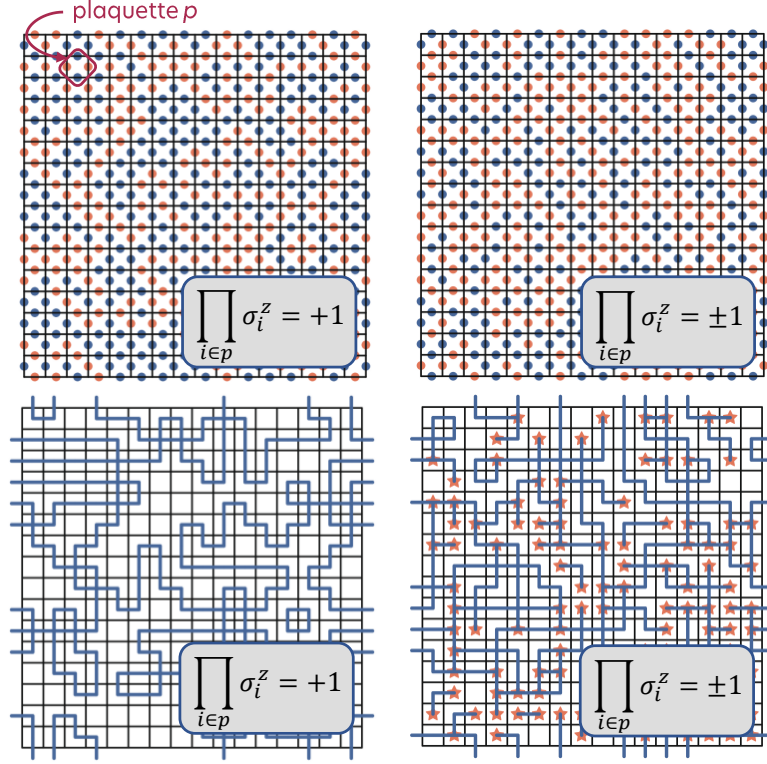
Figure 3.2: The upper panel show example spin configuration samples of IGT at $T = 0$ (left panels) and $T \to \infty$ (right panels) where local constraints are satisfied for all (some) plaquettes, respectively. An exemplary plaquette is marked in red. The lower panels show the corresponding dual representation, where the stars highlight loop breakage. Reproduced with [32, Notebook A1].

alignment of spins and a zero magnetization is observed. As such, the magnetization serves as an order parameter, which is zero within the disordered (paramagnetic phase) and approaches one in the ordered (ferromagnetic phase), see fig. 3.1(b).

3.1.2 Ising gauge theory

One of the most exciting research areas is the classification of phases that do not have a local order parameter, but rather a global one. Examples of systems that exhibit such phases are band topological insulators and topological superconductors [95]. Detecting topological phases is a challenging task from the experimental point of view because, in general, experimentalists have access only to local observables. In this context, ML techniques can be of great help [96–102].

The Ising gauge theory (IGT) [91] is the prototypical example of a system which exhibits a topological phase of matter. Like the Ising model, the IGT is also a classical spin model ($\sigma_k \in \{+1, -1\}$) defined on a square lattice (with periodic boundary conditions). Here, however, the spins are placed on the lattice bonds. It is described by the following Hamiltonian

$$H(\boldsymbol{\sigma}) = -J \sum_p \prod_{i \in p} \sigma_i, \tag{3.6}$$

where p refers to plaquettes on the lattice, see fig. 3.2. The ground state of this Hamiltonian is a highly degenerate manifold spanned by all states that meet the local constraint that the

product of spins along each plaquette is $\prod_{i \in p} \sigma_i = 1$. As such, this ground state corresponds to a topological phase of matter. In systems of finite size, the violations of the local constraints are strongly suppressed, and the system exhibits a slow transition from the low-temperature topological phase to the high-temperature phase with violated constraints. This allows for the definition of a crossover temperature T_c defined by the first appearance of a violated local constraint.[3]

There exists an interesting representation that highlights the topological character of the ground state of the IGT: connect the edges of the lattice that contain spins with the same orientation and form loops. The ground-state phase is then characterized by the property that all these loops are closed; the violation of a constraint results in the appearance of an open loop, see fig. 3.2. Looking at typical spin configuration samples of the IGT makes clear that its phases are hard to distinguish visually without prior knowledge of the local constraints or the corresponding dual representation. As such, IGT and other systems characterized by non-local and long-range correlations pose a hard problem for any phase classification algorithm.

3.2 Unsupervised phase classification without neural networks

Having introduced the Ising model and the IGT, let us discuss how we can classify their respective phases of matter. In particular, we are concerned with unsupervised ML algorithms. They work with training data that do not need to be labeled (see section 1.5). Unsupervised learning algorithms must *by itself* discover the relevant patterns in a training data set. As such, these algorithms represent a primary candidate for the autonomous discovery of new phases as they do not require prior labelling of the samples by the phase they belong to.

In particular, we discuss algorithms that perform a dimensionality reduction. In dimensionality reduction, we are concerned with projecting the input data into a lower-dimensional space. While any dimensionality reduction necessarily leads to an information loss, one aims to discard only information in the input data that is less relevant to the problem at hand. In particular, it is believed that real-world data often resides on a low-dimensional manifold within the original space [103]. For example, one expects that the set of images one would like to classify constitutes a small subspace of all possible images. In this case, the data can be effectively described by fewer degrees of freedom. Clearly, such an approach lends itself naturally to distinguish between different phases of matter and detect phase transitions in condensed matter systems: we want to discard the information-rich but complicated microscopic description of the system for the sake of a simpler macroscopic description, e.g., in the form of an order parameter.

Once we have performed the dimensionality reduction, we may already learn a lot about the given problem by visualising the data within the low-dimensional representation space. We tend to think that samples from the same phase of matter should be more similar to each other than to samples from another phase. If the dimension reduction technique preserves some of this similarity, we expect this to reveal itself in the data visualization. However, this is not guaranteed to work in general. We see an example of such a failure in the following.

Going beyond visualization, we can process the data further, e.g., using *clustering* methods. Clustering is one of the most fundamental unsupervised learning methods used to group unlabeled data into clusters of similar data points, where the similarity is assessed by a distance measure. In our context, the clusters would ideally correspond to the different phases of matter present in the data. There exist many different clustering algorithms suited for differ-

---

[3]Note that as we increase the system size $T_c \to 0$, i.e., the crossover temperature vanishes in the thermodynamic limit. As such, the IGT does not exhibit a phase transition at a non-zero temperature.

ent types of data, with k-means clustering being one of the simplest (see Ref. [85] for further details).

Clustering can, in principle, be performed without dimensionality reduction as a pre-processing step. However, dimensionality reduction may help in several aspects [85, 104]. Firstly, clustering typically relies on the Euclidean distance being a good measure of similarity.[4] The distance between two data points in the original high-dimensional representation may, however, not be particularly relevant as it is believed to often reside on a non-euclidean manifold. Dimensionality reduction techniques can allow for the identification of a low-dimensional Euclidean representation of the data. The Euclidean distance between data points within this representation is often physically more meaningful, resulting in a better clustering. Secondly, performing dimensionality reduction as a pre-processing step helps to alleviate the problems of the curse of dimensionality experienced when clustering data in high-dimensional spaces. Finally, identifying a low-dimensional representation also helps to better visualize and understand the clustering that is eventually obtained.

3.2.1 Principal component analysis

As an example, we consider principal component analysis (PCA) which is a common method to perform dimensionality reduction. PCA identifies mutually orthogonal directions, called principal components (PCs), in the data space along which the linear correlation in the data vanishes. We rank each PC based on the variance of the data along the corresponding direction. To reduce the dimensionality of our space, we discard the PCs along which the data shows the least variance. As such, in PCA directions along which the data exhibits a *large variance* are considered to contain the most *important information*. In our case, ideally the data (raw spin configuration samples) naturally splits into different clusters corresponding to the individual phases of the system when displayed in their low-dimensional representation.

To be more precise, we consider the case where we are given n data points $\{x_1, x_2, ..., x_n\}$ each living in a m-dimensional feature space $\mathbb{R}^m$ with zero mean $\bar{x} = \frac{1}{n} \sum_{i=1}^{n} x_i = 0$. Note that real-life data typically does not have zero mean. In this case, the data first needs to be transformed by subtracting the mean element-wise. We define the $n \times m$ design matrix $X = [x_1, x_2, ..., x_n]^{\mathsf{T}}$. The symmetric $m \times m$ empirical covariance matrix is then given as $\Sigma = \frac{1}{n} X^{\mathsf{T}} X$. Here, the i-th diagonal entry of the covariance matrix Σ_{ii} corresponds to the variance of the i-th feature over the entire data and the off-diagonal entries Σ_{ij} correspond to the covariance between feature i and feature j. The basis in which the correlations between features vanish corresponds to the eigenbasis of Σ in which Σ appears diagonal. Consequently, the problem of finding directions along which the linear correlation in the data vanishes reduces to diagonalizing Σ, i.e., finding its eigenvectors (or PCs) $\{v_1, v_2, ..., v_m\}$ and eigenvalues $\{\lambda_1, \lambda_2, ..., \lambda_m\}$. Here, the eigenvalue λ_i corresponds to the variance of the data along the direction given by v_i. We denote $\tilde{\lambda}_j = \lambda_j / \sum_{i=1}^{m} \lambda_i$ as the ratio of explained variance contained in the j-th PC. We refer to the appendix for a mathematical derivation of the procedure. Dimensionality reduction is then performed by selecting the first k PCs with the largest ratios of explained variance $\tilde{\lambda}$, and projecting the data into this space of reduced dimensionality. The projection is performed by the linear transformation $\tilde{X} = X\tilde{V}$, where $\tilde{V} = [v_1, v_2, ..., v_k]$ and $\tilde{X}$ is the projected design matrix. Note that one has to choose k, the number of PCs to keep. This can be done in an *ad-hoc* fashion that may be problem specific or, e.g., by choosing the minimal number of PCs such that $\sum_{i=1}^{k} \tilde{\lambda}_i \geq \tilde{\lambda}_{\mathrm{thresh}}$, where $\tilde{\lambda}_{\mathrm{thresh}}$ is the desired threshold explained variance ratio. The procedure is summarized in algorithm 2. For an intuitive under-

---

[4]In general, whether clustering succeeds or not depends on whether the choice of distance measure (be it Euclidean or not) is a good measure of similarity.
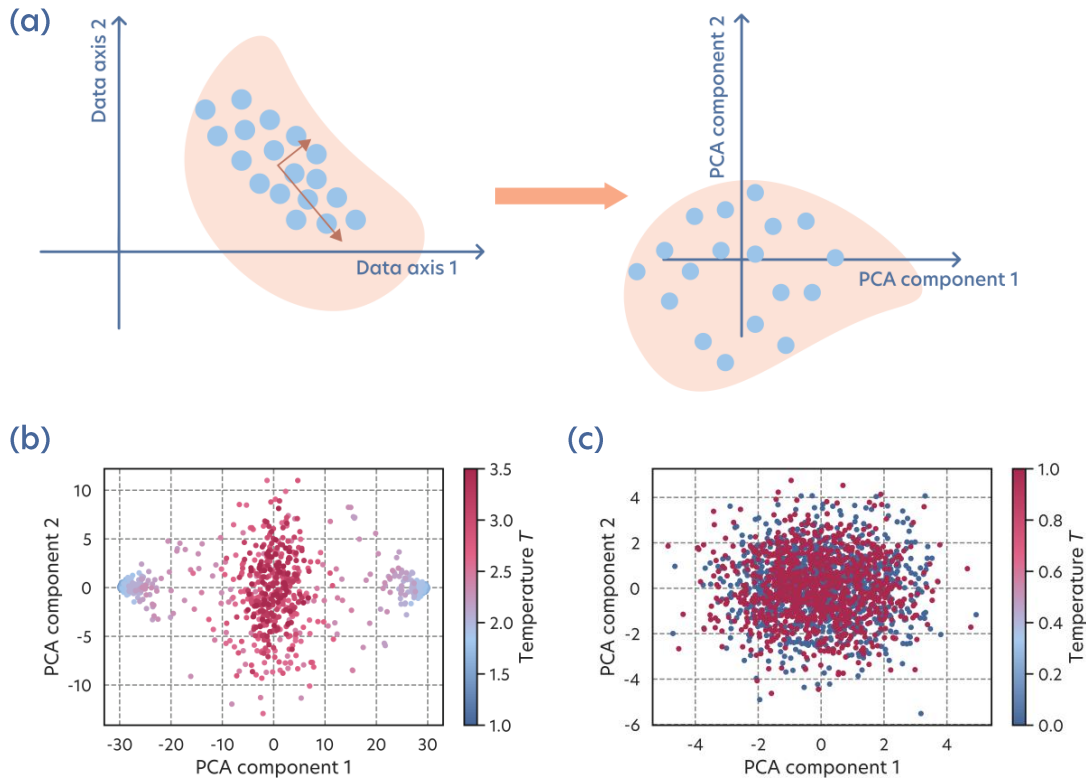
Figure 3.3: (a) Illustration of the principle behind PCA applied to data points (blue) living in a two-dimensional feature space. Orange vectors denote the first two principal components on which we project the data (right panel). PCA applied to the spin configuration samples of (b) the Ising model and (c) IGT with $k = 2$. For the Ising model, the data consists of 50 spin configurations (linear lattice size $L = 30$) sampled using Monte Carlo methods at temperatures T ranging from $T_1 = 1$ to $T_{20} = 3.5$ in equidistant steps. For the IGT, the data consists of 1000 spin configurations (linear lattice size $L = 16$) drawn within the topological phase and the disordered phase at high temperature. Panels (b) and (c) reproduced from [32, Notebook A1].

standing of the procedure, we refer to fig. 3.3(a) & (b): in this example, the data resides in a two-dimensional feature space. After subtracting the data mean, PCA identifies the first PC that contains the largest proportion of the data variance. PCA can not only be understood as variance maximization, but also as a minimization of a reconstruction error of a linear transformation. The prove of this equivalence can be found in appendix A. For further details, see, e.g., Ref. [85].

Now, we can readily apply PCA to our spin configuration samples. Figure 3.3(b,c) shows the results of PCA applied to spin configuration samples of the Ising model and IGT, respectively. For the Ising model, PCA separates the data into three clusters – a high temperature cluster corresponding to the disordered phase, as well as two low temperature clusters corresponding to the ordered phase with either positive or negative magnetization. Further analysis shows that the first PC corresponds to the magnetization [104]. By drawing a vertical decision boundary (perpendicular to PC1) which separates the high temperature cluster and a low temperature cluster a rough estimate of the critical transition temperature can be obtained as $T_{\mathrm{c,PCA}} \approx 2.3$ which is in agreement with the Onsager solution. In case of the IGT, PCA fails

---

Algorithm 2 Principal component analysis (PCA)

Require: Hyperparameter k (dimensionality of the projected data)
Require: Design matrix $X \in \mathbb{R}^{n \times m}$

$\quad X \leftarrow X - \text{mean}(X)$ $\qquad\qquad\qquad\qquad\qquad$ ▷ Remove mean element-wise
$\quad \Sigma \leftarrow X^\intercal X / n$ $\qquad\qquad\qquad\qquad$ ▷ Construct empirical covariance matrix
$\quad V \leftarrow \text{Eigenvectors}(\Sigma)$ $\qquad$ ▷ Find eigenvectors and sort them descendingly by eigenvalue
$\quad \tilde{V} \leftarrow V[:, :k]$ $\qquad\qquad\qquad$ ▷ Keep only first k eigenvectors **return** $\tilde{X} \leftarrow X\tilde{V} \in \mathbb{R}^{n \times k}$

---

to cluster the data into the two prevalent phases [see fig. 3.3(c)]. This is because PCA is restricted to linear transformations of the input data. While this is sufficient to encode simple local order parameters [104–106], such as the magnetization in case of the Ising model, linear transformations are not sufficient to compute topological features, i.e., non-local correlations in the data [106].

As illustrated by the failure of PCA in the case of the IGT, the restriction of PCA to linear transformations of the input space severely limits its performance. That is, one may not be able to find the optimal set of directions to perform dimensionality reduction using PCA. In particular, the low-dimensional manifold on which the data resides within the original space may not necessarily be parametrized by linear transformations of the original coordinates. In such cases, a dimensionality reduction using PCA does not preserve the relative pairwise distance, or similarity, between data points with respect to the manifold. However, this is a desired property for any algorithm that aims at performing dimensionality reduction. This problem is tackled by non-linear dimensionality reduction techniques, such as the kernel PCA (kPCA) (see chapter 4 on the kernel trick), the t-distributed stochastic neighbour embedding (t-SNE) [107], or uniform manifold approximation and projection (UMAP) [108]. In the following section, we briefly describe t-SNE.

3.2.2 t-Distributed stochastic neighbor embedding

Stochastic neighbor embedding [109] and its variant called t-distributed stochastic neighbour embedding (t-SNE) [107] are techniques for non-linear dimensionality reduction, which aim to preserve the local structure of the original data. That is, points which are close in the high-dimensional data set tend to be close to one another in the low-dimensional representation.

Let us consider an initial m-dimensional space with n points, i.e., $x_i \in \mathbb{R}^m$. We define the conditional probability $p_{i|j}$ that two points x_i and x_j are similar (i.e., close to one another) as

$$p_{i|j} = \frac{e^{-||x_i - x_j||^2 / 2\sigma_i^2}}{\sum_{k \neq l} e^{-||x_k - x_l||^2 / 2\sigma_i^2}}, \tag{3.7}$$

where $||x_i - x_j||$ is the Euclidean distance between the two points. The fact that Gaussian likelihoods are used in $p_{i|j}$ implies that only points near x_i contribute significantly to its probability. The variance σ_i^2 depends on the *perplexity* defined as

$$P_i = 2^{-\sum_{j=1}^n p_{j|i} \log_2 p_{j|i}}, \tag{3.8}$$

which is a measure based on Shannon entropy. In the first step of the t-SNE algorithm, the variances σ_i^2 are optimized for each point x_i to have a fixed perplexity value $P_i = \text{const}$. Points in regions of high density have smaller variance, while regions of low density have larger variance. In practice, the perplexity usually is set between 5 and 50. Note that $p_{i|j} \neq p_{j|i}$ due to the dependence on σ_i^2. To recover a symmetric relation $p_{i|j} = p_{j|i}$, we define the joint

probability distribution as

$$p_{ij} = \frac{p_{i|j} + p_{j|i}}{2n}. \tag{3.9}$$

The objective of the t-SNE algorithm is to find another set of points in lower dimensional representation $\boldsymbol{y}_i \in \mathbb{R}^{n \times d_{\text{red}}}, d_{\text{red}} < m$ and corresponding probability distribution q_{ij} in a new representation for which the KL divergence

$$D_{KL}(p||q) = \sum_{i,j} p_{ij} \log \frac{p_{ij}}{q_{ij}} \tag{3.10}$$

is minimal.

The procedure starts with randomly sampling n points $\boldsymbol{y}_i(z_1, z_2, \ldots, z_{d_{\text{red}}})$ in a d_{red}-dimensional space. For each point we define the probability distribution q_{ij} in a similar way as in the high-dimensional space but using the t-Student probability distribution instead of Gaussian distributions:

$$q_{ij} = \frac{(1 + ||\boldsymbol{y}_i - \boldsymbol{y}_j||^2)^{-1}}{\sum_{k \neq l}(1 + ||\boldsymbol{y}_k - \boldsymbol{y}_l||^2)^{-1}}. \tag{3.11}$$

In the last step, we minimize the Kullback-Leibler (KL) divergence from eq. (3.10) (see section 2.3) by optimizing the position $(z_1, z_2, \ldots, z_{d_{\text{red}}})$ of each point $\boldsymbol{y}_i = \boldsymbol{y}_i(z_1, z_2, \ldots, z_{d_{\text{red}}})$ in the d_{red}-dimensional space which eventually yields a low-dimensional data representation. The t-SNE algorithm is summarized in algorithm 3.

The low-dimensional data representation preserves the local structure of the original data set, i.e., similar points in original data set are now clustered in the d_{red}-dimensional representation space. However, the distance between the resulting clusters looses its meaning in representation space.

Algorithm 3 t-distributed stochastic neighbour embedding (t-SNE)

Require: Hyperparameters: d (dimensionality of the projected data), perplexity P, learning rate η
Require: Original data set of n points in m dimensional space $\boldsymbol{X} \in \mathbb{R}^{n \times m}$
Require: Random set of n points in lower dimensional $d_{\text{red}} < m$ representation $\boldsymbol{Y}^{(0)} \in \mathbb{R}^{n \times d_{\text{red}}}$
  for each $\boldsymbol{x}_i$ **do**
    for each $\boldsymbol{x}_j$ **do**
      Calculate pairwise conditional probability distribution $p_{i|j}$ with fixed perplexity P
    end for
  end for
  Calculate probability distribution p_{ij}
  for $t = 1$ to T **do**
    for each $\boldsymbol{y}_i^{(t-1)} \in \boldsymbol{Y}^{(t-1)}$ **do**
      for each $\boldsymbol{y}_j^{(t-1)} \in \boldsymbol{Y}^{(t-1)}$ **do**
        Calculate probability distribution q_{ij}
      end for
      Calculate gradients of the KL divergence with respect to coordinates of each $\boldsymbol{y}_i^{(t-1)}(z_1^{(i)}, z_2^{(i)}, \ldots, z_{d_{\text{red}}}^{(i)}) \in \boldsymbol{Y}^{(t-1)}$, i.e., $\frac{\partial D_{KL}(p||q)}{\partial \boldsymbol{z}^{(i)}}$
    end for
    $\boldsymbol{Y}^{(t)} \leftarrow \boldsymbol{Y}^{(t-1)} - \eta \frac{\partial D_{KL}(p||q)}{\partial \boldsymbol{z}}$ ▷ Update the coordinates of each point
  end for

> In general, clustering in combination with dimensionality reduction works elegantly for simple problems, such as the Ising model. However, such approaches typically do not perform well when applied to more difficult phase classification tasks, e.g., in the presence of topological phases such as in the IGT [110], or when a large number of phases is present [111].

3.3 Supervised phase classification with neural networks

One may wonder whether the issues encountered by clustering methods introduced in the previous section can be tackled by making use of the powerful machinery of NNs introduced in section 2.4.4. The idea is the following [112]. We train an NN to take spin configuration samples as input and correctly label them by the phase they belong to, see fig. 3.4(a). Typically, the label is encoded as a binary bit string in a *one-hot encoding*. In case of the Ising model this would correspond to the label 1 for all samples drawn within the ordered phase ($T < T_c$) or the label 0 for all samples drawn within the disordered phase ($T > T_c$).[5] To ensure that the output of the NN can be used to predict a binary label, we choose the output layer to be composed of two nodes to which we apply the softmax activation function introduced in eq. (2.37) over the activations x_j of all nodes within the output layer. This ensures that the output layer encodes a valid probability distribution over the classes. The predicted label is then typically chosen based on the node which yields the maximum probability. For training, one typically employs the binary cross-entropy (see eq. (2.2)) which, for a fixed input x is given as

$$\mathcal{L} = -\sum_j p_j(\boldsymbol{x}) \log\big(\mathrm{NN}(\boldsymbol{x})_j\big). \tag{3.12}$$

Here, $\mathrm{NN}(\boldsymbol{x})$ denotes the output of an NN, which contains a softmax activation function in its last layer, applied to the input $\boldsymbol{x}$. The sum runs over all output nodes, i.e., the number of distinct classes. $p_j(\boldsymbol{x})$ is the true label of the input $\boldsymbol{x}$ as specified by the one-hot encoding. For example, given two classes and an input whose true label is 0, we have $p_0(\boldsymbol{x}) = 1$ and $p_1(\boldsymbol{x}) = 0$ such that $\sum_j p_j(\boldsymbol{x}) = 1$. In eq. (3.12), this is compared to $\mathrm{NN}(\boldsymbol{x})_j$ which is the activation of the j-th output node and corresponds to the predicted probability of the input $\boldsymbol{x}$ to belong to class j.

In our example, the training set consists of labeled spin configuration samples for a wide range of temperatures far above and below T_c, whereas the test set is chosen over the entire temperature range. After training the NN (see section 2.4.4) on the training set, it is evaluated on the test set. In particular, we average the activation of the two nodes in the output layer, which encode the probability of the input sample belonging to phase 0 or 1, respectively, over the test set. Remarkably, fig. 3.4(b) shows that these activations cross over precisely at T_c enabling us to extract the correct critical temperature. Similarly, this method is capable of correctly identifying the crossover temperature in the IGT [112]. The fact that NNs can generalize to unseen input data can, for example, be exploited as follows. An NN trained on configurations for the square-lattice ferromagnetic Ising model can also highlight the critical temperature of Ising model with a different lattice geometry, such as a triangular lattice [112]. Note that the ferromagnetic Ising model on a triangular lattice is an typical example of a frustrated system.

---

[5]Of course, the opposite choice for labelling the two phases with label 0 for the ordered phase and 1 for the disordered phase is equally good.
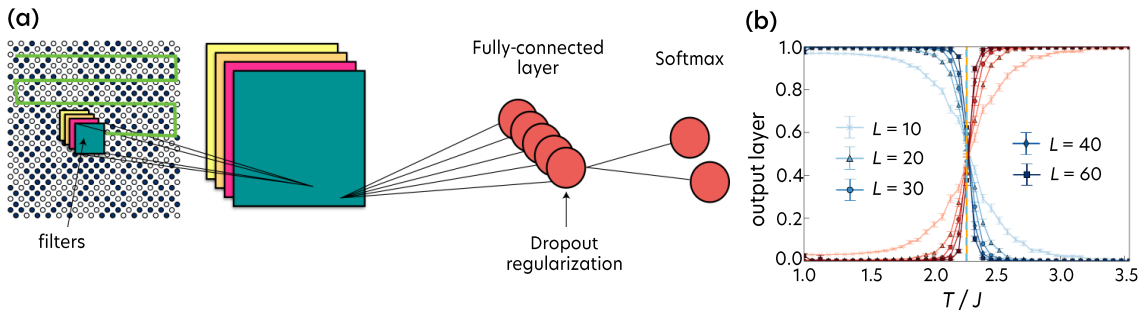
Figure 3.4: Supervised phase classification with an NN performed on the Ising model of varying linear lattice size L ($N = L^2$) (see [112] for further details). (a) (Convolutional) NN applied to a configuration sample of the Ising model. (b) The average activation of the two nodes in the output layer are given by blue and red curves, respectively. The predicted critical temperature is marked by their crossover and is in good agreement with the Onsager solution [eq. (3.5)] depicted as an orange vertical line. Adapted from Ref. [112].

3.4 Unsupervised phase classification with neural networks

In section 3.3, we showed that NNs can perform supervised phase classification. Due to its supervised nature this approach requires partial knowledge of the phase diagram of the system. One can determine the critical temperature (through "interpolation") if one knows the labels of samples deep within two neighboring phases. Ideally, in order to discover new phases of matter a phase classification algorithm should not rely on such *a priori* knowledge about the phases, i.e, it should be unsupervised in that regard. While clustering is unsupervised, we have seen that its power can be limited. In the following, we discuss four methods that use NNs to perform unsupervised phase classification.

3.4.1 Learning with autoencoders

A natural NN-based unsupervised method is based on the analysis of the latent data representation given by an autoencoder (AE). As we have briefly explained in section 2.4.5, AEs are NNs with a bottleneck in their center which are trained to reconstruct the input at the output. The architecture of a typical AE is depicted in fig. 3.5. Due to the bottleneck, the information passing through the network needs to get compressed at the bottleneck, and then decompressed to recover the input. As a consequence of the compression, some information may be lost.[6] However, the retained information in the bottleneck should ideally contain everything relevant for the reconstruction of the input. Therefore, the bottleneck forms a *latent space* which contains a compressed representation of the input data. This is akin to the dimensionality reduction schemes we discussed previously (see section 3.2), which preserve the most important features for the reconstruction. As such, we can analyze the latent representation of the input data in a similar way as the lower-dimensional representation obtained by PCA in section 3.2.1.

Let us apply an AE to reconstruct Monte Carlo samples of the two-dimensional Ising model [105]. Clearly, this represents an unsupervised phase classification scheme, because we do not provide any labels. The relevant loss function to be minimized is given by the reconstruction error between the input and output spin configurations (e.g., mean-squared

---

[6]In general, it is possible that NNs could compress more dimensions into a single neuron. However, in practice NNs tend to learn smooth functions, which penalizes this behavior.
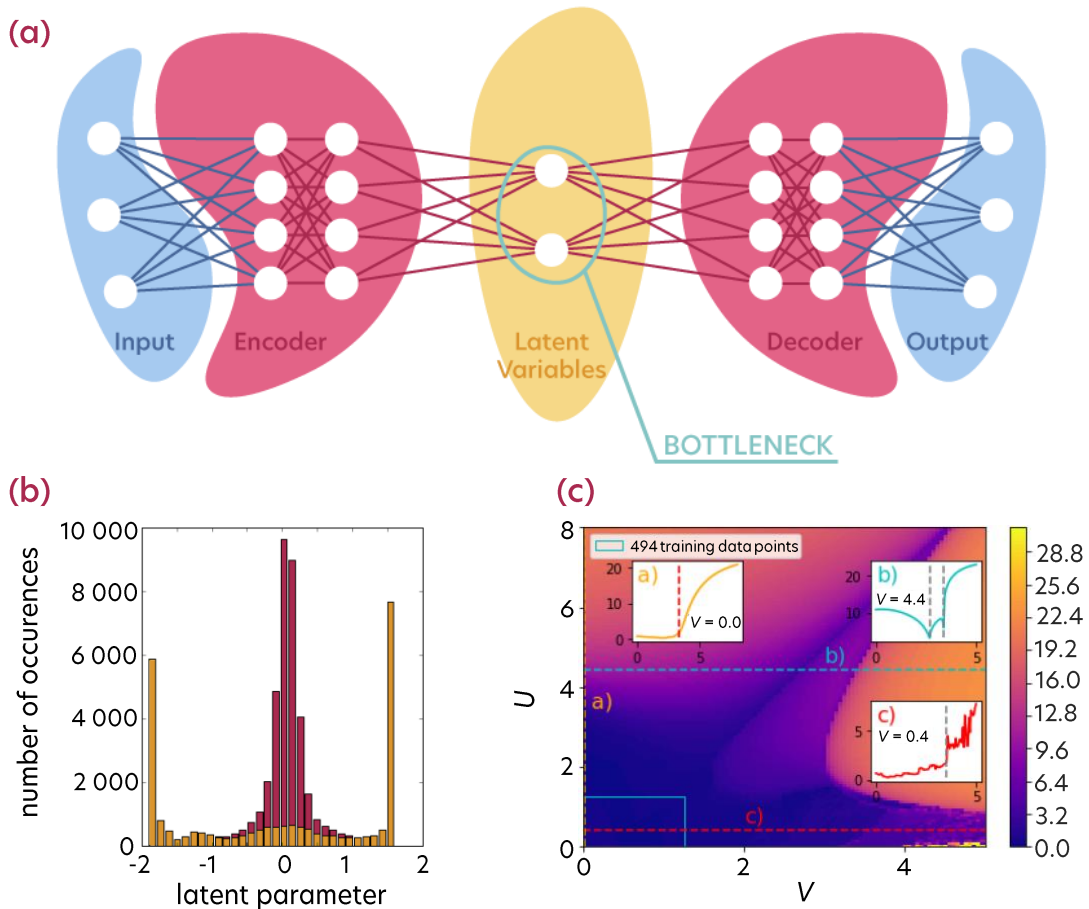
Figure 3.5: (a) Illustration of a natural bottleneck (here two neurons) in an AE architecture. (b) Analysis of bottleneck neurons of an AE trained to reconstruct spin configurations of a two-dimensional Ising model. Latent representation of Ising configurations clusters into two phases visible as a histogram. (c) Anomaly detection scheme allows for the recovery of the phase diagram from the reconstruction loss of an AE trained on one phase (blue box in bottom left). Panel (b) is taken from Ref. [105], (c) from Ref. [113].

error (MSE)). If we look at how the latent representation of the spin configurations in the trained AE change with the temperature (see fig. 3.5[b]), we can immediately observe a clustering of the latent parameters. The clusters correspond to the two phases of the Ising model.[7] Red points correspond to the high-temperature paramagnetic phase, while yellow points correspond to the low-temperature ferromagnetic phase. Note the two large yellow bins at the edges of the histogram in fig. 3.5(b). These are formed due to the degeneracy of the ground state, which has either all spins pointing up or all spins pointing down.

Analysis of the AE latent representation of the input data is not the only way of an AE-based unsupervised phase classification. Another successful and robust scheme based on anomaly detection was presented in Ref. [113]. The basic idea is as follows. Imagine training an AE to reconstruct states coming from one phase. Then, the AE is used to reconstruct states coming

---

[7]Beware, clustering of data in the latent space according to the phases present in the system is not a general property of AEs. The clustering occurs when input data causes distinctive activations in the bottleneck which *often* corresponds to different phases.

from the rest of the phase diagram. Such a task is difficult, because the training data is limited only to one phase, and the AE is bound to make reconstruction errors in other phases. Moreover, we expect that the error is lower for phases that are similar to the "training" phase and higher for phases which contain states that look very different. Finally, the quantum states from the transition regimes are usually distinctive and the most unique from the rest of the phase diagram. Altogether, the reconstruction error across the phase diagram, made by an AE trained to reproduce states from one phase, is expected to vary according to the phases and the phase boundaries in the system. This scheme enables the discovery of phases in a fully unsupervised way. The authors of Ref. [113] used this scheme based on anomaly detection to recover a full phase diagram of the extended Bose-Hubbard model in one dimension at exact integer filling. This result is presented in panel (c) of fig. 3.5. Interestingly, their work also revealed within the phase diagram a phase-separated region[8] with unexpected properties which may be one of the first fully unsupervised discoveries in the ML-guided phase classification.

3.4.2 Learning by confusion

Learning by confusion [114] is another NN-based unsupervised method and works as follows. We start by partitioning the temperature range into two regions with distinct labels. Based on these labels, we perform supervised learning over the entire temperature range as described in section 3.3 and keep track of the final overall classification accuracy of the model. This classification accuracy is associated with the guess for the critical temperature located at the boundary of the two regions. We repeat this procedure systematically for multiple bi-partitions of the temperature range, i.e., guesses for the critical temperature. Finally, we plot the classification accuracy against the guessed critical temperature. This procedure is summarized in algorithm 4. Note that each partitioning requires the training of a separate NN.[9] The results of this algorithm applied to the Ising model are depicted in fig. 3.6. We observe that the classification accuracy is *W-shaped*. The high classification accuracy at the end points of the temperature range arises due to the fact that in these cases almost all samples are assigned the same label. In particular, in the extreme case where all samples are assigned the same label a classification accuracy of 1 can be achieved trivially because the NN simply needs to learn to

---

[8]This phase-separated region is located between supersolid and superfluid phases, for more details see Ref. [113].

[9]Retraining a model for each choice of a bi-partition can become computationally expensive, in particular when increasing the resolution of the method. There has been an extension of the learning-by-confusion scheme which uses two neural networks [115] to try to circumvent this issue by choosing bi-partition points one at a time in a guided manner.

Algorithm 4 Learning by confusion

Require: Data set of (spin configuration) samples $\mathcal{D}_0 = \{x\}$, guesses for critical temperature
$\quad \mathcal{T} = \{T_1, ..., T_{\max}\}$
$\quad$ **for** $T_c^* \in \mathcal{T}$ **do**
$\qquad$ Partition data set $\mathcal{D}_0$ into two regions with $T \leq T_c^*$ and $T > T_c^*$
$\qquad$ Set label y of all samples in region with $T \leq T_c^*$ as 0 and $T \leq T_c^*$ as 1
$\qquad$ Split resulting data set into training and test set
$\qquad$ Perform supervised learning on the training set, i.e., train an NN to minimize loss in
$\quad$ eq. (3.12)
$\qquad$ Evaluate classification accuracy on test set
$\quad$ **end for**
$\quad$ Plot accuracy vs. $T_c^* \; \forall \, T_c^* \in \mathcal{T}$ (see fig. 3.6) ▷ Critical temperature T_c^* at which the accuracy
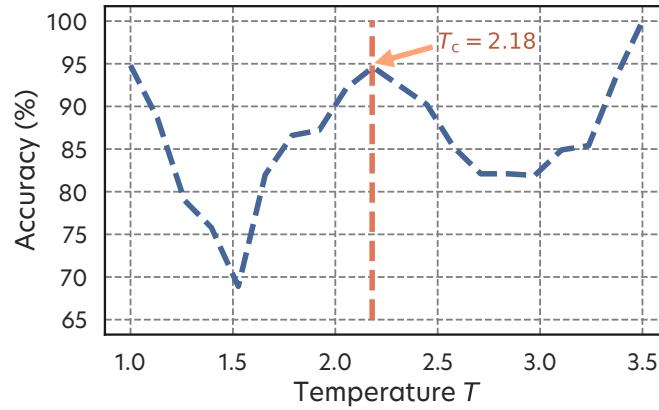$\quad$ peaks corresponds to the best guess for the location of the phase transition

Figure 3.6: Result of the learning by confusion scheme applied to the Ising model. The data consists of 100 spin configurations (linear lattice size $L = 30$) sampled using Monte Carlo methods at temperatures T ranging from $T_1 = 1$ to $T_{20} = 3.5$ in equidistant steps. The data set is split into equally-sized training and test sets (such that 50 spin configurations are present at each sampled temperature). The blue curve shows the classification accuracy on the test set for various choices of bi-partitions. It has a characteristic W-shape whose middle peak is at $T \approx 2.3$, which is in good agreement with the Onsager solution. Reproduced with [32, Notebook A3].

output the same label independent of the input. The middle peak, however, is non-trivial and corresponds to the predicted critical temperature of the method. Here, the predicted critical temperature is in good agreement with the Onsager solution. The presence of this middle peak can be explained as follows. Let us assume that the data can naturally be classified into two distinct groups realized by a particular choice for the bi-partition of the temperature range. Then, the closer our choice of bi-partition matches the "correct" bi-partition underlying the data the larger the classification accuracy of our algorithm.

Here, we have discussed the case where there are precisely two distinct phases present in the parameter range under consideration. In this case, the accuracy ideally displays a characteristic W-shape, see fig. 3.6. If there are multiple phases present, this characteristic W-shape is modified. The shape of the signal (in particular the number of obtained peaks) could then be used to identify the number of different phases present in the data [114, 116].

3.4.3 Prediction-based method

The learning by confusion scheme is difficult to efficiently extend to high dimensional parameter spaces which may feature several distinct phases.[10] Moreover, it has been shown that the learning by confusion scheme has difficulties to correctly identify the crossover in the IGT [110]. These limitations can be circumvented through the so-called *prediction-based method* [110, 111, 117], which works as follows.

We train an NN to predict the tuning parameter (here the temperature) for each configuration sample. The value of the tuning parameter at which a given configuration samples has been generated is readily available both in experiment and simulation. If the system does not undergo any phase transition, the predicted tuning parameter is *linearly* dependent on the true tuning parameter as shown in fig. 3.7(a). Consequently, the derivative of the predicted

---

[10]In Ref. [115] an approach to extend the scheme to two-dimensional parameter spaces featuring two distinct phases is presented.
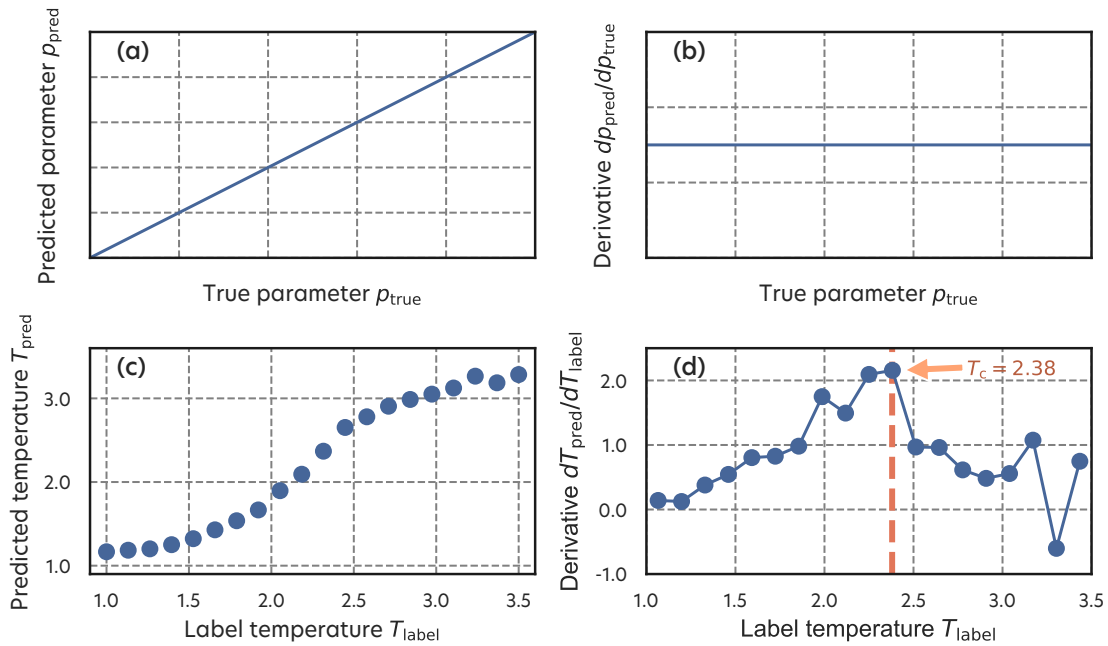
Figure 3.7: (a,b) Illustration of the output of the prediction-based method if the system does not undergo any phase transition. (c,d) Result of the prediction-based method applied to the Ising model. The data consists of 100 spin configurations (linear lattice size $L = 30$) sampled using Monte Carlo methods at temperatures T ranging from $T_1 = 1$ to $T_{20} = 3.5$ in equidistant steps. The data set is split into equally-sized training and test sets (such that 50 spin configurations are present at each sampled temperature). (c) Average predicted temperature for the test data as a function of the true underlying temperature. (d) Derivative of the average predicted temperature for the test data as a function of the true underlying temperature which peaks at the critical temperature of the Ising model. Panels (b) and (c) reproduced from [32, Notebook A3].

tuning parameter with respect to the true tuning parameter is constant, see fig. 3.7(b). For systems which exhibit a phase transition the situation is different. In this case, the tuning parameter cannot be predicted with perfect accuracy resulting in a *non-linear* relationship between the predicted and the true value of the tuning parameter. Figure 3.7(c) illustrates this in the case of the Ising model. Consequently, the derivative is not constant and at the critical tuning parameter the largest rate of change occurs, see fig. 3.7(c) and (d). In other words, the parameter value for which the NN predictions are most susceptible identifies the position of the phase transition.

Let us elaborate on this point: While the tuning parameter only changes marginally in the vicinity of the phase transition, the system's state and its corresponding order parameter change dramatically as the tuning parameter crosses its critical value. As a result, the NN is the best at distinguishing samples originating from two different phases whereas it has difficulties to distinguish samples from within the same phase. That is, its predictions change the most as the tuning parameter is swept across its critical value. Figure 3.7(c) shows that the predictions start to saturate deep within each phase, whereas they vary most strongly with the tuning parameter around the transition point.

So far, we have seen that phase classifications methods based on NNs are capable of locating the phase transition of the two-dimensional Ising model. To date, these methods have successfully revealed a plethora of other phase transitions in various physical systems.[11] This fact highlights that these methods are *generic* and have been formulated in a system-agnostic fashion. There may exist various physical observables (such as order parameters) that can be used to identify a given phase transition. However, finding these quantities is typically a hard task and requires a deep understanding of the physical system at hand. Remarkably, the NN-based methods we showcased here can successfully classify different phases of matter in an automated fashion without *a priori* knowledge of the underlying physics. Note that there exist similar system-agnostic tools which do no rely on ML, such as the specific heat for thermal phase transitions or the fidelity susceptibility [119] for quantum phase transitions.[12] However, these tools can still fail for a given system and can be expensive to compute or difficult to measure in an experiment. For example, the specific heat fails to locate the crossover temperature in the IGT. In case of the fidelity susceptibility, one investigates the change in the overlap $\langle \Psi_0(p) | \Psi_0(p + \epsilon) \rangle$, where $|\Psi_0(p)\rangle$ is the ground state of the Hamiltonian $H(p)$, p is the tuning parameter, and ϵ is an infinitesimal perturbation. Because one typically does not have access to the full wave-function, the fidelity susceptibility typically remains difficult to evaluate. The NN-based methods we discussed constitute alternative tools. In particular, they can *in principle* be applied using various properties of the system's state at different values of the tuning parameter as input. This allows them to identify phase transitions based on experimentally accessible measurement data [120].

While the phase classifications methods we discussed up to now are capable of locating phase transitions, we have not yet gained any insights into the specific type of the phase transition that the system undergoes. The crucial question is whether one can extract physical insights from the NNs concerning the underlying phase classification tasks. In particular, one can ask whether it is possible to extract novel order parameters from such NNs, which is an ultimate goal of the interpretable ML applied to phase classification problems.

3.5   Interpretability of machine learning models

As seen in the previous sections, NNs are powerful tools to identify phases in physical data. Now imagine applying these methods to a novel physical system whose phases and corresponding order parameters are not yet known. The natural questions that arise in this scenario are: Can we trust the NN predictions? In particular, how can we know that the model correctly located a phase transition in the parameter space? Moreover, assuming that the methods correctly classified the data into different phases of matter, how can we gain physical insights into the problem at hand? For instance, can we analyze the trained NNs to determine what types of phase transitions the system undergoes? Or would it even be possible to extract novel order parameters from them? When using ML (and especially DL) models, answers to these questions are not easy to find. Such challenges are being addressed by the research on the ML reliability and interpretability.[13]

---

[11]There exist various other ML methods for detecting phase transitions and classifying phases of matter. For example, in Ref. [118] phase transitions can be inferred by training an ML model to fit the properties within one phase and extrapolating toward other regions in parameter space. Here, the model is based on a Gaussian process (GP) utilizing kernels. We discuss kernel methods, including GPs, in detail in chapter 4.

[12]A quantum phase transition [88] corresponds to non-analytic behavior of the ground-state properties at the critical value of the tuning parameter p_c, where the system Hamiltonian is $H(p)$. It emerges due to the competition of individual terms in the Hamiltonian, which dependent on the tuning parameter.

[13]Note, that the formal definitions of these terms are not agreed upon in either the physical or computer science community [121]. To circumvent the problem, here we provide intuitions about meaning of these terms.

> Reliability is about trusting our ML model predictions. Our trust in the model is increased, e.g., when we have access to the uncertainty of model predictions. Interpretability is about understanding what an ML model learns and how it makes its predictions. As such, these two ideas are closely intertwined.

Both concepts are particularly important on our way toward scientific discovery using ML. If we are not able to understand what an NN learns when given a problem, *our* understanding of the problem remains limited![14]

We already mentioned that, *a priori*, DL models are usually neither reliable nor interpretable. As such, they largely serve as black-box models that provide us with suitable predictions (from which we, e.g., can locate phase transitions in the underlying input data). There are several reasons for that: firstly, their learning dynamics are largely opaque and not well understood.[15] Secondly, the direct analysis of trained NNs is challenging, as we explain in the next section. In particular, the "reasoning" of NNs does not necessarily have to be based on the same observations on which a human would base its decisions. Tackling these challenges is important for all ML applications, but especially crucial, e.g., for medical diagnosis or insurance and hiring decisions.

3.5.1 Difficulty of interpreting parameters of a model

When looking at a DNN with possibly billions of trainable parameters, it is hard for us humans to decipher what the NN is really doing under the hood. It may be that an NN actually computes a simple, physically relevant function, such as an order parameter, to make its predictions. Recognizing whether that is the case is hard because the computation and relevant information is spread over the multiple layers containing a large number of neurons each. However, if an NN is sufficiently small, the direct interpretation by looking at its trainable parameters may be possible. Consider the limiting case of a single-layer NN without any non-linear activation function. This corresponds to a simple linear regression model, described in section 2.4.1:

$$\hat{y} = \theta x + b, \tag{3.13}$$

where θ is a matrix of weights and b is a vector of biases. Evidently, such a linear model allows for a direct interpretation in terms of its weights: the larger the magnitude of a given weight (connection), the more important is the corresponding normalized feature for solving the problem at hand. For an example of weight interpretation in the context of phase classification, see Ref. [123].

However, this reduction in depth and loss of non-linearity comes at the cost of expressivity. In order for such a model to be accurate, it generally requires highly pre-processed inputs x which "contain" the necessary non-linearities. Moreover, the importance of a given feature has more meaning if it is already present in a compact, physically relevant form. This largely limits the domain of applicability of small predictive models to problems for which we (at least) have partial knowledge.

3.5.2 Interpretability via bottlenecks

As we have explained in the previous section, interpretability is an inherent characteristic of small models. Fortunately, there are alternative approaches to interpretability that are not lim-

---

[14]We can imagine a non-interpretable black-box NN that after training can give insights to the problem, e.g., Ref [122]. However, the model still needs to be reliable so we can trust the new insights, and we need to have previous deep insights into the problem.

[15]We show you how some of these questions can be answered with tools from statistical physics in section 8.1.

ited to simple small models. What we can do in large architectures is to identify bottlenecks in the information flow and focus our attention there. A bottleneck in an NN is just a layer with fewer neurons than the layer before and after it. An example of a NN with a natural bottleneck has already appeared in section 3.4.1 and in fig. 3.5(a), namely an autoencoder (AE). Its bottleneck forces the NN to distill the relevant information within the inputs, such that it can flow through this constriction. As such, the NN performs a dimensionality reduction and finds a suitable low-dimensional feature representation. While the entire NN architecture can be large and have many trainable parameters, the bottleneck itself is described only by few parameters. Because all the relevant information for the predictions of the NN must eventually flow through the bottleneck, we can limit our analysis to the small number of trainable parameters of the bottleneck as opposed to the entire NN. In particular, we can perform a regression on the output of such bottleneck neurons and extract the mapping between the input features and the activations of the bottleneck neurons. There is a natural bottleneck in almost every NN – its output neuron. However, performing a regression on it without imposing any additional bottlenecks is challenging, because you need to take into account all input features which can grow quickly in number. Apart from the output neuron, there are also other types of bottlenecks which can appear naturally in NNs architectures, such as in AEs (see section 2.4.5) [105, 124] and CNNs (see section 2.4.4) [125].[16] However, we can also introduce bottlenecks into our architecture on purpose to have more interpretable ML models. This idea gave birth to, e.g., Siamese NNs [127]. We look at these approaches in more detail in the next paragraphs and see what information on physical systems we can extract with them.

Interpretability with autoencoders (AEs). As we have explained in sections 2.4.5 and 3.4.1, AEs are NNs with a bottleneck in the middle that are trained to reconstruct the input at the output. We have already shown in section 3.4.1 and in fig. 3.5(b) that we can obtain clustering in the latent representation corresponding to phases present in the input data, achieving the unsupervised phase classification. Moreover, thanks to the bottleneck, which ideally should contain all information that is relevant for the reconstruction, we can also extract additional information and interpret what property of the input data is preserved by an AE. In particular, if we plot the latent parameter against the magnetization of the respective two-dimensional Ising spin configuration, as in fig. 3.8(a), we see a linear dependence. This suggests that the compressed representation learned by the AE is connected to the magnetization. To be more precise, the behavior deviates from a strict linear dependence at values of the magnetization close to -1. However, we still can make the statement that the AE learned a property related to the magnetization given that the mapping between the latent parameter and the magnetization is bijective. For example, such a statement would hold even if the latent parameter as a function of the magnetization would vary according to a sigmoid function.

Another example of analysis of latent space of AEs is work by Iten *et al.* [124]. They used a special AE architecture with a *question neuron*, i.e., an additional neuron connected to the first decoding layer after the bottleneck. The input of this question neuron is provided by a user. You can think of it as an alternative way of providing data to the network. The authors

---

[16]Alternatively, a "bottleneck" can be enforced through regularization – in particular the addition of a L_1 regularization term in the loss function given by $L_1 = \lambda \sum_i |w_i|$, where λ parametrizes the regularization strength and the sum runs over all (trainable) weights within the NN. This term enforces the weights to vanish, i.e., for connection to be cut. Ideally this results in a sparser, and thus effectively smaller, NN which enables interpretability. For example, the authors of Ref. [126] could extract analytical expressions for force laws and dark matter distributions from graph neural networks trained to predict planetary and dark matter dynamics. This was achieved by performing symbolic regression on the corresponding sparse networks. Note that such a regularization is also important when interpreting linear models as in eq. (3.13). Often learning problems do not have a unique solution. This means that the weights can vary given the same data and optimization procedure, which would result in different "interpretations" of the NN's inner workings. The regularization terms helps to remove the remaining degrees of freedom of the weights and enforce Occam's razor.
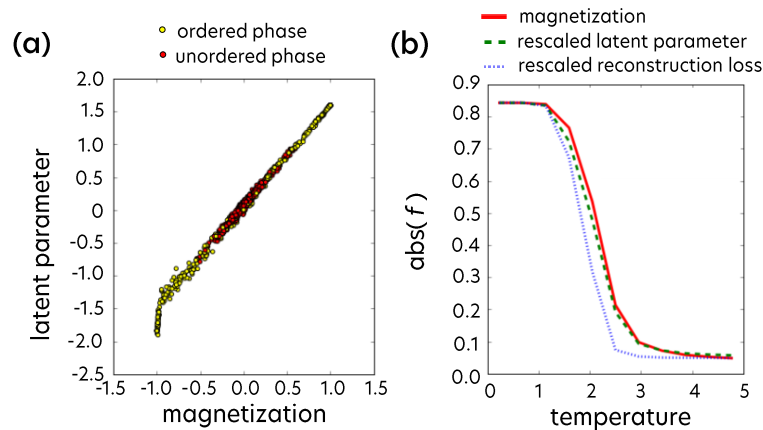
Figure 3.8: Analysis of bottleneck neurons of an AE trained to reconstruct spin configurations of a two-dimensional Ising model. (a) Dependence of latent space parameter on the magnetization. Red (yellow) color corresponds to samples from the low(high)-temperature regime. (b) Absolute magnetization, absolute rescaled values of latent parameter and reconstruction loss, averaged for fixed temperature. Adapted from Ref. [105].

showed that you can train such a special AE in a way that a user can ask a question via the question neuron and the answer is encoded in the latent space.

As you see, AEs are to some degree inherently interpretable by virtue of their low-dimensional latent space. However, the analysis of latent space does not give us any hint on the order parameter or important features. We can only compare it against the quantities or features we suspect to be important. If you look for a more automated way of detecting order parameters, we can turn to very special CNNs.

Extracting order parameters with convolutional neural networks (CNNs). We have already mentioned that CNNs have natural bottlenecks in their architectures. These bottlenecks are their filters or kernels, i.e., the structures with which they "scan" the data. Their size can be thought of as a receptive field size and tells us how many neighboring features (e.g., pixels) the network can analyze at the same time. Of course, if you have multiple convolutional layers with multiple kernels of different sizes, intertwined with pooling layers, their analysis is still challenging. But if you consider a simple CNN with only one or few subsequent convolutional layers with kernels of a fixed size and only one averaging layer at the end of the architecture, as presented in fig. 3.9(a), such a regression becomes tractable[17]. The mentioned architecture was proposed by Wetzel *et al.* (2017) [125] and is called *Interpretation Net* or *Correlation-Probing Neural Network,* see fig. 3.9(a). Such an architecture allows us to perform a regression on the output neuron with features extracted by kernels. Eventually, we obtain an analytical expression for the CNN decision function. If applied to a phase classification problem, such a decision function could unravel the order parameter. It seems, however, that such a decision function, and therefore the order parameter which may potentially be discovered through the CNN, depends on the choice of kernel size. What is the appropriate choice of kernel size, and thus decision function? Occam's razor tells us that we should be interested in the simplest decision function. That is, one should aim to take into account only a small number of input

---

[17]It remains non-trivial and involves careful zeroing of weights, Fourier series, and other tricks. If you are interested, see Ref. [125]
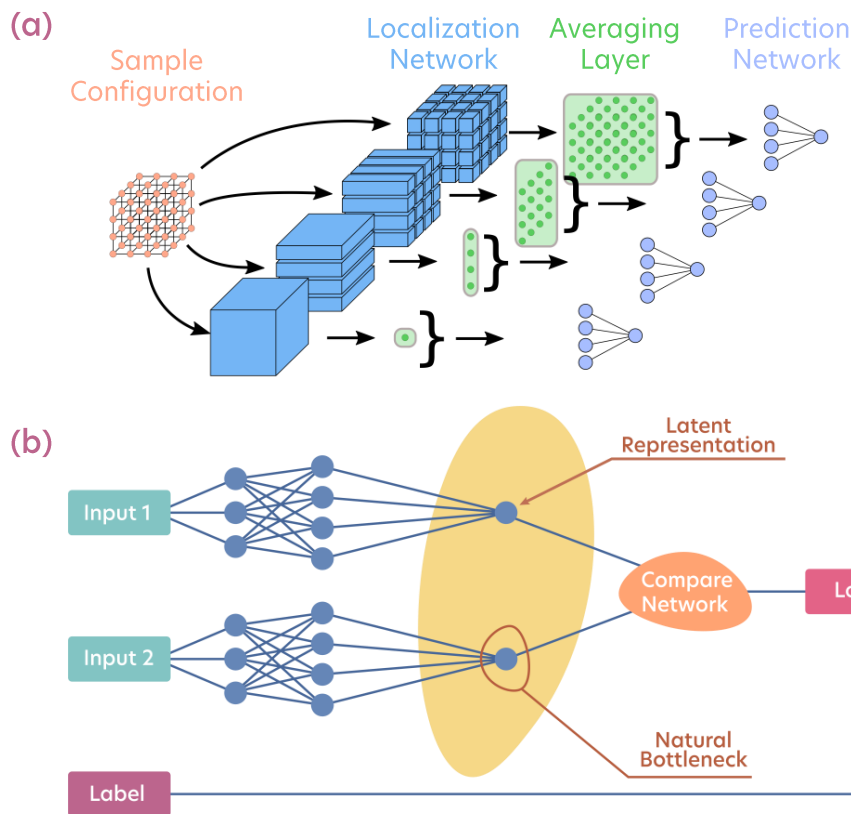
Figure 3.9: (a) Correlation-probing NN where the size of the receptive field is systematically reduced in each training step. Localization Network is one or more subsequent convolutional layers. Averaging layer collapses convolved features to a single number. (b) Scheme of a Siamese NN, whose two subnets are identical and share the same tunable parameters. The input is a pair of data points and the resulting label is either "same" or "different". Panel (a) is adapted from Ref. [125].

features. Crucially, this also makes the task of symbolic regression easier.

> Therefore, the idea of the correlation-probing convolutional network is to systematically reduce the size of the kernel (and thus the input dimension for the symbolic regression task) by cutting connections until there is a significant drop in the CNN performance. This drop corresponds to the CNN becoming "blind" to the correlations which are crucial for detecting and distinguishing different phases.

Imagine starting from a large kernel whose size corresponds to the size of the entire input image, e.g., 28×28. We train our *Interpretation Net* with such 28×28 kernels and see that it yields good results. Now, we reduce the receptive field size, e.g., to 20×20, retrain, and observe the performance. We repeat this process of reducing the kernel size and retraining until we see a significant drop in the CNN performance. Such a drop occurs as soon as the CNN gets blind to correlations in the system which are crucial for the phase classification, e.g., nearest-neighbor correlations. Finally, we can perform a regression on the output neuron of the CNN with the smallest kernel size that still yields good performance. The decision function we recover in the process is ideally connected to the underlying order parameter. With this

approach, the Interpretation Net is capable of successfully classifying the phases of the two-dimensional Ising model[18] or $SU(2)$ lattice gauge theory and one extract the corresponding decision functions. We stress that *the learned decision function can strongly depend on the choice of model architecture and training procedure (data)*. Therefore, various networks can detect different order parameters, e.g., in the Ising model, they can detect the expected energy per site, magnetization, or a scaled combination of those.

A related approach was used by Miles *et al.* (2021) [128] when designing a so-called *Correlator Convolutional Neural Network*. This CNN performs automatic feature engineering by probing for correlations in the first few layers. The subsequent layers are designed to check which correlations are the most important for the classification. By discovering which many-body correlations were the most important for the classification, they could distinguish between two distinct quantum models for their experimental results. This represents one of the first examples of scientific discovery with NNs.

Interpretable Siamese neural networks. Finally, you can create even more complex architectures with artificial bottlenecks allowing for an interpretation via symbolic regression. An interesting example is a Siamese NN [127], presented in fig. 3.9(b). It takes two input data points at the same time and is composed of two twin subnetworks with the same parameters and architecture. Their output neurons form two bottlenecks which in turn are inputs for the third subnetwork whose aim is to connect and compare the twin outputs. The task of the network is to determine whether two input data points are similar or not. This means that Siamese NNs are able to perform a multiple-class classification without a fixed number of classes and with relatively little training data per class. Moreover, by analyzing the bottlenecks we can extract what the NN learns in a problem.

Let us show an example. The authors of Ref. [127] applied the Siamese NN, e.g., to the motion of a particle in a central potential. The task was to learn whether two observations of the same particle correspond to the same particle trajectory. After successful training, we can perform a polynomial regression on the bottleneck with respect to the input data features. In this case, features are a position of the particle in the two-dimensional space and its velocity in both directions. By analyzing the dominant regression terms, they observed that the result of regression is proportional to the angular momentum of the particle. Such an analysis of bottlenecks of the successfully trained Siamese NN indicates that it learns conserved quantities and invariants.[19] Similar results can be observed for problems from special relativity and electromagnetism [127].

So far, we have learned that we can interpret ML models by analyzing bottlenecks in their architecture. These bottlenecks can either appear naturally (like in autoencoders (AEs)) or be imposed explicitly (like in CNNs, where the kernel size is systematically reduced, or in Siamese NNs). Another approach is based on the analysis of the minimum of the training loss function, reached by a model during the optimization. Because it is based on the minimum, this approach is very general and independent of the particular choice of the ML model architecture or the learning process.

---

[18]Interestingly, in their paper, the quantity which leads to the better CNN performance in case of the Ising model is the expected energy per site ($\frac{-J}{N}\sum_{(i,j)}\sigma_i\sigma_j$) which can still be detected with a 2×1 kernel, not the magnetization ($\frac{1}{N}\sum_i\sigma_i$) which can still be detected with a 1×1 kernel.

[19]Note that it is much easier to detect invariants which can be represented as polynomial function of input features.
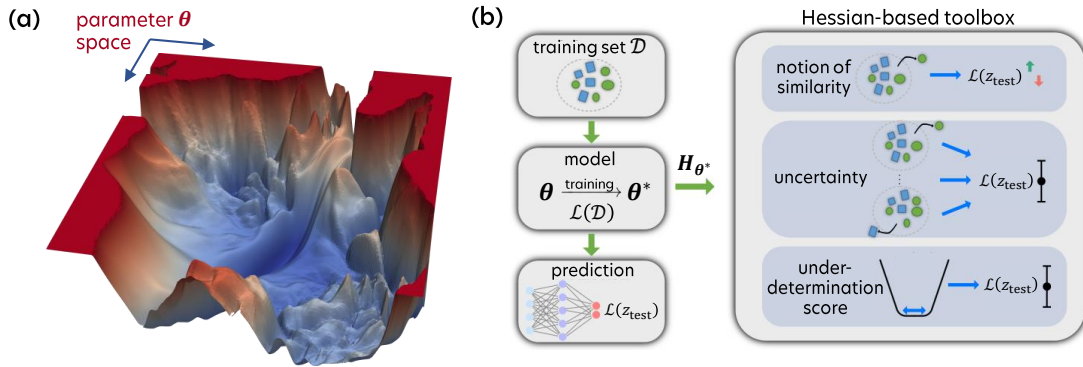
Figure 3.10: (a) Low-dimensionality visualization of a non-convex loss landscape of a DNN called VGG-56 trained on CIFAR-10 [39]. (b) Hessian-based toolbox [134] for increasing the interpretability and the reliability of a trained ML model. It is based on the Hessian of the training loss at the minimum (or an approximation thereof).

3.5.3 Hessian-based interpretability

As described in section 2.1, ML models learn by minimizing a training loss function $\mathcal{L}$ describing the problem through the variation of their parameters $\boldsymbol{\theta}$. The training loss landscape of deep NNs is, however, highly non-convex. This renders the optimization problem difficult, e.g., due to the presence of many local minima [see fig. 3.10(a)]. Moreover, these minima may not have equally good generalization properties that can be connected to the curvature around a minimum.[20] An analysis of how the generalization ability depends on the local curvature is an example for a case where the shape of the reached minimum can tell us something useful about trained ML models. The shape or curvature around the minimum $\boldsymbol{\theta} = \boldsymbol{\theta}^*$ is described by a Hessian matrix calculated at the minimum, i.e.:

$$H_{\boldsymbol{\theta}^*,ij} = \frac{\partial^2}{\partial\,\theta_i\theta_j}\mathcal{L}_{\text{train}}|_{\boldsymbol{\theta}=\boldsymbol{\theta}^*} . \tag{3.14}$$

The knowledge of the curvature around the minimum also allows us to approximate how our ML model (and as a result, its predictions) would change upon some action. Possible actions could be the removal of a single training point or a slight modification of $\boldsymbol{\theta}^* \to \tilde{\boldsymbol{\theta}}$, resulting in a shift to an adjacent minimum with identical training error. The study of how a model reacts to such actions is at heart of the Hessian-based toolbox summarized in fig. 3.10(b), which contains influence functions [135], the resampling uncertainty estimation (RUE) [136], and LEs [137] whose conceptual ideas we introduce in the following.

Influence functions are an approximation of the procedure known as leave-one-out training[21] and estimate how the model prediction on a test point x_{test} change, if a certain training point x_{R} is removed from the training set. You can imagine three outcomes of such a removal: (1) the prediction stays the same because the removed training point has no influence on the model prediction, (2) the prediction gets better (i.e., it leads to a lower test loss for x_{test}),

---

[20]There is a general consensus that wide, flat minima generalize better than sharp minima [129–132]. Keep in mind that flatness is not a well-developed concept in non-convex landscapes of deep models [133].

[21]Leave-one-out training for DL models with non-convex loss landscapes is tricky, because if we land in a different local minimum, we cannot make any claims on the perturbation caused by removal of a single training point. This is why usually we retrain carefully, starting from the minimum reached by the original model.

so x_{R} is a "harmful" training point for making a prediction on z_{test}, (3) the prediction gets worse (i.e., it leads to a larger test loss for x_{test}), so x_{R} is a "helpful" training point for making a prediction on z_{test}, and its removal made the task of constructing an accurate model harder. With such an analysis we can determine how influential training data points are to predictions at test points, which may give us a hint at how the model reasons. We can even go a step further and say that if two data points strongly influence each other, it is because they are very similar from the model's perspective.[22] This concept of similarity learned by a ML model can be understood as a distance between data points in the internal model representation and is a powerful tool for *detecting additional phases in mislabeled data* [96, 138], *detecting influential features* [96], and *anomaly detection* [134].

Another tool in the Hessian-based toolbox is the *resampling uncertainty estimation (RUE)* [136]. Its aim is to estimate the uncertainty of model predictions. It is an approximation of the classical procedure known as bootstrapping. You start with your original training set containing each training data point once. Imagine now that you create b new training sets by drawing samples uniformly with replacement from the original data set. Due to replacement, your new sets contain some training points in more than one copy and some points are omitted. Now you can train b models on these b training sets and make b predictions on the same test point, z_{test}. These predictions generally vary due to the distinct nature of the training sets. Computing the variance of these predictions on z_{test} gives us an estimate for the uncertainty of the original model prediction. A small variance signals that one can trust the prediction of the original model, because small random modifications to the training set do not change its prediction too much. A large variance signals that the prediction is based on a small number of training points and is therefore not reliable. In Ref. [134], you can see how such error bars indicate the *sharpness of quantum phase transitions*.

Finally, *local ensembles (LEs)* [137] allow us to detect the *underspecification* of a given model at the test point. A trained model is underspecified at a test input if many different predictions at that input data are all equally consistent with the constraints posed by the training data and the learning problem specification (i.e., the model architecture and the loss function). As described in section 2.1, the minimum reached within the optimization is usually surrounded by a mostly flat landscape. This means that if the model would have ended up in one of these flat neighboring points, the training error would have stayed exactly the same. Thus, such changes should not impact the predictions – unless a prediction is *underdetermined*, i.e., unstable and not well-explained by the training data. Therefore, we can again create multiple models by shifting the parameters of the original model by small amounts. As such, these new models explore the flat landscape around the original minimum. Eventually, we make predictions with these new models. If a prediction on a test point z_{test} changed due to such modifications, this point may be an out-of-distribution point, i.e., a point coming from a distribution that is significantly different from the distribution underlying the training data. LEs allow for the detection of such out-of-distribution test points which increases the reliability of the ML model. Moreover, the authors of Ref. [137] successfully used LEs for active learning, i.e., they built a much smaller, yet similarly informative training data set by iteratively adding to it test points with the largest underspecification score detected by LEs.

---

[22]This argument is well based in the geometric interpretation of influence functions, for details see section 2.3.3 in Ref. [134].

Therefore, we have answered our initial questions regarding interpretability: It is indeed possible to look inside the black box of ML models. If you focus your attention on the bottlenecks present in NN architectures, you can determine which quantities dominate in the NN prediction using regression methods. If these quantities are physically relevant, we can argue that the NN indeed bases its predictions on physically relevant quantities. For architectures without bottlenecks, you can turn your attention to the curvature around the minimum of the training loss. It contains information on the similarity learned by a model and allows for estimating the uncertainty.

3.6 Outlook and open problems

Over the last five years, there have been many works applying supervised and unsupervised phase classification algorithms, including supervised learning (section 3.3), learning by confusion (section 3.4.2), and the prediction-based method (section 3.4.3), to models with well-known phases. However, there have been only few works that applied unsupervised phase classification methods to experimental data. Moreover, the discovery of a novel phase of matter using unsupervised phase classification methods still remains to be demonstrated. This would constitute a major step toward the automation of scientific discovery.

While there has been significant progress regarding the interpretability of phase classification methods in recent years, we still lack a deeper understanding of these methods. In particular, it remains difficult to tell when and why a given method fails or succeeds [139]. With the goal of automated scientific discovery in mind and having demonstrated that phase classification methods are capable of dealing with a vast range of physical systems, addressing these gaps in knowledge and developing corresponding interpretability tools is of crucial importance.

Further reading

- Carleo, G. *et al.* (2019). *Machine learning and the physical sciences*. Rev. Mod. Phys. 91, 045002. An overview of the current state of the phase classification landscape is presented in section 4C [30].

- Neupert, T. *et al.* (2021). *Lecture notes: Introduction to machine learning for the sciences*. An introduction to fundamentals of ML and clustering algorithms for scientists [85].

- Molnar, C. (2019). *Interpretable Machine Learning: A Guide for Making Black Box Models Explainable*. An introductory book on interpretable machine learning [140].

- Jupyter notebook on phase classification [32].

4   Gaussian processes and other kernel methods

This section deals with the so-called kernel methods of which support vector machines (SVMs) and Gaussian processes (GPs) are prominent examples. These methods are particularly well-suited in the case of the low availability of labeled data. This usually happens when the creation of a large data set is expensive in terms of money, time, effort, and so on. As a second advantage, the predictions of GPs, in particular, are accompanied by their uncertainties which other methods typically do not provide. We see how this property arises from the design choice of the models in section 4.2.

But first, we have to introduce the notion of the *kernel* that is the integral part of all methods discussed in this chapter. The introduction of the kernel allows us to extend the range of problems we are able to tackle substantially. Before properly defining the mathematical foundation of kernels, we start by providing some intuition on how to use them in practice by means of the *kernel trick* and its implications. Afterwards, we show how to extend the aforementioned methods via this kernel trick and discuss how to train each of them given data. For example, it turns out that GPs can be approached from an information-theoretic perspective. Moreover, we explain how we can make use of concepts from information theory for a guided data acquisition procedure, as well as to select a good model among various possible ones. We end the chapter by showcasing the power of these methods at tackling quantum chemistry problems in section 4.5.

4.1   The kernel trick

As we have seen in section 2.4, simple approaches such as the linear regression model or the linear SVM have severe limitations with respect to the properties of data. They are applied to the input data *as is*, i.e., they are bound to the given representation of the input data. In order to avoid confusion later on, we refer to this data space as the *input space*. In this input space, it can, for example, happen that the given input data is not linearly separable. One possible remedy consists of extending the classification power of the model by first transforming the input data into an alternative *feature space*. In contrast to what we have said earlier in chapter 1, we explicitly distinguish between the input and the feature space in the following.[1] Ideally, in this new representation, the data possesses a more convenient structure compared to the original representation. For example, the data that was initially not linearly separable may be linearly separable in this new space. In particular, it is often useful to transform into a higher-dimensional feature space in which our data is now nested on a manifold which (ideally) possesses beneficial additional structure.

One may think that this makes the kernel methods extremely costly (or even infeasible if the dimension of the feature space approaches infinity).

> This is where the *kernel trick* comes in: it allows one to efficiently calculate distances in the feature space, which is all that is needed for many ML algorithms, without ever explicitly transforming the data into the feature space.

This trick is called the *kernel* trick because the kernel is the mathematical object we associate with such a feature space. As such, the kernel trick allows one to retain all the benefits of high-dimensional feature spaces at a manageable computational cost. Moreover, the mathe-

---

[1]Each element of a data point is still called a *feature* – in this chapter, we are, however, only interested in finding the most convenient representation of the data whose space we hence call the *feature* space.
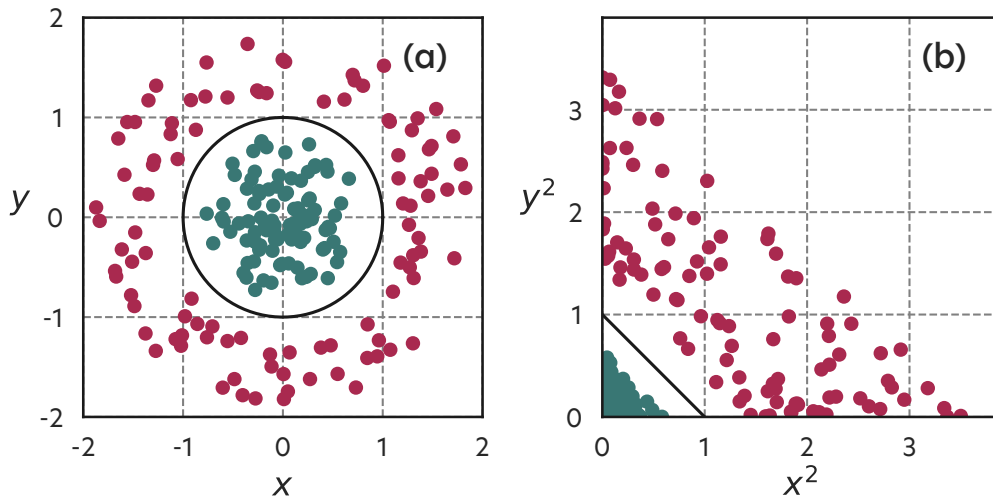
Figure 4.1: Toy example of a labeled two-dimensional data set. The data points are labeled according to their position with respect to the decision boundary indicated by the black circle in (a). In this *input space*, such a data set is not linearly separable. After a transformation of the input variables into a non-linear *feature space*, however, the data becomes linearly separable as indicated by the black line in (b).

matical foundation of kernels allow us, as we see in the next section, to enrich our motivation with rigorous, analytical validity. Especially important from a practical point of view is the *representer theorem*: so far, we have set out to find a suitable transformation, i.e., function to simplify our task at hand. However, it is unclear how to optimize over functions instead of parameters. The representer theorem endows us with both: in essence, it assures that the optimization over the function space is equivalent to optimizing the coefficients of a closed form solution which, in turn, allows us to devise feasible numerical optimization routines.

In the following, we start with an intuitive example to illustrate why and how the transformation into the feature space can be beneficial. Afterwards, we properly introduce the mathematical notion of kernels that gives us the analytical tools at hand that are required to understand the representer theorem.

4.1.1 Intuition behind the kernel trick

To gain some intuition, let us consider a labeled two-dimensional data set as depicted in fig. 4.1. In this toy example, the black line indicates the underlying decision boundary, i.e., the line that separates input data with different labels. In higher dimensions, the decision boundary generalizes to a hyperplane. In our example, one label refers to the center of the data cloud and the other label to its outskirts. A label distribution is said to be separable if one can draw such a decision boundary, i.e., it is separable if we can find at least one hyperplane separating the two class sets. If, furthermore, this decision boundary is linear, the data is called linearly separable.[2] Clearly, our toy data set is not linearly separable in the input space. As a consequence, we cannot find a straight line that fully separates the two data classes by means of a simplistic linear classifier. Additionally, other linear methods such as PCA (see chapter 3) fail to cluster this data.

---

[2]Whether a given data set actually is (linearly) separable or not, is not easily detectable. In practice, we can at least run algorithms such as an SVM explained in section 2.4.3 which are guaranteed to find the corresponding separating hyperplane if it exists.

However, as shown in the right panel in fig. 4.1, the data set becomes linearly separable if we transform the data in the appropriate way. Here, we have applied the transformation $(x_1, x_2) \mapsto \phi(x_1, x_2) = (x_1^2, x_2^2)$ to map the input data non-linearly to the so-called feature space. Hence, the map ϕ is called the feature map. There are two important caveats: firstly, finding a useful feature map is a highly-non-trivial task. In our toy example, the labeling procedure has considered the data points in polar coordinates and used the radial distance r to the origin as the label criterion. Using the connection $r^2 = x_1^2 + x_2^2$, we motivate our feature map ϕ whose choice is by no means unique. Secondly, even if we had found a good feature map, it could be infinite-dimensional.[3] In that case it would not be feasible to transform the data with the feature map. In our example, we only considered a polynomial expansion of the input variables in order to achieve linear separability. However, there can be instances where the polynomial expansion has to be taken to infinite order. We encounter such an example where the most suitable feature space is infinite dimensional later on when we come back to our toy example at the end of section 4.2.2.

> Fortunately, it turns out that many ML algorithms can be expressed only in terms of inner products between data points x, y.[a] As such, we do not need to consider the individual inputs x and their representation in feature space $\phi(x)$ explicitly. The *kernel trick* simply consists of exchanging the inner product $\langle x, y \rangle = x^\mathsf{T} y$ in the corresponding algorithms by the function $K(x, y) = \phi(x)^\mathsf{T} \phi(y)$.
>
> ---
> [a]We remind the reader that these data points are, in general, vectors, i.e., they may live in a high-dimensional space.

The function K can be efficiently evaluated even for an infinite-dimensional feature map ϕ and yields a single real non-negative number regardless of the data under consideration or the dimension of the feature space. As we see later, the function K is referred to as the kernel function. This way, the kernel trick allows for a feasible non-linear extension of a variety of ML-algorithms, such as ridge regression, SVMs, or PCA. We detail the mathematical foundation of kernels in the next sections.

4.1.2 The function space as a Hilbert space

As we have sketched above, we want to find a suitable choice for our feature map, i.e., search for a function that lives in some function space. A mathematical space is a set of elements that obey a set of common rules specifying the relationship between them. As we want to search in a function space, it is reasonable to assume it to be a vector space. In such a space, we are allowed to add functions to each other or rescale them by a constant without leaving the function space. This assumption is necessary to express the unknown target function by a weighted sum of other known functions. Fortunately, how to optimally tune these weights is something we are familiar with in ML. As a second ingredient, we require some distance measure or, equivalently, a measure of similarity between functions. This is achieved by enriching our vector space with an inner product $\langle \cdot, \cdot \rangle$, turning the function space into an Hilbert space. Since we have some freedom on how to define the inner product, different choices of inner products lead to different notions of distance, i.e., different spaces altogether. We see shortly why we need this similarity measure by the end of this section.

If we consider the space of real-valued functions and restrict ourselves to the condition of

---

[3]In a sense, we do the opposite of a dimensionality reduction method such as PCA in section 3.2.1 – usually, we drastically increase the dimension of the feature space in order to rearrange the data most conveniently. Another difference is that we do not loose any information in the data by embedding them into a high-dimensional space.

square-integrability, the corresponding function space is such a Hilbert space. This effectively turns the function space into something akin to the more intuitive Euclidean space. It is called the L^2-space.[4] Square-integrability refers to the fact that the integral over the full domain D remains finite, i.e., $\int_{\mathbb{D}} f^2(\boldsymbol{x})\, d\boldsymbol{x} < \infty \ \forall f \in L^2$. The domain $\mathbb{D}$ is often given by $\mathbb{R}^m$ with some dimension m in typical ML-scenarios as it corresponds to our input space. The L^2-space readily comes along with a canonical choice for the inner product given by

$$\langle f, g \rangle = \int_{\mathbb{D}} f(\boldsymbol{x}) g(\boldsymbol{x})\, d\boldsymbol{x} \tag{4.1}$$

that provides the notion of orthogonality as $\langle f, g \rangle = 0$, and a norm $\|f\|_{L^2}^2 = \langle f, f \rangle$. Since a Hilbert space is a vector space, we can find an orthogonal basis set $\{\phi_n(\boldsymbol{x})\}$ that spans the space. In case of the L^2-space it is of infinite (but countably infinite) dimension. This basis allows for any function $f \in L^2$ to be decomposed as

$$f(\boldsymbol{x}) = \sum_n a_n \phi_n(\boldsymbol{x}), \tag{4.2}$$

with real coefficients $\{a_n\}$. Lastly, any two Hilbert spaces have the same geometric structure, regardless of their respective elements – this is the whole reason we can draw the analogies between the L^2 and the intuitive Euclidean space in the first place. This can be made more formal by the representation theorem of Riesz [141]: we can express certain linear functionals by means of the Hilbert space's inner product. The functional of interest is the *evaluation* of the function f at any point $\boldsymbol{x} \in \mathbb{D}$, i.e., $f \in L^2 \mapsto f(\boldsymbol{x}) \in \mathbb{R}$ since this is what we are trying to achieve in our task. Furthermore, Riesz theorem tells us that this can, in principle, be achieved by a particular, unique function living in the Hilbert space via the inner product, i.e., the evaluation is of the form $\langle \cdot, K \rangle$ with K a member of the same Hilbert space. This function is called the *kernel function* but is not guaranteed to exist in every Hilbert space – we introduce it and its constraints properly in the next section.

4.1.3 Reproducing kernel Hilbert spaces

As already anticipated, we want to make use of Riesz theorem to connect the function space to the evaluation of its members. That is, we want to be able, once provided with a trial function f from the Hilbert space $\mathcal{H}$, to evaluate its output $f(\boldsymbol{x})$ at an arbitrary domain location $\boldsymbol{x}$. In order to use the theorem, we have to restrict the function K, which we subsequently call the *kernel function*, to fulfill the following integral transformation:

$$f(\boldsymbol{x}) = \int_{\mathbb{D}} K(\boldsymbol{x}, \boldsymbol{x}') f(\boldsymbol{x}')\, d\boldsymbol{x}' \quad \forall\, f \in \mathcal{H}, \tag{4.3}$$

while also requiring that $K(\cdot, \boldsymbol{x}) = K(\boldsymbol{x}, \cdot) =: k_{\boldsymbol{x}} \in \mathcal{H} \ \forall\, \boldsymbol{x} \in \mathbb{D}$. The equation relates the evaluation of the trial function f to the kernel – and we see how we can make use of it in the following. Actually, the integral transformation resembles one of the defining properties of the δ-distribution and we would be inclined to choose $K(\boldsymbol{x}, \boldsymbol{x}') \equiv \delta(\boldsymbol{x} - \boldsymbol{x}')$. However, the problem lies in the fact that the δ-distribution (when indexed by one of its components) is not square-integrable, i.e., $\langle \delta, \delta \rangle \notin \mathbb{R}$, and thus $\delta \notin L^2$.[5] We can solve this conundrum by

---

[4]Of course, not all functions we are interested in finding are necessarily members of this function space. Because we are always presented with a finite data set, however, we usually do not care what happens very far outside this regime. Even though our target function might not be a member of this space, we should be able to find a member that resembles the target function in the region of interest, nevertheless. This is why we can restrict ourselves with the L^2-space in the first place.

[5]At least not in the case where the domain corresponds to the whole $\mathbb{R}^m$. If we restrict the frequency domain to some bounded subset, we can, in fact, construct a kernel function. However, this function is not the δ-distribution.

setting up a *new* Hilbert space $\mathcal{H}$ (which cannot be identical to the L^2) equipped with a kernel function K that actually fulfills eq. (4.3). As a member of the Hilbert space $\mathcal{H}$, the kernel (when indexed by either one of its arguments) can be decomposed as in eq. (4.2). We can actually go one step further: due to Mercer's theorem [142], this basis set can be used to symmetrically decompose the kernel into

$$K(x, x') = \sum_n \lambda_n \phi_n(x) \phi_n(x') = K(x', x) \tag{4.4}$$

with coefficients $\{\lambda_n\}$. Moreover, for an orthonormal basis set, the coefficients λ_n are all equal to one. We can prove this by choosing $f = \phi_k$ for some integer k. Then from eq. (4.3) and the decomposition of the kernel, we require that

$$\phi_k(x) = \sum_n \lambda_n \phi_n(x) \int_{\mathbb{D}} \phi_n(x') \phi_k(x') \, dx' = \lambda_k \phi_k(x). \tag{4.5}$$

Since k was chosen arbitrarily, we find that $\lambda_n = 1 \ \forall n$ iff we select an orthonormal basis set. We can convince ourselves that this kernel representation actually performs the integral transformation in eq. (4.3). Therefore,

$$\int_{\mathbb{D}} K(x, x') f(x') \, dx' = \sum_{n,k} a_n \phi_k(x) \int_{\mathbb{D}} \phi_k(x') \phi_n(x') \, dx' = \sum_n a_n \phi_n(x) = f(x) \tag{4.6}$$

as intended. Having introduced the kernel function $K(x, x')$, let us examine more of its properties. First, let us fix one of the arguments and consider the kernel only as a function of the second argument. Due to the symmetry in the arguments, we choose x without loss of generality. We indicate this choice by a different notation as $K_x(x') := K(x, x') = \sum_n a_{x,n} \phi_n(x')$ where the last equation is just eq. (4.2) with $a_{x,n} = \lambda_n \phi_n(x)$ due to eq. (4.4). This newly introduced function K_x is just another function in our Hilbert space $\mathcal{H}$. However, we can express any other function $f \in \mathcal{H}$ in the same Hilbert space as an inner product with K_x: using the integral transformation of eq. (4.3) and the definition of the inner product as in eq. (4.1), we see that

$$f(x) = \int_{\mathbb{D}} K(x, x') f(x') \, dx' = \int_{\mathbb{D}} K_x(x') f(x') \, dx' = \langle K_x, f \rangle = \langle f, K_x \rangle. \tag{4.7}$$

At this point, we understand how Riesz' theorem applies to the function evaluation: the kernel function K turns the inner product in the Hilbert space $\mathcal{H}$ into the function evaluation. Due to this reproducing capability, the function K_x is called the *reproducing kernel* of the Hilbert space $\mathcal{H}$, which itself is dubbed the reproducing kernel Hilbert space (RKHS). Instead of indexing over the first argument x, we can also define $K_{x'}(x) := K(x, x')$ by indexing over the second argument x'. As both belong to the same Hilbert space $\mathcal{H}$, we faithfully reproduce $K_{x'}$ by K_x (or vice versa):

$$K_{x'}(x) = K(x, x') = \langle K_x, K_{x'} \rangle = K_x(x') \tag{4.8}$$

Furthermore, we see that the kernel function $K(x, x')$ is just the inner product between the reproducing kernel K_x with itself $K_{x'}$.

The choice of the reproducing kernel is unique as shown by the Moore-Aronszajn theorem [143] granted that we have a positive definite kernel, i.e., $K(x, x') \geq 0 \ \forall x, x' \in \mathbb{D}$. This condition is necessary in order to represent the kernel function as an inner product as in eq. (4.8). The theorem then tells us that for every positive definite kernel, there exists a unique RKHS and vice versa.

The theorem begs the question whether *any* positive definite function can actually be a kernel function. This is the case as we show now. To this end, consider a positive definite function K which takes two elements from our domain $\mathbb{D}$ as arguments, i.e., $K : \mathbb{D} \times \mathbb{D} \to \mathbb{R}$. Mercer's theorem also holds for positive definite functions and, thus, the decomposition in eq. (4.4) is valid with $\lambda_n \geq 0$ (but not necessarily equal to one anymore) due to the positivity of K. This decomposition, moreover, is unique and obeys the eigenvalue equation

$$\int_{\mathbb{D}} K(\boldsymbol{x}, \boldsymbol{x}')\phi_n(\boldsymbol{x}')\, d\boldsymbol{x}' = \lambda_n \phi_n(\boldsymbol{x}) \; \forall n \,. \tag{4.9}$$

Using eq. (4.2), we rewrite the inner product in the L^2 of eq. (4.1) as

$$\langle f, g \rangle = \int_{\mathbb{D}} f(\boldsymbol{x})g(\boldsymbol{x})\, d\boldsymbol{x} = \sum_{m,n} a_m b_n \underbrace{\int_{\mathbb{D}} \phi_m(\boldsymbol{x})\phi_n(\boldsymbol{x})\, d\boldsymbol{x}}_{=\langle \phi_m, \phi_n \rangle = \delta_{m,n}} = \sum_n a_n b_n$$

$$= \sum_n \int a_m \phi_m(\boldsymbol{x})\phi_n(\boldsymbol{x})\, d\boldsymbol{x} \int b_k \phi_k(\boldsymbol{x}')\phi_n(\boldsymbol{x}')\, d\boldsymbol{x}' = \sum_n \langle f, \phi_n \rangle \langle g, \phi_n \rangle \,. \tag{4.10}$$

However, in order for K to be a valid kernel, it has to obey eq. (4.7) as well. Plugging this into the first step of eq. (4.10) together with Mercer's decomposition as in eq. (4.4), we see that

$$\langle f, g \rangle = \int f(\boldsymbol{x})g(\boldsymbol{x})\, d\boldsymbol{x} = \int \langle f, K_{\boldsymbol{x}} \rangle\, g(\boldsymbol{x})\, d\boldsymbol{x}$$

$$= \sum_n \lambda_n \int \phi_n(\boldsymbol{x}) \langle f, \phi_n \rangle\, g(\boldsymbol{x}) = \sum_n \lambda_n \langle f, \phi_n \rangle \langle g, \phi_n \rangle \tag{4.11}$$

Comparing the two previous results, we see a discrepancy in terms of the prefactors λ_n of the Mercer decomposition of the (not yet) kernel function K. In order to compensate for this, we can redefine the inner product as

$$\langle f, g \rangle_{\mathcal{H}} = \sum_{n=1}^{\infty} \frac{\langle f, \phi_n \rangle \langle g, \phi_n \rangle}{\lambda_n} \,, \tag{4.12}$$

which is equivalent to the previous inner product in eq. (4.1) iff $\lambda_n = 1 \; \forall n$. With this definition of the inner product, we have

$$\langle f, K_{\boldsymbol{x}} \rangle_{\mathcal{H}} = \sum_{n=1}^{\infty} \frac{\langle f, \phi_n \rangle \langle K_{\boldsymbol{x}}, \phi_n \rangle}{\lambda_n} = \sum_{n=1}^{\infty} \langle f, \phi_n \rangle \phi_n(\boldsymbol{x}) = f(\boldsymbol{x}) \,. \tag{4.13}$$

Here, we have used eq. (4.9) in the second step and the last equality follows from the fact that the set $\{\phi_n\}$ forms a complete basis, i.e., eq. (4.2). This now fulfills eq. (4.7) as intended and, furthermore, renders the Hilbert space $\mathcal{H}$ an RKHS, and K, any arbitrary positive definite function, is indeed a kernel function. Lastly, we remark that the redefinition of the inner product is crucial in order for every RKHS to be associated with a unique positive definite kernel.

4.1.4 The representer theorem

Finally, we have all the ingredients necessary for the representer theorem [144]: by virtue of eq. (4.7), we have that $f(x) = \sum_{m=1}^{\infty} a_m K(\boldsymbol{x}, \boldsymbol{x}_m)$ for any function f in general. Given a loss function $\mathcal{L}$ (including a regularization term) and n training samples $\{(\boldsymbol{x}_i, y_i)\}_{i=1}^{n}$, the theorem asserts that

$$f^*(\boldsymbol{x}) := \arg \min_f \mathcal{L}\Big(\{(f(\boldsymbol{x}_i), y_i)\}_{i=1}^{n} \Big) = \sum_{i=1}^{n} a_i K(\boldsymbol{x}, \boldsymbol{x}_i), \tag{4.14}$$

i.e., the loss is minimized by resorting to the *finite* amount of training data only. Moreover, we only require the knowledge of our kernel function K – the heavy machinery, e.g., its unique RKHS with Riesz theorem telling us how to *evaluate* the unknown target function f^*, remains hidden in the proof and we can happily live with the resulting theorem only.

> The representer theorem guarantees that we can formulate the search for a function f^* that minimizes a specific loss function over an infinite-dimensional function space as a search over n kernel coefficients $\{a_i\}_{i=1}^n$. Thus, it significantly reduces the complexity of the minimization problem at hand and renders it computationally tractable.

Finally, our mathematical efforts have come to fruition: the reproducing property of the kernel in eq. (4.3) allows us to *implicitly* embed the input data in a (possibly) high-dimensional feature space in which we calculate the similarities to a test point x. Because we only require to calculate the similarity measure between data points, we do not loose efficiency here. We see how to practically do this in the following when we extend some of the models of section 2.4 via the kernel trick in section 4.2.

4.1.5 Consequences of the kernel trick

We have gone to somewhat lengthy details on the maths behind kernels, in particular, concerning the RKHS. Despite the perceived detour through Hilbert spaces and a redefinition of the inner product in the RKHS, this leg work equips us with all the necessary foundation to the theory of kernels: the reproducing feature of eq. (4.3) is not a mere mathematical curiosity but has straightforward implications in terms of the representer theorem. Secondly, the kernel allows us to solve our initial problem (finding the unknown target function) by finding the right kernel. The kernel can be understood as a similarity measure between functions. This similarity between two inputs can easily be calculated even if the underlying feature space is high- or even infinite-dimensional.

One important consequence of implicitly switching from the input to the feature space by means of the kernel trick is that we have to rethink our intuition of regularization: now, we have to perform the regularization of the learned function in the function space given by the RKHS as discussed in the previous section. Thus, we have to start from the inner product in the RKHS, i.e., eq. (4.12). By virtue of Mercer's theorem in eq. (4.4), the coefficients λ_n correspond to the weights of the basis functions of the kernel and are non-negative by construction. In particular, they depend on the actual choice of the kernel function K. For instance, our kernel decomposition could include zero entries for some of the basis functions. This is not an issue per se: the function f we are interested in might still lie entirely in the RKHS. Using eq. (4.2), we can decompose it as $f(x) = \sum_{n=1}^{\infty} a_n \phi_n(x)$. Its corresponding L^2-norm is $\|f\|_2^2 = \sum_n |a_n|^2$. Due to eq. (4.12), this translates to a norm in the RKHS as

$$\|f\|_{\mathcal{H}}^2 = \sum_{n=1}^{\dim(\mathrm{RKHS})} \frac{|a_n|^2}{\lambda_n}. \tag{4.15}$$

Thus, we see that we potentially run in to trouble in case of zero entries for some of the coefficients λ_n as our norm may diverge. It remains finite iff the corresponding function coefficient a_n is equal to zero at the same time. This is the case if the function is entirely in the RKHS provided by the kernel function. If not, i.e., when choosing the wrong kernel function, we cannot regularize our model and cannot expect to learn the unknown target function f.

Table 1: Examples of kernel functions, where θ, θ_1 and θ_2 are free parameters [118].

Kernel function	Mathematical form
Linear	$K_{\text{LIN}}\left(\boldsymbol{x}, \boldsymbol{x}'\right) = \boldsymbol{x}^{\intercal}\boldsymbol{x}' + \theta$
Radial basis	$K_{\text{RBF}}\left(\boldsymbol{x}, \boldsymbol{x}'\right) = \exp\left(-\frac{1}{2\theta^2}\|\boldsymbol{x} - \boldsymbol{x}'\|^2\right)$
Matérn 5/2	$K_{\text{MAT}}\left(\boldsymbol{x}, \boldsymbol{x}'\right) = \left(1 + \frac{\sqrt{5}}{\theta}\|\boldsymbol{x} - \boldsymbol{x}'\| + \frac{5}{3}\|\boldsymbol{x} - \boldsymbol{x}'\|^2\right) \times \exp\left(-\frac{\sqrt{5}}{\theta^2}\|\boldsymbol{x} - \boldsymbol{x}'\|\right)$
Rational quadratic	$K_{\text{RQ}}\left(\boldsymbol{x}, \boldsymbol{x}'\right) = \left(1 + \frac{\|\boldsymbol{x} - \boldsymbol{x}'\|}{2\theta_1\theta_2^2}\right)^{-\theta_1}$

> The theory of RKHS' can give us an intuition on why certain choices of kernel function seem to work while others fail: the function f we are interested to re-express with our kernel function K has to fully lie in the RKHS uniquely defined by K. If not, our approach is doomed to fail in learning the function from the start. Because a systemic check in the (usually) infinite dimensional function space is not feasible, we can only resort to the trial-and-error approach. Luckily for us, there are ways to systematically build better kernels (which provide a more suitable RKHS) presented in section 4.4.2.

4.2 Kernel methods

In section 4.1, we have presented the mathematical foundation of kernels. In short, we want to map our data to a feature space which possesses a more suitable structure for the task at hand. Instead of explicitly defining a feature map ϕ, we introduce a kernel function K which provides a similarity measure between data points in the underlying feature space. As such, we exchange the problem of searching for a (potentially) high-dimensional feature map to finding an optimal kernel function, which is rigorously easier. This constitutes the kernel trick.

Kernel methods correspond to all classification and regression methods that take advantage of the kernel trick. The validity of these approaches is ensured by the representer theorem, see section 4.1.4. The first step of every kernel method is to choose a kernel function. As discussed previously, any positive definite function can be used as a kernel function. Typically, one starts by assuming some functional form (see examples in table 1). These functions are parametrized by a few parameters, such as θ, or θ_1 and θ_2 in these examples. Having chosen a particular functional form of the kernel function, one varies these parameters to find the best kernel in the corresponding functional ansatz class. This makes the optimization already easier as we now have to optimize over a set of parameters and not over a set of functions. Also note that given a set of kernels, there exist many transformations which yield new valid kernels. For example, any linear combination of kernel functions $\sum_i c_i K_i\left(\boldsymbol{x}, \boldsymbol{x}'\right)$ with positive coefficients $c_i \geq 0$ constitutes a valid kernel. For a more exhaustive list of techniques for constructing new kernels, see [83]. We explicitly make use of these rules in section 4.4.2 where we discuss how to construct good kernels systematically through composition.

We turn to three prominent kernel methods in the remainder of this subsection: kernel ridge regression (KRR), support vector machines (SVMs) and Gaussian processes (GPs).

4.2.1 Kernel ridge regression

Kernel ridge regression (KRR) is an extension of ridge regression (presented in section 2.4.1) to a non-linear and possibly high-dimensional space. The functional we want to minimize is very similar to the one of ridge regression, but this time, the model f lives in the RKHS $\mathcal{H}$

corresponding to the particular choice of the kernel function (note the use of MSE!):

$$\mathcal{L}_{\text{KRR}} = \sum_i^n (y_i - f(\boldsymbol{x}_i))^2 + \lambda \|f\|_{\mathcal{H}}^2 = \mathcal{L}_{\text{MSE}} + \mathcal{L}_{\text{reg}} \tag{4.16}$$

with a regularizing term introduced in eq. (4.15). Here, f is not restricted to a linear function of its parameters (as in linear ridge regression). Instead, f can, in principle, be arbitrary. As such, KRR is capable of building highly expressive models given an appropriate choice of the kernel. Solving a problem with kernel methods translates to finding the optimal kernel. This functional form in eq. (4.16) does not yet look like it is the case. Let us then reformulate it so it becomes apparent. A kernel model $f(\boldsymbol{x})$ based on a kernel function $K(\boldsymbol{x}, \boldsymbol{x}')$ can be written as the following sum over the training data:

$$f(\boldsymbol{x}) = \sum_{j=1}^n \alpha_j K(\boldsymbol{x}, \boldsymbol{x}_j). \tag{4.17}$$

This formulation is an instance of the already discussed representer theorem, see eq. (4.14). Apart from K which we know how to compute given the data, we also have here coefficients α_j of our kernel model $f(\boldsymbol{x})$ which we need to find. Now we can express eq. (4.16) with eq. (4.17) in matrix form:

$$\mathcal{L}_{\text{MSE}} = \sum_i^n (y_i - f(\boldsymbol{x}_i))^2 = (\boldsymbol{y} - \boldsymbol{K}\boldsymbol{\alpha})^{\mathsf{T}}(\boldsymbol{y} - \boldsymbol{K}\boldsymbol{\alpha}), \tag{4.18}$$

$$\mathcal{L}_{\text{reg}} = \lambda \|f\|_{\mathcal{H}}^2 = \lambda \boldsymbol{\alpha}^{\mathsf{T}} \boldsymbol{K} \boldsymbol{\alpha}, \tag{4.19}$$

where the matrix $\boldsymbol{K}$ is called the *kernel matrix*. It is a positive-semidefinite, square $n \times n$ matrix with elements $K(\boldsymbol{x}, \boldsymbol{x}')$ with training points $\boldsymbol{x}$ and $\boldsymbol{x}'$ belonging to the training set: $\boldsymbol{x}_1, \boldsymbol{x}_2, \boldsymbol{x}_3, \ldots, \boldsymbol{x}_n$. The vector $\boldsymbol{y}$ represents the targets for the corresponding training input $\boldsymbol{x}$. Finally, if we put the derivative of the sum of these two components to zero, we can find a solution for $\boldsymbol{\alpha}$ which is:

$$\hat{\boldsymbol{\alpha}} = [\boldsymbol{K} + \lambda \mathbb{1}]^{-1} \boldsymbol{y}. \tag{4.20}$$

Given $\hat{\boldsymbol{\alpha}}$, we can write the estimator of the model $\hat{f}$ at a test point $\boldsymbol{x}^*$ as

$$\hat{f}(\boldsymbol{x}^*) = \boldsymbol{k}^{\mathsf{T}}(\boldsymbol{x}^*) \hat{\boldsymbol{\alpha}} = \boldsymbol{k}^{\mathsf{T}}(\boldsymbol{x}^*) [\boldsymbol{K} + \lambda \mathbb{1}]^{-1} \boldsymbol{y}, \tag{4.21}$$

where $\boldsymbol{k}(\boldsymbol{x}^*) = [k(\boldsymbol{x}^*)_i] = [K(\boldsymbol{x}^*, \boldsymbol{x}_i)]$. The analogous and thorough derivation of the kernel trick on the example of KRR is provided in appendix B. Finally, we can see that the prediction of the output for an unseen input $\boldsymbol{x}^*$ can be written in terms of:

- The target vector $\boldsymbol{y}$,

- The kernel matrix $\boldsymbol{K}$, whose elements are the kernel functions $K(\boldsymbol{x}_i, \boldsymbol{x}_j)$, which takes advantage of the kernel trick,

- The column vector $\boldsymbol{k}(\boldsymbol{x}^*)$, whose elements are the kernel functions $K(\boldsymbol{x}^*, \boldsymbol{x}_i)$, which also takes advantage of the kernel trick,

- The regularization term of magnitude λ.

So, as anticipated earlier in the chapter, successfully applying KRR boils down to finding the appropriate kernel function K.

4.2.2 Support vector machines

In the previous section, we have discussed how to use kernel methods for regression problems (in particular ridge regression). In this section, we show how can we use them for classification. In this context, the intuition behind the kernel approach is to embed the input space into the feature space in such a way that the data becomes linearly separable with a hyperplane (as described already in section 4.1.1). The most common ML-classification method utilizing the kernel trick are support vector machines (SVMs).[6]

SVMs have been introduced already in section 2.4.3 as geometric linear classifiers. Before we see how kernels enter SVMs, let us make a reminder how linear SVMs work and rephrase the optimization problem that we have described in section 2.4.3. The problem there is to find an optimal hyperplane separating data from different classes. The optimal hyperplane is defined as the one with the maximal distance between the hyperplane and the data points. In other words, we can say that all data points need to be at least the distance M away from the hyperplane. The data points that are separated from the hyperplane exactly by M, so are the closest to the hyperplane, become support points, $x_{s,i}$. The classification problem boils down to finding such a hyperplane described by θ that maximizes the margin between the hyperplane and support points $x_{s,i}$ (see fig. 2.5). As we can rescale the hyperplane in an arbitrary way, we can have $|\theta| = 1/M$. Then maximizing a margin, becomes minimizing θ that in turn comes down to minimizing the Lagrange function L in eq. (2.41), which we write here again for the readability:

$$L = \frac{1}{2}|\theta|^2 - \sum_{i=1}^{n} \alpha_i \left[y_i \left(\theta^\mathsf{T} x_i + \theta_0 \right) - 1 \right], \tag{4.22}$$

where the Lagrange multipliers α_i are chosen such that

$$\alpha_i \left[y_i \left(\theta^\mathsf{T} x_i + \theta_0 \right) - 1 \right] = 0 \quad \forall\, i = 1, \dots, n. \tag{4.23}$$

As we have already discussed, α_i is non-zero (and positive) only for $x_{s,i}$. In practice, rather than minimizing L, we go for the dual formulation of the problem, and we maximize a Lagrange dual, L_D, which provides the lower bound for L. L_D remains a quadratic program similarly as L as we have discussed in section 2.4.3. To express the problem via L_D, we firstly take the derivative of L with respect to θ and θ_0 and set it to zero. We arrive at:

$$\begin{aligned} \theta &= \sum_{i=1}^{n} \alpha_i y_i x_i \\ 0 &= \sum_{i=1}^{n} \alpha_i y_i. \end{aligned} \tag{4.24}$$

We can see that the coefficients θ are given by the Lagrange multipliers α_i, which can be found numerically. When we plug these equations back to the Lagrange function in eq. (4.22), we arrive to the Lagrange dual:

$$L_D = \sum_{i=1}^{n} \alpha_i - \frac{1}{2} \sum_{i=1}^{n} \sum_{j=1}^{n} \alpha_i \alpha_j y_i y_j x_i^\mathsf{T} x_j \quad \text{subject to } \alpha_i \geq 0. \tag{4.25}$$

Finally, to put kernels in the picture, we change the notation from $x_i^\mathsf{T} x_j$ to $\langle x_i, x_j \rangle$. For now, it remains a linear model. To deal with non-linearities in the input space, we can now

---

[6]There is a variant of this approach designed for regression called support vector regression that is almost identical with KRR but minimizes a different form of a loss function.
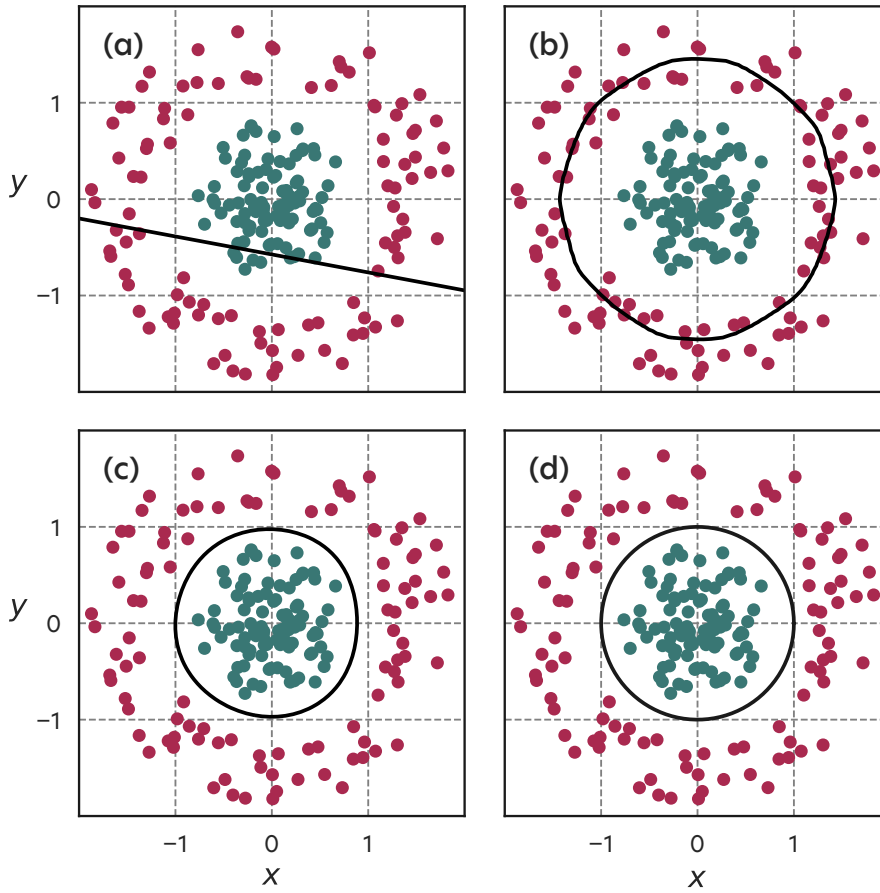
Figure 4.2: The kernel form makes a difference! The same data as in fig. 4.1 is classified using an SVM with different kernel choices. The black line corresponds to each underlying decision boundary. (a) As the data is not linearly separable, a linear kernel does not work. (b) A polynomial kernel up to degree 50 does the trick with the expense of signs of overfitting. (c) Due to the rotation symmetry, an RBF kernel is best suited for classifying this data set whose decision boundary closely resembles the actual underlying decision boundary of the data shown in (d).

introduce a feature map, $x_i \to \Phi(x_i)$, which gives us

$$L_D = \sum_{i=1}^{n} \alpha_i - \frac{1}{2} \sum_{i=1}^{n} \sum_{j=1}^{n} \alpha_i \alpha_j y_i y_j \left\langle \Phi(x_i), \Phi(x_j) \right\rangle. \tag{4.26}$$

So we finally see our kernel function, $K(x_i, x_j) = \left\langle \Phi(x_i), \Phi(x_j) \right\rangle$, appearing. In this kernel formulation, the margin we maximize is between the hyperplane and the support points *in the feature space*. Therefore, the SVM problem boils down to maximizing L_D numerically to find the coefficients α_i and the parameters of the kernel function K, e.g., using sequential minimal optimization [61]. Once these are known, the hyperplane separating the classes in the typically high-dimensional space is also known. With the optimal hyperplane $\hat{f}$ we can then make predictions at an arbitrary test point x^*:

$$\hat{f}(x^*) = \theta^{\mathsf{T}} \phi(x) + \theta_0 = \sum_i \alpha_i y_i \left\langle \phi(x_i), \phi(x_i) \right\rangle + \theta_0 = \sum_i \alpha_i y_i K(x_i, x) + \theta_0. \tag{4.27}$$
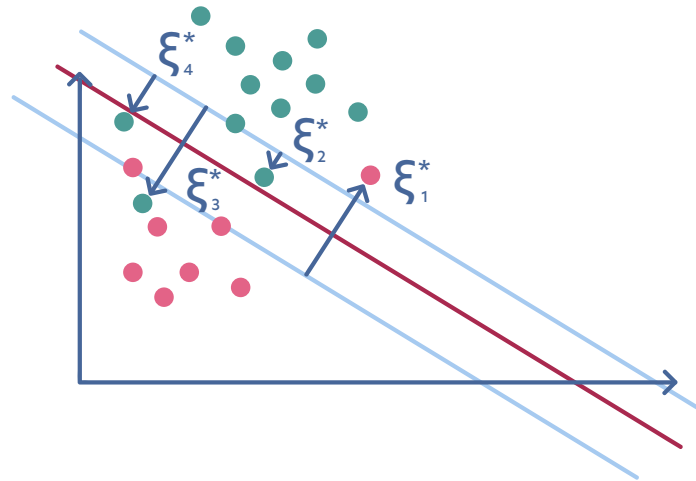
Figure 4.3: A linear SVM applied to a data set that is not linearly separable. The SVM tries to minimize the total distance of all misclassified data points ξ_i called slack variables. $\xi_i \geq 1$ for misclassified x_i (here, $i = 1, 3, 4$) and $0 < \xi_i < 1$ for points on the correct side of the decision boundary but within the margin (here, $i = 2$).

Finally, in order to turn this value into a class prediction, we take the sign of $\hat{f}$ as the corresponding class label. Note that the choice of the kernel function here matters as discussed in the opening of section 4.2. We visualize this problem in fig. 4.2.

While we can put lots of effort into finding a kernel function that renders our problem linearly separable, we can also relax the problem by allowing some misclassification. Let us thus move to the *problems that are not linearly separable*. The derivations above still hold with one modification: we now allow a number of data points to be on the wrong side of the margin, as shown in fig. 4.3. This modifies our constraint from eq. (2.40) to $y_i(\boldsymbol{\theta}^\intercal \boldsymbol{x}_i + \theta_0) \geq 1 - \xi_i$, where $\xi_i = 0$ if the data point is on the correct side of the margin. The variables ξ_i are often referred to as *slack variables*. We can incorporate the control over how "wrong" the hyperplane can be by adding another constraint, i.e., $\sum_i \xi_i < C = \text{const}$, which also adds terms to the Lagrange function:

$$L = \frac{1}{2}|\boldsymbol{\theta}|^2 - \sum_i \alpha_i \left[y_i \left(\boldsymbol{\theta}^\intercal \boldsymbol{x}_i + \theta_0 \right) - (1 - \xi_i) \right] + C \sum_i \xi_i. \tag{4.28}$$

Now, we maximize the margin while minimizing the violation of the margin constraints. This loss function is still a quadratic program but now has also a largely increased number of optimization variables (one slack variable per data point). As previously, instead of minimizing L you can maximize L_D. Note that in this case you get an additional regularization term with magnitude C. Large C allows for more misclassified data points but promotes simpler decision boundaries. In contrary, small C forces model to better fit training data, sometimes at the expense of the validation data.[7]

Finally, we can make a connection between SVMs and KRR. We started by saying that we

---

[7]Beware of various definitions and notations regarding regularization strength, in particular in SVMs. For example, in Scikit-learn decreasing a hyperparameter C corresponds to more regularization.

need to minimize $|\boldsymbol{\theta}|^2$ subject to the following conditions:

$$y_i(\boldsymbol{\theta}^\mathsf{T}\boldsymbol{x}_i + \theta_0) \geq 1 - \xi_i \text{ with } \xi_i \geq 0$$
$$\sum_i \xi_i < C = \text{const}. \tag{4.29}$$

If we simply write

$$\xi_i \geq 1 - y_i(\boldsymbol{\theta}^\mathsf{T}\boldsymbol{x}_i + \theta_0) \tag{4.30}$$

and vary $\boldsymbol{\theta}$ and θ_0 to find the minimum of the following function:

$$L(\boldsymbol{\theta}, \theta_0) = \frac{1}{2}|\boldsymbol{\theta}|^2 + C\sum_i [1 - y_i(\boldsymbol{\theta}^\mathsf{T}\boldsymbol{x}_i + \theta_0)]_+ , \tag{4.31}$$

the problem is equivalent to minimizing the following function:

$$L(\boldsymbol{\theta}, \theta_0) = \frac{1}{2C}|\boldsymbol{\theta}|^2 + \sum_{i=1}^n [1 - y_i(\boldsymbol{\theta}^\mathsf{T}\boldsymbol{x}_i + \theta_0)]_+ , \tag{4.32}$$

which is the same as

$$L(\boldsymbol{\theta}, \theta_0) = \frac{1}{2}\lambda|\boldsymbol{\theta}|^2 + \sum_{i=1}^n \max[0, 1 - y_i f(\boldsymbol{x}_i)] . \tag{4.33}$$

Finally, let us compare it to the functional of KRR from eq. (4.16): the regularization term is the same, the only difference is that KRR uses the squared error loss, while SVMs uses a function called the Hinge loss.

4.2.3 Gaussian processes

So far, we have already covered powerful and general regression tools. We learned about the kernel trick and what it means to learn in feature spaces rather than in the input space. Moreover, we have seen how this is useful in particular for high dimensional features spaces and examined in more depth some tools which manifestly use the kernel trick to perform good learning tasks. In this section we cover an additional tool, namely Gaussian processes (GPs). However, since we have already introduced powerful regression models such as KRR, a natural question to ask is: *why do we need another regression model?*. The short answer is that Gaussian process regression (GPR) allows to do what KRR does not: to calculate Bayesian uncertainties on our predictions. As we shall see, this tool can be used for (at least) two powerful applications: Bayesian optimization [145] and sampling. In the remainder of this section we describe what GPs are and how GPR works.

Considering a linear regression function in an m-dimensional space, as in section 2.4.1:

$$f(\boldsymbol{x}) = (\theta_0, \theta_1 \ldots \theta_m)^\mathsf{T}(1, \phi_1(\boldsymbol{x}), \ldots, \phi_m(\boldsymbol{x})) \tag{4.34}$$

where each of the functions $\phi_i(\boldsymbol{x})$ is some non-linear function of $\boldsymbol{x}$ such as

$$\phi_i(\boldsymbol{x}) = \tanh\left[w_i\sum_{j=1}^m x_j + b_i\right] \tag{4.35}$$

and $\boldsymbol{x}$ is m-dimensional, $\boldsymbol{x} = (x_1, \ldots, x_m)^\mathsf{T}$.

Equation (4.34) can be visualized as the NN from fig. 4.4. If all the weights of the network are fixed, the network is deterministic and maps any given data point $\boldsymbol{x}$ to a single value
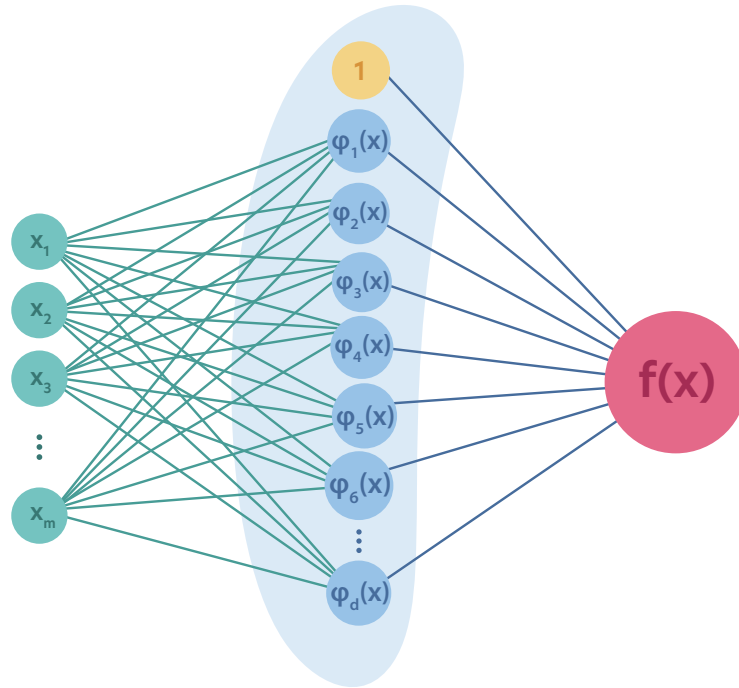
Figure 4.4: Sketch of a Bayesian NN. The features in the hidden layer (blue) are multiplied by random variables as shown in eq. (4.34). This way, the NN is no longer deterministic and its output $f(\boldsymbol{x})$ given the input $\boldsymbol{x}$ is itself a random variable.

$f(\boldsymbol{x})$. However, if we now assume all the parameters $\theta_0, \ldots \theta_m$ to be instantiations of random variables, distributed according to some distribution, we incorporate randomness into the network's output. The output of the NN for a fixed $\boldsymbol{x}$ thus itself becomes a random variable. Such an NN thus becomes a Bayesian NN. Assuming that all θ_i are i.i.d. random variables and letting $N \to \infty$, the central limit theorem[8] tells us that the distribution over the output of the Bayesian NN [146] is Gaussian. Because the distribution must remain Gaussian for any given input $\boldsymbol{x}$, $f(\boldsymbol{x})$ is a first example of a GP applied in the context of NNs. The upshot of this preliminary example is that by incorporating noise into the model, under the assumption of infinitely many independent randomly sampled parameters, the output of the model is, again, Gaussian. The advantage of all this, compared to what we have previously analyzed, is that one can obtain a closed-form expression for log marginal likelihood and the predictive distribution. So, a GP can be viewed as a probability distribution over possible functions fitting a set of data points. Its output is an instantiation of a random variable, distributed according to a multivariate density.

Our goal is to infer a function that describes a given data set. The data are usually noisy which we model with Gaussian-distributed noise with zero mean and variance σ^2:

$$y = f(\boldsymbol{x}) + \epsilon, \quad \epsilon \sim \mathcal{N}(0, \sigma^2). \tag{4.36}$$

Let us first consider a linear model, i.e., ϕ being the identity map, eq. (4.34) becomes:

$$f(\boldsymbol{x}) = \boldsymbol{\theta}^\mathsf{T} \boldsymbol{x} \tag{4.37}$$

---

[8]The central limit theorem states that the sum of many independent random variables is approximately normally distributed. E.g., if you roll two six-sided dice multiple times, the sum of the obtained results converges to the Gaussian distribution centered at seven in the limit of an infinite number of rolls.

hence a linear model. Let us now assume each data point x_i is independent of the others. For any given point, the model likelihood is expressed as $p(y_i \mid \boldsymbol{\theta}, x_i)$. Due to the independence, for a labeled training data set $\mathcal{D} = (\boldsymbol{X}, \boldsymbol{y})$ the joint likelihood reads (see also section 2.3):

$$p(\boldsymbol{y} \mid \boldsymbol{\theta}, \boldsymbol{X}) = \prod_{i=1}^{n} p(y_i \mid \boldsymbol{\theta}, x_i). \tag{4.38}$$

Because of our assumption of Gaussian distributed noise (see eq. (4.36)), we can explicitly rewrite each term of the product from the right-hand side of the equation above as:

$$p(y_i \mid \boldsymbol{\theta}, x_i) = \frac{1}{\sqrt{2\pi}\sigma} \exp\left[-\frac{(y_i - \boldsymbol{\theta}^T x_i)^2}{2\sigma^2}\right]. \tag{4.39}$$

Hence, the model likelihood given the data $\mathcal{D}$ is a product of Gaussians. Thus, eq. (4.38) can be explicitly rewritten as:

$$p(\boldsymbol{y} \mid \boldsymbol{\theta}, \boldsymbol{X}) = \prod_{i=1}^{n} p(y_i \mid \boldsymbol{\theta}, x_i) = \frac{1}{(2\pi\sigma^2)^{n/2}} \exp\left[-\frac{|\boldsymbol{y} - \boldsymbol{X}\boldsymbol{\theta}|^2}{2\sigma^2}\right]. \tag{4.40}$$

Our goal now is to use the Bayes' theorem to calculate the posterior over the weights $\boldsymbol{\theta}$ (see section 2.3). Using eq. (2.19)), we obtain

$$p(\boldsymbol{\theta} \mid \boldsymbol{y}, \boldsymbol{X}) = \frac{p(\boldsymbol{y} \mid \boldsymbol{\theta}, \boldsymbol{X})p(\boldsymbol{\theta})}{p(\boldsymbol{y} \mid \boldsymbol{X})} \tag{4.41}$$

where $p(\boldsymbol{y} \mid \boldsymbol{X})$ is just a normalization constant not depending on $\boldsymbol{\theta}$ and $p(\boldsymbol{\theta})$ and represents our prior (again see section 2.3). In principle, we have freedom over choosing the prior. Nevertheless, it would always be better in practice to choose this prior wisely. Hence, one should choose it according to the prior knowledge on the problem at hand. For instance, thinking about physical problems, one can use some context or prior knowledge on the system to set the prior appropriately. Of course, the better the prior is chosen, the more effective the model is. One though needs to be careful in this choice since restricting the prior or choosing it to be subjected to unreasonable constraints would make the whole learning process much harder. More specifically, a bad prior translates into a requirement of more data in order to build a good model. Thus, in light of all the considerations above we set the prior to be $\boldsymbol{\theta} \sim \mathcal{N}(0, \Sigma_{m+1})$ which is a joint normal distribution with zero mean and covariance matrix Σ_{m+1}. For instance, under the assumption of independent parameters, Σ_{m+1} can be chosen to be a diagonal matrix.[9]

Getting back to the posterior, we can collect all the $\boldsymbol{\theta}$-independent terms under a normalization constant A and rewrite the likelihood using eq. (4.38) and (4.41) as

$$p(\boldsymbol{\theta} \mid \boldsymbol{y}, \boldsymbol{X}) = \frac{p(\boldsymbol{y} \mid \boldsymbol{\theta}, \boldsymbol{X})p(\boldsymbol{\theta})}{p(\boldsymbol{y} \mid \boldsymbol{X})} = \frac{1}{A} \exp\left[-\frac{|\boldsymbol{y} - \boldsymbol{X}\boldsymbol{\theta}|^2}{2\sigma^2}\right] \exp\left[-\boldsymbol{\theta}^{\intercal}\Sigma_{m+1}^{-1}\boldsymbol{\theta}\right]. \tag{4.42}$$

Rearranging the expressions in the exponentials, the posterior becomes:

$$p(\boldsymbol{\theta} \mid \boldsymbol{y}, \boldsymbol{X}) = \frac{1}{A} \exp\left[-\frac{1}{2}(\boldsymbol{\theta} - \boldsymbol{\mu})^{\intercal}C(\boldsymbol{\theta} - \boldsymbol{\mu})\right] \tag{4.43}$$

where we used the following definitions

$$\boldsymbol{\mu} = \sigma^{-2}\left[\sigma^{-2}\boldsymbol{X}^{\intercal}\boldsymbol{X} + \Sigma_{m+1}^{-1}\right]^{-1}\boldsymbol{X}^{\intercal}\boldsymbol{y} \tag{4.44}$$

$$C^{-1} = \left[\sigma^{-2}\boldsymbol{X}^{\intercal}\boldsymbol{X} + \Sigma_{m+1}^{-1}\right]^{-1} \tag{4.45}$$

---

[9]As we include a possible bias term in eq. (4.34), we have $m+1$ tunable parameters.

with $\boldsymbol{\mu}$ being the posterior mean and $\boldsymbol{C}^{-1}$ the posterior covariance matrix. Finally, eq. (4.43) gives us access to the analytical form for the distribution of the model parameters $p(\boldsymbol{\theta} \mid \boldsymbol{y}, \boldsymbol{X})$ given the data $\mathcal{D}$. This, again, is a normal distribution with updated mean and covariance. These new values intrinsically posses the information of the training data as inferred from their analytical forms. Hence, $p(\boldsymbol{\theta} \mid \boldsymbol{y}, \boldsymbol{X}) \sim \mathcal{N}(\boldsymbol{\mu}, \boldsymbol{C}^{-1})$. Once we have our updated distribution over our model's parameters, the next step is to predict the output y^* for a previously unseen data point $\boldsymbol{x}^*$. To do this, we need to multiply the posterior with the likelihood for y^* and integrate over all possible parameters. This yields:

$$p(y^* \mid \boldsymbol{x}^*) = \int_{\mathbb{R}^{m+1}} p(y^* \mid \boldsymbol{x}^*, \boldsymbol{\theta}) p(\boldsymbol{\theta} \mid \boldsymbol{y}, \boldsymbol{X}) \, \mathrm{d}\boldsymbol{\theta} \tag{4.46}$$

$$\propto \int_{\mathbb{R}^{m+1}} \exp\left[-\frac{(y^* - \boldsymbol{\theta}^{\mathsf{T}} \boldsymbol{x}^*)^2}{2\sigma^2}\right] \exp\left[-\frac{1}{2}(\boldsymbol{\theta} - \boldsymbol{\mu})^{\mathsf{T}} C(\boldsymbol{\theta} - \boldsymbol{\mu})\right] \mathrm{d}\boldsymbol{\theta} \, . \tag{4.47}$$

It is easy to notice that this distribution is again going to be Gaussian. We can also analytically compute the conditional mean and variance:[10]

$$\hat{\mu} = \boldsymbol{x}^{*\mathsf{T}} \boldsymbol{\mu} = \boldsymbol{x}^{*\mathsf{T}} \sigma^{-2} \boldsymbol{C}^{-1} \boldsymbol{X}^{\mathsf{T}} \boldsymbol{y} \tag{4.48}$$

$$\hat{\sigma}^2 = \boldsymbol{x}^{*\mathsf{T}} \boldsymbol{C}^{-1} \boldsymbol{x}^* \, . \tag{4.49}$$

The mean can be used to make predictions while the variance gives the uncertainty over such estimation. It is now time to compare these results with previously introduced methods:

$$\text{Linear Regression: } x^{*\mathsf{T}} \hat{\boldsymbol{\theta}} = x^{*\mathsf{T}} (\boldsymbol{X}^{\mathsf{T}} \boldsymbol{X})^{-1} \boldsymbol{X}^{\mathsf{T}} \boldsymbol{y} \tag{4.50}$$

$$\text{Linear Ridge Regression: } x^{*\mathsf{T}} \hat{\boldsymbol{\theta}} = x^{*\mathsf{T}} (\boldsymbol{X}^{\mathsf{T}} \boldsymbol{X} + \lambda \mathbb{1})^{-1} \boldsymbol{X}^{\mathsf{T}} \boldsymbol{y} \tag{4.51}$$

$$\text{Linear GPR: } \hat{\mu} = \boldsymbol{x}^{*\mathsf{T}} \sigma^{-2} \left[\sigma^{-2} \boldsymbol{X}^{\mathsf{T}} \boldsymbol{X} + \Sigma_{m+1}^{-1}\right]^{-1} \boldsymbol{X}^{\mathsf{T}} \boldsymbol{y} \, . \tag{4.52}$$

This entire derivation, which we have been doing for the linear case, can easily be generalized to non-linear regression. In such case, we map $x \mapsto \phi = \phi(x)$, embedding our input data with a feature map into a potentially high-dimensional space. It follows that $\boldsymbol{X} \mapsto \boldsymbol{\Phi} = \phi(\boldsymbol{X})$ and the conditional mean and variance can be derived accordingly. Substituting the terms appropriately and doing a little bit of math adjustments, under the assumption of unit variance $\Sigma_{m+1} = \mathbb{1}$, we obtain:

$$\hat{\mu} = \phi^{*\mathsf{T}} \boldsymbol{\Phi}^{\mathsf{T}} \left[\boldsymbol{\Phi}^{\mathsf{T}} \boldsymbol{\Phi} + \sigma^2 \mathbb{1}\right]^{-1} \boldsymbol{y} \tag{4.53}$$

$$\hat{\sigma}^2 = \phi^{*\mathsf{T}} \phi^* - \phi^{*\mathsf{T}} \boldsymbol{\Phi}^{\mathsf{T}} \left[\boldsymbol{\Phi}^{\mathsf{T}} \boldsymbol{\Phi} + \sigma^2 \mathbb{1}\right]^{-1} \boldsymbol{\Phi} \phi^* \, . \tag{4.54}$$

Looking closely at these expressions, we can rewrite them in terms of the kernel function K:

$$\hat{\mu} = \boldsymbol{k}^{\mathsf{T}}(\boldsymbol{x}^*) \left[\boldsymbol{K} + \sigma^2 \mathbb{1}\right]^{-1} \boldsymbol{y} \tag{4.55}$$

$$\hat{\sigma}^2 = K(\boldsymbol{x}^*, \boldsymbol{x}^*) - \boldsymbol{k}^{\mathsf{T}}(\boldsymbol{x}^*) \left[\boldsymbol{K} + \sigma^2 \mathbb{1}\right]^{-1} \boldsymbol{k}(\boldsymbol{x}^*) \tag{4.56}$$

where we used the following definitions:

$$\phi^{*\mathsf{T}} \phi^* = K(\boldsymbol{x}^*, \boldsymbol{x}^*), \tag{4.57}$$

$$(\boldsymbol{\Phi} \phi^*)_i = \boldsymbol{k}(\boldsymbol{x}^*)_i = K(\boldsymbol{x}_i, \boldsymbol{x}^*), \tag{4.58}$$

$$(\boldsymbol{\Phi}^{\mathsf{T}} \boldsymbol{\Phi})_{ij} = \boldsymbol{K}_{ij} = K(\boldsymbol{x}_i, \boldsymbol{x}_j). \tag{4.59}$$

One important remark with respect to the covariance matrix: though we set Σ_{m+1} to be the identity, this might not be the best choice in practice. Nevertheless, this does not represent

---

[10]with $\boldsymbol{C} = [\sigma^{-2} \boldsymbol{X}^{\mathsf{T}} \boldsymbol{X} + \Sigma_{m+1}^{-1}]$ already defined above

a problem as one can always rewrite the identities above such that they take the covariance matrix into account (in particular, eq. (4.57) becomes $\phi^{*\mathsf{T}}\Sigma_{m+1}\phi^{*\mathsf{T}} = K(\boldsymbol{x}^*, \boldsymbol{x}^*)$).

Thus, looking at the conditional mean from eq. (4.55) one can directly see the parallelism with the result of KRR from eq. (4.21) where our regularization strength λ corresponds to the data noise assumption, parametrized by σ^2. This comes to no surprise as the conditional mean from eq. (4.55) simply is the MLE introduced in section 2.4.1. However, GPR also yields the uncertainty of the prediction. Furthermore, we see, once again, the consequence of the representer theorem in eq. (4.14) on the form of the conditional mean $\hat{\mu}$, i.e., $\boldsymbol{\alpha} = (\boldsymbol{K} + \sigma^2\mathbb{1})^{-1}\boldsymbol{y}$.

4.2.4 Training a Gaussian process

In the previous section, we have seen what a GP is, how we construct it and how it allows us to obtain an analytical expression for the conditional mean and the Bayesian uncertainty for the output over one (or more) unseen data point(s) $\boldsymbol{x}^*$. We understand that the performance of the GP strongly relies on the choice of the prior and on the amount of data the model is exposed to. So at this point one natural question which might arise is: how do we train a GP? Let us dive into this. First and foremost, we need to choose an appropriate kernel function K which defines the kernel matrix $\boldsymbol{K}_{ij} = K(\boldsymbol{x}_i, \boldsymbol{x}_j)$ accordingly. The parameters of this function (e.g., as in table 1) are tuned in order to maximize the so-called marginal likelihood $p(\boldsymbol{y} \mid \boldsymbol{X})$. This name comes from the fact that this quantity is obtained from the Bayes' theorem eq. (4.41) when marginalizing over the set of model parameters (i.e., taking the integral over $\boldsymbol{\theta}$). Here, our goal is to express the marginal likelihood of a GP in terms of the kernels. To this end, we choose the covariance matrix of the GP to be the kernel matrix such that $\mathrm{Cov}(\boldsymbol{x}, \boldsymbol{x}') = \boldsymbol{K}$[11] which turns out to be equivalent to the choice of the prior made previously $\boldsymbol{\theta}_{\mathrm{prior}} \sim \mathcal{N}(0, \Sigma_{m+1})$. Our ultimate goal is to evaluate the marginal likelihood

$$p(\boldsymbol{y} \mid \boldsymbol{X}) = \int_{\mathbb{R}^{m+1}} p(\boldsymbol{y} \mid \boldsymbol{\theta}, \boldsymbol{X}) p(\boldsymbol{\theta} \mid \boldsymbol{X}) \, \mathrm{d}\boldsymbol{\theta} \,. \tag{4.60}$$

Given that the prior's covariance is the kernel matrix and the integrand is a product of two Gaussians, it is actually possible to write this in terms of the kernel matrix. Working with the logarithm of the marginal likelihood it follows that our objective of the training process is

$$\log p(\boldsymbol{y} \mid \boldsymbol{X}) = -\frac{1}{2}\boldsymbol{y}^{\mathsf{T}}\left(\boldsymbol{K} + \sigma^2\mathbb{1}\right)^{-1}\boldsymbol{y} - \frac{1}{2}\log\left|\boldsymbol{K} + \sigma^2\mathbb{1}\right| - \frac{n}{2}\log 2\pi \,. \tag{4.61}$$

When training a GP one aims to find the parameters of the kernel function that maximize the logarithm of marginal likelihood from eq. (4.61). Moreover, a GP does the fine-tuning of the parameters automatically (either by gradient descent or cross validation), while in case of the SVM one needs to validate the kernel parameters instead. On the other hand, the training a GP requires the inversion of the kernel matrix whose size coincides with the training set. This already gives an intuition why GPs are the tool of choice in a regime of a few data points where they can be very effective and relatively cheap.

4.3 Bayesian optimization

In the previous section, we have discussed Gaussian process regression (GPR) and how to train a Gaussian process (GP). Furthermore, we have shown that GPs allow to derive an analytical form for the estimate of the output for an test data point $\boldsymbol{x}^*$, conditioned to a set of given data $\mathcal{D}$, in a similar fashion to KRR. Moreover and contrary to KRR, GPR also comes with

---

[11]On the notation: when providing the inputs of the covariance matrix we use Cov while when they are implicit we just use $\boldsymbol{C}$.

Algorithm 5 Bayesian Optimization

Require: initial data set $\mathcal{D}_0 = \{(\boldsymbol{X}, \boldsymbol{y})\}$
Require: initial surrogate model GP trained on $\mathcal{D}_0$ with mean and variance $\hat{\mu}, \hat{\sigma}^2$
Require: acquisition function to be maximized
    for iteration $t < T_{\max}$ **do**
        Sample a set of candidate points $\boldsymbol{X}_{\mathrm{cand}}$ ▷ batch optimization
        $\boldsymbol{x}^* \leftarrow \max_{\boldsymbol{x} \in \boldsymbol{X}_{\mathrm{cand}}} a(\boldsymbol{x}, \hat{\mu}, \hat{\sigma})$
        $y^* \leftarrow f_{\mathrm{BB}}(\boldsymbol{x}^*)$ at $\boldsymbol{x}^*$
        $\mathcal{D} \leftarrow \mathcal{D}_t \bigcup \{(\boldsymbol{x}^*, y^*)\}$ ▷ update data set
        Update the surrogate model's parameters $\hat{\mu}$ and $\hat{\sigma}^2$
    end for
    return $\hat{\mu}$ and $\hat{\sigma}^2$ ▷ prediction and uncertainty of the surrogate model

---

a prediction uncertainty over the conditional mean. This is of a great relevance as it can be used for Bayesian optimization (BO) [145]. As such, depending on the problem and the use-case one approach may be preferred to the other. GPR is certainly more versatile but also more expensive to train compared to KRR and one may want to prefer the latter toward a more efficient computation when uncertainty over the estimate is not needed.

BO is a technique used for the optimization of expensive black box functions where gradients can not be easily computed or estimated (i.e., experimental setups). Here, the term *expensive* is very important. Indeed, the optimization of black box functions is the general goal of a big set of ML-models and techniques. Such optimization usually relies on efficient computation, arbitrarily many data and so forth. However, this might not always be the case. Sometimes, we might be facing problems where the amount of data is rather limited, or the routine to extract additional experimental data is very expensive. In this context, the interplay between GP and BO becomes extremely important. It is also worth mentioning that contrary to the optimization methods used in most ML-approaches we have encountered so far (in particular NNs), BO is a gradient-free method. Therefore, it is particularly well suited for functions that are very difficult or expensive to evaluate. The way BO works in the context of GPR is that BO takes GPs *as surrogate models of the black-box function to be optimized*. Recalling the results of the previous section, GPR gives us access to a conditional prediction along with an estimate for its uncertainty. This said, the next important thing to notice is that BO is an iterative process. This process works as follows (see algorithm 5 for the pseudo-code): The BO procedure starts with a few evaluations of the black box function at some random locations. We refer to this initial data set as $\mathcal{D}_0 = \{(\boldsymbol{X}, \boldsymbol{y})\}$. These evaluations are used to train a first version of a GP, hence, we can think of those to be our training data.[12] Once we have our first surrogate model, we introduce the so-called *acquisition function*. The acquisition function is typically a function of both $\hat{\mu}$ and $\hat{\sigma}$ and essentially tells us where to perform the next evaluation x in order to maximize the knowledge we gain about the underlying black-box function. In the next section, we see how the acquisition function looks like. For now, we can just think of it to be an arbitrary function $a(\boldsymbol{x}, \hat{\mu}, \hat{\sigma})$. The prediction and its uncertainty are fixed given a surrogate GP prior. Thus, the acquisition function is only a function of a new candidate point $\boldsymbol{x}$. Our goal is now to find such candidate point to be as informative as possible. As such, the next point to evaluate by maximizing the acquisition function, i.e., $\boldsymbol{x}^* := \max_{\boldsymbol{x} \in D} a(x, \hat{\mu}, \hat{\sigma})$, where D is the domain of $\boldsymbol{x}$. Once the new target location $\boldsymbol{x}^*$ is found, the next step is to evaluate the black box function such that $y^* = f_{\mathrm{BB}}(\boldsymbol{x}^*)$. The result of the evaluation is appended to the

---

[12]Since we work in a Bayesian setting, the data noise is taken into account in eq. (4.36) and all predictions are based on top of that assumption.
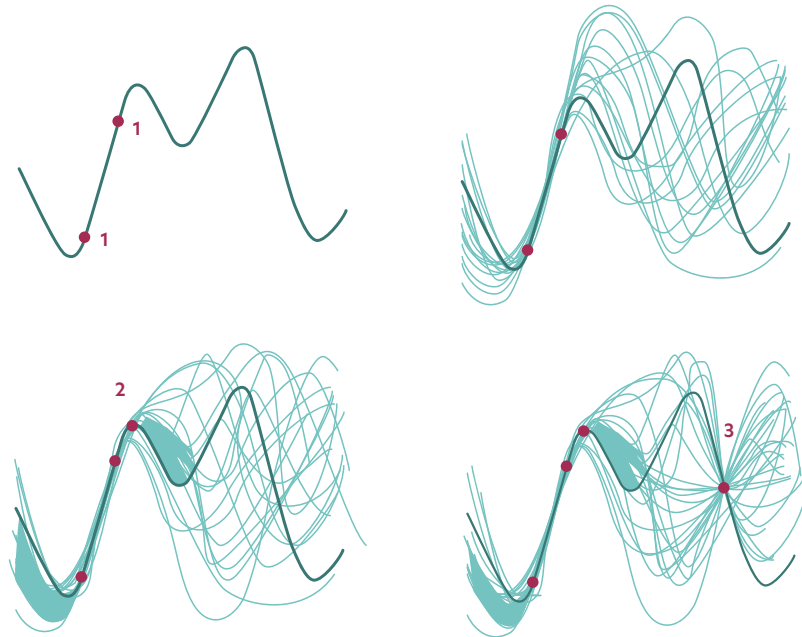
Figure 4.5: Example of how BO can be applied to GPR. A GP represents a surrogate model (light green lines) trained on an initial set of observations (red dots in the upper left panel). At each BO-step, a new point is added to the previous set of observations such that the surrogate model becomes increasingly certain as more points are added. The dark green line represents the underlying black box function.

training set for GP such that $\mathcal{D} = \mathcal{D}_0 \bigcup \{(\boldsymbol{x}^*, y^*)\}$ and a new, less uncertain, surrogate model is trained on the updated $\mathcal{D}$. From this point on, the iteration starts over: every time we update the surrogate model, we have new predictions and uncertainties, hence a new acquisition function. At each step of the BO a new point is thus added to $\mathcal{D}$ and the entire process goes on until a maximum number of iterations $T_{\max}$ is reached or some convergence criterion is met. The plot in fig. 4.5 shows how three subsequent steps of BO results in an increasingly more certain surrogate model of the underlying black box function (dark green line). The BO is, therefore, an example of the active learning where the training data set is built iteratively with the aim of minimizing the number of training points while maximizing the information it contains.

BO with GPR has the following advantages over other regression models:

- smaller training sets are enough (rule of thumb: 10× number of trainable parameters[a]),

- provides uncertainties to the predictions,

- gradient-free so the optimization works even if you cannot compute gradients.

---

[a]A suitable choice for the kernel typically lowers the number of function calls. Moreover, it is preferable to have smaller training sets for this method. Equation (4.55) shows that the kernel matrix needs to be inverted for each trial kernel which adds a computational constraint.

The acquisition function

In the previous section, we have briefly described the idea of BO and how it operates combined with GPs. In this context, we have introduced the acquisition function. This quantity is very important as it represents a mathematical technique which guides the exploration of the entire parameter space during the BO-routine. We have previously defined the acquisition function as a general function of x, the surrogate's prediction and its uncertainty. There are different kinds of acquisition functions, and most of the time the choice is problem-dependent. However, most importantly, its mathematical form should always incorporate the trade-off between exploration and exploitation. In other words, the goal of the acquisition function is to evaluate the usefulness of the next data location to look at in order to achieve the maximization of the surrogate model of our black box function and thus to approximate the target function with lower uncertainty. As such, the ultimate goal in BO is to find the next point to evaluate by maximizing such acquisition function. One example, commonly used and easy to interpret is the Upper Confidence Bound (UCB):

$$a_{\mathrm{UCB}}(x, \hat{\mu}, \hat{\sigma}) = \hat{\mu}(x) + \beta \hat{\sigma}(x) \tag{4.62}$$

where $\beta \geq 0$ is an arbitrary parameter which ideally should be tuned during the optimization routine. Here, the first term drives the exploitation while the second drives the exploration. In the remainder we refer to those as the *exploitation* and the *exploration* terms respectively.

Depending on the value of β, the exploration term might dominate in the maximization. By looking at eq. (4.62) it is immediately clear that a new candidate point with the higher variance is preferred as the model rewards the evaluation of currently unexplored regions of the domain. That is not surprising as the model seeks to explore what it does not know yet. With respect to the mean, according to the UCB, higher values for the mean are preferred. That is because by definition, we are seeking for an upper bound hence enhancing sampling in the upper quartile of the surrogate model. In other words, in the extreme case where $\beta \gg 0$, the exploration dominates, hence regions of higher variance are preferred (see fig. 4.6 leftmost plot).

When instead $\beta \to 0$, the acquisition function becomes far more conservative, hence samples aggressively around the best solution, i.e., exploiting the region where the surrogate model feels confident as visible in the rightmost panel of fig. 4.6. In fig. 4.6 the middle plot shows a good balance between the exploration and the exploitation. Hence, for two candidate points with comparable predicted mean, the one with higher uncertainty is preferred. As a consequence, the acquisition function, at least in the beginning of the optimization, prefers to explore rather than exploit.

Moreover, looking at the analytical form from eq. (4.55) (which appears as the first term in eq. (4.62)), the acquisition function might not always be easy to maximize (minimize) in practice. Therefore, one needs to leverage efficient numerical optimization routines. As acquisition functions are highly non-convex, what is done in practice is to do *batch optimization*. At each BO step, starting points x_{cand} are randomly sampled over a specified domain D, then one takes the best one of the sampled points (that maximizes the acquisition function) as the actual candidate. Other prominent examples of widely used acquisition functions are: Expected Improvement, Noisy Expected Improvement, Probability of Improvement. For a deeper yet more detailed overview on other type of acquisition functions the reader is referred to [147].
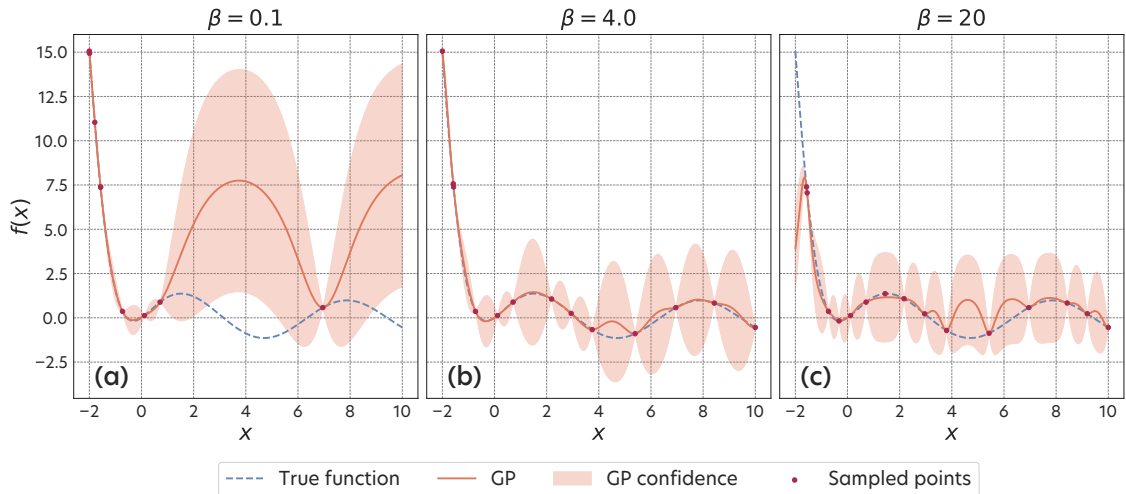
Figure 4.6: Selection of new candidate points via Bayesian optimization (BO) using the Upper Confidence Bound acquisition function. The target function is represented by the blue dashed line. The solid orange line is the surrogate model (GP) while the orange shading represents its uncertainty. The left most plot exhibits exploitative behavior, i.e., the most selected points are around the peak(s). Contrarily, in the rightmost plot, the parameter choice for β heavily enforces exploration. As such, new sampled points (red dots) are evenly distributed though some part of the domain (e.g., $x \sim 2$ would require more exploitation). The middle plot shows a trade-off between exploration and exploitation: the sampled candidates are well-distributed across the entire domain thus approximating the target function efficiently even around the peak(s) and boundaries.

4.4 Choosing the right model

Having introduced the powerful toolbox of kernels, a natural question arises: Suppose we are given a set of "noisy" data points, forming a data set $\mathcal{D}$, and two distinct models $\mathcal{M}_1$ and $\mathcal{M}_2$ possibly based on two different kernels, which one should we choose? This is the central question behind the field of *model selection*. To answer this question, we again take a Bayesian approach (see section 2.3). Applying Bayes' theorem from eq. (2.19) to each model $\mathcal{M}_i$ yields

$$p(\mathcal{M}_i \mid \mathcal{D}) = \frac{p(\mathcal{D} \mid \mathcal{M}_i) p(\mathcal{M}_i)}{p(\mathcal{D})} \,. \tag{4.63}$$

We combine the expressions of the two models to obtain

$$\frac{p(\mathcal{M}_1 \mid \mathcal{D})}{p(\mathcal{M}_2 \mid \mathcal{D})} = \frac{p(\mathcal{D} \mid \mathcal{M}_1)}{p(\mathcal{D} \mid \mathcal{M}_2)} \frac{p(\mathcal{M}_1)}{p(\mathcal{M}_2)} \,. \tag{4.64}$$

Here, the ratio of the posterior probabilities $P(\mathcal{M}_i \mid \mathcal{D})$ is equal to the ratio of the prior probabilities $P(\mathcal{M}_i)$ times the so-called *Bayes factor*

$$\frac{p(\mathcal{D} \mid \mathcal{M}_1)}{p(\mathcal{D} \mid \mathcal{M}_2)} \,. \tag{4.65}$$

Equation (4.64) gives us a first answer to our question: In a Bayesian framework, the ratio of posterior probabilities can be used to decide which model is superior given the data at hand, i.e., the model with the larger posterior probability is superior. In scenarios where we do not

know anything about the data, we can set the prior probabilities equal to each other, which leaves us with the Bayes factor

$$\frac{p(\mathcal{M}_1 \mid \mathcal{D})}{p(\mathcal{M}_2 \mid \mathcal{D})} = \frac{p(\mathcal{D} \mid \mathcal{M}_1)}{p(\mathcal{D} \mid \mathcal{M}_2)}. \tag{4.66}$$

To calculate the Bayes factor in eq. (4.65), we need to compute $p(\mathcal{D} \mid \mathcal{M}_i)$ for each model which can be viewed as a *marginal likelihood*, i.e., a likelihood function in which some variables have been marginalized out (integrated out). Let us define the likelihood as $p(\mathcal{D} \mid \boldsymbol{\theta}, \mathcal{M}_i)$, such that the marginal likelihood can be obtained as

$$p(\mathcal{D} \mid \mathcal{M}_i) = \int_{\mathbb{R}^d} p(\mathcal{D} | \boldsymbol{\theta}, \mathcal{M}_i) p(\boldsymbol{\theta} \mid \mathcal{M}_i) \, d\boldsymbol{\theta}, \tag{4.67}$$

where we integrate over the distribution of model parameters $\boldsymbol{\theta} \in \mathbb{R}^d$ given by $p(\boldsymbol{\theta} \mid \mathcal{M}_i)$. Unfortunately, marginal likelihoods are typically hard to compute as they involve high-dimensional integrals. Choosing a kernel with d parameters results in a d-dimensional integral for its marginal likelihood.

Having encountered this problem, let us take a step back: When we train a model, we minimize a loss function (or equivalently, we maximize the log-likelihood). Therefore, why not simply choose the model that gives the lowest loss or largest likelihood? Intuitively, this leads to *overfitting*. This intuition is formalized by the *bias-variance trade-off* (see section 2.2). In particular, the bias-variance trade-off makes clear that the ideal model realizes an optimal trade-off between the training error and the model complexity. Rather than choosing the model that results in the lowest loss during training, we thus need to take its complexity into account.

4.4.1 Bayesian information criterion

A computationally tractable criterion for model selection which takes model complexity into account is the Bayesian information criterion (BIC) [148] defined as

$$\text{BIC} = -2\max(\ell) + d\log(n), \tag{4.68}$$

where $\max(\ell)$ is the maximum of the log likelihood, n is the number of training points, and d is the number of model parameters. The lower the BIC, the better the model. Clearly, the BIC reflects the trade-off between bias, here given by $\max(\ell)$, and the model complexity as measured by $d\log(n)$. Moreover, it turns out that the BIC is very close to the logarithm of the marginal likelihood in the large n-limit [149]:

$$\log p(\mathcal{D} \mid \mathcal{M}_i) \approx \log p(\mathcal{D} \mid \boldsymbol{\theta}^*, \mathcal{M}_i) - \frac{d}{2}\log(n), \tag{4.69}$$

where $\boldsymbol{\theta}^*$ are the model parameters which maximize the likelihood. This expression reveals that the model selection criterion given in eq. (4.64) based on the Bayesian approach does indeed take the model complexity into account. Moreover, we see that the criterion can be used to estimate the posterior probability of a model $\mathcal{M}_i$ as

$$p_i = \frac{\exp\left(-\frac{1}{2}\text{BIC}_i\right)}{\mathcal{N}}. \tag{4.70}$$

Here, the normalization constant $\mathcal{N} = \sum_i e^{-\text{BIC}_i/2}$ ensures that each model $\mathcal{M}_i$ is assigned a valid probability p_i to enable comparability. As such, the BIC gives us a tractable way to select
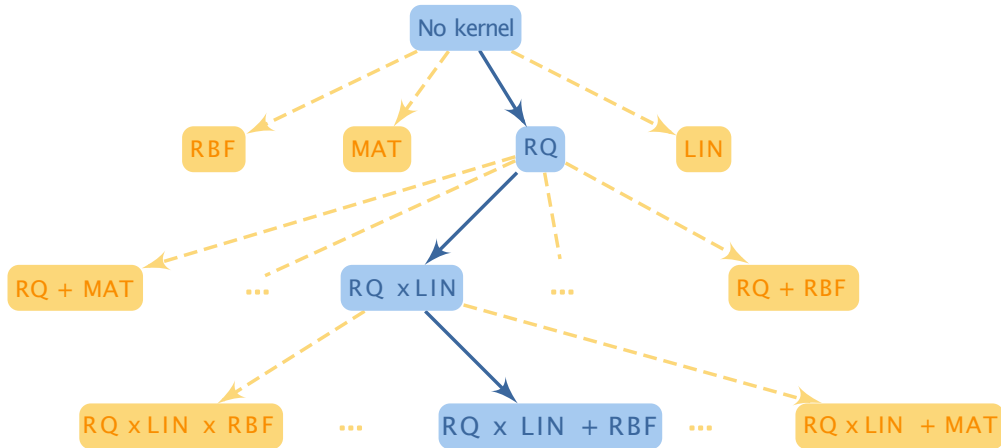
Figure 4.7: Illustration of the search tree behind the algorithm for the optimal kernel construction in GPR. It utilizes the BIC for the model selection introduced in eq. (4.68). For an overview of possible kernel functions and corresponding abbreviations, see table 1. Adapted from [118].

models according to the criterion given in eq. (4.64). In fact, BIC is asymptotically consistent as a model selection metric: Given a family of models, including the model underlying the data, the probability that BIC correctly selects the model underlying the data approaches one as $n \to \infty$.[13]

Inspired by these finding, we can adapt the criterion to GPR based on the log marginal likelihood which is optimized during training (at fixed kernel parameters) and the number of kernel parameters in the GPR. This criterion is computationally tractable and thus allows one to select between different kernels in the regression task using GPs.

4.4.2 Kernel search

Choosing the right kernel is crucial when using kernel-based method, as we have seen, e.g., for the performance of SVMs for different kernels in fig. 4.2. When performing Gaussian process regression (GPR) in a *naive* manner, we simply select a fixed kernel from a set of conventional kernels such as listed in table 1. We then optimize their hyperparameters by maximizing the marginal likelihood during training. There are now several possible routes toward achieving a more accurate model. Clearly, we may improve the model accuracy by providing more training points. However, keeping the number of training points low is one of the main advantages of GPR compared to other methods and constituted our main initial motivation. At a fixed number of training data the result from GPR can only be improved through a better kernel. Moreover, while BO is guaranteed to converge, the exact number of iterations may vary drastically. The choice of a good kernel can significantly speed up the convergence of BO.

The construction of good kernels ultimately boils down to a (possibly high-dimensional)

---

[13]While the BIC criterion approximates the log marginal likelihood in the large n-limit, it can still be applied as a heuristic model selection criterion at low values of n and can be confirmed empirically to often still yield good results. There exist many other model selection criteria (see [149] for a review), a popular one being the Akaike information criterion [150] which closely resembles the BIC. The crucial difference between the BIC and many other methods is its asymptotic consistency. One may question the importance of asymptotic consistency due to the fact that the ground-truth model typically is not present in the candidate set of models in practice.

optimization problem [151]. This happens, for example, when constructing a good kernel through optimization of the kernel hyperparameters itself. The key challenge is posed by the fact that the parametric form of the kernel must be proposed by the user itself. This is a non-trivial task which relies on trial-and-error – even for experts. In Refs. [118,151,152] the kernel learning problem was reframed as a search tree problem (see fig. 4.7): the space of parametric forms of kernels is constructed as a tree which can be searched systematically in an automated fashion, where the powerful BIC is used for the kernel selection and new kernels are proposed via composition.

We start by selecting each kernel from a set of conventional kernels and training a GP for each of them on the same data set. Then, we select the one which achieves the lowest value of BIC as given by eq. (4.68) (highlighted in blue). This kernel serves as the base kernel for the subsequent round where it is combined with the various kernels from the starting set to create new candidate kernels by forming products or combining them linearly. Again, the best one is selected according to the BIC and the process is repeated. The complexity of the model, i.e., of the composite kernel, increases as one progresses in the search tree. Eventually, increasing the kernel complexity further leads to overfitting, i.e., does not improve the BIC value compared to the kernel of the previous round and the algorithm is stopped. The algorithm can also be stopped prematurely if the number of kernel parameters becomes large and the associated training simply takes too long to be practical. Other than greedily searching the tree, the reformulation of the kernel construction as a search tree problem opens up the possibility for more advanced strategies which could yield better kernels more efficiently [153].

4.5 Bayesian optimization and Gaussian processes for quantum sciences

In the previous sections, we have motivated Gaussian processes (GPs) and Bayesian optimization (BO) as powerful methods which together allow us to build expressive ML models. Importantly, they are equipped with an intrinsic measure for uncertainty and can be trained using a small amount of training data. In this section, we discuss how these two methods can be useful in the context of quantum sciences, as sketched in fig. 4.8. In particular, GP and BO can be used to tackle inverse problems, to construct accurate extrapolations, and to increase the accuracy of quantum dynamics calculations.

4.5.1 Inverse problems

As explained in section 4.3, BO is very useful when you need to optimize black-box functions that are expensive to evaluate. This property proves extremely useful in inverse quantum problems aiming at finding theoretical description of the system by experimentally measuring its observables. The idea is related to a popular experimental approach known as *optimal control*. The optimal control approach aims at designing external field parameters that yield the desired quantum dynamics. It is usually achieved by a feedback loop which iteratively modifies experimental parameters such that they yield system dynamics advancing to the target one.

We can imagine applying a similar feedback loop for the inverse quantum problems. It would consist of iterative modifications of parameters of the theoretical description (such as Hamiltonian parameters) till the observables predicted theoretically agree with those measured experimentally. However, solving the iterative inverse quantum problem is challenging. Each iteration requires an additional run of theoretical calculations, e.g., the numerical solution of the Schrödinger equation, which is time-consuming. The optimization itself is also difficult as we do not explicitly know the range of parameters that need to be explored. Finally, the curse of the scaling of the Hilbert space dimension with the complexity of the quantum systems is definitely not helping. How to make it more feasible? Both inverse quantum problems
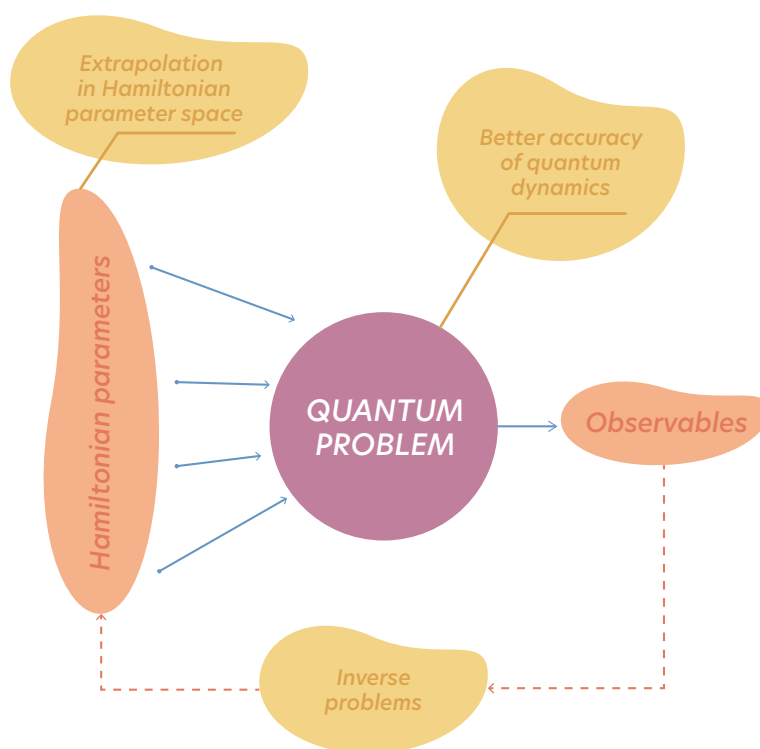
Figure 4.8: Illustration of the three main classes of problems in quantum sciences (marked in yellow) that have been successfully tackled with BO and GPs.

and optimal control become easier when the expensive black box (either the experimental set-up or the theoretical calculations) is replaced by a trained surrogate ML model such as a GP. Finally, instead of a blind search for the optimal parameters, we can employ BO.

As a practical example of the inverse problems solved with BO and GPs, let us consider the application to *scattering experiments*. Outcomes of such experiments are determined by the microscopic interactions between scattered particles. We have a quantum theory that describes these interactions and can predict the outcome of such scattering events. Therefore, our aim, in case of an inverse problem, may be to infer these microscopic interactions from the experiment. More concretely, the authors of Ref. [156] aimed to recover a global potential energy surface (PES)[14] governing the chemical reaction $H + H_2 \longrightarrow H_2 + H$, using as little experimental measurements of the reaction rates (depending on the constituents' translational energy) as possible. The feedback loop that needed to be solved is presented in fig. 4.9(a). Firstly, they trained a GP to surrogate a quantum scattering theory on a series of PESs and predicted reaction rates. Secondly, they modeled the PES with another GP. Finally, they used BO to find the three-dimensional potential energy surfaces (PESs) recovering the measured reaction rates. Only eight iterations of BO (where every iteration rebuilds the PES completely) were required to reach the accuracy of conventional approaches! Moreover, in this case a traditional approach of building a PES requires around 8 700 points – their GP was modeled

---

[14]A potential energy surface (PES) describes interactions between some particles. As a result, it models landscapes of chemical reactions, which can be used to predict reactive pathways and final products. Traditionally, it is constructed as an analytic fit to many, usually costly *ab initio* quantum chemical calculations of potential energy for reactants for various relative positions.
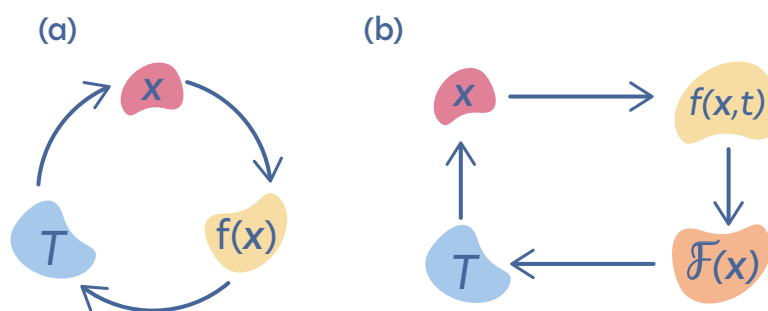
Figure 4.9: Examples of feedback loops whose optimization becomes feasible when implemented with BO and GPs. (a) x corresponds to PES, $f(x)$ is quantum scattering calculations taking the PES as an input, T is the difference between reaction probabilities calculated by $f(x)$ and measured in the experiment across various collisional energies. Search for optimal x would require minimization of T via optimization of $f(x)$. It becomes feasible when we surrogate $f(x)$ with one GP and x with another GP and apply BO. (b) x are Hamiltonian parameters, $f(x, t)$ is the time-dependent observable f (e.g., molecular orientation or alignment), $\mathcal{F}(x)$ is the time-dependent Schrödinger equation, T - difference between calculated and measured time-dependent observable f. When $\mathcal{F}(x)$ is surrogated by a GP, BO is used to minimize T and find x of the underlying Hamiltonian. Adapted from Ref. [154].

based only on 30 points![15] This impressive scaling is presented in fig. 4.10. As a result, they successfully surrogated two complex models (PES and quantum scattering calculations using PES as an input) with two GPs trained on much smaller number of data points than needed to build the original complex models. They also used this approach for a six-dimensional PES of OH + H_2, where BO beat the traditional approach with 290 points compared to 17 000 points.[16]

Another example of an inverse quantum problem is the task of inferring molecular properties from time-dependent observables. Authors of Ref. [154] tackled the reconstruction of molecular polarizability tensors from the observed time evolutions of the orientation or alignment signals of SO_3 and propylene oxide induced by strong laser pulses. The feedback loop that was solved is in fig. 4.9(b). They used a GP with a vector output whose each element corresponded to a prediction of a chosen observable (orientation or alignment) in a different time step. The GP was trained to surrogate the numerical integration of the time-dependent Schrödinger equation given the Hamiltonian parameters. Interestingly, the authors showed what we discussed already in section 4.4: that a proper choice of the kernel can result in a two times faster convergence of BO. Analogous approaches were used for the reconstruction of scattering matrices of molecules from molecular hyperfine experiments [157] and for

---

[15]Remember, these are not any 30 points, but points indicated by BO as needed for the optimal description.

[16]The number of points needed for efficient BO scales roughly like 10 times the number of PES dimensions. We can raise an interesting point which is, how are we even sure that we faithfully reproduce the PES if we build it only from reaction probabilities? It may happen that we capture the reactive chemical channels accurately, but the remaining parts of the surface are unconstrained and as a result may be nonphysical. One can argue that we ultimately do not need a complete faithful reproduction of the underlying PES. We only need a PES that allows us to accurately predict what we are interested in, here reaction probabilities. Note, however, that if we take a PES built from a particular set of observables and we use it to calculate another type of observable, the result may be wrong.
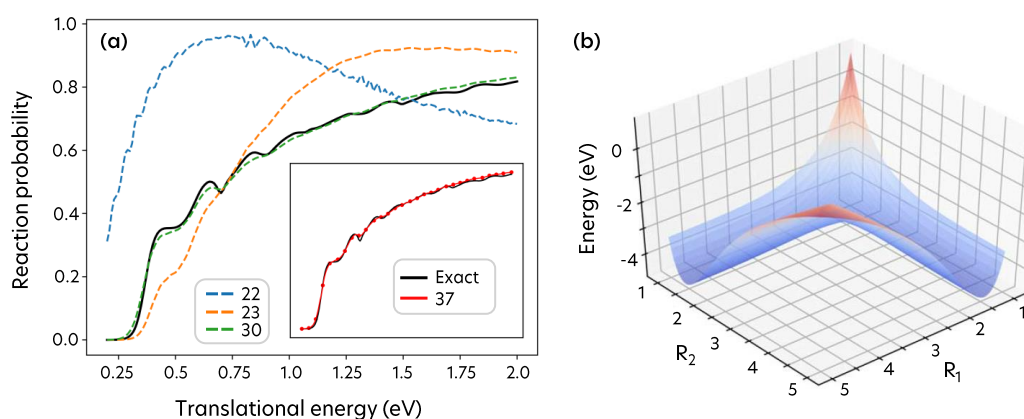
Figure 4.10: (a) The reaction probability for the $H_2 + H \longrightarrow H + H_2$ reaction as a function of the collision energy. The black solid curve is calculations from Ref. [155] based on the surface with 8701 *ab initio* points. The dashed blue/orange/ green/red curves are calculations based on the GP PES obtained with 22/23/30/37 *ab initio* points. (b) GP model of the PES for the H_3 reaction system constructed with 30 *ab initio* points. R_1 and R_2 are the distances between atoms 1 and 2 and atoms 2 and 3, respectively. Adapted from Ref. [156].

optimizing energetic chemistry synthesis experiment [158].

4.5.2 Improving quantum dynamics, physical models, and experiments

GP and BO can also be used for transfer learning in the context of quantum dynamics calculations. These are typically very difficult and one quickly has to rely on approximations. The authors of Ref. [159] proposed to apply GPs to correct such approximate quantum calculations on the example of molecular collisions and their cross-sections. The idea is to train a model on a small number of exact results and a large number of approximate calculations, resulting in ML models that can generalize exact quantum results to different dynamical processes.

Moreover, as the minimization of any function using BO bypasses the need of computing gradients [145], successful applications of BO includes optimization of parameters of physical models. The majority of such models do not have a close form solution and conventionally have to be approximated numerically using finite differences. For example, Refs. [160,161] showed that BO could efficiently optimize density functional models to improve their accuracy and minimize the energy of the Ising model [162]. Furthermore, BO was recently used to generate low-energy molecular conformers [163,164], tuning the parameters of various models used to simulate *cis–trans* photoisomerization of retinal in rhodopsin [165], and the optimization of lasers [166–168]. BO has also been impactful in material science in chemical compounds screening [169–174] and optimization of experimental setups [175–179].

4.5.3 Extrapolation problems

The second class of problems that seems perfect for GPs are extrapolation tasks: given some function values for data points in one regime the goal is to accurately predict the function values of data points in different regimes. This section touches upon two possible applications that are (1) learning PES from a possibly smallest number of *ab initio* calculations in one regime and (2) predicting existence of quantum phases without knowledge of the full phase diagram.
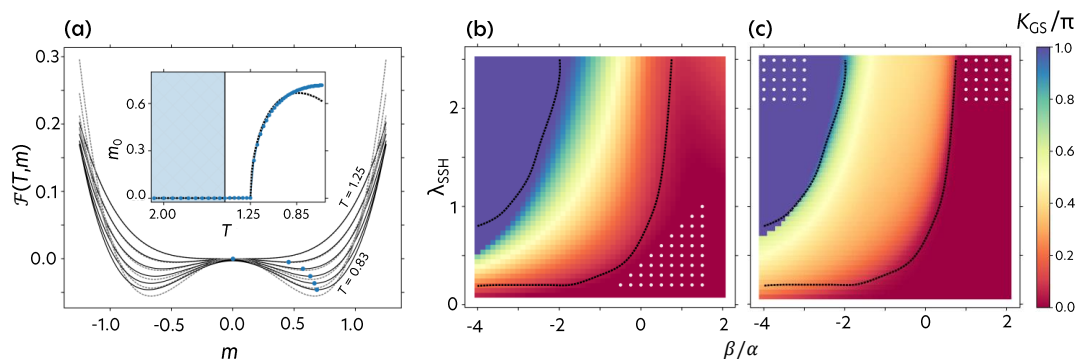
Figure 4.11: GPs for extrapolation to non-seen quantum phases. (a) The mean-field Heisenberg spin model in the nearest-neighbor approximation, where black dots are mean-field results and blue dots are GP predictions. GP was trained on the high-temperature shadowed regime of the data. (b)-(c) generalized lattice polaron model with different GP training regimes (marked with white dots). In both cases, GP correctly predicted the phase transitions (color map) as compared to the quantum calculations (black lines). Adapted from Ref. [118].

An example of a successful extrapolation in the case of PES-learning was shown in Ref. [153] where authors studied the six-dimensional PES of H_3O^+. They trained GP models on 1000 *ab initio* geometries from a low-energy regime (up to ≈ 7000 cm^{-1}) and checked that the model predictions in higher energy regimes match the full calculations with a high level of accuracy. If you doubt it, this result can be reproduced using the published code and data [32]. It gets better! You can get similarly accurate extrapolations from a GP model trained on 5000 molecular geometries of a 51-dimensional problem of a protonated imidazole dimer, which contains 19 atoms [180]. The scaling of the extrapolation accuracy with respect to the number of training points seems to be even more favorable for large molecules: high accuracy was reached already for 1000 randomly sampled geometries of the 57-dimensional aspirine.[17]

Another example of extrapolation, this time in the space of Hamiltonians, is task of inferring properties of other phases of a system given knowledge of one particular phase. In Ref. [118] the authors proposed to train a GP on one phase of the system and expected the model to predict phase transitions and properties of other phases. Let us start by discussing how they achieved this for the example of the mean-field Heisenberg spin model in the nearest-neighbor approximation. They trained the GP on the free energy of the system in the high-temperature regime, where the average spin magnetization is zero, far from the phase transition point. Then the trained GP was asked to extrapolate within the low-temperature regime, and it predicted correctly both the location of the phase transition as well as the free energy (and consequently non-zero magnetization) of the system as presented in fig. 4.11(a).

The authors also applied this approach to a much more complex system[18] whose Hamilto-

---

[17]More precisely, the test energy mean absolute error was 0.177 kcal/mol. Is this error small? Are these PESs accurate enough for modern spectroscopic applications? Spectroscopy discerns two kinds of accuracies. The spectroscopic accuracy is 1 cm^{-1}, while the chemical accuracy is 1 kcal/mol ≈ 350 cm^{-1}. Modern spectroscopic applications need a spectroscopic accuracy and this result has an error that is 60 times larger than spectroscopic accuracy - so no, it is not yet good enough. But it is more than enough, e.g., for simulations of molecular dynamics or reactions, especially at room temperature [181].

[18]The studied system was a generalized lattice polaron model [182] describing an electron in a one-dimensional lattice with $N \to \infty$ sites coupled to a phonon field. The interaction between an electron and a phonon field was a combination of two qualitatively different terms: the Su-Schrieffer-Heeger (SSH) electron-phonon coupling and

nian can be written in the following generic form:

$$H = H_0 + \alpha H_1 + \beta H_2, \tag{4.71}$$

where α and β are tunable parameters along which phase transitions occur. They trained a GP in some parameter regime of the Hamiltonian and were able to successfully extrapolate to others.[19] This approach proves to be useful for such a class of Hamiltonians for another reason. Usually, we are able to easily compute or measure the eigenspectrum in certain limits of α and β, but not at arbitrary points within the parameter space. We can then train a GPs in these limits and can expect them to extrapolate successfully to other parameter regimes where the direct calculation is more difficult. Finally, in the same system, the authors of Ref. [156] studied the importance of the choice of the kernel. They compared the results from the original work [118] obtained for kernels found with the BIC as described in section 4.4.1 and section 4.4.2 to the results obtained for kernels with the same complexity (i.e., at the same search tree level, see fig. 4.7) but chosen at random. Predictions of such GPs were much worse and were prone to overfitting, which stresses the power of the BIC as selection criterion for kernels. The appropriate choice of the kernel is therefore crucial as it determines how far the model can accurately extrapolate.

4.6 Outlook and open problems

- While GPs successfully surrogate PESs and need much smaller number of *ab initio* calculations, it is challenging to reach the spectroscopic accuracy with this approach. What is stopping us from achieving such accuracy levels with GPs? The major limitation is the number of training data. In practice, it is often observed that the error during learning eventually decreases by a factor of $1/n$, where n is the number of training points. As such, the number of training points required to reach a level of accuracy on the order of 10 cm^{-1} for a 57-dimensional surfaces is still manageable. However, reaching spectroscopic accuracy requires an excessive amount of training data. In particular the size of the training data set grows beyond the regime where GP are useful [183]. The high-accuracy limit may be obtained if one incorporates some knowledge on the system to the kernel. An open question of how to do that remains to be answered.

- In section 4.5 we have presented how BO and GPs can be used to tackle optimization of expensive set-ups gradients are not accessible. Such is also the case of quantum NNs or VAEs. Therefore, this approach may prove useful in the optimization of a quantum model!

- An interesting research direction is combining the power of automatic differentiation (AD), described in section 7.1, and kernel methods. Already, AD has played a major role in the development of more robust kernel functions for GP models. For example, Ref. [184] showed that by maximizing the log marginal likelihood, (eq. (4.61)), one could jointly optimize the weights and biases of a deep NN combined with any parameter of a standard kernel function. A more recent work [185] also showed that learning the composition of kernels is differentiable under the AD framework, and more complex kernels could be parametrized. Currently, there are two main ecosystems for GPs based on AD, `GPytorch` [186, 187], and `GPflow` [188].

---

the breathing-mode model with the Holstein coupling.

[19]How is this even possible? The intuition behind it is that the evolution of physical properties that are given to the ML model as input should somehow reflect the fact that there is a phase transition. The model probably picks up on the prevalent correlations within one phase and it observes that these correlations change when crossing to other phases.

- The training procedure of kernel ridge regression (KRR) could also be differentiated using AD bypassing the need of using a cross-validation scheme [189].

- With the advent of quantum extensions of classical ML-methods for near-term quantum devices, there are several paths on how to encode a data point x in a Hilbert space as $|x\rangle$. As a consequence, the kernel function has to be promoted to its quantum version. Interestingly, there is a provable advantage of such kernels based on measurement results of the quantum state [190]. We give a bit more detail in section 8.2.

Further reading

1. Rasmussen, C. E. & Williams, C. K. I. (2006). Gaussian Processes for Machine Learning. The MIT Press. The standard go-to reference on kernel methods and GPs in particular [191].

2. Krems, R. V. (2019). *Bayesian machine learning for quantum molecular dynamics*. PCCP, 21(25), 13392–13410. Discusses various applications of GPs for quantum molecular dynamics [192].

3. Jupyter notebook allowing to faithfully reproduce a six-dimensional PES with a GP and BO including optimal kernel search using the BIC criterion for the H_3O^+ [32].

4. Vargas-Hernández, R. A., & Krems, R. V. (2020). *Physical extrapolation of quantum observables by generalization with Gaussian processes*. Lect. Notes Phys., 968, 171–194. In-depth review of possible applications of GPs and BO for extrapolation problems in quantum sciences [193].

5. Huang, H. et al. (2021). *Provably efficient machine learning for quantum many-body problems*. arXiv:2106.12627. It introduces quantum-measurement inspired kernels for a provable advantage of kernel methods over classical methods that do not use measurement data [194].

5   Neural-network quantum states

In the early days of quantum mechanics, it soon became clear that approximation methods would be needed to solve most relevant real-world problems [195]. Indeed, in most cases one cannot exactly solve the Schrödinger equation for systems of more than a few interacting particles. This came to be referred as the *quantum many-body problem*. In this chapter, we show how neural networks (NNs) have been introduced to tackle this problem [196], in a variety of applications including ground-state and quantum dynamics of interacting quantum systems. For the sake of simplicity, we mainly focus our discussion on spin systems, and discuss applications to fermions [197] and bosons [198] only toward the end.

According to the axioms of quantum mechanics, the state of an isolated quantum system is encoded into a complex-valued probability amplitude commonly known as the wave function. In the case of a single spin-$\frac{1}{2}$, the wave function in the computational z-basis $\hat{Z}$ is $|\Psi\rangle = C_\uparrow|\uparrow\rangle + C_\downarrow|\downarrow\rangle$. The coefficients $C_\uparrow$ and $C_\downarrow$ are the complex-probability amplitudes of the spin being aligned along ($C_\uparrow$) or opposite to ($C_\downarrow$) the direction of the computational basis, and they are subject to the normalization condition $|C_\uparrow|^2 + |C_\downarrow|^2 = 1$. For many-body quantum systems of N spins, where N can be any large number from tens to the order of the Avogadro number $\sim 10^{23}$, the number of coefficients in the wave function scales as 2^N. Following up on the spin example, the wave function can be expressed as follows

$$
\begin{aligned}
|\Psi\rangle &= C_{\uparrow\uparrow\cdots\uparrow}|\uparrow\uparrow\cdots\uparrow\rangle + C_{\uparrow\uparrow\cdots\downarrow}|\uparrow\uparrow\cdots\downarrow\rangle + \cdots + C_{\downarrow\downarrow\cdots\downarrow}|\downarrow\downarrow\cdots\downarrow\rangle \\
&= \sum_{\sigma_1,\sigma_2,\cdots,\sigma_N} C_{\sigma_1,\sigma_2,\ldots,\sigma_N}|\sigma_1\rangle \otimes |\sigma_2\rangle \otimes \cdots \otimes |\sigma_N\rangle,
\end{aligned}
\tag{5.1}
$$

where the $|s\rangle = |\sigma_1\rangle \otimes |\sigma_2\rangle \otimes \cdots \otimes |\sigma_N\rangle$ are the basis vectors of the Hilbert space that describes the N spin system, and $C_{\sigma_1,\sigma_2,\ldots,\sigma_N}$ are their associated amplitudes.

The *quantum many-body problem* originates from the exponential scaling of the number of the basis elements, which leads to an exponential computational complexity in the system size. In particular, the memory required to naively store the wave function of just 60 spins is $16 \cdot 2^{60} \approx 18$ exabytes, about 500 times more than what is available on the world's largest supercomputer, as of 2022.

Nevertheless, while the Hilbert space of many-body quantum systems is exponentially large, physically-relevant states are typically confined to a corner of the Hilbert space that is of limited dimension. For instance, many physical Hamiltonians only contain *local* interactions, which significantly constraints the form of the associated many-body wave functions.

> The main idea behind variational methods is to find a computationally efficient representation of the physically relevant quantum states within the Hilbert space of interest.

Variational methods circumvent the issue of an exponential complexity by encoding the complex amplitudes of the wave function onto a parametrized function (often called the *ansatz*) which depends on a set of parameters $\boldsymbol{\theta}$. If the number of parameters is polynomial in the system size, the state can be efficiently stored with limited computational resources. In general, the variational state $|\Psi_{\boldsymbol{\theta}}\rangle$ can be expanded onto the computational basis as

$$
|\Psi_{\boldsymbol{\theta}}\rangle = \sum_{s=1}^{2^N} \Psi_{\boldsymbol{\theta}}(s)|s\rangle,
\tag{5.2}
$$

where $\Psi_{\boldsymbol{\theta}}(s) = \langle s|\Psi_{\boldsymbol{\theta}}\rangle$ denotes the probability amplitude corresponding to the state $|s\rangle$. The

task is then to find the parametrization $\boldsymbol{\theta}$ that best describes our desired quantum state of interest, such as the ground state of a given Hamiltonian.

5.1 Variational methods

Even when using variational states, computing expectation values can still be of exponential complexity since one must perform sums over all the basis elements of the Hilbert space for these calculations. Among the variational states that are practically usable, there are two possible approaches, which distinguish two families of variational ansätze: those that can be used to compute expectation values exactly with a polynomial cost, and those that do so only approximately, with an accuracy improvable at a polynomial cost in system size. In the former, the only source of error in the expectation value of observables comes from the truncation of (exponentially large) regions of the Hilbert space, limiting its ability of representing wave functions. In the latter, an additional source of error typically comes from sampling, which however does not necessarily add a systematic error and can be improved upon for an additional computational cost.

A third category consists of parameterized quantum states whose cost for computing expectation values scales exponentially with system size. In practical applications, for example in the case of tensor networks in two dimensions, approximate algorithms for computing expectation values are introduced. Strictly speaking, however, these are not variational methods, as we cannot compute expectation values to arbitrary accuracy in polynomial time, and introduce a systematic bias that goes beyond the pure variational error.

5.1.1 Variational states with exact expectation values

In the first kind of variational states, we mainly encounter locally constrained ansätze, for which mean-field and matrix-product states are notable examples.

Mean-field Ansatz   Mean-field states are one of the simplest variational quantum states. With these, we model our variational wave function by the mean-field approximation, that is, as the tensor product of single-spin wave functions

$$
\begin{aligned}
|\Psi_{\boldsymbol{\theta}}\rangle &= |\phi_1(\theta_\uparrow^{(1)}, \theta_\downarrow^{(1)})\rangle \otimes |\phi_2(\theta_\uparrow^{(2)}, \theta_\downarrow^{(2)})\rangle \otimes \cdots \otimes |\phi_N(\theta_\uparrow^{(N)}, \theta_\downarrow^{(N)})\rangle \\
&= \bigotimes_{i=1}^{N} |\phi_i(\theta_\uparrow^{(i)}, \theta_\downarrow^{(i)})\rangle,
\end{aligned}
\tag{5.3}
$$

where $|\phi_i\rangle$ are the single-spin wave functions at site i. They are subject to the orthogonality condition $\langle \phi_i | \phi_j \rangle = \delta_{ij}$, with δ_{ij} denoting the Kronecker delta. This way, $|\phi_i\rangle$ has only two coefficients corresponding to the probability amplitudes of the spin being up or down, which we take as variational parameters

$$
|\phi_i\rangle = \theta_\uparrow^{(i)} |\uparrow\rangle + \theta_\downarrow^{(i)} |\downarrow\rangle
\tag{5.4}
$$

$$
\left| \theta_\uparrow^{(i)} \right|^2 + \left| \theta_\downarrow^{(i)} \right|^2 = 1,
\tag{5.5}
$$

resulting into $2N$ complex parameters in total, i.e., $\boldsymbol{\theta} = \left\{ \theta_\uparrow^{(i)}, \theta_\downarrow^{(i)} \middle| i = 1, 2, \ldots, N \right\}$.

With this family of wave functions, we can compute expectation values of quantum Hamiltonians exactly. This is a consequence of the fact that we can exploit the tensor product structure of our wave function to simplify the expectation values over many-body states to the expectation over the corresponding single-body ones. For example, the expectation value of

the σ_i^x Pauli operator acting on the *i*-th site can be obtained as $\langle \Psi_{\boldsymbol{\theta}} | \sigma_i^x | \Psi_{\boldsymbol{\theta}} \rangle = \langle \phi_i | \sigma_i^x | \phi_i \rangle$. The calculation is straightforward, as $|\phi_i\rangle$ is a two-dimensional vector and σ_i^x is a 2×2 matrix.

Tensor network states However, mean-field states are not able to capture correlations between local degrees of freedom. Tensor network states (TNSs) are a family of quantum states that improve upon such a limitation, and a subset of TNSs also allow to compute expectations exactly. One of the most broadly used TNSs with this property are matrix product state (MPS), which predominate in the study of one-dimensional systems.

Let us consider the coefficients $C_{\sigma_1, \sigma_2, \dots, \sigma_n}$, defined in eq. (5.1). We can consider $C_{\sigma_1, \sigma_2, \dots, \sigma_N}$ as a tensor with N indexes, which we can always express as the contraction of tensors A^{σ_i}, such that:

$$C_{\sigma_1, \dots, \sigma_N} = \sum_{\alpha, \beta, \dots, \gamma} A^{\sigma_1}_{\alpha, \beta} A^{\sigma_2}_{\beta, \delta} \dots A^{\sigma_N}_{\gamma, \alpha} \tag{5.6}$$

where the maximal dimension of the Greek indices $\alpha, \beta, \dots$ is the bond dimension χ. This way, an exact representation of $C_{\sigma_1, \dots, \sigma_N}$ requires an exponentially large number of parameters. This means that the bond dimension, χ, must increase exponentially with N. The idea of the MPS ansatz resides in the truncation of the dimension of the indices of the tensors A^{σ_i}. With the truncation, we reduce the number of parameters of our ansatz to be $\mathcal{O}(dN\chi^2)$, where d is the local Hilbert space dimension, e.g., two for a spin-1/2 particle. We usually truncate the bond dimension in an elegant and controlled way using the singular value decomposition of the tensors A^{σ_i}, which has a strict connection with the maximal entanglement entropy the MPS can contain,[1] as we discuss in section 5.2.3.

As a final remark, let us mention an important algorithm proposed by S. White for the energy minimization of variational quantum states, known as density matrix renormalization group [199]. This algorithm is particularly well-suited for MPSs, and their combination is the current state-of-the-art technique to compute the ground state wave function of one dimensional systems. However, the description of this algorithm falls out of the scope of these lecture notes. We refer to [200] for a complete review of the use of MPS, and to [201] for a review of methods based on tensor networks (TNs).

5.1.2 Variational states with approximate expectation values

The second family of variational states we encounter are known as *computationally tractable states* [202].

> Variational ansätze must satisfy two conditions in order to be computationally tractable:
>
> - Amplitudes for arbitrary single basis elements $\Psi_{\boldsymbol{\theta}}(s) = \langle s | \Psi_{\boldsymbol{\theta}} \rangle$ can be computed efficiently.
>
> - It is possible to efficiently generate samples s from the Born distribution $P(s) = \frac{|\langle s | \Psi_{\boldsymbol{\theta}} \rangle|^2}{\langle \Psi_{\boldsymbol{\theta}} | \Psi_{\boldsymbol{\theta}} \rangle}$.

If these two conditions are met, we can estimate expectation values of arbitrary *k*-local operators efficiently, and the statistical error due to the stochastic sampling can be rigorously controlled by increasing the number of samples. Therefore, the computational time to compute expectation values is polynomial in both the size of the system and the accuracy.

---

[1] The bond dimension is in fact the rank of the Schmidt decomposition of the quantum state.

A *k*-local operator is an operator that contains terms acting on at most *k* local quantum numbers at the same time. For instance, a nearest-neighbour Hamiltonian is a 2-local Hamiltonian because it contains terms acting on 2 qubits.

In general, given a variational state $|\Psi_\theta\rangle$, we can obtain the expression for the expectation value of an operator $\hat{O}$ as follows

$$\langle\hat{O}\rangle = \frac{\langle\Psi_\theta|\hat{O}|\Psi_\theta\rangle}{\langle\Psi_\theta|\Psi_\theta\rangle} \tag{5.7}$$

$$= \frac{\sum_{s,s'}\langle\Psi_\theta|s\rangle\langle s|\hat{O}|s'\rangle\langle s'|\Psi_\theta\rangle}{\sum_s|\langle\Psi_\theta|s\rangle|^2} \tag{5.8}$$

$$= \frac{\sum_s\langle\Psi_\theta|s\rangle\frac{\langle s|\Psi_\theta\rangle}{\langle s|\Psi_\theta\rangle}\sum_{s'}\langle s|\hat{O}|s'\rangle\langle s'|\Psi_\theta\rangle}{\sum_s|\langle\Psi_\theta|s\rangle|^2} \tag{5.9}$$

$$= \frac{\sum_s|\langle\Psi_\theta|s\rangle|^2\sum_{s'}\langle s|\hat{O}|s'\rangle\frac{\langle s'|\Psi_\theta\rangle}{\langle s|\Psi_\theta\rangle}}{\sum_s|\langle\Psi_\theta|s\rangle|^2}, \tag{5.10}$$

where we have added two identities of the form $\sum_s|s\rangle\langle s| = \mathbb{1}$ in the numerator, and one in the denominator. Then, we have multiplied by $\frac{\langle s|\Psi_\theta\rangle}{\langle s|\Psi_\theta\rangle}$ in the numerator.[2] We identify two main terms:

$$P(s) = \frac{|\langle\Psi_\theta|s\rangle|^2}{\sum_s|\langle\Psi_\theta|s\rangle|^2} \tag{5.11}$$

$$O_{\text{loc}}(s) = \sum_{s'}\langle s|\hat{O}|s'\rangle\frac{\langle s'|\Psi_\theta\rangle}{\langle s|\Psi_\theta\rangle}, \tag{5.12}$$

where $O_{\text{loc}}(s)$ is the so-called *local estimator* of $\hat{O}$. Therefore, we can write the quantum expectation value of an observable $\hat{O}$ as the statistical expectation value of its local estimator O_{loc} over the probability distribution $P(s)$:

$$\langle\hat{O}\rangle = \sum_s P(s)O_{\text{loc}}(s) = \langle O_{\text{loc}}(s)\rangle_P. \tag{5.13}$$

Let us stress that these calculations only hold for operators with the property that the number of states s' such that $|\langle s|\hat{O}|s'\rangle| \neq 0$, for arbitrary s is at most polynomial in the number of spins. For example, it is easy to convince one-self that *k*-local operators satisfy this property. Conversely, evaluating $O_{\text{loc}}(s)$ would not be tractable, given that the sum over s' in eq. (5.12) would be over an exponential number of elements.

The procedure described above allows to obtain a controlled, stochastic estimate of the expectation values by directly sampling a series of states, $s^{(1)}, s^{(2)}, \ldots, s^{(M)}$, from $P(s)$, and approximating $\langle\hat{O}\rangle$ with the following arithmetic mean

$$\langle\hat{O}\rangle \approx \frac{1}{M}\sum_{i=1}^{M}O_{\text{loc}}(s^{(i)}). \tag{5.14}$$

The statistical error associated with such an estimate is $\varepsilon = \sqrt{\sigma^2/M}$, and it is bounded as long as the variance σ^2 of O_{loc} is finite. For example, when $\hat{O}$ is a k-local spin operator with

---

[2]Notice that this manipulation is always valid, since amplitudes with $\langle s|\Psi_\theta\rangle = 0$ never appear in the summation over s.

bounded coefficients, its variance is strictly finite, since it can be shown that $\sigma^2 = \langle \hat{O}^2 \rangle$. [3] Therefore, the error in the estimate of expectation values decreases as $\varepsilon \sim 1/\sqrt{M}$, which allows us to reach arbitrary accuracy in the estimation by increasing the number of samples M, given that $\lim_{M \to \infty} \varepsilon = 0$. However, generating a set of samples according to the Born distribution, $\{s^{(i)}\} \sim P(s)$, is in general a non-trivial computational task in the case where the variational ansatz, $\Psi_{\boldsymbol{\theta}}(s)$, is parameterized by an efficiently computable, yet arbitrary function. One of the most commonly adopted strategies to sample from $P(s)$ is through *Markov chain Monte Carlo* methods, including the Metropolis-Hastings method, which generate a sequence of correctly distributed samples $s^{(i)}$.

Metropolis-Hastings methods construct a markovian stochastic process which satisfies the *detailed balance* relation for the target probability distribution

$$P(s)\mathcal{T}(s \to s') = P(s')\mathcal{T}(s' \to s), \tag{5.15}$$

where $\mathcal{T}(s^{(i)} \to s^{(i+1)})$ is the probability that the state $s^{(i)}$ at step i transitions to the state $s^{(i+1)}$ at the following step. As the process is markovian, the transition probability at every step depends exclusively on the current configuration. The detailed balance condition ensures that, regardless of the initial configuration $s^{(0)}$, the sequence eventually converges to the correct distribution $P(s)$ in the long time limit.

One possible choice of the transition probability $\mathcal{T}$ is given by the *Metropolis-Hastings algorithm* [203]. The main idea is to express $\mathcal{T}$ in terms of a local transition kernel T and an acceptance probability A such that

$$\mathcal{T}(s \to s') = T(s \to s')A(s \to s'). \tag{5.16}$$

This way, we split the global stochastic process into the product of two local subprocesses that we can compute efficiently. For instance, it is very easy to find a normalized local transition kernel that allows us to modify only a few degrees of freedom, like flipping a single spin in a given configuration. Conversely, it is hard to find a normalized global kernel that would act on all spins.

The acceptance probability to go from a configuration s to s' through a local transition is defined as

$$A(s \to s') = \min\left(1, \frac{P(s')T(s' \to s)}{P(s)T(s \to s')}\right). \tag{5.17}$$

Notice that the normalization of the Born probabilities cancel out, giving the expression

$$\frac{P(s')}{P(s)} = \left| \frac{\langle s'|\Psi_{\boldsymbol{\theta}}\rangle}{\langle s|\Psi_{\boldsymbol{\theta}}\rangle} \right|^2, \tag{5.18}$$

which allows us to consider unnormalized variational ansätze. Additionally, if the variational state is computationally tractable, the transition probability also has a tractable complexity, provided it only acts on the basis elements.

Choosing a valid transition rule $T(s \to s')$ is not trivial, and we must take special care in the case of systems with symmetries. For example, if the total magnetization along the direction of the computational basis is known, we might want to fix it and use a transition rule that does not project the Markov chain outside of a certain region. In general, a computationally

---

[3]It is also simple to prove that, when $|\psi_{\boldsymbol{\theta}}\rangle$ approaches an eigenstate of $\hat{O}$, the variance vanishes. Consequently, considering $\hat{O} = \hat{H}$, the statistical error vanishes as we approach the ground (or any excited) state.

expensive, yet effective choice for the transition kernel is to use the Hamiltonian itself:

$$T(s \rightarrow s') = \frac{\left|\langle s|\hat{H}|s'\rangle\right|(1 - \delta_{s,s'})}{\sum_{'\neq s}\left|\langle s|\hat{H}|s'\rangle\right|},$$
(5.19)

which is known as Hamiltonian transition rule [196].

> This way, with the Metropolis-Hastings algorithm, starting from a random configuration $s^{(0)}$, we can sample from $P(s)$ by iteratively proposing local modifications s' according to $T(s \rightarrow s')$, and accepting them according to $A(s \rightarrow s')$.

Nonetheless, this sampling procedure is imperfect, and it can fail to converge for a reasonable number of iterations if the sampled distribution is too complex. In addition, the procedure suffers from the fact that the samples are correlated, since we flip spins iteratively. See algorithm 6 for further details.

Algorithm 6 Metropolis-Hastings algorithm

$s \leftarrow \text{uniform} \in [1, 2^N]$ ▷ sample initial state uniformly at random
for i = 1 to M **do**
    propose s' according to $T(s \rightarrow s')$
    $A \leftarrow \frac{P(s')T(s'\rightarrow s)}{P(s)T(s\rightarrow s')}$ ▷ calculate acceptance probability
    $\xi \leftarrow \text{uniform} \in [0, 1]$
    if $\xi \leq A$ **then**
        $s \leftarrow s'$ ▷ update state
    end if
end for

5.2   Representing the wave function

Now that we have seen how to compute the quantities of interest using parametrized quantum states, let us dive into how to devise expressive variational states in practice. The main idea is that we need to represent high-dimensional functions with a parametrization that is flexible and general enough to describe physical systems, while involving only a polynomial amount of parameters.

Traditionally, researchers have relied on physically-inspired variational ansätze. The Jastrow wave function [204,205] stands out as one of the most successful and widely used ones. It is based on the assumption that two-body interactions are the most physically relevant, and it assigns a trainable potential to every interacting pair. Formally,

$$\Psi_{\boldsymbol{\theta}}(s) = e^{-\frac{1}{2}\sum_{i\neq j}\theta_{ij}\sigma_i\sigma_j},$$
(5.20)

where the sum runs over all possible spin pairs, and θ_{ij} are the parameters encoding pairwise spin correlations. Therefore, for a system of N spins, the resulting wave function has $\mathcal{O}(N^2)$ parameters. Moreover, in translationally invariant systems, the parameters θ_{ij} can be made depend exclusively on the distance between i and j, resulting in a reduced number, $\mathcal{O}(N)$, of parameters.

More recently, ANNs have taken over more traditional ansätze to approximate the wave function itself [196]. This family of variational states is known as neural quantum states

(NQSs). For instance, we can write a parametrized wave function as a feed-forward NN. In this case, $\Psi_{\theta}(s)$ corresponds to the output of a NN that takes the configuration s as input in the form of a vector.

In a feed-forward neural network of depth D, every layer l consists of a non-linear activation function $g^{(l)}$ that acts, component-wise, on a vector resulting from applying the weight matrix $W^{(l)}$ to the output of the previous layer. This way, it is possible to write the variational state as the composition of operations $g^{(l)} \cdot W^{(l)}$, where "·" indicates point-wise operation, such that

$$\Psi_{\theta}(s) = g^{(D)} \cdot W^{(D)} \ldots g^{(2)} \cdot W^{(2)} g^{(1)} \cdot W^{(1)} s. \tag{5.21}$$

Hence, the output is a scalar, complex or real, representing the probability amplitude of configuration s.

From a mathematical perspective, these ansätze are of great interest given that NNs are subject to universal representation theorems [64], as we explain in section 2.4.4. According to eq. (2.46), we could represent the many-body wave function with a polynomial number $\mathcal{O}(N^2)$ of one-dimensional non-linear functions, with N denoting the number of spins.

However, these results hold for arbitrary non-linear functions, Φ_q, $\phi_{q,p}$ in eq. (2.46), that must be appropriately found in order to represent the target function. In practice, NNs use a fixed non-linear activation, and we can only adjust the number of operations. In these cases, the number of neurons does not have a strict polynomial scaling and it can be, in the worst case, exponential in N [65]. Nevertheless, the state-of-the-art results in computer vision and natural language processing [206–208] should be sufficient motivation to employ similar techniques to represent quantum states. Note that the NN representation of quantum states does not preserve the Hilbert space structure, which means that for two NN representations $|\psi_1\rangle$ and $|\psi_2\rangle$ it is not possible to construct a valid wave function $|\psi\rangle = |\psi_1\rangle + |\psi_2\rangle$ represented by a NN of the same size as the ones representing $|\psi_1\rangle$ and $|\psi_2\rangle$ by simply adding up the parameters together, as the ansatz is generally nonlinear.

5.2.1 Restricted Boltzmann machines

NQS were first introduced using *restricted Boltzmann machines (RBMs)* [196]. RBMs are shallow models featuring two fully-connected layers: a *visible* layer, consisting of N units, and a *hidden* layer, consisting of M units. A scheme of an RBM architecture is presented in fig. 5.1. The wave function amplitudes of an RBM ansatz are given by:

$$\Psi_{\theta}(s) = \sum_{h} e^{b_v^{\dagger} s + b_h^{\dagger} h + h^{\dagger} W s}. \tag{5.22}$$

where s, h represent the visible and hidden units, respectively, and the parameters $\theta = \{b_v, b_h, W\}$ represent the visible and hidden biases and the weight matrix, respectively. In the NN picture, the RBM is a single-layer nonlinear feed-forward NN, with the visible units serving as inputs and the exponential serving as the activation function. While it is common to have biases for the hidden layer (see section 2.4.4), RBMs have also somewhat unusual biases connected to the input values, which is explained in the next paragraph.

By construction, RBMs are designed in such a way that computing the summation over hidden units, as in eq. (5.22), can be done analytically. To see this, we can rewrite eq. (5.22) in a tractable form considering binary hidden units $h_i \in \{-1, 1\}$, leading to

$$\Psi_{\theta}(s) = e^{b_v^{\dagger} s} \prod_{i=1}^{M} 2 \cosh \left(b_{h,i} + W_i \cdot s \right), \tag{5.23}$$
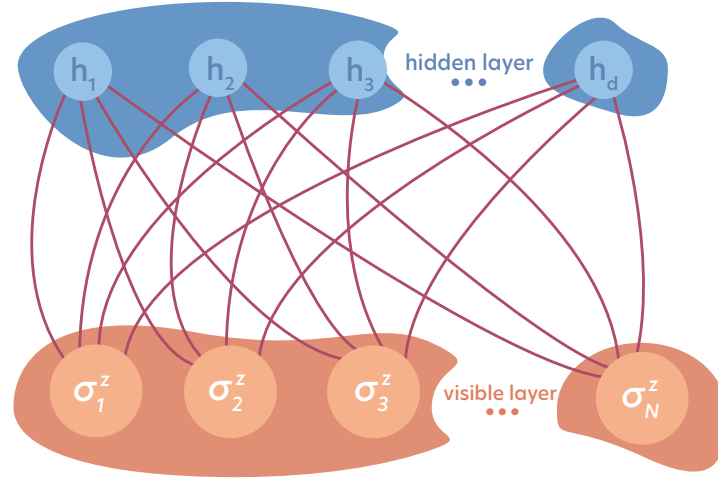
Figure 5.1: Pictorial representation of a restricted Boltzmann machine (RBM) that represents the wave function of an N-spin system, with $\boldsymbol{s} = (\sigma_1, \sigma_2, \ldots, \sigma_N)$ and $\boldsymbol{h} = (h_1, h_2, \ldots, h_d)$ the hidden units.

where $\boldsymbol{b}_{h,i}$ and $\boldsymbol{W}_{i\cdot}$ denote the i-th hidden bias and weight matrix row, respectively. To treat spin systems, the visible units will represent the N physical spins, thus the input of the RBM is simply the spin configuration $\boldsymbol{s}$. In this way we obtain an analytical expression to evaluate the amplitude for a given spin configuration, and thus represent the full wave function with this ansatz. One can also interpret the hidden units as M hidden spins, and in this picture the RBM can be thought of as an interacting spin model with interaction strengths $\boldsymbol{W}_{ij}$. Moreover, we can treat an RBM as a model with an associated energy depending on its parameters, input, and hidden spin values. This is known as an energy-based model, and explains why input biases are present in eq. (5.22). In fact, the RBM is equivalent to a Hopfield network, a type of spin glass [209]. For more details on this view, see [210].

Being the first to be introduced in this context, most of the early works about NQS employ RBMs, but other architectures have been systematically explored in more recent years. The capacity of RBMs and its relationship to quantum entanglement has been examined in various works [211, 212]. An extension of this architecture, the deep RBMs, has also been introduced to solve more complex problems [213], which consists in stacking more than two fully connected layers.

5.2.2 Autoregressive and recurrent neural networks

ARNNs, as presented in section 2.4.6, can also be used for constructing NQS, as introduced in Ref. [82] and later applied to both quantum [214] and classical problems [78]. Their main advantage is that their Born probability distribution is normalized, allowing for direct (autoregressive) sampling, which is easier to parallelize than Markov chain Monte Carlo. A pictorial representation of both the network and the sampling algorithm is presented in fig. 5.2.

Analogously to eq. (2.47), we express the many-body wave function in terms of a product
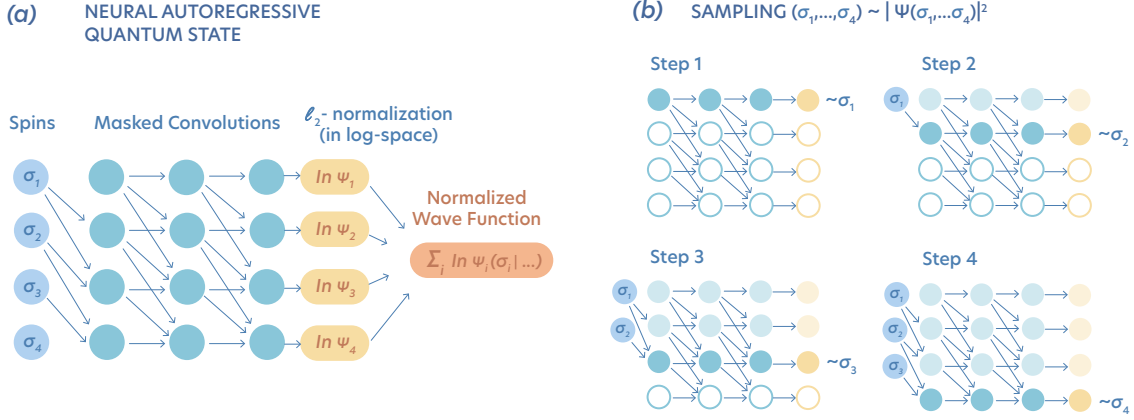
Figure 5.2: Example of an ARNN quantum state for four spins. (a) Pictorial representation of the network. The arrows representing the weights of the model are skewed in order not to break the conditional structure of the output probability distribution. These layers are "masked", due to some connections being deleted. (b) Sampling algorithm. One samples consecutive spins using direct sampling on the conditional probabilities at each step. Adapted from [82].

of conditional complex amplitudes:

$$\Psi_{\boldsymbol{\theta}}(s) = \prod_{i=1}^{N} \phi_i(\sigma_i | \sigma_{i-1}, \dots, \sigma_1), \tag{5.24}$$

which is subject to the normalization condition $\sum_{\sigma} \left| \phi_i(\sigma | \sigma_{i-1}, \dots, \sigma_1) \right|^2 = 1$. With this kind of architecture, we can compute expectation values by directly sampling state configurations instead of building a Markov Chain through the Metropolis-Hastings algorithm, for example (see algorithm 6). We sample state configurations by iteratively sampling one spin after the other: we start sampling the first spin σ_1 from the reduced probability distribution $|\phi(\sigma_1)|^2$. Then, we sample the second one σ_2 according to the conditional probability distribution $|\phi_2(\sigma_2|\sigma_1)|^2$, then the next one $|\phi(\sigma_3|\sigma_2, \sigma_1)|^2$, and so on until σ_N. This sampling procedure is embarrassingly parallel.[4]

This sampling procedure yields independent identically distributed samples. Conversely, Markov chain Monte Carlo methods may suffer from highly correlated consecutive samples,[5] which is problematic for complex probability distributions, e.g. that are far from Gaussian. Consider a quantum state that spans several separated regions in the Hilbert space, where the probability is concentrated. In this case, Markov chains generally remain stuck in one of the regions, given that it must take several penalizing steps to travel from one to another, resulting into a highly inaccurate sampling. In contrast, the direct sampling procedure can seamlessly draw spin configurations belonging to all the regions according to the probability distribution, yielding much better samples.

---

[4]We can use the intermediate conditional probabilities to draw samples for a low computational cost, e.g., use the probabilities for $N-1$ spins and sample from the last one, to obtain new samples; with Markov chain Monte Carlo we cannot do this.

[5]Markov chain Monte Carlo methods such as the Metropolis-Hastings algorithm, generally rely on performing modifications to the spin configurations to sample subsequent states. Therefore, this process could yield highly correlated consecutive samples that may have a negative impact on the results. In order to compute expectation values, we need to estimate the autocorrelation time to draw uncorrelated samples from the resulting chain. Moreover, when approaching a phase transition points, such methods suffer from critical slowing down, making the sampling of uncorrelated configurations unfeasible in many situations.
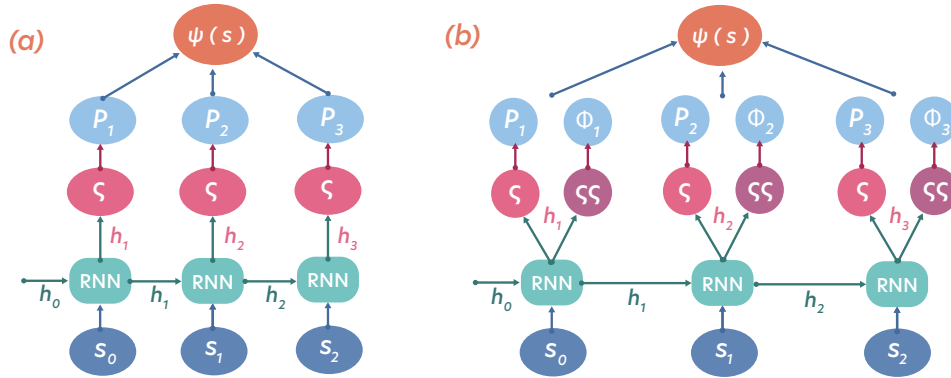
Figure 5.3: Pictorial representation of an RNN architecture for NQS. Panel (a) is for real-valued wave functions, which can be relevant for a certain class of problems, and panel (b) is for complex-valued wave functions. In both schemes, a local spin configuration s_i and a hidden vector h_i are fed into an RNN cell, which performs a non-linear transformation. Then an activation function (ς, for softmax and/or $\varsigma\varsigma$, for softsign) is applied to obtain the final probability and/or phase corresponding to the configuration. At the end, the probabilities (and phases) are combined to obtain the final wave function amplitudes $\psi(\boldsymbol{s})$.

While the first autoregressive models used in quantum physics were built from masked dense or convolutional layers, mimicking the so called PixelNet architecture [215], recurrent neural networks were later introduced [216] RNNs, inspired by natural language processing models, are also generative models. We can draw a simple analogy between correlations in sentences, with their elements living in a large "word space", and spin configurations. Considering spin systems, and supposing some hidden structure, quantum states are correlated and its base elements are elements of the Hilbert space. Following this analogy, Hibat-Allah *et al.* introduced RNN wave functions [216], obtaining impressive results even for frustrated systems. An example of such an architecture is shown in fig. 5.3. Clearly, many different NN architectures that can work. A plethora of different architectures have been implemented as NQS in recent years, such as CNN wave functions [217], and, more recently, group convolutional NNs [218], which are specially convenient to implement certain symmetries, something we examine in section 5.2.4.

5.2.3 Capacity and entanglement

As we show in sections 5.1 and 5.2, there is a whole plethora of methods to represent quantum many-body wave functions. For instance, only in NQSs, we already encounter substantial differences between ansäzte based on different NN architectures. Hence, a natural question arises regarding their expressive capacity and how they compare to each other.

TNs have been a recurrent tool to perform this kind of studies, provided that they are well established and characterized, and they constitute a theoretical language to study quantum many-body phenomena. For this reason, there has been a significant community effort to study the relationship between TNSs and NQSs [212, 219, 220] , which provides insight about the expressive capacity of NQSs [221]. Following the first introduction of NQSs implementing RBMs [196], early works focused on finding direct relationships between various kinds of RBM-based states and TNSs [212, 219]. Recently, it has been proven that NNs can efficiently approximate, in logarithmic space, all efficiently contractible TNs with arbitrary precision. Therefore, for every TNS there exists an equivalent NQS of polynomial size. Conversely, there
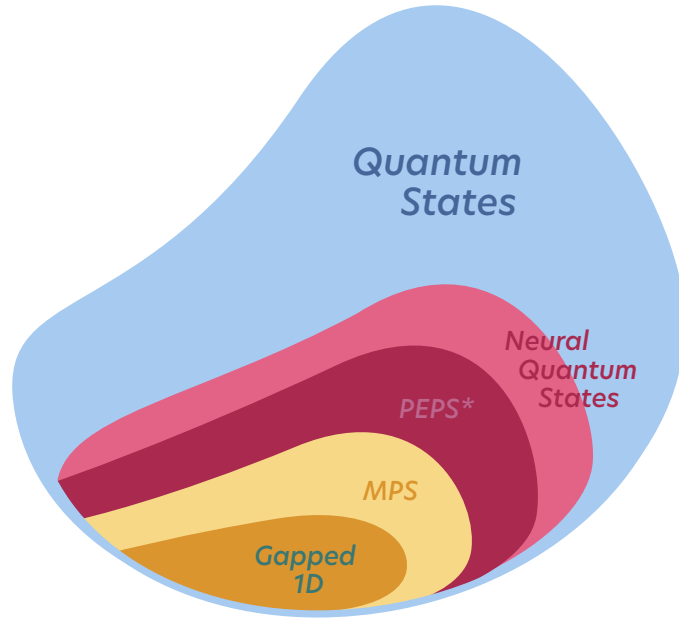
Figure 5.4: Expressive capacity of different classes of variational states, as explicitly proven in Ref. [220] by mapping TNSs to NQS. PEPS* refers to a sub-class of projected entangled pair states, a generalization of MPSs. Adapted from [220].

are quantum states that can be efficiently described by NQSs, whose representation in terms of TNSs requires an exponential amount of parameters. Hence, TNSs are a subset of NQSs [220], as depicted in fig. 5.4.

As a measure of expressive capacity, we often rely on the entanglement that the different ansätze can capture. For instance, the mean field ansatz is, by construction, a product state (recall eq. (5.3)). Hence, it can capture less entanglement than TNSs or NQSs, wich do not have such strong local limitations. This way, TNSs and NQSs have higher expressive capacity than the mean field ones.

More precisely, we study the entanglement scaling captured by the different ansätze. In a generic quantum many-body system with density matrix ρ, the entanglement entropy is defined as

$$S(\rho) = -\operatorname{Tr}\left[\rho \log_2 \rho\right], \tag{5.25}$$

which is zero for any pure state. Let us consider a partition of the system in two subsets: I and its complementary O, as well as the reduced density matrix $\rho_I = \operatorname{Tr}_O[\rho]$. In general, ρ_I represents a mixed state, which can have nonzero von Neumann entanglement entropy. For a generic quantum state, the entanglement entropy of ρ_I grows with the volume of the cut. Thus, it corresponds to a *volume-law* scaling. NQSs can efficiently capture such scaling with architectures ranging from very basic shallow ones, such as RBMs [211], to more modern and deeper approaches, such as CNNs or RNNs [221]. Some traditional ansätze, such as the Jastrow wave function (see eq. (5.20)), can also capture volume-law entanglement.[6]

---

[6]The Jastrow ansatz is, indeed, a specific case of RBM wave function with $N(N-1)/2$ hidden neurons [219].
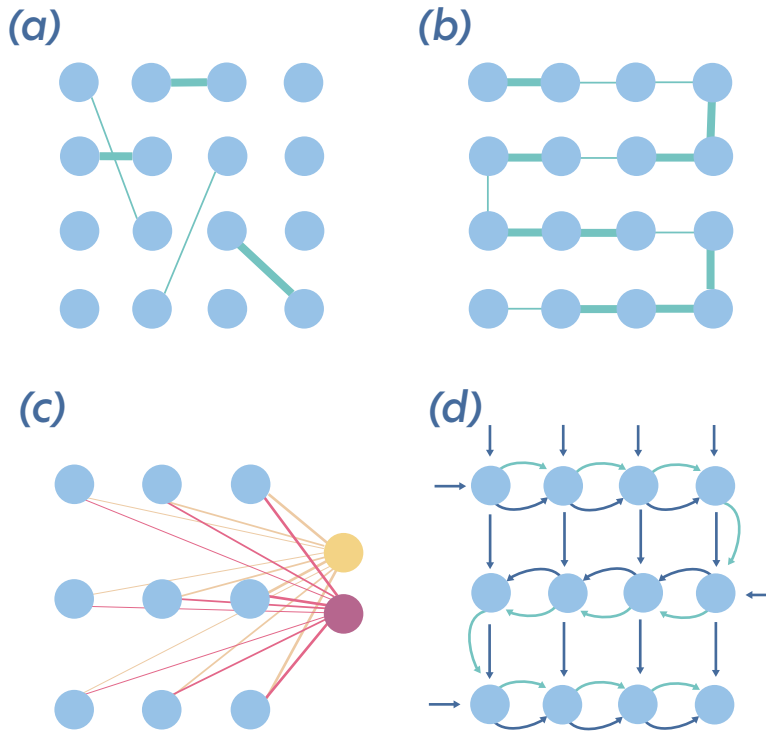
Figure 5.5: Schematic representation of various ansätze inspired by [219]. (a) The Jastrow ansatz draws connections between all possible pairs of sites. (b) The MPS ansatz draws connections between nearest-neighbour sites along a line. (c) The RBM ansatz connects all the sites to every hidden neuron, illustrated in different colours. (d) The RNN ansatz processes the state sequentially, following the green arrows. The dark blue arrows indicate the flow of information within the model. Arrows without a starting site correspond to free parameters. Sketch inspired by [224].

However, there is a subclass of states in which the entanglement entropy grows, at most, as the boundary area between two regions. This is known as *area-law* scaling, and it is a property of ground states of local and gapped Hamiltonians [222]. Due to their local nature, TNSs can efficiently capture area-law entanglement [223]. For instance, in a one-dimensional chain, the area of the cut between two subsystems is constant, meaning that the entanglement entropy is a constant, and not an extensive quantity, in the infinite volume limit. For an MPS with bond dimension χ, the von Neumann entanglement entropy of any possible bi-partition of the system is bounded from above as $S \leq \mathcal{O}(\log_2 \chi)$, thus making the MPS ansatz an excellent candidate to study one-dimensional systems.

We can understand most differences between the ansätze at an intuitive level by, simply, looking at how they are built. In fig. 5.5, we provide a pictorial representation of the different connections that some ansätze can draw in a bi-dimensional system. Clearly, the MPS ansatz, depicted in fig. 5.5(b), is the most locally restricted one, as it can only account for nearest neighbour connections in a snake-like pattern. This effectively limits the entanglement that MPS can capture. The RNN ansatz, illustrated in fig. 5.5(d), while it is limited to parse the state in the same pattern as the MPS, it has the freedom to account for additional information, allowing it to capture richer correlations.

In contrast, other ansätze such as the Jastrow or RBM wave functions, respectively illustrated in fig. 5.5(a) and (c), can draw connections between arbitrary sites. The Jastrow ansatz

can account for all possible pairs in the system, regardless of the distance. Then, the RBM anstaz is a generalization of the Jastrow by means of an auxiliary hidden layer of variable size. Through the hidden neurons, the ansatz is no longer limited to pairs, and it can actually consider up to all-to-all connections. This non-local character allows them to capture volume-law entanglement.

5.2.4 Implementing symmetries

Encoding symmetries in NQSs allows us to reduce the number of parameters in the NN, restricting the region of the Hilbert space that our ansatz can cover to a subspace of interest, thus improving the accuracy of the results. Let us first explain what we mean by symmetry in this context. Consider a group of linear transformations: if the Hamiltonian is invariant under those transformations, meaning that they all commute with the Hamiltonian, then the Hamiltonian is symmetric under that group. Some of the most common symmetries in lattice models are the translation symmetry, the rotation symmetry in two or higher dimensions, the inversion or reflection symmetries, and all the compositions of those.

It is possible to show that, if the Hamiltonian commutes with a set of operators $\mathcal{T} = \{\hat{T}_k\}_{k=1}^K$, its ground state must also be left invariant under those transformations. Therefore, the amplitude for two configurations $|s\rangle$ and $|s(k)\rangle = \hat{T}_k |s\rangle$ must be invariant for any $\hat{T}_k$: $\Psi_{\boldsymbol{\theta}}(s) = \Psi_{\boldsymbol{\theta}}(\hat{T}_k s) \, \forall k$.[7] One way to introduce symmetries in our NQS is to take, as output, the sum of the ansatz evaluated on the set of symmetry-invariant configurations $\{s(k)\}$. This way, the output is invariant by construction. However, we do not improve the performance of our model with this approach.

A more efficient approach is to build a dense layer at the beginning of the NQS model that fulfills the symmetry condition [217]. We can use this technique to encode any symmetry group isomorphic to a polynomially large permutation group. This usually comprises the set of all *lattice symmetries* (translations, rotations, reflections...), global discrete symmetries, such as a global spin-flip, but it cannot deal with continuous symmetries, such as SU(2). For instance, we can implement translation symmetries through a convolution with a kernel as wide as the system itself. Since the convolution is translationally invariant by definition, it's easy to see that the output of the layer is symmetry-invariant.

In the case of RBMs, we can rearrange the terms of eq. (5.22) to make it invariant under the elements of a symmetry group. Let us denote the transformation of local spins as $\sigma_j(k) = \hat{T}_k \sigma_j$. We can write our symmetry-invariant amplitude as:

$$\Psi_{\boldsymbol{\theta}}(s) = \sum_{\boldsymbol{h}} \exp\left\{ \sum_f^{\alpha} b_v^f \sum_k^K \sum_j^N \sigma_j(k) + \sum_f^{\alpha} b_h^f \sum_k^K h_{f,k} + \sum_f^{\alpha} \sum_k^K h_{f,k} \sum_j^N W_j^f \sigma_j(k) \right\}, \quad (5.26)$$

where we have explicitly written the matrix products as sums. The important point here is that b_v^f, b_h^f are now vectors in a feature space with $f = 1, \ldots, \alpha$, and the matrix W^f is now of size $\alpha \times N$.[8] If we consider translational invariance, the corresponding symmetry group is made of N translation operators. In this case, W^f can be seen as a kernel acting over configurations to which we have applied the translation operators.

There are, in fact, many ways to directly encode symmetries in NQSs. For more details, we refer to [225] for general feedforward networks, or [217] for an example with CNNs.

---

[7]Up to a phase on the right hand side, but let us ignore it for convenience.
[8]Note that this expression is equivalent to eq. (5.22) with $M = K \times \alpha$ hidden variables.

5.2.5 Limitations

Similar to many ML methods, NQSs suffer from an interpretability problem, as we have discussed extensively in section 3.5 for generic ML approaches. However, there has been substantial progress since the seminal paper from Carleo & Troyer [196]. For instance, a recent work introduced an interpratable RBM ansatz, in which the authors add some correlation terms to the expression of the probability distribution given by eq. (5.22). With this, one can look at the magnitude of the trained parameters to understand which correlations are more important for the given physical problem [226].

Another route to gain further understanding of NQSs is through the mapping of NQS architectures to other known ansätze, such as TNSs. By exploiting this idea, works have shown NQSs to be capable of describing volume-law states, as opposed to TNSs, as we show in section 5.2.3. In terms of expressive capacity, NQSs can efficiently represent the ground states of one-dimensional gapped Hamiltonians, all the TNSs that are efficiently contractable in classical computers, and volume-law states [220]. Furthermore, there have been found exact NQS representations of several interesting phases of matter, such as topological states and stability codes [211,213,219,227–231]. However, not all quantum states can be efficiently represented in terms of NQSs. For instance, we cannot represent random states, since there do not have structure.

Another important aspect is choosing the right NN architecture and training strategy for the problem. For instance, we may be interested in implementing certain symmetries, as we discuss in section 5.2.4. However, on a given problem, a certain NQS ansatz may be well-suited for the task, but the training procedure can fail numerically. Some works have analyzed the training procedure involving stochastic reconfiguration [232]. Others have found that states involved in the dynamics of non-integrable systems are not representable by various architectures, but their entanglement structure can be recovered, hinting at a different limit from the built-in limitation on entanglement in TN-based ansätze [233].

These findings, along with state-of-the-art results, point toward a superior expressive power of NQS over existing simulation methods, but many research routes have to be taken to fully understand their capabilities, much like many ML methods discussed in these lecture notes.

5.3 Applications

In this section, we present various applications of NQS, ranging from the ground state search to quantum state tomography, featuring real-time dynamics, quantum circuits, and fermionic systems. In addition to presenting how the methods described previously apply to such problems, we provide results for each application and compare them to other state-of-the-art methods. By doing this we hope to show both the potential and versatility of NQS approaches, that is still a young field of research.

5.3.1 Finding the ground state

As common in many ML tasks, we define a loss function $\mathcal{L}$ that depends on the trainable parameters of the NN. In this situation, this corresponds to the variational energy, i.e., the expectation value of the Hamiltonian in the variational state:

$$\mathcal{L}(\boldsymbol{\theta}) = E(\boldsymbol{\theta}) = \langle \Psi_{\boldsymbol{\theta}} | \hat{H} | \Psi_{\boldsymbol{\theta}} \rangle. \tag{5.27}$$

This choice of the loss function is naturally introduced since it follows from the variational principle in quantum mechanics.

The *variational principle* states that given an Hamiltonian $\hat{H}$, the energy $E(\theta)$ of a variational wave function $|\Psi_\theta\rangle$ is greater or equal than the exact ground state energy, i.e.,

$$E(\boldsymbol{\theta}) = \frac{\langle \Psi_\theta | \hat{H} | \Psi_\theta \rangle}{\langle \Psi_\theta | \Psi_\theta \rangle} \geq E_0. \tag{5.28}$$

Therefore the energy is a valid loss function, as the *lower* the expectation value of the energy, *the better the approximation is[a]*.

---
[a]We stress that the principle is only valid when computing expectation values exactly. When the energy is computed as a stochastic average, its estimated average can be lower than the exact energy. Nethertheless, as discussed previously, the increase of the number of samples and the use of an efficient sampling approach reduce fluctuations below the exact energy systematically.

In fact, having a loss function strongly rooted in a principle of physics is crucial, since it also allows to compare different methods. By looking at the variational energy, we can for example understand how a method performs at solving a given problem: if the resulting approximate ground state energy is significantly lower than what was found by alternative techniques, we can be reasonably sure that the solution found is of better quality. Following the general discussion on expectation values of operators, the variational energy can be stochastically approximated as

$$E(\boldsymbol{\theta}) \approx \frac{1}{M} \sum_i^M E_{\text{loc}}(\boldsymbol{s}^{(i)}), \tag{5.29}$$

where E_{loc} is the local estimator and is defined as $E_{\text{loc}}(\boldsymbol{s}) = \sum_{\boldsymbol{s}'} \langle s | \hat{H} | s \rangle \frac{\langle s' | \Psi \rangle}{\langle s | \Psi \rangle}$. We aim to minimize this loss function by means of gradient-based optimization algorithms. The energy gradients can also be written in terms of expectation values[9]:

$$\frac{\partial E(\boldsymbol{\theta})}{\partial \theta_p} = 2 \operatorname{Re}\left[\langle E_{\text{loc}}(\boldsymbol{s}) O_p^*(\boldsymbol{s}) \rangle - \langle E_{\text{loc}}(\boldsymbol{s}) \rangle \langle O_p^*(\boldsymbol{s}) \rangle \right] \tag{5.30}$$

$$= 2 \operatorname{Re}\left[\langle (E_{\text{loc}}(\boldsymbol{s}) - \langle E_{\text{loc}}(\boldsymbol{s}) \rangle) O_p^*(\boldsymbol{s}) \rangle \right] \tag{5.31}$$

where we have assumed that the parameters are real[10] and that θ_p is the p-th parameter of the NQS. The diagonal operator $\hat{O}_p$ is defined as

$$O_p(\boldsymbol{s}) = \frac{\partial}{\partial \theta_p} \log\langle s | \Psi_\theta \rangle = \langle s | \hat{O}_p | s \rangle. \tag{5.32}$$

---
[9]Computationally speaking, one does not need to store in memory the full Jacobian matrix $O_p(\boldsymbol{s})$, but can compute this gradient directly through the vector-Jacobian product (reverse-mode differentiation) of the vector $v = E_{\text{loc}}(\boldsymbol{s}) - \langle E_{\text{loc}}(\boldsymbol{s}) \rangle$ and the Jacobian $O_p(\boldsymbol{s})$. This approach lowers considerably the memory and computational cost. For more details, see section 7.1.

[10]The requirement of real parameters is not actually necessary. For complex parameters the expression is very similar, though care has to be taken in order to consider non-holomorphic ansätze. Note that many common ansätze, in particular most autoregressive ones, are not holomorphic. A discussion of this can be found in the appendix of Ref. [234].

We also remark that the expression used in eq. (5.31) has the form of a covariance, and therefore it is therefore particularly stable with respect to sampling noise. Most notably, when the wave function is close to the exact ground state, statistical fluctuations in the local energy are suppressed, implying that also statistical fluctuations of the gradients are small, because of the covariance structure.

The learning algorithm is thus straightforward. First, we initialize the weights $\theta^{(0)}$. Next, at each step a sequence of M configurations is sampled according to the Born distribution: $P(s; \theta^{(s)}) \sim s^{(1)} \dots s^{(M)}$. This can be done with a Markov chain or with direct sampling techniques as explained above.

The next step is to compute the mean of the local energy $E(\theta)$, which gives us the estimate of the expectation value of the Hamiltonian. Additionally, the gradients can also be calculated as shown in eq. (5.31). For the last step, we can use a gradient-based optimizer of our choice, to update the parameters for the next step, i.e., $\theta_p^{(s+1)} = \theta_p^{(s)} - \eta \frac{\partial E(\theta)}{\partial \theta_p}$ for vanilla gradient descent where η is the learning rate.

The procedure is repeated until it converges to a minimum of the energy landscape. Here, there is no training data set as the approach is not based on any supervised learning method. The presented task is in fact to determine the optimal (unknown) wave function by drawing samples from the associated Born distribution and using a neural network to model the state itself. These steps are summarized in algorithm 7. Note that this algorithm is not the most commonly used, as it is less accurate than imaginary-time evolution, which is presented in section 5.3.3.

Algorithm 7 Ground state search with NQS

   Initialize θ randomly
   for i = 1 to n_{steps} **do**
       Generate M samples according to some algorithm (usually a Markov chain)
       Calculate the gradient of the energy $\partial E(\theta)/\partial \theta_p$
       Update parameters as $\theta_j \leftarrow \theta_j - \eta \partial E(\theta)/\partial \theta_j$ (or with a more advanced update rule)
   end for
   return Optimized parameters θ

5.3.2 Real-time evolution

NQSs can also be used to variationally perform real-time evolution [235] through a procedure known as time-dependent variational Monte-Carlo (t-VMC) [196, 217, 236, 237]. This is of particular interest for non-equilibrium quantum dynamics of closed, interacting quantum systems. Studying these problems enables one to understand critical properties, entanglement spectra, and many other physical quantities of interest in complex many-body quantum systems. The problem one wants to solve is to integrate the time-dependent Schrödinger equation ($\hbar = 1$ in the following) in time, using a parametrized wave function $|\Psi_\theta(t)\rangle$:

$$\mathrm{i}\frac{d|\Psi_\theta(t)\rangle}{dt} = \hat{H}|\Psi_\theta(t)\rangle, \tag{5.33}$$

i.e., find the correct form of $|\Psi_\theta(t)\rangle \ \forall t$. Expanding eq. (5.33) at first order in δ and taking the inner product with $\langle s|$, we obtain:

$$\Psi_\theta(t+\delta)(s) = 1 - \mathrm{i}\delta\langle s|\hat{H}|\Psi_\theta(t)\rangle + O(\delta^2) \tag{5.34}$$

$$= 1 - \mathrm{i}\delta E_{\text{loc}}(s) + O(\delta^2), \tag{5.35}$$

where we used $E_{\text{loc}}(s)$ as defined in the previous section. In order to get a good variational approximation of the state at the next time step, $t + \delta$, it is natural to define the cost function $\mathcal{L}(\tilde{\boldsymbol{\theta}})$:

$$\mathcal{L}(\tilde{\boldsymbol{\theta}}) = \text{dist}\left(|\Psi_{\tilde{\boldsymbol{\theta}}}\rangle, |\Psi_{\boldsymbol{\theta}}(t + \delta)\rangle\right), \tag{5.36}$$

with $\boldsymbol{\theta}$ the variational parameters at the previous time step, and $\tilde{\boldsymbol{\theta}}$ variational parameters to be determined. The loss function can be minimized analytically, if the time step is sufficiently small. One starts by noticing that $\tilde{\boldsymbol{\theta}} = \boldsymbol{\theta} + \delta\dot{\boldsymbol{\theta}} + \mathcal{O}(\delta^2)$. One can therefore expand the variational state $|\Psi_{\tilde{\boldsymbol{\theta}}}\rangle$ at first order and take its inner product with $\langle s|$, much like we did for eq. (5.34):

$$\Psi_{\boldsymbol{\theta}+\tau\dot{\boldsymbol{\theta}}}(s) = \left(1 - \delta\dot{\boldsymbol{\theta}}\partial_{\boldsymbol{\theta}}\Psi_{\boldsymbol{\theta}}(s)\right)\Psi_{\boldsymbol{\theta}}(s) + \mathcal{O}(\delta^2). \tag{5.37}$$

We need to consider a distance measure between the two states $|\Psi\rangle$ and $|\phi\rangle$ which can be efficiently sampled. There is a certain freedom in this choice, which can lead to slightly different variational principles. For an extensive discussion of these issues, see [235]. By considering the infidelity, keeping in mind that for many NQS architectures the quantum states are unnormalized, we have [11]:

$$\text{dist}\left(|\Psi\rangle, |\phi\rangle\right) = 1 - \frac{\langle\phi|\Psi\rangle\langle\Psi|\phi\rangle}{\langle\phi|\phi\rangle\langle\Psi|\Psi\rangle}. \tag{5.38}$$

By plugging eq. (5.37) and eq. (5.34) into the distance of eq. (5.38), minimising it, and keeping the leading terms in δ one obtains an equation giving the time derivative of the variational parameters $\dot{\boldsymbol{\theta}}$, enabling high-order integration methods such as Runge-Kutta integration:

$$S\dot{\boldsymbol{\theta}} = -\mathrm{i}\boldsymbol{f} \tag{5.39}$$

with the *quantum geometric tensor* S and the vector $\boldsymbol{f}$, whose elements are given by:

$$S_{pp'} = \langle O_p^* O_{p'}\rangle - \langle O_p^*\rangle\langle O_{p'}\rangle \tag{5.40}$$

$$f_p = \langle E_{\text{loc}} O_p^*\rangle - \langle E_{\text{loc}}\rangle\langle O_p^*\rangle \tag{5.41}$$

with the O_ps given by eq. (5.32) and E_{loc} is the local energy. The vector $\boldsymbol{f}$ is the gradient of the local energy with respect to the variational parameters and, in analogy with classical mechanics, it is often called the vector of *forces*. The spectrum of the geometric tensor instead encodes the (linearized) curvature of the variational space, akin to the Hessian discussed in section 4.5. For a full derivation and an in-depth discussion of the time-dependent variational principles, see [235]. The spectrum of S has been extensively studied in the case of ground state optimization with RBMs [232], where it has been connected to the different regimes of considered physical system. In practice, solving the linear system eq. (5.39) implies either using an iterative solver (for example, conjugate gradient) or a direct solver (for example, QR factorization). An important pratical numerical issue is that the matrix S is often singular. Some techniques have been found to regularize S and obtain more stable dynamics [217,238]. In all cases, since only stochastic averages for both S and $\boldsymbol{f}$ are available, stable and accurate long time dynamics are still a challenge for NQS [238]. As an example, in fig. 5.6 we show the quench dynamics of a one-dimensional spin chain, subject to the Ising Hamiltonian with a transverse field:

$$\hat{H}_{\text{TFI}} = -J\sum_j \hat{\sigma}_j^z \hat{\sigma}_{j+1}^z + h\sum_j \hat{\sigma}_j^x. \tag{5.42}$$

J is the nearest-neighbor coupling, and h is the transverse field strength. This model exhibits a second-order phase transition in one dimension at $h = J$, that separates a ferromagnetic

---

[11]Rigorously, one should consider the Fubini-Study metric, but taking this distance leads to the same equations.
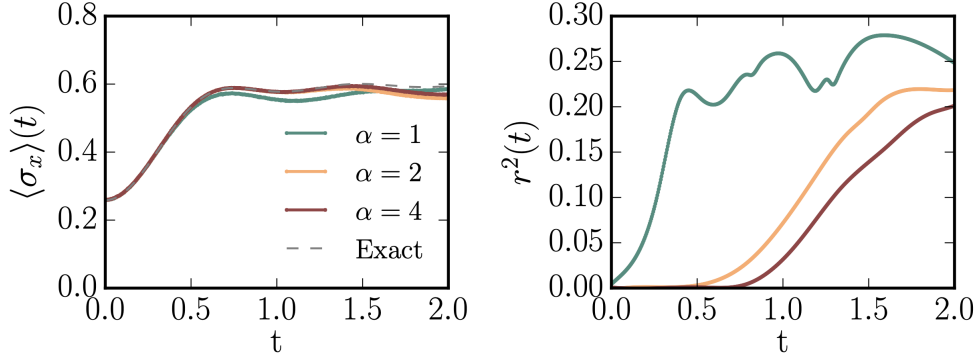
Figure 5.6: Critical quench dynamics with an RBM, preparing the system in the ground state of $\hat{H}_{\mathrm{TFI}}$ for $h_i/J = 1/2$, then suddenly quenching to $h_f/J = 1$. This excites many eigenstates of the system at criticality (which exhibit long-range correlations, making the dynamics difficult to capture). Left panel: average magnetization along x for different values of the number of hidden layers α of the RBM. Right panel: integrated error, systematically reduced by increasing α. Taken from [196].

(for $J > 0$, or antiferromagnetic for $J < 0$) phase from a paramagnetic phase, with all spins aligned along the transverse-field for $h \gg J$. Critical quench dynamics can be investigated by preparing the system in an eigenstate of the Hamiltonian for some value of $h = h_i$, then suddenly switching the Hamiltonian parameters to $h_f/J = 1$. As seen in fig. 5.6, an RBM captures the dynamics up to about $Jt = 1.5$, and increasing the number of hidden layers α systematically improves the precision. As mentioned, more recent results have also been obtained using a CNN on a two-dimensional system, whose dynamics are a challenge for TN methods [217].

5.3.3 Imaginary-time evolution

The first-order optimization scheme presented in section 5.3.1 to estimate the ground state of many-body systems can be improved to yield more accurate results. For this purpose, it is useful to consider imaginary time evolution, through Wick's rotation $t \to i\tau$:

$$|\psi_{\boldsymbol{\theta}}(\tau)\rangle = \exp\left(-\tau\hat{H}\right)|\psi_{\boldsymbol{\theta}}(0)\rangle, \tag{5.43}$$

where $\hat{H}$ is the Hamiltonian, and τ is a real number. It can be shown that $\lim_{\tau\to\infty}|\phi(\tau)\rangle = |\phi_0\rangle$, with $|\phi_0\rangle$ the exact ground state of the Hamiltonian, and provided $|\langle\psi_{\boldsymbol{\theta}}(\tau)|\phi_0\rangle| \neq 0$. Furthermore, it can be shown that the convergence of imaginary-time evolution toward the exact ground state is exponentially fast with τ, thus offering a systematic way to find the ground state. Analogously to real-time evolution, imaginary-time evolution can also be performed variationally. This leads to the same type of equation as eq. (5.39):

$$S\dot{\boldsymbol{\theta}} = -\boldsymbol{f}, \tag{5.44}$$

with the factor i missing due to the form of the exponent in eq. (5.43). Hence, a very similar procedure is obtained as for the real time evolution in which we can update the weights according to the update given by the equation above. To summarize both real and imaginary time, the algorithm for variational time evolution is given in algorithm 8. In the case of imaginary-time evolution, the algorithm is typically modified in such a way that the S matrix is regularized by adding a constant, $\Lambda > 0$, proportional to the identity: $S \to S + \Lambda I$. In this case, one recovers the stochastic reconfiguration method, as originally introduced by S. Sorella [239,240]. In fig. 5.7, results are shown for imaginary-time evolution performed on

---

Algorithm 8 Real ($\xi = i$) or imaginary ($\xi = 1$) time evolution algorithm for NQS

   $\boldsymbol{\theta} \leftarrow$ random initialization
   for i $= 1$ to n_{steps} **do**
       Calculate $S_{pp'}$ and F_p
       Get $\dot{\boldsymbol{\theta}}$ by inverting the equation $\sum_{p'} S_{pp'} \dot{\theta}_{p'} = -\xi F_p$ (and possibly regularizing)
       Update $\boldsymbol{\theta}$ using an ODE integrator
   end for
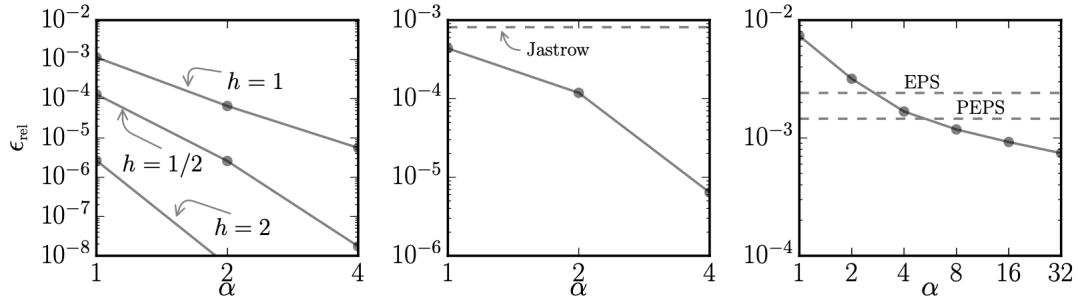
Figure 5.7: Relative error of the ground state search using imaginary time evolution with respect to the exact solution. Left panel: relative error for the ground state of the transverse-field Ising model, for various values of h/J as a function of the number of $\alpha = M/N$, M being the number of hidden units for $N = 80$ spins. Center panel: Same plot for the ground state of the antiferromagnetic Heisenberg model, compared to another variational ansatz, the Jastrow wave function. Right panel: comparison with state-of-the-art TN results, showing that NQSs perform at least as good. Taken from [196].

the transverse-field Ising model and the Heisenberg model [196]. These results show two important features: (i) using an RBM ansatz, the relative error can be systematically reduced by increasing $\alpha = M/N$, with M the number of hidden units and (ii) the results achieve a higher precision than state-of-the-art TN methods.

5.3.4 Fermionic systems

The classical simulation of fermionic systems is known to be a very interesting and difficult problem. Its difficulty arises from the fact that fermionic operators obey anti-commutation relations which constrain the wave functions of fermionic systems to be anti-symmetric under particle exchange. Due to the infamous sign problem [241], all the known quantum Monte Carlo methods become computationally extremely expensive. Nevertheless, fermionic systems are ubiquitous in many-body quantum physics, and in high energy physics as the elementary constituents of the matter, i.e., quarks and leptons, are fermions. Also, in chemical reactions, electrons play a fundamental role, and they are fermionic particles as well.

   One convenient approach to simulate fermionic systems is based on the mapping of the fermionic degrees of freedom to spins. A generic protocol is the Jordan-Wigner transformation, which enables us to map fermionic problems to interacting spin problems.[12] Historically, this technique has been used to solve spin models [243]. However, here we do the opposite: we map fermionic operators to spin operators in order to use NQSs and the techniques presented throughout the chapter.

---

[12]There are other transformations that have been developed in the context of quantum simulation, such as the Bravyi-Kitaev encoding [242].

Let us consider the creation and annihilation fermionic operators acting on site j, $\hat{c}_j^\dagger$ and $\hat{c}_j$, respectively. The Jordan-Wigner transformation prescribes:

$$\hat{c}_j = \left(\prod_{k=1}^{j} \hat{\sigma}_k^z\right) \hat{\sigma}_j^- \tag{5.45}$$

$$\hat{c}_j^\dagger = \left(\prod_{k=1}^{j} \hat{\sigma}_k^z\right) \hat{\sigma}_j^+, \tag{5.46}$$

where $\hat{\sigma}_j^\pm = \frac{1}{2}\left(\hat{\sigma}_j^x \pm i\hat{\sigma}_j^y\right)$ denote the spin raising and lowering operators. The first term in the transformation provides a phase that can be ± 1 depending on whether the number of occupied fermionic modes is even or odd in sites $k = 1,\ldots,j$. We can conveniently rewrite this term using the relations $\hat{\sigma}_j^z = 2\hat{\sigma}_j^+\hat{\sigma}_j^- - 1$, and $\hat{\sigma}_j^+\hat{\sigma}_j^- = \hat{c}_j^\dagger \hat{c}_j = n_j$. This ensures that the resulting operators fulfill fermionic anti-commutation relations.

For example, using this transformation, we can map a free fermions Hamiltonian in one dimension:

$$\hat{H} = -\frac{1}{2}\sum_j \hat{c}_j \hat{c}_{j+1}^\dagger + \hat{c}_j^\dagger \hat{c}_{j+1} \tag{5.47}$$

to an interacting spin Hamiltonian of the form:

$$\hat{H} = -\frac{1}{2}\sum_j \hat{\sigma}_j^+\hat{\sigma}_{j+1}^- + \hat{\sigma}_{j+1}^+\hat{\sigma}_j^- \tag{5.48}$$

In this form, we can implement all the methods described throughout this chapter 5.

The main issue with this transformation is that it does not generalize well for arbitrary dimensions. In higher dimensions, the Jordan-Wigner transformation makes the Hamiltonian non-local, making it unfeasible to tackle with most standard techniques. Recently, different mappings for fermionic degrees of freedom that work in higher dimensions have been proposed. These are not general mappings, but rather are tailored to specific problems. For example, we can map local Hamiltonians in more than one dimension to local bosonic Hamiltonians for certain specific gauge theories [244, 245].

As mentioned, a problem of current interest is calculating the electronic structure of molecules [197]. This problem is important for applications in chemistry, and was in fact known as one of the first instances of the quantum many-body problem mentioned by Dirac [195]. In this context one is generally interested in finding the ground state energy as a function of some physical parameter, such as the distance between two nuclei for a diatomic molecule. This way, by looking at the minimum of the energy, one can know what the stable geometry of the molecule of interest is.

This is done by finding the ground state of an interacting fermionic Hamiltonian on a lattice, usually of the form:

$$\hat{H} = \sum_{i,j} t_{ij}\hat{c}_i^\dagger \hat{c}_j + \sum_{i,j,k,l} U_{ijkl}\hat{c}_i^\dagger \hat{c}_j^\dagger \hat{c}_k \hat{c}_l, \tag{5.49}$$

where t_{ij} is a single-body hopping term, U_{ijkl} is a two-body interaction strength, and $\hat{c}_i(\hat{c}_i^\dagger)$ is a fermionic annihilation (creation) operator for mode i. [13] The Jordan-Wigner transformation changes this Hamiltonian to the form

$$\hat{H} = \sum_r a_r \mathbf{S}_r \tag{5.50}$$

---

[13]this can be in a real-space or a momentum-space basis, which we leave unspecified for the sake of generality.
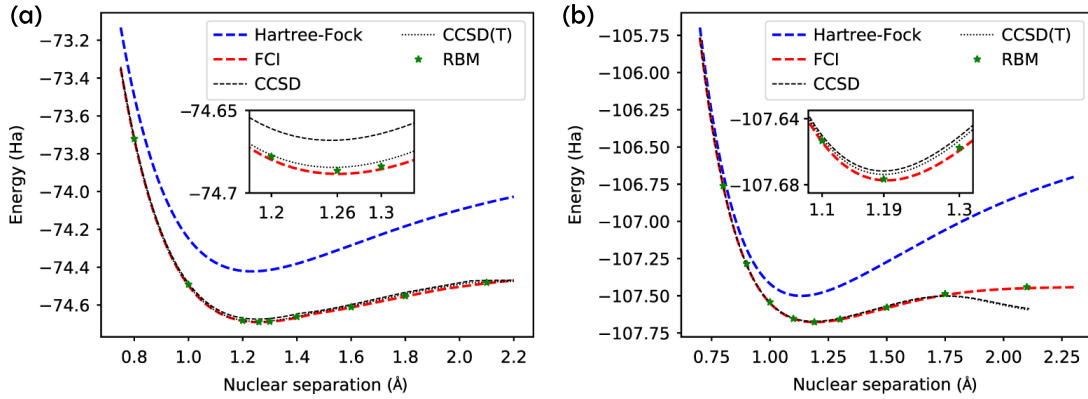
Figure 5.8: Ground state energies of (a) C_2 and (b) N_2 molecules as a function of nuclear separation, given by various techniques compared with results for an RBM ansatz with $M = 40$ hidden units. CCSD(T): coupled-cluster approaches, FCI: full-configuration interaction. Taken from [197].

with a_r some coefficients and $\mathbf{S}_r$ Pauli strings formed of compositions of elements of the set of single-qubit operators $\{\mathbb{1}, \hat{\sigma}^x, \hat{\sigma}^y, \hat{\sigma}^z\}$. In other words, we now have an interacting spin problem and, while the resulting Hamiltonian is not necessarily $k-$local, it can be shown that the computation of the local energy estimator is still efficiently realized. These mappings are therefore amenable to variational searches based of the ground states based on NQS.

In fig. 5.8, we show the dissociation curves (ground state energies) as a function of the nuclear separation for molecules of C_2 and N_2 provided by various numerical methods. By using an RBM ansatz and a simple Jordan-Wigner transformation, one is able to recover results that are competitive with recent full-configuration interaction results, which demonstrates the versatility and power of NQS. Finally, we mention that since the introduction of NQS, there has been a large number of different architectures proposed for quantum chemistry, that construct antisymmetric wave functions explicitly [246, 247].

5.3.5 Classical simulation of quantum circuits

Another promising direction for NQS is the classical simulation of quantum circuits. Indeed, current classical simulation methods for large quantum circuits (of the order of at least 50 qubits) rely on TN methods that are explicitly restricted by entanglement. In particular, TNSs cannot capture volume-law entanglement scaling, which quickly arises in quantum circuits, whereas certain NQS architectures such as deep CNNs can [220]. In this context, NQSs can be investigated in two somewhat orthogonal directions: one could use quantum circuits to probe the limits of their capacity and trainability, and NQSs can be used to push the classical simulation limits of quantum hardware.

Let us consider a quantum circuit defined by a set of D gates $\mathcal{G} = \{\hat{G}_i\}_{i=1}^{D}$, each gate being defined by a unitary operator $\hat{G}_i$. After each gate, the variational state must be updated so as to capture the application of the previous gate. The following variational distance must therefore be minimized, for each gate:

$$\mathcal{L}(\tilde{\boldsymbol{\theta}}) = \text{dist}\left(|\Psi_{\tilde{\boldsymbol{\theta}}}\rangle, \hat{G}_i|\Psi_{\boldsymbol{\theta}}\rangle\right), \tag{5.51}$$

with $\tilde{\boldsymbol{\theta}}$ the parameters to be optimized, $\boldsymbol{\theta}$ the parameters of the previous variational state, and $\hat{G}_i$ the unitary operator corresponding to gate G (for instance, for a NOT gate, $\hat{G}_i = \hat{\sigma}^x$). One can apply this procedure for each gate G and obtain the output state at the end of a circuit, after D optimizations. Note that $\hat{G}_i$ must be a $k-$local gate, or else the minimization procedure

cannot be carried out (this is reminiscent of ground state search). This is rarely a problem, since universal gate sets can be constructed with only single- and two-qubit gates. With this condition, minimizing eq. (5.51) resembles closely the ground state optimization. One can develop this expression using the infidelity, see eq. (5.38)], and obtain:

$$\mathcal{L}(\tilde{\boldsymbol{\theta}}) = 1 - \langle G_{\text{loc}}(\boldsymbol{\theta}, \tilde{\boldsymbol{\theta}}) \rangle_{|\Psi_{\tilde{\boldsymbol{\theta}}}|^2} \langle G_{\text{loc}}(\tilde{\boldsymbol{\theta}}, \boldsymbol{\theta}) \rangle_{|\Psi_{\boldsymbol{\theta}}|^2} \tag{5.52}$$

$$\text{with } G_{\text{loc}}(\boldsymbol{\theta}, \tilde{\boldsymbol{\theta}})(s) = \sum_{s'} \frac{\langle s | \hat{G}_i | s' \rangle}{\Psi_{\tilde{\boldsymbol{\theta}}}(s)} \Psi_{\boldsymbol{\theta}}(s'), \tag{5.53}$$

where we have defined G_{loc} as a local estimator, similarly to the procedure desribed for ground state search. As often in ML, the minimization of $\mathcal{L}(\tilde{\boldsymbol{\theta}})$ may be inaccurate, which reduces the overall fidelity of the simulation. Using an RBM architecture, however not all gates need to be approximated through minimization of the loss above. Some gates can be applied "analytically", i.e., it is possible to find the exact update on the parameters of the network so as to match the applied gate. In general, it is not possible to realize these exact updates for all gates of a universal gate set, or else one could simulate any quantum circuit with an RBM with infinite precision by obtaining the exact parameter update for each gate. For example, let us consider a Z gate acting on spin s_j defined by the operator $\hat{G} = \hat{\sigma}_j^z$. The action of such an operator on a basis state $|s\rangle$ is simply $\hat{G}|s\rangle = (-1)^{s_j}|s\rangle$. The RBM parameters before the gate are defined as $\boldsymbol{\theta} = (\boldsymbol{b}_v, \boldsymbol{b}_h, \boldsymbol{W})$ and the parameters after the gate are defined as $\tilde{\boldsymbol{\theta}} = (\tilde{\boldsymbol{b}}_v, \tilde{\boldsymbol{b}}_h, \tilde{\boldsymbol{W}})$. The parameter update is given by the solution of the following equation (with C a constant):

$$\Psi_{\tilde{\boldsymbol{\theta}}}(s) = C \langle s | \hat{G} | \Psi_{\boldsymbol{\theta}} \rangle \tag{5.54}$$

$$e^{\tilde{b}_{v,j} s_j} = C(-1)^{s_j} e^{b_{v,j} s_j}, \tag{5.55}$$

which is simply $\tilde{b}_{v,j} = b_{v,j} + i\pi$ for $C = 1$. The simplification in the previous equation is due to the fact that this gate acts trivially on the other parts of the RBM amplitude, defined in section 5.2.1. Details of how to apply other gates analytically can be found in Ref. [248] and [249]. In this last reference, authors classically simulate the circuit corresponding to the quantum approximate optimization algorithms (QAOA) using an RBM ansatz. This quantum algorithm enables one to access the solution of a certain class of combinatorial optimization problems. The corresponding circuit, which is quite shallow, can be implemented on current hardware [250]. In fig. 5.9, one can see that the results obtained by simulating the quantum circuit with the RBM ansatz closely matches the result of the exact simulation, enabling one to find the solution of the optimization problem for large systems. Authors also estimate a significant advantage over TN methods.[14] Indeed, in the left panel of fig. 5.9, one can see that the required bond dimension required to reach the same results to that of the RBM would quickly become dauntingly large when using an MPS.

Alternatively, authors of Ref. [251] have proposed to simulate quantum circuits using a transformer architecture. A transformer is a deep learning model that adopts the mechanism of self-attention, differentially weighting the significance of each part of the input data [252]. Using this framework, a practical algorithm to simulate quantum circuits using a transformer ansatz responsible for the most recent breakthroughs in natural language processing was introduced in Ref. [251]. This framework allows for the simulation of circuits that build Greenberger-Horne-Zeilinger and linear graph states of up to 60 qubits.

5.3.6 Open quantum systems

The idea of using NNs to represent quantum states was also applied to open quantum systems. An open quantum system is a physical system that interacts with an environment, for example

---

[14]Based on an extrapolation of numerical simulation data.
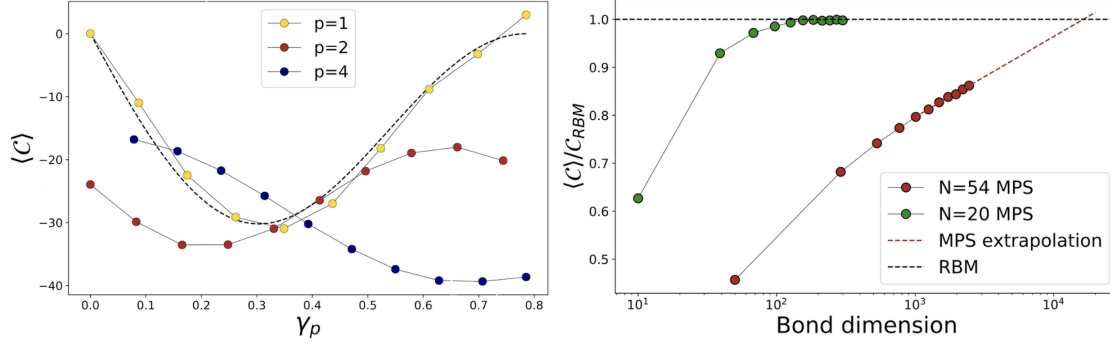
Figure 5.9: Results for the classical simulation of QAOA for a 3-planar graph. The left panel shows $\langle\mathcal{C}\rangle$, the approximated cost function for various values of p, the depth of the quantum circuit. The dashed line corresponds to the exact simulation of the $p = 1$ quantum circuit which the RBM simulation accurately reproduces for this task. Right panel: Estimation of the required bond dimension in a Matrix Product State (MPS) simulation of the QAOA circuit to match the accuracy of the RBM. For $N = 54$ qubits, the required bond dimension is of about 10^4, which amounts to using billions of parameters, whereas the RBM uses a few hundred. Taken from [249].

an array of atoms interacting with an electromagnetic field. Rather than describing the full system+environment ensemble, one is generally only interested in properties of the system (in the example above, the atoms) and one only keeps an effective description of its interaction with the environment (the field). This description enables one to understand effects such as decoherence. In the Born-Markov approximation, the time evolution of an open quantum system is given by the Lindblad master equation [253]

$$\partial_t \hat{\rho} = -\mathrm{i}[\hat{H}, \hat{\rho}] + \sum_{i=1}^{D}\big(\hat{J}_i \hat{\rho} \hat{J}_i^\dagger - \frac{1}{2}\{\hat{J}_i^\dagger \hat{J}_i, \hat{\rho}\}\big) \equiv \mathbf{L}[\hat{\rho}], \tag{5.56}$$

where $\hat{\rho}$ is the system density operator, $\hat{H}$ is the system Hamiltonian ($\hbar = 1$), and $\hat{J}_i$ are so-called jump operators, that describe the system-environment interaction. We have also defined $\mathbf{L}$, the Liouvillian, which is to open quantum systems what the Hamiltonian is to closed quantum systems (up to an i) – their time evolution generator. Many works focus on finding the steady state that corresponds to the state $\hat{\rho}$ which satisfies $\mathbf{L}[\hat{\rho}] = 0$, or the dynamics of particular systems, which means one must in general integrate eq. (5.56) in time, analogously to non-equilibrium dynamics of closed systems. A first difficulty one faces is finding a correct representation for $\hat{\rho}$ in terms of an NN. Indeed, a density matrix is harder to represent than a wave function, because it has to be Hermitian, semi-positive, and of trace one. In fact, a general method to encode a density matrix into arbitrary NNs has still not been found. The key point of these works is that one can always purify a density matrix, and write its elements as

$$\langle s|\hat{\rho}|s'\rangle = \sum_{s'} \Psi(s,s')\Psi^*(s,s'), \tag{5.57}$$

with $\Psi(s,s')$ the purification that belongs to the joint Hilbert space composed of the system and an imaginary ancilla (whose Hilbert space is of at least the same dimension as the system's Hilbert space). With an RBM architecture, one can encode the purification $\Psi_\theta(s,s')$ with an NN, and the RBM architecture enables one to analytically trace out the ancilla spins s' without explicitly performing the summation which in general requires exponentially many operations. For more details, see [254–257] and references therein.
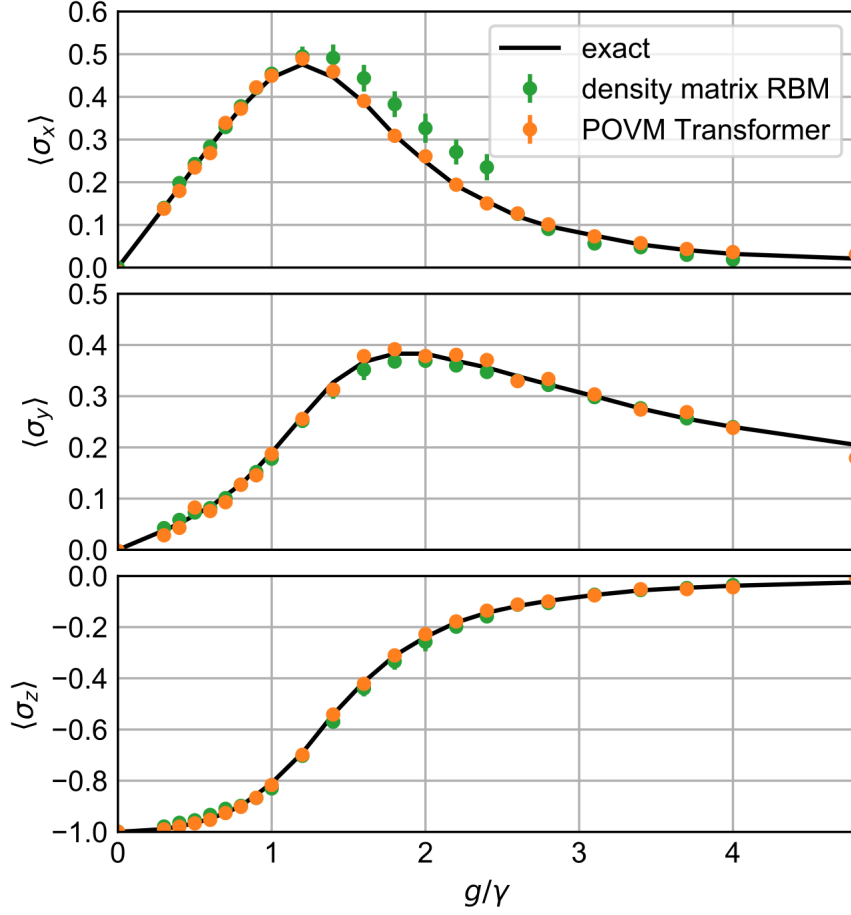
Figure 5.10: Expectation values of observables $\hat{\sigma}_k = 1/N \sum_i \hat{\sigma}_i^k$, $k \in \{x, y, z\}$ at the steady state of the open system described by the transverse-field Ising Hamiltonian and jump operators $\hat{J}_i = \sqrt{\gamma} \hat{\sigma}_i^-$ as a function of g/γ, with g the magnetic field strength. Results are shown for both the purified RBM approach and the POVM approach with a Transformer network. Taken from [258].

A second more recent approach proposes to view the density matrix as a probability distribution over positive operator-valued measures (POVMs), and represent the resulting distribution using models employed in general density estimation, such as RNNs and ARNNs. In this formalism, the density matrix is simply written as:

$$\hat{\rho}_{\boldsymbol{\theta}} = \sum_a p_{\boldsymbol{\theta}}(a) \hat{M}_a, \tag{5.58}$$

with $\hat{M}_a$ POVMs that belong to a chosen complete set of POVMs. This could, for example, be all the operators composed as tensor products of the Pauli operators and the identity. In this picture, one simply needs to encode the probability distribution $p_{\boldsymbol{\theta}}(a)$ with an NN. This POVM-based representation is motivated by the fact that the density matrix can be viewed as an ensemble of 4^N measurements, which is naively how experimentally one performs tomography to reconstruct the density matrix. This method alleviates the constraint on using an RBM for open systems, but does not guarantee positivity of the density matrix, which can lead to unphysical states. However, a certain number of results using the POVMs encoding are promising [258, 259], and understanding in which regime they work best is a key research direction.

Finding the steady-state(s) of open quantum systems is both challenging, due to the daunting size of the Liouvillian one would need to diagonalize (4^N for a spin system of N spins), and interesting, for example, for the study of dissipative phase transitions [260]. Once a parametrization $\hat{\rho}_{\boldsymbol{\theta}}$ of the density matrix is constructed, one can simply minimize the following cost function:

$$\mathcal{L}(\boldsymbol{\theta}) = \langle \hat{\rho}_{\boldsymbol{\theta}} \mathbf{L}^{\dagger} \mathbf{L} \hat{\rho}_{\boldsymbol{\theta}} \rangle. \tag{5.59}$$

The obtained state corresponds to the zero eigenvalue is zero of the Liouvillian, which is the steady-state. For details about the procedure and how to retrieve the gradients, see [254–257]. As one can see in fig. 5.10, this method has been applied to the dissipative version of the transverse-field Ising model, with good results for both a POVM approach and an RBM approach. In the former case, the expressive power of the network is higher, but the positivity of the density matrix is not enforced. A clear picture of when each approach fails or succeeds is still lacking, and is an important research direction. The dynamics of open quantum systems is not described in detail here, but stochastic reconfiguration can also be used for open systems in both the RBM [257] and POVM [259] approaches.

5.3.7 Quantum tomography

Reconstructing a quantum state from measurement data is a challenging task, as one is faced with an exponentially large number of snapshots in the system size to obtain a faithful reconstruction.

> Quantum tomography is the task of reconstructing a quantum state from measurement data. Fully reconstructing a state is tedious as it requires an exponential number of measurements in the system size. This is a major problem for experimentalists who want to demonstrate quantum effects and protocols. Neural networks can once again help in this task, and they have been successfully applied to reconstruct non-trivial quantum states from a polynomial number of measurements.

Let us consider the task of reconstructing a wave function $|\psi\rangle$ from a limited number of snapshots $|\psi(s)|^2$ obtained by performing projective measurements in some basis spanned by $|s\rangle = |s_1, s_2, \ldots, s_N\rangle$, with s_i some local quantum numbers and N the size of the system. Then, the task, in the NQS language, is simply to minimize:

$$\min_{\boldsymbol{\theta}} \operatorname{dist}\left(|\psi_{\boldsymbol{\theta}}\rangle, |\psi\rangle\right) \tag{5.60}$$

with $\boldsymbol{\theta}$ being some variational parameters, and $|\psi_{\boldsymbol{\theta}}\rangle$ the variational state to optimize, parametrized by a neural network. The architecture of this network is left unspecified here, and all architectures work provided training can be performed efficiently. Many distances can be considered, but we here focus on the Kullback-Leibler (KL) divergence (see section 2.3) as was first presented in the work by Torlai *et al.* [261]. It is defined as:

$$D_{\mathrm{KL}}(p||q) = \sum_{x \in \mathcal{P}} p(x) \frac{\log p(x)}{\log q(x)} \tag{5.61}$$

for two probability distributions p and q, defined on the same space $\mathcal{P}$. The application to quantum states is straightforward, as one can obtain probability distributions from the Born rule, i.e., $p_{\boldsymbol{\theta}}(s) = |\psi_{\boldsymbol{\theta}}(s)|^2$, $q(s) = |\psi(s)|^2$. By taking x to be configurations s in some set S of snapshots, one can simply minimize:

$$D_{\mathrm{KL}}(\boldsymbol{\theta}) = \sum_{s \in S} |\psi_{\boldsymbol{\theta}}(s)|^2 \frac{\log |\psi_{\boldsymbol{\theta}}(s)|^2}{\log |\psi(s)|^2} \tag{5.62}$$

which concludes one possible approach.

However, recall that a quantum state is not simply a probability distribution. A probability distribution can *always* be defined from a quantum state, but *not the reverse*. More explicitly, we want to reconstruct the full quantum state whose amplitudes are $\psi(s) = \sqrt{Q(s)}e^{i\phi(s)}$. By minimizing eq. (5.62), *information about the phase, $\phi(s)$, is lost.* This difference is crucial and is at the heart of many issues in learning quantum states. As mentioned in chapter 5, learning the phase of a frustrated quantum state is challenging [262]. The elegant solution to this issue is to *consider measurements performed in different bases*. Indeed, the form of the quantum state in a different basis involves the interference between amplitudes in different bases. Hence, matching the probability distribution defined by snapshots in different measurement bases leads to the correct quantum state as long as the bases contain enough information about the quantum state. Mathematically, one can simply replace eq. (5.62) by:

$$\mathrm{D_{KL}}(\boldsymbol{\theta}) = \sum_B \sum_{s \in S_B} |\psi_{\boldsymbol{\theta}}^B(s)|^2 \frac{\log |\psi_{\boldsymbol{\theta}}^B(s)|^2}{\log |\psi^B(s)|^2} \tag{5.63}$$

where S_B is the set of snapshots of the quantum state in basis B, and $\psi^B(s) = \langle s| \hat{U}_B |\psi\rangle$ with $\hat{U}_B$ a unitary operator. Then, gradients are found as usual, either with automatic differentiation or analytically with simple models such as RBMs.

In fig. 5.11, various observables are shown for a synthetic state and a reconstructed state. The synthetic state approximates the ground state of the Heisenberg model in a triangular lattice, that authors of the corresponding work generated with tensor network simulations [81]. The reconstructed state was reconstructed employing ideas presented in this section with an RNN architecture (for more details, see the introduction or chapter 5 and section 7.2), using a POVM representation of quantum states (for more details, see section 5.3.6). Note that the approach has been extended to reconstructing mixed states [263], although supplemental care must be taken to avoid issues linked to positivity of the reconstructed density matrix, similarly to what was presented in the above.

Experimentally, one can implement this strategy by applying rotations with, for instance, laser pulses, and then measure the system repeatedly. In Ref. [264], authors demonstrate the first state reconstruction from experimental data from a programmable array of Rb atoms, using an RBM architecture. Here snapshots of the wave function in the $\hat{\sigma}^z$ basis are obtained through site-resolved fluorescence imaging. A challenge that arises when using real data is that noise is introduced, which stems from measurement errors, leading to a set of snapshots $|\psi(s)|^2$ that imperfectly match the state of the system. This is taken care of in this work by adding a noise layer to the neural network, with which the snapshots are transformed in order to filter out the noise during training. At the expense of increasing the total number of parameters in the network, this is a quick and easy strategy to deal with experimental noise, that has enabled high fidelity state reconstruction. The underlying principle behind these approaches is that with a polynomial number of bases B and a polynomial number of snapshots, one should be able to reconstruct states belonging to a certain class (not fully random states, for instance, which contain almost no structure). As underlined previously, this class is not exactly known, and is the subject of current research. To draw an analogy with images, images are not fully random; they contain a lot of hidden structure, that can be learned by a properly designed and trained neural network. The hope is that the same is true for quantum states, and investigating the limits of such techniques could also help us understand in more detail their hidden structure, beyond what has been found with entanglement properties through the study of TNs. As a final consideration, let us mention that in recent years there has been a significant number of results that show that one can in fact predict selected properties of
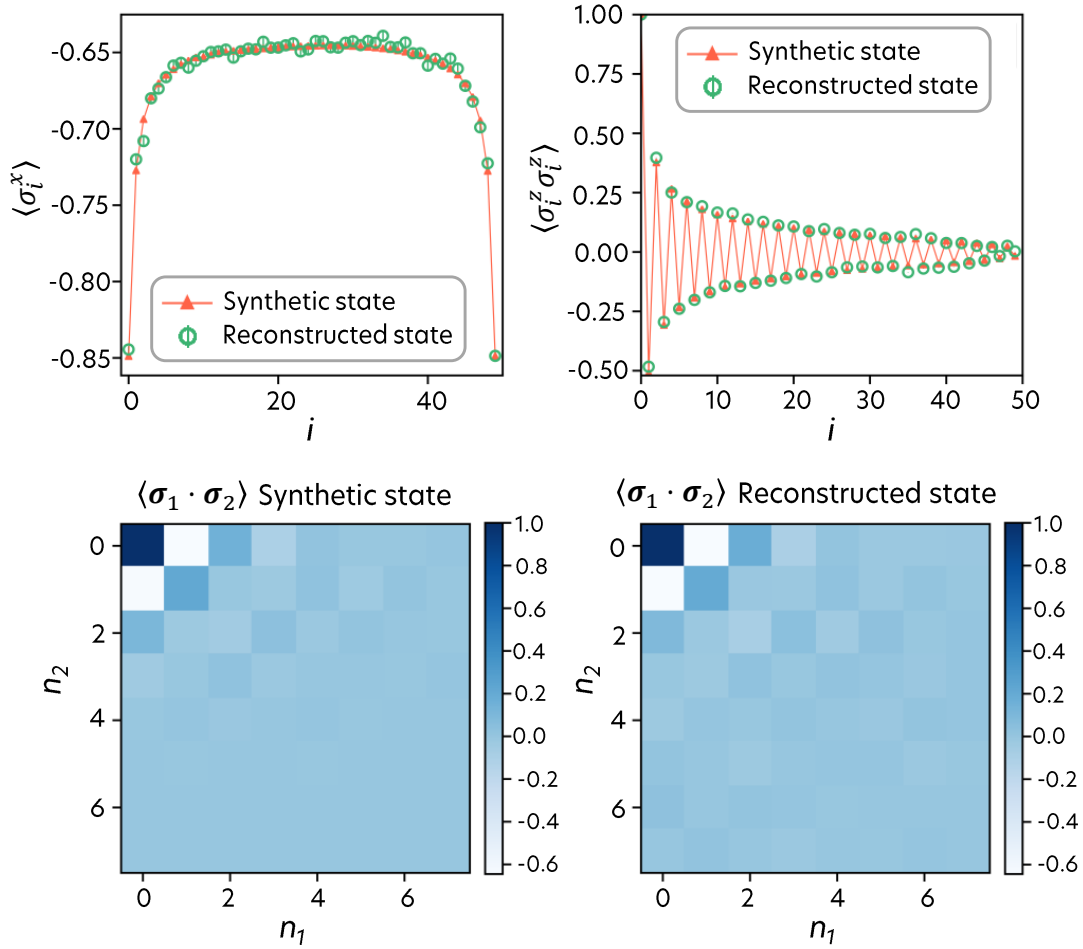
Figure 5.11: Various observables corresponding to the ground state of the Heisenberg model on a triangular lattice with $N = 50$ spins. (a) Average magnetization along x for each spins i. (b) Spin-spin correlation function between the spin at site 1 with spins at site i. (c) and (d) Average spin-spin correlation between the first and the i-th spin. One can see that all observables are reproduced with a very high precision. Adapted from Ref. [81].

complex quantum systems without reconstructing the full quantum state. This field has been coined under the name of "shadow tomography" (see [190, 265]) and is very active. The price to be paid in these methods however is that the number of required measurements typically scales exponentially with the locality of the operator averages to be reconstructed, albeit with a runtime that is typically better than the naive direct measurement of the observables from data. In contrast to these approaches, in this section we have instead considered the task of training a low-dimensional representation of the full wave function from a limited number of measurements.

5.4   Outlook and open problems

We hope to have provided enough material to stimulate further research in the growing field of NQSs. Here is a non-exhaustive list of open problems and challenges related to the above discussion:

- **Capacity of NQS**. Some works have proven the capability of NQSs to represent volume-law entanglement, which means they could outperform TNSs for strongly correlated and two- and three-dimensional systems [211,220,221]. Others have proven the equivalence of RBMs with matrix-product states, meaning that the former cannot represent more states than the latter [212]. Even though general theorems have been found, knowledge about specific architectures is still rare, and understanding which architectures perform better on which problems is a crucial point. In addition, proving representativity does not mean that the models can be efficiently trained, thus understanding how the training of NQS models works is key.

- **Long-time dynamics**. To this day, no method has proven to show stable long time dynamics for NQSs [238]. However, progress has been made thanks to regularization techniques [217]. A recent work has proposed to use an implicit method [237], enabling one to go beyond stochastic reconfiguration. However, ample results on large lattices are still lacking for such an approach .

- **Open quantum systems**. No general method of encoding a density matrix into an arbitrary neural network has been found yet; one is either forced to use an RBM, which has known limitations, or one can use a POVM approach, which may fail due to non-positive density matrices.

- **Frustrated systems**. Finding the ground state of frustrated systems with an NQS approach has proved to be challenging [262], and understanding exactly how one can improve the optimization of the procedure to learn the phase (which has a nontrivial sign structure) is of particular interest.

- **Simulation of quantum circuits**. Few results have been obtained with networks other than RBMs, and investigating how different circuits affect the accuracy of the chosen ansatz can lead to results in two ways: understanding the complexity of a given circuit and the limitations of the chosen ansatz.

- **Quantum tomography.** Quantum state tomography based on neural networks is still in its beginnings. So far, it has only been explored numerically on toy models and small experimental settings where traditional quantum state tomography is still feasible. It is likely that its real benefits may emerge in the context of estimation of difficult quantities in quantum simulation. In this setting, the complexity of estimation arises because even simple quantities such as the energy and other correlation functions can have high variance. This implies that some of these quantities have a sample complexity which can grow quickly with the size of the system.

- **Extension to continuous Hilbert spaces and bosonic systems.** For now most techniques and works have focused on systems with discrete degrees of freedom (such as spins). Extensions to continuous Hilbert spaces have been only recently directly addressed, for example in the context of quantum chemistry [246, 266] and nuclear matter [267]. Efficient encodings for bosonic Hilbert spaces would also be of particular interest for photonic systems, for example, that are usually treated with mean-field-like approaches.

Further reading

- Carleo, G. & Troyer, M. (2017). *Solving the quantum many-body problem with artificial neural networks*. The original paper by Carleo and Troyer that introduced NQS [196].

- Becca F. and Sorella, S. (2017). *Quantum Monte Carlo Approaches for Correlated Systems*. A comprehensive book that includes details on quantum Monte-Carlo methods, and variational states [240].

- Vicentini, F. *et al.* (2021). *NetKet 3: Machine learning toolbox for many-body quantum systems*. The paper accompanying the open-source library NetKet 3, which contains an extensive discussion of how to implement several algorithms introduced in this chapter, as well as a collection of tutorials showing how to solve some benchmark problems with NQS [234, 268].

- Carrasquilla, J. & Torlai, G. (2021). *How to use neural networks to investigate quantum many-body physics*. A recent tutorial by Carrasquilla and Torlai that includes interesting applications and code snippets can help anyone who wants to start in the field [269].

- Carleo, G. (2017). Repository for example codes presented at the "Machine Learning and Many-Body Physics" workshop. Notes, exercises, and code produced for the 2017 Beijing workshop on Machine Learning and Many-Body Physics [270].

6   Reinforcement learning

So far, we have encountered multiple ML scenarios featuring supervised or unsupervised learning problems where we want to infer some labels, predict certain values, or find patterns in the data. In this chapter, we describe a different approach: *learning strategies*.

In the supervised learning framework, we can think of a student that learns from a teacher who knows the correct answers to all possible questions within a given domain. In this scheme, the student is limited by the knowledge of their teacher and can never surpass it or address questions outside the teacher's expertise. To overcome this limitation, in reinforcement learning (RL), we get rid of the teacher and let the student try things out and learn from the resulting experience. Just like us, humans, the student learns from the interaction with an environment, understands the consequences of its actions, and finds strategies to achieve particular goals. In RL, we refer to the student as the *agent*, as it can interact with its environment.

For instance, let us consider the case in which we teach an agent to play chess. A supervised learning approach would consist of training a ML model to reproduce the moves from recorded chess games from the best players in the world. In this setting, given a state of the game, i.e., the position of the remaining pieces on the chessboard, the model predicts the move such as reference players would do. However, this approach suffers from some major shortcomings. For example, there is no single optimal move for every situation, and they strongly depend on the game strategy taken by the players. As a result, the agent may be unable to consistently execute a strategy through various actions. Additionally, the agent's performance is ultimately limited by the quality of the training data, meaning that it may be impossible to outperform the reference players. We refer to section 6.6.2 for a related example.

Instead, we can let the agent play chess games, either against various opponents or even against itself, without providing any additional knowledge besides the rules. In that case, it develops its own understanding of the game and devise its own strategies. The resulting agent's potential is far superior to the previous one, as it is not limited by its teacher. Nevertheless, learning from experience may be challenging, provided that the quality of the actions is only assessed at the very end of the game when the outcome is decided: victory or loss.[1] Hence, the agent must develop a deep understanding of the long-term consequences of the actions from sparse environment feedback.

In this chapter, we introduce the field of RL. We start with an intuitive view on the concept of learning from experience and its mathematical foundations in section 6.1. Then, we present two main approaches: value-based RL in section 6.2, and policy gradient in section 6.3. In section 6.4, we combine the two paradigms, introducing actor-critic algorithms. Then, we provide an alternative approach to RL, projective simulation, in section 6.5. Finally, we present a series of application examples of RL in section 6.6, featuring superhuman performance in games as well as various problems in quantum technologies.

6.1   Foundations of reinforcement learning

The general setting of any RL problem consist of two main elements: an *agent*, and an *environment* that it interacts with, as illustrated in fig. 6.1. The environment contains all the information defining the problem at hand, e.g., the rules of a game, and it provides the agent with observations and feedback according to its *actions*. The environment defines the set of

---

[1]In some cases, we may be tempted to add intermediate rewards, such as a bonus for taking out a piece from the opponent. However, in doing so we effectively change the game and its goal and, as a consequence, we might fail to find the optimal strategy of the original problem.

all possible *states*, $s \in \mathcal{S}$, which can range from an empty set, in the case of a stateless environment (see the first example in section 6.6.1), to a multi-dimensional continuous space. For example, these could be all the possible configurations of a board game or all the possible combinations of joint angles in a robot.

The agent can observe (sometimes only partially) the state s of the environment, and it can choose an action a to perform, which may include the possibility to remain idle. The action is chosen from the set of possible actions, $a \in \mathcal{A}$, which is defined by the environment and can be state-dependent. For instance, the action of pushing forward a pawn in chess is only possible if there is a free position in front of it. The actions may alter the state in which the environment is found, and they can have deterministic or stochastic outcomes. In the chess example, all the actions are deterministic. In contrast, in the case of a walking robot, the action to move forward may have different results: it can succeed in doing so, the robot may trip, or it may even remain idle with a certain probability due to a hurdle or malfunctioning. This information is encoded in the environment, and the agent may not have access to it.

Nevertheless, every time the agent performs an action, the environment provides it with an observation of the new state together with a feedback signal called *reward*, r. The reward can take any numerical value. It may depend on the previous state, the new state, and the action that was taken. The main purpose of the agent is to maximize the obtained rewards by the end of the task, and it is, therefore, the quantity that defines the objective task. Hence, the agent obtains higher rewards when accomplishing the objective task or progressing toward the goal, e.g., winning a game, while it might receive penalties when performing harmful or bad actions, e.g., losing a game.

> The central objective of any RL problem is to learn the *optimal policy*, π^*, that maximizes the obtained rewards. A policy, π, dictates which actions to take given the observations, and thereby defines the strategy followed by the agent.

In general, the policy can take any form, as we show in forthcoming sections. For example, it can be a table assigning the best possible action to every possible state or a ML model that, given a state, provides a probability distribution over all the possible actions. However, the learned policy is specific to the problem. We summarize the introduced key elements of the RL setting in fig. 6.1.

Let us provide some insight on the main elements of the RL setting with a couple of examples. In the case of the chess game from chapter 6, the agent is one of the players. The environment models the rules of the game, the opponent,[2] and its states, that correspond to the piece positions on the board.[3] The state space contains all the possible board configurations that can be reached within a game, e.g., excluding those where one of the kings is missing. The action space corresponds to all the possible legal moves that can be made every turn. In this case, the agent does not obtain rewards until the game is resolved. At this point, the agent receives a positive or negative reward upon victory or defeat, respectively. In case of a draw, the final reward could be zero or even negative. The goal is to learn the policy that yields the highest possible number of victories.

---

[2]The opponent could be the same agent, which would play against itself, but each agent would perceive the other as part of their respective environment. This is known as *self-play*, and it helps exploring new strategies faster.

[3]The state for chess can also contain extra information, such as whether castling is still possible. For the purpose of this example, and to keep it simpler, we restrict ourselves only to the piece positions here
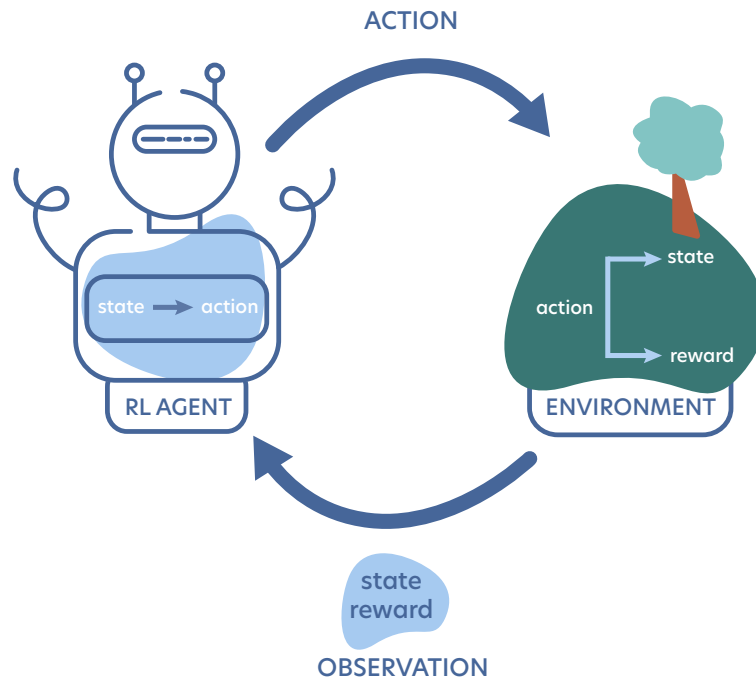
Figure 6.1: Overview of the basic RL setting. The agent receives an observation from the environment. Given the observation, it chooses the next action according to its policy. The environment determines the outcome of the action, and it returns an observation to the agent consisting of the new state and a potential reward.

As a second example, we consider a robot trapped in a maze. The robot can only see its immediate surroundings and has to maneuver to reach a target location. In this case, the agent is the robot, and the environment models the maze, its walls, and the target location. The state is the current position of the agent plus its immediate surroundings, and the state space comprises all the reachable locations. The action space contains the moves in all possible directions, and the environment ensures that the agent does not cross the walls. Hence, moving into a wall would leave the agent in the same position and, therefore, would not modify the state. As a reward, we can provide the agent with a constant negative reward after every move in order to encourage it to take the least amount of steps toward the goal.

6.1.1 Delayed rewards

As we have previously introduced, the reward r is a key concept in RL. The agent learns to maximize the reward and, therefore, it is the quantity that defines the problem. At a given discrete time t, the agent observes a state s_t and performs an action a_t according to its policy. Then, the environment presents the agent with a new state s_{t+1} and a reward r_{t+1}. Hence, r is time-dependent and it may depend on any of the other three quantities $r_t = r(s_{t-1}, a_{t-1}, s_t)$ (see section 6.1.3 for further details).

So far, we have briefly talked about maximizing the rewards. In order to formalize the RL objective, we need to introduce the notion of *delayed rewards*. They introduce the idea of "looking ahead" to the agent, allowing it to account for the future rewards obtained along a trajectory through the state space. However, we can penalize the rewards that are far into
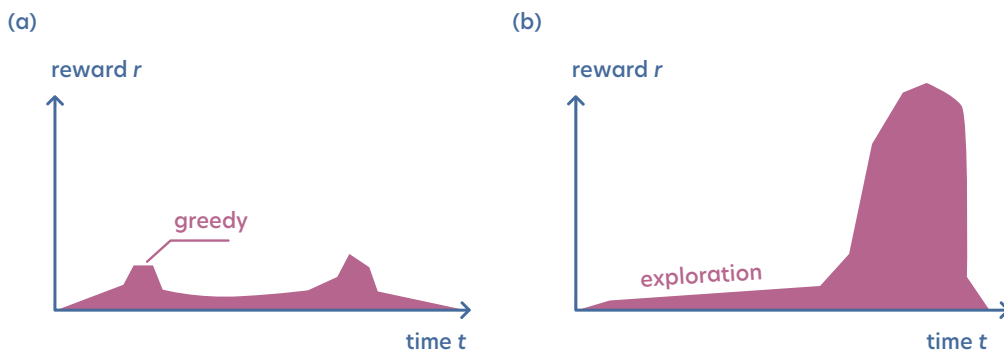
Figure 6.2: Impact of the discount factor, γ, in RL algorithms. (a) A myopic algorithm ($\gamma \to 0$) may settle for a greedy policy that leads to early immediate rewards, even if they are smaller than possible latter ones. (b) However, a long-term oriented algorithm ($\gamma \to 1$) might sacrifice early rewards in favor of larger late ones.

the future with a discount factor $\gamma \in [0, 1]$.

> The discount factor weights the rewards according to their temporal separation. This way, immediate rewards have larger weights than those that are far into the future. The RL objective is to maximize the *discounted return*, defined as the weighted sum of future rewards
>
> $$G_t = \sum_{k=0}^{T-t-1} \gamma^k r_{t+k+1}, \tag{6.1}$$
>
> which accounts for the rewards obtained starting at time t until the final time T.[a]
>
> ---
> [a]In RL, we typically consider finite trajectories. However, a discount factor $0 \le \gamma < 1$ allows us to consider infinite trajectories $T = \infty$ with finite returns.

Notice that the return presents a recursive form that is essential for many RL algorithms

$$G_t = r_{t+1} + \gamma G_{t+1}. \tag{6.2}$$

This concept draws inspiration from human psychology, and it mimics our daily observation that far-term rewards, even if high, are less desired than near-term ones, e.g., we favor procrastinating instead of reading this article. We can distinguish two limits: for a small discount factor, $\gamma \to 0$, the return becomes myopic, i.e., immediate rewards predominate over any other possible future ones. On the other hand, large discount factors, $\gamma \to 1$, result in equal weights for early and late rewards, which encourage long-term oriented strategies. This includes, in particular, the deliberate choice to perform a few seemingly sub-optimal choices in the beginning that, however, result in a far greater final return. We depict the two cases in fig. 6.2.

Hence, the discount factor strongly affects the resulting policy. In fact, it defines the RL task, as the agent aims to maximize the return, introduced in eq. (6.1). Nevertheless, we often rely on trial-and-error methods to find the discount factor that best suits our needs.

6.1.2 Exploration and exploitation

In RL we encounter a trade-off between exploration and exploitation. In order to maximize the return, the agent must *exploit* its knowledge about good strategies. However, the agent must

explore other different actions in order to improve them, or even discover better strategies in the future.

However, a learning algorithm cannot rely on exploration alone, as it would be reduced to a brute-force search algorithm. Conversely, in a case of pure exploitation, the agent would blindly commit to the first working strategy that it found, even if it was highly sub-optimal. Hence, we need to find a balance between both regimes in which the agent can try several actions and progressively favor the best ones. This way, the exploration is conducted around the most promising areas of the state and action spaces, heavily reducing the amount of experience that the agent must gather in order to find the optimal policy.

A common strategy to balance exploration and exploitation is the so-called *ε-greedy policy*. In this case, the agent follows its policy to perform actions (exploits), and it may take a random action (explores) with probability $\varepsilon \in [0,1]$ at any point. This approach encompasses both paradigms: for $\varepsilon = 1$, we have full exploration, whereas we have full exploitation for $\varepsilon = 0$. By tuning ε, we interpolate between both regimes. A common practice is to start with high ε, to enforce early exploration, and decrease it during the training process.

6.1.3 Markov decision process

All RL problems are modeled by the same underlying mathematical structure: Markov decision processes (MDPs). They constitute a general framework to model environments in which there exists a notion of sequentiality between states. In such environments, the future is independent of the past given the present. This is known as the *Markov property*.

> In essence, the *Markov property* means that the current state is a sufficient statistic containing all the required information relevant to the possible evolution of the environment. In particular, we do not have any memory effects from previously visited states. Formally, at any time step t,
>
> $$p(s_{t+1}|s_0, \ldots, s_t) = p(s_{t+1}|s_t). \tag{6.3}$$

Mathematically, an MDP is a tuple $(\mathcal{S}, \mathcal{A}, p, G, \gamma)$, respectively denoting the state space $\mathcal{S}$, the action space $\mathcal{A}$, the *dynamics p*, the set of total returns G, and the discount factor γ. In this formalism, the return G, together with the discount factor γ, determines the objective, and p describes the dynamics of the environment,

$$p(s', r|s, a) = p(s_{t+1} = s', r_{t+1} = r|s_t = s, a_t = a), \tag{6.4}$$

which corresponds to the joint probability of observing a new state s' and obtaining a reward r by performing action a in state s. For fully deterministic environments, $p(s', r|s, a)$ is either zero or one.

From eq. (6.4) we can derive all the relevant information about the environment. For instance, *state-transition probabilities* are a central quantity in many RL algorithms:

$$p(s'|s, a) = \sum_r p(s', r|s, a). \tag{6.5}$$

Furthermore, it allows us to determine the reward functions. In section 6.1.1 we briefly introduce the reward function $r(s, a, s')$. In the most general form, the reward is jointly determined with the state s', as shown in eq. (6.4).[4] However, in many cases, we may need to consider

---

[4]In stochastic environments, the reward can be inherently sampled from a probability distribution. Consider

the expected rewards for state–action pairs and state–action–next-state triplets:

$$r(s,a) = \sum_r \sum_{s' \in \mathcal{S}} r p(s', r | s, a), \tag{6.6}$$

$$r(s,a,s') = \sum_r r \frac{p(s', r | s, a)}{p(s' | s, a)}. \tag{6.7}$$

In the iterative interaction between agent and environment, the agent chooses the actions according to a *policy*. The policy is a mapping from states to the probability of performing each possible action

$$\pi(a|s) = p(a_t = a \mid s_t = s). \tag{6.8}$$

In the limit of deterministic policies, $\pi(a|s)$ is one for a single action and zero for the rest.

The goal in RL is to modify the policy with the experience gathered from the interaction with the environment to achieve the goal. This interaction generates *trajectories* of the form

$$s_0, a_0, r_1, s_1, a_1, r_2, s_2, a_2, \ldots, s_T,$$

where all states, actions and rewards are random variables. This way, the agent performs a trajectory through the state-action space $\tau = a_0, s_1, a_1, \ldots, s_T$ with probability

$$p(\tau) = \prod_{t=0}^{T-1} p(s_{t+1}|s_t, a_t) \pi(a_t|s_t), \tag{6.9}$$

starting from an initial state s_0. We denote the discounted return associated to the trajectory as $G(\tau) = \sum_{t=0}^{T-1} \gamma^t r_{t+1}$.

This entire formalism holds assuming the Markov property from eq. (6.3), which implies that the environment is memory-less. However, we may encounter situations in which the environment has certain memory effects, such as games in which the execution of a sequence of actions yields an additional effect at the end. In these cases, we may recover the Markov property by considering an extended state space that already includes the memory. In return, this implies that even deterministic Markovian dynamics on the full state space can give rise to non-deterministic and non-Markovian dynamics on the smaller state space.[5]

6.1.4 Model-free vs. model-based reinforcement learning

We can distinguish between two main paradigms in RL: model-free and model-based RL. In the first setting, the agent does not have any kind of information about the underlying mechanisms of the environment and it must purely learn by trial and error. In the second one, the agent either has access to a *model of the environment* or it builds one from the gathered experience. Then, the agent can use this model in order to plan ahead, inferring the result of a sequence of actions before executing any of them, in order to choose the best possible ones.

Although we focus on model-free RL in the remainder of the chapter, we briefly elaborate on how to exploit the knowledge of a model. Building a model of the environment provides the agent with an enhanced understanding of the problem and can potentially help it face new situations. For example, in a case where an agent juggles a set of balls, if it has a good model

---

the game of blackjack: with the same hand (state) the action of settling may have different rewards depending on the opponent's hand (environment). Hence, the reward is stochastic.

[5]An analogous situation is encountered in the discussion of open quantum systems: non-unitary dynamics in the subsystems arise despite a global unitary evolution of the system and its bath.

of the laws of physics, it is much easier for it to learn to juggle a new set of balls with different shapes and weights.

These models can take various forms, but a general formulation are fully characterizable MDPs. This way, the model approximates the dynamics of the underlying MDP of the problem. In some situations, the true model is too complex to be grasped, and we may simply try to approximate the parts of the dynamics that are the most relevant for the problem. An example of a simple model would be a ML algorithm that predicts both the expected next state and the reward (s_{t+1}, r_{t+1}) given the current state and an action (s_t, a_t) at any time step t. Such a model allows us to predict the outcome of a series of future actions given the current state, and we can train it in a supervised way directly from the experience gathered by the agent.

In continuous-action spaces, the model provides a direct connection between the input action and the received reward, allowing us to employ backpropagation methods to maximize the return instead of mere sampling from the environment. See section 7.1 for examples that illustrate the process. In the case of discrete-state spaces, the model typically takes the form of a search tree that we can explore at our advantage. Models are especially convenient in situations where the interaction cost with the environment is very high, such as the realization of a physical or chemical experiment. In these cases, we try to augment our dataset of actual samples from the environment with artificial samples drawn from the model in order to minimize the total sampling costs.

However, we do not always have access to a model or it may not be in our interest to build one. Building models is costly, especially in cases where we have limited knowledge about the environment, and they are only helpful when they are accurate. Furthermore, models are often tailored to the specific problems. On the contrary, model-free RL algorithms come with the advantage that they are agnostic to the problem at hand and, thus, they are more versatile. Therefore, we focus on model-free RL for the rest of the chapter for pedagogical purposes, as they prove useful on the full range of RL tasks. In particular, we provide an introduction to policy-based and value-based RL in section 6.3 and section 6.2.1, respectively.

6.1.5 Value functions and Bellman equations

As we mention in the previous sections, the goal in RL is to find the optimal policy π^* that maximizes the return, introduced in eq. (6.1). Such a clear objective allows us to define *value functions* that estimate how convenient it is for the agent to be in a given state or to perform a certain action to accomplish the task. For instance, consider the case in which we are looking for a treasure on a map. Being one step away from the treasure is, overall, much better than being ten steps away. However, not all actions in the close position are equally good, provided that one leads to the treasure but the others move away from it. This is quantified by the expected future return that the agent may obtain given the current conditions. However, given that the future rewards strongly depend on the actions that the agent will take, value functions are defined with respect to the policy.

The *state-value function*, $V_\pi(s)$, of a state s under the policy π is the expected return when starting at state s and following the policy π thereafter. We formally define it as

$$V_\pi(s) = \mathbb{E}[G_t|s_t = s, \pi] = \mathbb{E}\left[\sum_{k=0}^{T-t-1} \gamma^k r_{t+k+1} \bigg| s_t = s, \pi\right] \tag{6.10}$$

In a similar way, the *action-value function*, $Q_\pi(s,a)$, is the expected return when starting at state s, performing action a, and then following the policy π:

$$Q_\pi(s,a) = \mathbb{E}[G_t|s_t = s, \ a_t = a, \pi] = \mathbb{E}\left[\sum_{k=0}^{T-t-1} \gamma^k r_{t+k+1} \bigg| s_t = s, a_t = a, \pi\right] \tag{6.11}$$

The *advantage*, $A_\pi(s,a)$, is the additional expected return obtained by following an action a at state s, over the expected policy behavior:

$$A_\pi(s,a) = Q_\pi(s,a) - V_\pi(s). \tag{6.12}$$

The value functions fulfill a recursive relationship that is exploited by many RL algorithms, which stems from the recursive nature of the return eq. (6.2). This allows us to write the state-value function $V_\pi(s)$ as a function of the next states

$$
\begin{aligned}
V_\pi(s) &= \mathbb{E}[G_t|s_t = s, \pi] = \mathbb{E}[r_{t+1} + \gamma G_{t+1}|s_t = s, \pi] \\
&= \sum_a \pi(a,s) \sum_{s',r} p(s',r|s,a)\left(r + \gamma \mathbb{E}[G_{t+1}|s_{t+1} = s', \pi]\right) \\
&= \sum_a \pi(a,s) \sum_{s',r} p(s',r|s,a)\left(r + \gamma V_\pi(s')\right) \\
&= \mathbb{E}[r_{t+1} + \gamma V_\pi(s_{t+1})|s_t = s, \pi].
\end{aligned} \tag{6.13}
$$

We can do the analogous derivation for the action-value function $Q_\pi(s,a)$

$$
\begin{aligned}
Q_\pi(s,a) &= \mathbb{E}[G_t|s_t = s, a_t = a, \pi] = \mathbb{E}[r_{t+1} + \gamma G_{t+1}|s_t = s, a_t = a, \pi] \\
&= \sum_{s',r} p(s',r|s,a)\left(r + \gamma \mathbb{E}[G_{t+1}|s_{t+1} = s', \pi]\right) \\
&= \sum_{s',r} p(s',r|s,a)\left(r + \gamma V_\pi(s')\right) \\
&= \mathbb{E}[r_{t+1} + \gamma V_\pi(s_{t+1})|s_t = s, a_t = a, \pi],
\end{aligned} \tag{6.14}
$$

from which the relationship $V_\pi(s) = \sum_a \pi(a|s)Q_\pi(s,a)$ becomes evident. These are the *Bellman equations* for the value functions, and they lie at the core of RL as they define the relation between the value of a state s and its successors s', recursively capturing future information.

These concepts introduce the notion of partial ordering between policies. A policy π is better than another policy π' if it yields a higher return. Hence, $\pi > \pi'$ if and only if $V_\pi(s) > V_{\pi'}(s) \ \forall s \in \mathcal{S}$. Therefore, the optimal policy π^* is such that it is better than or equal to all the other possible policies.[6] Hence, the optimal policy maximizes the value function.

---

[6]The ordering operator is not always defined between policies. Two policies π, π' cannot be ordered iff $\exists s, s' \in \mathcal{S} : \ V_\pi(s) > V_{\pi'}(s), V_\pi(s') < V_{\pi'}(s')$. However, for MDPs there always exist an optimal policy π^* s.t. $\pi^* \geq \pi \ \forall \pi$ [271].

Taking the Bellman equations, eqs. (6.13) and (6.14), π^* is such that

$$
\begin{aligned}
V_{\pi^*}(s) &= \max_a \mathbb{E}[G_t | s_t = s, a_t = a, \pi^*] \\
&= \max_a \mathbb{E}[r_{t+1} + \gamma V_{\pi^*}(s_{t+1}) | s_t = s, a_t = a, \pi^*] \\
&= \max_a Q_{\pi^*}(s, a).
\end{aligned}
\tag{6.15}
$$

Notice that in this new Bellman equation there is a maximization over the first action, as opposed to the expectation over actions from eq. (6.13). This is because the value of a state under the optimal policy must be equal to the expected return for the best action. In a similar way, we can find the Bellman equation for the action-value function $Q_\pi(s, a)$ for an optimal policy π^*. Together, they define the set of the *Bellman optimality equations*:

$$
\begin{aligned}
V_{\pi^*}(s) &= \max_a \sum_{s', r} p(s', r | s, a)\big[r + \gamma V_{\pi^*}(s')\big] \\
Q_{\pi^*}(s, a) &= \sum_{s', r} p(s', r | s, a)\big[r + \gamma \max_{a'} Q_{\pi^*}(s', a')\big]
\end{aligned}
\tag{6.16}
$$

These equations fulfill

$$
\begin{aligned}
Q_{\pi^*}(s, a) &= \max_\pi Q_\pi(s, a) \\
V_{\pi^*}(s) &= \max_\pi V_\pi(s) = \max_a Q_{\pi^*}(s, a).
\end{aligned}
\tag{6.17}
$$

We can define the optimal policy $\pi^*(a|s)$ and action a^* at a given state s as:

$$
\begin{aligned}
\pi^* &= \arg\max_\pi V_{\pi^*}(s) \\
a^* &= \arg\max_a Q_{\pi^*}(s, a).
\end{aligned}
\tag{6.18}
$$

The optimal policy π^* corresponds to the deterministic choice of the best action a^* for a given state s according to the optimal action-value function $Q_{\pi^*}(s, a)$. Due to the recursive nature of the value functions, a greedy action according to V_{π^*} or Q_{π^*} is optimal in the long term.

The Bellman optimality equations eq. (6.16) are, indeed, a system of equations with one for every state. In order to solve them directly, we need to explicitly use $p(s', r | s, a)$.[7] If $p(s', r | s, a)$ is known, we know the underlying model of the system, and thus we deal with model-based RL, as discussed in the previous section. In a general model-free RL scenario, it is unknown and, as such, we need additional methods to solve them, such as the ones we introduce in the following sections.

6.2 Value-based methods

In value-based RL, the goal is to obtain the optimal policy $\pi^*(a|s)$ by learning the optimal value functions, as in eq. (6.18). This way, we start with an initial estimation of the value function for every state, $V_\pi(s)$, or state–action pairs, $Q_\pi(s, a)$. Then, we progressively update them with the experience gathered by the agent following its policy.

Given that the value functions are defined with respect to a policy (recall section 6.1.5), we need to define a fixed policy for this family of algorithms. A common choice is an ε-greedy

---

[7]Due to the maximization step in eq. (6.16), this is a non-linear optimization problem.

policy, as introduced in section 6.1.2, provided that the optimal policy is greedy with respect to the optimal value function. Hence, learning the value function for such policy provides us with the optimal one in the greedy limit.

One of the most straightforward and naive approaches to learn the value function would be to sample trajectories $\tau \sim p(\tau)$ (eq. (6.9)), and then use the return G_t to update our value function estimation[8] for every visited state s_t along the way:

$$V_\pi(s_t) = V_\pi(s_t) + \eta(G_t - V_\pi(s_t)), \tag{6.19}$$

where η is a learning rate. We can do an analogous process for every visited state and action along the trajectory to learn $Q_\pi(s, a)$ instead.

However, with this approach we can only learn at the end of each trajectory, also known as *episodes*, which can be very inefficient in problems involving long episodes, or even infinite ones. On the contrary, temporal-difference (TD) algorithms exploit the recursive nature of the value functions, eqs. (6.13) and (6.14), to learn at every time step:

$$V_\pi(s_t) = V_\pi(s_t) + \eta\left(r_{t+1} + \gamma V_\pi(s_{t+1}) - V_\pi(s_t)\right). \tag{6.20}$$

Notice that, while $V_\pi(s_t)$ is an estimate, $V_\pi(s_{t+1})$ is also an estimate. This is known as a *bootstrapping* method, as the update is partially based on another estimate. Nevertheless, it is proven to converge to a unique solution. The term in brackets is known as *TD error*.

The algorithm implementing eq. (6.20) is known as TD(0), which is a special case of the TD(λ) algorithms [272]. The analogous algorithm for the action-value function is known as SARSA [273, 274]:

$$Q_\pi(s, a) = Q_\pi(s, a) + \eta\left(r + \gamma Q_\pi(s', a') - Q_\pi(s, a)\right), \tag{6.21}$$

where we have recovered the notation s', a', r to denote the next state, action and reward. Replacing the term $Q_\pi(s', a')$ by an expectation over the next possible actions, such as $\sum_{a'} \pi(a'|s')Q_\pi(s', a')$, we obtain the expected SARSA algorithm [275]. If, instead, we take a maximization, as in eq. (6.22) below, we obtain Q-learning [276], for which we provide a detailed introduction in the following section 6.2.1.

6.2.1 Q-learning

Q-learning is one of the most widely used TD algorithms due to its desirable properties [276]. Most of the TD algorithms that we introduce in the previous section learn the value functions for their given policies, mainly ε-greedy policies. These include exploratory random actions (recall section 6.1.2) that have an impact on the learned value functions. Therefore, the policy determines the result, and we must adjust ε during the training process to ensure their proper convergence toward the optimal value functions. However, Q-learning always learns the optimal action-value function regardless of the policy followed during the training.[9]

> The goal is to directly learn the optimal Q-values, $Q_{\pi^*}(s, a)$, hence the name Q-learning, in order to obtain $\pi^*(s|a)$ by performing greedy actions over them, as in eq. (6.18).

---

[8]The return is an unbiased estimator for the expectation $V_\pi(s_t) = \mathbb{E}[G_t|s_t, \pi]$ from eq. (6.10). This is known as a sample update, as we only use a single sample to determine the expectation.

[9]Q-learning is an off-policy algorithm, which means that the policy it learns (optimal $\pi^*(a|s)$) is different from the one it follows in the training episodes. Algorithms like SARSA are on-policy, and learn the value function that corresponds to the policy with which they generate the training data.

We start by arbitrarily initializing our estimates $Q_\pi(s, a) \ \forall s \in \mathcal{S}, a \in \mathcal{A}$, which are typically stored in a table (see section 6.2.3 for an implementation with NNs). Then, we sample trajectories $\tau \sim p(\tau)$ according to the policy to progressively update our estimates with the relation

$$Q_\pi(s, a) = Q_\pi(s, a) + \eta \left(r + \gamma \max_{a'} Q_\pi(s', a') - Q_\pi(s, a) \right). \tag{6.22}$$

We illustrate the process in algorithm 9.

Algorithm 9 Q-learning

Require: learning rate η, maximum time T, policy parameter ε
  Initialize $Q(s, a) \ \forall s \in \mathcal{S}, a \in \mathcal{A}$
  while not converged **do**
    Initialize s_0
    for $t = 0$ to $T - 1$ **do**
      $\xi \leftarrow \text{uniform} \in [0, 1]$
      $a \leftarrow \text{uniform } a$ **if** $\xi \leq \varepsilon$ **else** $\arg\max_a Q_\pi(s, a)$ ▷ ε-greedy policy
      Move to next state s' and obtain reward r
      $Q(s, a) \leftarrow Q(s, a) + \eta \left(r + \gamma \max_{a'} Q(s', a') - Q(s, a) \right).$
    end for
  end while
  return $Q(s, a)$ ▷ Optimal action-value function for all states and actions

---

This method is guaranteed to converge to the optimal action-value function as long as all possible state—action pairs continue to be updated. This is a necessary condition for all the algorithms that converge to the optimal behavior and it can become an issue for fully deterministic policies. However, with Q-learning, we can have an ε-greedy policy with $\varepsilon \neq 0$ that ensures that this condition is fulfilled.

The key element is that, while the policy determines which states and actions are visited by the agent, the Q-value update is performed over a greedy next action, as shown in eq. (6.22). This way, the learned Q-values are those corresponding to the greedy policy over them, which is the one fulfilling the Bellman optimality equations eq. (6.16).

6.2.2 Double Q-learning

Most of the TD algorithms suffer from a maximization bias that results in an overestimation of the Q-values, which can harm the performance. Specially, in Q-learning, we encounter two maximizations: one in the ε-greedy policy and one in the greedy target policy (eq. (6.22)). This way, we use a maximum overestimated value (see below) to update the maximum Q-value, which corresponds to the greedy action taken by the policy, potentially incurring into a significant positive bias for $Q_\pi(s, a)$.

The maximization over next possible actions in eq. (6.22) is a sample estimate for the maximum expected value $\max_{a'} \mathbb{E}[Q_\pi(s', a')]$. However, it is a positively biased estimator, provided that the sample estimate actually corresponds to the expected maximum value $\mathbb{E}[\max_{a'} Q_\pi(s', a')]$ [277]. In Ref. [271] they provide a simple example to develop intuition on the matter: suppose that the true Q-values for all actions in a state are zero and that our estimates $Q_\pi(s, a)$ are distributed around them taking positive and negative values. The maximum value is positive and, hence, it is an overestimation. The overestimation of the Q-values can prevent the algorithm from learning the optimal policy [278].

We overcome this issue with double Q-learning [279]. This way, instead of learning a single set of Q-values, we learn two: $Q_\pi^A(s, a)$, and $Q_\pi^B(s, a)$. However, in order to update one, we

use the other to estimate the value of its corresponding next greedy action:

$$Q_\pi^A(s,a) = Q_\pi^A(s,a) - \eta \left(r + \gamma Q_\pi^B \left(s', \arg\max_{a'} Q_\pi^A(s',a') \right) - Q_\pi^A(s,a) \right), \qquad (6.23)$$

where *A, B* are interchangeable. This approach avoids using the same estimate to determine both the maximizing action and its value, yielding an unbiased estimate.

We learn both sets of values by randomly updating one at a time at every time step. The only additional difference with respect to standard Q-learning is that we take actions following an ε-greedy policy that combines the information of both $Q_\pi^A(s,a)$ and $Q_\pi^B(s,a)$, e.g., using their sum or mean. With double Q-learning, we overcome a major limitation of Q-learning at the price of doubling the memory requirements.

6.2.3   Implementing Q-learning with a neural network

In Q-learning, as we have introduced it in section 6.2.1, we store the Q-values, $Q_\pi(s,a)$, for every possible state−action pair. This approach allows us to find the exact optimal action-value function. However, it is only viable for small problems, as the memory requirement quickly becomes unfeasible for moderately large ones.

In these cases, we must rely on an efficient way to represent $Q_\pi(s,a) \; \forall s \in \mathcal{S}, a \in \mathcal{A}$. NNs are a prominent candidate to approximate the action-value function, as introduced in Ref. [18], with significantly less parameters than state−action pairs (recall section 2.4.4). Using NNs to learn the Q-values is known as *deep Q-learning* and the network is commonly referred to as deep Q-network (DQN). DQNs take a representation of state in the input layer $\phi(s)$, and have as many neurons as possible actions in the output layer, which encode $Q_\pi(s,a;\boldsymbol{\theta}) \; \forall a \in \mathcal{A}$. Here, $\boldsymbol{\theta}$ denotes the set of learnable parameters of the neural network. This way, the DQN provides the Q-value of all possible actions given a state.

Nevertheless, DQNs may become highly unstable when directly applying algorithm 9 with an update rule for the network parameters:

$$\boldsymbol{\theta} = \boldsymbol{\theta} + \eta \left(r + \gamma \max_{a'} Q_\pi(s',a';\boldsymbol{\theta}) - Q_\pi(s,a;\boldsymbol{\theta}) \right) \nabla_{\boldsymbol{\theta}} Q_\pi(s,a;\boldsymbol{\theta}), \qquad (6.24)$$

which is analogous to a regression problem in which we minimize the MSE loss (eq. (2.1)) between the target, $r + \gamma \max_{a'} Q_\pi(s',a';\boldsymbol{\theta})$, and the prediction, $Q_\pi(s,a;\boldsymbol{\theta})$, through gradient descent. The instabilities are mainly due to correlations in consecutive observations along the trajectories, correlations between target and prediction, and significant changes in the data distribution due to small variations in the parameters. The latter happen because the agent follows an ε-greedy policy, and small changes in the parameters may change the actions that have the maximum Q-value for the states, abruptly altering the course of the trajectories.[10] We overcome these limitations with *experience replay* [280], and introducing a *target network*.

With experience replay, instead of learning at every time step, we store the experience gathered along the episodes in a memory, which keeps the information of every transition (s,a,r,s'). Then, once the agent has gathered enough experience, it replays a randomly sampled batch of transitions in its memory to compute the loss and update the DQN parameters. This way, the agent alternates between episodes to gather experience and replaying it to perform the learning process. This technique removes the correlation between training samples

---

[10]Consider the case of two separate paths that lead to different treasures. We initialize the Q-values arbitrarily, and the ε-greedy policy mainly takes the path with the highest one, while casually following the other with small probability ε. However, if the second one leads to a bigger treasure, its Q-value will eventually become the highest, and the data distribution will suddenly change to mainly sample this path and casually take the other.

and mitigates the sudden changes in data distribution. Furthermore, it allows the agent to reuse the experience to prevent forgetting and re-learning.[11]

In order to remove the correlation between target and prediction, we consider a target network, which is a clone of the DQN that we update at a different rate. While we update the DQN parameters, $\boldsymbol{\theta}$, at every iteration, we only update the parameters of the target network, $\boldsymbol{\theta}^-$, copying $\boldsymbol{\theta}$ every few iterations. Then, we use it to predict the target term $\max_{a'} Q_\pi(s', a'; \boldsymbol{\theta}^-)$, hence the name of the network. This ensures that the prediction, $Q_\pi(s, a; \boldsymbol{\theta})$, and the target are uncorrelated.

Additionally, we can go a step further and use the target network for double Q-learning (see section 6.2.2) in order to prevent the DQN from overestimating the action-value function, as introduced in Ref. [281]. Thus, the overall implementation consists on gathering experience by following an ε-greedy policy on the Q-values, $Q_\pi(s, a; \boldsymbol{\theta})$. Then, the agent replays randomly selected transitions from the experience to compute the MSE loss function between the target and the prediction, but using a target network to perform double Q-learning:

$$\mathcal{L} = \frac{1}{n} \sum_{i=1}^n \left(r_i + \gamma Q_\pi \left(s_i', \arg\max_{a'} Q_\pi(s_i', a'; \boldsymbol{\theta}); \boldsymbol{\theta}^- \right) - Q_\pi(s_i, a_i; \boldsymbol{\theta}) \right)^2, \qquad (6.25)$$

where i denotes the index in a batch of n randomly sampled transitions from the memory. Then, we perform a gradient descent step over the loss in eq. (6.25) to update $\boldsymbol{\theta}$. Finally, every few iterations, we update the target network $\boldsymbol{\theta}^- \leftarrow \boldsymbol{\theta}$.

6.3 Policy gradient methods

The main goal of RL is to find the optimal policy $\pi^*(a|s)$ that maximizes the expected return for a given task. In policy gradient algorithms we try to directly find the optimal policy by proposing a parametrized ansatz $\pi_{\boldsymbol{\theta}}(a|s)$ and optimizing its parameters $\boldsymbol{\theta}$, similar to the variational wave functions from chapter 5. Hence, finding the optimal policy $\pi^*(a|s)$ is equivalent to finding the optimal set of parameters $\boldsymbol{\theta}^*$ that best approximates it $\pi_{\boldsymbol{\theta}*}(a|s) \approx \pi^*(a|s)$. This parametrization can take several forms, such as a NN, and controlling the shape of the policy may allow us to leverage prior knowledge about the task to obtain better results. Furthermore, the policies are stochastic, which have a natural exploratory character and the flexibility to also approximate deterministic policies.

In order to optimize the parameters, we use an objective function O_π that we aim to maximize. This can be any figure of performance, such as the state-value function V_π, the action-value function Q_π, or the return G. Having continuous parametrized policies, the objective function changes smoothly with changes in the parameters, which allows us to compute their derivatives. We approach the optimization by a gradient ascent method: we compute the gradient of the expectation value $\nabla_{\boldsymbol{\theta}} \mathbb{E}[O_\pi|\pi_{\boldsymbol{\theta}}]$, and perform a small update of the parameters $\boldsymbol{\theta}$. The expectation value is taken over the trajectories τ sampled according to the policy (recall eq. (6.9)).

Directly evaluating the gradient is not straightforward because it depends on the stationary distribution of the states, to which we do not have access in model-free RL. Hence, it is difficult to estimate the effect of the policy update on the state distribution. However, the *policy gradient theorem* [282,283] provides us with an analytical form for the gradient of the objective function that does not involve the derivative over the state distribution.

---

[11]This is specially valuable when the experience is costly to obtain. For instance, if a robot receives severe damage, having a memory allows it to keep learning from the situation without receiving further injuries.

Policy gradient theorem: For any differentiable policy $\pi_{\boldsymbol{\theta}}(a|s)$ and objective function O_π, the gradient of its expectation value $\nabla_{\boldsymbol{\theta}} \mathbb{E}[O_\pi|\pi_{\boldsymbol{\theta}}]$ can be expressed in terms of derivatives acting exclusively on the logarithmic policy $\nabla_{\boldsymbol{\theta}} \log \pi_{\boldsymbol{\theta}}(a|s)$. The term $\nabla_{\boldsymbol{\theta}} \log \pi_{\boldsymbol{\theta}}(a|s)$ is often referred to as the *score function*.

To get some additional intuition on the above theorem, let us consider an example with the total return $G(\tau)$ as objective function (see [271] for an extended proof with $V_\pi(s)$). Thus, we are interested in maximizing the expectation value $\mathbb{E}[G|\pi_{\boldsymbol{\theta}}]$, which is performed over the trajectories $\tau \sim p_{\boldsymbol{\theta}}(\tau)$. We restate eq. (6.9) to explicitly show the parameter dependence

$$p_{\boldsymbol{\theta}}(\tau) = \prod_{t=0}^{T-1} p(s_{t+1}|s_t, a_t)\pi_{\boldsymbol{\theta}}(a_t|s_t). \tag{6.26}$$

Therefore, we can write the expectation as

$$\mathbb{E}[G|\pi_{\boldsymbol{\theta}}] = \sum_\tau p_{\boldsymbol{\theta}}(\tau)G(\tau). \tag{6.27}$$

In order to take the gradient, let us first recall the property of logarithmic derivatives $\nabla_{\boldsymbol{\theta}} p_{\boldsymbol{\theta}} = p_{\boldsymbol{\theta}} \nabla_{\boldsymbol{\theta}} \log p_{\boldsymbol{\theta}}$, wich we apply in the following derivation:

$$
\begin{aligned}
\nabla_{\boldsymbol{\theta}} \mathbb{E}[G|\pi_{\boldsymbol{\theta}}] &= \sum_\tau G(\tau)\nabla_{\boldsymbol{\theta}} p_{\boldsymbol{\theta}}(\tau) \\
&= \sum_\tau G(\tau)p_{\boldsymbol{\theta}}(\tau)\nabla_{\boldsymbol{\theta}} \log p_{\boldsymbol{\theta}}(\tau).
\end{aligned}
\tag{6.28}
$$

Then, from eq. (6.26), we see that the only dependence on $\boldsymbol{\theta}$ from $p_{\boldsymbol{\theta}}(\tau)$ is in the policy. Therefore,

$$\nabla_{\boldsymbol{\theta}} \log p_{\boldsymbol{\theta}}(\tau) = \sum_{t=0}^{T-1} \nabla_{\boldsymbol{\theta}} \log \pi_{\boldsymbol{\theta}}(a_t|s_t), \tag{6.29}$$

which, combined with eq. (6.28), we obtain the expression

$$
\begin{aligned}
\nabla_{\boldsymbol{\theta}} \mathbb{E}[G|\pi_{\boldsymbol{\theta}}] &= \sum_\tau p_{\boldsymbol{\theta}}(\tau)G(\tau) \sum_{t=0}^{T-1} \nabla_{\boldsymbol{\theta}} \log \pi_{\boldsymbol{\theta}}(a_t|s_t) \\
&= \mathbb{E}\left[G(\tau) \sum_{t=0}^{T-1} \nabla_{\boldsymbol{\theta}} \log \pi_{\boldsymbol{\theta}}(a_t|s_t) \middle| \pi_{\boldsymbol{\theta}} \right]
\end{aligned}
\tag{6.30}
$$

The importance of the policy gradient theorem lies in the fact that it yields a closed form for the gradient as an expectation value. As a consequence, we can estimate it via Monte-Carlo sampling over different trajectories τ. Furthermore, the gradient of the objective function is independent of the initial state s_0, as it does not depend on the policy.

6.3.1 REINFORCE

The REINFORCE algorithm [284] is one of the most commonly used policy gradient algorithms and it uses the return as objective $O_\pi = G(\tau)$.[12]

---

[12]In section 6.1.5 we mention that the optimal policy maximizes $V_\pi(s) \; \forall s \in \mathcal{S}$. Taking $V_\pi(s)$ as objective, the gradient is $\nabla_{\boldsymbol{\theta}} \mathbb{E}[V_\pi(s)|\pi_{\boldsymbol{\theta}}] = \mathbb{E}[Q_\pi(s,a)\nabla_{\boldsymbol{\theta}} \log \pi_{\boldsymbol{\theta}}(a|s)|\pi_{\boldsymbol{\theta}}]$ (see [271]). In REINFORCE, G_t acts as an unbiased estimator of $Q_\pi(a_t,s_t)$ to find the optimal policy, since $Q_\pi(a_t,s_t) = \mathbb{E}[G_t|s_t,a_t,\pi_{\boldsymbol{\theta}}]$ from eq. (6.11).

> The main principle of REINFORCE is to directly modify the policy to favor series of actions within the agent's experience that lead to a high return. This way, previously beneficial actions are more likely to happen the next time the agent interacts with the environment.

Formally, we solve the optimization problem $\boldsymbol{\theta}^* = \arg\max_{\boldsymbol{\theta}} \mathbb{E}[G|\pi_\theta]$. We find $\boldsymbol{\theta}^*$ via an iterative update rule in which we estimate the gradient $\nabla_{\boldsymbol{\theta}} \mathbb{E}[G|\pi_{\boldsymbol{\theta}}]$ and perform a gradient ascent step in its direction. In practice, we estimate it by sampling a batch of trajectories $\tau \sim p_{\boldsymbol{\theta}}(\tau)$, also known as *episodes*, and then we evaluate eq. (6.30). This way, at learning iteration i,

$$\Delta\boldsymbol{\theta}_i = \frac{1}{\Omega} \sum_\tau G(\tau) \sum_{t=0}^{T-1} \nabla_{\boldsymbol{\theta}} \log \pi_{\boldsymbol{\theta}}(a_t|s_t) \tag{6.31}$$

$$\boldsymbol{\theta}_{i+1} = \boldsymbol{\theta}_i + \eta \Delta\boldsymbol{\theta}_i, \tag{6.32}$$

where η is the learning rate and $\Omega = \sum_\tau G(\tau)$.[13] We illustrate the procedure in algorithm 10.

Algorithm 10 REINFORCE

Require: learning rate η, number of trajectories n, maximum time T
Require: randomly initialized differentiable policy $\pi_{\boldsymbol{\theta}}(a|s)$
  while not converged **do**
    for $i = 1$ to n **do**
      Initialize s_0
      for $t = 0$ to $T - 1$ **do**
        Take action $a_t \sim \pi_{\boldsymbol{\theta}}(a_t|s_t)$ and store $\nabla_{\boldsymbol{\theta}} \log \pi_{\boldsymbol{\theta}}(a_t|s_t)$
        Move to next state s_{t+1} and store reward r_{t+1}
      end for
      $G^{(i)} \leftarrow \sum_t \gamma^t r_{t+1}$
      $z^{(i)} \leftarrow \sum_t \nabla_{\boldsymbol{\theta}} \log \pi_{\boldsymbol{\theta}}(a_t|s_t)$
    end for
    $\Omega \leftarrow \sum_i G^{(i)}$
    $\Delta\boldsymbol{\theta} \leftarrow (1/\Omega) \sum_i G^{(i)} z^{(i)}$
    $\boldsymbol{\theta} \leftarrow \boldsymbol{\theta} + \eta\Delta\boldsymbol{\theta}$
  end while
  return $\boldsymbol{\theta}$ ▷ Optimal policy parameters

However, the trajectory sampling introduces significant fluctuations to the expected quantities that result in large training variances, which is a general problem with any Monte-Carlo-based approach. Some episodes may be quite successful whereas some others could be a complete failure with very low returns. Such high variance results into unstable policy updates, which increase the convergence time toward the optimal policy. A common technique to tackle this issue is to introduce a *baseline* into the returns, which reduces the variance of the method without incurring any bias, and therefore *should always be used*.

In order to provide a better description of the baseline, let us first rewrite eq. (6.30) in

---

[13]The expectation of the gradient over trajectories is a weighted sum with respect to their returns. Unlike normalizing by the number of trajectories, this approach disregards trajectories with zero return, which do not contribute to the gradient and would dilute the information, yielding very small updates $\Delta\boldsymbol{\theta}_i \to 0$.

a more convenient way, and omitting the condition $\mathbb{E}[\cdot|\pi_\theta]$ for the rest of the chapter:

$$
\begin{aligned}
\nabla_\theta \mathbb{E}[G|\pi_\theta] &= \mathbb{E}\left[\left(\sum_{t'=0}^{T-1}\gamma^{t'}r_{t'+1}\right)\sum_t \nabla_\theta \log \pi_\theta(a_t|s_t)\right] \\
&= \mathbb{E}\left[\sum_{t'=0}^{T-1}\gamma^{t'}r_{t'+1}\sum_{t=0}^{t'}\nabla_\theta \log \pi_\theta(a_t|s_t)\right] \\
&= \mathbb{E}\left[\sum_{t=0}^{T-1}\nabla_\theta \log \pi_\theta(a_t|s_t)\sum_{t'=t}^{T-1}\gamma^{t'}r_{t'+1}\right] \\
&= \mathbb{E}\left[\sum_{t=0}^{T-1}\gamma^t G_t \nabla_\theta \log \pi_\theta(a_t|s_t)\right],
\end{aligned}
\tag{6.33}
$$

where in the first equation we write the explicit form of $G(\tau)$. In the second equation we use the relation

$$
\begin{aligned}
\nabla_\theta \mathbb{E}[G|\pi_\theta] &= \nabla_\theta \mathbb{E}\left[\sum_{t'=0}^{T-1}\gamma^{t'}r_{t'+1}\right] = \sum_{t'=0}^{T-1}\nabla_\theta \mathbb{E}_{\tau_{t'}}\left[\gamma^{t'}r_{t'+1}\right] \\
&= \sum_{t'=0}^{T-1}\mathbb{E}_{\tau_{t'}}\left[\gamma^{t'}r_{t'+1}\sum_{t=0}^{t'}\nabla_\theta \log \pi_\theta(a_t|s_t)\right] \\
&= \mathbb{E}\left[\sum_{t'=0}^{T-1}\gamma^{t'}r_{t'+1}\sum_{t=0}^{t'}\nabla_\theta \log \pi_\theta(a_t|s_t)\right],
\end{aligned}
\tag{6.34}
$$

where $\mathbb{E}_{\tau_{t'}}$ denotes expectation over trajectories up to time t'. Then, in the third line of eq. (6.33), we rearrange the terms in the summations and we find the explicit form of G_t offset by a γ^t factor. In the final expression, it becomes clearer how past rewards in the trajectories do not contribute to the gradient of the policy from a given time onwards, which recovers the Markov property.

We can reduce the variance in the gradient by introducing a state-dependent baseline $b(s_t)$ in eq. (6.33) such that

$$
\nabla_\theta \mathbb{E}[G|\pi_\theta] = \mathbb{E}\left[\sum_{t=0}^{T-1}\gamma^t \left(G_t - b(s_t)\right)\nabla_\theta \log \pi_\theta(a_t|s_t)\right].
\tag{6.35}
$$

Any baseline is appropriate as long as it does not depend on the actions. This way, we do not introduce any bias, given that

$$
\begin{aligned}
\mathbb{E}\left[b(s_t)\nabla_\theta \log \pi_\theta(a_t|s_t)\right] &= \mathbb{E}_{\tau_t}\left[b(s_t)\mathbb{E}_{\tau_{t:T}}\left[\nabla_\theta \log \pi_\theta(a_t|s_t)\right]\right] \\
&= \mathbb{E}_{\tau_t}\left[b(s_t)\sum_{a_t}\pi_\theta(a_t|s_t)\nabla_\theta \log \pi_\theta(a_t|s_t)\underbrace{\sum_{s_{t+1}}p(s_{t+1}|s_t,a_t)}_{1}\underbrace{\sum_{\tau_{t+1:T}}p_\theta(\tau_{t+1:T})}_{1}\right] \\
&= \mathbb{E}_{\tau_t}\left[b(s_t)\nabla_\theta \underbrace{\sum_{a_t}\pi_\theta(a_t|s_t)}_{1}\right] = \mathbb{E}_{\tau_t}\left[b(s_t)\cdot 0\right] = 0,
\end{aligned}
\tag{6.36}
$$

where $\tau_{t:T}$ indicates a trajectory from time t until the end T. We move from the second to the third line using the property of logarithmic derivatives, as in eq. (6.28). Notice that the expectation remains unbiased even if the baseline depends on θ.

While the expectation is unaffected, the baseline can have a major impact in the variance.[14] Let us consider the case of a state-independent baseline. We can find the optimal baseline that minimizes the variance in the gradient for each parameter. In order to simplify the notation, let z_k and b_k be the k-th components of the score function $z_k = \partial_{\theta_k} \log \pi_{\theta}(a|s)$ and a state-independent baseline vector, respectively. Hence, the goal is to minimize the variance of the term $(G_t - b_k)z_k$,[15] which is the argument of eq. (6.35). Formally, we aim to find $b_k^* = \arg\min_{b_k} \text{Var}[(G_t - b_k)z_k]$, that is such that $\partial_{b_k^*}\text{Var}[(G_t - b_k)z_k] = 0$. Therefore,

$$\text{Var}[(G_t - b_k)z_k] = \mathbb{E}[((G_t - b_k)z_k)^2] - \mathbb{E}[G_t z_k]^2 \tag{6.37}$$

$$\partial_{b_k}\text{Var}[(G_t - b_k)z_k] = -2\,\mathbb{E}[(G_t - b_k)z_k^2] \tag{6.38}$$

$$b_k^* = \frac{\mathbb{E}[G_t z_k^2]}{\mathbb{E}[z_k^2]}\,, \tag{6.39}$$

where in the first equation we have used eq. (6.36) to remove b_k in the second term.

There are several other valid baselines that we can consider, besides the state-independent example above, with which we may obtain better results. For instance, an estimation of the value function $\hat{V}_{\pi}(s_t) \approx \mathbb{E}[G_t|s_t]$ is a common state-dependent baseline. This can either be learned, either directly from G_t or as we show in section 6.4, or it can be estimated through sampling in self-critic schemes (see [285]). With such baseline, actions that lead to returns higher than expected with the current policy are reinforced, while those that lead to lower rewards are penalized. This is equivalent to weighting the score function by the advantage. Given that $\mathbb{E}[G_t|s_t, a_t] = \mathbb{E}[Q_{\pi}(s_t, a_t)|s_t, a_t]$, from eq. (6.11), subtracting a baseline $b(s_t) = V_{\pi}(s_t)$, we obtain the expectation of the advantage (recall eq. (6.12)). Hence, $\nabla_{\theta}\mathbb{E}[G|\pi_{\theta}] = \mathbb{E}\left[\sum_t \gamma^t A(s_t, a_t)\nabla_{\theta}\log\pi_{\theta}(a_t|s_t)\right]$. Directly estimating the advantage provides the least possible variance, see [286] for further reference on this matter.

Another common practice is to *whiten* the return. This consists of subtracting the mean of the return along all the time steps of a trajectory and dividing by its standard deviation $\bar{G}_t = (G_t - \langle G \rangle)/\sigma_G$. Since this is not exactly a baseline, this method *does* introduce a bias.

6.3.2 Implementing REINFORCE with a neural network

The parametrized policy π_{θ} is a central quantity in policy gradient methods and it can take any form as long as it is differentiable with respect to its parameters. One of the most common approaches in discrete action spaces is to define action probabilities according to a *softmax* distribution:

$$\pi_{\theta}(a|s) = \frac{e^{x(s,a)}}{\sum_{a' \in \mathcal{A}} e^{x(s,a')}}\,, \tag{6.40}$$

where $x(s, a)$ is the *action preference* for action a in state s.

The simplest way to define action preferences is through a set of linear parameters $\boldsymbol{\theta}$ applied to a feature representation of the state and action $\phi(s, a)$, such that $x(s, a) = \boldsymbol{\theta}^T\phi(s, a)$. However, this approach may lack the expressive power to approximate the optimal policy π^* in complex problems.

In these cases, we may need to use a deep NN to parametrize the action preferences. NNs are a natural generalization of the linear parameter approach that we can tune to increase the expressive power by, e.g., increasing the number of hidden layers or their size. This way, the

---

[14]Recall that $\text{Var}[x] = \mathbb{E}[x^2] - \mathbb{E}[x]^2$. Hence, adding a term with null expectation does not affect the second term but it does have an impact on the first one $\text{Var}[x - b] = \mathbb{E}[(x - b)^2] - \mathbb{E}[x - b]^2 = \mathbb{E}[(x - b)^2] - \mathbb{E}[x]^2$.

[15]In this case, we take the approximation $\text{Var}\left[\sum_t X_t\right] \approx \sum_t \text{Var}[X_t]$

NN parametrizing the policy takes a state representation in the input layer $\phi(s)$, and has as many neurons as possible actions in the output layer, which encode $x(s, a)\ \forall a \in \mathcal{A}$. Applying a softmax activation function in the output layer (see eq. (2.37)), we obtain $\pi_\theta(a|s)\ \forall a \in \mathcal{A}$, as in eq. (6.40).

The training process is analogous to training a supervised classifier on the experience gathered by the agent. Implementing REINFORCE with gradients from eq. (6.35) is equivalent to performing gradient descent with a modified categorical cross-entropy loss (recall eq. (2.3)):

$$\mathcal{L} = -\frac{1}{n}\sum_{i=1}^{n}\sum_{t=0}^{T-1}\gamma^t(G_{ti} - b(s_{ti}))\log\pi_\theta(a_{ti}|s_{ti}),\tag{6.41}$$

where i denotes the index in a batch of n trajectories. This way, the procedure is analogous to training an NN classifier in which the actions act as state labels. The main difference with supervised classification problems is that, given a state, we do not know the true probability distribution of the actions (true labels), as that would be the optimal policy. Instead, we assign the obtained return G_t as true label for the taken action a_t.[16] Intuitively, in classification problems we aim to enhance the probability that the NN provides the right label, whereas here we reinforce the actions with high returns.

In many situations, actions can take a range of continuous values rather than a discrete set of categories. For instance, a robotic arm may rotate by a certain angle or we can tune various continuous parameters in an experimental setup. Sometimes, we can discretize the action space into small intervals at the cost of a loss in precision and an increasing amount of actions. Nevertheless, this may not always be possible depending on the problem requirements and the resulting number of actions.

In these cases, we model the stochastic continuous actions with a mean μ and a standard deviation σ, such that

$$a = \mu + \sigma\xi,\tag{6.42}$$

where ξ is a random normal variable with unit variance. Analogously to the action preferences above, we can parametrize $\mu_\theta(s), \sigma_\theta(s)$ in various ways, ranging from a set of linear parameters, e.g., $\mu_\theta(s) = \theta^T\phi(s)$, to an NN with two output neurons that determine both $\mu_\theta(s)$ and $\sigma_\theta(s)$ for the given observation. Formally,

$$\pi_\theta(a|s) = \frac{1}{\sigma_\theta(s)\sqrt{2\pi}}\exp\left(-\left(\frac{a - \mu_\theta(s)}{2\sigma_\theta(s)}\right)^2\right).\tag{6.43}$$

In many cases, as the learning advances, and the agent becomes better at taking the right actions (choosing $\mu_\theta(s)$), the deviations decrease and we obtain a quasi-deterministic policy.

6.4 Actor-critic methods

In section 6.2, we introduce value-based RL, featuring the Q-learning algorithm in section 6.2.1. These methods excel at dealing with discrete state–action spaces, and their TD character makes them data efficient and allows them to tackle continuing tasks (infinite

---

[16]The standard categorical cross entropy would be $\mathcal{L} = -\frac{1}{n}\sum_n\sum_k p(a_k)\log\pi_\theta(a_k|s)$, where $p(a_k)$ is the true probability distribution that we want to learn. In standard classification problems, this is typically 1 for the true label and 0 for the rest. Here, it corresponds to the optimal policy $p(a_k) = \pi^*(a_k|s)$. Since we do not have access to π^* (it is our goal!), we use the return G_t for the chosen action in its place, as π^* would favor actions with high returns. This effectively removes the expectation over actions, and we make the sum over time explicit in eq. (6.41).

episodes). However, they experience difficulties to deal with large state—action spaces, and can't deal with their continuous version. Furthermore, they are bound to implement deterministic greedy policies, while many problems present stochastic optimal policies. Finally, small changes in the value functions can cause large variations in the policy, which may cause instabilities in learning.

On the other hand, we introduce policy-gradient methods in section 6.3, featuring the REINFORCE algorithm in section 6.3.1. These algorithms overcome the aforementioned limitations of value-based methods, provided that they can deal with continuous (infinite) state—action spaces, and they are based on continuous stochastic policies, which ensure smooth changes in the policy throughout the learning process, and can become deterministic when needed. However, the learning happens at the end of the episodes, once we know the return, which is an issue for long trajectories or continuing tasks.

> Actor-critic algorithms combine value-based and policy-based methods in order to obtain the best of both approaches. We can understand actor-critic methods as the TD version of policy gradient, with which we retain all its advantages and overcome its major limitation. It features two main elements: the *actor*, a parametrized policy that dictates the decisions, and the *critic*, a model that evaluates them.

The presence of the critic allows the agent to immediately learn from each action without waiting for the outcome at the end of the episode. Evaluating the policy mainly consists on learning its value functions, which allows the critic to assess whether the actions are more or less favorable. In section 6.3.1, we introduce the state-value function, $V_\pi(s)$, as the optimal baseline to reduce the variance in policy gradient. Although, in this case, we only look at $V_\pi(s)$ of the initial state in in the transitions, which does not allow us to evaluate the actions.[17]

However, we sow that, with such baseline, we can compute the gradient in terms of the advantage $A(s,a)$, introduced in eq. (6.12). The explicit form of the advantage sets the foundation for actor-critic methods [287–289]:

$$A(s_t, a_t) = \mathbb{E}[r_{t+1} + \gamma V_\pi(s_{t+1}) - V_\pi(s_t)], \tag{6.44}$$

which is derived from eqs. (6.12) and (6.14). This expression lies at the core of TD algorithms, as it corresponds to the TD error from eq. (6.20).

In eq. (6.44), we use $V_\pi(s)$ to evaluate both the initial and final states of a given transition, thus constituting a critic of the action. This allows the agent to learn from every time step in REINFORCE, processing states, actions and rewards as they occur, like the TD algorithms from section 6.2. Nevertheless, this advantage comes as the cost of learning two models: the policy $\pi_\theta(a|s)$, and the state-value function $V_\pi(s; w)$, which are usually parametrized with NNs with parameters θ and w, respectively. The NN parametrizing the state-value function takes a feature representation of the state, $\phi(s)$, in the input layer, and has a single output neuron encoding $V_\pi(s; w)$. The policy parametrization is the same as in section 6.3.2. We train both models simultaneously by following algorithm 11.

We train the actor with the methods from section 6.3, and the critic using the principles from section 6.2. Hence, all the methods in both sections apply to this algorithm. The

---

[17]In order to determine the quality of an action, we need to compare the initial and final positions. In a game, an action that escapes from the brink of a loss toward a less disadvantageous position may be more valuable than one that moves from an already favorable position to a slightly better one, despite the latter providing a higher final state-value function.

Algorithm 11 Actor-critic

Require: learning rates $\eta_{\boldsymbol{\theta}}, \eta_{\boldsymbol{w}}$, maximum time T
Require: randomly initialized differentiable policy $\pi_{\boldsymbol{\theta}}(s|a)$
Require: randomly initialized differentiable state-value function $V_{\pi}(s; \boldsymbol{w})$
   while not converged **do**
      Initialize s_0
      for $t = 0$ to $T - 1$ **do**
         Take action $a \sim \pi_{\boldsymbol{\theta}}(a|s)$
         Move to next state s' and obtain reward r
         $A \leftarrow r + \gamma V_{\pi}(s'; \boldsymbol{w}) - V_{\pi}(s; \boldsymbol{w})$
         $\boldsymbol{\theta} \leftarrow \boldsymbol{\theta} + \eta_{\boldsymbol{\theta}} \gamma^t A \nabla_{\boldsymbol{\theta}} \log \pi_{\boldsymbol{\theta}}(a|s)$ ▷ Update actor
         $\boldsymbol{w} \leftarrow \boldsymbol{w} + \eta_{\boldsymbol{w}} A \nabla_{\boldsymbol{w}} V(s; \boldsymbol{w})$ ▷ Update critic
      end for
   end while
   return θ, w ▷ Optimal actor and critic parameters

---

parameter updates in algorithm 11 come from performing gradient ascent with eq. (6.35) on the actor, and an analogous update rule to eq. (6.22) for the critic, using $V_{\pi}(s)$ instead of $Q_{\pi}(s, a)$. The process is equivalent to perform gradient descent on the losses $\mathcal{L}_{\boldsymbol{\theta}} = \frac{1}{n} \sum_n \sum_t \gamma^t A(s_t, a_t; \boldsymbol{w}) \log \pi_{\boldsymbol{\theta}}(a_t|s_t)$, and $\mathcal{L}_{\boldsymbol{w}} = \frac{1}{n} \sum_n A(s, a; \boldsymbol{w})^2$, respectively, in which we omit the index for the sum over n samples. They are based on the same principles as the ones in eqs. (6.25) and (6.41).

This method is often referred to as advantage actor-critic (A2C). It has been further enhanced using asynchronous actors, giving raise to the asynchronous advantage actor-critic (A3C) algorithm [290]. Other improvements rely on implementing more advanced optimization techniques, such as the natural gradient [291], as in natural policy gradient [292], natural actor-critic [293, 294], and trust-region methods [295–297].

6.5   Projective simulation

In recent years, there have been introduced novel approaches to RL that explore techniques beyond the prototypical value-based and policy gradient methods that we introduce in sections 6.2 and 6.3. Among those, projective simulation (PS) [298] is of particular interest for the physics community, due to its numerous applications in the field.

PS considers an agent based on an episodic and compositional memory (ECM), a mathematical object capable of storing the information about visited states and actions, and drawing connections between them. This way, the ECM is continuously updated as the agent gathers experience, and it ultimately determines the policy at any given state, as we show below. Usually, the ECM is represented as a directed weighted graph, as shown in fig. 6.3(a). The nodes, defined here as *clips*, represent either visited states, actions, or hidden information learned by the agent. As the agent explores, clips corresponding to new visited states are added to the graph. Similarly, an agent may create additional ones to accommodate new actions, e.g., the combination of two actions, or hidden information. The edges are weighted, and every new node is initialized with uniform edge weights. The weights determine the transition probability between clips, and they are updated as the agent gathers rewards.

As we have previously mentioned, the ECM defines the policy of the PS agent. In the vanilla version of PS, given an observed state, the agent performs a weighted random walk
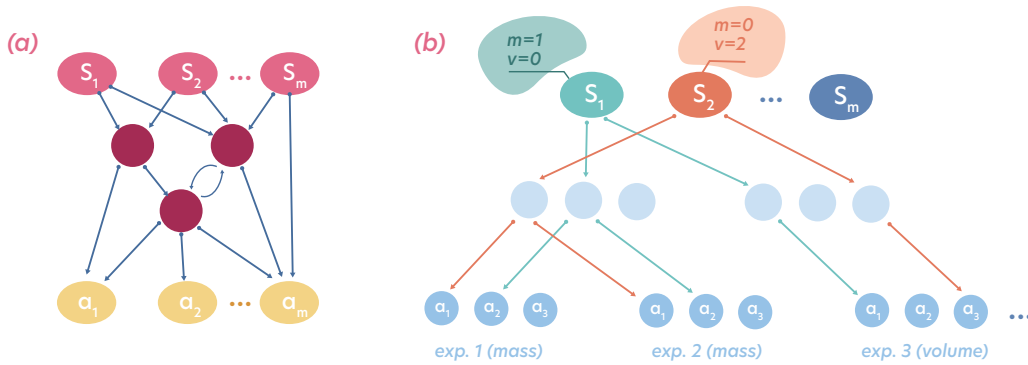
Figure 6.3: Schematic representation of the episodic and compositional memory (ECM) of various projective simulation (PS) agents. (a) A multi-layer ECM with m state nodes (pink), three hidden nodes (red) and m action nodes (yellow). The connectivity of the graph can also be set as a (b) A three-layer ECM, used to demonstrate the possibility of feature extraction by the PS model. See the main text for details.

through the ECM starting on the corresponding state clip. The walk ends as soon as it lands in an action node, and the corresponding action is chosen. The probability to jump from one clip, c_i, to another, c_j, can be any normalized function of the edge weights $h(c_i, c_j)$, such as

$$P(c_i, c_j) = \frac{h(c_i, c_j)}{\sum_{j \in \mathcal{I}} h(c_i, c_j)}, \tag{6.45}$$

where $\mathcal{I}$ is the set of edges of c_i. Other transition functions have also been introduced, such as softmax transitions, which allow us to have arbitrary h-values.

Following the previous scheme, training a PS agent consists on updating the ECM by adding new nodes, and learning the edge weights. The goal is that, for every state clip, the path through the ECM leads to the correct action with high probability. Thus, the training can then be reduced to the update of the h-values at every time-step via

$$h(c_i, c_j) \leftarrow h(c_i, c_j) + \gamma(h(c_i, c_j) - 1) + r \tag{6.46}$$

where c_i and c_j represent the clips traversed during the random walk through the ECM, γ is a damping parameter, and r is the reward given by the environment after performing the chosen action.

With this update rule, for every agent's decision, i.e., every time it performs a walk from a state node to an action node, all h-values of the visited edges are updated. In this way, the h-values along the walk are always damped by a factor γ, and, in the case that they led to a rewarded action, they also increase their value by a factor r.

In many practical scenarios, rewards are obtained at the end of a long series of actions, e.g., performing various steps in a grid-world to reach a target. Hence, it is important to "*backpropagate*" such reward through the sequence of all the actions that led to it. For instance, in TD algorithms, this is achieved by considering the expected value of future states to perform the updates, as we introduce in section 6.2. To accommodate such property, we can generalize the update rule from eq. (6.46) by introducing the concept of an *edge glow*: every time an edge is traversed, it starts to glow decaying with time. This feature allows the agent to update all

the edges in the ECM involved in the decisions to describe a trajectory $\tau = a_0, s_1, a_1, \dots$ [18] which led to a certain reward. The update rule can then be rewritten as

$$h(c_i, c_j) \leftarrow h(c_i, c_j) + \gamma(h(c_i, c_j) - 1) + g(c_i, c_j)r \,, \tag{6.47}$$

where g is the glow value.

Each time a certain edge is visited, its corresponding glow value is set to 1. Then, at every step, all the glow values are dampened via

$$g(c_i, c_j) \leftarrow g(c_i, c_j)(1 - \eta) \,, \tag{6.48}$$

effectively decreases all of them with a rate η. This means that edges that have been recently visited and led to a reward $r \neq 0$ are strengthened, while those visited earlier on received a lesser update, analogous to TD algorithms. We refer to [299, 300] for an in-depth and practical description of the usage of the PS models.

The presented approach to PS is a tabular method, similarly to Q-learning from section 6.2.1, as the agent's deliberation is saved in the adjacency matrix of the ECM, namely the h-matrix. As commented previously, tabular methods have strong limitations when dealing with large action and state spaces. Recently, non-tabular approaches for PS have been proposed [301]. In that case, a neural network (and more precisely, an energy-based model) is trained to output the h-value for a certain state-action pair, analogously to how DQNs are used to predict Q-values, as we introduce in section 6.2.3.

An important feature of the PS model is its transparency and potential interpretability power, in contrast to other approaches such as Q-learning. In the latter, the Q-values encode the expected reward received from an action-state tuple. As the policy relies on performing the action with largest Q-value, there is little to no room for interpretability, aside from such maximization. Conversely, PS constructs a visible graph encoding the probabilities to hop between nodes, which may represent both direct information from the RL task, i.e., actions and states, but also hidden information extracted by the agent. For instance, as we describe in section 6.6.6, the authors of Ref. [302] were able to interpret the hidden structure of the ECM, related in that example to different optical devices. Interestingly, the PS agent was able to create useful optical gadgets composed of multiple devices by composing actions together into new joint nodes (see [298]). Nonetheless, when working in the so-called two-layer PS (one layer of nodes for the states and one for the actions), PS reduces to a very similar model to Q-learning. Indeed, recent works have extensively compared both approaches [303]. However, we can introduce further *hidden* nodes to build deeper PS models, as shown in fig. 6.3(a).

Recently, there have been multiple efforts to build such deep PS architectures and to show that they are indeed able to extract relevant hidden features from the environment or the task at hand [304, 305]. An enlightening example is shown in Ref. [305], which we schematically reproduce in fig. 6.3(b). In this work, an agent is given a set of objects with different physical properties, such as mass, charge and volume. For simplicity, these quantities can take only one of three values: 0, 1 or 2. The agent has access to different experiments, which measure each of this quantities separately. The states are then different objects with certain properties, e.g., in fig. 6.3(b), S_2 is an object of mass 0 and volume 2, obviously in arbitrary units or categories. On the other hand, the actions are the predictions over the various experiments. For instance,

---

[18]Be careful to not confuse the trajectories through the ECM with the trajectories through the state and action spaces. Given a state s_t, the PS agent chooses the action a_t by performing a trajectory through the ECM that starts on the corresponding s_t node until it reaches an action node. Then, the corresponding action a_t is performed to move toward the next state s_{t+1}.

a_1 corresponds to the prediction that the object has the lowest value measured by experiment one (related in this case to mass), a_2 to an intermediate value of that same experiment, etc. The authors show that the PS agent would assign the hidden nodes to meaningful features of the problem. In particular, each hidden node would represent a particular value of a physical quantity, as shown in fig. 6.3(b). Such interesting feature is not only a valuable sign of the interpretability of the PS model, but also was shown to increase its generalization performance.

6.6 Examples and applications

In this section, we showcase a series of prominent applications of RL. Between all the examples, we find instances of each RL paradigm that we discuss in the previous sections. We start with two toy examples to settle the theoretical foundations of policy gradient, as they have analytical solutions. Then, we briefly comment on some of the most famous examples of RL: Atari video games, and Go. Finally, we highlight a few applications of RL to quantum physics, more precisely, in the context of future quantum technologies such as quantum circuits, error correction, and certification.

6.6.1 Toy examples

Let us illustrate the REINFORCE algorithm, from section 6.3.1, by solving a couple of toy examples. These simple scenarios allow us to solve all the equations analytically in order to lay down the foundations and become familiar with the basic concepts.

The random walker Consider an agent that can move along a one-dimensional path with only two actions: move up or down. Every time the agent goes up, it receives a positive reward $r_t = +1$ and every time it goes down it receives a negative reward $r_t = -1$. Considering the undiscounted case, $\gamma = 1$, the return of a trajectory of T steps is the final position $G(\tau) = x_T$. We can also express it in terms of the number of times the agent has taken the actions to go up or down $G(\tau) = n_{\text{up}} - n_{\text{down}} = 2n_{\text{up}} - T$. Clearly, the optimal policy is to always go uphill regardless of the current position.

In such a simple scenario, there is no notion of a state for the agent. Therefore, the policy only depends on the action. Furthermore, since there are only two possible actions, we can define the parametrized policy for one, e.g., $\pi_\theta(\text{up}) \in [0, 1]$, and take the other as $\pi_\theta(\text{down}) = 1 - \pi_\theta(\text{up})$. Let us consider the parametrized sigmoid policy

$$\pi_\theta(\text{up}) = \frac{1}{1 + e^{-\theta}}, \ \pi_\theta(\text{down}) = \frac{1}{1 + e^\theta}, \tag{6.49}$$

which determine the probability to move upwards or downwards, respectively, in terms of the single parameter θ. Their score functions are

$$\nabla_\theta \log \pi_\theta(\text{up}) = \pi_\theta(\text{down}), \ \nabla_\theta \log \pi_\theta(\text{down}) = -\pi_\theta(\text{up}). \tag{6.50}$$

With eqs. (6.49) and (6.50), we can compute the parameter update rule from eq. (6.31) analytically. We can express each of its terms as a function of $\pi_\theta(\text{up})$:

$$\mathbb{E}\left[G(\tau) \sum_{t=0}^{T-1} \nabla_\theta \log \pi_\theta(a_t)\right] = \mathbb{E}\left[\left(n_{\text{up}} - n_{\text{down}}\right)\left(n_{\text{up}} \pi_\theta(\text{down}) - n_{\text{down}} \pi_\theta(\text{up})\right)\right]$$

$$= \mathbb{E}\left[\left(2n_{\text{up}} - T\right)\left(n_{\text{up}} - T\pi_\theta(\text{up})\right)\right] \tag{6.51}$$

$$= 2\mathbb{E}\left[\left(n_{\text{up}} - T/2\right)\left(n_{\text{up}} - \langle n_{\text{up}}\rangle_{\pi_\theta}\right)\right]$$

$$= 2\text{Var}\left[n_{\text{up}}\right] = 2T\pi_\theta(\text{up})(1 - \pi_\theta(\text{up})),$$
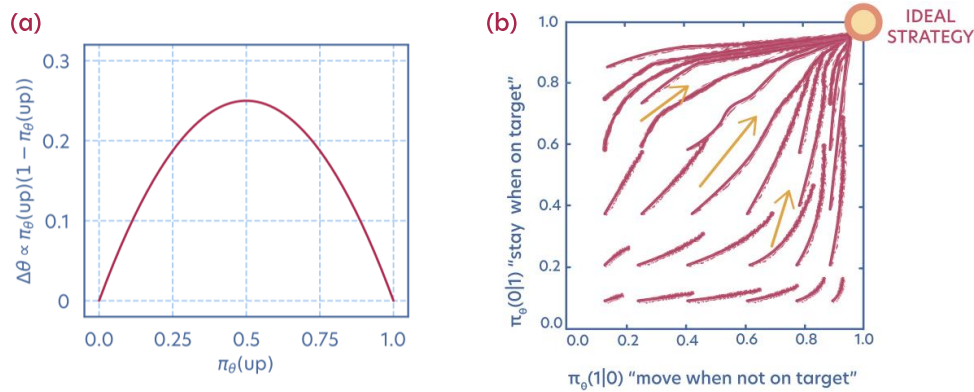
Figure 6.4: Walkers and RL. (a) Parameter update from eq. (6.52) for the random walker. (b) Evolution of various policies trained on the walker with target.

where we have taken $T\pi_\theta(\text{up})$ as the expected number of upwards moves $\langle n_{\text{up}} \rangle_{\pi_\theta}$. With this, we are able to reach a closed analytical form for the parameter update rule in this simplistic scenario, which is not the usual case in RL. This allows us to understand the way that actions are reinforced. For instance, the term $n_{\text{up}} - \langle n_{\text{up}} \rangle_{\pi_\theta}$ reinforces actions that lead toward higher upwards moves than expected following the policy, and it penalizes those that lead to fewer.

The parameter update is a quadratic function on the policy, such that

$$\Delta\theta \propto \pi_\theta(\text{up})(1 - \pi_\theta(\text{up})), \tag{6.52}$$

which is minimal either close to the optimal policy $\pi_\theta(\text{up}) \simeq 1$ or far from it $\pi_\theta(\text{up}) \simeq 0$, as shown in fig. 6.4(a). We can understand this in a very intuitive way: if the agent is already prioritizing the action to move upwards, it has very little to learn from there on. Conversely, if it barely takes this action, it cannot learn that it is the right choice. Hence, the agent learns the most whenever it takes both of actions at a similar rate. This also reflects the importance of the initialization. If we initialize the policy to $\pi_{\theta_0}(\text{up}) \simeq 0$, the agent takes much longer to converge to the optimal policy than with $\pi_{\theta_0}(\text{up}) \simeq 0.5$.

The walker with target Consider now a slightly more complex situation in which the agent moves along a one-dimensional path and has to stop at a target location. In this case, the two actions are to move forward, or to stay. The agent receives a reward every time step it stays at the target location. In this example, the optimal policy is to move forward until the agent reaches the target, and then stop.

In contrast to the previous example, the agent is no longer blind, and the policy does depend on the state. Notice that, even though the agent moves in space, the actual position is completely irrelevant to the problem, and the only important information is whether the agent is in the right position or not. Therefore, we encode this information with Boolean indicators, assigning $s = 1$ when the agent is at the target location, and $s = 0$ elsewhere. Hence, despite the agent moving in real space, it only navigates in a two-state MDP.[19] Then, we denote the actions "stay" and "move" with $a = 0$ and $a = 1$, respectively. This way, the optimal policy always takes the action to move when not in target, and to stay when in target. We illustrate the optimal policy in table 2. Additionally, we illustrate the convergence of various policies to the optimal one with REINFORCE in fig. 6.4(b).

---

[19]We emphasize that, when we frame a problem as an RL instance, we only need to model and encode the information that is relevant to the problem. Hence, the resulting state and action spaces do not need to correspond directly to those in the "real world". The simpler the MDP, the easier it is be for the agent.

	stay $a = 0$	move $a = 1$
out of target $s = 0$	0	1
on the target $s = 1$	1	0

Table 2: Optimal policy $\pi^*(a|s)$ for the walker with target example.

6.6.2 Go and Atari games

Games are one of the most natural applications for RL, and they serve as a benchmark for the state of the art methods. Most games involve long-term strategies, and early actions may lead to completely different outcomes, even in short time scales. Furthermore, many games involve vast state spaces, or even infinite ones. Overall, they pose a great challenge that has motivated some of the greatest advances in the field.

The first applications of RL to games were board games. Achieving superhuman performance in chess was a milestone in the field when, in 1997, *Deep Blue* [306] beat Garry Kasparov, the highest-rated chess player in the world at the time. A more recent breakthrough has been achieving superhuman performance in the game of Go [20]. Go is a Chinese board game which is over 3,000 years old. Two players take turns to place stones on the board. The goal is to conquer as much space as possible, either by strategically surrounding empty spaces, or capturing the opponent's stones by surrounding them. Once all stones are allocated, the player with the largest captured territory wins. Even with this simple set of rules, there are 10^{172} possible board configurations, making this game order of magnitudes more complex than chess [307].

The computer program developed by DeepMind, AlphaGo [20], combines a technique called Monte Carlo tree search [308] with deep NNs. With this approach, the goal is to progressively build a search tree of the state space that grows as the agent gathers experience. In the tree, each edge contains the learned action-value function $Q(s, a)$, which partially determines the policy, similar to Q-learning from section 6.2.1. However, since the state space is virtually infinite, they implement two NNs that guide the search through the regions outside of the tree: a parametrized policy that guides the exploration, and a parametrized value function that predicts the probability to win from each state. See [20] for a detailed explanation.

Initially, they train the policy network by supervised learning, taking example moves from expert games. This provides them with an early advantage with respect to starting tabula rasa to build the search tree from already functional strategies. However, they then proceed to train the whole pipeline through *self-play*, i.e., playing against itself, further refining the policy via policy gradient, as shown in section 6.3. This model defeated the world champion of Go in 2015.

This approach has been improved by removing the initial supervised training over expert human games, and purely training through self-play from scratch. This algorithm is known as AlphaGo Zero [309]. This new version defeated the previous one by a hundred games to zero. In fig. 6.5, we see the performance of AlphaGo and AlphaGo Zero with training time in terms of Elo rating.[20] Initially, AlphaGo has a substantial advantage thanks to the previous

---

[20]The Elo rating system, named after its creator Arpad Elo, is a method to calculate the relative skill level of players in zero-sum games. After every game, the winning player takes points from the losing one. The difference in rating between players determines the total number of points gained or lost after a game. If the higher-rated
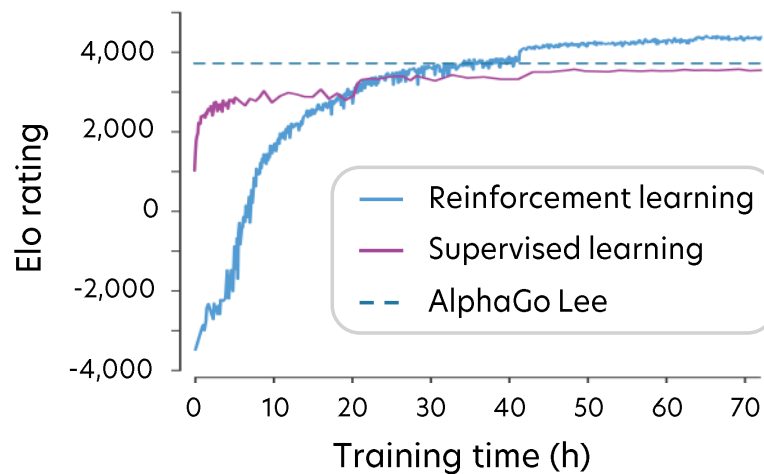
Figure 6.5: Performance comparison between AlphaGo (initial supervised learning) [20], and AlphaGo Zero (pure RL) [309] at the game of Go. Initially, AlphaGo has an advantage thanks to the initial supervised training. However, it limits its capabilities and it is quickly outperformed by AlphaGo Zero. The horizontal dashed line corresponds to the Elo rating of Lee Sedol during his match with AlphaGo being a reference point for the supervised/pure RL performance. Taken from [309].

supervised learning phase. However, this pre-training ultimately limits its capabilities, and AlphaGo Zero outperforms it in just a few hours of training. Furthermore, while these algorithms are generally tailored to the specific game, more general and recent approaches, defeated the previous benchmarks in chess, shogi, and Go at the same time [310].

Another exciting avenue for RL in games are video games. One of the first applications were Atari games, achieving superhuman performance with deep Q-learning [18], as we explain in section 6.2.3. In this case, the state space is also infinite and the agent receives the screen pixels as input, together with the current score. However, the action space is limited by the game controller, which is very convenient for Q-learning. This approach achieved superhuman performance in forty nine different games with the same algorithm.

Some other recent outstanding results in video games include competitive performance in StarCraft II [19], Dota 2 [311], and Minecraft [312]. Furthermore, advances in model-free RL have motivated the research on planning with model-based algorithms, with which some of the benchmarks that we introduce above have been bested [313]. This approach does not even require the explicit encoding of the game rules, as it builds a model of them while playing.

6.6.3 Quantum feedback control

Quantum control is a research direction in quantum technologies aiming to improve initialization and stabilization of a desired quantum state. Already, deep RL algorithms have been successfully employed in a wide range of applications for quantum feedback control [315–318]. In general, a quantum system is controlled by an NN based on a feedback loop with some measurements that have been performed on the system. These measurement results are fed as an input to the NN whose output guides the control scheme. In Ref. [316], authors considered a single-mode quantum cavity. The cavity mode is leaking from the cavity and this signal

---

player wins, only a few rating points are taken from the lower-rated player. However, in the opposite case, the lower-rated player takes many points from the higher-rated one.
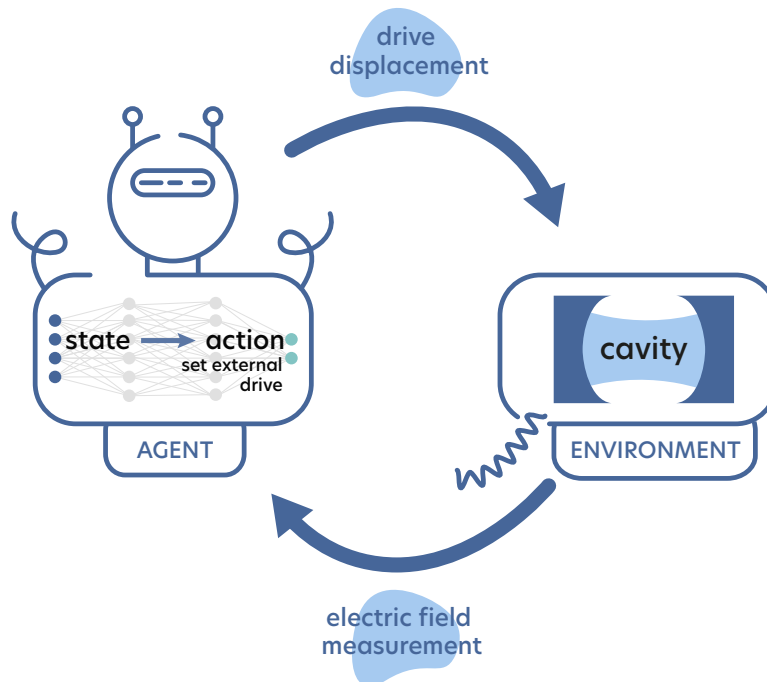
Figure 6.6: Driven single mode microcavity as an RL environment. The mode decays from the cavity. Its measurement serves as the observation for the agent represented by an NN. The network converts a measurement trace into probabilities for all the available actions, which give feedback for the displacement drive of the cavity. Adapted from [314].

can be measured. Additionally, the cavity mode can be controlled via an external drive. The goal is to adjust the drive amplitude of a beam entering the cavity to create and then stabilize a cavity quantum state with a single photon as depicted in fig. 6.6.

The input to the network, i.e., the observed state s, is the measured electric field leaked from the cavity. The only action in this scenario is to set the value of the driving laser amplitude as a function of time. After a short evolution time step, the NN is queried again. Given the updated measurement of the electric field, the network decides on the next action probabilities. One of these actions is selected and the next system evolution in the next step is executed. This procedure is performed until a fixed end of the trajectory, before the network's parameters are updated according to the policy gradient approach from section 6.3. Many different training episodes start with the cavity vacuum state. During training, the agent (in form of an NN) eventually finds a strategy to compete losses with the proper drive ending up in the stabilized target cavity state.

6.6.4 Quantum circuit optimization

Quantum computing based on quantum gates requires designing a quantum circuit for a specific quantum algorithm. However, there can be many different sequences of quantum gates implementing the same algorithm. Additionally, due to the fact that quantum gates have non-perfect fidelity, the more gate operations are performed, the more errors appear during the algorithm execution. As such, quantum circuits should be designed in the most optimal way, im-
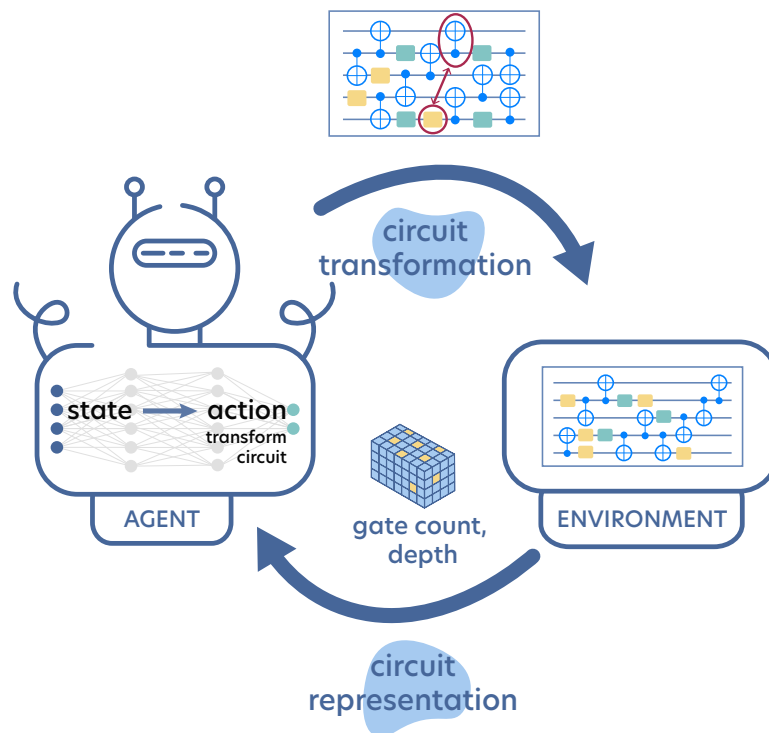
Figure 6.7: Schematic representation of the RL framework for circuit optimization. The agent observes a representation of a quantum circuit given by the environment. Then, it can choose to perform a modification to the circuit. The environment calculates a reward depending on the gate count (or another metric) of the resulting circuit, and it provides the agent with the new circuit and the reward. Adapted from [320].

plementing the least possible number of quantum gates. This is especially important for noisy intermediate-scale quantum (NISQ) devices, which currently allow for > 100 qubits [319] but, at the same time do not allow for high-level logical quantum error correction.[21] Quantum circuit optimization utilizes the fact that there exist certain sets of transformation rules that allow us to replace sequences of quantum gates by others that yield the same output. For example, these transformations could involve swapping the position of two gates, or moving one gate to a different position relative to another. Furthermore, some sequences of gates can be shortened by merging gates without changing the output.

We can naturally formulate the problem quantum circuit optimization as an RL problem [320]. In the resulting framework, depicted in fig. 6.7, the environment holds the quantum circuit, containing information about the different gates, such as their error rates. Te agent can observe a representation of the quantum circuit, which corresponds to the state, and it can decide to perform a transformation to the circuit from a set of possible transformation rules. The environment can evaluate the resulting circuit after the transformation, and provide the agent with a reward. The reward can account for various aspects, such as the reduction in the total gate count, the reduction in depth (the time needed for the circuit to run), or the combination of both. Additionally, the reward function can also depend on a decoherence estimate for the whole circuit, based on the decoherence that happens on each the gates.

---

[21]In fact, we show how to employ RL methods to tackle quantum error correction in section 6.6.5
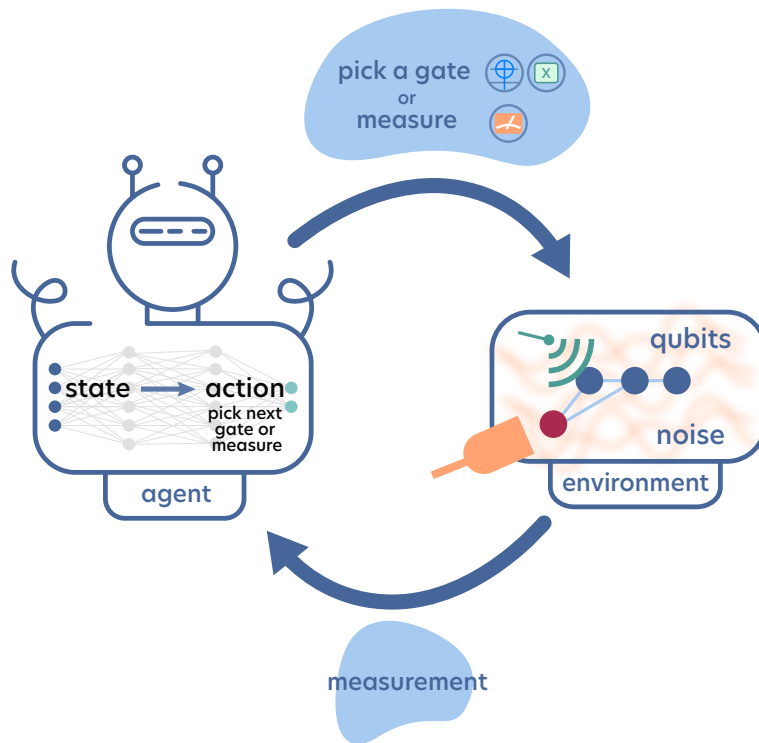
Figure 6.8: Schematic representation of the RL-based error correction framework. The agent can choose the next gate or measurement to be applied to an ensemble of a few, possibly error-affected, qubits in order to protect a single target qubit. Adapted from [316].

This way, the resulting circuit optimization is an autonomous process that can account for specific information about the hardware when chosing the actions, e.g., some gates involve longer execution times, or a given qubit may be prone to further errors than others. In the future, quantum compilers will be able to optimize circuits tailored to the hardware specifications and native gate implementation.

6.6.5 Quantum error correction

Whenever we perform any kind of computation, we have to ensure that it is performed flawlessly. In both classical, and quantum computation, we require a mechanism to mitigate any possible effect of errors occurring during the computation. Whereas classical error corrections methods have long been established, the current quantum error correction schemes come with a daunting overhead in the number of qubits. Moreover, classical correction schemes cannot be transferred directly to the quantum case, since we can neither simply copy arbitrary quantum states (known as the no-cloning-theorem [321]) nor measure the quantum computer's state arbitrarily to find possible errors, as we would erase the state's superposition. Some error correction implementations tackle these challenges using RL methods. Here, we discuss two different approaches.

Error correction with qubit interaction The first one proposes a suitable error correction scheme from scratch, simply interacting with a collection of qubits [316], as sketched in fig. 6.8. This approach treats the actual hardware as a black-box, and therefore it is versatile regarding the hardware's constraints, as it does not require any prior knowledge about the

task. In this setting, the goal is to preserve an arbitrary single-qubit state, $|\phi(0)\rangle = \alpha |0\rangle + \beta |1\rangle$, over time. In order to do so, the agent can choose to apply gates from a given set, or to perform measurements on auxiliary qubits. This way, any hardware limitation can readily be incorporated by a suitable choice of the avilable gates, which conforms the action space. Then, we can measure the performance in terms of the fidelity $F = |\langle \phi(T)|\phi(0)\rangle| \in [0, 1]$ after some arbitrary, but fixed time T.

However, a naive RL approach is bound to fail when we only consider the fidelity as the reward. Almost all possible circuit transformations reduce the fidelity, thus making random strategies worse than remaining idle. This happens even when considering the fidelity after each new gate or measurement, as the optimal scheme initially decreases the fidelity, and applies a recovery sequence to restore it afterwards. Hence, the chance of finding the right gate sequence to protect the state vanishes for large times T. In order to overcome these challenges, the authors in Ref. [316] propose a two-stage learning scheme, and a more convenient reward function.

> The two-stage learning consist of training two models. First, we train an RL agent which has access to enhanced information with respect to what it is available in an actual device, such as a full description of the multi-qubit state. This also allows us to use a more convenient reward function: the *recoverable quantum information*
>
> $$r_t = \frac{1}{2} \min_{\vec{n}} \|\hat{\rho}_{\vec{n}}(t) - \hat{\rho}_{-\vec{n}}(t)\|_1, \tag{6.53}$$
>
> where $\vec{n}$ denotes the vector in the Bloch sphere corresponding to the initial state. This reward uses the idea that $\vec{n}$ and $-\vec{n}$ are orthogonal to provide a reward at every time-step that guides the agent toward the optimal gate sequence. See [316] for details.
> Then, we train the second model using the first one as a teacher. The second model only has access to the information available in a real device, such as the gates it applies, and the occasional measurement outcomes. Instead of using RL, we train it in a supervised way to mimic the behavior of the first one. The process is analogous to training a supervised classifier in which the labels are the actions of the first model.

The overall process of two-stage learning is way faster, and much less computationally demanding than directly solving the original problem. The main limitation is that the teacher model requires a full state description of the multi-qubit system, which limits the application to just a few qubits, and requires a well-characterized noise map of the device that might not be known, in practice.

Error correction with stabilizer codes Whereas the first approach aimes at discovering the best error correction scheme from direct qubit interaction, the second one implements a quantum code to represent logical qubits [322]. The implementation in this example uses stabilizer codes to achieve error correction via redundancy. In order to properly understand the process, let us build some basic intuition about the stabilizer formalism. Consider a precursory code to correct arbitrary single bit flips of the physical qubits, $|0\rangle \leftrightarrow |1\rangle$ with the encoding

$$|0_L\rangle = \frac{1}{\sqrt{2}} (|000\rangle + |111\rangle)$$

for a single logical qubit state $|0_L\rangle$ in terms of three physical qubits. We can jointly measure subsets of qubits without changing the state with *stabilizer operations*. In this case, we can apply the operations $Z_1 Z_2$, and $Z_2 Z_3$ without altering the qubit state: $Z_1 Z_2 |0_L\rangle = |0_L\rangle = Z_2 Z_3 |0_L\rangle$. Moreover, we can use these operators to detect bit-flip errors on one of the physical qubits,

as the stabilizer operators are designed to not alter the erroneous state either.[22] The stabilizer measurements have an outcome of ± 1, and applying them successively we can identify whether any qubit suffered an error to proceed with the correction. The series of outcomes is known as the *syndrome*, and, in practice, these can also have errors.

In this example, we can deal with single bit-flip errors, but not with phase errors represented by Z_i operators. For the error correction of arbitrary single-qubit errors, we need five physical qubits with four stabilizer operations [323]. The amount of qubit overhead grows quickly with the number of qubit error classes to cover. The stabilizer code in Ref. [322], is a surface code to protect a single logical qubit against arbitrary errors affecting up to d qubits while using, at most, d^2 physical ones.

To properly perform error correction, we need a combination of accuracy, scalability, and speed to detect and correct errors. We can formulate this as an RL task [322, 324, 325] implementing the full toolbox introduced in this chapter. In the setting from [322], the environment tracks the underlying quantum state, accounting for possible stochastic errors on the physical qubits in the form of depolarizing and bit-flip noise. The agent can choose to perform single-qubit X-, Y-, or Z- rotations,[23] or to perform syndrome measurements. Then, the environment provides the agent with the (possibly faulty) measurement outcome, and a reward, from which the agent can decide the new set of actions to perform. The environment employs a *referee decoder* that checks whether the multi-qubit state after the agent's actions leads to the same logical qubit state. If it is the case, the reward is positive, otherwise, it is negative and the episode terminates.

> The authors in Ref. [322] consider an agent based on a DQN which they train with Q-learning algorithm, as we explain section 6.2.3. After training, the average lifetime of the encoded logical qubit can be extended drastically as shown in fig. 6.9.
> Furthermore, they implement an alternative genetic algorithm within the described framework that results into significantly smaller ML models, which are better suited to run in actual devices.

6.6.6 Quantum experiment design

The design of new experiments is key for the development of the quantum sciences. The more complex the applications become, the harder it is to find suitable setups to test our ideas. In the context of quantum physics, this can be illustrated in an optical experiment, where we combine different components such that the final quantum state has certain desired properties. For instance, finding the appropriate set of components to create multipartite entanglement in high dimensions is a non-trivial task, and usually relies on sophisticated previous knowledge on the states, and involved mathematical approaches. Nonetheless, such states are of great importance in applications of quantum information and computation, and hence they are highly coveted.

In Ref. [302], the authors propose an autonomous approach to build experiments with RL, using the PS algorithm that we introduce in section 6.5. The goal is to create high-dimensional many-particle entangled states, based on the orbital angular momentum of light. To do so, the agent has access to a set of optical elements, and the actions consist on placing one of such components in the optical table. The states are the different configurations of optical com-

---

[22]In practice, we would first devise a set of stabilizer operators, and then, we would define the logical 0 and 1 states as the simultaneous eigenstates of all of the stabilizers.

[23]Given that XZ = iY, we can reduce the action space in certain cases.
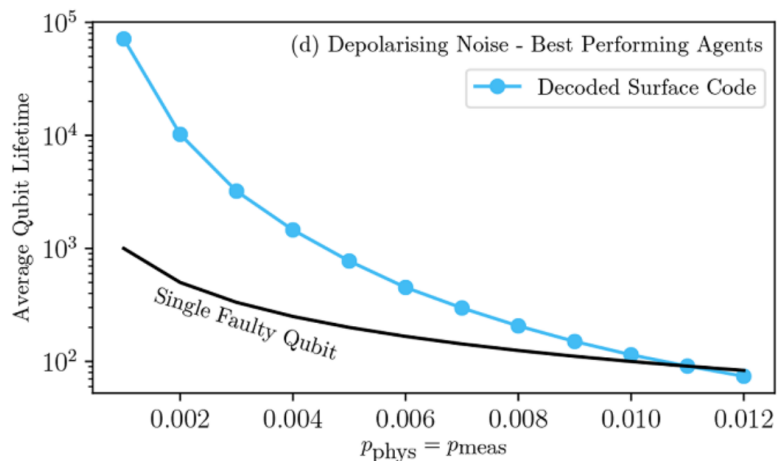
Figure 6.9: Average lifetime of the logical qubit encoded with the surface code. The physical qubits are affected by depolarising noise with parameter p_{phys} that drastically decreases the unprotected qubit lifetime (black line). With agents trained on various noise levels, p_{phys}, we can dramatically increase the qubit lifetime (blue dots). Taken from [322].

ponents in the table. After each placement, the environment analyzes the resulting quantum state generated by the setup. If it corresponds to the desired quantum state, it provides the agent with a reward and the episode ends. If not, the agent continues placing more elements. It is important to note that, due to the presence of noise in optical setups, the more elements, the harder it becomes to correctly find the target quantum state. Hence, the agent is given a maximal number of elements to reach its goal, after which the episode ends and the table resets.

From a technical point of view, the agent has a 2-layer ECM: one representing the table configurations (states), and one representing the optimal components (actions). An interesting feature of PS is *action composition*: the agent can create new composite actions from simpler ones that where found useful in previous episodes. In the current context, if the agent finds a particular profitable action sequence leading to a reward, the actions can be added combined as a new single one in the ECM, hence allowing the agent to access rewarded experiments in a single decision step. This way, the agent can distill combinations of components that lead to well known setups, such as optical interferometers, as well as completely novel ones, such as a non-local version of the Mach-Zender interferometer.

Hence, we can divide the general task of generating quantum states in two: finding the simplest optical configuration leading to the target state, and finding as many experiments as possible that produce it. The former is crucial in terms of practical applications of quantum technologies, as shorter experiments are less noisy, and usually easier to implement. The latter allows us to explore to the full extent all possibles solutions to the problem, which may lead to the discovery of new approaches to create the desired quantum states.

6.6.7 Building optimal relaxations

In physics we often encounter optimization tasks that we cannot solve in a reasonable amount of time. In these cases, we rely on approximate methods to obtain solutions that are as close as possible to the exact one. There are two paradigmatic approaches: variational and relaxation methods. In the former, we parametrize a family of solutions with the hope that it contains the exact one, such as the variational quantum states introduced in chapter 5. In the latter, we
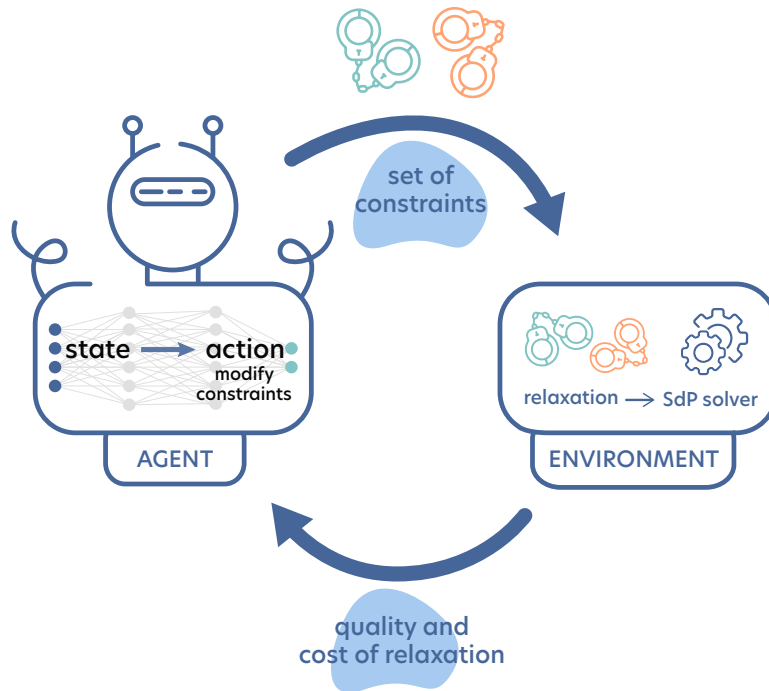
Figure 6.10: Schematic representation of the RL framework to find optimal relaxations. The agent can modify the set of active constraints of a problem with its actions. These constraints go into the environment, which solves the constrained optimization problem. Then, the agent observes a reward that depends on both the result of the problem and the computational cost incurred by the environment. Given this observation, it can decide to further modify the constraints.

build a relaxed (easier) version of the problem in order to provide the optimization process with desirable properties, such as convexity.

Relaxation methods are broadly used in quantum physics and they lie at the core of quantum information processing. One of the most paradigmatic examples in entanglement theory is the relaxation from the set of separable states to those that are positive under partial transposition (PPT) [326]. Determining whether a state belongs to the first class is hard, whereas it is straightforward to check the membership to the second one. This greatly simplifies the problem of determining whether a state is entangled: we simply need to check it is not PPT. However, while all the product states are PPT, there are some entangled states which also belong to this class, thus resulting into an outer bound to the set of separable states.

Just like with variational methods, we often encounter a trade-off between the computational cost that we can incur and the accuracy of the method. Hence, given a limited computational budget, it is crucial to find the relaxation that best approximates the optimal solution. Nevertheless, there is no clear way to know such optimal relaxation beforehand. The most common practice relies on exploiting specific knowledge of the given problem, such as symmetries, to build hand-crafted relaxations which, in general, are suboptimal. However, we can combine RL with semidefinite programming to systematically build optimal relaxations [327].

A natural way to build relaxations is to remove or relax constraints of the optimization

problem at hand. In the proposed RL framework, presented schematically in fig. 6.10, the states encode the active constraints of the problem and the agent can loosen or strengthen them with its actions. The environment acts as a black box that provides the agent with the associated reward to the action and the new state, i.e., the new set of constraints. The rewards are engineered to guide the agent toward the optimal relaxation, evaluating both the quality and the cost associated to the current one.

The RL agent is completely agnostic to the problem. Therefore, the method can be applied in a wide variety of relevant problems in physics and optimization, such as building entanglement witnesses, optimizing outer approximations to the quantum set of correlations or finding better sum-of-squares representations of multivariate polynomials, to name a few. In Ref. [327], the authors show a particular application to find the ground state energy of quantum many-body Hamiltonians. They can infer properties of the system from the resulting optimal relaxations, such as changes in the ground state, and, even more, they can explore the phase diagram in an autonomous way using transfer learning.

6.7 Outlook and open problems

In this chapter, we have introduced the field of RL and its main paradigms, featuring value-based RL (section 6.2), policy gradient methods (section 6.3), and actor-critic algorithms (section 6.4). Additionally, we have explored other methods that present an alternative approach to RL, such as the PS algorithm (section 6.5). These lay down the conceptual foundations to understand a whole plethora of other advanced RL techniques, while already being competitive, as we show in section 6.6.

In the context of quantum technologies, RL has been widely applied to quantum control problems. Specially, in quantum simulation, and with the current boom in quantum computation, many problems involving state preparation, error correction, or controlling and preparing qubits have a natural mapping to the RL framework. Furthermore, RL serves as an optimization tool for large problems with a clear structure, with applications as varied as quantum circuit optimization, the design of optical experiments, or the construction of relaxations in quantum information processing problems.

Similar to unsupervised learning, RL is an appealing technique for autonomous scientific discovery, as it does not require explicit fully-characterized learning instances. However, while we can identify some previously known strategies in the resulting RL applications, as in the section 6.6.4 example, there is still the need to develop further analysis techniques in order to fully understand the nature and rationale behind some of the most prominent results.

A big concern in the field of RL algorithms is data efficiency, which is crucial in applications involving costly experiments or simulations. In this regard, the field of RL can greatly benefit from the latest advances in physics, such as devising optimal exploration strategies for the most challenging problems, or leveraging the latest advances in quantum technologies to enhance RL, as we show in section 8.2.7.

Further reading

- Sutton, S. R. & Barto, A. G. (2018). Reinforcement Learning: An Introduction. This textbook provides a comprehensive review on RL [271]. Specifically, chapters 7 and 12 expand the TD concept, and chapter 13 contains a full complementary derivation of policy gradient, actor-critic, and their application to continuing problems (infinite time).

- Marquardt, F. (2021). *Machine learning and quantum devices*. SciPost Phys. Lect. Notes 29. An introduction to RL for physicsts [314].

- Silver, D. *et al.* (2014). *Deterministic policy gradient algorithms*. PMLR, 387–395 [328]. We have introduced policy gradient methods in section 6.3 with stochastic policies. Here, the authors introduce policy gradient with deterministic policies and its corresponding implementation in actor-critic algorithms.

- Some of the current state-of-the-art algorithms, such as the ones we mention at the end of section 6.4, feature additional terms in the objective function, usually in the form of an entropy or a Kullback-Leibler (KL) divergence. This results into more robust algorithms, and it is tightly close to the formulation of RL as probabilistic inference. We recommend reading Ref. [329] for a tutorial, Ref. [330] for a prominent algorithm, and Ref. [331] for another algorithm, featuring a great overview of the field, which recently proved its performance in experimental control [332].

7 Deep learning for quantum sciences – selected topics
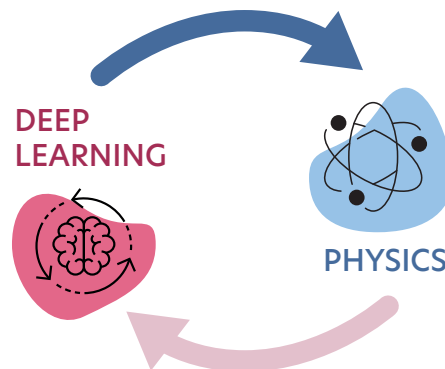
Figure 7.1: There exists a dual relationship between machine learning (ML) and physics. In this chapter, we focus on the more popular direction, where techniques from ML, in particular deep learning (DL), are used to solve problems in physics.

So far, these Lecture Notes have focused on four broad fields at the intersection of quantum sciences and ML: phase classification with unsupervised and supervised ML methods in chapter 3, use of kernel methods especially in quantum chemistry in chapter 4, representation of quantum states with ML models in chapter 5, and use of reinforcement learning (RL) in quantum sciences in chapter 6. We have presented each of these ideas in detail after a (hopefully) exhaustive introduction. As such, chapter 3 through chapter 6 have highlighted a plethora of ML applications in quantum sciences. However, they obviously do not constitute a complete overview of the field.

To fill these gaps, the following two chapters aim at addressing more specialized topics located at the intersection of ML and quantum sciences. This chapter, in particular, discusses further how ML can be used to solve problems in quantum sciences (see fig. 7.1). We start by explaining the concept of differentiable programming (∂P) and its use cases in quantum sciences in section 7.1. Section 7.2 describes generative models and how they can tackle density estimation problems in quantum physics. Finally, we describe selected ML applications for experimental set-ups in section 7.3.

7.1 Differentiable programming

Differentiable programming (∂P) represents a fundamental shift in software development that emerged from DL [333]. In "standard" programming each instruction is explicitly specified in the code, i.e., one specifies a point in *program space* with some desirable behavior (see fig. 7.2). In ∂P computer programs are instead composed of parametrized elements of code (such as an NN) which are then tuned to minimize a given loss function using derivative information. Here, the programmer only specifies the desired behavior of the program (e.g., to correctly classify a given image or to win a game of Go) via a loss function. The program space is then searched for a program with the desired behavior by tuning the code parameters.

In most real-world problems, collecting data – instances in which a given task has been correctly solved, reproducing the output of an ideal program – is easier than writing a program that solves the task. Under these circumstances ∂P shines, as demonstrated by the success of programs generated through deep learning. There have been many instances where ∂P lead to algorithms which even outperformed humans, such as in AlphaGo [20].

∂P also has multiple other advantages compared to conventional programming. One aspect regards the possibility to develop customized optimization strategies. The typical instruction set of NNs consists of matrix multiplication, vector addition, element-wise application of nonlinearities: such a set is limited and much smaller compared to the instruction set associated with the entire class of standard computer programs. In the future, this will allow us to move programs which are based on parametrized elements that are tuned via gradient-based optimization much closer to silicon, i.e., design hardware that is optimized for the limited instruction set underlying ∂P. Note that such considerations already lead to the design of graphics processing units (GPUs) and tensor processing units (TPUs), which are examples of application-specific hardware.

∂P also allows for more flexible programming: consider the situation where you had standard code that performs a certain task and someone wanted you to make it twice as fast, possibly at the expense of its accuracy. This would be a highly non-trivial task. However, it is easy to incorporate such constraints by means of a cost function and hyperparameters in ∂P. For example, given that one uses an NN this could be accomplished by cutting the network's size in half and retraining it. Moreover, consider the situation where programs which were first optimized or coded individually are merged together in a modular fashion to create a new larger program. Then, ∂P offers an easy solution for optimizing the performance of this new program: simple fine-tuning of the individual components in the given configuration through optimization. The benefits of ∂P come at the cost of program interpretability. At the end of the optimization we obtain code that works well, but which is very hard to read for a human and understand in intuitive terms. As such, we typically are left with the choice between a fairly accurate model that is understandable in human terms, and a more accurate model that is difficult to interpret.[1]

Recently, widespread interest in ∂P has arisen in the area of scientific computing [334].

> In ∂P, arbitrary computer program structures can be differentiated in an automatic fashion. Importantly, this allows for NNs to be embedded into a plethora of existing scientific simulations and computations, because the gradients required for training the NNs can be computed efficiently. In particular, one can differentiate through the NN, as well as surrounding non-parametrized/non-trainable parts of the program.

Examples for algorithms which have been written in a fully differentiable way are Fourier transforms, eigenvalue solvers, singular value decompositions, or ordinary differential equations (ODEs) [335, 336]. As such, one is able to differentiate through domain-specific computational processes to solve inverse problems, such as learning or control tasks: Tensor networks [337–339], molecular dynamics [340, 341], quantum chemistry [342–348], quantum optimal control [349–359], or quantum circuits [360, 361] have all been formulated in a fully-differentiable manner. We discuss several examples in detail in section 7.1.2.

Notably, ∂P enables scientific ML which combines the best of two worlds: in general, black-box ML approaches are flexible but require a large amount of data to be trained successfully. The amount of required data can be reduced by incorporating our scientific knowledge on the structure of a problem into the program. The training of the parametrized program part is then enabled via ∂P. This allows for the learning task to be simplified because only the parts of the model that are "missing" need to be learned.

Perhaps the biggest feat of ∂P is the ability to compute gradients of loss functions with

---

[1]Again, interpretability appears as a central issue (see section 3.5).
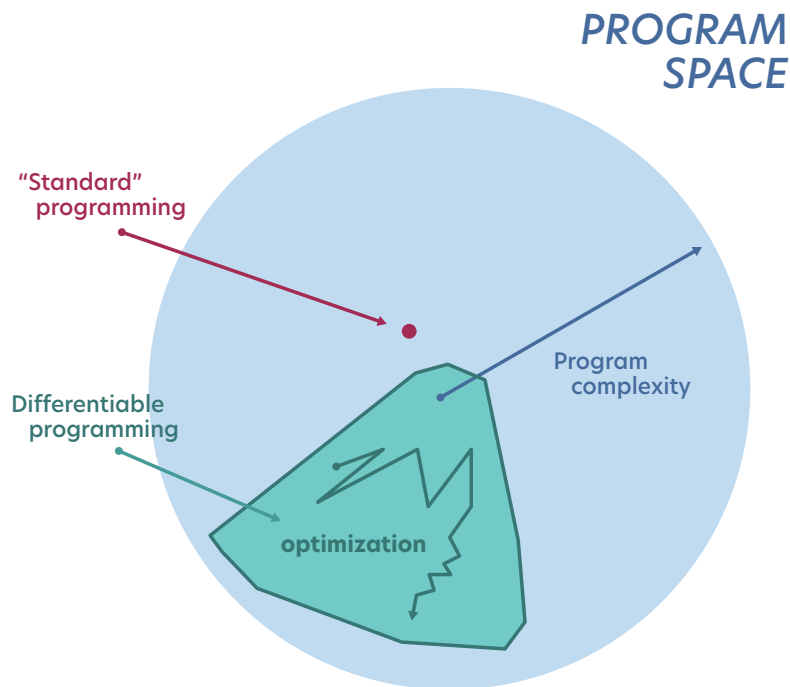
Figure 7.2: Illustration of the difference between "standard" programming and differentiable programming. In some cases, the complexity of programs found by ∂P exceeds human capabilities. Adapted from [333].

respect to NN parameters. Recall that we require these gradients for NN training when using gradient-based optimizers (as is typically done), see section 2.1. Crucially, the computation is efficient, precise, and occurs in an automated fashion. In particular, it allows for arbitrary NN architectures to be differentiated automatically without implementation overhead. Compare this to the tedious computation of analytical gradients which needs to be performed again given different NN architectures.

However, ∂P is not restricted to the computation of gradients with respect to NN parameters for NN training. It enables the automatic computation of gradients and higher-order derivatives of arbitrary program variables. These can, for example, be tunable parameters of a Hamiltonian whose ground state we are interested in. Being able to differentiate through the eigensolver, we can tune the Hamiltonian's parameters via a derivative-based optimizer such that its ground state satisfies desired properties (as specified by a loss function), see section 7.1.2 for details. This is an example of an *inverse problem* which can be solved efficiently through ∂P. However, the applicability of ∂P goes beyond solving optimization tasks. Gradients and higher-order derivatives contain highly valuable information on the relationship between model parameters and outputs which can, e.g., facilitate the interpretation of phase classification methods [134] (see section 3.5.3) or help to characterize variational quantum circuits [362].

7.1.1 Automatic differentiation

∂P allows us to compute the gradients and higher-order derivatives of arbitrary computer programs.

> In general, methods for the computation of derivatives in computer programs can be classified into four categories [363]: (1) manually working out derivatives and coding them, (2) numerical differentiation using finite difference approximations, (3) symbolic differentiation using expression manipulation,[a] and (4) automatic differentiation (AD) which is the workhorse behind ∂P.
>
> ---
>
> [a]This is done by computer algebra systems such as `Mathematica`, `Maxima`, or `Maple`.

Let us briefly discuss these different approaches.

Manual differentiation is time consuming and prone to errors. *Numerical differentiation* is quite simple to implement. Its most basic form is based on the limit definition of a derivative: given a multivariate function $f : \mathbb{R}^m \to \mathbb{R}$, the components of its gradient $\nabla f = (\frac{\partial f}{\partial x_1}, \ldots, \frac{\partial f}{\partial x_m})$ can be approximated as

$$\frac{\partial f}{\partial x_i}\bigg|_{\boldsymbol{x}} \approx \frac{f(\boldsymbol{x} + h\boldsymbol{e}_i) - f(\boldsymbol{x})}{h}, \tag{7.1}$$

where $\boldsymbol{e}_i \in \mathbb{R}^m$ is the i-th unit vector and h is a small step size. Approximating ∇f in such a fashion requires $\mathcal{O}(m)$ evaluations of f. This is the main reason why numerical differentiation is not useful in ML where the number of trainable parameters m can be as large as millions or billions. Also note that for the gradient approximation to be somewhat accurate, the step size h needs to be carefully chosen: while the truncation error of the approximation in eq. (7.1) can be made arbitrarily small as $h \to 0$, eventually round-off errors due to floating-point arithmetic dominate the calculation.[2]

Symbolic differentiation is the automated manipulation of mathematical expressions for obtaining explicit derivative expressions, e.g., by using simple derivative rules such as the product rule

$$\frac{d}{dx}(f(x)g(x)) = \frac{df(x)}{dx}g(x) + f(x)\frac{dg(x)}{dx}. \tag{7.2}$$

Symbolic expressions have the benefit of being interpretable and allow for analytical treatments of problems. However, symbolic derivatives generated through symbolic differentiation typically do not allow for efficient calculation of derivative values. This is because they can quickly get substantially larger than the expression whose derivative they represent. Consider a function of the form $h(x) = f(x)g(x)$ and its derivative, which can be evaluated by the product rule in eq. (7.2). Note that $f(x)$ and $\frac{df(x)}{dx}$, for example, appear separately in such an expression. A naive calculation of the derivative according to eq. (7.2) thus involves duplicate computations of any expressions that appear both in $f(x)$ and $\frac{df(x)}{dx}$. Moreover, manual and symbolic methods require the underlying function to be defined in a closed-form expression. As such, they cannot easily deal with programs that involve conditional branches, loops, or recursions. That means, for symbolic differentiation to be efficient there must exist a convenient symbolic expression for computing the derivative under consideration.

When we are concerned with the accurate numerical evaluation of derivatives and not their symbolic form, it is possible to significantly simplify computations by storing the values of intermediate sub-expressions in memory. This is the basic idea behind automatic differentiation (AD). AD provides numerical values of derivatives (as opposed to symbolic expressions) and it does so by using symbolic rules of differentiation (but keeping track of derivative values,

---

[2]In computing, floating-point numbers are typically represented approximately through a fixed number of significant digits that are scaled through an exponent in some fixed basis $a \times b^c$, where a, b, and c are all integers. Because of the limited number of representable numbers, round-off errors can occur when performing computations.
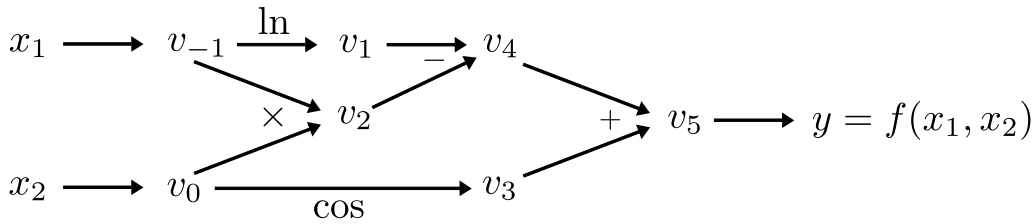
Figure 7.3: Computation graph associated with the forward evaluation trace of $f(x_1, x_2) = \ln(x_1) + \cos(x_2) - x_1 x_2$.

as opposed to the entire symbolic expression). As such, it may be viewed as an *intermediate between numerical and symbolic differentiation*. AD makes use of the fact that every computer program, no matter how complicated it may look, simply executes a sequence of elementary arithmetic operations (e.g., additions or multiplications) and elementary functions (e.g., exp or sin). We refer to the sequence of elementary operations that a computer program applies to its input values to compute its output values as *evaluation trace* [364]. The derivative of every computer program can therefore be computed in an automated fashion through repeated application of the chain rule. As such, the number of arithmetic operations required to compute the derivative are on the same order as for the original program. Moreover, this results in derivatives which are accurate up to machine precision. In the following we illustrate how AD is done in practice.

Forward-mode AD Conceptually, AD in so-called *forward-mode* is the simplest type. Consider the evaluation trace of the function

$$f(x_1, x_2) = \ln(x_1) + \cos(x_2) - x_1 x_2 \tag{7.3}$$

given in table 3(left). The associated computation graph is shown in fig. 7.3, where the computation of a function f is decomposed into variables v_i. We follow the standard notation used in Ref. [365], where v_{1-i}, $i = 1, \ldots, n$ are the input variables, v_i, $i = 1, \ldots, l$ are intermediate variables, and v_{l+i}, $i = 1, \ldots, m$ are output variables. For computing the derivative of f with respect to x_1, we start by associating with each variable v_i a derivative

$$\dot{v}_i = \frac{\partial v_i}{\partial x_1}. \tag{7.4}$$

Applying the chain rule to each elementary operation in the evaluation trace, we generate the corresponding derivative trace, given in table 3(right). In forward-mode AD the desired derivative $\dot{v}_5 = \frac{\partial y}{\partial x_1}$ (where y is the output variable) is obtained by computing the intermediate variables v_i in sync with their corresponding derivatives $\dot{v}_i$.

This can be generalized to the computation of the full Jacobian of a function $f : \mathbb{R}^m \to \mathbb{R}^n$ with m input variables x_i and n output variables y_j. In this case, each forward pass of AD is initialized by setting $\dot{x}_i = 1$ for a single variable x_i and zero for the rest. That is, we choose $\dot{x} = e_i$ where e_i is the i-th unit vector. The forward pass with given input values $x = a$ then computes

$$\dot{y}_j = \left.\frac{\partial y_j}{\partial x_i}\right|_{x=a} \quad \text{for } j = 1, \ldots, n. \tag{7.5}$$

$v_{-1} = x_1$	$= 2$	$\dot{v}_{-1} = \dot{x}_1$	$= 1$
$v_0 = x_2$	$= 1$	$\dot{v}_0 = \dot{x}_2$	$= 0$
$v_1 = \ln v_{-1}$	$= \ln 2$	$\dot{v}_1 = \dot{v}_{-1}/v_{-1}$	$= 1/2$
$v_2 = v_{-1}v_0$	$= 2$	$\dot{v}_2 = \dot{v}_{-1}v_0 + v_{-1}\dot{v}_0$	$= 1$
$v_3 = \cos v_0$	$= \cos 1$	$\dot{v}_3 = -\dot{v}_0 \sin v_0$	$= 0$
$v_4 = v_1 - v_2$	$= -1.307$	$\dot{v}_4 = \dot{v}_1 - \dot{v}_2$	$= -1/2$
$v_5 = v_3 + v_4$	$= -0.767$	$\dot{v}_5 = \dot{v}_3 + \dot{v}_4$	$= -1/2$
$v_5 = y$	$= -0.767$	$\dot{v}_5 = \dot{y}$	$= -1/2$

Table 3: Workflow for computation of derivatives in forward-mode AD given the function $f(x_1, x_2) = \ln(x_1) + \cos(x_2) - x_1 x_2$. Left: Forward evaluation trace for the choice of initial inputs $(x_1, x_2) = (2, 1)$. Right: Forward derivative trace resulting in the computation of $\frac{\partial f}{\partial x_1}$ at $(x_1, x_2) = (2, 1)$.

This corresponds to the i-th column column of the Jacobian matrix

$$J_f = \begin{bmatrix} \frac{\partial y_1}{\partial x_1} & \cdots & \frac{\partial y_1}{\partial x_m} \\ \vdots & \ddots & \vdots \\ \frac{\partial y_n}{\partial x_1} & \cdots & \frac{\partial y_n}{\partial x_m} \end{bmatrix}\Bigg|_{x=a}. \tag{7.6}$$

Thus, the full Jacobian can be computed in m forward passes, i.e., m evaluations of the function f. As such, forward-mode AD is efficient if $m \ll n$. In the other limit, so-called reverse-mode AD is preferred which we discuss shortly.

In practice, forward-mode AD is implemented by augmenting the algebra of real numbers and introducing a new arithmetic: to every number one associates an additional component which corresponds to the derivative of a function computed at that particular value. We call this composite number a *dual number*

$$\text{dual}(v) = v + \dot{v}\epsilon, \tag{7.7}$$

where $\epsilon \neq 0$ is a number such that $\epsilon^2 = 0$. The extension of all arithmetic operators to dual numbers allows for the dual number algebra to be defined. Observe, for example, that

$$f(\text{dual}(v)) = f(v) + \dot{f}(v)\dot{v}\epsilon, \tag{7.8}$$

where we obtain the function value in the first part and the corresponding derivative $\dot{f}(v)\dot{v}$ in the ϵ part.[3] This follows from expanding the function in its Taylor series and noting that terms $\mathcal{O}(\epsilon^2)$ vanish due to the property that $\epsilon^2 = 0$. Equation (7.8) resembles the computation of the derivative using the chain rule.

Reverse-mode AD As the name suggests, in reverse-mode AD the derivatives are propagated backwards from a given output.[4] This is in contrast to forward-mode AD where we saw that the derivatives are propagated forwards in sync with the function evaluation. Reverse-mode AD is done by complementing each intermediate variable v_i with a so-called adjoint

$$\bar{v}_i = \frac{\partial y_j}{\partial v_i}, \tag{7.9}$$

---

[3]Under the hood dual numbers are typically handled through so-called operator overloading, i.e., overloading all functions to work appropriately on the new algebra.

[4]Historically, reverse-mode AD can be traced back to the master thesis of Seppo Linnainmaa in 1970 [366] in which he described explicit, efficient error backpropagation in arbitrary, discrete, possibly sparsely connected, NN-like networks [367].

where y_j is the output variable with respect to which we desire to compute derivatives. In reverse mode AD, derivatives are computed in the second phase of a two-phase process. In the first phase, the original function code is run forward: intermediate variables v_i are populated and their dependencies in the computational graph are tracked through a bookkeeping procedure. In the second phase, derivatives are calculated by propagating adjoints $\bar{v}_i$ in reverse, i.e., from the outputs to the inputs. This is illustrated in table 4 for the function given in eq. (7.3), where the reverse pass is started with $\bar{v}_5 = \bar{y} = \frac{\partial y}{\partial y} = 1$. As a result, we obtain both $\bar{x}_1 = \frac{\partial y}{\partial x_1}$ and $\bar{x}_2 = \frac{\partial y}{\partial x_2}$ in a single reverse pass.

$v_{-1} = x_1$	$= 2$	$\bar{v}_5 = \bar{y}$		$= 1$
$v_0 = x_2$	$= 1$			
$v_1 = \ln v_{-1}$	$= \ln 2$	$\bar{v}_4 = \frac{\partial v_5}{\partial v_4}\bar{v}_5 = \frac{\partial v_3 + v_4}{\partial v_4}\bar{v}_5$		$= 1$
$v_2 = v_{-1} v_0$	$= 2$	$\bar{v}_3 = \frac{\partial v_5}{\partial v_3}\bar{v}_5$		$= 1$
$v_3 = \cos v_0$	$= \cos 1$	$\bar{v}_2 = \frac{\partial v_4}{\partial v_2}\bar{v}_4$		$= -1$
$v_4 = v_1 - v_2$	$= -1.307$	$\bar{v}_1 = \frac{\partial v_4}{\partial v_1}\bar{v}_4$		$= 1$
$v_5 = v_3 + v_4$	$= -0.767$	$\bar{v}_0 = \frac{\partial v_2}{\partial v_0}\bar{v}_2 + \frac{\partial v_3}{\partial v_0}\bar{v}_3$		$= -2.841$
		$\bar{v}_{-1} = \frac{\partial v_1}{\partial v_{-1}}\bar{v}_1 + \frac{\partial v_2}{\partial v_{-1}}\bar{v}_2$		$= -1/2$
$v_5 = y$	$= -0.767$	$\bar{v}_0 = \bar{x}_2$		$= -2.841$
		$\bar{v}_{-1} = \bar{x}_1$		$= -1/2$

Table 4: Workflow for computation of derivatives in reverse-mode AD given the function $f(x_1, x_2) = \ln(x_1) + \cos(x_2) - x_1 x_2$. Left: Forward evaluation trace for the choice of initial inputs $(x_1, x_2) = (2, 1)$. Right: Reverse (adjoint) derivative trace resulting in the computation of $\frac{\partial f}{\partial x_1}$ and $\frac{\partial f}{\partial x_2}$ at $(x_1, x_2) = (2, 1)$.

This example illustrates the complementary nature of the reverse mode compared to the forward mode: The reverse-mode is cheaper to evaluate than the forward mode for functions with a large number of inputs, i.e., where $m \gg n$ with $f : \mathbb{R}^m \to \mathbb{R}^n$. As we just saw, in the extreme case of $f : \mathbb{R}^m \to \mathbb{R}$, only one application of the reverse mode is sufficient to compute the full gradient compared with the m passes of the forward mode. The typical case encountered in ML applications corresponds to the evaluation of the derivatives of a loss function $y_j = \mathcal{L} : \mathbb{R}^m \to \mathbb{R}$ with respect to m trainable parameters, where m is typically large. As such, reverse-mode AD is the preferred method for computing gradients automatically as it is computationally more efficient compared to forward-mode AD.[5] In the context of ML, in particular NNs, reverse-mode AD is typically referred to as backpropagation. It is the working horse behind NN training as it allows for efficient computation of the gradients for arbitrary NN-based architectures in an automated fashion. In the following, we discuss several ways how reverse mode AD is implemented in practice.

Static graph AD A basic implementation of reverse-mode AD makes use of static computation graphs. This choice is natural, given that we chose to illustrate reverse-mode AD using computation graphs [368]. Tensorflow is an example of a platform which uses this approach. Here, the user must define variables and operations in a graph-based language. Subsequent executions of the computation graph allow for the program to be differentiated in a straightforward

---

[5]Note that forward-mode and reverse-mode AD are just two (extremal) ways of applying chain rules. Finding the optimal way to traverse the chain rule to compute a Jacobian for a given function (i.e., the choice which results in the smallest number of arithmetic operations) is known as the optimal Jacobian accumulation problem and is NP-complete.

manner. However, this requires all existing programs to be rewritten as a static computation graph which is inconvenient.

Tracing-based AD   This can be circumvented by building computation graphs *dynamically* at runtime which is achieved by "tracing" all the operations encountered in the forward pass given a particular input [368]. Dynamic computation graphs are the basis of many reverse-mode AD implementations in Julia (Tracker.jl, ReverseDiff.jl, or Autograd.jl) or Python (PyTorch, Tensorflow Eager, Autograd [JAX]). The fact that it is simple to implement makes this approach widely adopted in practice. An issue of such tracing-based implementations is that each trace is value-dependent, meaning that each run of a program (with different inputs) can build a new trace. Moreover, these traces can be much larger than the code itself, for example, because loops are completely unravelled.

Source-to-source AD   In source-to-source AD one overcomes these issues by generating source code for the backward pass that is able to handle all input values [368]. In particular branches, loops, and recursions are not explicitly unrolled. The right branch in the reverse pass through recall of the intermediates values used in the forward pass. It turns out that the implementation of a source-to-source AD system poses many requirements on the underlying language.[6] Source-to-source AD is used in programming languages such as Julia (Zygote.jl).[7]

High-level adjoint rules   The advantages of reverse-mode AD in ML applications come at the cost of increased storage requirements which (in the worst case) is proportional to the number of operations in the evaluated function. This is because the values of the intermediate variables populated during the forward pass need to be stored when using reverse-mode AD, whereas they can be directly used for the derivative computation within forward-mode AD. Improving storage requirements in reverse-mode AD implementations is an active research area. In general, reverse-mode AD can be made more efficient by deriving adjoint rules at a higher level. Consider, for example, the case where your program involves solving a non-linear problem $f(x, p) = 0$ with an iterative method, such as Newton's method. A naive application of the reverse-mode AD system results in a backward pass through all iteration steps. Not only is this computationally expensive, but also requires storing the values of all intermediate iteration steps. Instead of unrolling the entire computation, one can analytically derive an appropriate adjoint rule which can be used to compute the derivatives in reverse-mode via a separate linear equation. In particular, it only requires knowledge of the final solution x of the non-linear problem as opposed to values in the intermediate iterations. For further details, see Ref. [189,335]. Other examples for which adjoint rules can be derived also include ODEs [336,356,368,369] and eigenvalue solvers [335]. In case of ODEs, for example, the adjoint rule involves solving a second, augmented ODE backwards in time.

7.1.2   Application to quantum physics problems

In this section, we illustrate the application of $\partial \mathrm{P}$ to problems from quantum physics through two simple examples.

Inverse Schrödinger problem   As a concrete example of an inverse-design problem, we consider the time-independent Schrödinger equation in one dimension

$$\left[-\frac{1}{2}\frac{d}{dx^2} + V(x) \right] \Psi(x) = E\Psi(x), \tag{7.10}$$

---

[6]In particular, it should possess a strong internal graph structure.

[7]TensorFlow considered building a source-to-source AD based on the Swift language. Older AD systems for Fortran were also source-to-source.
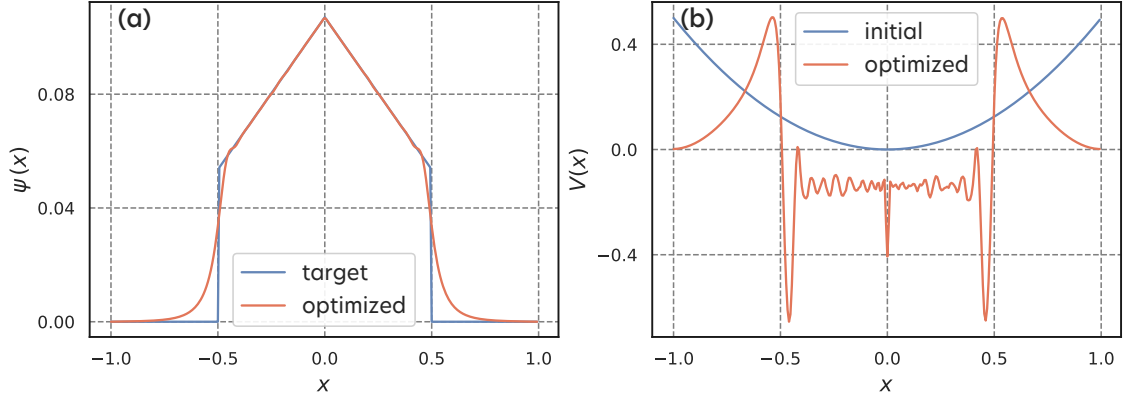
Figure 7.4: (a) Optimized ground-state wave function $\Psi_0(x)$ after ≈ 1000 iterations of the L-BFGS algorithm with box constraints (L-BFGS-B) given the target wave function $\Psi(x) = 1 - |x|$ with $|x| < 0.5$. (b) Optimized potential $V(x)$ (rescaled by $1/300$) and the initial harmonic potential. Figure reproduced from [370].

where we set $\hbar = m = 1$ [335]. Typically, we are given a potential $V(x)$ and solve for the corresponding eigenfunctions Ψ and energies E. Here, we consider the inverse problem. Given a particular wave function $\Psi(x)$ we want to construct a potential $V(x)$ with a ground-state wave function $\Psi_0(x)$ that closely matches $\Psi(x)$. We restrict ourselves to the domain $x \in [-1, 1]$ and define the following mean-squared error (MSE) function

$$\mathcal{L} = \int_{-1}^{1} |\Psi(x) - \Psi_0(x)|^2 dx. \tag{7.11}$$

The potential $V(x)$ is discretized on a grid and each individual amplitude is tuned using gradient-based optimization methods in order to minimize eq. (7.11). An implementation of this problem in JAX can be found at [370]. The results are illustrated in fig. 7.4. Here, the gradient is calculated by the AD system underlying JAX and involves propagating the derivative through the eigenvalue solver. For more details on ∂P applied to inverse-design problems in quantum mechanics and adjoints for eigensolvers, see Ref. [371].

Quantum optimal control Next, we consider a problem from quantum optimal control. We would like to find the time-dependent amplitudes $\{u_i(t)\}$ of the following Hamiltonian

$$\hat{H} = \hat{H}_0 + \sum_{i=1}^{n_{\text{ctrl}}} u_i(t) \hat{H}_i, \tag{7.12}$$

such that the time-evolution under $\hat{H}$ realize a CNOT gate. Here $\hat{H}_i$ with $i \in [1, n_{\text{ctrl}}]$ are time-independent Hamiltonians that can be tuned through the time-dependent amplitudes $\{u_i(t)\}$. We parametrize these amplitudes using Fourier series $u_i(t) = \sum_{j=1}^{n_{\text{basis}}} u_{ij} \sin(\pi j t/T)$, where we introduce n_{basis} as a cutoff enabling numerical evaluations. To find the gate which a given choice of $\{u_i(t)\}$ implements we integrate the time-dependent Schrödinger equation from 0 to T under initial conditions $U(0) = \mathbb{1}$ with

$$\frac{dU}{dt} = -i\hat{H}(t)U, \tag{7.13}$$

where we set $\hbar = 1$. Ideally, $U(T)$ realizes a CNOT operation ($U_{\text{target}} = \text{CNOT}$). Hence, we setup our loss function as

$$\mathcal{L} = 1 - \frac{1}{d} |\text{tr}(U(T)^\dagger U_{\text{target}})|, \tag{7.14}$$

where d is the dimension of the associated Hilbert space. Note that when $U(T) = U_{\text{target}}$ we reach the global minimum of $\mathcal{L} = 0$. The coefficients $\{u_{ij}\}$ are tuned to minimize the loss function in eq. (7.14) using gradient-based optimization methods. An implementation of this problem in JAX can be found at [372], where the gradient is calculated via AD in JAX and involves propagating the derivative through the ODE solver (eq. (7.13)). For more details on differentiable programming applied to quantum optimal control, see Refs. [117, 350].

Outlook and open problems

In this chapter, we have introduced the novel programming paradigm that is ∂P. Most notably, ∂P enables NNs training via the efficient, precise, and automated calculation of the corresponding gradients. Having the ability to differentiate arbitrary computer programs, in addition, allows for NNs to be seemingly incorporated in scientific workflows. By now there are many applications of ∂P in scientific computing, including quantum physics. However, the field is still in its infancy and many open problems remain to be tackled. For instance, finding efficient high-level adjoint rules for algorithms used in quantum physics problems, such as solvers for stochastic dynamics, is still a current topic of research [359]. Another example are chaotic systems for which standard AD methods can fail [373, 374]. The development of AD systems is also still an ongoing effort: In Enzyme.jl [375], for example, the idea is to perform reverse-mode AD on the portable, low-level intermediate representation of Julia which is language-agnostic. This allows for performance improvements due to low-level optimizations. NiLang.jl [376] on the other hand tries to build a reverse-mode AD system based on the paradigm of reversible programming. Running the program in reverse in the backward pass allows the overhead in memory in standard reverse-mode AD to be circumvented.

Further reading

- Baydin, A. G. *et al.* (2018). *Automatic differentiation in machine learning: a survey*. J. Mach. Learn. Res. 18(1), 5595–5637. Good overview on AD in the context of ML [363].

- Innes, M. *et al.* (2019). *Differentiable programming system to bridge machine learning and scientific computing*. arXiv:1907.07587. Discussion on the role of ∂P in scientific computing [334].

- Google Colab notebooks by Lei Wang [370, 372].

7.2 Generative models in many-body physics

Deep generative models are (mostly) neural-network architectures designed to approximate the probability density underlying the system we aim to describe. In this section we revise some of the most relevant algorithms in the field. We mainly focus on autoregressive (AR) networks and normalizing flows (NFs). With deep generative models, one often associates the term *density estimation* which similarly refers to the construction of the probability density function underlying a given problem [377]. The difficulty of this task comes from the fact that the relevant probability density functions cannot be dealt with analytically in most cases. For a large class of cases, these problems can be attributed to the difficulty of calculating normalization constants (i.e., partition functions in statistical mechanics). As such, one often has to resort to different methods and techniques which approximate the underlying probability density functions.

Throughout this manuscript, one encounters a variety of instances of density estimation tasks in quantum physics. For example, finding a variational representation of quantum-many

body system wave function can be viewed as a density estimation task, see chapter 5. More generally, in quantum physics the concept of density estimation often appears in the context of reconstructing the many-body state from measurements performed on a quantum many-body system – a task known as *quantum state tomography*, which is described in more detail in section 5.3.7. This is particularly challenging, because only a reduced set of quantities are experimentally accessible, such as single-body density matrix, or higher-order correlation functions [378–380]. Moreover, the corresponding experiment can be very demanding, and a single experimental run can take a long time (i.e., hours or days). As such, one is faced with the task of estimating a high-dimensional probability density function given a small number of measurements of a restricted set of observables.

In general, one can think of two different approaches to density estimation: *parametric* and *non-parametric* density estimation. In parametric approaches, one fixes a parametrized functional form for the density. The free parameters are then tuned such that the trial density best matches the density of the system under consideration. This can be done by comparing the trial density against training data, which corresponds to observations drawn from the target density, or against an unnormalized target probability density (e.g., an unnormalized Boltzmann distribution). A simple example of a parametrized trial density would be a Gaussian, where its mean and variance can be adjusted accordingly. In parametric approaches, one reduces the problem of finding an appropriate density function to the problem of finding appropriate parameters. Clearly, the choice of functional form of the density is crucial for the success of this approach, as it can (potentially) restrict the family of target densities which can be approximated well.

In contrast, in non-parametric approaches to density estimation the structure of the trial density function is not set *a priori*.[8] Instead, a trial density function is directly constructed based on the training data. The simplest example of a non-parametric approach to density estimation corresponds to the construction of a histogram. Clearly, histogram binning comes with some drawbacks. For example, one must carefully choose the size and location of bins. Moreover, histograms are non-differentiable functions. In general, non-parametric methods rely on less knowledge about the system at hand compared to parametric methods. While this makes non-parametric methods robust and generally applicable, they typically also require more samples to reach a given level of accuracy.

In recent years, several new methods for density estimation have emerged from the interplay of ML and physics based on learning an approximate density underlying a given physical system. These approaches are typically parametric in nature: the parameters $\boldsymbol{\theta}$ of a suitable variational (parametric) ansatz for the trial density $p_{\boldsymbol{\theta}}$ are optimized systematically to match the target density p. A natural way to achieve this is based on the MLE principle, where a likelihood function is maximized (or equivalently, a log-likelihood is minimized) by optimizing the parameters $\boldsymbol{\theta}$ (see eq. (2.26)). For a given data set of independent observations $\mathcal{D} = \{\boldsymbol{x}\}$, the loglikelihood function of the model is defined as

$$\ell(\boldsymbol{\theta}|\mathcal{D}) = \log\left[\prod_{\boldsymbol{x} \in \mathcal{D}} p_{\boldsymbol{\theta}}(\boldsymbol{x})\right], \tag{7.15}$$

where $p_{\boldsymbol{\theta}}(\boldsymbol{x})$ is the probability assigned to each independent observation of the system $\boldsymbol{x}$. The observations $\mathcal{D}$ can, for example, refer to a set of spin configurations $\boldsymbol{x}$ drawn from an Ising model at a fixed temperature. As a parametrization for the trial density function, one can choose an NN. The fact that NNs are universal function approximators (see section 2.4.4)

---

[8]The trial density functions in non-parametric approaches to density estimated do not completely lack parameters. It simply means that the parametrization of the trial density functions is not fixed in advance.

makes this ML-based approach to parametric density estimation very powerful. In this context, the approximation capabilities of NNs guarantee that any target densities can be approximated well.

The optimization based on the MLE principle requires training data. However, in some cases data may not be readily available, because it is difficult or expensive to generate. For such cases, the data-driven procedure described above may not be optimal – in particular because NNs typically require a generous amount of data to be trained. To this end, we discuss an alternative approach to density estimation, sometimes referred to as *Hamiltonian-driven approach*, which is based on encoding physical laws and physical prior knowledge of the system into the learning process. Let us consider the Ising model, for example. We know the Hamiltonian of the system and we know that spin configurations $\boldsymbol{\sigma}$ are distributed according to a properly normalized Boltzmann distribution,

$$p(\boldsymbol{\sigma}) = e^{\frac{-H(\sigma)}{k_{\mathrm{B}}T}}/Z\,. \tag{7.16}$$

In practice, the partition function Z is difficult to compute, as it involves a summation over all possible spin configurations [9]. However, one can use the knowledge that the system follows a Boltzmann distribution to efficiently train an ML model which approximates the target density $p(\boldsymbol{x})$ successfully. In this case, one does *not need training data*. The parameters are optimized to minimize the so-called *reverse* Kullback-Leibler (KL) divergence

$$\mathrm{KL}(p_{\boldsymbol{\theta}}||p) = \int_{\mathcal{D}} \log \frac{p_{\boldsymbol{\theta}}(\boldsymbol{x})}{p(\boldsymbol{x})} d\boldsymbol{x}, \tag{7.17}$$

where $\mathcal{D}$ is the relevant integration domain. This quantity measures the discrepancy between the target density and the trial density.[10] Minimizing the KL divergence is equivalent to minimizing the variational free energy. As such, one could see the optimization through KL divergence minimization as being an equivalent formulation for the variational principle in statistical mechanics [78, 79]. Given a trial density function that can be efficiently sampled, eq. (7.17) can be approximated using Monte Carlo integration. The ratio $p_{\boldsymbol{\theta}}(\boldsymbol{x})/p(\boldsymbol{x})$ can be efficiently computed, because the normalization constant inside the logarithm becomes a constant shift and does not need to be computed when training the variational ansatz $p_{\boldsymbol{\theta}}$. For example applications of this approach in the context of lattice physics, see [79, 381, 382]. For a general overview, see [383, 384].

The remainder of this chapter is structured as follows. In the next section, we introduce deep generative models for density estimation based on several examples. Afterwards, we analyze a few of those in more depth, putting additional emphasis on normalizing flows (NFs) in the last paragraph of section 7.2.2.

7.2.1 Deep generative models

The tools of choice for density estimation and synthetic data generation are the so-called generative neural sampler (GNS), sometimes also referred to as deep generative models. Generative neural samplers include amongst other NFs [385], ARNNs [386], VAEs [387], generative adversarial networks (GANs) [388, 389]. These methods represent a very important assortment of the whole plethora of ML algorithms, especially when it comes to unsupervised learning. The usual setting where they are deployed is when, given a set of data, one wants to learn (or approximate) the underlying probability density of such training data. This way,

---

[9]In eq. (7.16) σ is used to indicate the general configuration of a spin system. In the remainder of the section the more general variable **x** is used to indicate the point at which the probability density is evaluated.

[10]Note that this metric may lead to some pathological behavior, mentioned briefly in section 2.3.

one is then able to generate new artificial samples resembling the true ones. For instance, if we give to a GNS a stack of images of dogs, once trained, we expect this to generate unseen images of dogs. Thus what happens in practice is that the algorithm learns the salient, yet recurrent, features which are more important to shape something which looks like a dog. Images are just a prominent example, but of course this idea can be broadly applied, especially to physics. In physics, though, we have one further advantage. Sometimes we have to deal with systems of which we know the underlying density up to a normalization factor (e.g., the partition function in the Boltzmann distribution of a thermodynamic system). As such, we can deploy such tools in a slightly different way, dealing better with the problem at hand. Therefore, we can follow two distinct approaches when it comes to apply GNS to physics problems. The first option is to naively learn from data (e.g., data configurations) in order to learn how to generate seemingly reasonable unseen configurations, the same approach we would use with dog images. This way we could infer something on the underlying structure of the physical systems. For instance, we can learn the underlying density to generate new configurations and relate such density to a theoretical distribution. Doing so, one could infer on some order parameters (i.e., critical exponents) or the temperature at which the training configurations were generated (or measured experimentally). The second approach, instead, relies on some prior knowledge of the system. For example, we may know the underlying density we try to approximate is a Boltzmann-like distribution with some unknown normalization factor. Leveraging on this information we can structure the learning problem in a slightly different fashion though the goal remains the same: to estimate the underlying target density of the system at hand.

As mentioned above, there are many tools which fall under the category of GNSs and all of them come with different features and are suitable for different situations. As such, neural samplers can be divided into two categories: the ones which give access to a *tractable density*, i.e., thus allowing to compute $p(x)$ for any x in polynomial time in the system size N, and the ones which do not. Under the latter category we find GANs. With GANs we can generate artificial samples looking like the training data. These algorithms consist of two agents trained within a game theoretic context: a generator network learns how to produce (realistic) samples to fool a discriminator network which task is to recognize whether a samples is real or artificially generated. The joint optimization of those two agents makes the generator more and more capable of generating realistic samples. This approach works well in practice but unfortunately does not allow access to tractable densities. In turn, GANs work if we want to generate unseen configurations but do not allow much more than that. In Ref. [390] the authors used a GAN to enhance Markov chain Monte Carlo (MCMC) methods in lattice simulations. The second category of GNS refers to those algorithms which instead allow access to exact (or approximate) sampling probabilities along with normalized (or unnormalized) densities. Under this category we find: autoregressive neural networks (ARNNs) [78–82] and recurrent neural networks (RNNs) [216, 224], restricted Boltzmann machines (RBMs) [391], and latent variable models such as variational autoencoders (VAEs) and normalizing flows (NFs) [381, 382, 392]

In the remainder of this section, we provide examples on how to deploy three kind of deep generative models with some applications. Our focus is on ARNNs and RNNs (already introduced in section 2.4.6), and NFs.

7.2.2 Applications and examples

Autoregressive models As previously mentioned in chapter 5, one can resort to a certain class of models called autoregressive (AR) models for the task of density estimation. The main advantage in using an AR model is that it enables for (i) uncorrelated and (ii) fast [393] sampling. The samples are uncorrelated because thanks to the AR structure of the probability
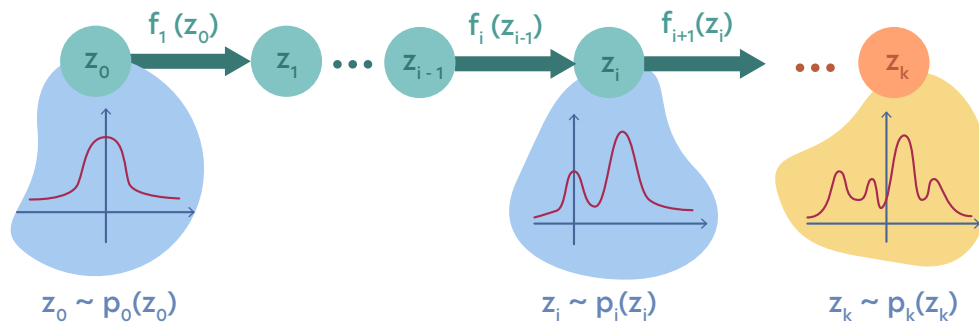
Figure 7.5: Sketch of a normalizing flow (NF) architecture. A sequence of bijective transformations is combined in order to achieve a complex non-linear invertible transformation which describes the probability mass transport from a base distribution toward a learned density which would, upon training, approximate the target density of the problem at hand. The learned density is tractable and properly normalized which enables fast yet efficient sampling.

distribution, a direct sampling algorithm can be performed, rather than MCMC whose performance is hindered by the correlation of the samples and can severely fail in the case of multimodal distributions (where different blobs of probability are far apart in the configuration space). Direct sampling with AR models goes as the following: sample state x_1 from $p_\theta(x_1)$, then sample from $p_\theta(x_2|x_1)$ and so on until x_N. Direct sampling from a probability distribution over an exponentially large configuration space (e.g., if the x_i are binary variables) is possible with AR models, and makes them extremely powerful. The sampling can also be made faster as many samples can be processed in parallel in a single pass. Note that imposing an AR structure on a model constrains it: for instance, to build a deep CNN one must introduce masked layers (to keep the AR structure), which alter the representability of such models.

Recurrent neural networks A general introduction to RNNs is provided in section 2.4.6 and we refer the reader to that section for a more comprehensive introduction. RNNs are a special type of AR models, among which one can find a plethora of sub-models, such as the Long-Short Term Memory (LSTM) and the Gated Recurrent Unit (GRU). The latter has been used in the context of ground state search [216]. In the context of statistical mechanics, an RNN model has been applied to difficult problems such as spin glasses. These models are typically hard to sample, therefore the direct sampling helped in reaching a high accuracy in a simulated annealing task [224].

Normalizing flows NFs are an ML algorithm that learns complicated probability densities from data or (when unavailable) unnormalized probability densities (see [385, 394] for a review). Recently, many works applying flows in the field of lattice physics have been proposed [381, 382, 392]. NFs rely on the very simple idea of the change of variables formula. They work as follows: first they sample a latent random variable from a tractable, known distribution (e.g. a normal or uniform one). Successively, a bijective mapping under specific constraints is learned. This map transforms the probability mass of the base distribution toward a new one which approximates the target density we want to model. By leveraging the change of variable formula, one can thus obtain a variational approximation of the target density, properly normalized and easy to handle. We refer to fig. 7.5 for a sketch of an NF architecture.

In a normalizing flow (NF), rather than mapping one density to another, we define a diffeomorfic transportation map which redistribute the probability mass from an easy-to-treat base distribution to a more complicated target one.

We now dive into the mathematical intricacies of NFs in the remainder of this section. Let us assume we have a set of unlabelled data x of which we want to learn the underlying density. To make it practical, let us be more specific and assume to have a set of lattice configurations (irrespective of the physical system, spin glass, lattice field theory and so forth). One may know that these configurations are distributed according to a normalized density (e.g. Boltzmann like distribution $p = Z^{-1} \cdot e^{-H[x]}$) although its normalization factor Z, known as the partition function, is generally not tractable and easy to compute. Hence, to access the probability density of a given configuration, even knowing the unnormalized distribution $\hat{p} = e^{-H[x]}$ is not an easy task. NFs can overcome this issue by learning an efficient approximation of p properly normalized and fully tractable. Now that we have the problem outlined, let us go back to our configurations. We define a latent variable $z \in \mathbb{R}^D$ distributed according to a known easy to treat distribution. A common choice is a normal Gaussian $q_0 = \mathcal{N}(0, 1) : \mathbb{R}^D \rightarrow \mathbb{R}^D$. The task of NFs is now to learn a bijective mapping between the data space and the latent space which transforms the probability density of the given base distribution $\mathcal{N}$ into a variational density q_{θ} which should approximate the target density p. The approximation ansatz q_{θ} is parametrized by a set of parameters θ which are optimized during training, see fig. 7.5 for a visual representation of this scheme. We know where we start and where we want to get. What is left now is to construct the bijective transformation and see how the parameters are encoded into such a map. Let us define an invertible and differentiable transformation $f_{\theta} : z \rightarrow x = f_{\theta}(z)$ with inverse $f^{-1}(x) = g(x) = z$. In other words, what learning this f does in practice is to redistribute the probability mass of some random signal into some complex unknown target density. In the context of generative models, one says that the function f "pushes forward" the base density q_0 to a more complex density q_{θ}. Once the mapping is learned, one can generate a new data point x^* by sampling in the latent space from the base distribution $z \sim q_0$ and apply the bijection to obtain a corresponding sample in the data space. Reversely, one can also take a sample, plug it into the inverse of f and thus obtain the probability density of such sample as a function of the base distribution and the Jacobian of the transformation. More specifically:

$$q_{\theta}(x) = q_0(f_{\theta}^{-1}(x)) \left| \frac{df_{\theta}}{dz} \right|^{-1}. \tag{7.18}$$

where f_{θ} is invertible by assumption. By applying the change of variable theorem one can obtain eq. (7.18) with $x \sim q_{\theta}$. In order to make such transformation more general yet flexible, one can write f_{θ} as a composition of many transformations (known as coupling blocks) all of which should be to invertible and differentiable and parametrized with their own subset of parameters θ_i. The general composite transformation then reads:

$$f_{\theta}(z) = \left(f_{\theta_N} \cdots \circ f_{\theta_i} \circ \cdots \circ f_{\theta_1} \right)(z). \tag{7.19}$$

In order to make the learning process smooth and efficient one additional requirement is that the determinant of the Jacobian of such transformation should be tractable and efficient to compute since it enters in eq. (7.18) and is used to estimate the approximated density of a given sample. We refer the reader to the above mentioned review paper on NFs for details about how to build these transformations. By training our NF, we train the joint set of parameters for all the different transformation (or coupling blocks) f_{θ_i}. Given a set of data observed from some complicated distribution, $\mathcal{D} = \{x^{(i)}\}_{i=1}^n$, we can then perform likelihood-based estimation of

the parameters. The data log-likelihood in this case simply reads:

$$\log p(\mathcal{D}|\boldsymbol{\theta}) = \sum_{i=1}^{n} \log q_\theta(\boldsymbol{x}_i|\boldsymbol{\theta}). \tag{7.20}$$

Minimizing this objective optimizes the set of $\boldsymbol{\theta}$ such that $q_{\boldsymbol{\theta}}$ matches as close as possible with the target density p. Let us now go back to the practical problem as stated above. One goal of density estimation is to be able to generate configurations for a physical system. One way this is usually done, is by means of MCMC. However, as one might know, these chain have some pathological behavior in the presence of phase transitions as the samples generated by such chains become highly correlated and the generative process by means of MCMC shows exploding autocorrelation times [395, 396]. To phrase it differently, the samples obtained by MCMC when a phase transition is involved may not be that reliable. One should now be able to foresee where the advantages of NFs come into play. Under certain circumstances, not difficult to be realized in practice, a flow trained in a particular point in parameter space, is completely agnostic to the region of the phase space at which it is sampling. As such, when sampling from a trained flow, no matter where, one always efficiently samples highly decorrelated configurations for the system at hand. For a more detailed yet mathematical description of how flows work in practice the reader is once again referred to the review paper [385]. As a last further example in the domain of quantum field theory is presented in Ref. [382]. In this application, no data are required but the NF is trained by optimizing a different objective known as reverse KL divergence eq. (7.17). Leveraging on the fact that one knows the Hamiltonian of the system we want to investigate, one consequently knows the shape of the unnormalized underlying Boltzmann density.

Outlook and open problems

As stated above in the recent years NFs have become the most promising tool to address the problem of density estimation in the physical sciences. However, many challenges still need to be faced. First and foremost volume scaling is currently the main issue. All the promising results achieved so far by deploying such tool in the context of lattice field theory, for instance, have been proved only on relative small lattices. One would expect that approaching the continuum limit, hence scaling the volume of a lattice up to a reasonable shape, would have a serious impact on the flow performance. One way to tackle this problem would be to leverage more on the physical knowledge by incorporating existing symmetries into flow so that the network does not have to learn the physics from scratch. The paper [397, 398] gives a nice overview on how this can be applied. Another relevant challenge briefly mentioned above is the problem of mode collapse. This has been analyzed in Refs. [383, 384] and is currently an open problem not only in the domain of NFs in physics but also in the entire ML community. Having a multi-modal distribution to model makes the learning problem much more complex as the algorithm may perfectly cover one mode of such distribution but completely neglect the others being stuck there. As such, when sampling from the learned variational density, we would never cover the full statistics of the underlying density. This is a relevant problem especially in this context as it may hard to detect in some scenarios and at the same time be very harmful when it comes to a accurate estimation of some observables.

Further reading

- Wang, L. (2018). *Generative models for physicists* [399].

- Noe, F. *et al.* (2019). *Boltzmann generators*. Science, 365, eaaw1147. Application of normalizing flows (NFs) in the context of quantum chemistry [400].

- Nicoli, K. A. *et al.* (2021). *Machine learning of thermodynamic observables in the presence of mode collapse*. arXiv:2111.11303 [384]. Hackett, D. *et al.* (2021). *Flow-based sampling for multimodal distributions*. arXiv:2107.00734 [383]. Overviews on the problem of mode collapse.

- Köhler, J. *et al.* (2020). *Equivariant flows*. arXiv:2006.02425 [397], Satorras, V. G. *et al.* (2022). *E(n) equivariant normalizing flows*. arXiv:2105.09016 [398]. Incorporating symmetries into normalizing flows (NFs).

- Albergo, M. S. *et al.* (2021). *Flow-based sampling for fermionic lattice field theories*. Phys. Rev. D, 104, 114507. Using normalizing flows (NFs) in the context of fermion densities [401].

7.3 Machine learning for experimental data

Performing quantum experiments poses tough technical challenges and the task of optimizing their performance while interpreting the output data can seem daunting. It is informative to note that the output of quantum devices naturally generates large-scale data in whose regime ML thrives. In chapter 3, we have already seen how ML can be used to detect phases, and while such efforts are much more challenging when dealing with experimental data, a few works managed to successfully address this real-world problem [96, 402, 403]. In section 5.3.7 we have also demonstrated how ML can boost quantum tomography with NQSs presented in chapter 5. Another research direction pursued in the context of quantum experiments is the application of RL for quantum feedback control, quantum error correction, quantum circuit, and experiment design, all described in sections 6.6.3 to 6.6.6.

This section focuses on three other ML approaches for experimental data. Firstly, we acknowledge that there is an important niche of experimental physics that can be revolutionized by ML, i.e., automation of (tedious) repetitive tasks. We show examples of successful realizations of this idea with actual experimental data in section 7.3.1. In section 7.3.2 we discuss the theoretical proposal of ML-based analysis of time-of-flight images which pose the standard measurement technique in ultracold-atom setups. We conclude this section with describing a powerful scheme for quantum experiments, i.e., learning the Hamiltonian governing the system in section 7.3.3.

7.3.1 Automation of experimental setups

This section is devoted to novel ideas for automation of physical experiments. Specifically, we present the automated identification of nanomaterial samples for quantum device technologies [404] and the automated tuning of double quantum dots [405] for quantum information devices. Both of these examples have one thing in common: at some point in the execution of their respective experiments, a large amount of human labor becomes necessary that is tedious and repetitive with respect to the decision making process a worker employs but not trivial enough to be replaced by a simple looping algorithm.

Automated identification of nanomaterials In the case of the preparation of nanomaterials for quantum devices as detailed in Ref. [404], an important step is the selection of appropriate two-dimensional flakes from a wafer under a microscope. The flakes in question can differ depending on their desired use in the final device, but they all share their flat shape and approximate size due to the exfoliation-based technique with which they are prepared beforehand. Examples include hexagonal boron-nitride (hBN), graphite and bilayer-graphene. Figure 7.6 depicts the scanning setup along with a typical image for hBN. The microscope in a typical setup can operate at different magnifications and can scan a 1 cm^2 wafer in roughly three
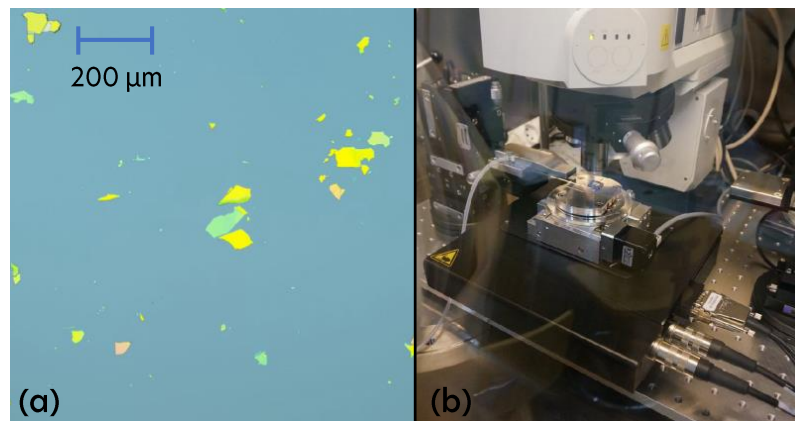
Figure 7.6: Experimental nanoflake setup. (a) A typical microscope image of hBN from Ref. [404]. (b) Typical microscope setup with waver already placed under the microscope. Photo credit: Klaus Ensslin Lab, ETH Zürich.

minutes. In practice, however, this takes much longer as the human operator has to slowly move the frame across the wafer and decide for each frame which of the depicted flakes are suitable for future device building. In short, the human operator classifies the flakes; a well-trained NN could do this as well. Hence, the design and training of a suitable NN architecture was at the core of the automation scheme developed in Ref. [404]. However, it is worth noting that the automation scheme did more than just the classification task as is summarized in fig. 7.7. For example, prior to even implementing anything network related, they provided the experimental team with a program with a simple GUI for click-based flake labeling of pre-processed images to simplify the generation of an adequate data set. This is pointed out here to truly reflect the additional steps that need to be taken into consideration when working with experimental setups.
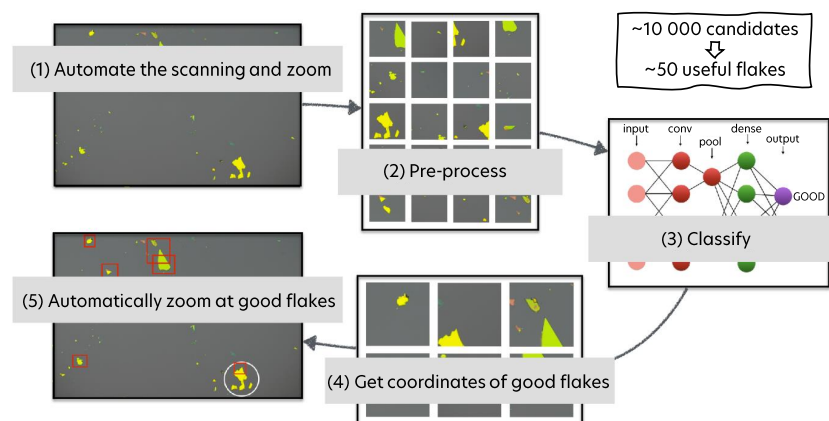
Figure 7.7: The full automation procedure consisted of scanning, *labeling*, pre-processing, *training*, classifying, and then collecting and presenting the good flakes. The steps marked with italics were done only prior to application. Figure credit: QMAI group at TU Delft.

In this work more than one network was used to minimize classification errors: Three networks were used and applied consecutively, each consisting of four convolutional layers and one dense layer. The reason this stacking of networks was necessary is the immense imbalance between good and bad flakes in the data set. While a batch optimization procedure
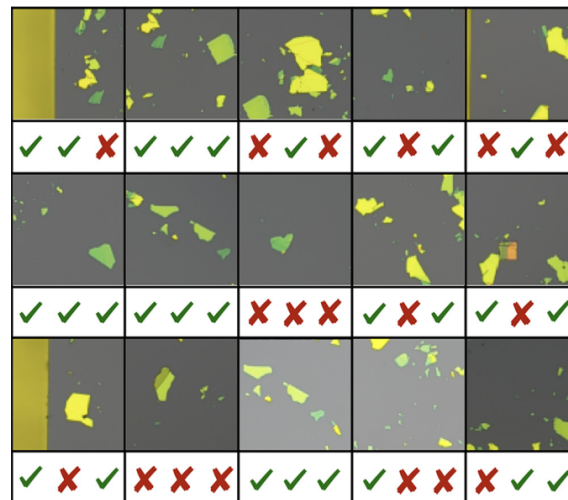
Figure 7.8: Differences of human judgement visualized. Selection of 15 frames that were to be judged on whether they contained good flakes or not along with the judgement results from three different human operators. Adapted from Ref. [404].

paired with data augmentation can usually account for this to some extent, here this was not sufficient: after passing new data that contained approximately 1000 flakes, 10.8% of which were good, through only one trained network, the classified results yielded the 86% accuracy with 13% of false positives (bad flakes classified falsely as good) and 1% of false negatives (good flakes classified falsely as bad). Since there are so few truly good flakes, avoiding false negatives is of utmost importance.

An important and more practical aspect of this number and accuracy of leftover "good" (correctly or incorrectly classified) flakes is concerned with the additional human labour that would follow this classification result: after classifying, the automation scheme (compare fig. 7.7) goes on to automatically zoom in on the good flakes after which a human operator steps in again. More specifically, this means that instead of manually scanning the probe, looking at the, e.g., 1000 flakes available and zooming in on the selected flakes in order to then decide whether they are good or not, in the automated scheme the human operator only acts after the entire wafer is scanned and the microscope is shifted to the different locations of the good flakes on which it appropriately zooms in. In this way, the experimentalist only makes the final decision on which flakes to use; this represents a substantial workload reduction from 944 flakes to 224, approximately 44% of which are actually good. However, since there is still work involved, three instead of one networks are used to reduce the amount of flakes that need to be looked at even further. After passing the data through all three networks only 150 flakes need to be looked at, approximately 57% of which are good.

One of the reasons why the accuracy is still comparatively low is due to the discrepancies of classification choices among the humans who did the labeling beforehand. Given that it was already time consuming enough to label a large enough data set even with the helpful GUI program written for that purpose, every flake was only labeled once by one of the many experimentalists taking part in this project. Figure 7.8 captures the differences in judgement of three different participants all looking at a selection of single shot frames. It is important to note that while here, we were able to explicitly show one source of uncertainty and errors in preparation of the data, usually we do not see it directly. We should always assume possibility of their existence! Evidently, there is a degree of uncertainty and disagreement about whether the individual frames contain good flakes which introduced a bound on the model

performance. This is reflected by the classification accuracy.

All in all, the developed automation procedure including and revolving around the NN is still clearly a success: this type of material control is a common step in the field of nanomaterial device development and the method generalizes satisfyingly to, e.g., graphite and bi-layer graphene (compare Ref. [404]). The implementation is available on GitHub [406].

Quantum dot tuning   The next example is the automated tuning of double quantum dots in quantum information technology research. A detailed discussion can be found in Ref. [405]. A quantum dot is a nanostructure that is confined so heavily in all three spatial dimensions that it is essentially zero dimensional. The confinement, similar to a particle-in-a-box scenario, leads to the emergence of quantum effects, i.e., energy quantization (as opposed to having a continuous energy spectrum in larger structures) and thus discrete states.

In quantum information research, quantum dots are used to create qubits by putting together two dots as discrete states. There are various reasons why this technology is challenging in the context of universal quantum computation: on the one hand, there are difficulties associated with making two dots interact in a controlled manner and, on the other hand, there are issues associated to reproducibility. Both concerns are related to the preparation techniques and the example discussed here offers a new ML-based remedy for the former.

Like in the previous example, the experimental procedure contains a tedious step that one can seek to automate. While in the flake example this step revolved around human operators looking at images from a probe under a microscope, in this quantum dot setup the human operator looks at graphs created from changes in current measurements in the quantum device with changing applied voltages. When conducting a measurement like this, the quantity of interest is the occupation of the quantum dots, i.e., the state of the quantum dot. The occupation can be changed by applying a voltage to the dot: as seen in fig. 7.9(a), every one of the three quantum dots has a plunger gate (PG) associated with it that is used to tune the voltage. Underneath these dots, the current of a quantum point contact is measured.[11] As defined in Coulomb's law, the occupation of the dots, i.e., the negative charge of the respective electrons, affects the electric current close to it. Hence, a change in the electron occupation causes a discrete change in the current flow which corresponds to spikes in the conductance ($\partial I_{\text{QPC}}/\partial V_{\text{PG}}$) measurement. Those spikes are the dark blue lines in the charge-stability diagram showcased in fig. 7.9(b). Figure 7.9(b) can then be interpreted as follows. At the bottom left corner, both quantum dots (QDs) are unoccupied but whenever a vertical (horizontal) line is crossed, an electron is added to QD1 (QD2).

The goal in the device preparation and tuning is to prepare different discrete states by applying the adequate voltages that corresponds to the correct current-spike-line framed, diamond shaped area in the charge-stability diagram. To do this, the operator needs the knowledge of the charge-stability diagram. Thus, tuning a double quantum dot device, such as this one, requires measuring the entire charge-stability diagram, i.e., performing many subsequent measurements where one voltage is kept constant and the other one is gradually changed. In this very time-consuming scenario a classification-based ML scheme can be of help. For ML to bring a significant improvement, it is essential that measuring the entire charge-stability diagram is not required for the input data. A suitable scheme should be able to produce the two plunger gate voltages for a specified desired occupation state from any starting state (corresponding to a starting pair of voltages along with their current flow). However, without the charge-stability diagram, there is no way of knowing which occupational state two starting

---

[11]The quantum point contact in fig. 7.9(a) is formed by the three gates at the bottom responsible for the measurement.
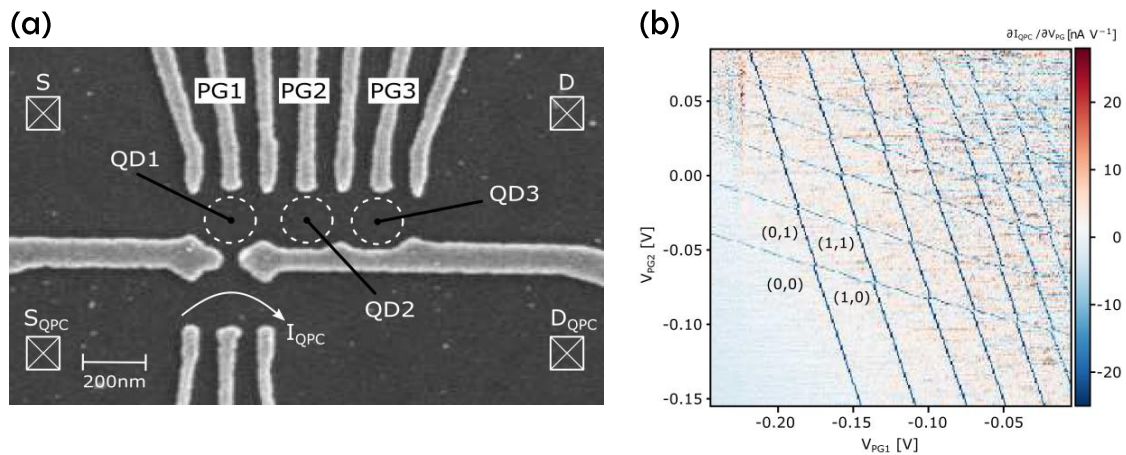
Figure 7.9: Experimental setup for quantum dots. The device is built and then tuned using measurements that are made possible by the quantum point contact built into it. (a) Scanning microscope image of an example device. Base material is a GaAs heterostructure with an electron gas embedded at the position where the three quantum dots (QD1, QD2, QD3) are intended to be. It also contains a number of finger gates for confinement and measurement. The gates responsible for the measurement are the three at the bottom (quantum point contact). (b) The charge-stability diagram for a double quantum dot device that uses QD1 and QD2 in (a). Correspondingly, the changed voltages are the ones for PG1 (corresponds to QD1) and PG2 (corresponds to QD2). Taken from Ref. [405].

voltages correspond to. For example, if the starting state had both voltages at $0\,V$, then a human operator with knowledge of fig. 7.9(b) would know that this places the state somewhere in the top right of the diagram and would, by means of counting lines, be able to specify the state.

To avoid having to measure the whole diagram, the ML scheme uses an approach for which small, low-resolution excerpts of the diagram suffice:

1. **Finding the (0,0) state:** In a first step, one utilizes the fact that any state except the (0,0) state is framed by four lines in the diagram, whereas the (0,0) state only has neighboring lines in the positive x- and y-direction. Therefore, a first classification network is trained to recognize whether there are more lines to cross in the negative x- or y-direction. The output is either true or false. If there are more lines, both plunger voltages are lowered by a set amount (as depicted in fig. 7.10(a)) and the classification is performed again until there are no more line to be crossed.

2. **Finding any desired, given state:** To get from the (0,0) state to any desired state (m,n), one has to cross *exactly* m vertical lines and n horizontal lines. Thus, a second network is now trained to more accurately classify which lines there are. This network uses smaller frames of a higher resolution that allow a more differentiated distinction between the cases of there being no lines, there being one vertical line, there being a horizontal line and there being both in the considered frame (compare fig. 7.10(b)). Just like in the first step, each classification is followed by a change in voltages and this 2-step procedure is repeated until the desired state is reached.
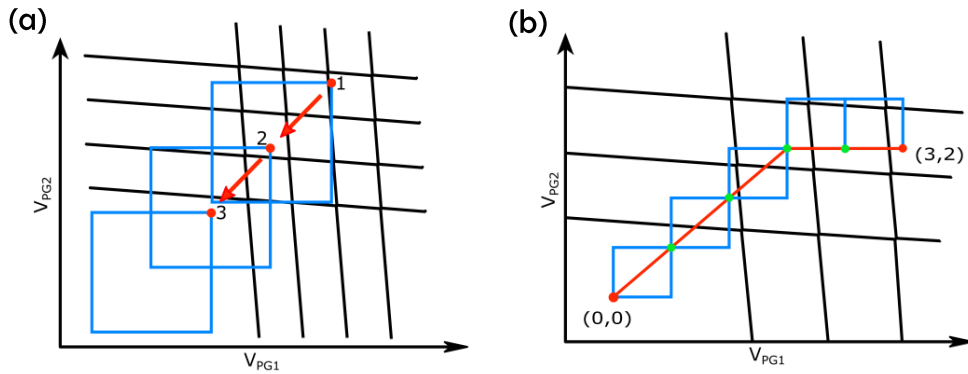
Figure 7.10: (a) Finding the (0,0) state using a first classification network: Starting at random initial voltages corresponds to point "1". In this example the network had to be run through three iterations of classification and frame shifting until (0,0), here marked by "3", was reached. (b) Finding the state of desired occupation (m,n): Depending on the different classification results the frame can be shifted either only to higher PG1 voltages (in case of one vertical line), only to higher PG2 voltages (in case of one horizontal line) or diagonally, increasing both gate voltages (in case of two lines). Adapted from Ref. [405].

For the training of the first network, 470 charge stability diagrams were measured in fairly low resolution, whereas for the second network 128 charge stability diagrams were measured in higher resolution. The plunger gate voltage ranges were varied for the different measurements to foster better generalization later on. In both cases, data sets were created by cutting out numerous random frames from the diagrams and labeling them with a script. Note that while full charge stability diagrams were measured for the generation of the training data set, the input for the eventual application of the network only needs the small windows. Measuring full charge stability diagrams and using many windows therein was just a convenient way to create a data set.

When testing on the actual device, the success rates of the two loops were 90% (step 1 loop) and 63% (step 2 loop) which combines to an overall success rate of 57%. It is important to keep in mind that those individual success rates are not the equivalents of the accuracy rates of the two networks: each loop calls the network multiple times, so errors are doomed to accumulate and the second loop usually requires more calls to the network than the first loop, because the frames are smaller, see panels (a) and (b) of fig. 7.10. In fact, when tested separately and only a single time on a labeled data set, the accuracy rates reached by the two networks were 98.9% and 96%. In the article, the authors stated that the primary error source was identified as a weak signal-to-noise ratio and improving on this would surely improve the scheme. In conclusion, the integration of deep networks into a larger scheme can lead to the accumulation of errors and this needs to be taken into consideration when planning the implementation of the automation routine. In general, the integration of ML gadgets into broader automation schemes call for different levels of network accuracy and, as it was the case in the first example, some scenarios might even have limited network accuracy overall. It is important to take these things into account ahead of the implementation and gauge the benefits of automation versus the remaining workload.
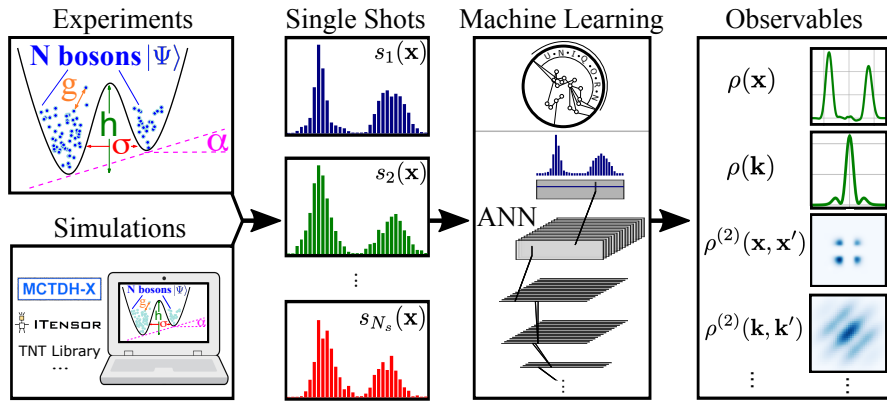
Figure 7.11: Implementing ML into the extraction of observables from measurements of ultracold atoms: Conventional experimental approaches are usually only able to extract the first and second order density matrix through averaging approaches, whereas the ML approach also extracts real space observables from momentum space measurements as well as correlation functions. Taken from Ref [407].

7.3.2 Machine-learning analysis of time-of-flight images

When it comes to analysis of experimental data, we present one more example related to ultracold-atom experiments. In contrast to the two highly specialized applications to actual experimental data discussed so far in section 7.3.1, we consider a proposal that is based on theoretical data but is readily extendable to experiments [407]. There is a number of theory-based, yet application-oriented proposals which are currently being published and discussing their differences should prove insightful. The focus of this discussion is to be put on the feasibility of making the transition from theory to application.

For any such transition from theory to experiment within an ML scope, the following aspects should be examined:

- *Specificity vs. flexibility of the method:* as was discussed in the two earlier examples, when the ML model does not provide truly new insights into the physics of the model, the automation should instead yield a significant reduction of human labour. This can either be achieved by designing a specific scheme for *one* scenario that requires a large expenditure of work or by designing a flexible scheme for a large number of scenarios of medium expenditure.

- *Similarity of theoretical and experimental results:* more often than not, theoretical models produce results that diverge quite significantly from their experimental counterparts. This can be due to experimental noise or limitations in the theoretical model. For a model that has been trained on theoretical results only, it is important to evaluate whether further pre-processing, such as the inclusion of artificial noise could be sufficient to prepare the network architecture for an input of experimental data and/or how much the network needs to be retrained.

Unlike the work done with quantum dots and flakes that utilized *specific schemes with high impact*, the scheme proposed now is very general and profits from the *flexibility* of the probed system: ultracold atoms. Due to the high level of control available in such setups, ultracold atoms represent an exemplary quantum simulator for a large variety of few to many-body
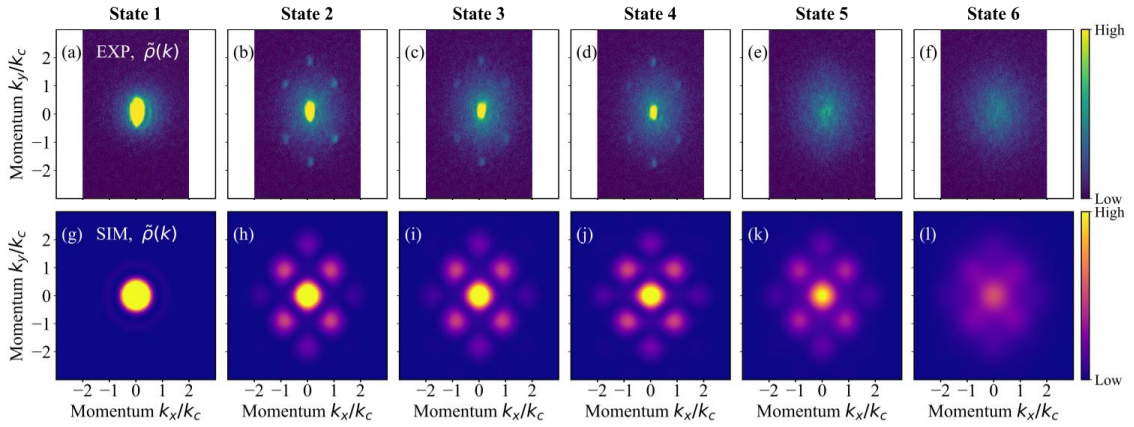
Figure 7.12: Comparison of experimentally measured (upper row) and simulated (bottom row) momentum space density distributions of a system undergoing a phase transition from a superfluid self-organized phase (State 1) to a superfluid Mott insulating phase (State 6). Adapted from Ref [408].

physics phenomena. It is worth noting that independently of whether the considered experimental effect is a dynamic transition from superfluid to Mott-insulating states, the quantization of conductance through a quantum point contact, or simply the many-body nature of condensed versus fragmented states in a double-well potential, the standard output of experiments remains similar. It is namely a time-of-flight image.

In an experimental setup, an initially trapped cloud of ultracold atoms is let expand and time-of-flight imaging captures snapshots of the cloud. These single shots carry an amount of information as they can unambiguously be linked to a large variety of physical quantities and phases. While experimentalists can usually only extract a few observables through averaging techniques, it is shown that an ML tool should be able to harness the information contained in the data more accurately and access a larger selection of observables (compare fig. 7.11). The ANN-based approach proposed by the authors exploits the shot-to-shot fluctuations in order to implicitly reconstruct the many-body state. This is promising for widespread application in experimental realizations.

When it comes to compare theoretical predictions and experimental results, noise becomes an important factor. In ultracold atoms, Lode *et al.* (fig. 7.11) proposed a method for an optimized observable readout from single-shot images of ultracold atoms, arguing that the similarity of theoretically simulated and experimentally detected single-shots is good enough that the addition of artificial Gaussian noise to the theoretical data during training should suffice. Figure 7.12 shows a comparison of simulated and experimental single-shots of ultracold atoms at different points of a phase transition in an optical cavity upon increase of one of the external laser intensities. While this example comes from a different framework, both publications used the same simulation method for the single-shot generation [408, 409]. Noise is evidently present but the agreement is satisfactory for the different stages of the phase transition. An alternative to adding artificial noise to the theoretical data is attempting to subtract noise from experimental data, e.g., by means of denoising autoencoders. Which option is eventually chosen naturally depends on the given experimental and theoretical data. In the case of single shot images, denoising methods may not be ideal owing to the presence of quantum noise, inherent in many-body systems, which is difficult to discern from other noise sources and therefore to selectively remove.

Overall, we have seen that ML techniques can contribute in bridging the gaps between theoretical models and noisy or resource-constrained experimental realizations and measurements. These findings represent a solid groundwork demonstrating experimental quantum physics enhancement via ML and indicate a promising avenue toward the hybridization of ML and the quantum realm in the coming years.

7.3.3 Hamiltonian learning

The focus of this section is the verification of quantum simulators such as trapped ions, Rydberg atoms, superconducting qubits, or ultracold atoms in optical lattices [410–413].[12] These experimental setups are well understood and can be used to simulate more complex and challenging systems governed by the same Hamiltonians. We enter exciting times when quantum simulators start to be very complex and, in particular, not solvable with classical computers. For example, when working with quantum simulators with 50 qubits we have to deal with enormous Hilbert spaces of the order of 10^{15}. Therefore, the question arises how can we know that these simulators are working as they should be if we can not verify their results with classical computers? One possible solution to this problem is called *Hamiltonian learning* which is the main topic of this section and presented in Ref. [414].

> The main idea of Hamiltonian learning is to reconstruct the map from experimentally accessible measurements to the parameters of the underlying Hamiltonian. NNs are a specific example to extract these parameters governing the created quantum simulator. These quantum simulators create experimentally accessible data (e.g., real space images) for the corresponding Hamiltonian whose parameter are known. Then, the NNs are trained via supervised learning to predict the parameters of these Hamiltonians. It is also possible to reverse the procedure: given the defining parameters of the Hamiltonian of a quantum system, relevant characteristics of the system can be efficiently learned by an NN [415].

A very simple example to illustrate the process of Hamiltonian learning with NNs is a single spin system as shown in fig. 7.13. Firstly, we prepare an initial state of a known Hamiltonian, H_0. In this case, it is an eigenstate of σ_z (spin "up"). Secondly, we perform a unitary evolution under an unknown Hamiltonian, H_1, which leads to a precession of the spin around the axis of the Bloch sphere. We now want to learn from measurements the unknown H_1, i.e., how fast the spin precesses around the sphere. In this case, a sequence of measurements is required to obtain the oscillation frequency, ω. This procedure can be generalized to arbitrary known initial H_0 and unknown H_1, driving the unitary evolution of the system.

Now, we focus on another experimental setup of a quantum simulator consisting of neutral atoms in a harmonic potential in a system of 2×50 lattice sites. The initial states of this system are the positions of the atoms in the optical lattice and this experimental setup can be described by the Bose-Hubbard Hamiltonian

$$H_{BH} = -\sum_{\langle i,j \rangle} J_{i,j}\hat{a}_i^\dagger\hat{a}_j + \sum_i \frac{U_i}{2}\hat{a}_i^\dagger\hat{a}_i(\hat{a}_i^\dagger\hat{a}_i - 1) - \sum_i \mu_i\hat{a}_i^\dagger\hat{a}_i \qquad (7.21)$$

where $J_{i,j}$ describes the hopping between lattice sites i and j, U_i the onsite energies, and μ_i is the chemical potential of the atoms in the optical lattice. If we consider only ten particles in this

---

[12]Different experimental setups have different advantages and disadvantages for specific quantum simulation problems and Hamiltonians. A difference between quantum simulation and quantum computation is that quantum simulators are engineered for specific problems and quantum computing is more versatile and able to solve general problems.
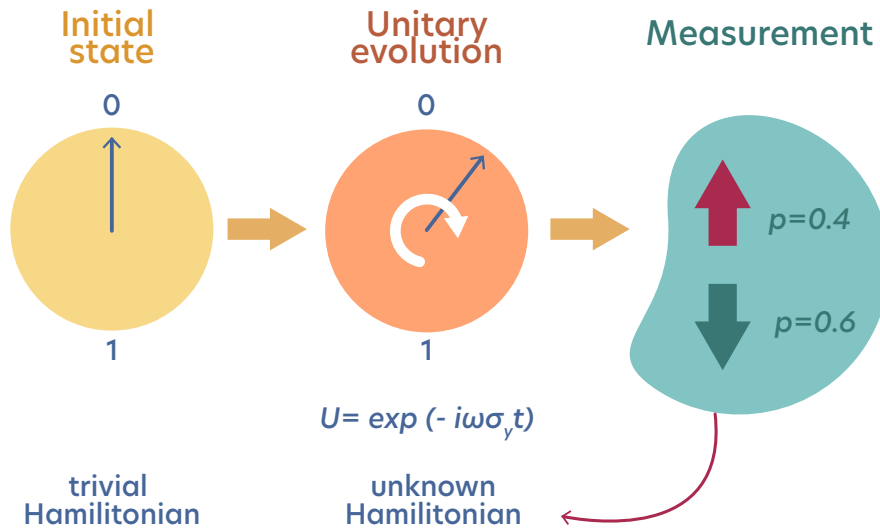
Figure 7.13: Illustration of the procedure of Hamiltonian learning of a one-spin system. The spin is prepared in an initial state and driven by an unknown Hamiltonian. The rotation frequency can be learned from experimental measurements.

lattice, the corresponding Hilbert space is of dimension 10^{13} with 350 parameters to estimate. This leads to two main issues: first, the wave function is too large making it impossible to simulate this system, and, second, it leads to a 350-dimensional optimization problem. Therefore, let us first consider a small system consisting of 4 atoms as illustrated in fig. 7.14(a), which reduces the number of parameters to 25 and the Hilbert space size to 330. This eliminates the problem of the large Hilbert space and leaves us with the optimization problem.

Now, we want to create a mapping from the measurements to the parameters of the Hamiltonian eq. (7.21).[13] To do so, supervised learning is used to train an NN and perform regression. The challenge in this setup is the scaling of the training data with the output size. To train a single NN to predict all parameters, as shown in fig. 7.14(b), several examples for all combinations of the 25 parameters are required which is unfeasible for most applications due to the enormous size of the required training set. The solution to this problem is quite simple: instead of using a single NN to predict all parameters, 25 NNs are trained to predict each parameter separately with continuous regression.

Moreover, the experimental snapshots may not be the best representation of the data set. A more effective representation is to switch from experimental snapshot batches to the correlators of the specific Hamiltonian. In this example, density correlators are used which enable a way more efficient way to train the NN by reducing the input dimension. This approach is shown in fig. 7.14(d). After successful training, the NN achieves around 0.1% error rates for experimental parameters with 2500 snapshots. Using Bayesian inference as a benchmark, the NN approach outperforms the Bayesian results for small data sets of 2500 snapshots. However, for large data sets of about 20 000 samples, both approaches achieve the same accuracy in predictions of the parameters.

So far, we have only considered small system sizes of four atoms which can be solved exactly with classical computers. In the following, we present a scheme to scale to larger

---

[13]Here, exact simulations were used as "measurements" instead of experimental snapshots and the input images are the real space positions of the atoms in the optical lattice.
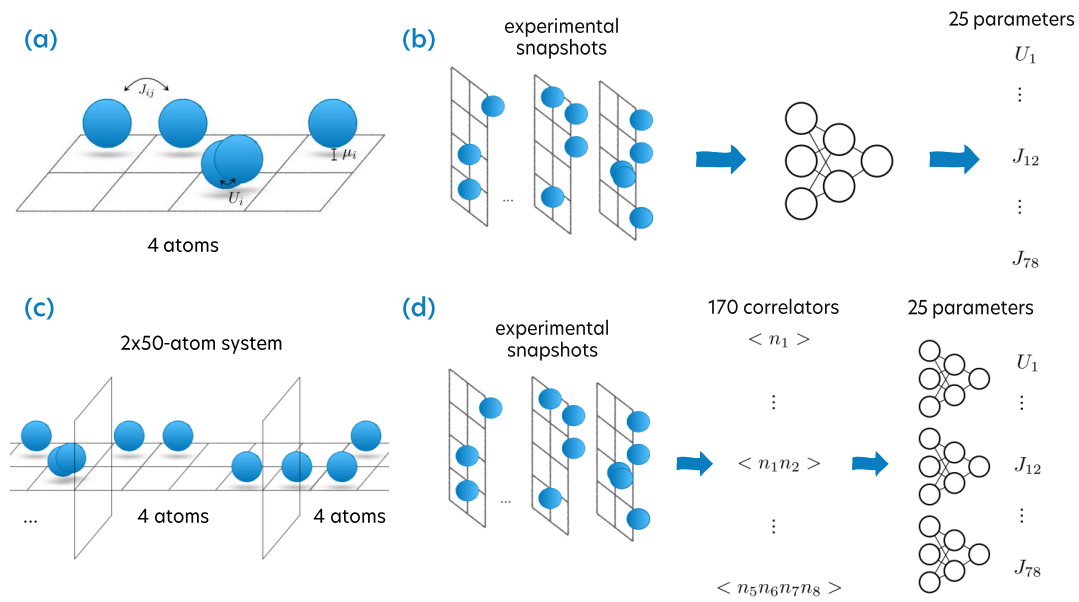
Figure 7.14: (a) Illustration of a four atom system with 25 parameters. (b) Mapping from the experimental snapshots to the Hamiltonian parameters using one NN and supervised learning. (c) Extension to larger system sizes by "dividing" the lattice into subsystems with walls. (d) More efficient way to map measurements to the parameters. Adapted from Ref. [414]. Additional credit: QMAI group at TU Delft.

system sizes of this specific Hamiltonian. In this experimental setup, it is possible to modulate the lattice and to create walls in order to separate the chain of 50 lattice sites into four-site units (see fig. 7.14(c)). In this system, the parameters of the Hamiltonian are local and only the terms of H which are unaffected by the boundary have to be learned which are called the "effective parameters" (see fig. 7.15). Now, the boundary is shifted by one lattice site at a time and 2500 shots are measured for each position. Once the system is shifted up to the point of translational invariance, all parameters were at least in one configuration unaffected by the boundary wall and successfully learned by the NN.

As mentioned before, this procedure is very specific for this system and cannot easily be generalized to different systems. The field of Hamiltonian learning is still in its early stages and general schemes for large systems and complex Hamiltonians have still to be developed. However, it is a promising approach for the important task of validating if quantum simulators work correctly which becomes more and more important with the increasing size and applicability of these simulators which might have the possibility to go beyond classical computation.

Outlook and open problems

The efficient characterization of quantum systems, the verification of quantum devices, and the validation of underpinning physical models are central challenges for modern quantum technologies. ML is expected to improve the computational cost of those tasks. As a result, ML-based Hamiltonian learning is becoming a widely used technique to verify quantum experiments. Interesting examples are its application to nitrogen-vacancy centre setups [416] and to nuclear magnetic resonance measurements [417].

Scaling of ML approaches to larger sizes of quantum devices remains an important challenge. Even though ML algorithms perform exceptionally well on the large experimental data
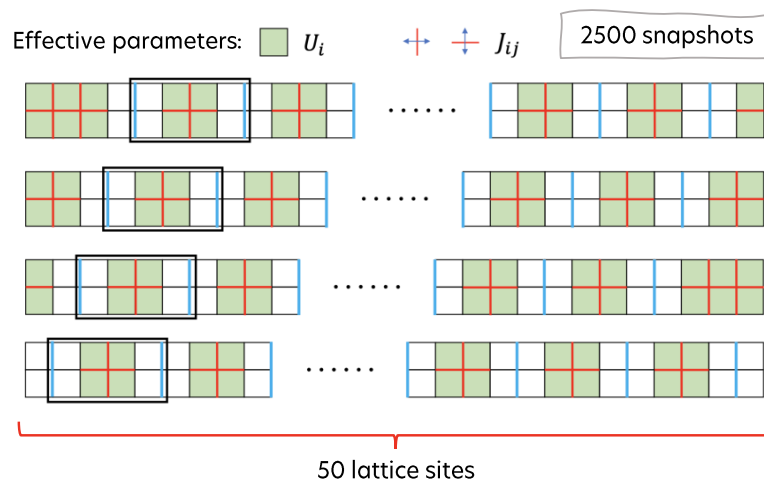
Figure 7.15: Scaling scheme from four lattice sites to 50 for this specific system and Hamiltonian. For each of the four wall configurations, 2500 snapshots were taken in order to train the NN and learn all parameters. Adapted from Ref. [414].

sets, adding more qubits (and therefore tuning parameters) generates learning difficulties. It is especially recognized in the quantum dot tuning. There are efforts toward tuning multiple parameters at once [418, 419] or toward significant reduction of the experimental data needed for tuning [420]. However, to quickly tune large scale quantum devices with hundreds of parameters requires new methods.

Finally, there are interesting works exploring the possibility of ML approaches designing quantum experiments [304] with a special focus on quantum optics [421, 422].

Further reading

- King, R. D. *et al.* (2009). *The automation of science*. Science, 324, 85-89. Report on building one of the first "robot scientists" named "Adam" which aimed at the automation of hypothesis forming and recording of experiments [423].

- Wiebe, N. *et al.* (2014). *Hamiltonian learning and certification using quantum resources*. Phys. Rev. Lett. **112**, 190501. The first proposal of Hamiltonian learning combining quantum simulators and the Bayesian inference [424].

- Raccuglia, P. *et al.* (2016). *Machine-learning-assisted materials discovery using failed experiments*. Nature 533, 73–76. Example of ML use for discovery of materials that outperforms traditional human approaches [425].

- Häse, F., Roch, L. M., & Aspuru-Guzik, A. (2019). *Next-generation experimentation with self-driving laboratories*. Trends Chem. 1, 282-291. Perspective concerning self-driving laboratiories and their role in scientific discovery [426].

8 Physics for deep learning
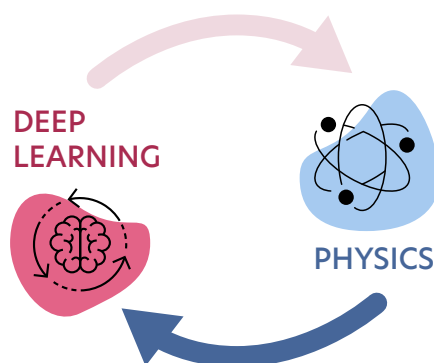
Figure 8.1: There exists a two-way influence between machine learning (ML) and physics. In this chapter, we focus on the less known approach, i.e., physics for ML.

So far, we have discussed different applications of ML which aim at solving various problems in quantum science. In contrast, in this chapter we focus on how physics (in particular statistical and quantum physics) influences ML research. In section 8.1, we explain fundamental theoretical challenges of ML and show how tools of statistical physics can shed some light on these problems. In section 8.2 we discuss quantum computing and promises of quantum machine learning (QML).

8.1 Statistical physics for machine learning

In this section, we present how to apply concepts from physics (in particular, tools of statistical physics like the thermodynamic limit, or order parameters describing phase transitions) to develop theory of ML (see fig. 8.2) [427]. This idea was born already in 1980s, but the DL revolution in 2010s has caused a renewed surge of interest in this approach.

Indeed, help from statistical physics is very needed, as we do not understand many conundrums in ML! For example, modern NNs can have billions of trainable parameters.[1] How can we even find well-generalizing minima within such enormous, non-convex loss landscapes?

---

[1]One of the latest champions is Microsoft's GPT-3 with over 175 billion parameters.
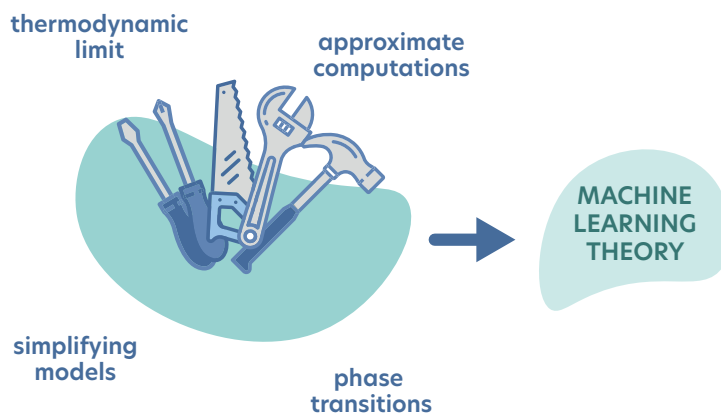
Figure 8.2: Statistical physics toolbox for understanding ML theory
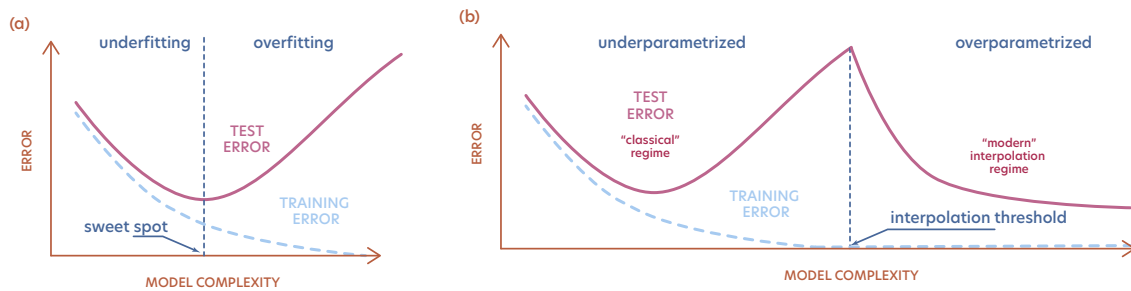
Figure 8.3: Classical and modern understanding of the generalization. (a) The classical U-shaped error curve arising from the bias-variance trade-off. (b) The double descent error curve incorporating the classical U-shape in the classical regime and low generalization errors of modern overparametrized models. Adapted from Ref. [428].

Another riddle is connected to the so-called bias-variance trade-off, which we have shown in section 2.2 and which indicates that in the regime of large model complexity models should heavily overfit their data sets as presented in fig. 8.3(a). But in practice, we see that these gigantic overparametrized DL models generalize very well as seen in fig. 8.3(b). So how do they escape this traditional bias-variance trade-off? We have a long way toward a full understanding of these puzzles. A way of tackling them is to study simple, solvable models, following a traditional approach of physicists to study new systems. Results from toy problems can give us hints on how more complex models work.

This section has four parts. Firstly, in section 8.1.1, we go through the seminal study on the capacity of the perceptron, which gives an idea how statistical physics can be useful for learning problems. Then, we discuss three directions of this interdisciplinary research, i.e., the teacher-student paradigm for studying generalization in section 8.1.2, how we can model the structure of data in section 8.1.3, and how to study the dynamics of learning in section 8.1.4.

8.1.1 Capacity of the perceptron

The simplest ML model we can think of is a single perceptron, f, presented already in section 2.4.4 (see fig. 2.6(b)). In this section, we focus on its capacity, i.e., the question of how many data points it can fit. To answer it, let us make the additional assumption that the data set is in *general position*.[2] The assumption is reasonable – if we have many copies of the same training point, they should not contribute to the estimation of the model capacity.

A single perceptron is only capable of learning linearly separable patterns. Therefore, we can reformulate the question of its capacity to the question whether randomly labeled data sets of size n with binary labels are linearly separable. The probability of such a linear separability, $p_R(\alpha)$, is a function of α, which is the ratio between the number of training points, n, and the number of data features (or data dimensionality), m. In the case of the perceptron, the number of features is equal to the number of perceptron weights, d,[3] therefore $\alpha = \frac{n}{d}$. In this problem, you can understand the parameter α as the difficulty of the classification task, which increases with the number of training points and decreases with the number of parameters.

---

[2]The set of points in $\mathbb{R}^d$ is in general position if and only if every set of $(d+1)$ points are not in any possible hyperplane of dimension d. In other words, as long as there is no three data points on a single line or four points on a single plane, etc., the set is in general position. Intuitively, any random data set is in general position.

[3]In general, a perceptron is parametrized by weights and biases. For the remainder of this section, we ignore biases, therefore weights are all model parameters, $\boldsymbol{\theta}$, of size d.

To calculate p_R we could resolve to geometric arguments. This approach was chosen by Thomas Cover in 1960s [429]. However, here we choose to rephrase this problem in the language of statistical physics as was done by Elizabeth Gardner in 1987 [430].

> Namely, we can take the space of all possible weights, so $\mathbb{R}^d$, and calculate the volume of those weights that fulfill all the constraints of the random labeling.

In other words, we calculate how many sets of weights could solve the problem of separating randomly labeled training data, $\mathcal{D} = \{\boldsymbol{x}^{(k)}, y^{(k)}\}_{k=1}^n$:

$$V_{n,d} = \int_{\mathbb{R}^d} d\theta \prod_{k=1}^n \delta(f(\boldsymbol{x}^{(k)}; \boldsymbol{\theta}) - y^{(k)}). \tag{8.1}$$

The δ-function in eq. (8.1) is 1 only when the ground-truth label is equal to the label predicted by the perceptron. With each new data point k, we are adding a new constraint, and the volume of possible weights shrinks. To have at least one set of such weights, the volume has to be larger than zero, $V_{n,d} > 0$. Therefore, we define the critical task difficulty, α_c, as the value of α for which $V_{n,d}$ goes down to zero. If we can calculate this, we solve the problem of the perceptron capacity.

Let us make one modification to the equation that leads us closer toward statistical physics. We introduce an effective Hamiltonian counting the number of missclassified training data points

$$H(\theta; \mathcal{D}) = \sum_{k=1}^n \Theta(-f(\theta; x^{(k)}) y^{(k)}) \tag{8.2}$$

where the Heaviside function $\Theta(\cdot)$ is equal to 1 if its argument is positive and 0 otherwise. We can substitute the Dirac δ-distribution above by the Boltzmann factor of $H(\theta; \mathcal{D})$. Up to a multiplicative constant, eq. (8.1) becomes

$$V_{n,d} \propto \lim_{\beta \to +\infty} \beta \int_{\mathbb{R}^d} d\theta \, e^{-\beta \sum_{k=1}^n \Theta(-f(\theta; x^{(k)}) y^{(k)})} = \lim_{\beta \to +\infty} \int_{\mathbb{R}^d} d\theta e^{-\beta H(\theta; \mathcal{D})}. \tag{8.3}$$

Suddenly, the volume $V_{n,d}$ in eq. (8.3) resembles the canonical *partition function*[4] from statistical physics with β playing the role of an inverse temperature, defined as $\frac{1}{k_B T}$. The limit $\beta \to \infty$ therefore corresponds to the zero temperature limit. The problem is that this integral is hard to calculate as it lives in a huge d-dimensional space of all real numbers.[5] Moreover, the "effective energies" in the exponent depend on the training set. As such, each training set requires a separate calculation of the volume $V_{n,d}$.

Fortunately, the physics of *disordered systems* comes to the rescue. It has been applied to learning theory since 1980s [431–437]. Namely, if we recognize a disordered system in eq. (8.3), we can use solutions from statistical physics to compute this high-dimensional integral. Let us give a brief introduction to disordered systems. A disorder system is described by two types of random variables. The first type concerns states of the system $s \in \mathbb{R}^d$. For example, for a system of d spins - $\frac{1}{2}$, $s \in \{-1, 1\}^d$, because each spin can be up or down. The

---

[4]A partition function for a many-body classical discrete system is equal to $Z = \sum_i e^{-\beta \varepsilon_i}$, where i iterates over all possible microstates and ε_i is the energy of the i-th microstate. If we go to a continuous system with n identical particles described by properties $\boldsymbol{\theta}$, the partition function is $Z \propto \int \exp\left(-\beta \sum_{i=1}^n H(\boldsymbol{\theta}_i)\right) d\theta_1 \cdots d\theta_n$, where H is a classical Hamiltonian.

[5]This is also a reason why computation of any interesting partition function is hard.

second type concerns interactions between the degrees of freedom which can be parametrized by couplings $J \in \mathbb{R}^n$. For example, J can describe whether spins want to align or anti-align. The distribution of states in disordered systems is then described by the Boltzmann distribution:

$$p(s \mid J) = \frac{1}{Z_J} e^{-\beta H(s;J)}, \tag{8.4}$$

where $H(s; J)$ is an energy function depending on both s and J, and $Z_J = \int_{\mathbb{R}^d} ds e^{-\beta H(s;J)}$ is the partition function equal and plays the role of a normalization.

As an example of a disordered system, let us consider a *spin glass* [438, 439], where the energy function is $H(s; J) = -\sum_{<i,j>} J_{ij} s_i s_j$ (resembling Ising-type interaction, see eq. (3.1)), where couplings J_{ij} are i.i.d. according to the normal distribution $p(J_{ij}) \propto \exp\{-(J_{ij} - J_0)/2J^2\}$ where J_0 and J^2 are the mean and the variance. If all the J_{ij} are positive, the system is ferromagnetic, and the ground state of the system is easy to find. With random couplings complications arise along with the frustration of the system: at a given site, a spin can be encouraged by neighbors to point in conflicting directions. Finding the ground state of such systems is a numerical challenge of its own. While in one dimension the solution is trivial and can be solved by a deterministic algorithm whose cost scales as $\mathcal{O}(n)$, the complexity grows in two dimensions and reaches NP-completeness in three and more dimensions [440].[6]

Now, let us tackle the exponent in eq. (8.3) which we treat as an energy function. If we do that, there is a property of the free energy[7] which can help us in simplifying the calculations. Namely, free energy is self-averaging.

> If a random quantity is *self-averaging*, two conditions are met: its mean value and the most probable value coincide in the thermodynamic limit, and fluctuations around this mean value are sufficiently small. In other words, the system *concentrates on typical states*.

This property often holds for the free energy of disordered systems. Consider the following argument: imagine dividing the macroscopic system into many subsystems and each subsystem is still large enough to be considered macroscopic. Their interaction can be viewed as a surface effect and is negligible when compared to the bulk. Therefore, each subsystem has a well-defined free energy and realization of disorder, even if the specific values vary between subsystems. In the limit of an infinite number of subsystems (whose interactions can be ignored to first order), the disorder average of the free energy is automatically the average free energy across the disordered subsystems [439, 442, 443]. That is, for d large enough, the physics of the system is independent of the disorder realization:

$$\frac{1}{d} \ln Z_J \approx \lim_{d \to \infty} \mathbb{E}_J \left[\frac{1}{d} \ln Z_J \right]. \tag{8.5}$$

The free energy being extensive, note that the converging quantity in the thermodynamic limit is the free-energy per spin. This result is highly non-trivial, tools like replica computations, variational mean-field methods, and high-temperature expansions are necessary to identify where self-averaging applies and to compute the disorder averages.[8] In the following para-

---

[6]There are proposals to tackle this challenge with reinforcement learning (RL) [441].

[7]In the thermodynamic limit, the free energy of the system is $F = U - TS = -\frac{1}{\beta} \ln Z$, where U is the energy of the system and S is its entropy.

[8]It is interesting to note that these non-rigorous physical approaches for disordered systems developed in the 1970s [439, 442, 443] are now being put on a more rigorous footing by mathematicians [444, 445]!

graph, we provide the intuition behind only one of the concepts behind eq. (8.5), namely *the replica trick*. The reader interested in more detailed explanations should turn to the tutorial reviews [446, 447].

Replica trick. In statistical physics calculating averages makes sense only for extensive observables. The replica method is a way to calculate these averages with respect to disorder variables. We are particularly interested in the averaged value of the system free energy $F_J = -\frac{1}{\beta} \ln Z_J$. To obtain the averaged free energy $\mathbb{E}_J[F_J]$ we have to obtain the averaged value of the logarithm of the partition function $\mathbb{E}_J[\ln Z_J]$. It turns out that averaging the logarithm is challenging but the averages of powers of the partition function, $\mathbb{E}_J[Z^n]$ for $n \in \mathbb{N}$, can be estimated. Then, by using the identity

$$\ln x = \lim_{n \to 0} \frac{x^n - 1}{n}, \tag{8.6}$$

we can write

$$\mathbb{E}_J[\ln Z] = \lim_{n \to 0} \frac{\mathbb{E}_J[Z^n] - 1}{n}. \tag{8.7}$$

As we can see the limit $n \to 0$ requires $n \in \mathbb{R}$. However, what we can do is to calculate Z^n for $n \in \mathbb{N}$. The partition function Z is an integral of the form $\int e^{-\beta H(s,J)}$, thus we can write Z^n as

$$Z^n = \int ds^{(1)} \dots ds^{(n)} \prod_{a=1}^{n} e^{-\beta H(s^a, J))} = \int ds^{(1)} \dots ds^{(n)} e^{-\beta \sum_{a=1}^{n} H(s^a, J))}, \tag{8.8}$$

where the exponent contains a sum over n independent samples, or replicas. The replica trick consists in defining a function $\phi(n)$ being an analytic continuation of the function in the exponent. As such $n \in \mathbb{R}$ becomes a continuous variable, and we can take limit $n \to 0$ in eq. (8.7). In summary, assuming we are able to calculate averaged value $\mathbb{E}_J[Z^n]$, we can calculate the averaged value of the free energy F_J.

Finally, having eq. (8.5), we can come back to the volume $V_{d,n}$ in eq. (8.3).

> We associate this volume $V_{d,n}$ now with the partition function of a spin system. Spins (s) are now model parameters (θ), and couplings (J) are training data ($\mathcal{D}$), posing the constraints to learn.

Applying the same analysis as in the paragraph before, we can state that the free energy for a given realization of the data set is just the free energy averaged over the data set distribution when we consider large data sets and large perceptron with fixed ratio $\alpha = n/d$:

$$V_{d,n} \simeq \lim_{n \to \infty} \mathbb{E}_{\mathcal{D}}[V_{d,n} \mid \mathcal{D}] = V(\alpha). \tag{8.9}$$

Therefore, if you fix the distribution of data (disorder realization), you can find the α_c for which $V_{d,n} = 0$ and as a result, the perceptron capacity. To be more exact, we can calculate it only for the large ("thermodynamic") limit of n for an arbitrary fixed α as V is actually expressed in terms of α.

We remind you that α_c indicates the critical task difficulty for which the volume of perceptron weights fulfilling the constraints of the random labelling goes to zero. It means that for the lower task difficulty, $\alpha < \alpha_c$, the randomly labeled data is linearly separable, while for the higher task difficulty, $\alpha > \alpha_c$, the data are no longer linearly separable. The probability, p_R, is therefore a step function of α in the thermodynamic limit. We plot p_R for real-valued parameters coming from a Gaussian distribution in blue in fig. 8.4. To show finite-size effects,
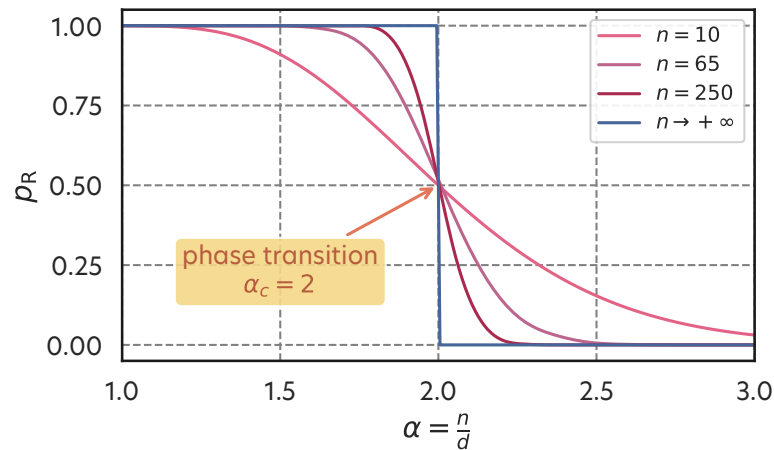
Figure 8.4: Probability of the randomly labeled data being linearly separable, p_R, as a function of the difficulty of the task, $\alpha = \frac{n}{d}$. Finite size results were obtained analytically by Cover [429].

Table 5: The capacity of the perceptron depending on the distribution of the data and type of weights. The capacity is expressed as the minimal task difficulty, $\alpha_c = \frac{n}{d}$, for which the volume of possible solutions goes down to zero, $V(\alpha_c) = 0$.

	Distribution of data		Critical task difficulty, α_c
1	Gaussian inputs Real weights	$p(x_i^{(k)}) = \mathcal{N}(x_i; 0, 1)$ $\boldsymbol{\theta} \in \mathbb{R}^d$	$\alpha_c = 2$
2	Binary inputs Binary weights	$p(x_i^{(k)}) = \text{Bernoulli}(0.5)$ $\boldsymbol{\theta} \in \{-1, 1\}^d$	$\alpha_c \approx 0.83$

we can also compute $p_R(\alpha)$ below the thermodynamic limit following Cover's argument [429]. To vary α, we can either change n or d. In case of perceptron, it is easier to keep d fixed and calculate p_R as a function of α for increasing n.

> In the equivalent of the thermodynamic limit, so $n \to \infty$, we see a phase transition for a critical $\alpha_c = 2$, which means that the most difficult task that the perceptron is able to solve is when the number of training points (in general position) is twice as large as the number of parameters.

Interestingly, the solution for α_c (for which $V_{d,n} = 0$) depends on the setup of the problem, namely the random data distribution and the allowed values of parameters (spin values). While the previous discussion has been conducted for Gaussian distribution of inputs and real perceptron parameters, $\boldsymbol{\theta}$, different critical task difficulty is obtained for binary inputs and parameters, as presented in table 5.

In this section we have looked at the problem of perceptron capacity which is well-known and decades old. As such, it serves well the educational purpose. In particular, we have seen that the statistical approach to learning focuses on simple solvable models (here, perceptrons). Moreover, we have seen that the statistical approach aims to express learning problems in terms

of statistical problems, e.g., disordered spin systems,[9] where physicists have already developed useful analytical tools.

In the next sections, we briefly discuss selected modern results from the intersection of ML and statistical physics. For the more thorough review on this intersection, we refer to [30]. Moreover, the outstanding retrospective of these developments can be found in the lecture titled "Statistical physics and ML: A 30-year perspective" of the late Naftali Tishby.

8.1.2 The teacher-student paradigm: a toy model to study the generalization

Our motivation for this section is to tackle the riddle of generalization, which is the ability of a model to make correct predictions on data unseen during training. However, our goal for this section is not to build new useful ML models or to distinguish between bad and good modern models in terms of generalization. Rather, we want to understand why useful modern ML models generalize so well. To do so, let us consider all learning task elements (such as the model, optimization method, and data) in their simplest form. The toy model which helps us in this ambitious task falls under the teacher-student paradigm.

> The teacher-student paradigm consists of two main elements: a teacher which is a data-generating model, and a student which is a model trying to learn the data generated by a teacher.

Teacher consists of an input distribution $p_x(\boldsymbol{x})$, e.g. Gaussian or binary, and an input-output rule $p(y_t \mid \boldsymbol{x}) = f_t(\boldsymbol{x}, \boldsymbol{\theta}^*)$. For now, let us assume the teacher is a perceptron. On top of the input-output rule, we may assume a ground-truth distribution on the weights $p_\theta(\boldsymbol{\theta})$, from which the parameters $\boldsymbol{\theta}^*$ of the teacher model were drawn. Once we decide on how a teacher looks like, it can generate training data: $\mathcal{D} = \{\boldsymbol{x}^{(k)}, y_t^{(k)}\}_{k=1}^n = \{\boldsymbol{x}^{(k)}, f_t(\boldsymbol{x}^{(k)}, \theta^*)\}_{k=1}^n$.

> The second element is the student whose aim is to learn the distribution underlying the training data. In the teacher-student scheme, we know exactly what the data-generating distribution is. Therefore, we can easily distinguish between a student that simply fits the training data (limited generalization) and a student that recovers a teacher's input-output rule (perfect generalization). In other words, we can measure the generalization ability of the student.

To continue with the teacher-student strategy, we need to decide on a model for the student, $f_s(\boldsymbol{x}, \boldsymbol{\theta})$, but also on a learning strategy. Let us start with the simplest scenario when a student is also a perceptron (like the teacher). To train, we could use the standard empirical loss minimization strategy, e.g.,

$$\boldsymbol{\theta}^* = \text{argmin}_{\boldsymbol{\theta}} \left\{ \sum_{k=1}^n \mathcal{L}\left(y_t^{(k)}, f_s\left(\boldsymbol{x}^{(k)}, \boldsymbol{\theta}\right)\right) \right\}, \tag{8.10}$$

where we aim to minimize a given distance between the teacher outputs $y_t^{(k)}$ and student outputs $y_s^{(k)} = f_s(\boldsymbol{x}^{(k)}, \boldsymbol{\theta})$. Alternatively, we can instead maximize the following Bayesian posterior:

$$p(\boldsymbol{\theta} \mid \mathcal{D}) \propto \prod_{k=1}^n p\left(y_t^{(k)} \mid \boldsymbol{\theta}, \boldsymbol{x}^{(k)}\right) p(\boldsymbol{\theta}). \tag{8.11}$$

---

[9]This also tells us that NNs with binary weights may be especially approachable for physicists. These are spin-1/2 problems!

Equation (8.11) denotes the posterior distribution, i.e., the belief on the student model weights $\boldsymbol{\theta}$ given the data set $\mathcal{D}$ and the prior assumption on the student weights $p(\boldsymbol{\theta})$.

Assuming, e.g., a MSE loss, the student generalization error for given weights $\boldsymbol{\theta}$ is defined as the expected error over the entire data distribution:

$$\mathcal{E}_g(\boldsymbol{\theta}) = \mathbb{E}_{\boldsymbol{x},y}\left[(y - f_s(\boldsymbol{x}, \boldsymbol{\theta}))^2 \right]. \tag{8.12}$$

In the best possible scenario, the student model $f_s(\cdot, \cdot)$ is identical the teacher model $f_t(\cdot, \cdot)$ underlying the generated data. When a student is identical to the teacher, we call the setting *Bayes optimal* and define the Bayes optimal error of the student (see section 2.3),

$$\mathcal{E}_g^{\text{opt}}(\mathcal{D}) = \mathbb{E}\left[\mathbb{E}_{\boldsymbol{x},y}\, (y - f_s(\boldsymbol{x}, \boldsymbol{\theta}))^2 \mid p(\boldsymbol{\theta} \mid \mathcal{D}) \right], \tag{8.13}$$

which is a mean error for student parameters $\boldsymbol{\theta}$ drawn from the posterior distribution in eq. (8.11). This is a fundamental quantity from the point of view of information theory: it quantifies how much information on the weights $\boldsymbol{\theta}$ the training data set $\mathcal{D}$ provides assuming the student has perfect knowledge of the form of the problem. We can use the same tools as in the previous section (disorder average, thermodynamic limit, and replica computation) to obtain:

$$\mathcal{E}_g^{\text{opt}}(\mathcal{D}) \underset{n \to \infty}{\to} \quad \mathbb{E}[\mathcal{E}_g^{\text{opt}}(\mathcal{D}) \mid \mathcal{D}] = \mathcal{E}_g^{\text{opt}}(\alpha). \tag{8.14}$$

Here again, the limiting generalization error takes the form of a function of the ratio $\alpha = \frac{n}{m}$ between the number of data points and the number of data features or weights. We no longer interpret this ratio as the difficulty of the classification task as in the capacity computation. Instead, in generalization problems, it is more useful to think of α as the sample complexity, that is the amount of training data available to infer the input-output rule. In the following paragraphs, we examine generalization for a few different pairs of teacher and student.

Two perceptrons. The generalization error from eq. (8.14) is shown in fig. 8.5. We can compare the limiting Bayesian optimal generalization error (red line in panels (a) and (b)) with the training of a perceptron at finite m by minimizing a loss function, such as performing a logistic regression with gradient descent (blue squares). In panel (a), for binary weights, we have a first-order phase transition [435, 436]. In panel (b), for real-valued weights, there is a smooth decrease of the generalization error [448]. In both cases, there is a computational gap between the optimal generalization error and logistic regression with gradient descent.

Finally, the same generalization error of the student perceptron can be studied when learning occurs with algorithms called generalized approximate message passing (GAMP). For the introduction to these methods, see Ref. [447, 449, 450]. For our needs, it is enough to know that these algorithms provide an alternative to convex optimization and allow for efficient calculations of quantities based on graphs (like perceptrons or NNs) which are sampled from distributions like eqs. (8.12) to (8.14). Moreover, they are remarkable in that their asymptotic $(n, d \to \infty,\ n/d = \alpha)$ performance can be analyzed rigorously using the so-called state evolution (SE). Armed with this knowledge, we now see that the generalization error obtained using GAMP in fig. 8.5 is much closer to the Bayes error compared to the optimization with gradient descent. In panel (b), the gap completely disappears. In panel (a), there is a remaining computational gap between GAMP and the exact Bayes error. This regime is called a *hard phase*. It comes from the fact that, in practice, our computational time is limited to the polynomial regime. Interestingly, there is no known efficient algorithm which would beat GAMPs in the hard phase of this perceptron learning [448].
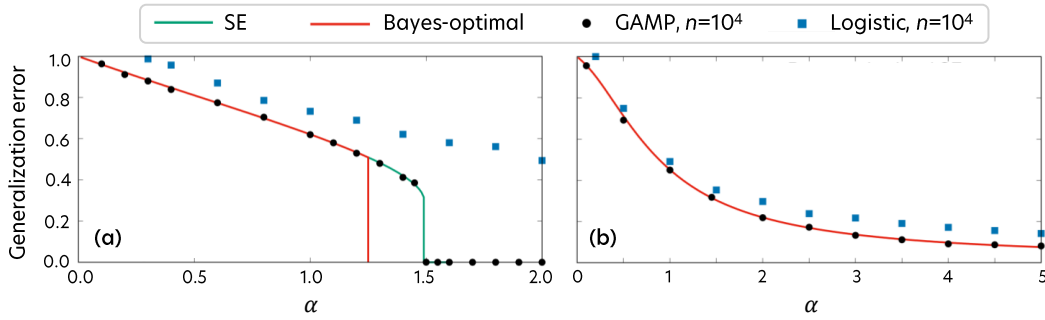
Figure 8.5: Generalization error as a function of the task difficulty α, which is the ratio between the number of training points and the number of (student) model parameters for perceptrons with (a) $\boldsymbol{\theta} \in \mathbb{R}^d$ or (b) $\boldsymbol{\theta} \in \{-1, 1\}$. The red line is the exact Bayes-optimal generalization error. The blue squares are for a fine-tuned perceptron with gradient-based minimization of the error. We see the computational gap between those results. The gap (a) gets smaller or (b) disappears for message-passing algorithms. Black circles are results for $n = 10^4$ obtained using generalized approximate message passing (GAMP), and the green line denotes the results of state evolution (SE) which approximates the limit $n \rightarrow \infty$. Adapted from [448].

Two-layer NNs. So far, both the teacher and the student have been modeled with perceptrons. We can switch to more complex models. For the reminder of this section, we use two special two-layer NNs with a rich history in statistical physics. We start with *committee machines* [451, 452] shown in fig. 8.6(a). Their analytical treatment is possible in the limit of an infinite number of input features, m, and data size, n, while keeping a finite number of hidden units. In particular, we present here soft committee machines which allow for an even simpler analysis. In soft committee machines, we train only parameters belonging to the first layer of the machine, $\boldsymbol{\theta}_1$, of size $d_1 = d = mD$, where m is the number of features and D is the number of hidden units. The second layer is fixed and identical for both the teacher and the student. The second NN used in this section is a *random feature model* [453, 454] presented in fig. 8.6(b). Interestingly, their analytical analysis is enabled by a fixed first layer whose parameters are set to random values. The number of those parameters is also $d_1 = d = mD$. Therefore, only parameters of the second layer are trainable. The idea behind the random first layer is that projecting a lower-dimensional input onto a much higher dimensional space leads to better separation of the data which then can be successfully processed by a single-layer NN.[10] Also note that random feature models can have an arbitrary number of hidden units, in particular larger than the number of input features, which allows for a study of over-parametrization.

Two committee machines. Now, we are ready to tackle generalization with more complex models. Here, we use soft committee machines. For now, a teacher and a student share the same architecture. The formulation of the problem stays the same. We calculate the generalization error from eq. (8.14) of the student committee machine when learning data generated by the teacher committee machine [452]. We plot generalization errors in fig. 8.7(a)-(b) for committee machines with two hidden neurons. Similarly as before, we see in panel (a) that

---

[10]In other words, you can think of such a projection as mapping input data to a feature space as discussed in section 4.2 on kernel methods. Interestingly, Refs. [453, 454] showed that random data projection onto a feature space is not much worse compared to projecting onto an optimized feature space. However, randomization is much cheaper than optimization.
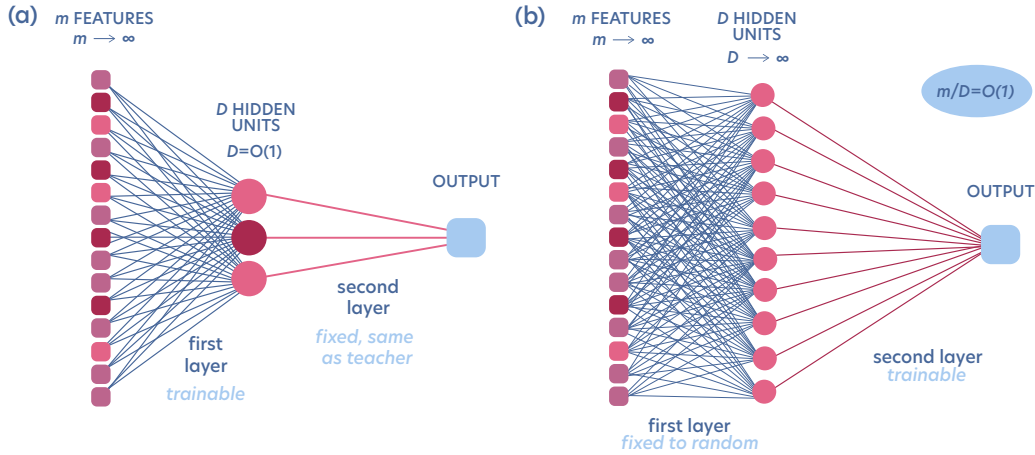
Figure 8.6: Schematic illustration of used two-layer NNs. (a) Soft committee machine. Parameters belonging to the first layer, $\boldsymbol{\theta}_1 \in \mathbb{R}^{m \times D}$, are trainable, whereas the parameters of the second layer, $\boldsymbol{\theta}_2 \in \mathbb{R}^{D \times 1}$, are chosen identical to the parameters of the teacher. Its analytical treatment is possible if $m \to \infty$ and $D = O(1)$. (b) Random feature model. Its first layer is fixed to random parameter values. The second layer is trainable. The number of hidden units can be varied to study overparametrization. In the analysis, the number of hidden units $D \to \infty$ scales linearly with the number of inputs $m \to \infty$, i.e., $m/D = O(1)$.

for real-valued weights the generalization error (obtained with GAMP and SE) is equal to the Bayes one, while for binary weights in panel (b) there is a computational gap between both errors. This time, we also look at the overlap between hidden neurons of the student and of the teacher, which measures the similarity neuron-by-neuron between the teacher and the student. To be more precise, we look at the matrix $Q = [q_{jj'}] = \frac{1}{m} \sum_{i=1}^m \Theta^*_{1,ij} \theta_{1,ij'}$, where $\boldsymbol{\Theta}_1$ and $\boldsymbol{\theta}_1$ are the parameters of the teacher and student first layers, respectively. It turns out that there is a so-called *specialization* phase transition [455, 456].

> In the regime of low task complexity, both hidden units of the student committee machine learn the same function. After crossing the critical α, when enough data is available, hidden neurons of the student start to *specialize*. Each student neuron selects a different teacher neuron to converge to. The specialized phase is associated with lower generalization error than the non-specialized, see fig. 8.7.

The specialization for teacher and student committee machines with two hidden neurons ($D = 2$) takes place for $\alpha_c \approx 2$ for real-value weights and for $\alpha_c \approx 1.5$ for binary weights, which means that specializing neurons require at least 2 and 1.5 times more training data than the number of data features, m, i.e., approximately as much training data as the number of parameters in the first layer, $d_1 = 2m$. Similar observations hold if both teacher and student committee machines have a large number of hidden neurons ($D \gg 2$). We can plot a phase diagram of the generalization error as a function of a rescaled task difficulty, $\tilde{\alpha} = \frac{\alpha}{D} = \frac{n}{Dm}$ for real-valued weights. It is presented in fig. 8.7(c). In total, we find three distinct phases: two correspond to specialized and non-specialized hidden neurons, and above the specialized phase, there is a computational gap where a model in principle has enough information to specialize but is unable to due to shortcomings of its optimization.
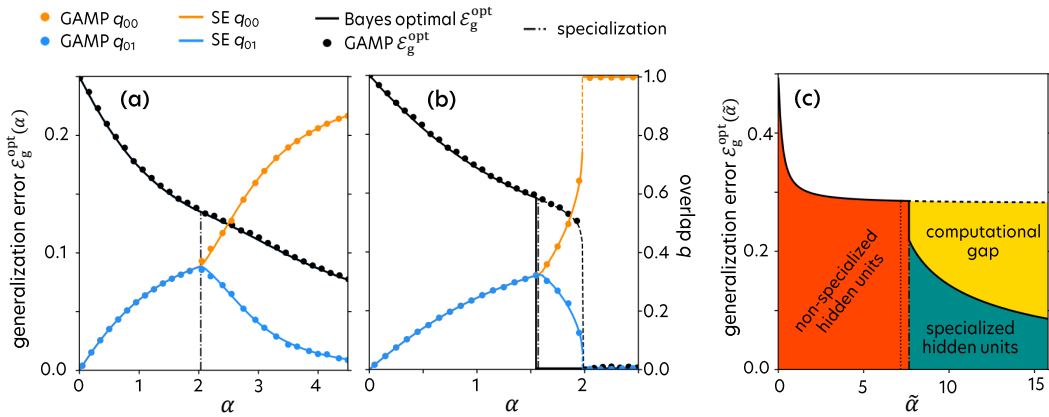
Figure 8.7: Generalization error and specialization in committee machines as functions of the task difficulty $\alpha = \frac{n}{m} \propto \frac{n}{d}$, which is the ratio of the number of training points and the number of input features. We consider committee machines with (a) $\boldsymbol{\theta} \in \mathbb{R}^{m \times D}$, $D = 2$, or with (b) $\boldsymbol{\theta} \in \{-1, 1\}^{m \times D}$, $D = 2$. The black line is the exact Bayes-optimal generalization error, black dots are obtained by studying the committee machine with GAMP. The orange and blue lines and dots indicate the overlap of the two hidden neurons of the student committee machine with the two hidden neurons of the teacher committee machine, calculated with GAMP and SE, respectively. We see that specialization is responsible for the rapid decrease in generalization error. (c) Generalization of panel (a) to large number of hidden neurons, D. Phase diagram calculated for the task difficulty, $\tilde{\alpha} = \frac{\alpha}{D}$. Adapted from [452].

Overparametrization. As we have already mentioned in the introduction, one of the most puzzling phenomena in modern ML is the generalization capability of heavily overparametrized models. In real-world setups, it is natural to think of the level of the model overparametrization as the ratio between number of model parameters, d, and number of available training data points, n. Surprisingly, we see in practice that models with large d are able to extract meaningful relations from much fewer training data points. In turn, with the teacher-student scheme, we can make the definition of overparametrization more rigorous, because we have direct access to the "ground-truth" number of parameters needed to describe the input-output rule, which is the number of teacher parameters. Therefore, the level of overparametrization can be understood as a ratio between the number of student and teacher parameters. In particular, the student can have much more parameters than the teacher. To study overparametrization, it is then a necessity to have mismatched teacher-student architectures. Crucially, this mismatch of architectures means that the student cannot achieve a Bayes optimal error anymore.

For the remainder of this section, we study the generalization error of overparametrized student models. This time we employ as a student a random feature model, presented already in fig. 8.6(b). The analysis requires the model's first layer weights to be fixed to random values. The number of student parameters in the second layer can vary as compared to the teacher.[11] As such, we have a full control over how overparametrized the student is. We come back to the study of overparametrization in committee machines in section 8.1.4.

---

[11]Ref. [457] interprets the same exact setting as a teacher generating labels with a perceptron, itself acting on a low dimensional latent space, and input data generated with a one layer generative NN from this latent space. A student perceptron is trained in the input data-label pairs.
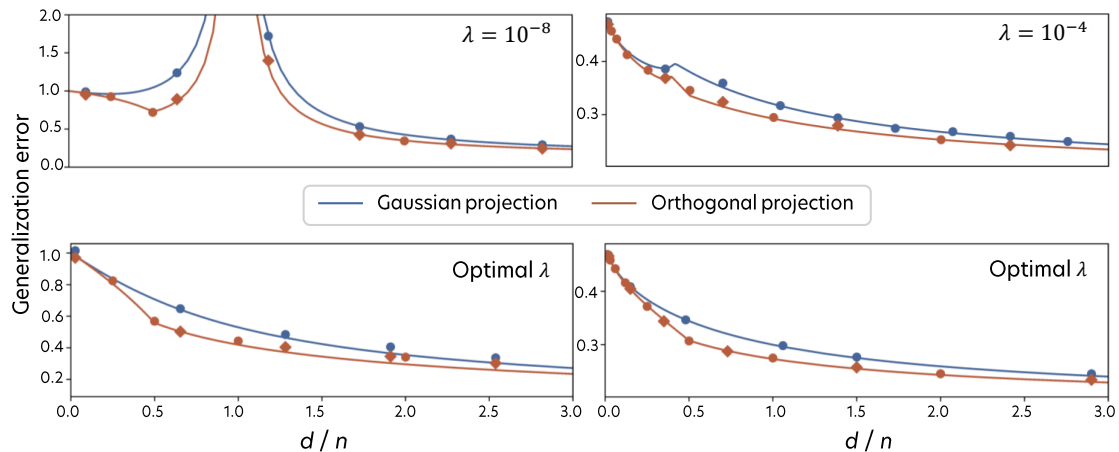
Figure 8.8: Generalization errors as functions of the ratio of the number of model parameters and number of training data points for mismatched teacher-student models where the student is a random feature model. First (second) column shows the generalization error in the case of a regression (classification) problem. The upper row shows results for sub-optimal regularization strengths, where the generalization error curves exhibit a double descent. The bottom row shows results for optimal regularization, where the double descent disappears. Adapted from Ref. [457].

With a student random feature model, we are ready to study the generalization error as a function of overparametrization, $\frac{1}{\alpha} = \frac{d}{n}$, where $d = d_1$ is the number of parameters in the first fixed random layer of the student. As the student cannot achieve a Bayes optimal error anymore, we need to change the training objective, e.g., to a MSE with ℓ_2 regularization. Using various analytical tools, we can still approximate the generalization error of the student and plot it as a function of overparametrization $\frac{d}{n}$. In Ref. [457], the generalization error in regression and classification tasks was analyzed for various regularization strengths. Their results are shown in fig. 8.8. The left (right) column shows the generalization error of the mismatched student for optimal and sub-optimal regularization strengths in a regression (classification) problem.

> Remarkably, in the case of mismatched student-teacher architectures, the generalization error curve exhibits a characteristic double descent. Moreover, the optimal choice of regularization cancels the first error descent, resulting in the generalization error steadily decreasing with increasing number of model parameters.

Therefore, these results on toy models give us a hint on the origin of the double descent phenomenon. It occurs when the student and teacher have mismatched architectures, and the choice of regularization strength is sub-optimal. Interestingly, Ref. [457] also showed that the magnitude of the initial generalization error ascent in the double descent phenomenon depends on whether the problem is a classification or regression task.

In summary, the study of toy models indicates that there are numerous reasons for the generalization error being larger than the Bayes optimal error. In general, the generalization capabilities depend on:

- whether a data-generating model (teacher) and learning model (student) have mis-

matched architectures,

- whether the model aims at solving a regression or classification problem,

- the choice of optimization method, target function, and available computation time,

- the sample complexity (how much training data is available and, for teacher-student committee machines, the degree of specialization of the neurons).

8.1.3 Models of data structure

So far, while studying sources of generalization errors, we have mainly played with the architectures of teacher and student models, which specifies the structure of the input-output rule underlying the data. In particular, we have only considered random input data sets where all input features are independent. Clearly, while such isotropic data simplifies the analytical analysis, it is quite unrealistic. Ideally, we would like to study prototypical data sets, like MNIST [21] or ImageNet [24], but these are difficult to treat analytically. Instead, let us move one step away from data sets given by white noise and use teacher-student paradigm to study the impact of data anisotropy on the generalization error. To this end, we employ *salient and weak feature models* [458]. Within these feature model, the data remains Gaussian (as in most of the previous sections), $x \sim \mathcal{N}(0, \Sigma_x)$, but the covariance is not isotropic as if $\Sigma_x = I_d$. Instead, it is anisotropic:

$$\Sigma_x = \begin{bmatrix} \sigma_{x,1} I_{\phi_1 d} & 0 \\ 0 & \sigma_{x,2} I_{\phi_2 d} \end{bmatrix}, \tag{8.15}$$

where $\sigma_{x,1} \gg \sigma_{x,2}$, and $\phi_{1/2} d$ denotes the number of data features (equal to the number of perceptron parameters) that are affected by the variance $\sigma_{x,1/2}$ (with $\phi_1 + \phi_2 = 1$). The parameters affected by the large variance, $\sigma_{x,1}$, form the salient subspace, whereas the ones with a small variance, $\sigma_{x,2}$, form the weak subspace as presented in fig. 8.9(a). We assume the weak subspace to be much larger than the salient one, $\phi_2 \gg \phi_1$.

If we add such a structure to our input data and run the teacher-student scheme with mismatched architectures (here, the teacher is a perceptron and the student is a random feature model), we can still compute the generalization error exactly in the high-dimensional limit [458]. Importantly, this generalization error now depends on the input data anisotropy. In particular, it depends on how the teacher perceptron is aligned with respect to the weak and salient data subspaces as presented in fig. 8.9(a). The dashed hyperplanes mark the separation of the input space by the teacher percepton and lie perpendicular to the perceptron parameter vector, θ. This vector can be aligned in various ways with the data anisotropy. If θ is aligned with the salient subspace, the hyperplane cuts along the weak subspace, and the only subspace relevant to discriminate the data points is the salient subspace, in which the variance of the data is concentrated, and the weak subspace can be effectively ignored. In this case, due to the data structure, the problem has a small effective dimension corresponding to the salient space $\phi_1 d$, therefore it is easier to solve. In turn, if θ is aligned with the weak subspace, the impact of the data structure is negligible as the student needs to discriminate along an axis where data has low variance comparatively to the typical variance of the data. Here, the problem closely resembles the (fully) isotropic case.

The impact of the data structure on the generalization curve as a function of the ratio of the number of student model parameters and the data dimensionality, $\frac{d}{m}$, is shown in fig. 8.9(b).
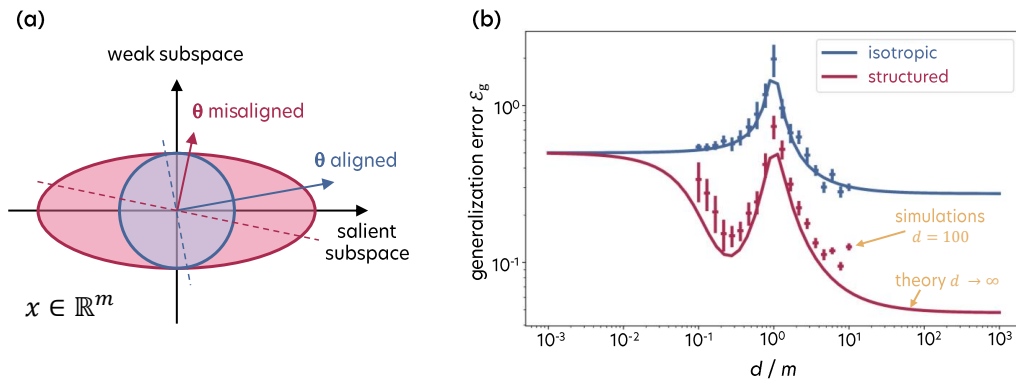
Figure 8.9: Data structure entering the teacher-student scheme. (a) The data space can be separated into a weak and salient subspaces, where the data is characterized by a small or large variance, respectively. The teacher perceptron with parameters θ can be either aligned (blue vector) or misaligned (purple vector) with the salient subspace. The classification task specified by the teacher (represented as a line separating the data) is easier (compared to the isotropic case) if θ is aligned with the salient subspace. (b) The model can detect the structure existing in the data. As a result, the generalization error is lower for the structured than for the fully isotropic case. Results for the isotropic data are similar to the results for anisotropic data where the teacher perceptron is misaligned. The generalization curve shows a double descent. Adapted from Ref. [458].

Interestingly, the structure in the data is detected during training before the generalization error peaks due to overfitting and improves the generalization error as compared to the isotropic case.

Why does the structure help? Because, in practice, the model can ignore the weak subspace and focus on the salient one, which lowers the dimensionality of the problem. The fact that the generalization error is lower in the anisotropic case compared to the isotropic case remains true even in the highly overparametrized regime ($\frac{d}{m} = 10^3$). Moreover, the double descent phenomenon is also exacerbated in presence of data structure. Note that both these effects take place only when the teacher perceptron is aligned with the salient subspace. Otherwise the setup closely resembles the isotropic case.

It turns out that many more questions can be addressed with the teacher-student paradigm using salient and weak feature models. In particular, the authors of Ref. [458] checked the interplay between the data structure and other elements of ML problems, like the choice of the loss function. Recalculating the quantities in fig. 8.9(b) for the MSE and logistic loss, one observes that the overfitting peak is attenuated in the case of logistic loss. Therefore, it seems that the logistic loss takes more advantage of the existing data structure. We can confirm this further by computing the generalization error for both loss functions as a function of the teacher-data alignment. As discussed earlier, this alignment determines how much of data structure is *effectively* present in the problem. In agreement with the results described above, when increasing the alignment, the gap between the generalization error of MSE and logistic loss grows.
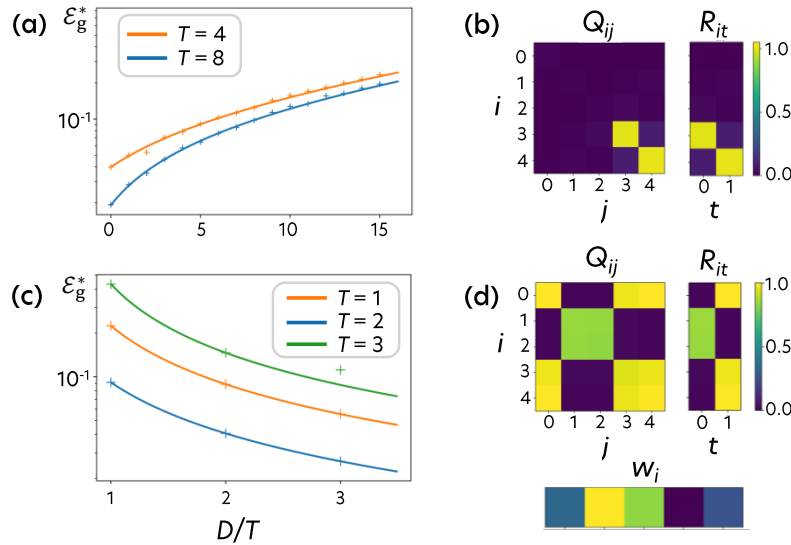
Figure 8.10: Dynamics of learning in overparametrized committee machines. In panels (a)-(b), we allow only a single trainable student layer, another layer is fixed. In panels (c)-(d), we train the whole student model. (a),(c) Generalization error vs. student overparametrization which occurs when the number of student hidden units, D, is larger than the number of teacher hidden units, T. (b),(d) Self-overlaps of the student (Q matrix) and overlaps between the overparametrized student and the teacher (R matrix). Vector w contains the second layer weights of the student. Adapted from Ref. [459].

8.1.4 Dynamics of learning

Finally, we can investigate the dynamics of learning and its dependence on the model over-parametrization using the teacher-student schemes described above. An example of a simplified model of learning is *online learning*, which has been analyzed since the 1990s. In online learning, the model is fed a stream of data, where the model sees each data point only once. We build a loss function based on this example and perform a parameter update according to the gradient of this loss function. In fact, we perform a parameter update after each data point encounter. Thus, the number of optimization steps is equal to number of seen training data points. If we take the continuous time and high-dimensional limit, and average over all random variables (which is doable with the replica method if we assume samples at distinct times are uncorrelated), we can again calculate the generalization error explicitly. In particular, we can calculate how it changes during the training. In other words, we can track the quality of the model predictions over the course of the training.

Such an analysis has already been conducted in the 1990s for perceptrons and committee machines [460, 461]. It showed, for instance, that during online training, the generalization error decreases with different convergence rates given different learning rates. Recently, the same analysis was revisited for soft committee machines [459] considering the impact of overparametrization. In the simplified case of matching teacher-student models and training limited to only a single student layer, results show how the generalization error drops the moment the student neurons specialize and attain a large overlap with the teacher neurons. We can also investigate the effect of overparametrization on the learning dynamics using committee machines as presented in fig. 8.6(a) in the regime of the number of data features, $m \to \infty$, with the sigmoidal activation function, $g(x) = \text{erf}(x/\sqrt{2})$. Here, we study the generalization

error as a function of the ratio between the number of hidden units of the student D and the teacher T given by $\frac{D}{T}$. Figure 8.10 shows two cases of online learning of such overparametrized students. In the first case, shown in panels (a)-(b), only the first hidden layer of the student model can be trained, whereas the parameters of the second hidden layer are fixed and identical to the respective teacher layer. In the second case, presented in panels (c)-(d), both student layers are trained. Panel (a) shows that the generalization error actually increases with the size of the trainable student layer, proving that overparametrization can be detrimental in some scenarios. To understand the reason, we analyze the teacher-student overlaps at the end of the training in the form of the $\boldsymbol{R} = [R_{it}]$ where each matrix element measures the similarity between the weights of the i-th student node and the t-th teacher node. We also study the overlap of the weights of different student nodes with each other ($\boldsymbol{Q} = [Q_{ij}]$). We plot both matrices in panel (b). We see that in the case of soft committee machines only the number of student neurons equal to the number of teacher neurons specialize. The rest simply picks up the noise present in the available data, which impairs generalization. However, if we allow all layers to be trained, a very different behavior is observed. In panel (c), we see that the generalization error decreases as one overparametrizes the student model. This time, all neurons learn something related to the teacher neurons. Thanks to that, additional neurons are beneficial as each teacher neuron can be learned by an ensemble of student neurons which contributes to "denoising" the estimation of the teacher parameters.

Outlook and open problems

In this section, we have seen how to use analytical tools from statistical physics to study problems in ML. In particular, we have discussed the seminal problem of perceptron capacity. Subsequently, we have focused on a powerful paradigm for studying the generalization error: the teacher-student scheme. This scheme is amendable to various modifications addressing every element of the learning problem.

We can study different teacher and student architectures, and they can be mismatched. We have shown results for perceptrons, committee machines, and random feature models, but in general, we can have, e.g., a pre-trained generative model (described in more detail in section 7.2.1) playing a role of a teacher as it was done in Ref. [462]. One can also analyze more complex data sets than those provided by a salient and weak feature model. In particular, is is possible to confirm intuitions gained from the analytical analysis of simple models with simulations on standard benchmark data sets [458], such as MNIST [21] and CIFAR [23]. Finally, one can go beyond online gradient descent and study multi-pass stochastic gradient descent (which involves multiple encounters of the same data points) with dynamical mean-field theory [463], bringing us closer and closer to modern optimization methods.

Moreover, one can investigate the capacities of large ML architectures (in contrast to simple perceptrons). Statistical tools play also an increasingly important role in the research on quantum machine learning (QML). For example, the Gardner approach was successfully applied to quantum perceptrons [464, 465] and quantum NNs [466]. In particular, it turned out that the quantum perceptron has some advantages over its classical counterparts when it comes to capacity [465]. Moreover, the teacher-student scheme was proposed to systematically compare different quantum NN architectures [467]. Finally, there is an increasing body of works searching for phases in the learning dynamics of ML models [468, 469].

Further reading

- Gabrié, M. (2020). *Mean-field inference methods for neural networks*. J. Phys. A: Math. Theor. 53, 223002. Review on the mean-field methods mentioned within this section. In particular, it contains principles of derivations of high-temperature expansions, the

replica method, and message passing algorithms [447].

- Zdeborová, L. (2020). *Understanding deep learning is also a job for physicists*. Nat. Phys. 16, 602–604. Short and friendly introduction to how physics can help ML [427].

- Castellani, T. & Cavagna, A. (2005). *Spin-glass theory for pedestrians*. J. Stat. Mech. P05012. Pedagogical review on mean-field methods for spin glasses [446].

8.2   Quantum machine learning

This section explores yet another direction: how quantum mechanics and quantum technologies can be used to solve data-driven tasks. This recent field is called quantum machine learning (QML)[12]. This field started with the development of quantum algorithms aiming for a potential quantum advantage. In recent years, there has been an increasing interest in another direction: studying hybrid quantum-classical algorithms (also often called quantum-enhanced algorithms), where part of the algorithm is performed on a quantum device. With the development of new experimental platforms for quantum computation, researchers are now looking for applications tailored to these hybrid algorithms and trying to determine if and how quantum advantage can arise in such systems. While the quantum advantage would represent a breakthrough, the study of the quantum-enhanced algorithms running on these hybrid devices is an interesting problem in itself and can potentially lead to the discovery of exciting physics.

In the following sections, we provide an overview of the recent advances in the field. We do not aim to provide a complete review, but rather an introduction to selected topics. In the last section, we refer to recent reviews of the field for the interested reader.

8.2.1   Gate-based quantum computing

In the following sections, we focus on the description of *gate-based quantum computation*. These concepts are used throughout the whole section.

> The most common building blocks of gate-base quantum computation are *qubits* and quantum gates. A gate-based quantum algorithm, specified as a sequence of gate operations and measurements performed on qubits, can be conveniently represented as a *quantum circuit*.

Qubits are two-level quantum systems that can be realized by isolating two degrees of freedom in several experimental platforms, such as photonic platforms [470], superconducting circuits [471], trapped ions [472], or Rydberg atoms in optical tweezers [473, 474]. When performing a calculation, a quantum computer modifies the state of the qubits or entangles them with quantum gates.

Quantum gates are unitary operations and can be represented by unitary matrices. The dimensions of these matrices depend on the number of qubits on which these gates act. The scaling of their dimension is exponential in the number of qubits.

Examples of single qubit gates are the Hadamard and Pauli-X gates , which read in the

---

[12]Often in literature, quantum machine learning (QML) incorporates both quantum-enhanced ML and ML applied to quantum, e.g. ML for quantum information processing. In this section, we use QML for quantum-enhanced ML. A detailed discussion about this convention can be found in section 8.2.2
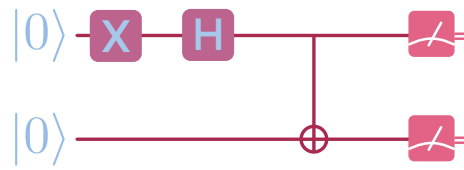
Figure 8.11: Illustration of a quantum circuit diagram with two initialized qubits, q_0 and q_1, and three different quantum gates: the Hadamard gate H and the σ_x gate X, both acting on q_0, and a two-qubit gate (CNOT). The final element is the measurement on q_0 and q_1.

single qubit basis $\{|0\rangle, |1\rangle\}$

$$H = \frac{1}{\sqrt{2}} \begin{pmatrix} 1 & 1 \\ 1 & 1 \end{pmatrix}, X = \begin{pmatrix} 0 & 1 \\ 1 & 0 \end{pmatrix}, \tag{8.16}$$

or parametrized gates such as the single qubit rotation gate

$$R_X(\theta) = \frac{1}{\sqrt{2}} \begin{pmatrix} \cos\theta & -i\sin\theta \\ -i\sin\theta & \cos\theta \end{pmatrix}, \tag{8.17}$$

parametrized in terms of the angle θ. An example of a two-qubit gate is the controlled NOT gate (CNOT), which reads in the two qubit basis $\{|00\rangle, |01\rangle, |10\rangle, |11\rangle\}$

$$\text{CNOT} = \begin{pmatrix} 1 & 0 & 0 & 0 \\ 0 & 1 & 0 & 0 \\ 0 & 0 & 0 & 1 \\ 0 & 0 & 1 & 0 \end{pmatrix}. \tag{8.18}$$

In general, *quantum circuits* can be illustrated in quantum diagrams, as exemplarily shown in fig. 8.11. Each line corresponds to a qubit. This circuit has two gates acting on a single qubit (X and H) and an entangling gate (CNOT) acting on two qubits. The last part of the diagram is the measurement, which is an interaction with individual qubits that forces their collapse to one of the two levels. As the measurements are destructive, the careful choice of a set a measurements is necessary to propely extract the needed information from the quantum circuit.

8.2.2 What is quantum machine learning?

To understand better quantum machine learning (QML), let us first have a look at fig. 8.12(a). Generally, ML algorithms are run on classical data, e.g., image classification or natural language processing. We have thus a classical algorithm dealing with classical data (CC). These Lectures Notes focus mainly on the case of classical ML applied to quantum data (CQ), e.g. quantum states. On the other hand, quantum machine learning (QML) deals with the integration of quantum devices in ML algorithms. Therefore, the algorithms can be quantum, and the data can be either classical (QC) or quantum (QQ). In this section, we focus mainly on the QC side, as the QQ side is only at its early stage of development [475–478].

Let us discuss an elementary example to introduce the revised building blocks of ML in the context of the QC QML. We consider the classification problem of one-dimensional data on a ring. We sketch each step of this QML classification problem in fig. 8.12(b). Firstly, the classical data (x_i, y_i) is encoded in a quantum computer. Here, for example, we encode
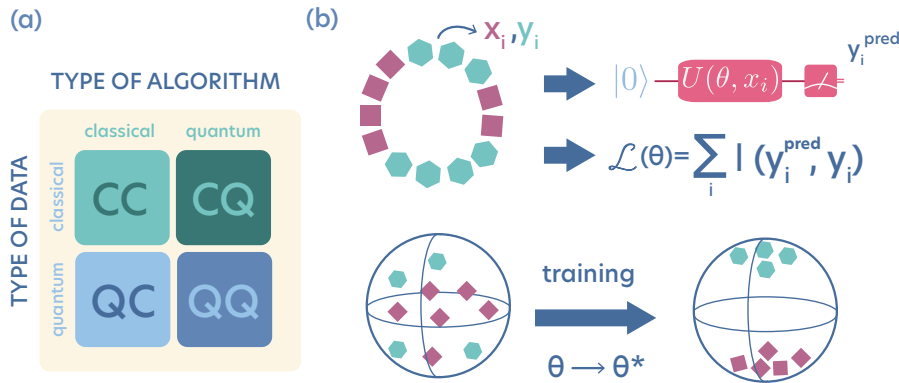
Figure 8.12: (a) Table of the different types of data and algorithms. (b) Sketch of an example of a classification task on one qubit.

them on a single qubit through the action of a parametrized unitary $U_{\boldsymbol{\theta}}(\boldsymbol{x}_i)$, where $\boldsymbol{\theta}$ are the parameters of this unitary transformation (for example $R_X(\theta)$ introduced in section 8.2.1). Then, a measurement is performed, and one can define the output of the measurement y_{pred} as a label (here 1 or 0). We then construct a loss function $\mathcal{L}(\boldsymbol{\theta})$ depending on the predicted and ground-truth labels. We can see here that the *quantum-enhanced* part corresponds to the evaluation of y_{pred} on a quantum computer. Once the loss function is defined, the minimization can be performed on a classical computer with the method of your choice, such as gradient descent or a gradient-free optimizer (e.g., Nelder mead). In this simple example, the training has a physical interpretation. Initially, the weights $\boldsymbol{\theta}$ of the unitary are randomly distributed. Consequently, the mapping of our classical data to the qubit is randomly distributed on the Hilbert space. The optimization procedure aims to push the two classes toward the opposite poles of the Bloch sphere. Therefore, for the weights after training $\boldsymbol{\theta}^*$, we expect that data on the Bloch sphere is much more ordered.

8.2.3   Ideal quantum computers and quantum machine learning

Computational complexity theory is a field of computer sciences that focuses on classifying computational problems in terms of the resources they need. In particular, classical computers are known to excel at solving problems belonging to two complexity classes: solvable in polynomial time (P) and bounded-error probabilistic polynomial time (BPP). Having an ideal quantum computer, a natural question arises: what types of problems can be solved in a polynomial time on a quantum computer while taking an exponential time on a classical computer? In this context, another complexity class was defined and includes all problems which can be solved and verified with a quantum computer in polynomial time (BQP).

One of the first quantum algorithm with an exponential speed-up has been proposed in the context of discrete Fourier transform. The quantum Fourier transform algorithm [479] performs the discrete Fourier transform on 2^n amplitudes using a quantum circuit consisting of only $\mathcal{O}(n \log(n))$ quantum gates. The classical algorithm needs $\mathcal{O}(n 2^n)$ operations to perform the same task. Another example of an algorithm with such a speed-up is the Shor algorithm for efficient number factorization [480]. It uses building blocks from the quantum phase estimation algorithm [481] and the quantum Fourier transform to gain an exponential speed-up with repsect to the best classical algorithm for this task. The Harrow-Hassidim-Lloyd (HHL)

algorithm [482] is another very famous algorithm that was designed to solve a system of linear equations

$$\boldsymbol{A}\boldsymbol{x} = \boldsymbol{b}, \tag{8.19}$$

where $\boldsymbol{A}$ is an $n \times n$ sparse matrix with condition number k. The algorithm is able to find the vector $\boldsymbol{x}$ in $\mathcal{O}(\log(n)k^2)$ time instead of the typical $\mathcal{O}(nk)$ for standard algorithms. This is an exponential speed up in the size of the system, however one crucial remark to keep in mind is that the classical algorithm returns the full solution, while the HHL can only approximate functions of the solution vector.

Machine learning (ML) algorithms largely rely on linear algebra, which generally constitutes the most costly part of the algorithm. For example, the classification problem with a support vector machine (SVM) generally requires quadratic progamming (see section 2.4.3 for the general idea of SVM) but a special form of support vector machine (SVM)[13] boils down to solving a system of linear equations. In this context, quantum computers might speed up such costly operation. One application of the HHL algorithm have been proposed, e.g., in the context of SVMs [483] (see [484] for a recent experimental realization on a four-qubit quantum computer) and data fitting [485]. It is worth noticing that the quantum speed-up provided by the HHL algorithm with respect to classical algorithms is under debate [486].

8.2.4 Quantum computing in the noisy intermediate-scale quantum era

Until now, we have only considered ideal quantum computers to run the most famous quantum algorithms, including the Shor, the quantum Fourier transform, and HHL algorithms. However, the realization of these algorithms for a number of qubits where such advantage matters is not yet feasible in near-term quantum computers. The main reasons are that (i) quantum computers currently contain *too few qubits* (nowadays in the order of hundreds) and (ii) they perform imperfect operations (noisy).

Furthermore, algorithms such as the Shor algorithm have to be compiled on real devices. This means that unitaries acting on several qubits have to be *decomposed in elementary gates* that can be physically realized in the experimental platform. Such a transformation might lead to complex quantum circuits with native gates [487]. For example, for the IBM-Q Washington platform, only the CNOT, ID, RZ, $\sqrt{X}$, and X gates are native gates. Any other gate must be decomposed into these gates. Since these gates form a set of universal quantum gates [488], this is, in theory, sufficient but, in practice, it can lead to very quantum circuits with an important number of gates. For example, we consider the decomposition of the Shor algorithm to these gates, as shown in fig. 8.13. An apparently simple circuit consists, in practice, of many operations on real quantum devices. The latter might be especially problematic due to *noise and decoherence* that are intrinsically present in the physical devices.

In modern quantum computers, we can identify three primary sources of errors: gate errors (generated by a non-precise application of the desired gate), decoherence errors (loss of coherence of the wave function as a function of time), and read-out errors (erroneous read-out of the qubits state during the measurement procedure).

---

[13]For the special case of least-squares support-vector machine, the problem can be written as a solving a linear system of equations.

INTEGER FACTORIZATION: SHOR'S ALGORITHM
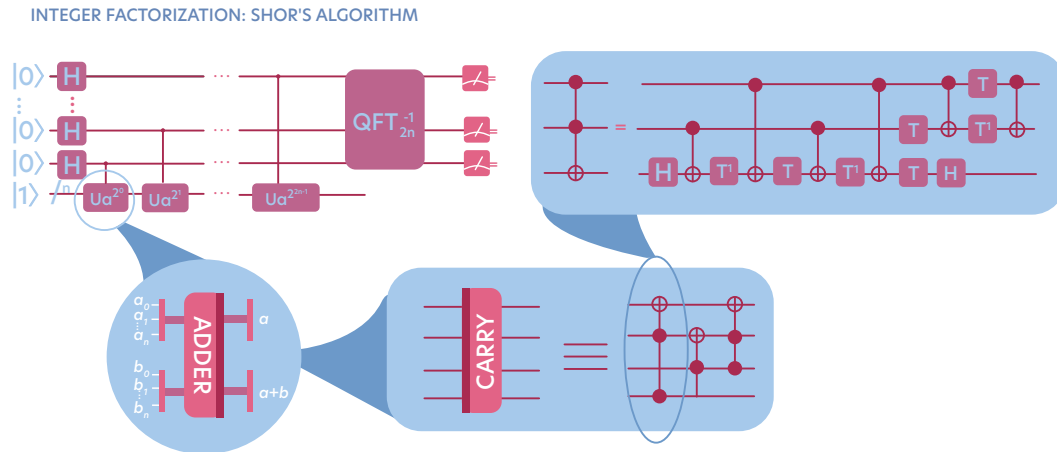
Figure 8.13: Realization of the famous Shor algorithm in a real quantum computer. Top left diagram presents a concise theoretical circuit of this algorithm. Due to the limitation to certain gates (CNOT and SWAP), generic gates have to be decomposed and the circuit requires more gates and higher depths.

> Due to many different noise and error sources in real quantum computers, we are far from the fault-tolerant quantum computation. Instead, we are in the so-called *noisy intermediate-scale quantum (NISQ)* era [489]. The qubits of the current quantum processors are noisy and require quantum error correction. Nevertheless, the study of the physics of such systems is interesting in itself. In particular, there might be applications with a quantum speed-up within this regime, as in the case of the recent quantum advantage experiment [471].

It is now clear that we cannot run algorithms requiring many gates or implement gates with low error rates in NISQ circuits. If the circuit contains too many gates, the coherence gets lost as well as the superposition and entanglement between different qubits. A natural question arises: Can we design algorithms that perform well on NISQ devices and do not require fully error corrected quantum computers? This means one has to find clever ways to explore the exponentially big Hilbert space without exact algorithms. One approach is using quantum computers to generate variational states and to find a procedure to converge iteratively to the solution instead of taking a direct deterministic path (for example by performing the optimization on a classical computer). We go into more detail into these variational approaches in section 8.2.6. Before, in section 8.2.5, we present how NISQ devices can be used for SVM with kernels.

To sum up, the NISQ era has still many open problems in experimental quantum computing and in quantum error correction. State-of-the-art devices include 50-100 qubits with error rates of less than 0.5%[14]. Nonetheless, recent years showed many examples of useful variational quantum simulations that can be performed with the near-term devices, e.g., see Ref. [490]. Moreover, many error mitigation routines have been developed to ease the noise effects in quantum computers, allowing for extraction of useful information from noisy devices

---

[14]In the quantum advantage experiment [471], the authors reported single-qubit gate fidelities of 99.85% and two-qubit gates fidelities of 99.64%
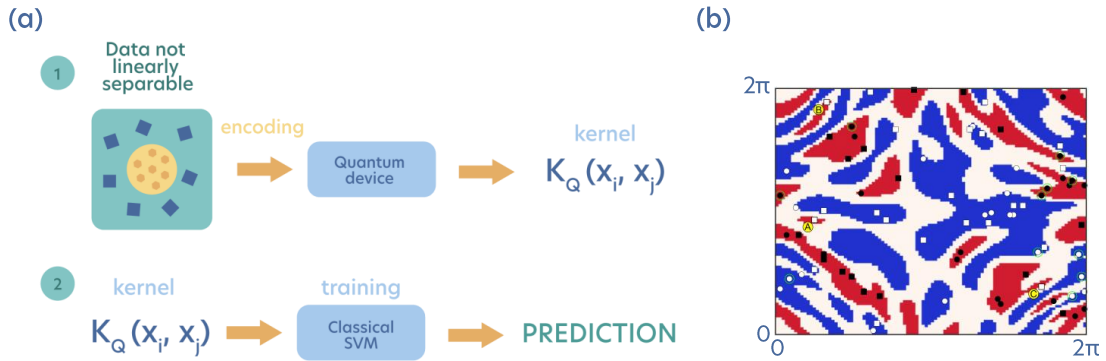
Figure 8.14: Quantum SVM enhanced by a quantum device. (a) Sketch of the steps of the SVM enhanced by a quantum kernel. The data are encoded in a quantum device, such as a quantum circuit, which computes the kernel. These kernels are then used in classical SVM. (b) Example of a dataset used in Ref. [495] to show the capacity of quantum kernels. Blue (red) regions correspond to label 1 (0).

in the near term [491–494]. NISQ devices are also an excellent trial field to study physics without building a fault-tolerant quantum computer. Finally, useful applications of NISQ devices can still be found, and they can be considered as a step toward fault-tolerant quantum computing.

8.2.5 Support vector machines with quantum kernels

We have seen in section 8.2.3 that ideal quantum computers could allow one to accelerate the numerically costly parts of the support vector machine (SVM) algorithm by implementing the HHL algorithm. There, the key element has been to use the quantum computer to solve the linear system of equations. In 2018, two independent works [495, 496] followed an interesting alternative direction: using kernels evaluated directly on quantum devices, while performing the rest of the SVM algorithm classically.

The idea is sketched in fig. 8.14(a). Let us consider a dataset that is not linearly separable. We therefore want to non-linearly embed it in a higher dimensional space such that the data is linearly separable in this space (see section 4.2 for more detail). We here use a quantum device to encode classical data $\boldsymbol{x}$ into a high-dimensional Hilbert space $|\psi(\boldsymbol{x})\rangle$, or even infinite in the case of squeezed states considered in Ref. [496]. In this case, the choice of the encoding of the classical state into the quantum state is crucial as it determines the quality of the feature map. More importantly, quantum devices and in particular quantum circuits can allow for the efficient computation of the scalar product between two quantum states, which allows one to define a quantum kernel

$$K_Q(\boldsymbol{x}_i, \boldsymbol{x}_j) = |\langle \psi(\boldsymbol{x}_i)|\psi(\boldsymbol{x}_j)\rangle|^2 = \sum_n \lambda_n \phi_n(\boldsymbol{x}_i)\phi_n(\boldsymbol{x}_j), \tag{8.20}$$

which has all the properties of a classical kernel with a feature map ϕ and defines an RKHS (see section 4.1.3)[15]. As such, quantum kernels can be directly used in classical algorithms such as kPCA or kSVM or Gaussian processes (GPs) [497] rendering them quantum algorithms.

---

[15]The careful reader may notice that eq. (8.20) is the norm squared of the inner product instead of the typical inner product expected for kernels. This becomes clearer when writing the kernel in terms of density matrices $K_Q(\boldsymbol{x}_i, \boldsymbol{x}_j) = \text{Tr}(\rho_i \rho_j)$. The kernel is then corresponding to the Frobenius inner product of density matrices ρ_i and ρ_j.

To be more concrete, we explain the main ingredients of the quantum kernel introduced in Ref. [495]. Given a data set of points $\{x_i\}$ with labels $\{y_i\}$, the feature map is defined in terms of the unitary transformation $U(x_i)$ that can be realized in a quantum circuit of qubits

$$x_i \mapsto |\psi(x_i)\rangle = U(x_i)|0\rangle, \tag{8.21}$$

where $|0\rangle$ stands for the product state $|0\rangle^{\otimes n}$. Typically, the classical data encoding into the quantum circuit can be done through parametric local rotations of single qubits. The unitary is then built through repeated application of these data dependent gates and other nonparametric gates, such as entangling gates and Hadamard gates. We do not enter into the details of the construction of the circuit, but the interested reader can have a look at the following Qiskit tutorial for more details [498].

The quantum kernel can then be computed on a quantum circuit with the compute-uncompute trick: one basically implements the following quantum circuit $U^\dagger(x_j)U(x_i)|0\rangle$ and measures in the z basis. the frequency of the all-zero outcome estimates, therefore, gives an estimate of the kernel $K_Q(x_i, x_j)$.

Given these kernels, the optimization of the parameters of the SVM can be performed on a classical computer (see section 4.2.2) using, e.g., Bayesian optimization [497] presented in section 4.3. Ref. [495] generated a complex classification problem, shown in fig. 8.14(b), where the blue (red) region corresponds to label 0 (1). They then generated a training set by selecting random points these regions and performed the SVM enhanced by the quantum kernel. The algorithm yields very good results with around 95% of accuracy on the test set for this synthetic data set.

The previous example shows that quantum kernels can represent complex data sets. Nevertheless, the quantum advantage has yet to be seen for a general data set [499,500]. A recent important step in this direction has been achieved in Ref. [475], where the authors constructed data sets that cannot be classified efficiently on a classical computer. Another exciting question concerns the best ways to build quantum kernels, i.e., how should one perform the encoding of the inputs $x \mapsto |\psi(x)\rangle$? This is still a very active line of research and these questions do not have yet an answer. We refer to [495] for further information.

8.2.6 Variational approaches

This section deals with the optimization of quantum circuits that can be realized in NISQ devices. In particular, we focus here on the so called variational quantum algorithms. This idea generalizes the toy example we introduced in section 8.2.2. We define a parametrized quantum circuit (PQC), a circuit that depends on a set of parameters $\{\theta\}$ (θ can be, for example, the angles of single qubit rotations). Then, one defines an objective function $C(\theta)$ that we aim to minimize. Such an objective function can always be written as a function depending on a set of observables and on the PQC. Our goal is then to find the optimal set of parameters θ^* minimizing the objective function. Such variational approach has applications in many fields such as ML (classification, generative models), many-body physics and quantum chemistry (ground state finding), combinatorial optimization, etc.

We illustrate the building blocks of the variational approach with the example of the variational quantum eigensolver (VQE) [501]. Given an Hamiltonian $\hat{H}$, the goal of the VQE is to minimize the energy $E = \langle\psi|\hat{H}|\psi\rangle$. The general principle of the VQE is shown in fig. 8.15. The process starts with an initial state which is easy to prepare on the quantum computer, e.g., the product state $|0\rangle^{\otimes n}$, which for simplicity we denote by $|0\rangle$. This is followed by the parametrized quantum circuit (PQC) including, e.g., all the parameters θ of the quantum gates and which can be seen, at this point, as a black box which prepare a quantum state. In the
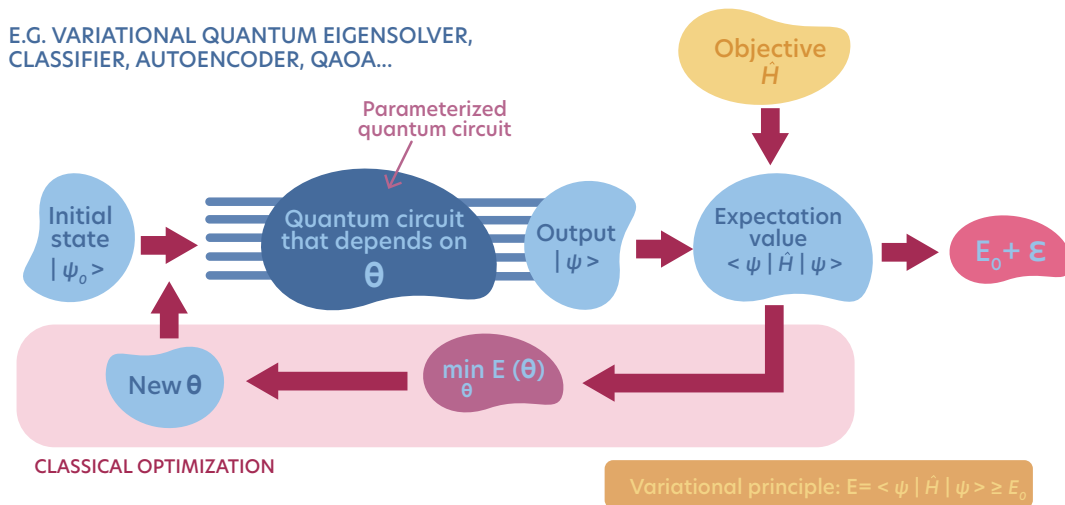
Figure 8.15: Variational optimization of quantum circuits, including the initial state, parametrized quantum circuit (PQC), output, objective, measurement, and classical optimization.

first iteration, this state is just a random state and is used as the initial state for the expectation function, which is in general the Hamiltonian of the physical system we want to study, up to a global phase. The Hamiltonian can describe the interaction within a molecule or a spin system, but can, in general, be any kind of cost function in operational form that can be written in the computational basis of the quantum hardware we are using. The next step is the minimization of the cost function with a classical subroutine to converge toward the lowest energy state of the physical system in the space of the quantum sopate that can be reached by our parametrized quantum circuit (PQC) in a self-consistent manner. We also know that, if the system is gapped and the ground state unique, the minimal value of the expectation value of the Hamiltonian is the ground-state energy and the corresponding eigenvalue is the ground state wave function.[16]

Going a bit more into detail, for the PQCs we are computing the energy of the ansatz

$$E_0 = \min_{\boldsymbol{\theta}} \langle \psi(\boldsymbol{\theta}) | \hat{H} | \psi(\boldsymbol{\theta}) \rangle = \min_{\boldsymbol{\theta}} \langle 0 | U^{\dagger}(\boldsymbol{\theta}) \hat{H} U(\boldsymbol{\theta}) | 0 \rangle \,,$$

where $\boldsymbol{\theta}$ are the parameters of the gates which are optimized to minimize the expectation value. The variational state is the unitary state, i.e., our *parametrized quantum circuit (PQC)* applied to the initial state $|0\rangle$. However, in order to run and work with the PQC we have to make several assumptions: first, we are assuming the existence of a set of parameters that approximates the ground state and that our PQC can represent that specific solution. Second, that it is possible to converge to the solution without being stuck in local minima and, finally, that the circuit can be run on a NISQ computer. Taking all these assumptions into account, there are two ways to design a PQC. The first option is the problem-inspired design which we can use when we exploit some physical properties of the system we want to represent, e.g. by using the Hamiltonian representation to design the unitary operation as happens in the variational quantum eigensolver (VQE) algorithm. However, these kinds of ansatz require, in general, many gates or a particular qubit connectivity, making it unfeasible for bigger sys-

---

[16]The energy measured at each iteration is an upper bound of the ground state energy, according to the variational principle. The ability to reach the global minimum, of course, depends on the capacity of the circuit. If the circuit does not contain the solution, such an ansatz will never reach the minimal energy [502].

(a)

(b)
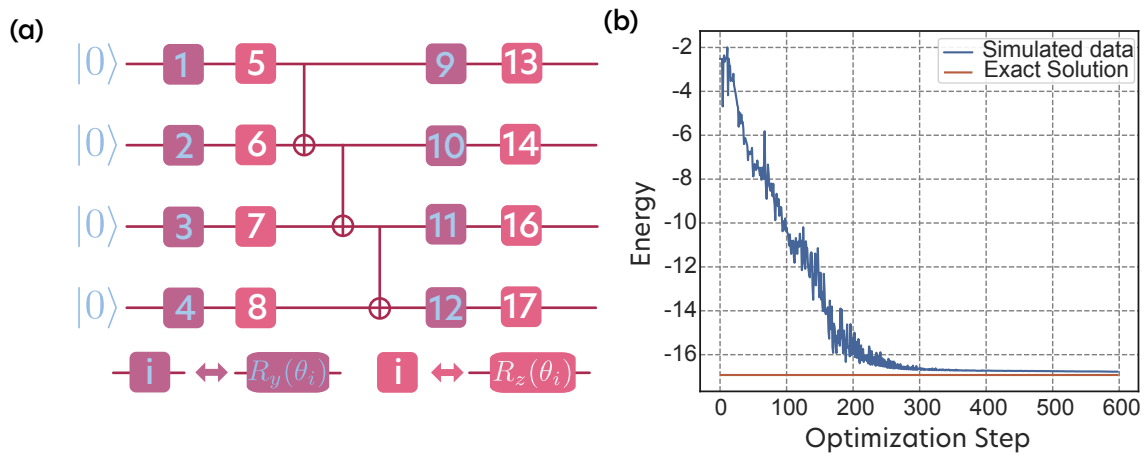
Figure 8.16: In this figure we show an example of a variational quantum simulation. In sub-figure (a) we show the parametric quantum circuit used for the simulations. In sub-figure (b) we plot the energy of the system during the optimization algorithm.

tems in current quantum computers. Another way is the hardware-efficient ansatz, which is a heuristic method that requires way less quantum gates and that consists of preparing a PQC that uses the native gate set and respects the quantum computer connectivity. In general, problem-inspired ansatz use to be more precise but less feasible to implement in current quantum computers, while this happens otherwise with the hardware-efficient ansatz

The next step after defining the PQC is the choice of the *objective function* which can be everything that encodes our problem in a quantum operator, e.g., a Hamiltonian as shown in fig. 8.15. The objective function is then decomposed into Pauli strings whose expectation value can be measured with the quantum computer. The expectation value of a hermitian operator is computed on the quantum hardware by making the wave function collapse in the computational basis. From this measurement, we can extract bit strings (i.e. lists of 0 and 1, e.g., $[(0, 0, 1, 1, 0, 0), (1, 0, 1, 0, 0, 0), (0, 0, 1, 0, 1, 0)]$). From these bit strings, we can reconstruct the expectation value of any operator that can be written as the tensor product of Pauli matrices. This leads to the next important step in the process, the measurement. In this step, we extract the information from our quantum computer or our quantum devices. These devices project in a particular basis, normally the z-basis, and the measured expectation values are from Pauli strings and not directly the Hamiltonian or the designed cost function.

The last step is the classical optimization in which we have to navigate through the PQC parameter space by using, e.g., a gradient-based approach. The gradients are expectation values of the quantum circuit derivatives with respect to a parameter, and we do not have direct access to the gradients of the quantum state. In NISQ devices, the gradient of the PQC can be computed with the parameter shift rule [503]: for each parameter θ, one can compute exactly its partial derivative by evaluating two PQCs. The problem in this step is the number of required measurements. In order to run the classical minimization algorithm, measurements of all gradients are required. Therefore, this method can be very expensive and includes a huge number of variables and multiple iterations to converge to the ground state, and that is why other gradient-free methodologies are exploited, like genetic algorithms or reinforcement learning strategies. After all, the combination of the variational optimization of the quantum circuit with classical optimization algorithms is an efficient way to use NISQ devices for real world problems.

Let us discuss a concrete example: the Heisenberg Hamiltonian acting on four spins, which

reads

$$\hat{H} = \sum_{i=1}^{3} J_1 \sigma_i^x \sigma_{i+1}^x + J_2 \sigma_i^y \sigma_{i+1}^y + J_2 \sigma_i^z \sigma_{i+1}^z + \sum_{j=1}^{4} h_1 \sigma_i^x + h_2 \sigma_i^y + h_3 \sigma_i^z . \tag{8.22}$$

We fix the parameters of the Hamiltonian to $\boldsymbol{J} = [1, 1, -1]$ and $\boldsymbol{h} = [1, 1.5, 3]$. These parameters are chosen to be far away from any phase transition point, not to make the problem too difficult. We can use this Hamiltonian as a benchmark for our algorithm. Let us also consider a very easy quantum ansatz for the four-qubit case. The ansatz consists in two rotation gates, applied to every qubits in Y and Z direction, three CNOT gates that connect every qubits, and two more rotations in Y and Z direction. The circuit is sketched in fig. 8.16(a).

In variational quantum eigensolvers (VQEs) we want to use the variational circuit to minimize the energy of the system. If we did this operation on a classical computer, the computational cost of the evaluation of the energy would scale exponentially with the number of qubits. The expectation value of the Hamiltonian of the system can be computed efficiently on a perfect quantum computer. The computational cost is linear in the number of qubits. We can feed this cost function to an optimizer, in this case we use the Nelder-Mead optimization routine. In fig. 8.16(b) we plot the value of the energy of the system as a function of the optimization step. We can find a relatively good approximation of the ground-state energy with few variational parameters and polynomial computational cost in the number of qubits. Many things can be improved in these kinds of simulations, both on the design of the variational ansatz, and on the optimization routine. In the design of variational quantum circuits, we can, for example, impose symmetries of the system we are studying. In the optimization routine, we could use stochastic gradient descent or other more efficient algorithms.

8.2.7 Parametrized quantum circuits for quantum machine learning

Classification tasks Variational quantum circuits can be used to perform the classification of classical data. The first non-trivial task in the construction of such a quantum algorithm is the loading of the classical data on the quantum hardware. Moreover, the algorithm must be able to process efficiently these data and have a way to perform the classification. In Ref. [504] the authors have shown that PQC with data reuploading can lead to a good classifier. In Ref. [505] the authors have introduced the concept of quantum convolutional neural networks. As for classical CNN, these variational quantum circuits have more capacity. In particular, the authors have shown how these circuits can be used to perform classification on symmetry-protected topological phase in the Haldane chain directly from the quantum state, that can be obtained with a VQE. This idea has been realized experimentally in a recent work [476]. Finally, it is worth to notice that the above-mentioned classifiers are closely related to quantum kernels [506, 507].

Quantum reinforcement learning Parametrized quantum circuit (PQC) can also be used to evaluate action-value functions (see section 6.2 for Q-learning and deep Q-learning) policies (see section 6.3 for an introduction to policy gradient). Two examples of algorithms that take advantage of PQCs in the context of RL can be found in Ref. [508, 509]. In Ref. [508], the quantum circuit is trained using a policy gradient algorithm and is used to solve classical environments, i.e., to find the optimal policy for the task at hand. The choice of the action, the probability of which occurring we want to fix, is going to be encoded in the measured observable – if we have a certain set of actions, we define a certain set of observables. The RL architecture states that the agent observes fixes a quantum state that the circuit will produce and the expectation value of such observable is going to encode $\pi(a|s)$ – the probability of the action a in a given RL state s, i.e., it corresponds to the policy π. In Ref. [509] the authors have used the OpenAI Gym [510] examples as benchmark environments for the variational

quantum algorithm for deep Q-learning, as for example, the *Cartpole* game (a cart that can move left and right and the agent is trying to balance the pole attached to the cart). Compared to the classical models (for which the exemplary environments were created), the quantum models can reach a similar accuracy using much fewer parameters (which alone does not imply better models but highlights their difference). An interesting and open question would be to understand whether these results can be generalized to other environments.

Quantum autoencoders   In the same spirit as their classical counterpart (see section 2.4.5), quantum autoencoders [511] are used to compress quantum data on a quantum computer. quantum autoencoders act directly on data encoded in qubits and can thus be used to compress quantum data without having the need to have a classical representation that would have an exponential cost. Since there are patterns that classical computation cannot generate, e.g. entanglement, the quantum version of an autoencoder might be able to recognize patterns beyond classical capabilities. The encoding done with quantum autoencoder transform quantum data into a latent space with fewer qubits. Let us consider a set of quantum data that can be encoded into n qubit. We want to find the representation of k qubit that encodes the properties of our data. To do so, we minimize a variational cost function. The quantum simulation is performed on $n + k$ qubits. This encoding is done via a variational map represented by a quantum circuit with a polynomial number of parameters $U(\theta)$. Since the encoding procedure is a unitary (quantum circuit), the decoding operator is just represented by the hermitian conjugate of $U^{\dagger}(\theta)$. It is still under debate whether this quantum algorithm can have a computational advantage with respect to their classical counterpart. Variational quantum autoencoders have also been proposed for various applications, such as quantum data denoising [512] or quantum error correction [513].

Generative models   Generative models are algorithms learning the distribution of a data set. In quantum mechanics, the inherent quantum nature of the devices can be of great help for learning probability distributions and in particular for quantum wave functions. Recently, diverse QML architectures have been proposed: these include quantum Hamiltonian-based models [514], quantum GANs [515, 516] and quantum Born machines [517, 518]. In particular, quantum circuit Born machines are generative model that can represent classical distribution of data, represented as pure quantum states. In this context, variational quantum circuits can provide a useful tool to represent these probabilities distribution and, moreover, an efficient way to sample from these distributions. The algorithm has comparable performance to its classical counterpart. In Ref. [519] the authors have proposed yet another quantum circuit Born machine that can learn the probability distribution of coherent thermal states, where the probability distribution is given by the Boltzmann weights. Such algorithms can be run on NISQ devices and are good candidates for quantum advantage in near term.

8.2.8   Current experimental and theoretical limitations

In this last section, we discuss some experimental and theoretical open problems which have to be overcome for successful applications and use of NISQ devices. One important topic is the *quantum error mitigation*, i.e., reducing or compensating errors. This includes classical post-processing techniques as well as active operations on the hardware itself. The former approach includes techniques as *stabilizer-based approaches* which rely on information associated with conserved quantities as spin or particle number [520], and mitigation scheme based on classical post-processing of data [491–494]. These methods are, however, only post-processing tools after we ran the circuit. Another way of error mitigation are *active mitigation techniques* or quantum optimal control strategies. In contrast to the post-processing techniques, these methods are directly related to experiments and the quantum hardware [521–526].

We are not only facing experimental but also theoretical open problems which have to be solved or overcome. One of these problems is the *barren-plateau problem* [527] which appears for global cost functions of quantum circuits parametrized with local unitaries. Without prior knowledge about the solution, the parameters $\boldsymbol{\theta}$ of the PQC are initialized randomly. As a consequence, we obtain a barren-plateau: the expected value of the gradient as well as the expected value of the variance are exponentially vanishing with the number of qubits and/or the circuit depth. In other words, this means that the loss landscape is mainly flat, with a narrow gorge hosting the global minimum [528]. Possible solutions to the barren-plateau problem consist in using parameters close to the solution, using a local cost function instead of global ones, or introducing correlations between parameters [527, 528]. The downside of the latter solutions are that these methods do not work well for strongly correlated systems. A general solution to the barren-plateau remains still an open theoretical problem. Moreover, it is totally unclear that there are any natural problems where a PQC will outperform a classical learning engine [507]. The loss landscape is, furthermore, characterized by the appearance of many local minima that can be far away from the global minimum [529]. A similar situation is known for the training of classical NNs [38] – it is an open question whether this observation poses an actual challenge in practical applications of PQCs.

Another theoretical obstacle includes the capacity of the PQC. When setting a PQC ansatz, we have to be careful not to narrow the Hilbert space accessible by the PQC too much. If we do so, we might end up in a wrong area of the Hilbert space and we cannot reach a good approximation of the solution [502, 530]. There are some measures (e.g. Haar distributions) but the capacity remains an open problem for the PQC ansatz.

Circuit compilation is another important challenge, involving both theory and experimental parts: the theoretical circuit, the decomposition into native gates, the simplification, and finally the mapping to the hardware and real qubit system. The circuit compilation relies on the Solovay-Kitaev theorem [488, 531] which states that with a universal gate set it is possible to approximate any SU(N) with a circuit of polynomial depth up to a certain accuracy. However, when it comes to the specific hardware implementation, some gates are easier to control than others. In PQC, one always try to use as many native gates as possible. This solution can make the quantum circuit shorter and simpler.

As a concluding remark, much effort has been devoted toward applications with a quantum advantage, i.e., where a quantum computer is required using less resources than the classical counterpart. The study of such algorithms is crucial and will probably require the integration of quantum devices in high performance computing facilities.

Outlook and open problems

We are currently in the NISQ era. Despite the complex theoretical and experimental challenges toward fault-tolerant quantum computation, the general objective in the NISQ era is to understand the possible algorithms that can be implemented in current experimental platforms. While the reduction of error rates affecting qubits and gates efficiency developments is a hard task demanding fundamental scientific and technological advances, there is a need to develop software tools to control quantum computers, develop error mitigation techniques and define quantum optimal control strategies in the meantime, as well as tools to characterize variational quantum algorithms such as the study of the loss landscape [362, 532], the entanglement properties [533], etc. Moreover, the development of algorithms taking advantage of quantum computers without having a direct classical counterpart is a very interesting but challenging direction beyond the CQ paradigm.

Further reading

- Biamonte, J. *et al.* (2017). *Quantum machine learning*. Nature **549**, 195. Very famous review on the subject of QML.

- Bharti, K. *et al.* (2022). *Noisy intermediate-scale quantum (NISQ) algorithms*. Rev. Mod. Phys. **94**, 015004. Review paper focused on the variational quantum circuits simulations in the NISQ era.

- Li, W. & Deng, D.-L. (2022). *Recent advances for quantum classifiers*. Sci. China: Phys. Mech. Astron. **65**, 220301. Recent review paper on classification algorithms with quantum computers.

- Cerezo, M. *et al.* (2021). *Variational quantum algorithms*. Nat. Rev. Phys. **3**, 625. Very nice review paper on the recent advances in variational quantum algorithms and their applications.

- Qiskit tutorial on quantum machine learning.

- Pennylane tutorials and demos on quantum machine learning.

- Tensorflow quantum tutorial on quantum reinforcement learning.

9   Conclusion and outlook

In the last decade, ML (and DL in particular) has been intensively studied and has revolutionized many topics, including computer vision and natural language processing.

The new toolbox and set of ideas coming from this field have also found successful applications in the sciences. In particular, ML and DL have been used to tackle problems in physical and chemical sciences, both in the classical and quantum regime. Their applications range from particle physics, fluid dynamics, cosmology, many-body quantum systems [29–31], to quantum computing and quantum information theory [534]. On the other hand, physicists have started to apply tools from statistical physics to try to understand the dynamics related to the training of DL [427] and are also exploring potential hardware based on quantum physics [535].

These Lecture Notes aim to introduce physicists and chemists to selected topics in ML and some of their applications in physics and chemistry. As this field is relatively new and quickly growing, we have decided to focus on explaining key concepts in ML for scientists with a physics or chemistry background and briefly reviewed some of the possible applications. We have also discussed how physics can help in gaining a deeper understanding of the intrinsic mechanisms governing DL and how quantum technologies can be used for data-driven tasks. The list of topics and applications covered in this book is, of course, not exhaustive. We nevertheless hope that we have been able to convey our enthusiasm for ML applied to quantum sciences and that we have properly introduced the necessary building blocks needed for the keen reader to dive into this field.

Finally, we would like to summarize the directions explored in this book and share our view on potential exciting developments.

Characterization and classification of trajectories and phases. Researchers have intensively studied different ML and DL methods to tackle the characterization and classification of trajectories and phases. While many of these techniques have been very successful [31, 536], many challenges remain. Most of the works focused on reproducing known phase diagrams with supervised learning schemes. The ability to process unlabeled data and apply unsupervised learning or self-supervised learning constitutes a big step forward in assisting physicists in the discovery of new exotic phases of matter. Furthermore, as the most powerful models are black boxes, interpretability techniques are essential to help physicists to discover relevant physical concepts learned by these models. For example, Refs. [124, 537] were able to discover physical concepts or recover conservation laws from trajectories. Another very interesting direction is the classification of phases directly from experimental data [96, 122, 402, 538, 539]. It would be interesting to understand the effect of the experimental noise on the classification with respect to simulated data.

Gaussian processes and kernel methods. Gaussian processes (GPs) and kernel-based regression methods are ML algorithms that are not considered to be suited for large dimensional systems due to their cubic scaling with the size of the training data set [191]. Nonetheless, kernel-based methods have proven to be robust regression tools with comparable accuracy to DL methods without the caveat of hyperparameter optimization. They have also played a significant role in the field of optimization thanks to the success of Bayesian optimization (BO) [145]. The advancement of kernel-based methods has been focused on two main challenges: (i) numerical routines for matrix inversion and (ii) more robust kernel functions. The rise of GPUs has allowed for the development of efficient algorithms for kernel-based methods (e.g., GPyTorch [186]). The accuracy of kernel-based methods is founded

on the learning capacity of the underlying kernel function. While algorithms similar to the Bayesian information criterion (BIC) have proven to be very useful for the construction of kernels well-suited for the data, the rise of the automatic differentiation (AD) and the ability to parametrize more complex kernels, along the lines of Ref. [184], offer exciting alternative directions. Finally, kernel-based methods have also been expanded to molecular systems where a string-based comparison is carried as the kernel function [540] and used for computing the similarities between Fock states [541].

Neural network quantum states. NN representation of the many-body wave function appeared to be very successful in predicting ground state properties of the system (such as the energy), even outperforming state-of-the-art techniques (PEPS) for the $J_1 - J_2$ model [542]. There is also great interest in using NQS for time evolution of the many-body wave function [233, 237, 543], especially in dimensions higher than one. Current challenges are the generalization of NQS to mixed states, e.g., for open quantum systems, and the implementations of symmetries in NQS. There is a particular interest in finding strategies to extend NQS to fermionic systems. Furthemore, the applications of NQS to *ab initio* studies of interacting electrons in continuous space is a promising direction for quantum chemistry and physics applications [246, 266]. An interesting other direction is to gain a better understanding of the internal structure and the capacity of NQS [544]. Finally, the application of NQS for quantum state reconstruction is a very active field.

Reinforcement learning. Reinforcement learning (RL) provides a powerful framework with a broad range of applications in the development of quantum technologies. There is an ongoing effort to combine RL techniques with experimental setups, which opens a variety of research avenues. One interesting direction is the real-time control of quantum simulators [545–547], which may allow us to prepare and study complex phases of matter beyond our current capabilities. Similarly, we can enhance NISQ devices with RL-based control to progress toward fault-tolerant quantum computation [316, 322, 548, 549]. Another possible direction is the design of experimental platforms with RL, with which we may discover new approaches for quantum experiments. In Ref. [302], the authors discover new optical setups to prepare highly entangled quantum states. In a similar fashion, we could explore new quantum computing architectures, or design new technical devices, for example. On a more theoretical level, RL is a powerful optimization tool that can help us solve challenging problems either on its own, or in combination with other established techniques [327]. A general interesting direction is bridging theoretical and experimental advances, for which we could use RL, for instance, to design Hamiltonians with certain desired properties of interest [550].

Differentiable programming. The application of differentiable programming (∂P) might be very beneficial in physics. It can be applied to different techniques such as variational Monte Carlo (for neural quantum state (NQS), see chapter 5), tensor network [337] or mean field [342]. These works show that such algorithms can remove the tedious part of calculating derivatives while retaining state-of-the-art results. The integration of automatic differentiation (AD) in other tasks such as differential equation solving is also very promising.

Machine learning for scientific discovery. Is AI capable of scientific discovery and understanding? The hopes and prospects coming from the use of ML in science are gigantic, but so far achievements that can be called "scientific discoveries" have been rare. In particular, the AlphaFold [551] algorithm by DeepMind may truly revolutionize biology and medicine thanks to its ability to predict the three-dimensional structure of a protein based solely on its genetic sequence (known as the protein folding problem). Automated and self-driving labs can change how we do experiments [426]. Another example is an ML-guided selection of preformulated hypotheses presented in Ref. [128]. The authors first trained a model on numerical

data coming from two different theories that were hypothesized to underlie the physical system in question and then asked the model which theory described the experimental snapshots of the system better. An exciting approach is using ML to guide scientists to interesting regimes of the problem as it was done in phase classification [113], mathematics [552], and quantum information [553]. Finally, note that having an omniscient oracle that can predict the outcome of any process does not *a priori* provide us with or prove scientific understanding [35]. Again, this points toward the key challenge of ML interpretability.

Statistical physics for machine learning. Statistical mechanics and the physicists view can help shed light on the inner workings of ML. Using computation methods coming from the physics of disordered systems and the teacher-student modelling of learning problems have already proven to be a powerful paradigm for studying a central puzzle of modern ML: generalization of overparametrized models [457, 458]. In parallel, the dynamics of learning can be studied with these same methods [459, 463], as well as with the Langevin equation [468]. Tools from statistical mechanics can also be of great help to improve the training of ML architectures. Recent works in this direction improved the training of restricted Boltzmann machines (RBMs) using a physical approach [469, 554]. Both the Gardner program and the teacher-student paradigm have been successfully used to study the capacity of quantum architectures [464–466] and the generalization of quantum NNs [467].

Potential hardware accelerators based on physical processes. Today, NNs are run on classical devices. While GPUs have become a game changer in the last decade in this field, the memory, computation time, and the energy used in the current NN architectures are constantly growing and will eventually become a bottleneck. As such, there is a great effort to find new devices implementing NNs in physical devices [555]. The main goal of this research direction is to construct a physical realization of NNs performing fully parallel and fast operations. Examples of such platforms are optical implementations of NNs [556–563], or exciton–polaritons [564–568]. Another direction has been discussed in section 8.2: the use of hybrid classical-quantum devices to perform data driven tasks. A crucial point in this direction is the integration of quantum devices in high performance computing facilities. Finally, recent works have explored yet another direction coming back to ideas from the early days of classical ML: designing quantum generalizations of Hopfield networks [569, 570].

Acknowledgments

A   Mathematical details on principal component analysis

We can motivate PCA from two different perspectives: The first one is sketched in the main text and is based on retaining the largest possible data variance when reducing the dimensionality of the data. As such, it corresponds to a constrained maximization problem. PCA can also be motivated as the algorithm which finds a low-rank approximation $\hat{X}$ to the design matrix X such that the distance between the two matrices is minimized. We will prove that these two approaches are equivalent. That is, we show that the projection matrix V is the solution to

$$V = \underbrace{\arg\min_{V} \min_{Z} \frac{1}{N}\|X - VZ\|^2}_{\text{min. error in high-dim. space}} = \underbrace{\arg\max_{V} \frac{1}{N}\|V^\intercal X\|^2}_{\text{max. variance in low-dim. space}}. \tag{A.1}$$

Because we deal with matrices, the norm refers to the Frobenius norm $\|A\|^2 := \operatorname{tr}[A^\intercal A]$.

Let us recap the approach from the main text, i.e., the variance maximization. We define the design matrix X from the N p-dimensional data points by stacking them together. However, for the mathematical proofs, we define it in its transposed version as an $(p \times N)$

matrix. We construct the empirical covariance matrix Σ (assuming zero mean in the data) as $\Sigma = (XX^{\mathsf{T}})/N = \Sigma^{\mathsf{T}}$. It contains all covariances between any two input features. We wish to find a linear transformation V that preserves the maximal variance of the data. As we assume data with zero mean, the projected data $V^{\mathsf{T}}X$ also has zero mean. The empirical variance of the input data is given by $\sum_{i=1}^{N} x_i^2/N$. We want to find the columns of the projection matrix iteratively. The first column v_1 of V is obtained by maximizing the variance $\sum_{i=1}^{N}(v_1^{\mathsf{T}}x_i)^2/N$. This can be summarized by the following optimization problem:

$$\max_{v_1} \frac{1}{N}\left\|v_1^{\mathsf{T}}X\right\|^2 = \max_{v_1}\frac{1}{N}v_1^{\mathsf{T}}XX^{\mathsf{T}}v_1 = \max_{v_1}v_1^{\mathsf{T}}\Sigma v_1 \quad \text{s.t. } v_1^{\mathsf{T}}v_1 = 1. \tag{A.2}$$

Here, the constraint enforces a finite value for the maximum and we have inserted the definition of the norm (of vectors here) and of the covariance matrix. We solve the constrained optimization problem using the method of Lagrange multipliers. To this end, we define the Lagrangian $\mathcal{L}(v_1) = v_1^{\mathsf{T}}\Sigma v_1 - \mu_1(v_1^{\mathsf{T}}v_1 - 1)$ and calculate its differential as $d\mathcal{L} = 2(v_1^{\mathsf{T}}\Sigma - \mu_1 v_1^{\mathsf{T}})dv_1$. The optimal solution requires $d\mathcal{L} = 0$. This is fulfilled, if $\Sigma v_1 = \mu_1 v_1$. We identify the eigenvalue problem, i.e., v_1 must be an eigenvector of Σ with eigenvalue μ_1. Choosing μ_1 to be the largest eigenvalue λ_1 of Σ then maximizes our objective.

For the next column v_2 of V, we start from eq. (A.2) and enforce orthogonality between v_1 and v_2 by adding the constraint $v_1^{\mathsf{T}}v_2 = 0$. We can write the modified Lagrangian and calculate its differential with respect to dv_2. This leaves us with the condition that $2\Sigma v_2 - 2\mu_2 v_1^{\mathsf{T}}v_2 - \kappa v_1 = 0$ with κ being the Lagrange multiplier for the orthogonality condition. Multiplying both sides with v_1^{T} from the left and applying the orthogonality condition we find that $\kappa = 0$. Plugging this into the previous condition, we again arrive at $\Sigma v_2 = \mu_2 v_2$. With the same reasoning as before, we see that μ_2 has to be the second-largest eigenvalue λ_2 of Σ with its corresponding eigenvector v_2. Iteratively, we can the other entries of V as the remaining eigenvectors of Σ ordered by their eigenvalues.

We now understand the reason behind the procedure discussed in the main text and why we can drop the eigenvectors that carry the least variance to achieve a dimensionality reduction. The dimensionality-reduced data now has a variance spread along each axis according to the respective PCs. This spread can also be transformed to unit variance along each axis by modifying the projected design matrix as $\tilde{X}_{\text{white}} = X\tilde{V}\tilde{\Lambda}^{-1/2}$ which is called *whitening* of the data. Here, $\tilde{\Lambda} = \text{diag}(\lambda_1, \lambda_2, \dots)$ is the diagonal matrix with the k largest eigenvalues of Σ in descending order.

As mentioned earlier, there is another, equivalent approach to find V by minimizing the approximation error between the design matrix X and its low-rank reconstruction $V\tilde{X}$. The mean-squared error (MSE) between the two matrices is given by the following constrained optimization problem:

$$\min_{V,Z}\|X - VZ\|^2 = \min_{V,Z}\text{tr}\left[(X - VZ)^{\mathsf{T}}(X - VZ)\right] \quad \text{s.t. } V^{\mathsf{T}}V = \mathbb{1} \tag{A.3}$$

where we inserted the definition of the Frobenius norm. The constraint can be placed without loss of generality: assume that $V^{\mathsf{T}}V = A \neq \mathbb{1}$. Consider the eigenvalue decomposition of $A = W\Lambda W^{\mathsf{T}}$ with $W^{\mathsf{T}}W = \mathbb{1}$. Thus, $V^{\mathsf{T}}V = A = W\Lambda W^{\mathsf{T}} \Rightarrow \Lambda = (VW)^{\mathsf{T}}(VW)$ and we recover our constraint by setting $\tilde{V} = \Lambda^{-1/2}VW$ and minimize over $\tilde{V}$ instead.

We solve this again with Lagrange multipliers. However, we now have a matrix constraint and therefore introduce the matrix-valued Lagrange multiplier M^{T}. Since distances between matrices are given by the Frobenius norm, the Lagrangian reads as

$$\mathcal{L}(V, Z) = \text{tr}\left[(X - VZ)^{\mathsf{T}}(X - VZ)\right] - \text{tr}\left[M(V^{\mathsf{T}}V - \mathbb{1})\right].$$

Using matrix calculus, the differential is $d\mathcal{L} = -2\operatorname{tr}\left[(X - VZ)^{\mathsf{T}}V\,dZ\right]$. Setting it to zero, we require that $X^{\mathsf{T}}V = Z^{\mathsf{T}}V^{\mathsf{T}}V = Z^{\mathsf{T}}$ and thus $Z = V^{\mathsf{T}}X$ which we plug into the objective as $\operatorname{tr}\left[(X - VZ)^{\mathsf{T}}(X - VZ)\right] = \operatorname{tr}\left[X^{\mathsf{T}}X - X^{\mathsf{T}}VV^{\mathsf{T}}X\right]$. The first term can be dropped as it does not depend on the minimization parameter V. We can rewrite the second term as $-\|V^{\mathsf{T}}X\|$ and absorb the minus sign by turning the minimization into a maximization of $\|V^{\mathsf{T}}X\|$. This is exactly the objective of the variance maximization principle eq. (A.2) and we see their equivalence. In our derivation, we did not discuss how the Lagrange multiplier M disappears. The reasoning, however, is similar to before where the eigenvalue decomposition of M has to be considered. This effectively only adds a rotation of V which can again be absorbed into the definition of V.

B   Derivation of the kernel trick

Here, we present a derivation of the kernel trick. The training data $\mathcal{D} = \{(X, y)\}$ is defined as

$$X = \begin{bmatrix} x_1^{\mathsf{T}} \\ x_2^{\mathsf{T}} \\ \vdots \\ x_n^{\mathsf{T}} \end{bmatrix} = \begin{bmatrix} x_{1,1} & x_{1,2} & \cdots & x_{1,m} \\ x_{2,1} & x_{2,2} & \cdots & x_{2,m} \\ \vdots & \vdots & \ddots & \vdots \\ x_{n,1} & x_{n,2} & \cdots & x_{n,m} \end{bmatrix} \text{ and } y = \begin{bmatrix} y_1 \\ y_2 \\ \vdots \\ y_n \end{bmatrix}, \tag{B.1}$$

where each row of X (i.e., x_i) is one data point associated with an observable y_i, n is the number of data points, and m is the number of features. Let us consider a linear model $f(x, \theta) = x^{\mathsf{T}}\theta$ as in section 2.4.1. In ridge regression, the loss function is then given as

$$\begin{aligned} \mathcal{L}(\theta, X, y) &= \|f(X, \theta) - y\|_2^2 + \lambda\|\theta\|_2^2 \\ &= \|X\theta - y\|_2^2 + \lambda\|\theta\|_2^2, \end{aligned} \tag{B.2}$$

where $\|\cdot\|_2$ denotes the ℓ_2-norm. The optimal set of parameters θ^* is found by minimizing $\mathcal{L}(\theta, X, y)$ with respect to θ,

$$\begin{aligned} \theta^* &= \arg\min_{\theta} \mathcal{L}(\theta, X, y) \\ &= \arg\min_{\theta} \|X\theta - y\|_2^2 + \lambda\|\theta\|_2^2. \end{aligned} \tag{B.3}$$

To validate that θ^* is the optimal solution of $\mathcal{L}$, we can verify that $\nabla_{\theta}\mathcal{L}|_{\theta^*} = 0$. Given the linear dependence of θ in f, $\nabla_{\theta}\mathcal{L}$ has a closed-form solution. Before we proceed with the derivation, let us first expand eq. (B.2):

$$\begin{aligned} \mathcal{L}(\theta, X, y) &= (X\theta - y)^{\mathsf{T}}(X\theta - y) + \lambda\theta^{\mathsf{T}}\theta \\ &= \theta^{\mathsf{T}}X^{\mathsf{T}}X\theta - \theta^{\mathsf{T}}X^{\mathsf{T}}y - y^{\mathsf{T}}X\theta + y^{\mathsf{T}}y + \lambda\theta^{\mathsf{T}}\theta. \end{aligned} \tag{B.4}$$

Solving for θ^* by setting the gradient of $\mathcal{L}$ w.r.t. θ to zero, we get

$$\nabla_{\theta}\mathcal{L} = 0 = 2X^{\mathsf{T}}X\theta - 2y^{\mathsf{T}}X + y^{\mathsf{T}}y + \lambda\theta. \tag{B.5}$$

Please consult Ref. [571] for the derivative identities needed to derive eq. (B.5). Solving for θ, we obtain

$$(X^{\mathsf{T}}X + \lambda\mathbb{1})\theta = X^{\mathsf{T}}y, \tag{B.6}$$

where

$$\theta^* = (X^{\mathsf{T}}X + \lambda\mathbb{1})^{-1}X^{\mathsf{T}}y. \tag{B.7}$$

Before we proceed further, let us examine the $\boldsymbol{X}^\mathsf{T}\boldsymbol{X}$ term

$$\boldsymbol{X}^\mathsf{T}\boldsymbol{X} = \begin{bmatrix} \boldsymbol{x}_1 & \boldsymbol{x}_2 & \cdots & \boldsymbol{x}_n \end{bmatrix} \begin{bmatrix} \boldsymbol{x}_1^\mathsf{T} \\ \boldsymbol{x}_2^\mathsf{T} \\ \vdots \\ \boldsymbol{x}_n^\mathsf{T} \end{bmatrix} = \begin{bmatrix} x_{1,1} & \cdots & x_{n,1} \\ x_{1,2} & \cdots & x_{n,2} \\ \vdots & \ddots & \vdots \\ x_{1,m} & \cdots & x_{n,m} \end{bmatrix} \begin{bmatrix} x_{1,1} & \cdots & x_{1,m} \\ x_{2,1} & \cdots & x_{2,m} \\ \vdots & \ddots & \vdots \\ x_{n,1} & \cdots & x_{n,m} \end{bmatrix}. \tag{B.8}$$

Here, $\boldsymbol{X}^\mathsf{T}\boldsymbol{X}$ is a $(m \times m)$ matrix, where the matrix elements represent the dot-product in the "number-of-data-points" space. Here, $\boldsymbol{\theta}^*$ is an m-dimensional vector.

The optimal solution $\boldsymbol{\theta}^*$ could be rewritten as

$$\boldsymbol{\theta}^* = \boldsymbol{X}^\mathsf{T}(\boldsymbol{X}\boldsymbol{X}^\mathsf{T} + \lambda \mathbb{1})^{-1}\boldsymbol{y}, \tag{B.9}$$

where we used the following matrix identity [571]

$$(\boldsymbol{A}\boldsymbol{B} + \mathbb{1})^{-1}\boldsymbol{A} = \boldsymbol{A}(\boldsymbol{B}\boldsymbol{A} + \mathbb{1})^{-1}. \tag{B.10}$$

In the same manner, let us examine the term $\boldsymbol{X}\boldsymbol{X}^\mathsf{T}$ given by

$$\boldsymbol{X}\boldsymbol{X}^\mathsf{T} = \begin{bmatrix} x_{1,1} & \cdots & x_{1,m} \\ x_{2,1} & \cdots & x_{2,m} \\ \vdots & \ddots & \vdots \\ x_{n,1} & \cdots & x_{n,m} \end{bmatrix} \begin{bmatrix} x_{1,1} & \cdots & x_{n,1} \\ x_{1,2} & \cdots & x_{n,2} \\ \vdots & \ddots & \vdots \\ x_{1,m} & \cdots & x_{n,m} \end{bmatrix}. \tag{B.11}$$

As we can observe, the matrix elements now represent the standard dot-product between two points of training data, $\boldsymbol{x}_i^\mathsf{T}\boldsymbol{x}_j$. This new representation also changes the dimensionality of $\boldsymbol{\theta}^*$. A disadvantage of using eq. (B.9) is that inverting $\boldsymbol{X}\boldsymbol{X}^\mathsf{T}$, a $n \times n$ matrix, becomes computationally more expensive when $n \gg m$.

By using eq. (B.10) to rewrite $\boldsymbol{\theta}^*$ (eq. (B.7)) into eq. (B.9), the prediction of a new point $\boldsymbol{x}_\text{new}$ becomes

$$\begin{aligned} f(\boldsymbol{x}_\text{new}, \boldsymbol{\theta}^*) &= (\boldsymbol{\theta}^*)^\mathsf{T}\boldsymbol{x}_\text{new} = \boldsymbol{x}_\text{new}^\mathsf{T}\boldsymbol{\theta}^* \\ &= \boldsymbol{x}_\text{new}^\mathsf{T}\boldsymbol{X}^\mathsf{T}(\boldsymbol{X}\boldsymbol{X}^\mathsf{T} + \lambda \mathbb{1})^{-1}\boldsymbol{y}, \end{aligned}$$

where the term $\boldsymbol{x}_\text{new}^\mathsf{T}\boldsymbol{X}^\mathsf{T}$ represent the dot-product between the point where the function is evaluated and the training data,

$$\boldsymbol{x}_\text{new}^\mathsf{T}\boldsymbol{X}^\mathsf{T} = \begin{bmatrix} x_1^\text{new} & x_2^\text{new} & \cdots & x_m^\text{new} \end{bmatrix} \begin{bmatrix} x_{1,1} & \cdots & x_{n,1} \\ x_{1,2} & \cdots & x_{n,2} \\ \vdots & \ddots & \vdots \\ x_{1,m} & \cdots & x_{n,m} \end{bmatrix} = \begin{bmatrix} \boldsymbol{x}_\text{new}^\mathsf{T}\boldsymbol{x}_1 \\ \boldsymbol{x}_\text{new}^\mathsf{T}\boldsymbol{x}_2 \\ \vdots \\ \boldsymbol{x}_\text{new}^\mathsf{T}\boldsymbol{x}_n \end{bmatrix}. \tag{B.12}$$

From eq. (B.12) and eq. (B.12), we can observe that a second linear model over the $\{\boldsymbol{x}_\text{new}^\mathsf{T}\boldsymbol{x}_i\}_{i=1}^n$ feature space could be defined,

$$f(\boldsymbol{x}_\text{new}, \boldsymbol{\theta}^*) = (\boldsymbol{\theta}^*)^\mathsf{T}\left(\boldsymbol{x}_\text{new}^\mathsf{T}\boldsymbol{X}^\mathsf{T}\right), \tag{B.13}$$

where $\boldsymbol{\theta}^*$ is $(\boldsymbol{X}\boldsymbol{X}^\mathsf{T} + \lambda \mathbb{1})^{-1}\boldsymbol{y}$ corresponding to an n-dimensional vector.

The initial model considered is a linear model on $\boldsymbol{x}$, $f(\boldsymbol{x}, \boldsymbol{\theta}) = \boldsymbol{x}^\mathsf{T}\boldsymbol{\theta}$. However, we could consider a linear model over a basis-set $\Phi = [\phi_0, \phi_1, \ldots, \phi_\ell]$ spanning an alternative *feature*

space. If we replace in our derivation $\boldsymbol{x}$ for $\Phi(\boldsymbol{x}) = [\phi_0(\boldsymbol{x}), \phi_1(\boldsymbol{x}), \ldots, \phi_\ell(\boldsymbol{x})]$, i.e., we transform our data into the corresponding feature space, we end up with the following model

$$
\begin{aligned}
f(\Phi(\boldsymbol{x}_{\text{new}}), \boldsymbol{\theta}^*) &= (\boldsymbol{\theta}^*)^\intercal \, \Phi(\boldsymbol{x}_{\text{new}}) = \Phi(\boldsymbol{x}_{\text{new}})^\intercal \boldsymbol{\theta}^* \\
&= \Phi(\boldsymbol{x}_{\text{new}})^\intercal \Phi(\boldsymbol{X})^\intercal \left(\Phi(\boldsymbol{X}) \Phi(\boldsymbol{X})^\intercal + \lambda \mathbb{1} \right)^{-1} \boldsymbol{y}.
\end{aligned}
$$

Here, $\Phi(\boldsymbol{x}_{\text{new}})^\intercal \Phi(\boldsymbol{X})^\intercal$ corresponds to the dot-product in the basis-set expansion between $\boldsymbol{x}_{\text{new}}$ and the training data $\boldsymbol{X}$. Moreover, $\Phi(\boldsymbol{X})\Phi(\boldsymbol{X})^\intercal$ corresponds to the dot-product in the basis-set expansion between all training data points, i.e., $[\Phi(\boldsymbol{X})\Phi(\boldsymbol{X})^\intercal]_{ij} = \Phi(\boldsymbol{x}_i)^\intercal \Phi(\boldsymbol{x}_j)$.

In the context of kernel methods $\Phi(\boldsymbol{X})\Phi(\boldsymbol{X})^\intercal$ is known as the design matrix $\boldsymbol{K}$. It should be stressed that, the computation of $f(\Phi(\boldsymbol{x}_{\text{new}}), \boldsymbol{\theta}^*)$ does only depend on the basis-set expansion via the dot-product $\Phi(\boldsymbol{x}_i)^\intercal \Phi(\boldsymbol{x}_j)$. This enables the kernel trick. Finally, our derivation was done for KRR, however, the logarithm of the likelihood of a GP (eq. (4.42)) has the same algebraic form. Therefore, our derivation also illustrates how GP models operate via kernels.

References

[1] C. Williams, *A brief introduction to artificial intelligence*, In *Proceedings OCEANS '83*, pp. 94–99, doi:10.1109/OCEANS.1983.1152096 (1983).

[2] R. Dearden and C. Boutilier, *Abstraction and approximate decision-theoretic planning*, Artif. Intell. **89**(1), 219 (1997), doi:10.1016/S0004-3702(96)00023-9.

[3] J.-D. Zucker, *A grounded theory of abstraction in artificial intelligence*, Phil. Trans. R. Soc. Lond. B **358**(1435), 1293 (2003), doi:10.1098/rstb.2003.1308.

[4] L. Saitta and J.-D. Zucker, *Abstraction in Artificial Intelligence and Complex Systems*, Springer, New York, NY, ISBN 978-1-4614-7051-9, doi:10.1007/978-1-4614-7052-6 (2013).

[5] M. Mitchell, *Abstraction and analogy-making in artificial intelligence*, Ann. N. Y. Acad. Sci. **1505**(1), 79 (2021), doi:10.1111/nyas.14619.

[6] H. Moravec, *Mind Children: The Future of Robot and Human Intelligence*, Harvard University Press, Cambridge, Massachusetts, ISBN 0674576160, doi:10.2307/1575314, P. 15 (1988).

[7] I. Goodfellow, Y. Bengio and A. Courville, *Deep Learning*, The MIT Press, ISBN 0262035618, doi:10.5555/3086952 (2016).

[8] G. Marcus, *Deep learning is hitting a wall*, Nautilus, Accessed: 2022-03-11 (2022).

[9] T. J. Sejnowski, *The Deep Learning Revolution: Machine Intelligence Meets Human Intelligence*, The MIT Press, ISBN 9780262038034 (2018).

[10] Y. LeCun, Y. Bengio and G. Hinton, *Deep learning*, Nature **521**(7553), 436 (2015), doi:10.1038/nature14539.

[11] G. E. Hinton, S. Osindero and Y.-W. Teh, *A fast learning algorithm for deep belief nets*, Neural Comput. **18**(7), 1527 (2006), doi:10.1162/neco.2006.18.7.1527.

[12] B. Marr, *How much data do we create every day? The mind-blowing stats everyone should read*, Forbes, Accessed: 2018-05-21.

[13] SeedScientific, *Volume of data/information created, captured, copied, and consumed worldwide from 2010 to 2025*, SeedScientific, Accessed: 2022-01-28 (2021).

[14] Statista Research Department, *Volume of data/information created, captured, copied, and consumed worldwide from 2010 to 2025*, Statista, Accessed: 2022-03-18 (2022).

[15] M. F. Dixon, I. Halperin and P. Bilokon, *Machine Learning in Finance: From Theory to Practice*, Springer, ISBN 9783030410674, doi:10.1007/978-3-030-41068-1 (2020).

[16] J. Eisenstein, *Introduction to Natural Language Processing*, The MIT Press, ISBN 9780262042840 (2019).

[17] S. Polu, J. M. Han, K. Zheng, M. Baksys, I. Babuschkin and I. Sutskever, *Formal mathematics statement curriculum learning* (2022), arXiv:1602.04915.

[18] V. Mnih, K. Kavukcuoglu, D. Silver, A. A. Rusu, J. Veness, M. G. Bellemare, A. Graves, M. Riedmiller, A. K. Fidjeland, G. Ostrovski, S. Petersen, C. Beattie *et al.*, *Human-level control through deep reinforcement learning*, Nature **518**(7540), 529 (2015), doi:10.1038/nature14236.

[19] O. Vinyals, I. Babuschkin, W. M. Czarnecki, M. Mathieu, A. Dudzik, J. Chung, D. H. Choi, R. Powell, T. Ewalds, P. Georgiev, J. Oh, D. Horgan *et al.*, *Grandmaster level in StarCraft II using multi-agent reinforcement learning*, Nature **575**(7782), 350 (2019), doi:10.1038/s41586-019-1724-z.

[20] D. Silver, A. Huang, C. J. Maddison, A. Guez, L. Sifre, G. van den Driessche, J. Schrittwieser, I. Antonoglou, V. Panneershelvam, M. Lanctot, S. Dieleman, D. Grewe *et al.*, *Mastering the game of Go with deep neural networks and tree search*, Nature **529**(7587), 484 (2016), doi:10.1038/nature16961.

[21] Y. Lecun, L. Bottou, Y. Bengio and P. Haffner, *Gradient-based learning applied to document recognition*, Proc. IEEE **86**(11), 2278 (1998), doi:10.1109/5.726791.

[22] R. A. Fisher, *The use of multiple measurements in taxonomic problems*, Ann. Eug. **7**, 179 (1936), doi:10.1111/j.1469-1809.1936.tb02137.x.

[23] A. Krizhevsky, *Learning multiple layers of features from tiny images*, Tech. rep., MIT & NYU, CiteSeer^X 10.1.1.222.9220 (2009).

[24] O. Russakovsky, J. Deng, H. Su, J. Krause, S. Satheesh, S. Ma, Z. Huang, A. Karpathy, A. Khosla, M. Bernstein, A. C. Berg and L. Fei-Fei, *ImageNet large scale visual recognition challenge*, Int. J. Comput. Vis. **115**(3), 211 (2015), doi:10.1007/s11263-015-0816-y.

[25] D. Gissin, *Active learning review*, GitHub.io, Accessed: 2022-04-08 (2020).

[26] P. Ren, Y. Xiao, X. Chang, P.-Y. Huang, Z. Li, B. B. Gupta, X. Chen and X. Wang, *A survey of deep active learning* (2020), arXiv:2009.00236.

[27] J. E. van Engelen and H. H. Hoos, *A survey on semi-supervised learning*, Mach. Learn. **109**(2), 373 (2020), doi:10.1007/s10994-019-05855-6.

[28] B. Blaiszik, *Charting ML publications in science*, GitHub repository (2021).

[29] V. Dunjko and H. J. Briegel, *Machine learning & artificial intelligence in the quantum domain: a review of recent progress*, Rep. Prog. Phys. **81**(7), 074001 (2018), doi:10.1088/1361-6633/aab406.

[30] G. Carleo, I. Cirac, K. Cranmer, L. Daudet, M. Schuld, N. Tishby, L. Vogt-Maranto and L. Zdeborová, *Machine learning and the physical sciences*, Rev. Mod. Phys. **91**, 045002 (2019), doi:10.1103/RevModPhys.91.045002.

[31] J. Carrasquilla, *Machine learning for quantum matter*, Adv. Phys.: X **5**(1), 1797528 (2020), doi:10.1080/23746149.2020.1797528.

[32] Summer School: Machine Learning in Science and Technology, GitHub repository with selected tutorials from the school (2021).

[33] A. Dawid, J. Arnold, B. Requena, A. Gresch, M. Płodzień, K. Donatella, K. Nicoli, P. Stornati, R. Koch, M. Büttner, R. Okuła, G. Muñoz–Gil *et al.*, GitHub repository with figures prepared for these Lecture Notes (2022).

[34] F. Chollet, *On the measure of intelligence* (2019), arXiv:1911.01547.

[35] M. Krenn, R. Pollice, S. Y. Guo, M. Aldeghi, A. Cervera-Lierta, P. Friederich, G. dos Passos Gomes, F. Häse, A. Jinich, A. Nigam, Z. Yao and A. Aspuru-Guzik, *On scientific understanding with artificial intelligence* (2022), arXiv:2204.01467.

[36] R. Bagheri, *Weight initialization in deep neural networks*, Towards Data Science, Accessed: 2022-02-16 (2020).

[37] T. Akiba, S. Sano, T. Yanase, T. Ohta and M. Koyama, *Optuna: A next-generation hyperparameter optimization framework* (2019), arXiv:1907.10902.

[38] A. L. Blum and R. L. Rivest, *Training a 3-node neural network is NP-complete*, Neural Netw. **5**(1), 117 (1992), doi:10.1016/S0893-6080(05)80010-3.

[39] H. Li, Z. Xu, G. Taylor, C. Studer and T. Goldstein, *Visualizing the loss landscape of neural nets*, In *NIPS 2018 - Adv. Neural. Inf. Process. Syst.*, pp. 6389–6399 (2018), arXiv:1712.09913.

[40] Y. Feng and Y. Tu, *The inverse variance–flatness relation in stochastic gradient descent is critical for finding flat minima*, Proc. Natl. Acad. Sci. **118**(9) (2021), doi:10.1073/pnas.2015617118.

[41] J. D. Lee, M. Simchowitz, M. I. Jordan and B. Recht, *Gradient descent converges to minimizers* (2016), arXiv:1602.04915.

[42] A. Choromanska, M. Henaff, M. Mathieu, G. Ben Arous and Y. LeCun, *The loss surfaces of multilayer networks*, In *AISTATS 2015 - Int. Conf. Artif. Intell. Stat.*, vol. 38, pp. 192–204. PMLR (2015), arXiv:1412.0233.

[43] Y. N. Dauphin, R. Pascanu, C. Gulcehre, K. Cho, S. Ganguli and Y. Bengio, *Identifying and attacking the saddle point problem in high-dimensional non-convex optimization*, In *NIPS 2014 - Adv. Neural. Inf. Process. Syst.*, vol. 27 (2014), arXiv:1406.2572.

[44] L. Sagun, L. Bottou and Y. LeCun, *Eigenvalues of the Hessian in deep learning: singularity and beyond* (2016), arXiv:1611.07476.

[45] G. Alain, N. Le Roux and P. A. Manzagol, *Negative eigenvalues of the Hessian in deep neural networks*, In *ICLR 2018 - Int. Conf. Learn. Represent.* (2018), arXiv:1902.02366.

[46] I. Sutskever, J. Martens, G. Dahl and G. Hinton, *On the importance of initialization and momentum in deep learning*, In *ICML 2013 - 30th Int. Conf. Mach. Learn.*, vol. 28, pp. 1139–1147 (2013).

[47] Y. Liu, Y. Gao and W. Yin, *An improved analysis of stochastic gradient descent with momentum* (2020), arXiv:2007.07989.

[48] J. Duchi, E. Hazan and Y. Singer, *Adaptive subgradient methods for online learning and stochastic optimization*, J. Mach. Learn. Res. **12**, 2121–2159 (2011), doi:10.5555/1953048.2021068.

[49] D. P. Kingma and J. Ba, *Adam: A method for stochastic optimization* (2014), arXiv:1412.6980.

[50] Z. Zhang, *Improved Adam optimizer for deep neural networks*, In *2018 IEEE/ACM 26th Int. Symp. Qual. Serv. IWQoS 2018*, pp. 1–2, doi:10.1109/IWQoS.2018.8624183 (2018).

[51] C. Zhu, R. H. Byrd, P. Lu and J. Nocedal, *Algorithm 778: L-BFGS-B*, ACM Trans. Math. Softw. **23**(4), 550 (1997), doi:10.1145/279232.279236.

[52] L. M. Rios and N. V. Sahinidis, *Derivative-free optimization: a review of algorithms and comparison of software implementations*, J. Glob. Optim. **56**(3), 1247 (2012), doi:10.1007/s10898-012-9951-y.

[53] C. Zhang, S. Bengio, M. Hardt, B. Recht and O. Vinyals, *Understanding deep learning requires rethinking generalization*, In *ICLR 2017 - Int. Conf. Learn. Represent.* (2017), arXiv:1611.03530.

[54] D. H. Wolpert, *What is important about the No Free Lunch theorems?* (2020), arXiv:2007.10928.

[55] P. Domingos, *A unified bias-variance decomposition for zero-one and squared loss*, In *NCAI 2000 - 17th National Conference on Artificial Intelligence*, pp. 564–569, doi:10.5555/647288.721421 (2000).

[56] K. Kawaguchi, L. P. Kaelbling and Y. Bengio, *Generalization in deep learning* (2020), arXiv:1710.05468.

[57] J. Frankle and M. Carbin, *The lottery ticket hypothesis: Finding sparse, trainable neural networks*, In *ICLR 2019 - Int. Conf. Learn. Represent.* (2019), arXiv:1803.03635.

[58] C. R. Rao, *Generalized inverse of a matrix and its applications*, pp. 601–620, University of California Press, doi:10.1525/9780520325883-032 (1972).

[59] R. Tibshirani, *Regression shrinkage and selection via the lasso*, J. R. Stat. Soc. Ser. B Methodol. **58**(1), 267 (1996), doi:10.1111/j.2517-6161.1996.tb02080.x.

[60] Z. Zhou, X. Li and R. N. Zare, *Optimizing chemical reactions with deep reinforcement learning*, ACS Cent. Sci **3**(12), 1337 (2017), doi:10.1021/acscentsci.7b00492.

[61] J. Platt, *Sequential minimal optimization: A fast algorithm for training support vector machines*, Tech. Rep. MSR-TR-98-14, Microsoft (1998).

[62] M. Minsky and S. Papert, *Perceptrons: an introduction to computational geometry*, MIT press, ISBN 0-262-13043-2 (1969).

[63] F. Rosenblatt, *The perceptron: A probabilistic model for information storage and organization in the brain*, Psychol. Rev. **65**(6), 386 (1958), doi:10.1037/h0042519.

[64] A. N. Kolmogorov, *On the representation of continuous functions of many variables by superposition of continuous functions of one variable and addition*, In *Doklady Akademii Nauk*, vol. 114, pp. 953–956. Russian Academy of Sciences (1957).

[65] G. Cybenko, *Approximation by superpositions of a sigmoidal function*, Math. Control Signals Syst. **2**(4), 303 (1989), doi:10.1007/BF02551274.

[66] K. Hornik, *Approximation capabilities of multilayer feedforward networks*, Neural Netw. **4**(2), 251 (1991), doi:10.1016/0893-6080(91)90009-T.

[67] D. E. Rumelhart, G. E. Hinton and R. J. Williams, *Learning representations by backpropagating errors*, Nature **323**(6088), 533 (1986), doi:10.1038/323533a0.

[68] D. P. Kingma and M. Welling, *Auto-encoding variational Bayes* (2013), arXiv:1312.6114.

[69] D. J. Rezende, S. Mohamed and D. Wierstra, *Stochastic backpropagation and approximate inference in deep generative models*, In *ICML 2014 - Int. Conf. Mach. Learn.*, vol. 32, pp. 1278–1286 (2014), arXiv:1401.4082.

[70] A. Ng *et al.*, *Sparse autoencoder*, CS294A Lecture notes, Stanford University (2011).

[71] A. Makhzani and B. Frey, *K-sparse autoencoders* (2013), arXiv:1312.5663.

[72] P. Vincent, H. Larochelle, Y. Bengio and P.-A. Manzagol, *Extracting and composing robust features with denoising autoencoders*, In *ICML 2008 - 25th Int. Conf. Mach. Learn.*, pp. 1096–1103, doi:10.1145/1390156.1390294 (2008).

[73] Y. Burda, R. Grosse and R. Salakhutdinov, *Importance weighted autoencoders* (2015), arXiv:1509.00519.

[74] B. Uria, M.-A. Côté, K. Gregor, I. Murray and H. Larochelle, *Neural autoregressive distribution estimation*, J. Mach. Learn. Res. **17**(1), 7184–7220 (2016), doi:10.5555/2946645.3053487.

[75] A. Paszke, S. Gross, F. Massa, A. Lerer, J. Bradbury, G. Chanan, T. Killeen, Z. Lin, N. Gimelshein, L. Antiga, A. Desmaison, A. Kopf *et al.*, *PyTorch: an imperative style, high-performance deep learning library*, In *NeurIPS 2019 - Adv. Neural. Inf. Process. Syst.* (2019), arXiv:1912.01703.

[76] S. Hochreiter and J. Schmidhuber, *Long short-term memory*, Neural Comput. **9**(8), 1735 (1997), doi:10.1162/neco.1997.9.8.1735.

[77] K. Cho, B. van Merriënboer, D. Bahdanau and Y. Bengio, *On the properties of neural machine translation: Encoder–decoder approaches*, In *SSST-8 - 8th Workshop on Syntax, Semantics and Structure in Statistical Translation*, pp. 103–111, doi:10.3115/v1/W14-4012 (2014).

[78] D. Wu, L. Wang and P. Zhang, *Solving statistical mechanics using variational autoregressive networks*, Phys. Rev. Lett. **122**(8), 080602 (2019), doi:10.1103/PhysRevLett.122.080602.

[79] K. A. Nicoli, S. Nakajima, N. Strodthoff, W. Samek, K.-R. Müller and P. Kessel, *Asymptotically unbiased estimation of physical observables with neural samplers*, Phys. Rev. E **101**(2), 023304 (2020), doi:10.1103/PhysRevE.101.023304.

[80] J.-G. Liu, L. Mao, P. Zhang and L. Wang, *Solving quantum statistical mechanics with variational autoregressive networks and quantum circuits*, Mach. Learn.: Sci. Technol. **2**(2), 025011 (2021), doi:10.1088/2632-2153/aba19d.

[81] J. Carrasquilla, G. Torlai, R. G. Melko and L. Aolita, *Reconstructing quantum states with generative models*, Nat. Mach. Intell. **1**(3), 155–161 (2019), doi:10.1038/s42256-019-0028-1.

[82] O. Sharir, Y. Levine, N. Wies, G. Carleo and A. Shashua, *Deep autoregressive models for the efficient variational simulation of many-body quantum systems*, Phys. Rev. Lett. **124**(2) (2020), doi:10.1103/PhysRevLett.124.020503.

[83] C. M. Bishop, *Pattern Recognition and Machine Learning*, Springer, Berlin, Heidelberg, ISBN 0387310738, doi:10.5555/1162264 (2006).

[84] A. Zhang, Z. C. Lipton, M. Li and A. J. Smola, *Dive into deep learning* (2021), arXiv:2106.11342.

[85] P. Mehta, M. Bukov, C.-H. Wang, A. G. Day, C. Richardson, C. K. Fisher and D. J. Schwab, *A high-bias, low-variance introduction to machine learning for physicists*, Phys. Rep. **810**, 1 (2019), doi:10.1016/j.physrep.2019.03.001.

[86] T. Neupert, M. H. Fischer, E. Greplova, K. Choo and M. Denner, *Introduction to machine learning for the sciences* (2021), arXiv:2102.04883.

[87] J. Carrasquilla and G. Torlai, *How to use neural networks to investigate quantum many-body physics*, PRX Quantum **2**, 040201 (2021), doi:10.1103/PRXQuantum.2.040201.

[88] S. Sachdev, *Quantum Phase Transitions*, Cambridge University Press, doi:10.1017/cbo9780511973765 (2011).

[89] N. Goldenfeld, *Lectures On Phase Transitions And The Renormalization Group*, CRC Press, doi:10.1201/9780429493492 (2018).

[90] L. Onsager, *Crystal statistics. I. A two-dimensional model with an order-disorder transition*, Phys. Rev. **65**, 117 (1944), doi:10.1103/PhysRev.65.117.

[91] F. J. Wegner, *Duality in generalized Ising models and phase transitions without local order parameters*, J. Math. Phys. **12**(10), 2259 (1971), doi:10.1063/1.1665530.

[92] L. D. Landau, *On the theory of phase transitions. I.*, Phys. Z. Sowjet. **11**, 26 (1937), Reprinted in Collected Papers of L. D. Landau.

[93] L. D. Landau, *On the theory of phase transitions. II.*, Phys. Z. Sowjet. **11**, 545 (1937), Reprinted in Collected Papers of L. D. Landau.

[94] X.-G. Wen, *Topological orders in rigid states*, Int. J. Mod. Phys. B **4**(02), 239 (1990), doi:10.1142/S0217979290000139.

[95] B. Bernevig and T. Hughes, *Topological Insulators and Topological Superconductors*, Princeton University Press, ISBN 9780691151755, doi:10.1515/9781400846733 (2013).

[96] N. Käming, A. Dawid, K. Kottmann, M. Lewenstein, K. Sengstock, A. Dauphin and C. Weitenberg, *Unsupervised machine learning of topological phase transitions from experimental data*, Mach. Learn.: Sci. Technol. **2**, 035037 (2021), doi:10.1088/2632-2153/abffe7.

[97] N. Sun, J. Yi, P. Zhang, H. Shen and H. Zhai, *Deep learning topological invariants of band insulators*, Phys. Rev. B **98**, 085402 (2018), doi:10.1103/PhysRevB.98.085402.

[98] P. Zhang, H. Shen and H. Zhai, *Machine learning topological invariants with neural networks*, Phys. Rev. Lett. **120**, 066401 (2018), doi:10.1103/PhysRevLett.120.066401.

[99] M. D. Caio, M. Caccin, P. Baireuther, T. Hyart and M. Fruchart, *Machine learning assisted measurement of local topological invariants* (2019), arXiv:1901.03346.

[100] N. L. Holanda and M. A. R. Griffith, *Machine learning topological phases in real space*, Phys. Rev. B **102**, 054107 (2020), doi:10.1103/PhysRevB.102.054107.

[101] P. Baireuther, M. Płodzień, T. Ojanen, K. Tworzydło and T. Hyart, *Identifying Chern numbers of superconductors from local measurements* (2021), arXiv:2112.06777.

[102] P. Huembeli, A. Dauphin and P. Wittek, *Identifying quantum phase transitions with adversarial neural networks*, Phys. Rev. B **97**, 134109 (2018), doi:10.1103/PhysRevB.97.134109.

[103] C. Fefferman, S. Mitter and H. Narayanan, *Testing the manifold hypothesis*, J. Am. Math. Soc. **29**(4), 983 (2016), doi:10.1090/jams/852.

[104] L. Wang, *Discovering phase transitions with unsupervised learning*, Phys. Rev. B **94**, 195105 (2016), doi:10.1103/PhysRevB.94.195105.

[105] S. J. Wetzel, *Unsupervised learning of phase transitions: From principal component analysis to variational autoencoders*, Phys. Rev. E **96**, 022140 (2017), doi:10.1103/PhysRevE.96.022140.

[106] W. Hu, R. R. Singh and R. T. Scalettar, *Discovering phases, phase transitions, and crossovers through unsupervised machine learning: A critical examination*, Phys. Rev. E **95**(6), 062122 (2017), doi:10.1103/PhysRevE.95.062122.

[107] L. Van der Maaten and G. Hinton, *Visualizing data using t-SNE*, J. Mach. Learn. Res. **9**(11) (2008).

[108] L. McInnes, J. Healy and J. Melville, *UMAP: Uniform manifold approximation and projection for dimension reduction* (2018), arXiv:1802.03426.

[109] G. E. Hinton and S. T. Roweis, *Stochastic neighbor embedding*, In *NIPS 2002 - Adv. Neural. Inf. Process. Syst.*, vol. 15 (2002).

[110] E. Greplova, A. Valenti, G. Boschung, F. Schäfer, N. Lörch and S. D. Huber, *Unsupervised identification of topological phase transitions using predictive models*, New J. Phys. **22**(4), 045003 (2020), doi:10.1088/1367-2630/ab7771.

[111] J. Arnold, F. Schäfer, M. Žonda and A. U. J. Lode, *Interpretable and unsupervised phase classification*, Phys. Rev. Res. **3**, 033052 (2021), doi:10.1103/PhysRevResearch.3.033052.

[112] J. Carrasquilla and R. G. Melko, *Machine learning phases of matter*, Nat. Phys. **13**(5), 431 (2017), doi:10.1038/nphys4035.

[113] K. Kottmann, P. Huembeli, M. Lewenstein and A. Acín, *Unsupervised phase discovery with deep anomaly detection*, Phys. Rev. Lett. **125**, 170603 (2020), doi:10.1103/PhysRevLett.125.170603.

[114] E. P. Van Nieuwenburg, Y.-H. Liu and S. D. Huber, *Learning phase transitions by confusion*, Nat. Phys. **13**(5), 435 (2017), doi:10.1038/nphys4037.

[115] Y.-H. Liu and E. P. L. van Nieuwenburg, *Discriminative cooperative networks for detecting phase transitions*, Phys. Rev. Lett. **120**, 176401 (2018), doi:10.1103/PhysRevLett.120.176401.

[116] S. S. Lee and B. J. Kim, *Confusion scheme in machine learning detects double phase transitions and quasi-long-range order*, Phys. Rev. E **99**, 043308 (2019), doi:10.1103/PhysRevE.99.043308.

[117] F. Schäfer and N. Lörch, *Vector field divergence of predictive model output as indication of phase transitions*, Phys. Rev. E **99**, 062107 (2019), doi:10.1103/PhysRevE.99.062107.

[118] R. A. Vargas-Hernández, J. Sous, M. Berciu and R. V. Krems, *Extrapolating quantum observables with machine learning: Inferring multiple phase transitions from properties of a single phase*, Phys. Rev. Lett. **121**, 255702 (2018), doi:10.1103/PhysRevLett.121.255702.

[119] S.-J. Gu, *Fidelity approach to quantum phase transitions*, Int. J. Mod. Phys. B **24**(23), 4371 (2010), doi:10.1142/S0217979210056335.

[120] A. Bohrdt, S. Kim, A. Lukin, M. Rispoli, R. Schittko, M. Knap, M. Greiner and J. Léonard, *Analyzing nonequilibrium quantum states through snapshots with artificial neural networks*, Phys. Rev. Lett. **127**, 150504 (2021), doi:10.1103/PhysRevLett.127.150504.

[121] Z. C. Lipton, *The mythos of model interpretability*, Commun. ACM **61**(10), 35 (2018), doi:10.1145/3233231.

[122] A. Bohrdt, C. S. Chiu, G. Ji, M. Xu, D. Greif, M. Greiner, E. Demler, F. Grusdt and M. Knap, *Classifying snapshots of the doped Hubbard model with machine learning*, Nat. Phys. **15**(9), 921 (2019), doi:10.1038/s41567-019-0565-x.

[123] Y. Zhang, P. Ginsparg and E.-A. Kim, *Interpreting machine learning of topological quantum phase transitions*, Phys. Rev. Res. **2**, 023283 (2020), doi:10.1103/PhysRevResearch.2.023283.

[124] R. Iten, T. Metger, H. Wilming, L. Del Rio and R. Renner, *Discovering physical concepts with neural networks*, Phys. Rev. Lett. **124**(1), 010508 (2020), doi:10.1103/PhysRevLett.124.010508.

[125] S. J. Wetzel and M. Scherzer, *Machine learning of explicit order parameters: From the Ising model to SU(2) lattice gauge theory*, Phys. Rev. B **96**(18), 184410 (2017), doi:10.1103/PhysRevB.96.184410.

[126] M. Cranmer, A. Sanchez-Gonzalez, P. Battaglia, R. Xu, K. Cranmer, D. Spergel and S. Ho, *Discovering symbolic models from deep learning with inductive biases*, In *NeurIPS 2020 - Adv. Neural. Inf. Process. Syst.*, pp. 1–25 (2020), arXiv:2006.11287.

[127] S. J. Wetzel, R. G. Melko, J. Scott, M. Panju and V. Ganesh, *Discovering symmetry invariants and conserved quantities by interpreting Siamese neural networks*, Phys. Rev. Res. **2**, 033499 (2020), doi:10.1103/PhysRevResearch.2.033499.

[128] C. Miles, A. Bohrdt, R. Wu, C. Chiu, M. Xu, G. Ji, M. Greiner, K. Q. Weinberger, E. Demler and E.-A. Kim, *Correlator convolutional neural networks: An interpretable architecture for image-like quantum matter data*, Nat. Commun. **12**(1), 1 (2021), doi:10.1038/s41467-021-23952-w.

[129] N. S. Keskar, J. Nocedal, P. T. P. Tang, D. Mudigere and M. Smelyanskiy, *On large-batch training for deep learning: Generalization gap and sharp minima*, In *ICLR 2017 - Int. Conf. Learn. Represent.* (2017), arXiv:1609.04836.

[130] L. Wu, Z. Zu and W. E, *Towards understanding generalization of deep learning: Perspective of loss landscapes* (2017), arXiv:1706.10239.

[131] P. Izmailov, D. Podoprikhin, T. Garipov, D. Vetrov and A. G. Wilson, *Averaging weights leads to wider optima and better generalization*, In *UAI 2018 - 34th Conf. Uncertain. Artif. Intell.*, vol. 2, pp. 876–885 (2018), arXiv:1803.05407.

[132] H. He, G. Huang and Y. Yuan, *Asymmetric valleys: Beyond sharp and flat local minima*, In *NeurIPS 2019 - Adv. Neural. Inf. Process. Syst.*, vol. 32 (2019), arXiv:1902.00744.

[133] L. Dinh, R. Pascanu, S. Bengio and Y. Bengio, *Sharp minima can generalize for deep nets*, In *ICML 2017 - 34th Int. Conf. Mach. Learn.*, vol. 3, pp. 1705–1714 (2017), arXiv:1703.04933.

[134] A. Dawid, P. Huembeli, M. Tomza, M. Lewenstein and A. Dauphin, *Hessian-based toolbox for reliable and interpretable machine learning in physics*, Mach. Learn.: Sci. Technol. **3**, 015002 (2022), doi:10.1088/2632-2153/ac338d.

[135] P. W. Koh and P. Liang, *Understanding black-box predictions via influence functions*, In *ICML 2017 - 34th Int. Conf. Mach. Learn.*, vol. 70, pp. 1885–1894. PMLR (2017), arXiv:1703.04730.

[136] P. Schulam and S. Saria, *Can you trust this prediction? Auditing pointwise reliability after learning*, In *AISTATS 2019 - Int. Conf. Artif. Intell. Stat.*, vol. 89, pp. 1022–1031. PLMR (2020), arXiv:1901.00403.

[137] D. Madras, J. Atwood and A. D'Amour, *Detecting extrapolation with local ensembles*, In *ICLR 2020 - Int. Conf. Learn. Represent.* (2020), arXiv:1910.09573.

[138] A. Dawid, P. Huembeli, M. Tomza, M. Lewenstein and A. Dauphin, *Phase detection with neural networks: interpreting the black box*, New J. Phys. **22**(11), 115001 (2020), doi:10.1088/1367-2630/abc463.

[139] J. Arnold and F. Schäfer, *Replacing neural networks by optimal analytical predictors for the detection of phase transitions* (2022), arXiv:2203.06084.

[140] C. Molnar, *Interpretable Machine Learning: A Guide for Making Black Box Models Explainable*, GitHub.io, ISBN 9780244768522 (2019).

[141] G. Bachman and L. Narici, *Functional analysis*, Dover Publications, Mineola, New York, ISBN 9780486136554 (2000).

[142] J. Mercer, *XVI. Functions of positive and negative type, and their connection the theory of integral equations*, Philos. Trans. Royal Soc. A **209**(441-458), 415 (1909), doi:10.1098/rsta.1909.0016.

[143] N. Aronszajn, *Theory of reproducing kernels*, Trans. Am. Math. Soc. **68**(3), 337 (1950), doi:10.2307/1990404.

[144] B. Schölkopf, R. Herbrich and A. J. Smola, *A generalized representer theorem*, In *Computational Learning Theory*, pp. 416–426. Springer, doi:10.1007/3-540-44581-1_27 (2001).

[145] R. Garnett, *Bayesian Optimization*, Cambridge University Press, in preparation (2022).

[146] R. M. Neal, *Bayesian learning for neural networks*, vol. 118 of *Lecture Notes in Statistics*, Springer, doi:10.1007/978-1-4612-0745-0 (2012).

[147] P. I. Frazier, *A tutorial on Bayesian optimization* (2018), arXiv:1807.02811.

[148] G. Schwarz, *Estimating the dimension of a model*, Ann. Stat. pp. 461–464 (1978), doi:10.1214/aos/1176344136.

[149] P. Stoica and Y. Selen, *Model-order selection: a review of information criterion rules*, IEEE Signal Process. Mag. **21**(4), 36 (2004), doi:10.1109/MSP.2004.1311138.

[150] H. Akaike, *A new look at the statistical model identification*, IEEE Trans. Automat. Contr. **19**(6), 716 (1974), doi:10.1109/TAC.1974.1100705.

[151] D. Duvenaud, J. Lloyd, R. Grosse, J. Tenenbaum and G. Zoubin, *Structure discovery in nonparametric regression through compositional kernel search*, In *ICML 2013 - Int. Conf. Mach. Learn.*, vol. 28, pp. 1166–1174. PMLR (2013), arXiv:1302.4922.

[152] D. Duvenaud, H. Nickisch and C. E. Rasmussen, *Additive Gaussian processes*, In *NeurIPS 2011 - Adv. Neural. Inf. Process. Syst.*, vol. 24 (2011), arXiv:1112.4394.

[153] J. Dai and R. V. Krems, *Interpolation and extrapolation of global potential energy surfaces for polyatomic systems by Gaussian processes with composite kernels*, J. Chem. Theory Comput. **16**(3), 1386 (2020), doi:10.1021/acs.jctc.9b00700.

[154] Z. Deng, I. Tutunnikov, I. S. Averbukh, M. Thachuk and R. V. Krems, *Bayesian optimization for inverse problems in time-dependent quantum dynamics*, J. Chem. Phys. **153**(16), 164111 (2020), doi:10.1063/5.0015896.

[155] N. Q. Su, J. Chen, Z. Sun, D. H. Zhang and X. Xu, $H + H_2$ *quantum dynamics using potential energy surfaces based on the XYG3 type of doubly hybrid density functionals: Validation of the density functionals*, J. Chem. Phys. **142**, 084107 (2015), doi:10.1063/1.4913196.

[156] R. A. Vargas-Hernández, Y. Guan, D. H. Zhang and R. V. Krems, *Bayesian optimization for the inverse scattering problem in quantum reaction dynamics*, New J. Phys. **21**, 22001 (2019), doi:10.1088/1367-2630/ab0099.

[157] J. T. Cantin, G. Alexandrowicz, G. Alexandrowicz and R. V. Krems, *Transfer-matrix theory of surface spin-echo experiments with molecules*, Phys. Rev. A **101**(6), 062703 (2020), doi:10.1103/PhysRevA.101.062703.

[158] N. Sugisawa, H. Sugisawa, Y. Otake, R. V. Krems, H. Nakamura and S. Fuse, *Rapid and mild one-flow synthetic approach to unsymmetrical sulfamides guided by Bayesian optimization*, Chem. Methods **1**(11), 484 (2021), doi:10.1002/cmtd.202100053.

[159] A. Jasinski, J. Montaner, R. C. Forrey, B. H. Yang, P. C. Stancil, N. Balakrishnan, J. Dai, R. A. Vargas-Hernández and R. V. Krems, *Machine learning corrected quantum dynamics calculations*, Phys. Rev. Res. **2**(3), 32051 (2020), doi:10.1103/PhysRevResearch.2.032051.

[160] R. A. Vargas Hernandez, *Bayesian optimization for calibrating and selecting hybrid-density functional models*, J. Phys. Chem. A **124**(20), 4053 (2020), doi:10.1021/acs.jpca.0c01375.

[161] J. Proppe, S. Gugler and M. Reiher, *Gaussian process-based refinement of dispersion corrections*, J. Chem. Theory Comput. **15**(11), 6046 (2019), doi:10.1021/acs.jctc.9b00627.

[162] R. Tamura and K. Hukushima, *Bayesian optimization for computationally extensive probability distributions*, PLoS One **13**(3), 1 (2018), doi:10.1371/journal.pone.0193785.

[163] S. Carr, R. Garnett and C. Lo, *BASC: Applying Bayesian optimization to the search for global minima on potential energy surfaces*, In *ICML 2016 - Int. Conf. Mach. Learn.*, vol. 48, pp. 898–907. PMLR (2016).

[164] L. Chan, G. R. Hutchison and G. M. Morris, *Bayesian optimization for conformer generation*, J. Cheminformatics **11**(1), 32 (2019), doi:10.1186/s13321-019-0354-7.

[165] R. A. Vargas-Hernández, C. Chuang and P. Brumer, *Multi-objective optimization for retinal photoisomerization models with respect to experimental observables*, J. Chem. Phys. **155**(23), 234109 (2021), doi:10.1063/5.0060259.

[166] J. Duris, D. Kennedy, A. Hanuka, J. Shtalenkova, A. Edelen, P. Baxevanis, A. Egger, T. Cope, M. McIntire, S. Ermon and D. Ratner, *Bayesian optimization of a free-electron laser*, Phys. Rev. Lett. **124**, 124801 (2020), doi:10.1103/PhysRevLett.124.124801.

[167] S. Jalas, M. Kirchen, P. Messner, P. Winkler, L. Hübner, J. Dirkwinkel, M. Schnepp, R. Lehe and A. R. Maier, *Bayesian optimization of a laser-plasma accelerator*, Phys. Rev. Lett. **126**, 104801 (2021), doi:10.1103/PhysRevLett.126.104801.

[168] R. J. Shalloo, S. J. D. Dann, J.-N. Gruse, C. I. D. Underwood, A. F. Antoine, C. Arran, M. Backhouse, C. D. Baird, M. D. Balcazar, N. Bourgeois, J. A. Cardarelli, P. Hatfield *et al.*, *Automation and control of laser wakefield accelerators using Bayesian optimization*, Nat. Commun. **11**(1), 6355 (2020), doi:10.1038/s41467-020-20245-6.

[169] T. Ueno, T. D. Rhone, Z. Hou, T. Mizoguchi and K. Tsuda, *COMBO: An efficient Bayesian optimization library for materials science*, Mater. Discov. **4**, 18 (2016), doi:10.1016/j.md.2016.04.001.

[170] R. Jalem, K. Kanamori, I. Takeuchi, M. Nakayama, H. Yamasaki and T. Saito, *Bayesian-driven first-principles calculations for accelerating exploration of fast ion conductors for rechargeable battery application*, Sci. Rep. **8**(1), 5845 (2018), doi:10.1038/s41598-018-23852-y.

[171] S. Ju, T. Shiga, L. Feng, Z. Hou, K. Tsuda and J. Shiomi, *Designing nanostructures for phonon transport via Bayesian optimization*, Phys. Rev. X **7**, 021024 (2017), doi:10.1103/PhysRevX.7.021024.

[172] J. Kuhn, J. Spitz, P. Sonnweber-Ribic, M. Schneider and T. Böhlke, *Identifying material parameters in crystal plasticity by Bayesian optimization*, Optim. Eng. (2021), doi:10.1007/s11081-021-09663-7.

[173] R.-R. Griffiths and J. M. Hernández-Lobato, *Constrained Bayesian optimization for automatic chemical design using variational autoencoders*, Chem. Sci. **11**, 577 (2020), doi:10.1039/C9SC04026A.

[174] A. Deshwal, C. M. Simon and J. R. Doppa, *Bayesian optimization of nanoporous materials*, Mol. Syst. Des. Eng. **6**, 1066 (2021), doi:10.1039/D1ME00093D.

[175] F. Häse, L. M. Roch, C. Kreisbeck and A. Aspuru-Guzik, *Phoenics: A Bayesian optimizer for chemistry*, ACS Cent. Sci. **4**(9), 1134 (2018), doi:10.1021/acscentsci.8b00307.

[176] F. Häse, M. Aldeghi, R. J. Hickman, L. M. Roch and A. Aspuru-Guzik, *Gryffin: An algorithm for Bayesian optimization of categorical variables informed by expert knowledge*, Appl. Phys. Rev. **8**(3), 031406 (2021), doi:10.1063/5.0048164.

[177] A. Biswas, A. N. Morozovska, M. Ziatdinov, E. A. Eliseev and S. V. Kalinin, *Multi-objective Bayesian optimization of ferroelectric materials with interfacial control for memory and energy storage applications*, J. Appl. Phys. **130**(20), 204102 (2021), doi:10.1063/5.0068903.

[178] Y. Wang, T.-Y. Chen and D. G. Vlachos, *NEXTorch: A design and bayesian optimization toolkit for chemical sciences and engineering*, J. Chem. Inf. Model. **61**(11), 5312 (2021), doi:10.1021/acs.jcim.1c00637.

[179] M. Aldeghi, F. Häse, R. J. Hickman, I. Tamblyn and A. Aspuru-Guzik, *Golem: An algorithm for robust experiment and process optimization*, Chem. Sci. **12**, 14792 (2021), doi:10.1039/D1SC01545A.

[180] H. Sugisawa, T. Ida and R. V. Krems, *Gaussian process model of 51-dimensional potential energy surface for protonated imidazole dimer*, J. Chem. Phys. **153**(11), 114101 (2020), doi:10.1063/5.0023492.

[181] C. Puzzarini, J. Bloino, N. Tasinato and V. Barone, *Accuracy and interpretability: The devil and the holy grail. New routes across old boundaries in computational spectroscopy*, Chem. Rev. **119**(13), 8131 (2019), doi:10.1021/acs.chemrev.9b00007.

[182] F. Herrera, K. W. Madison, R. V. Krems and M. Berciu, *Investigating polaron transitions with polar molecules*, Phys. Rev. Lett. **110**(22), 223002 (2013), doi:10.1103/PhysRevLett.110.223002.

[183] K. Asnaashari and R. V. Krems, *Gradient domain machine learning with composite kernels: improving the accuracy of PES and force fields for large molecules*, Mach. learn.: sci. technol. **3**(1), 015005 (2021), doi:10.1088/2632-2153/ac3845.

[184] A. G. Wilson, Z. Hu, R. Salakhutdinov and E. P. Xing, *Deep kernel learning*, In *AISTATS 2016 - Int. Conf. Artif. Intell. Stat.* (2016), arXiv:1511.02222.

[185] S. Sun, G. Zhang, C. Wang, W. Zeng, J. Li and R. Grosse, *Differentiable compositional kernel learning for Gaussian processes*, In *ICML 2018 - Int. Conf. Mach. Learn.* (2018), arXiv:1806.04326.

[186] J. Gardner, G. Pleiss, K. Q. Weinberger, D. Bindel and A. G. Wilson, *GPyTorch: Blackbox matrix-matrix Gaussian process inference with GPU acceleration*, In *NeurIPS 2018 - Adv. Neural Inf. Process. Syst.* (2018), arXiv:1809.11165.

[187] B. Charlier, J. Feydy, J. A. Glaunès, F.-D. Collin and G. Durif, *Kernel operations on the GPU, with Autodiff, without memory overflows*, J. Mach. Learn. Res. **22**(74), 1 (2021), arXiv:2004.11127.

[188] A. G. d. G. Matthews, M. van der Wilk, T. Nickson, K. Fujii, A. Boukouvalas, P. León-Villagrá, Z. Ghahramani and J. Hensman, *GPflow: A Gaussian process library using TensorFlow*, J. Mach. Learn. Res. **18**(40), 1 (2017), arXiv:1610.08733.

[189] M. Blondel, Q. Berthet, M. Cuturi, R. Frostig, S. Hoyer, F. Llinares-López, F. Pedregosa and J.-P. Vert, *Efficient and modular implicit differentiation* (2021), arXiv:2105.15183.

[190] H.-Y. Huang, R. Kueng and J. Preskill, *Predicting many properties of a quantum system from very few measurements*, Nat. Phys. **16**(10), 1050–1057 (2020), doi:10.1038/s41567-020-0932-7.

[191] C. E. Rasmussen and C. K. I. Williams, *Gaussian Processes for Machine Learning*, Adaptive Computation and Machine Learning. MIT Press, ISBN 9780262256834, doi:10.7551/mitpress/3206.001.0001 (2005).

[192] R. V. Krems, *Bayesian machine learning for quantum molecular dynamics*, Phys. Chem. Chem. Phys. **21**(25), 13392 (2019), doi:10.1039/c9cp01883b.

[193] R. A. Vargas-Hernández and R. V. Krems, *Physical Extrapolation of Quantum Observables by Generalization with Gaussian Processes*, pp. 171–194, Springer International Publishing, Cham, ISBN 978-3-030-40245-7, doi:10.1007/978-3-030-40245-7_9 (2020).

[194] H.-Y. Huang, R. Kueng, G. Torlai, V. V. Albert and J. Preskill, *Provably efficient machine learning for quantum many-body problems* (2021), arXiv:2106.12627.

[195] P. A. M. Dirac and R. H. Fowler, *Quantum mechanics of many-electron systems*, Proc. R. Soc. A: Math. Phys. Eng. Sci. **123**(792), 714 (1929), doi:10.1098/rspa.1929.0094.

[196] G. Carleo and M. Troyer, *Solving the quantum many-body problem with artificial neural networks*, Science **355**(6325), 602–606 (2017), doi:10.1126/science.aag2302.

[197] K. Choo, A. Mezzacapo and G. Carleo, *Fermionic neural-network states for ab-initio electronic structure*, Nat. Commun. **11**(1) (2020), doi:10.1038/s41467-020-15724-9.

[198] H. Saito, *Solving the Bose–Hubbard model with machine learning*, J. Phys. Soc. Jpn. **86**(9), 093001 (2017), doi:10.7566/jpsj.86.093001.

[199] S. R. White, *Density matrix formulation for quantum renormalization groups*, Phys. Rev. Lett. **69**, 2863 (1992), doi:10.1103/PhysRevLett.69.2863.

[200] U. Schollwöck, *The density-matrix renormalization group in the age of matrix product states*, Ann. Phys. (N. Y.) **326**(1), 96–192 (2011), doi:10.1016/j.aop.2010.09.012.

[201] R. Orús, *A practical introduction to tensor networks: Matrix product states and projected entangled pair states*, Ann. Phys. (N. Y.) **349**, 117–158 (2014), doi:10.1016/j.aop.2014.06.013.

[202] M. V. den Nest, *Simulating quantum computers with probabilistic methods* (2010), arXiv:0911.1624.

[203] W. K. Hastings, *Monte Carlo sampling methods using Markov chains and their applications*, Biometrika **57**(1), 97 (1970), doi:10.2307/2334940.

[204] R. Jastrow, *Many-body problem with strong forces*, Phys. Rev. **98**, 1479 (1955), doi:10.1103/PhysRev.98.1479.

[205] E. Manousakis, *The spin-½ Heisenberg antiferromagnet on a square lattice and its application to the cuprous oxides*, Rev. Mod. Phys. **63**, 1 (1991), doi:10.1103/RevModPhys.63.1.

[206] T. Brown, B. Mann, N. Ryder, M. Subbiah, J. D. Kaplan, P. Dhariwal, A. Neelakantan, P. Shyam, G. Sastry, A. Askell, S. Agarwal, A. Herbert-Voss *et al.*, *Language models are few-shot learners*, In *NeurIPS 2020 - Adv. Neural Inf. Process. Syst.* (2020), arXiv:2005.14165.

[207] M. Caron, H. Touvron, I. Misra, H. Jégou, J. Mairal, P. Bojanowski and A. Joulin, *Emerging properties in self-supervised vision transformers*, In *ICCV 2021 - Int. Conf. Comput. Vis.* (2021), arXiv:2104.14294.

[208] A. Nichol, P. Dhariwal, A. Ramesh, P. Shyam, P. Mishkin, B. McGrew, I. Sutskever and M. Chen, *GLIDE: Towards photorealistic image generation and editing with text-guided diffusion models* (2021), arXiv:2112.10741.

[209] A. Barra, A. Bernacchia, E. Santucci and P. Contucci, *On the equivalence of Hopfield networks and Boltzmann machines*, Neural Netw. **34**, 1 (2012), doi:10.1016/j.neunet.2012.06.003.

[210] G. Montufar, *Restricted Boltzmann machines: Introduction and review* (2018), arXiv:1806.07066.

[211] D.-L. Deng, X. Li and S. Das Sarma, *Quantum entanglement in neural network states*, Phys. Rev. X **7**(2) (2017), doi:10.1103/PhysRevX.7.021021.

[212] J. Chen, S. Cheng, H. Xie, L. Wang and T. Xiang, *Equivalence of restricted Boltzmann machines and tensor network states*, Phys. Rev. B **97**(8) (2018), doi:10.1103/PhysRevB.97.085104.

[213] X. Gao and L.-M. Duan, *Efficient representation of quantum many-body states with deep neural networks*, Nat. Commun. **8**(1) (2017), doi:10.1038/s41467-017-00705-2.

[214] D. Luo, G. Carleo, B. K. Clark and J. Stokes, *Gauge equivariant neural networks for quantum lattice gauge theories*, Phys. Rev. Lett. **127**, 276402 (2021), doi:10.1103/PhysRevLett.127.276402.

[215] A. Bansal, X. Chen, B. Russell, A. Gupta and D. Ramanan, *PixelNet: Representation of the pixels, by the pixels, and for the pixels* (2017), arXiv:1702.06506.

[216] M. Hibat-Allah, M. Ganahl, L. E. Hayward, R. G. Melko and J. Carrasquilla, *Recurrent neural network wave functions*, Phys. Rev. Res. **2**(2), 023358 (2020), doi:10.1103/PhysRevResearch.2.023358.

[217] M. Schmitt and M. Heyl, *Quantum many-body dynamics in two dimensions with artificial neural networks*, Phys. Rev. Lett. **125**, 100503 (2020), doi:10.1103/PhysRevLett.125.100503.

[218] C. Roth and A. H. MacDonald, *Group convolutional neural networks improve quantum state accuracy* (2021), arXiv:2104.05085.

[219] I. Glasser, N. Pancotti, M. August, I. D. Rodriguez and J. I. Cirac, *Neural-network quantum states, string-bond states, and chiral topological states*, Phys. Rev. X **8**, 011006 (2018), doi:10.1103/PhysRevX.8.011006.

[220] O. Sharir, A. Shashua and G. Carleo, *Neural tensor contractions and the expressive power of deep neural quantum states* (2021), arXiv:2103.10293.

[221] Y. Levine, O. Sharir, N. Cohen and A. Shashua, *Quantum entanglement in deep learning architectures*, Phys. Rev. Lett. **122**, 065301 (2019), doi:10.1103/PhysRevLett.122.065301.

[222] P. Calabrese and J. Cardy, *Entanglement entropy and quantum field theory*, J. Stat. Mech. **2004**, P06002 (2004), doi:10.1088/1742-5468/2004/06/p06002.

[223] J. Eisert, M. Cramer and M. B. Plenio, *Colloquium: Area laws for the entanglement entropy*, Rev. Mod. Phys. **82**, 277 (2010), doi:10.1103/RevModPhys.82.277.

[224] M. Hibat-Allah, E. M. Inack, R. Wiersema, R. G. Melko and J. Carrasquilla, *Variational neural annealing*, Nat. Mach. Intell. **3**, 952 (2021), doi:10.1038/s42256-021-00401-3.

[225] K. Choo, G. Carleo, N. Regnault and T. Neupert, *Symmetries and many-body excitations with neural-network quantum states*, Phys. Rev. Lett. **121**, 167204 (2018), doi:10.1103/PhysRevLett.121.167204.

[226] A. Valenti, E. Greplova, N. H. Lindner and S. D. Huber, *Correlation-enhanced neural networks as interpretable variational quantum states*, Phys. Rev. Res. **4**, L012010 (2022), doi:10.1103/PhysRevResearch.4.L012010.

[227] G. Carleo, Y. Nomura and M. Imada, *Constructing exact representations of quantum many-body systems with deep neural networks*, Nat. Commun. **9**, 5322 (2018), doi:10.1038/s41467-018-07520-3.

[228] R. Kaubruegger, L. Pastori and J. C. Budich, *Chiral topological phases from artificial neural networks*, Phys. Rev. B **97**, 195136 (2018), doi:10.1103/PhysRevB.97.195136.

[229] Y. Zheng, H. He, N. Regnault and B. A. Bernevig, *Restricted Boltzmann machines and matrix product states of one-dimensional translationally invariant stabilizer codes*, Phys. Rev. B **99**, 155129 (2019), doi:10.1103/PhysRevB.99.155129.

[230] S. Lu, X. Gao and L.-M. Duan, *Efficient representation of topologically ordered states with restricted Boltzmann machines*, Phys. Rev. B **99**, 155136 (2019), doi:10.1103/PhysRevB.99.155136.

[231] Y. Huang and J. E. Moore, *Neural network representation of tensor network and chiral states*, Phys. Rev. Lett. **127**, 170601 (2021), doi:10.1103/PhysRevLett.127.170601.

[232] C.-Y. Park and M. J. Kastoryano, *Geometry of learning neural quantum states*, Phys. Rev. Res. **2**, 023232 (2020), doi:10.1103/PhysRevResearch.2.023232.

[233] S.-H. Lin and F. Pollmann, *Scaling of neural-network quantum states for time evolution* (2021), arXiv:2104.10696.

[234] F. Vicentini, D. Hofmann, A. Szabó, D. Wu, C. Roth, C. Giuliani, G. Pescia, J. Nys, V. Vargas-Calderon, N. Astrakhantsev and G. Carleo, *NetKet 3: Machine learning toolbox for many-body quantum systems* (2021), arXiv:2112.10526.

[235] X. Yuan, S. Endo, Q. Zhao, Y. Li and S. C. Benjamin, *Theory of variational quantum simulation*, Quantum **3**, 191 (2019), doi:10.22331/q-2019-10-07-191.

[236] G. Carleo, F. Becca, M. Schiro and M. Fabrizio, *Localization and glassy dynamics of many-body quantum systems*, Sci. Rep. **2**, 243 (2012), doi:10.1038/srep00243.

[237] I. L. Gutiérrez and C. B. Mendl, *Real time evolution with neural-network quantum states*, Quantum **6**, 627 (2022), doi:10.22331/q-2022-01-20-627.

[238] D. Hofmann, G. Fabiani, J. H. Mentink, G. Carleo and M. A. Sentef, *Role of stochastic noise and generalization error in the time propagation of neural-network quantum states* (2021), arXiv:2105.01054.

[239] S. Sorella, *Green function Monte Carlo with Stochastic Reconfiguration*, Phys. Rev. Lett. **80**, 4558 (1998), doi:10.1103/PhysRevLett.80.4558.

[240] F. Becca and S. Sorella, *Quantum Monte Carlo Approaches for Correlated Systems*, Cambridge University Press, ISBN 9781316417041, doi:10.1017/9781316417041 (2017).

[241] D. Hangleiter, I. Roth, D. Nagaj and J. Eisert, *Easing the Monte Carlo sign problem*, Sci. Adv. **6**, eabb8341 (2020), doi:10.1126/sciadv.abb8341.

[242] S. B. Bravyi and A. Y. Kitaev, *Fermionic quantum computation*, Ann. Phys. **298**, 210 (2002), doi:10.1006/aphy.2002.6254.

[243] P. Jordan and E. Wigner, *Über das Paulische Äquivalenzverbot*, Zeitschrift für Physik **47**, 631 (1928), doi:10.1007/BF01331938.

[244] E. Zohar and J. I. Cirac, *Eliminating fermionic matter fields in lattice gauge theories*, Phys. Rev. B **98**, 075119 (2018), doi:10.1103/PhysRevB.98.075119.

[245] U. Borla, R. Verresen, F. Grusdt and S. Moroz, *Confined phases of one-dimensional spinless fermions coupled to Z_2 gauge theory*, Phys. Rev. Lett. **124**, 120503 (2020), doi:10.1103/PhysRevLett.124.120503.

[246] J. Hermann, Z. Schätzle and F. Noé, *Deep-neural-network solution of the electronic Schrödinger equation*, Nat. Chem. **12**, 891–897 (2020), doi:10.1038/s41557-020-0544-y.

[247] D. Luo and B. K. Clark, *Backflow transformations via neural networks for quantum many-body wave functions*, Phys. Rev. Lett. **122**, 226401 (2019), doi:10.1103/PhysRevLett.122.226401.

[248] B. Jonsson, B. Bauer and G. Carleo, *Neural-network states for the classical simulation of quantum computing* (2018), arXiv:1808.05232.

[249] M. Medvidović and G. Carleo, *Classical variational simulation of the quantum approximate optimization algorithm*, npj Quantum Inf. **7**, 101 (2021), doi:10.1038/s41534-021-00440-z.

[250] M. P. Harrigan, K. J. Sung, M. Neeley, K. J. Satzinger, F. Arute, K. Arya, J. Atalaya, J. C. Bardin, R. Barends, S. Boixo and et al., *Quantum approximate optimization of nonplanar graph problems on a planar superconducting processor*, Nat. Phys. **17**, 332–336 (2021), doi:10.1038/s41567-020-01105-y.

[251] J. Carrasquilla, D. Luo, F. Pérez, A. Milsted, B. K. Clark, M. Volkovs and L. Aolita, *Probabilistic simulation of quantum circuits using a deep-learning architecture*, Phys. Rev. A **104**, 032610 (2021), doi:10.1103/PhysRevA.104.032610.

[252] A. Vaswani, N. Shazeer, N. Parmar, J. Uszkoreit, L. Jones, A. N. Gomez, L. Kaiser and I. Polosukhin, *Attention is all you need*, In *Adv. Neural. Inf. Process. Syst.* (2017), arXiv:1706.03762.

[253] H.-P. Breuer and F. Petruccione, *The Theory of Open Quantum Systems*, Oxford University Press, ISBN 9780198520634, doi:10.1093/acprof:oso/9780199213900.001.0001 (2007).

[254] N. Yoshioka and R. Hamazaki, *Constructing neural stationary states for open quantum many-body systems*, Phys. Rev. B **99**, 214306 (2019), doi:10.1103/PhysRevB.99.214306.

[255] A. Nagy and V. Savona, *Variational quantum Monte Carlo method with a neural-network ansatz for open quantum systems*, Phys. Rev. Lett. **122**, 250501 (2019), doi:10.1103/PhysRevLett.122.250501.

[256] F. Vicentini, A. Biella, N. Regnault and C. Ciuti, *Variational neural-network ansatz for steady states in open quantum systems*, Phys. Rev. Lett. **122**, 250503 (2019), doi:10.1103/PhysRevLett.122.250503.

[257] M. J. Hartmann and G. Carleo, *Neural-network approach to dissipative quantum many-body dynamics*, Phys. Rev. Lett. **122**, 250502 (2019), doi:10.1103/PhysRevLett.122.250502.

[258] D. Luo, Z. Chen, J. Carrasquilla and B. K. Clark, *Autoregressive neural network for simulating open quantum systems via a probabilistic formulation* (2021), arXiv:2009.05580.

[259] M. Reh, M. Schmitt and M. Gärttner, *Time-dependent variational principle for open quantum systems with artificial neural networks*, Phys. Rev. Lett. **127**, 230501 (2021), doi:10.1103/PhysRevLett.127.230501.

[260] F. Minganti, A. Biella, N. Bartolo and C. Ciuti, *Spectral theory of Liouvillians for dissipative phase transitions*, Phys. Rev. A **98**, 042118 (2018), doi:10.1103/PhysRevA.98.042118.

[261] G. Torlai, G. Mazzola, J. Carrasquilla, M. Troyer, R. Melko and G. Carleo, *Neural-network quantum state tomography*, Nat. Phys. **14**, 447–450 (2018), doi:10.1038/s41567-018-0048-5.

[262] A. Szabó and C. Castelnovo, *Neural network wave functions and the sign problem*, Phys. Rev. Res. **2**, 033075 (2020), doi:10.1103/PhysRevResearch.2.033075.

[263] T. Schmale, M. Reh and M. Gärttner, *Scalable quantum state tomography with artificial neural networks* (2021), arXiv:2109.13776.

[264] G. Torlai, B. Timar, E. P. L. van Nieuwenburg, H. Levine, A. Omran, A. Keesling, H. Bernien, M. Greiner, V. Vuletić, M. D. Lukin, R. G. Melko and M. Endres, *Integrating neural networks with a quantum simulator for state reconstruction*, Phys. Rev. Lett. **123**, 230504 (2019), doi:10.1103/PhysRevLett.123.230504.

[265] S. Aaronson, *Shadow tomography of quantum states* (2018), arXiv:1711.01053.

[266] D. Pfau, J. S. Spencer, A. G. Matthews and W. M. C. Foulkes, *Ab initio solution of the many-electron Schrödinger equation with deep neural networks*, Phys. Rev. Res. **2**, 033429 (2020), doi:10.1103/PhysRevResearch.2.033429.

[267] C. Adams, G. Carleo, A. Lovato and N. Rocco, *Variational Monte Carlo calculations of $A \leq 4$ nuclei with an artificial neural-network correlator ansatz*, Phys. Rev. Lett. **127**, 022502 (2021), doi:10.1103/PhysRevLett.127.022502.

[268] F. Vicentini, *Machine learning toolbox for quantum many body physics*, Nat. Rev. Phys. **3**, 156 (2021), doi:10.1038/s42254-021-00285-7.

[269] J. Carrasquilla and G. Torlai, *Neural networks in quantum many-body physics: a hands-on tutorial* (2021), arXiv:2101.11099.

[270] G. Carleo, *Beijing lecture notes and code*, Lecture Notes (2017).

[271] S. R. Sutton and A. G. Barto, *Reinforcement Learning: An Introduction*, Bradford Book, ISBN 9780262352703, doi:10.5555/980651.980663 (2018).

[272] R. S. Sutton, *Learning to predict by the methods of temporal differences*, Mach. Learn. **3**, 9 (1988), doi:10.1007/BF00115009.

[273] G. A. Rummery and M. Niranjan, *On-line Q-learning using connectionist systems*, CUED/F-INFENG/TR 166, University of Cambridge, Department of Engineering (1994).

[274] H. van Seijen, A. R. Mahmood, P. M. Pilarski, M. C. Machado and R. S. Sutton, *True online temporal-difference learning*, J. Mach. Learn. Res. **17**, 1 (2016), doi:10.48550/arXiv.1512.04087.

[275] G. H. John, *When the best move isn't optimal: Q-learning with exploration*, In *Proc. 12th Nat. Conf. Artif. Intell. (Vol. 2)* (1994).

[276] C. J. C. H. Watkins and P. Dayan, *Q-learning*, Mach. Learn. **8**, 279 (1992), doi:10.1007/BF00992698.

[277] J. E. Smith and R. L. Winkler, *The optimizer's curse: Skepticism and postdecision surprise in decision analysis*, Manag. Sci. **52**, 311 (2006), doi:10.1287/mnsc.1050.0451.

[278] S. Thrun and A. Schwartz, *Issues in using function approximation for reinforcement learning*, In *Proc. 4th Connectionist Models Summer School* (1993).

[279] H. Van Hasselt, *Double Q-learning*, In *Conf. Neural Inf. Process. Syst.*, vol. 23 (2010).

[280] L.-J. Lin, *Reinforcement Learning for Robots Using Neural Networks*, Ph.D. thesis, Carnegie Mellon University, USA, UMI Order No. GAX93-22750 (1992).

[281] H. Van Hasselt, A. Guez and D. Silver, *Deep reinforcement learning with double Q-learning*, In *Proc. AAAI Conf. Artif. Intell.* (2016), arXiv:1509.06461.

[282] P. Marbach and J. N. Tsitsiklis, *Simulation-based optimization of Markov reward processes*, IEEE Trans. Automat. Contr. **46**, 191 (2001), doi:10.1109/9.905687.

[283] R. S. Sutton, D. McAllester, S. Singh and Y. Mansour, *Policy gradient methods for reinforcement learning with function approximation*, In *NeurIPS 2000 - Adv. Neural Inf. Process. Syst.* (2000).

[284] R. J. Williams, *Simple statistical gradient-following algorithms for connectionist reinforcement learning*, Mach. Learn. **8**, 229 (1992), doi:10.1007/BF00992696.

[285] S. J. Rennie, E. Marcheret, Y. Mroueh, J. Ross and V. Goel, *Self-critical sequence training for image captioning*, In *Proc. IEEE Conf. Comput. Vision and Pattern Recognition*, doi:10.1109/CVPR.2017.131 (2017).

[286] J. Schulman, P. Moritz, S. Levine, M. Jordan and P. Abbeel, *High-dimensional continuous control using generalized advantage estimation*, In *ICLR 2016 - Int. Conf. Learn. Represent.* (2016), arXiv:1506.02438.

[287] A. G. Barto, R. S. Sutton and C. W. Anderson, *Neuronlike adaptive elements that can solve difficult learning control problems*, IEEE Trans. Syst. Man Cybern. Syst. **5**, 834 (1983), doi:10.1109/TSMC.1983.6313077.

[288] V. Konda and J. Tsitsiklis, *Actor-critic algorithms*, In *Conf. Neural. Inf. Process. Syst.* (1999).

[289] T. Degris, M. White and R. S. Sutton, *Off-policy actor-critic*, In *ICML 2012 - Conf. Mach. Learn.*, p. 179–186. Omnipress (2012), arXiv:1205.4839.

[290] V. Mnih, A. P. Badia, M. Mirza, A. Graves, T. Lillicrap, T. Harley, D. Silver and K. Kavukcuoglu, *Asynchronous methods for deep reinforcement learning*, In *ICML 2016 - 33th Int. Conf. Mach. Learn.*, vol. 48, pp. 1928–1937 (2016), arXiv:1602.01783.

[291] S.-i. Amari, *Natural gradient works efficiently in learning*, Neural Comput. **10**(2), 251 (1998), doi:10.1162/089976698300017746.

[292] S. M. Kakade, *A natural policy gradient*, In *NeurIPS 2002 - Conf. Neural. Inf. Process. Syst.* (2002).

[293] J. Peters and S. Schaal, *Natural actor-critic*, Neurocomputing **71**(7), 1180 (2008), doi:10.1016/j.neucom.2007.11.026.

[294] S. Bhatnagar, R. S. Sutton, M. Ghavamzadeh and M. Lee, *Natural actor–critic algorithms*, Automatica **45**(11), 2471 (2009), doi:10.1016/j.automatica.2009.07.008.

[295] J. Schulman, S. Levine, P. Abbeel, M. Jordan and P. Moritz, *Trust region policy optimization*, In *ICML 2015 - Int. Conf. Mach. Learn.* (2015), arXiv:1502.05477.

[296] Y. Wu, E. Mansimov, R. B. Grosse, S. Liao and J. Ba, *Scalable trust-region method for deep reinforcement learning using Kronecker-factored approximation*, In *NeurIPS 2017 - Adv. Neural. Inf. Process. Syst.*, vol. 30 (2017), arXiv:1708.05144.

[297] J. Schulman, F. Wolski, P. Dhariwal, A. Radford and O. Klimov, *Proximal policy optimization algorithms* (2017), arXiv:1707.06347.

[298] H. J. Briegel and G. De las Cuevas, *Projective simulation for artificial intelligence*, Scientific reports **2**(1), 1 (2012), doi:10.1038/srep00400.

[299] J. Mautner, A. Makmal, D. Manzano, M. Tiersch and H. J. Briegel, *Projective simulation for classical learning agents: a comprehensive investigation*, New Gener. Comput. **33**(1), 69 (2015), doi:10.1007/s00354-015-0102-0.

[300] A. A. Melnikov, A. Makmal and H. J. Briegel, *Benchmarking projective simulation in navigation problems*, IEEE Access **6**, 64639 (2018), doi:10.1109/ACCESS.2018.2876494.

[301] S. Jerbi, L. M. Trenkwalder, H. P. Nautrup, H. J. Briegel and V. Dunjko, *Quantum enhancements for deep reinforcement learning in large spaces*, PRX Quantum **2**(1), 010328 (2021), doi:10.1103/PRXQuantum.2.010328.

[302] A. A. Melnikov, H. P. Nautrup, M. Krenn, V. Dunjko, M. Tiersch, A. Zeilinger and H. J. Briegel, *Active learning machine learns to create new quantum experiments*, Proc. Natl. Acad. Sci. U.S.A. **115**(6), 1221 (2018), doi:10.1073/pnas.1714936115.

[303] W. L. Boyajian, J. Clausen, L. M. Trenkwalder, V. Dunjko and H. J. Briegel, *On the convergence of projective-simulation–based reinforcement learning in Markov decision processes*, Quantum machine intelligence **2**(2), 1 (2020), doi:10.1007/s42484-020-00023-9.

[304] A. A. Melnikov, A. Makmal, V. Dunjko and H. J. Briegel, *Projective simulation with generalization*, Scientific reports **7**(1), 1 (2017), doi:10.1038/s41598-017-14740-y.

[305] K. Ried, B. Eva, T. Müller and H. J. Briegel, *How a minimal learning agent can infer the existence of unobserved variables in a complex environment* (2019), arXiv:1910.06985.

[306] M. Campbell, A. J. Hoane Jr and F.-h. Hsu, *Deep blue*, Artificial intelligence **134**(1-2), 57 (2002), doi:10.1016/S0004-3702(01)00129-1.

[307] A. Yee and M. Alvarado, *Pattern recognition and Monte-Carlo tree search for Go gaming better automation*, In *IBERAMIA 2012 – Adv. Artif. Intell.*, doi:10.1007/978-3-642-34654-5_2 (2012).

[308] R. Coulom, *Efficient selectivity and backup operators in monte-carlo tree search*, In *International conference on computers and games*, pp. 72–83. Springer, doi:10.1007/978-3-540-75538-8_7 (2006).

[309] D. Silver, J. Schrittwieser, K. Simonyan, I. Antonoglou, A. Huang, A. Guez, T. Hubert, L. Baker, M. Lai, A. Bolton, Y. Chen, T. Lillicrap *et al.*, *Mastering the game of Go without human knowledge*, Nature **550**(7676), 354 (2017), doi:10.1038/nature24270.

[310] D. Silver, T. Hubert, J. Schrittwieser, I. Antonoglou, M. Lai, A. Guez, M. Lanctot, L. Sifre, D. Kumaran, T. Graepel, T. Lillicrap, K. Simonyan *et al.*, *A general reinforcement learning algorithm that masters chess, Shogi, and Go through self-play*, Science **362**(6419), 1140 (2018), doi:10.1126/science.aar6404.

[311] OpenAI, C. Berner, G. Brockman, B. Chan, V. Cheung, P. Dębiak, C. Dennison, D. Farhi, Q. Fischer, S. Hashme, C. Hesse, R. Józefowicz *et al.*, *Dota 2 with large scale deep reinforcement learning* (2019), arXiv:1912.06680.

[312] W. H. Guss, C. Codel, K. Hofmann, B. Houghton, N. Kuno, S. Milani, S. Mohanty, D. Perez Liebana, R. Salakhutdinov, N. Topin *et al.*, *The MineRL 2019 competition on sample efficient reinforcement learning using human priors* (2019), arXiv:1904.10079.

[313] J. Schrittwieser, I. Antonoglou, T. Hubert, K. Simonyan, L. Sifre, S. Schmitt, A. Guez, E. Lockhart, D. Hassabis, T. Graepel, T. Lillicrap and D. Silver, *Mastering Atari, Go, chess and Shogi by planning with a learned model*, Nature **588**(7839), 604 (2020), doi:10.1038/s41586-020-03051-4.

[314] F. Marquardt, *Machine learning and quantum devices*, SciPost Phys. Lect. Notes p. 29 (2021), doi:10.21468/SciPostPhysLectNotes.29.

[315] R. Porotti, A. Essing, B. Huard and F. Marquardt, *A deep reinforcement learning for quantum state preparation with weak nonlinear measurements* (2021), arXiv:2107.08816.

[316] T. Fösel, P. Tighineanu, T. Weiss and F. Marquardt, *Reinforcement learning with neural networks for quantum feedback*, Phys. Rev. X **8**, 031084 (2018), doi:10.1103/PhysRevX.8.031084.

[317] S. Borah, B. Sarma, M. Kewming, G. J. Milburn and J. Twamley, *Measurement-based feedback quantum control with deep reinforcement learning for a double-well nonlinear potential*, Phys. Rev. Lett. **127**, 190403 (2021), doi:10.1103/PhysRevLett.127.190403.

[318] V. Nguyen, S. B. Orbell, D. T. Lennon, H. Moon, F. Vigneau, L. C. Camenzind, L. Yu, D. M. Zumbühl, G. A. D. Briggs, M. A. Osborne, D. Sejdinovic and N. Ares, *Deep reinforcement learning for efficient measurement of quantum devices*, npj Quantum Inf. **7**(1), 100 (2021), doi:10.1038/s41534-021-00434-x.

[319] J. Preskill, *Quantum computing in the NISQ era and beyond*, In *Quantum* [489], p. 79 (2018), doi:10.22331/q-2018-08-06-79.

[320] T. Fösel, M. Yuezhen Niu, F. Marquardt and L. Li, *Quantum circuit optimization with deep reinforcement learning* (2021), arXiv:2103.07585.

[321] W. K. Wootters and W. H. Zurek, *A single quantum cannot be cloned*, Nature **299**(5886), 802 (1982), doi:10.1038/299802a0.

[322] R. Sweke, M. S. Kesselring, E. P. L. van Nieuwenburg and J. Eisert, *Reinforcement learning decoders for fault-tolerant quantum computation*, Mach. Learn.: Sci. Technol. **2**(2), 025005 (2021), doi:10.1088/2632-2153/abc609.

[323] D. Gottesman, *An introduction to quantum error correction and fault-tolerant quantum computation* (2009), arXiv:0904.2557.

[324] D. Fitzek, M. Eliasson, A. F. Kockum and M. Granath, *Deep Q-learning decoder for depolarizing noise on the toric code*, Phys. Rev. Res. **2**, 023230 (2020), doi:10.1103/PhysRevResearch.2.023230.

[325] H. Théveniaut and E. van Nieuwenburg, *A NEAT Quantum Error Decoder*, SciPost Phys. **11**, 5 (2021), doi:10.21468/SciPostPhys.11.1.005.

[326] A. Peres, *Separability criterion for density matrices*, Phys. Rev. Lett. **77**(8), 1413 (1996), doi:10.1103/PhysRevLett.77.1413.

[327] B. Requena, G. Muñoz-Gil, M. Lewenstein, V. Dunjko and J. Tura, *Certificates of quantum many-body properties assisted by machine learning* (2021), arXiv:2103.03830.

[328] D. Silver, G. Lever, N. Heess, T. Degris, D. Wierstra and M. Riedmiller, *Deterministic policy gradient algorithms*, In *ICML 2014 - Int. Conf. Mach. Learn.*, doi:10.5555/3044805.3044850 (2014).

[329] S. Levine, *Reinforcement learning and control as probabilistic inference: Tutorial and review* (2018), arXiv:1805.00909.

[330] T. Haarnoja, A. Zhou, P. Abbeel and S. Levine, *Soft actor-critic: Off-policy maximum entropy deep reinforcement learning with a stochastic actor*, In *ICML 2018 - Int. Conf. Mach. Learn.*, pp. 1861–1870 (2018), arXiv:1801.01290.

[331] A. Abdolmaleki, J. T. Springenberg, Y. Tassa, R. Munos, N. Heess and M. Riedmiller, *Maximum a posteriori policy optimisation* (2018), arXiv:1806.06920.

[332] J. Degrave, F. Felici, J. Buchli, M. Neunert, B. Tracey, F. Carpanese, T. Ewalds, R. Hafner, A. Abdolmaleki, D. de las Casas, C. Donner, L. Fritz *et al.*, *Magnetic control of tokamak plasmas through deep reinforcement learning*, Nature **602**(7897), 414 (2022), doi:10.1038/s41586-021-04301-9.

[333] A. Karpathy, *Software 2.0*, Medium, Accessed: 2022-04-08 (2017).

[334] M. Innes, A. Edelman, K. Fischer, C. Rackauckas, E. Saba, V. B. Shah and W. Tebbutt, *A differentiable programming system to bridge machine learning and scientific computing* (2019), arXiv:1907.07587.

[335] S. G. Johnson, *Notes on adjoint methods for 18.335*, Introduction to Numerical Methods (2012).

[336] R. T. Chen, Y. Rubanova, J. Bettencourt and D. K. Duvenaud, *Neural ordinary differential equations*, In *NeurIPS 2018 - Adv. Neural. Inf. Process. Syst.* (2018), arXiv:1806.07366.

[337] H.-J. Liao, J.-G. Liu, L. Wang and T. Xiang, *Differentiable programming tensor networks*, Phys. Rev. X **9**(3), 031041 (2019), doi:10.1103/PhysRevX.9.031041.

[338] B.-B. Chen, Y. Gao, Y.-B. Guo, Y. Liu, H.-H. Zhao, H.-J. Liao, L. Wang, T. Xiang, W. Li and Z. Y. Xie, *Automatic differentiation for second renormalization of tensor networks*, Phys. Rev. B **101**, 220409 (2020), doi:10.1103/PhysRevB.101.220409.

[339] G. Torlai, J. Carrasquilla, M. T. Fishman, R. G. Melko and M. P. A. Fisher, *Wavefunction positivization via automatic differentiation*, Phys. Rev. Res. **2**, 032060 (2020), doi:10.1103/PhysRevResearch.2.032060.

[340] J. Ingraham, A. Riesselman, C. Sander and D. Marks, *Learning protein structure with a differentiable simulator*, In *ICLR 2018 - Int. Conf. Learn. Represent.* (2018).

[341] S. S. Schoenholz and E. D. Cubuk, *JAX, M.D.: A framework for differentiable physics*, In *NeurIPS 2020 - Adv. Neural Inf. Process. Syst.*, vol. 33 (2020), arXiv:1912.04232.

[342] T. Tamayo-Mendoza, C. Kreisbeck, R. Lindh and A. Aspuru-Guzik, *Automatic differentiation in quantum chemistry with applications to fully variational hartree–fock*, ACS Cent. Sci. **4**(5), 559 (2018), doi:10.1021/acscentsci.7b00586.

[343] L. Zhao and E. Neuscamman, *Excited state mean-field theory without automatic differentiation*, J. Chem. Phys. **152**(20), 204112 (2020), doi:10.1063/5.0003438.

[344] L. Li, S. Hoyer, R. Pederson, R. Sun, E. D. Cubuk, P. Riley, K. Burke *et al.*, *Kohn-sham equations as regularizer: Building prior knowledge into machine-learned physics*, Phys. Rev. Lett. **126**(3), 036401 (2021), doi:10.1103/PhysRevLett.126.036401.

[345] M. F. Kasim and S. M. Vinko, *Learning the exchange-correlation functional from nature with fully differentiable density functional theory*, Phys. Rev. Lett. **127**, 126403 (2021), doi:10.1103/PhysRevLett.127.126403.

[346] A. S. Abbott, B. Z. Abbott, J. M. Turney and H. F. Schaefer, *Arbitrary-order derivatives of quantum chemical methods via automatic differentiation*, J. Phys. Chem. Lett. **12**(12), 3232 (2021), doi:10.1021/acs.jpclett.1c00607, PMID: 33764068.

[347] M. F. Kasim, S. Lehtola and S. M. Vinko, *DQC: a Python program package for differentiable quantum chemistry* (2021), arXiv:2110.11678.

[348] V. Bergholm, J. Izaac, M. Schuld, C. Gogolin, M. S. Alam, S. Ahmed, J. M. Arrazola, C. Blank, A. Delgado, S. Jahangiri, K. McKiernan, J. J. Meyer *et al.*, *PennyLane: Automatic differentiation of hybrid quantum-classical computations* (2020), arXiv:1811.04968.

[349] N. Khaneja, T. Reiss, C. Kehlet, T. Schulte-Herbrüggen and S. J. Glaser, *Optimal control of coupled spin dynamics: design of NMR pulse sequences by gradient ascent algorithms*, J. Magn. Reson. **172**(2), 296 (2005), doi:10.1016/j.jmr.2004.11.004.

[350] N. Leung, M. Abdelhafez, J. Koch and D. Schuster, *Speedup for quantum optimal control from automatic differentiation based on graphics processing units*, Phys. Rev. A **95**(4) (2017), doi:10.1103/PhysRevA.95.042318.

[351] M. Abdelhafez, D. I. Schuster and J. Koch, *Gradient-based optimal control of open quantum systems using quantum trajectories and automatic differentiation*, Phys. Rev. A **99**, 052327 (2019), doi:10.1103/PhysRevA.99.052327.

[352] H. Jirari, *Optimal population inversion of a single dissipative two-level system*, Eur. Phys. J. B **92**(12), 265 (2019), doi:10.1140/epjb/e2019-100378-x.

[353] H. Jirari, *Time-optimal bang-bang control for the driven spin-boson system*, Phys. Rev. A **102**, 012613 (2020), doi:10.1103/PhysRevA.102.012613.

[354] F. Schäfer, M. Kloc, C. Bruder and N. Lörch, *A differentiable programming method for quantum control*, Mach. Learn.: Sci. Technol. **1**(3), 035009 (2020), doi:10.1088/2632-2153/ab9802.

[355] R. A. Vargas-Hernández, R. T. Q. Chen, K. A. Jung and P. Brumer, *Inverse design of dissipative quantum steady-states with implicit differentiation* (2020), arXiv:2011.12808.

[356] R. A. Vargas-Hernández, R. T. Q. Chen, K. A. Jung and P. Brumer, *Fully differentiable optimization protocols for non-equilibrium steady states*, New J. Phys. **23**(12), 123006 (2021), doi:10.1088/1367-2630/ac395e.

[357] I. Khait, J. Carrasquilla and D. Segal, *Optimal control of quantum thermal machines using machine learning*, Physical Review Research **4**(1) (2022), doi:10.1103/physrevresearch.4.l012029.

[358] L. Coopmans, D. Luo, G. Kells, B. K. Clark and J. Carrasquilla, *Protocol discovery for the quantum control of majoranas by differentiable programming and natural evolution strategies*, PRX Quantum **2**(2), 020332 (2021), doi:10.1103/PRXQuantum.2.020332.

[359] F. Schäfer, P. Sekatski, M. Koppenhöfer, C. Bruder and M. Kloc, *Control of stochastic quantum dynamics by differentiable programming*, Mach. Learn.: Sci. Technol. **2**(3), 035004 (2021), doi:10.1088/2632-2153/abec22.

[360] X.-Z. Luo, J.-G. Liu, P. Zhang and L. Wang, *Yao. jl: Extensible, efficient framework for quantum algorithm design*, Quantum **4**, 341 (2020), doi:10.22331/q-2020-10-11-341.

[361] O. Kyriienko, A. E. Paine and V. E. Elfving, *Solving nonlinear differential equations with differentiable quantum circuits*, Phys. Rev. A **103**(5), 052416 (2021), doi:10.1103/PhysRevA.103.052416.

[362] P. Huembeli and A. Dauphin, *Characterizing the loss landscape of variational quantum circuits*, Quantum Sci. Technol. **6**(2), 025011 (2021), doi:10.1088/2058-9565/abdbc9.

[363] A. G. Baydin, B. A. Pearlmutter, A. A. Radul and J. M. Siskind, *Automatic differentiation in machine learning: a survey*, J. Mach. Learn. Res. **18**(1), 5595–5637 (2018), doi:10.5555/3122009.3242010.

[364] R. E. Wengert, *A simple automatic derivative evaluation program*, Commun. ACM **7**(8), 463 (1964), doi:10.1145/355586.364791.

[365] A. Griewank and A. Walther, *Evaluating Derivatives: Principles and Techniques of Algorithmic Differentiation*, Society for Industrial and Applied Mathematics, ISBN 9780898716597, doi:10.5555/1455489 (2008).

[366] S. Linnainmaa, *The representation of the cumulative rounding error of an algorithm as a taylor expansion of the local rounding errors*, Master's Thesis (in Finnish), Univ. Helsinki pp. 6–7 (1970).

[367] A. Griewank, *Who invented the reverse mode of differentiation*, Documenta Math., Accessed: 2022-04-01 (2012).

[368] C. Rackauckas, *Parallel computing and scientific machine learning*, 18.337J/6.338J Lecture notes, MIT Lecture (2020).

[369] Y. Ma, V. Dixit, M. Innes, X. Guo and C. Rackauckas, *A comparison of automatic differentiation and continuous sensitivity analysis for derivatives of differential equation solutions* (2021), arXiv:1812.01892.

[370] L. Wang, *Implementation of an inverse Schrödinger problem in JAX*, Available as Google Colab Notebook: https://colab.research.google.com/drive/1e1NFA-E1Th7nN_9-DzQjAaglH6bwZtVU?usp=sharing (2021).

[371] H. Xie, J.-G. Liu and L. Wang, *Automatic differentiation of dominant eigensolver and its applications in quantum physics*, Phys. Rev. B **101**, 245139 (2020), doi:10.1103/PhysRevB.101.245139.

[372] L. Wang, *Implementation of a quantum optimal control problem in JAX*, Accessed: 2022-03-11. Available as Google Colab Notebook (2021).

[373] Q. Wang, R. Hu and P. Blonigan, *Least squares shadowing sensitivity analysis of chaotic limit cycle oscillations*, J. Comput. Phys **267**, 210 (2014), doi:10.1016/j.jcp.2014.03.002.

[374] L. Metz, C. D. Freeman, S. S. Schoenholz and T. Kachman, *Gradients are not all you need* (2021), arXiv:2111.05803.

[375] W. S. Moses and V. Churavy, *Instead of rewriting foreign code for machine learning, automatically synthesize fast gradients* (2020), arXiv:2010.01709.

[376] J.-G. Liu and T. Zhao, *Differentiate everything with a reversible embeded domain-specific language* (2020), arXiv:2003.04617.

[377] B. Silverman, *Density Estimation for Statistics and Data Analysis*, Chapman & Hall/CRC Monographs on Statistics & Applied Probability. Taylor & Francis, ISBN 9781315140919, doi:10.1201/9781315140919 (1998).

[378] Z. Hradil, *Quantum-state estimation*, Phys. Rev. A **55**, R1561 (1997), doi:10.1103/PhysRevA.55.R1561.

[379] M. Paris and J. Rehacek, *Quantum State Estimation*, Lecture Notes in Physics. Springer-Verlag Berlin/Heidelberg, ISBN 9783642061035, doi:10.1007/b98673 (2004).

[380] Y. S. Teo, *Introduction to quantum-state estimation*, World Scientific, ISBN 9789814678865, doi:10.1142/9617 (2015).

[381] G. Kanwar, M. S. Albergo, D. Boyda, K. Cranmer, D. C. Hackett, S. Racaniere, D. J. Rezende and P. E. Shanahan, *Equivariant flow-based sampling for lattice gauge theory*, Phys. Rev. Lett. **125**(12), 121601 (2020), doi:10.1103/PhysRevLett.125.121601.

[382] K. A. Nicoli, C. J. Anders, L. Funcke, T. Hartung, K. Jansen, P. Kessel, S. Nakajima and P. Stornati, *Estimation of thermodynamic observables in lattice field theories with deep generative models*, Phys. Rev. Lett. **126**(3), 032001 (2021), doi:10.1103/PhysRevLett.126.032001.

[383] D. C. Hackett, C.-C. Hsieh, M. S. Albergo, D. Boyda, J.-W. Chen, K.-F. Chen, K. Cranmer, G. Kanwar and P. E. Shanahan, *Flow-based sampling for multimodal distributions in lattice field theory* (2021), arXiv:2107.00734.

[384] K. A. Nicoli, C. Anders, L. Funcke, T. Hartung, K. Jansen, P. Kessel, S. Nakajima and P. Stornati, *Machine learning of thermodynamic observables in the presence of mode collapse* (2021), arXiv:2111.11303.

[385] I. Kobyzev, S. Prince and M. Brubaker, *Normalizing flows: An introduction and review of current methods*, IEEE Trans. Pattern Anal. Mach. Intell. **11**, 3964–3979 (2021), doi:10.1109/TPAMI.2020.2992934.

[386] A. Van den Oord, N. Kalchbrenner, L. Espeholt, O. Vinyals, A. Graves *et al.*, *Conditional image generation with PixelCNN decoders*, Advances in neural information processing systems **29** (2016), arXiv:1606.05328.

[387] D. P. Kingma and M. Welling, *An introduction to variational autoencoders*, Foundations and Trends® in Machine Learning **12**(4), 307 (2019), doi:10.1561/2200000056.

[388] A. Creswell, T. White, V. Dumoulin, K. Arulkumaran, B. Sengupta and A. A. Bharath, *Generative adversarial networks: An overview*, IEEE Signal Processing Magazine **35**(1), 53 (2018), doi:10.1109/MSP.2017.2765202.

[389] I. Goodfellow, J. Pouget-Abadie, M. Mirza, B. Xu, D. Warde-Farley, S. Ozair, A. Courville and Y. Bengio, *Generative adversarial nets*, Advances in neural information processing systems **27** (2014), arXiv:1406.2661.

[390] J. M. Pawlowski and J. M. Urban, *Reducing autocorrelation times in lattice simulations with generative adversarial networks*, Mach. Learn.: Sci. Technol. **1**(4), 045011 (2020), doi:10.1088/2632-2153/abae73.

[391] R. G. Melko, G. Carleo, J. Carrasquilla and J. I. Cirac, *Restricted Boltzmann machines in quantum physics*, Nat. Phys. **15**(9), 887 (2019), doi:10.1038/s41567-019-0545-1.

[392] M. S. Albergo, G. Kanwar and P. E. Shanahan, *Flow-based generative models for Markov chain Monte Carlo in lattice field theory*, Phys. Rev. D **100**, 034515 (2019), doi:10.1103/PhysRevD.100.034515.

[393] P. Ramachandran, T. L. Paine, P. Khorrami, M. Babaeizadeh, S. Chang, Y. Zhang, M. A. Hasegawa-Johnson, R. H. Campbell and T. S. Huang, *Fast generation for convolutional autoregressive models* (2017), arXiv:1704.06001.

[394] G. Papamakarios, E. Nalisnick, D. J. Rezende, S. Mohamed and B. Lakshminarayanan, *Normalizing flows for probabilistic modeling and inference* (2019), arXiv:1912.02762.

[395] U. Wolff, A. Collaboration *et al.*, *Monte Carlo errors with less errors*, Comput. Phys. Commun. **156**(2), 143 (2004), doi:10.1016/S0010-4655(03)00467-3.

[396] P. Białas, P. Korcyl and T. Stebel, *Analysis of autocorrelation times in neural Markov Chain Monte Carlo simulations* (2021), arXiv:2111.10189.

[397] J. Köhler, L. Klein and F. Noé, *Equivariant flows: exact likelihood generative learning for symmetric densities*, In *ICML 2020 - Int. Conf. Mach. Learn.*, pp. 5361–5370. PMLR (2020), arXiv:2006.02425.

[398] V. G. Satorras, E. Hoogeboom, F. B. Fuchs, I. Posner and M. Welling, *E(n) equivariant normalizing flows* (2021), arXiv:2105.09016.

[399] L. Wang, *Generative models for physicists*, Tech. rep., Institute of Physics, Chinese Academy of Sciences, GitHub.io (2018).

[400] F. Noé, S. Olsson, J. Köhler and H. Wu, *Boltzmann generators: Sampling equilibrium states of many-body systems with deep learning*, Science **365**(6457), eaaw1147 (2019), doi:10.1126/science.aaw1147.

[401] M. S. Albergo, G. Kanwar, S. Racanière, D. J. Rezende, J. M. Urban, D. Boyda, K. Cranmer, D. C. Hackett and P. E. Shanahan, *Flow-based sampling for fermionic lattice field theories*, Phys. Rev. D **104**, 114507 (2021), doi:10.1103/PhysRevD.104.114507.

[402] B. S. Rem, N. Käming, M. Tarnowski, L. Asteria, N. Fläschner, C. Becker, K. Sengstock and C. Weitenberg, *Identifying quantum phase transitions using artificial neural networks on experimental data*, Nat. Phys. **15**, 917 (2019), doi:10.1038/s41567-019-0554-0.

[403] E. Lustig, O. Yair, R. Talmon and M. Segev, *Identifying topological phase transitions in experiments using manifold learning*, Phys. Rev. Lett. **125**(12), 127401 (2020), doi:10.1103/PhysRevLett.125.127401.

[404] E. Greplova, C. Gold, B. Kratochwil, T. Davatz, R. Pisoni, A. Kurzmann, P. Rickhaus, M. H. Fischer, T. Ihn and S. D. Huber, *Fully automated identification of two-dimensional material samples*, Phys. Rev. Appl. **13**(6), 064017 (2020), doi:10.1103/PhysRevApplied.13.064017.

[405] R. Durrer, B. Kratochwil, J. V. Koski, A. J. Landig, C. Reichl, W. Wegscheider, T. Ihn and E. Greplova, *Automated tuning of double quantum dots into specific charge states using neural networks*, Phys. Rev. Appl. **13**(5), 054019 (2020), doi:10.1103/PhysRevApplied.13.054019.

[406] E. Greplova and S. Huber group, GitHub repository to "Fully automated search for 2D material samples" (2019).

[407] A. U. Lode, R. Lin, M. Büttner, L. Papariello, C. Lévêque, R. Chitra, M. C. Tsatsos, D. Jaksch and P. Molignini, *Optimized observable readout from single-shot images of ultracold atoms via machine learning*, Phys. Rev. A **104**(4), L041301 (2021), doi:10.1103/PhysRevA.104.L041301.

[408] R. Lin, C. Georges, J. Klinder, P. Molignini, M. Büttner, A. U. Lode, R. Chitra, A. Hemmerich and H. Keßler, *Mott transition in a cavity-boson system: A quantitative comparison between theory and experiment*, SciPost Phys. **11**(2), 030 (2021), doi:10.21468/SciPostPhys.11.2.030.

[409] R. Lin, P. Molignini, L. Papariello, M. C. Tsatsos, C. Lévêque, S. E. Weiner, E. Fasshauer, R. Chitra and A. U. Lode, *MCTDH-X: The multiconfigurational time-dependent Hartree method for indistinguishable particles software*, Quantum Sci. Technol. **5**(2), 024004 (2020), doi:10.1088/2058-9565/ab788b.

[410] J. Zhang, G. Pagano, P. W. Hess, A. Kyprianidis, P. Becker, H. Kaplan, A. V. Gorshkov, Z.-X. Gong and C. Monroe, *Observation of a many-body dynamical phase transition with a 53-qubit quantum simulator*, Nature **551**(7682), 601 (2017), doi:10.1038/nature24654.

[411] H. Bernien, S. Schwartz, A. Keesling, H. Levine, A. Omran, H. Pichler, S. Choi, A. S. Zibrov, M. Endres, M. Greiner *et al.*, *Probing many-body dynamics on a 51-atom quantum simulator*, Nature **551**(7682), 579 (2017), doi:10.1038/nature24622.

[412] B. Chiaro, C. Neill, A. Bohrdt, M. Filippone, F. Arute, K. Arya, R. Babbush, D. Bacon, J. Bardin, R. Barends *et al.*, *Direct measurement of non-local interactions in the many-body localized phase* (2019), arXiv:1910.06024.

[413] M. Rispoli, A. Lukin, R. Schittko, S. Kim, M. E. Tai, J. Léonard and M. Greiner, *Quantum critical behaviour at the many-body localization transition*, Nature **573**(7774), 385 (2019), doi:10.1038/s41586-019-1527-2.

[414] A. Valenti, G. Jin, J. Léonard, S. D. Huber and E. Greplova, *Scalable Hamiltonian learning for large-scale out-of-equilibrium quantum dynamics*, Phys. Rev. A **105**, 023302 (2022), doi:10.1103/PhysRevA.105.023302.

[415] A. Gresch, L. Bittel and M. Kliesch, *Scalable approach to many-body localization via quantum data* (2022), arXiv:2202.08853.

[416] A. A. Gentile, B. Flynn, S. Knauer, N. Wiebe, S. Paesani, C. E. Granade, J. G. Rarity, R. Santagati and A. Laing, *Learning models of quantum systems from experiments*, Nat. Phys. **17**(7), 837 (2021), doi:10.1038/s41567-021-01201-7.

[417] T. E. O'Brien, L. B. Ioffe, Y. Su, D. Fushman, H. Neven, R. Babbush and V. Smelyanskiy, *Quantum computation of molecular structure using data from challenging-to-classically-simulate nuclear magnetic resonance experiments* (2021), arXiv:2109.02163.

[418] N. M. van Esbroeck, D. T. Lennon, H. Moon, V. Nguyen, F. Vigneau, L. C. Camenzind, L. Yu, D. M. Zumbühl, G. A. D. Briggs, D. Sejdinovic and N. Ares, *Quantum device fine-tuning using unsupervised embedding learning*, New J. Phys. **22**(9), 095003 (2020), doi:10.1088/1367-2630/abb64c.

[419] B. Severin, D. T. Lennon, L. C. Camenzind, F. Vigneau, F. Fedele, D. Jirovec, A. Ballabio, D. Chrastina, G. Isella, M. de Kruijf, M. J. Carballido, S. Svab *et al.*, *Cross-architecture tuning of silicon and SiGe-based quantum devices using machine learning* (2021), arXiv:2107.12975.

[420] J. P. Zwolak, T. McJunkin, S. S. Kalantre, S. F. Neyens, E. MacQuarrie, M. A. Eriksson and J. M. Taylor, *Ray-based framework for state identification in quantum dot devices*, PRX Quantum **2**, 020335 (2021), doi:10.1103/PRXQuantum.2.020335.

[421] A. Cervera-Lierta, M. Krenn and A. Aspuru-Guzik, *Design of quantum optical experiments with logic artificial intelligence* (2021), arXiv:2109.13273.

[422] D. Flam-Shepherd, T. Wu, X. Gu, A. Cervera-Lierta, M. Krenn and A. Aspuru-Guzik, *Learning interpretable representations of entanglement in quantum optics experiments using deep generative models* (2021), arXiv:2109.02490.

[423] R. D. King, J. Rowland, S. G. Oliver, M. Young, W. Aubrey, E. Byrne, M. Liakata, M. Markham, P. Pir, L. N. Soldatova, A. Sparkes, K. E. Whelan *et al.*, *The automation of science*, Science **324**(5923), 85 (2009), doi:10.1126/science.1165620.

[424] N. Wiebe, A. Kapoor and K. M. Svore, *Quantum algorithms for nearest-neighbor methods for supervised and unsupervised learning*, Quantum Inf. Comput. **15**(3–4), 316–356 (2015).

[425] P. Raccuglia, K. C. Elbert, P. D. F. Adler, C. Falk, M. B. Wenny, A. Mollo, M. Zeller, S. A. Friedler, J. Schrier and A. J. Norquist, *Machine-learning-assisted materials discovery using failed experiments*, Nature **533**(7601), 73 (2016), doi:10.1038/nature17439.

[426] F. Häse, L. M. Roch and A. Aspuru-Guzik, *Next-generation experimentation with self-driving laboratories*, Trends Chem. **1**(3), 282 (2019), doi:10.1016/j.trechm.2019.02.007.

[427] L. Zdeborová, *Understanding deep learning is also a job for physicists*, Nat. Phys. **16**(6), 602 (2020), doi:10.1038/s41567-020-0929-2.

[428] M. Belkin, D. Hsu, S. Ma and S. Mandal, *Reconciling modern machine-learning practice and the classical bias–variance tradeoff*, PNAS **116**(32), 15849 (2019), doi:10.1073/pnas.1903070116, arXiv:https://www.pnas.org/content/116/32/15849.full.pdf.

[429] T. M. Cover, *Geometrical and statistical properties of systems of linear inequalities with applications in pattern recognition*, IEEE Trans. Comput. **EC-14**(3), 326 (1965), doi:10.1109/PGEC.1965.264137.

[430] E. Gardner, *Maximum storage capacity in neural networks*, EPL **4**(4), 481 (1987), doi:10.1209/0295-5075/4/4/016.

[431] D. J. Amit, H. Gutfreund and H. Sompolinsky, *Storing infinite numbers of patterns in a spin-glass model of neural networks*, Phys. Rev. Lett. **55**(14), 1530 (1985), doi:10.1103/PhysRevLett.55.1530.

[432] B. Derrida, E. Gardner and A. Zippelius, *An exactly solvable asymmetric neural network model*, EPL **4**(2), 167 (1987), doi:10.1209/0295-5075/4/2/007.

[433] B. Derrida and J. P. Nadal, *Learning and forgetting on asymmetric, diluted neural networks*, J. Stat. Phys. **49**(5-6), 993 (1987), doi:10.1007/BF01017556.

[434] C. Peterson, *A mean field theory learning algorithm for neural networks*, Complex Syst. **1**, 995 (1987).

[435] W. Krauth and M. Mézard, *Storage capacity of memory networks with binary couplings*, J. Phys. **50**(20), 3057 (1989), doi:10.1051/jphys:0198900500200305700.

[436] G. Györgyi, *First-order transition to perfect generalization in a neural network with binary synapses*, Phys. Rev. A **41**(12), 7097 (1990), doi:10.1103/PhysRevA.41.7097.

[437] M. Opper and D. Haussler, *Generalization performance of Bayes optimal classification algorithm for learning a perceptron*, Phys. Rev. Lett. **66**(20), 2677 (1991), doi:10.1103/PhysRevLett.66.2677.

[438] D. Sherrington and S. Kirkpatrick, *Solvable model of a spin-glass*, Phys. Rev. Lett. **35**(26), 1792 (1975), doi:10.1103/PhysRevLett.35.1792.

[439] M. Mézard, G. Parisi and M. A. Virasoro, *SK model: The replica solution without replicas*, EPL **1**(2), 77 (1986), doi:10.1209/0295-5075/1/2/006.

[440] F. Barahona, *On the computational complexity of Ising spin glass models*, J. Phys. A: Math. Gen. **15**, 3241 (1982), doi:10.1088/0305-4470/15/10/028.

[441] C. Fan, M. Shen, Z. Nussinov, Z. Liu, Y. Sun and Y.-Y. Liu, *Finding spin glass ground states through deep reinforcement learning* (2021), arXiv:2109.14411.

[442] S. F. Edwards and P. W. Anderson, *Theory of spin glasses*, J. Phys. F: Met. Phys. **5**, 965 (1975), doi:10.1088/0305-4608/5/5/017.

[443] D. J. Thouless, P. W. Anderson and R. G. Palmer, *Solution of 'Solvable model of a spin glass'*, Philos. Mag. **35**(3), 593 (1977), doi:10.1080/14786437708235992.

[444] M. Talagrand, *The Parisi formula*, Ann. Math. **163**(1), 221 (2006), doi:10.4007/annals.2006.163.221.

[445] D. Panchenko, *Introduction to the SK model*, Current Developments in Mathematics **2014**(1), 231 (2014), doi:10.4310/cdm.2014.v2014.n1.a4.

[446] T. Castellani and A. Cavagna, *Spin-glass theory for pedestrians*, J. Stat. Mech. p. P05012 (2005), doi:10.1088/1742-5468/2005/05/P05012.

[447] M. Gabrié, *Mean-field inference methods for neural networks*, J. Phys. A: Math. Theor. **53**(22), 223002 (2020), doi:10.1088/1751-8121/ab7f65, arXiv:1911.00890.

[448] J. Barbier, F. Krzakala, N. Macris, L. Miolane and L. Zdeborová, *Optimal errors and phase transitions in high-dimensional generalized linear models*, Proc. Natl. Acad. Sci. U.S.A. **116**(12), 5451 (2019), doi:10.1073/pnas.1802705116, arXiv:1708.03395.

[449] S. Rangan, *Generalized approximate message passing for estimation with random linear mixing*, In *2011 IEEE International Symposium on Information Theory Proceedings*. IEEE, doi:10.1109/isit.2011.6033942 (2011).

[450] L. Zdeborová and F. Krzakala, *Statistical physics of inference: thresholds and algorithms*, Adv. Phys. **65**(5), 453 (2016), doi:10.1080/00018732.2016.1211393.

[451] R. Monasson and R. Zecchina, *Learning and generalization theories of large committee machines*, Mod. Phys. Lett. B **09**(30), 1887 (1995), doi:10.1142/s0217984995001868.

[452] B. Aubin, A. Maillard, J. Barbier, F. Krzakala, N. Macris and L. Zdeborová, *The committee machine: computational to statistical gaps in learning a two-layers neural network*, J. Stat. Mech. Theor. Exp. **2019**(12), 124023 (2019), doi:10.1088/1742-5468/ab43d2.

[453] A. Rahimi and B. Recht, *Random features for large-scale kernel machines*, In *NIPS 2007 - Adv. Neural. Inf. Process. Syst.*, vol. 20, doi:10.5555/2981562.2981710 (2007).

[454] A. Rahimi and B. Recht, *Weighted sums of random kitchen sinks: replacing minimization with randomization in learning*, In *NIPS 2008 - Adv. Neural. Inf. Process. Syst.*, vol. 21, doi:10.5555/2981780.2981944 (2008).

[455] H. Schwarze and J. Hertz, *Generalization in fully connected committee machines*, EPL **21**(7), 786 (1993), doi:10.1209/0295-5075/21/7/012.

[456] H. Schwarze, *Learning a rule in a multilayer neural network*, J. Phys. A: Math. Gen. **26**(21), 5781 (1993), doi:10.1088/0305-4470/26/21/017.

[457] F. Gerace, B. Loureiro, F. Krzakala, M. Mézard and L. Zdeborová, *Generalisation error in learning with random features and the hidden manifold model*, J. Stat. Mech. **2021**(12), 124013 (2021), doi:10.1088/1742-5468/ac3ae6.

[458] S. D'Ascoli, M. Gabrié, L. Sagun and G. Biroli, *More data or more parameters? Investigating the effect of data structure on generalization*, In *NeurIPS 2021 - Adv. Neural Process. Syst.* (2021), arXiv:2103.05524.

[459] S. Goldt, M. S. Advani, A. M. Saxe, F. Krzakala and L. Zdeborová, *Dynamics of stochastic gradient descent for two-layer neural networks in the teacher-student setup*, J. Stat. Mech. Theor. Exp. **2020**(12), 1 (2020), doi:10.1088/1742-5468/abc61e.

[460] M. Biehl and P. Riegler, *On-line learning with a perceptron*, EPL **28**(7), 525 (1994), doi:10.1209/0295-5075/28/7/012.

[461] M. Biehl and H. Schwarze, *Learning by on-line gradient descent*, J. Phys. A: Math. Gen. **28**(3), 643 (1995), doi:10.1088/0305-4470/28/3/018.

[462] S. Goldt, B. Loureiro, G. Reeves, F. Krzakala, M. Mézard and L. Zdeborová, *The Gaussian equivalence of generative models for learning with shallow neural networks* (2020), arXiv:2006.14709.

[463] F. Mignacco, F. Krzakala, P. Urbani and L. Zdeborová, *Dynamical mean-field theory for stochastic gradient descent in Gaussian mixture classification*, In *NeurIPS 2020 - Conf. Neural. Inf. Process. Syst.* (2020), arXiv:2006.06098.

[464] M. Lewenstein, *Quantum perceptrons*, J. Mod. Opt. **41**(12), 2491 (1994), doi:10.1080/09500349414552331.

[465] A. Gratsea, V. Kasper and M. Lewenstein, *Storage properties of a quantum perceptron* (2021), arXiv:2111.08414.

[466] M. Lewenstein, A. Gratsea, A. Riera-Campeny, A. Aloy, V. Kasper and A. Sanpera, *Storage capacity and learning capability of quantum neural networks* (2020), arXiv:2011.06113.

[467] A. Gratsea and P. Huembeli, *Exploring quantum perceptron and quantum neural network structures with a teacher-student scheme* (2021), arXiv:2105.01477.

[468] Y. Feng and Y. Tu, *Phases of learning dynamics in artificial neural networks in the absence or presence of mislabeled data*, Mach. Learn.: Sci. Technol. **2**(4), 043001 (2021), doi:10.1088/2632-2153/abf5b9.

[469] A. Decelle, C. Furtlehner and B. Seoane, *Equilibrium and non-equilibrium regimes in the learning of restricted Boltzmann machines*, In *NeurIPS 2021 - Adv. Neural Process. Syst.* (2021), arXiv:2103.05524.

[470] H.-S. Zhong, H. Wang, Y.-H. Deng, M.-C. Chen, L.-C. Peng, Y.-H. Luo, J. Qin, D. Wu, X. Ding, Y. Hu *et al.*, *Quantum computational advantage using photons*, Science **370**(6523), 1460 (2020), doi:10.1126/science.abe8770.

[471] F. Arute, K. Arya, R. Babbush, D. Bacon, J. C. Bardin, R. Barends, R. Biswas, S. Boixo, F. G. Brandao, D. A. Buell *et al.*, *Quantum supremacy using a programmable superconducting processor*, Nature **574**(7779), 505 (2019), doi:10.1038/s41586-019-1666-5.

[472] C. D. Bruzewicz, J. Chiaverini, R. McConnell and J. M. Sage, *Trapped-ion quantum computing: Progress and challenges*, Appl. Phys. Rev. **6**(2), 021314 (2019), doi:10.1063/1.5088164, arXiv:https://doi.org/10.1063/1.5088164.

[473] M. Saffman, *Quantum computing with atomic qubits and Rydberg interactions: progress and challenges*, J. Phys. B: At. Mol. Opt. Phys. **49**(20), 202001 (2016), doi:10.1088/0953-4075/49/20/202001.

[474] L. Henriet, L. Beguin, A. Signoles, T. Lahaye, A. Browaeys, G.-O. Reymond and C. Jurczak, *Quantum computing with neutral atoms*, Quantum **4**, 327 (2020), doi:10.22331/q-2020-09-21-327.

[475] Y. Liu, S. Arunachalam and K. Temme, *A rigorous and robust quantum speed-up in supervised machine learning*, Nat. Phys. **17**(9), 1013 (2021), doi:10.1038/s41567-021-01287-z.

[476] J. Herrmann, S. Masot Llima, A. Remm, P. Zapletal, N. A. McMahon, C. Scarato, F. Swiadek, C. Kraglund Andersen, C. Hellings, S. Krinner, N. Lacroix, S. Lazar *et al.*, *Realizing quantum convolutional neural networks on a superconducting quantum processor to recognize quantum phases* (2021), arXiv:2109.05909.

[477] H.-Y. Huang, M. Broughton, J. Cotler, S. Chen, J. Li, M. Mohseni, H. Neven, R. Babbush, R. Kueng, J. Preskill and J. R. McClean, *Quantum advantage in learning from experiments* (2021), arXiv:2112.00778.

[478] M. Gong, H.-L. Huang, S. Wang, C. Guo, S. Li, Y. Wu, Q. Zhu, Y. Zhao, S. Guo, H. Qian, Y. Ye, C. Zha *et al.*, *Quantum neuronal sensing of quantum many-body states on a 61-qubit programmable superconducting processor* (2022), arXiv:2201.05957.

[479] L. Hales and S. Hallgren, *An improved quantum Fourier transform algorithm and applications*, In *FOCS 2000 - 41st Annu. IEEE Symp. Found. Comput. Sci.*, pp. 515–525, doi:10.1109/SFCS.2000.892139 (2000).

[480] P. Shor, *Algorithms for quantum computation: discrete logarithms and factoring*, In *FOCS 1994 - 35th Annu. IEEE Symp. Found. Comput. Sci.*, pp. 124–134, doi:10.1109/SFCS.1994.365700 (1994).

[481] A. Y. Kitaev, *Quantum measurements and the Abelian stabilizer problem* (1995), arXiv:quant-ph/9511026.

[482] A. W. Harrow, A. Hassidim and S. Lloyd, *Quantum algorithm for linear systems of equations*, Phys. Rev. Lett. **103**, 150502 (2009), doi:10.1103/PhysRevLett.103.150502.

[483] P. Rebentrost, M. Mohseni and S. Lloyd, *Quantum support vector machine for big data classification*, Phys. Rev. Lett. **113**, 130503 (2014), doi:10.1103/PhysRevLett.113.130503.

[484] Z. Li, X. Liu, N. Xu and J. Du, *Experimental realization of a quantum support vector machine*, Phys. Rev. Lett. **114**, 140504 (2015), doi:10.1103/PhysRevLett.114.140504.

[485] N. Wiebe, D. Braun and S. Lloyd, *Quantum algorithm for data fitting*, Phys. Rev. Lett. **109**, 050505 (2012), doi:10.1103/PhysRevLett.109.050505.

[486] A. Gilyén, S. Lloyd and E. Tang, *Quantum-inspired low-rank stochastic regression with logarithmic dependence on the dimension* (2018), arXiv:1811.04909.

[487] A. Ekert and R. Jozsa, *Quantum computation and Shor's factoring algorithm*, Rev. Mod. Phys. **68**, 733 (1996), doi:10.1103/RevModPhys.68.733.

[488] C. M. Dawson and M. A. Nielsen, *The Solovay-Kitaev algorithm* (2005), arXiv:quant-ph/0505030.

[489] J. Preskill, *Quantum computing in the NISQ era and beyond*, Quantum **2**, 79 (2018), doi:10.22331/q-2018-08-06-79.

[490] Y. Y. Atas, J. Zhang, R. Lewis, A. Jahanpour, J. F. Haase and C. A. Muschik, *SU(2) hadrons on a quantum computer via a variational approach*, Nat. Commun. **12**(1) (2021), doi:10.1038/s41467-021-26825-4.

[491] K. Temme, S. Bravyi and J. M. Gambetta, *Error mitigation for short-depth quantum circuits*, Phys. Rev. Lett. **119**, 180509 (2017), doi:10.1103/PhysRevLett.119.180509.

[492] S. Endo, S. C. Benjamin and Y. Li, *Practical quantum error mitigation for near-future applications*, Phys. Rev. X **8**(3) (2018), doi:10.1103/PhysRevX.8.031027.

[493] L. Funcke, T. Hartung, K. Jansen, S. Kühn, P. Stornati and X. Wang, *Measurement error mitigation in quantum computers through classical bit-flip correction* (2020), arXiv:2007.03663.

[494] A. D. Córcoles, E. Magesan, S. J. Srinivasan, A. W. Cross, M. Steffen, J. M. Gambetta and J. M. Chow, *Demonstration of a quantum error detection code using a square lattice of four superconducting qubits*, Nat. Commun. **6**(1), 6979 (2015), doi:10.1038/ncomms7979.

[495] V. Havlíček, A. D. Córcoles, K. Temme, A. W. Harrow, A. Kandala, J. M. Chow and J. M. Gambetta, *Supervised learning with quantum-enhanced feature spaces*, Nature **567**(7747), 209 (2019), doi:10.1038/s41586-019-0980-2.

[496] M. Schuld and N. Killoran, *Quantum machine learning in feature Hilbert spaces*, Phys. Rev. Lett. **122**, 040504 (2019), doi:10.1103/PhysRevLett.122.040504.

[497] J. Dai and R. V. Krems, *Quantum Gaussian process model of potential energy surface for a polyatomic molecule* (2022), arXiv:2202.10601.

[498] *Quantum feature maps and kernels*, chapter of the Qiskit textbook "Introduction to Quantum Computing", Accessed: 2022-03-02.

[499] E. Tang, *Quantum principal component analysis only achieves an exponential speedup because of its state preparation assumptions*, Phys. Rev. Lett. **127**(6), 060503 (2021), doi:10.1103/PhysRevLett.127.060503.

[500] J. M. Kübler, S. Buchholz and B. Schölkopf, *The inductive bias of quantum kernels* (2021), arXiv:2106.03747.

[501] A. Peruzzo, J. McClean, P. Shadbolt, M.-H. Yung, X.-Q. Zhou, P. J. Love, A. Aspuru-Guzik and J. L. O'Brien, *A variational eigenvalue solver on a photonic quantum processor*, Nat. Comm. **5**(1) (2014), doi:10.1038/ncomms5213.

[502] L. Funcke, T. Hartung, K. Jansen, S. Kühn and P. Stornati, *Dimensional expressivity analysis of parametric quantum circuits*, Quantum **5**, 422 (2021), doi:10.22331/q-2021-03-29-422.

[503] J. Li, X. Yang, X. Peng and C.-P. Sun, *Hybrid quantum-classical approach to quantum optimal control*, Phys. Rev. Lett. **118**, 150503 (2017), doi:10.1103/PhysRevLett.118.150503.

[504] A. Pérez-Salinas, A. Cervera-Lierta, E. Gil-Fuster and J. I. Latorre, *Data re-uploading for a universal quantum classifier*, Quantum **4**, 226 (2020), doi:10.22331/q-2020-02-06-226.

[505] I. Cong, S. Choi and M. D. Lukin, *Quantum convolutional neural networks*, Nat. Phys. **15**(12), 1273–1278 (2019), doi:10.1038/s41567-019-0648-8.

[506] M. Schuld, *Supervised quantum machine learning models are kernel methods* (2021), arXiv:2101.11020.

[507] S. Jerbi, L. J. Fiderer, H. P. Nautrup, J. M. Kübler, H. J. Briegel and V. Dunjko, *Quantum machine learning beyond kernel methods* (2021), arXiv:2110.13162.

[508] S. Jerbi, C. Gyurik, S. C. Marshall, H. J. Briegel and V. Dunjko, *Parametrized quantum policies for reinforcement learning* (2021), arXiv:2103.05577.

[509] A. Skolik, S. Jerbi and V. Dunjko, *Quantum agents in the Gym: a variational quantum algorithm for deep Q-learning* (2021), arXiv:2103.15084.

[510] G. Brockman, V. Cheung, L. Pettersson, J. Schneider, J. Schulman, J. Tang and W. Zaremba, *OpenAI Gym* (2016), arXiv:1606.01540.

[511] J. Romero, J. P. Olson and A. Aspuru-Guzik, *Quantum autoencoders for efficient compression of quantum data*, Quantum Sci. Technol. **2**(4), 045001 (2017), doi:10.1088/2058-9565/aa8072.

[512] D. Bondarenko and P. Feldmann, *Quantum autoencoders to denoise quantum data*, Phys. Rev. Lett. **124**(13) (2020), doi:10.1103/PhysRevLett.124.130502.

[513] D. F. Locher, L. Cardarelli and M. Müller, *Quantum error correction with quantum autoencoders* (2022), arXiv:2202.00555.

[514] G. Verdon, J. Marks, S. Nanda, S. Leichenauer and J. Hidary, *Quantum Hamiltonian-based models and the variational quantum thermalizer algorithm* (2019), arXiv:1910.02071.

[515] S. Lloyd and C. Weedbrook, *Quantum generative adversarial learning*, Phys. Rev. Lett. **121**, 040502 (2018), doi:10.1103/PhysRevLett.121.040502.

[516] P.-L. Dallaire-Demers and N. Killoran, *Quantum generative adversarial networks*, Phys. Rev. A **98**, 012324 (2018), doi:10.1103/PhysRevA.98.012324.

[517] J.-G. Liu and L. Wang, *Differentiable learning of quantum circuit Born machines*, Phys. Rev. A **98**, 062324 (2018), doi:10.1103/PhysRevA.98.062324.

[518] B. Coyle, D. Mills, V. Danos and E. Kashefi, *The Born supremacy: quantum advantage and training of an Ising Born machine*, npj Quantum Inf. **6**(1) (2020), doi:10.1038/s41534-020-00288-9.

[519] M. Benedetti, D. Garcia-Pintos, O. Perdomo, V. Leyton-Ortega, Y. Nam and A. Perdomo-Ortiz, *A generative modeling approach for benchmarking and training shallow quantum circuits*, npj Quantum Inf. **5**(1) (2019), doi:10.1038/s41534-019-0157-8.

[520] L. Viola and S. Lloyd, *Dynamical suppression of decoherence in two-state quantum systems*, Phys. Rev. A **58**, 2733 (1998), doi:10.1103/PhysRevA.58.2733.

[521] F. Kleißler, A. Lazariev and S. Arroyo-Camejo, *Universal, high-fidelity quantum gates based on superadiabatic, geometric phases on a solid-state spin-qubit at room temperature*, npj Quantum Inf. **4**(1) (2018), doi:10.1038/s41534-018-0098-7.

[522] M. Taherkhani, M. Willatzen, E. V. Denning, I. E. Protsenko and N. Gregersen, *High-fidelity optical quantum gates based on type-II double quantum dots in a nanowire*, Phys. Rev. B **99**, 165305 (2019), doi:10.1103/PhysRevB.99.165305.

[523] E. Zahedinejad, J. Ghosh and B. C. Sanders, *High-fidelity single-shot toffoli gate via quantum control*, Phys. Rev. Lett. **114**, 200502 (2015), doi:10.1103/PhysRevLett.114.200502.

[524] D. Yu, H. Wang, D. Ma, X. Zhao and J. Qian, *Adiabatic and high-fidelity quantum gates with hybrid Rydberg-Rydberg interactions*, Opt. Express **27**(16), 23080 (2019), doi:10.1364/OE.27.023080.

[525] F. Haddadfarshi and F. Mintert, *High fidelity quantum gates of trapped ions in the presence of motional heating*, New J. Phys. **18**(12), 123007 (2016), doi:10.1088/1367-2630/18/12/123007.

[526] S. Li, J. Xue, T. Chen and Z. Xue, *High-fidelity geometric quantum gates with short paths on superconducting circuits*, Adv. Quantum Technol. **4**(5), 2000140 (2021), doi:10.1002/qute.202000140.

[527] J. R. McClean, S. Boixo, V. N. Smelyanskiy, R. Babbush and H. Neven, *Barren plateaus in quantum neural network training landscapes*, Nat. Commun. **9**(1), 1 (2018), doi:10.1038/s41467-018-07090-4.

[528] M. Cerezo, A. Sone, T. Volkoff, L. Cincio and P. J. Coles, *Cost function dependent barren plateaus in shallow parametrized quantum circuits*, Nat. Commun. **12**(1), 1 (2021), doi:10.1038/s41467-021-21728-w.

[529] L. Bittel and M. Kliesch, *Training variational quantum algorithms is NP-hard*, Phys. Rev. Lett. **127**, 120502 (2021), doi:10.1103/PhysRevLett.127.120502.

[530] S. Sim, P. D. Johnson and A. Aspuru-Guzik, *Expressibility and entangling capability of parameterized quantum circuits for hybrid quantum-classical algorithms*, Adv. Quantum Technol. **2**(12), 1900070 (2019), doi:10.1002/qute.201900070.

[531] A. Y. Kitaev, *Quantum computations: algorithms and error correction*, Russ. Math. Surv. **52**(6), 1191 (1997), doi:10.1070/rm1997v052n06abeh002155.

[532] M. S. Rudolph, S. Sim, A. Raza, M. Stechly, J. R. McClean, E. R. Anschuetz, L. Serrano and A. Perdomo-Ortiz, *ORQVIZ: Visualizing high-dimensional landscapes in variational quantum algorithms* (2021), arXiv:2111.04695.

[533] J. Eisert, *Entangling power and quantum circuit complexity*, Phys. Rev. Lett. **127**, 020501 (2021), doi:10.1103/PhysRevLett.127.020501.

[534] H.-Y. Huang, R. Kueng and J. Preskill, *Information-theoretic bounds on quantum advantage in machine learning*, Phys. Rev. Lett. **126**, 190505 (2021), doi:10.1103/PhysRevLett.126.190505.

[535] K. Bharti, A. Cervera-Lierta, T. H. Kyaw, T. Haug, S. Alperin-Lea, A. Anand, M. Degroote, H. Heimonen, J. S. Kottmann, T. Menke *et al.*, *Noisy intermediate-scale quantum algorithms*, Rev. Mod. Phys. **94**(1), 015004 (2022), doi:10.1103/RevModPhys.94.015004.

[536] G. Munoz-Gil, G. Volpe, M. A. Garcia-March, E. Aghion, A. Argun, C. B. Hong, T. Bland, S. Bo, J. A. Conejero, N. Firbas, O. Garibo i Orts, A. Gentili *et al.*, *Objective comparison of methods to decode anomalous diffusion*, Nat. Commun. **12**(1), 6253 (2021), doi:10.1038/s41467-021-26320-w.

[537] Z. Liu and M. Tegmark, *Machine learning conservation laws from trajectories*, Phys. Rev. Lett. **126**, 180604 (2021), doi:10.1103/PhysRevLett.126.180604.

[538] G. Muñoz-Gil, M. A. Garcia-March, C. Manzo, J. D. Martín-Guerrero and M. Lewenstein, *Single trajectory characterization via machine learning*, New J. Phys. **22**(1), 013010 (2020), doi:10.1088/1367-2630/ab6065.

[539] G. Munoz-Gil, C. Romero-Aristizabal, N. Mateos, F. Campelo, L. I. de LLobet-Cucalon, M. Beato, M. Lewenstein, M. Garcia-Parajo and J. A. Torreno-Pina, *Particle flow modulates growth dynamics and nanoscale-arrested growth of transcription factor condensates in living cells*, bioRxiv (2022), doi:10.1101/2022.01.11.475940.

[540] H. B. Moss and R.-R. Griffiths, *Gaussian process molecule property prediction with FlowMO* (2020), arXiv:2010.01118.

[541] A. Glielmo, Y. Rath, G. Csányi, A. De Vita and G. H. Booth, *Gaussian process states: A data-driven representation of quantum many-body physics*, Phys. Rev. X **10**, 041026 (2020), doi:10.1103/PhysRevX.10.041026.

[542] K. Choo, T. Neupert and G. Carleo, *Two-dimensional frustrated $J_1 - J_2$ model studied with neural network quantum states*, Phys. Rev. B **100**(12) (2019), doi:10.1103/PhysRevB.100.125124.

[543] M. Secor, A. V. Soudackov and S. Hammes-Schiffer, *Artificial neural networks as propagators in quantum dynamics*, J. Phys. Chem. Lett. **12**(43), 10654 (2021), doi:10.1021/acs.jpclett.1c03117.

[544] V. Havlicek, *Amplitude ratios and neural network quantum states* (2022), arXiv:2201.09128.

[545] M. Bukov, A. G. R. Day, D. Sels, P. Weinberg, A. Polkovnikov and P. Mehta, *Reinforcement learning in different phases of quantum control*, Phys. Rev. X **8**, 031086 (2018), doi:10.1103/PhysRevX.8.031086.

[546] J. Yao, L. Lin and M. Bukov, *Reinforcement learning for many-body ground-state preparation inspired by counterdiabatic driving*, Phys. Rev. X **11**, 031070 (2021), doi:10.1103/PhysRevX.11.031070.

[547] F. Metz and M. Bukov, *Self-correcting quantum many-body control using reinforcement learning with tensor networks* (2022), arXiv:2201.11790.

[548] M. Y. Niu, S. Boixo, V. N. Smelyanskiy and H. Neven, *Universal quantum control through deep reinforcement learning*, npj Quantum Inf. **5**(33), 1 (2019), doi:10.1038/s41534-019-0141-3.

[549] H. P. Nautrup, N. Delfosse, V. Dunjko, H. J. Briegel and N. Friis, *Optimizing quantum error correction codes with reinforcement learning*, Quantum **3**, 215 (2019), doi:10.22331/q-2019-12-16-215.

[550] P. Peng, X. Huang, C. Yin, C. Ramanathan and P. Cappellaro, *Deep reinforcement learning for quantum Hamiltonian engineering*, In *APS March Meeting Abstracts*, vol. 2021, p. P33.001 (2021).

[551] A. W. Senior, R. Evans, J. Jumper, J. Kirkpatrick, L. Sifre, T. Green, C. Qin, A. Žídek, A. W. R. Nelson, A. Bridgland, H. Penedones, S. Petersen *et al.*, *Improved protein structure prediction using potentials from deep learning*, Nature **577**(7792), 706 (2020), doi:10.1038/s41586-019-1923-7.

[552] A. Davies, P. Veličković, L. Buesing, S. Blackwell, D. Zheng, N. Tomašev, R. Tanburn, P. Battaglia, C. Blundell, A. Juhász, M. Lackenby, G. Williamson *et al.*, *Advancing mathematics by guiding human intuition with AI*, Nature **600**(7887), 70 (2021), doi:10.1038/s41586-021-04086-x.

[553] A. Pozas-Kerstjens, N. Gisin and M.-O. Renou, *Proofs of network quantum nonlocality aided by machine learning* (2022), arXiv:2203.16543.

[554] A. Pozas-Kerstjens, G. Muñoz-Gil, E. Piñol, M. Á. García-March, A. Acín, M. Lewenstein and P. R. Grzybowski, *Efficient training of energy-based models via spin-glass control*, Mach. Learn.: Sci. Technol. **2**(2), 025026 (2021), doi:10.1088/2632-2153/abe807.

[555] L. G. Wright, T. Onodera, M. M. Stein, T. Wang, D. T. Schachter, Z. Hu and P. L. McMahon, *Deep physical neural networks trained with backpropagation*, Nature **601**(7894), 549 (2022), doi:10.1038/s41586-021-04223-6.

[556] K. Wagner and D. Psaltis, *Optical neural networks: an introduction by the feature editors*, Appl. Opt. **32**(8), 1261 (1993), doi:10.1364/AO.32.001261.

[557] Y. Zuo, B. Li, Y. Zhao, Y. Jiang, Y.-C. Chen, P. Chen, G.-B. Jo, J. Liu and S. Du, *All-optical neural network with nonlinear activation functions*, Optica **6**(9), 1132 (2019), doi:10.1364/OPTICA.6.001132.

[558] X. Sui, Q. Wu, J. Liu, Q. Chen and G. Gu, *A review of optical neural networks*, IEEE Access **8**, 70773 (2020), doi:10.1109/ACCESS.2020.2987333.

[559] H. Zhang and e. a. Gu, *An optical neural chip for implementing complex-valued neural network*, Nat. Commun. **12**(1), 457 (2021), doi:10.1038/s41467-020-20719-7.

[560] H. e. a. Zhang, *Efficient on-chip training of optical neural networks using genetic algorithm*, ACS Photonics **8**(6), 1662 (2021), doi:10.1021/acsphotonics.1c00035.

[561] X. Xu, M. Tan, B. Corcoran, J. Wu, A. Boes, T. G. Nguyen, S. T. Chu, B. E. Little, D. G. Hicks, R. Morandotti, A. Mitchell and D. J. Moss, *11 TOPS photonic convolutional accelerator for optical neural networks*, Nature **589**(7840), 44 (2021), doi:10.1038/s41586-020-03063-0.

[562] J. Liu, Q. Wu, X. Sui, Q. Chen, G. Gu, L. Wang and S. Li, *Research progress in optical neural networks: theory, applications and developments*, PhotoniX **2**(1), 5 (2021), doi:10.1186/s43074-021-00026-0.

[563] T. Wang, S.-Y. Ma, L. G. Wright, T. Onodera, B. C. Richard and P. L. McMahon, *An optical neural network using less than 1 photon per multiplication*, Nat. Commun. **13**(1), 123 (2022), doi:10.1038/s41467-021-27774-8.

[564] H. Xu, S. Ghosh, M. Matuszewski and T. C. Liew, *Universal self-correcting computing with disordered exciton-polariton neural networks*, Phys. Rev. Appl. **13**, 064074 (2020), doi:10.1103/PhysRevApplied.13.064074.

[565] D. Ballarini, A. Gianfrate, R. Panico, A. Opala, S. Ghosh, L. Dominici, V. Ardizzone, M. De Giorgi, G. Lerario, G. Gigli, T. C. H. Liew, M. Matuszewski *et al.*, *Polaritonic neuromorphic computing outperforms linear classifiers*, Nano Lett. **20**(5), 3506 (2020), doi:10.1021/acs.nanolett.0c00435.

[566] M. Matuszewski, A. Opala, R. Mirek, M. Furman, M. Król, K. Tyszka, T. Liew, D. Ballarini, D. Sanvitto, J. Szczytko and B. Piętka, *Energy-efficient neural network inference with microcavity exciton polaritons*, Phys. Rev. Appl. **16**, 024045 (2021), doi:10.1103/PhysRevApplied.16.024045.

[567] R. Mirek, A. Opala, P. Comaron, M. Furman, M. Król, K. Tyszka, B. Seredyński, D. Ballarini, D. Sanvitto, T. C. H. Liew, W. Pacuski, J. Suffczyński *et al.*, *Neuromorphic binarized polariton networks*, Nano Lett. **21**(9), 3715 (2021), doi:10.1021/acs.nanolett.0c04696.

[568] D. Zvyagintseva, H. Sigurdsson, V. K. Kozin, I. Iorsh, I. A. Shelykh, V. Ulyantsev and O. Kyriienko, *Machine learning of phase transitions in nonlinear polariton lattices*, Commun. Phys. **5**(1), 8 (2022), doi:10.1038/s42005-021-00755-5.

[569] J. J. Hopfield, *Neural networks and physical systems with emergent collective computational abilities*, Proc. Natl. Acad. Sci. U.S.A. **79**(8), 2554 (1982), doi:10.1073/pnas.79.8.2554.

[570] P. Rotondo, M. Marcuzzi, J. P. Garrahan, I. Lesanovsky and M. Müller, *Open quantum generalisation of Hopfield neural networks*, J. Phys. A: Math. Theor. **51**(11), 115301 (2018), doi:10.1088/1751-8121/aaabcb.

[571] K. B. Petersen and M. S. Pedersen, *The matrix cookbook,* Mathematics - Waterloo University, Accessed: 2022-03-04 (2012).

List of Figures

List of Algorithms

Nomenclature

Numbers and arrays

$\boldsymbol{A}$ matrix

A tensor

$\boldsymbol{a}$ vector

A random variable

a scalar

Physical constants and quantities

β $1/k_{\mathrm{B}}T$

δ Kronecker delta

$\langle x \rangle_p$ or $\mathbb{E}[x \mid p]$ Estimator of quantity x with respect to distribution p

$\hat{\sigma}$ Pauli matrix

$\hat{H}$ quantum Hamiltonian

$\mathcal{H}$ Hilbert space

σ spin variable

H classical Hamiltonian

k_{B} Boltzmann constant

m magnetization

s state

Z partition function

Machine learning quantities

$\boldsymbol{b}$ model biases

K_i or K i-th class or number of classes in a classification problem

$\mathcal{D}$ data set

n size of $\mathcal{D}$, i.e., number of training examples

η learning rate

ϕ feature map

m dimensionality of data point $\boldsymbol{x}$, i.e., number of data features

$\hat{f}$ model with converged $\boldsymbol{\theta}$

$\mathcal{L}$ loss (or cost/error) function

$\boldsymbol{H}$ Hessian matrix

d size of $\boldsymbol{\theta}$, i.e., number of model parameters

$\boldsymbol{\theta}$ model parameters or weights

$\boldsymbol{\theta}^*$ converged $\boldsymbol{\theta}$

π policy

π^* optimal policy

ℓ_n L(n) regularization

ς activation function

a action

D_{KL} Kullback-Leibler divergence

G return

r reward

List of acronyms

AD automatic differentiation

AE autoencoder

AI artificial intelligence

ANN artificial neural network

AR autoregressive

ARNN autoregressive neural network

BIC Bayesian information criterion

BO Bayesian optimization

CPU central processing unit

CE cross-entropy

CNN convolutional neural network

∂P differentiable programming

DL deep learning

DNN deep neural network

DQN deep Q-network

ECM episodic and compositional memory

GAMP generalized approximate message passing

GAN generative adversarial network

GNS generative neural sampler

GP Gaussian process

GPR Gaussian process regression

GPU graphics processing unit

IGT Ising gauge theory

KRR kernel ridge regression

KL Kullback-Leibler

L-BFGS limited-memory Broyden–Fletcher–Goldfarb–Shanno algorithm

LASSO least absolute shrinkage and selection operator

LE local ensemble

MAE mean absolute error

MAP maximum a posteriori estimator

MCMC Markov chain Monte Carlo

MDP Markov decision process

ML machine learning

MLE maximum likelihood estimation

MPS matrix product state

MSE mean-squared error

NF normalizing flow

NISQ noisy intermediate-scale quantum

NN neural network

NQS neural quantum state

ODE ordinary differential equation

PC principal component

PCA principal component analysis

PES potential energy surface

POVM positive operator-valued measure

PPT positive under partial transposition

PQC parametrized quantum circuit

PS projective simulation

QAOA quantum approximate optimization algorithms

QD quantum dot

QML quantum machine learning

RBM restricted Boltzmann machine

RKHS reproducing kernel Hilbert space

RL reinforcement learning

RNN recurrent neural network

RUE resampling uncertainty estimation

SGD stochastic gradient descent

SE state evolution

265

SVM support vector machine

t-SNE t-distributed stochastic neighbour embedding

t-VMC time-dependent variational Monte-Carlo

TD temporal-difference

TN tensor network

TNS tensor network state

VAE variational autoencoder

VQE variational quantum eigensolver

Index